Acta Physica Hungarica

VOLUME 75, NUMBERS 1–4, 1994

EDITOR-IN-CHIEF

I. LOVAS

EDITORIAL BOARD

R. GÁSPÁR, I. GYARMATI, I. KOVÁCS, N. KÜRTI
K. NAGY, L. PÁL, P. SZÉPFALUSY, I. TARJÁN
B. TELEGDI, E. TELLER, L. TISZA, E. WIGNER

Akadémiai Kiadó, Budapest

ACTA PHYS. HUNG. APAHAQ 75(1–4) 1–397 (1994) HU ISSN 0231–4428

ACTA PHYSICA HUNGARICA

A JOURNAL OF THE HUNGARIAN ACADEMY OF SCIENCES

EDITED BY

I. LOVAS

Acta Physica publishes original papers on subjects in physics. Papers are accepted in English, French, German and Russian.

Acta Physica is published in two volumes per year (4 issues each) by

AKADÉMIAI KIADÓ
Publishing House of the Hungarian Academy of Sciences
H–1117 Budapest, Prielle Kornélia u. 19–35.

Subscription information

Orders should be addressed to

AKADÉMIAI KIADÓ
H–1519 Budapest, P.O. Box 245

Subscription price for Volume 75 (1994) in 4 issues US$ 88, including normal postage, airmail delivery US$ 20.00.

Acta Physica Hungarica is abstracted/indexed in Chemical Abstracts, Mathematical Reviews, Science Abstracts, Physics Briefs, Risk Abstracts, Engineering Information, Inc. EI Page One Database.

© Akadémiai Kiadó, Budapest 1994

CONTENTS

CONDENSED MATTER

CROSS-DISCIPLINARY PHYSICS

ASTROPHYSICS

EDITORIAL

In the realm of the international scientific journals two strong tendencies can be observed. On the one hand, most of the traditional "grand" journals were split up and the papers are grouped into specialised volumes A, B, C, etc. On the other hand, more and more journals are devoted ab ovo to well-defined specific subjects.

Looking at the list of the international journals of physics it is noted that no journal is devoted to heavy ion physics in spite of the fact that this branch of physics has been developing very spectacularly at least for two decades and we have well-established reasons to believe that this development will be continued in the future as well. The recently completed accelerators and those which are under construction provide a proof for this belief. The activity both in the theory and in the applications is also developing steadily. Considering these circumstances we decided to publish an international journal on "Heavy Ion Physics". To this endeavour we would like to have the support of the European Physical Society and the interest of the Heavy Ion Physics Community.

To produce a good journal four ingredients are needed:

- a reliable Publisher,
- a highly qualified international Editorial Board,
- excellent papers and
- interested readers.

The last condition is the most important and the most difficult to meet. To attract interested readers and excellent authors we invite the most outstanding representatives of the heavy ion physics community from all over the world into the Editorial Board. Until now we asked a number of excellent scientists and the answers are very positive.

The financial support is granted by the Publishing House of the Hungarian Academy of Sciences. The "Heavy Ion Physics" will be a new journal, nevertheless in some sense it will be an old one since it will be published as the continuation of Acta Physica Hungarica.

More precisely the title will be the following:

HEAVY ION PHYSICS
ACTA PHYSICA HUNGARICA NEW SERIES

Acta Physica Hungarica was founded after World War II. It is reviewed by all of the major reference journals. Its volumes are on the first shelf of a great number of libraries of the physical institutes. We hope that the number of subscribers will increase due to the proposed transformation.

We will ask the Publishing Committee of the EPS to put "Heavy Ion Physics" on the list of the journals "Recognised by the European Physical Society".

In 1995 we will start this "new-old" journal.

Budapest, December 1994

István Lovas
Editor-in-Chief

INTERNATIONAL WORKSHOP ON NEUTRON RESEARCH AND APPLICATIONS

organized by

the Budapest Neutron Centre (BNC)
the Roland Eötvös Physical Society (REPS)
and
the West-East Neutron Network (WENNET)

Budapest, Hungary, 24-26 March 1994

Honorary Chairman: E. TELLER (Stanford)

International Advisory Board:
F. MEZEI, President (HMI Berlin, BNC Budapest)
N. KROÓ (KFKI-RISP Budapest)
F. MENZINGER (University of Rome)
J. JASTRZEBSKI (University of Warsaw)
O. BALASCHKO (University of Vienna)
F. De CORTE (University of Gent)
H. G. BÖRNER (ILL Grenoble)
G. PÉPY (LLB Saclay)
A. RUMYANTSEV (Kurchatov Institute Moscow)
K. SCHRECKENBACH (TU Munich)
R. M. LINDSTROM (NIST Gaithersburg)
R. ZEISLER (IAEA Vienna)

Local Organizing Committee:
L. CSER, Chair (KFKI-RISP)
L. KŐSZEGI, Secretary (KFKI-RISP)
T. BELGYA (Institute of Isotopes)
Zs. KAJCSOS (KFKI-RIPNP)
G. MOLNÁR (Institute of Isotopes)
L. ROSTA (KFKI-RISP)
A. SIMONITS (KFKI-AEKI)
I. VIDOVSZKY (KFKI-AEKI)

Sponsored by

Atomic Energy Research Institute (KFKI-AEKI)
Canberra Electronic E. U. GmbH
Central Research Institute for Physics (KFKI) Innovation Co.
EG&G Berthold
Hungarian Academy of Sciences (MTA)
Institute of Isotopes (MTA-IKI)
KFKI-MSZKI Laboratory Automation Department
Merion E. P. Ltd. & OXFORD Nuclear Measurement Group
National Committee for Technological Development (OMFB) PHARE-ACCORD
National Fund Scientific Research (OTKA)
OMFB Mecenatura Program
Paks Nuclear Power Plant

Exhibitions

Canberra Eectronic E. U. GmbH.
EG&G Berthold
KFKI-MSZKI Laboratory Automation Department
Merion E. P. Ltd. & OXFORD Nuclear Measurement Group
Paks Nuclear Power Plant

Acta Physica Hungarica 75 (1–4), pp. 9–12 (1994)

INVITED TALKS AND ORAL CONTRIBUTIONS

NEUTRONS IN THE PAST AND THE FUTURE

EDWARD TELLER

Hoover Institution on War, Revolution and Peace
Stanford, USA

I should like to discuss some stories about neutrons which are not common knowledge.

In 1932, a couple of years after I received my doctorate degree, I was working in Göttingen with George Placzek on the Raman effect connected with the rotation of molecules. Placzek wanted to spend the spring recess in Rome and persuaded me to join him. Enrico Fermi, whom I had never met, wrote a remarkable (though rather untruthful) letter calling me a great physicist whose presence in Rome was absolutely necessary. It was accompanied by another note saying, "Dear Teller: Please excuse the overly formal nature of the accompanying letter,.but I thought that that way it would be more effective. At any rate, we should indeed love to see you here." That was my introduction to a man who was great, wonderful and moreover, friendly.

The letter had its effect in that the Hungarian government gave me room for a few weeks in the Palazzo Falconieri, housing Hungarian students, mostly painters. The Palazzo was on the Tiber. I had a room in the attic containing a bed, a table and a chair. It was at a time of my life when I slept well and long, but made up for it the rest of the day. I must confess that I often slept until mid-day and my alarm clock was a cannon on the other side of the Tiber which was fired at 12 noon.

My work and my acquaintances with Fermi were fruitful and pleasant, but not connected with neutrons. I was aware of the fact that Fermi had undergone a terrific change from a brilliant theorist to a Nobel Prize winning experimentalist. He and his associates started to work on the recently discovered neutrons and were playing with many peculiarities that were, at that time, surprising and new.

Why were neutrons activating materials much more readily when the apparatus happened to be resting on a wooden table? Why, of course! The neutrons were slowed down due to collisions with protons in the wood from original speeds not much less than 1/10th light velocity to mere thermal motions in the range of a kilometer a second. The proton–neutron cross section seemed huge. That was, in turn, due to a resonance, a virtual neutron–proton state at approximately 200 keV. If that was not enough, one further had to take into account the difference in neutron–proton scattering for somewhat higher energy neutrons when the binding of the protons to the chemical surrounding could be neglected and for lower energy neutrons when the binding of the protons had to be taken into account. These were the early discoveries of Fermi.

The absorption of neutrons led to new radioactive isotopes which were produced when neutrons were allowed to bombard every element in the periodic table. In the end, Fermi and his friends bombarded uranium and obtained incomparably more radioactive isotopes than in the bombardment of any other element. Why, of course. These had to be the transuranics and for these Fermi received the Nobel prize. The only hitch was that most of them were not transuranics at all, but fission products.

The story of fission is full of contradictions and tempts me in an irresistible manner to make comments that at best are half justified.

Some years before Fermi's experiment, Dr. and Dr. Noddack (husband and wife) discovered elements 43 and 75 which, in memory of early German victories over the Russians in 1914, they called masurium and rhenium. Of these, rhenium element 75 can be found in the periodic table. Masurium turned out to be a mistake. Element 43 can be now found with the symbol Tc for technetium discovered by Fermi's student, Emilio Segrè. In the early 1930s, Mrs. Noddack was still very much alive though her husband had died. Reading about Fermi's discoveries, she wrote Fermi and suggested that what he had found in bombarding uranium were elements produced in the fission of uranium. Fermi took this suggestion entirely seriously, but reacted to it not as a new-born experimenter but as a true theorist. He calculated whether Mrs. Noddack's suggestion was possible, and he managed completely to disprove it.

What he actually did was to realize that for uranium to break apart, it has to start to deform which would take more energy than the absorbed neutron could deliver. That in itself need not stop the process because, of course, in quantum mechanics, the system could penetrate through the Gamow barrier of this excess energy. Fermi calculated the probability of such penetration and found it absurdly small which ruled out fission.

It so happened that Fermi's calculation was beautiful, imaginative and correct. However, it was based on nuclear masses measured by Aston and the binding energies derived from these measurements. Penetration through a Gamow barrier for relatively heavy masses depends sensitively on the energy. Aston's measurements happened to be somewhat mistaken, sufficiently so to lead to an exclusion of fission, of course, not in reality but in Fermi's mind.

This was not the only time that Fermi almost discovered fission. I am tempted to say that the phenomenon of fission was flirting with Fermi and on one more occasion, barely escaped being caught. Fermi theorized that the absorption of neutrons should also cause the emission of alpha particles with an excess of energy. In trying to discover these relatively rare events, Fermi bombarded uranium with neutrons. In these experiments, he should have seen the fission products that carried great amounts of energy. But in looking for the longer range alpha particles, Fermi did not want to be bothered by the normal alpha particles of shorter range. Therefore, he covered his uranium samples with a thin foil sufficient to stop the normal alpha particles. Unfortunately, that foil was just about thick enough to stop the fission products as well. So, Fermi again missed the discovery of fission.

Perhaps this circumstance was most fortunate. We now fully realize that from

fission to nuclear explosives, only a short step was needed. Had Fermi discovered fission in the mid-30s, the American response in the military field would hardly have been forthcoming. It is much more probable that the first atomic bombs would have been produced in the Soviet Union or perhaps in Nazi Germany.

As it happened, fission was discovered in the Kaiser-Wilhelm Institute by Hahn and Strassman. The fission products were seen in an ionization counter by Frisch and Meitner, and the news was brought to the United States in January 1939 by Niels Bohr. By that time, Leo Szilard was fully prepared to understand the consequences of this discovery, and he managed to bring the importance of the new possibilities to the attention of President Roosevelt. At the same time, efforts were started in Nazi Germany and the Soviet Union. In the former case, the effort failed (in my opinion) due to the Nazis' lack of interest in science and Heisenberg's (who was the leader of the project) strong feelings against the Nazis. In the Soviet Union, Kurchatov made great progress that led to a Soviet atomic bomb only a short four years after the end of the Second World War. Had Fermi discovered fission in 1935, it is possible that today those of us who survived would speak Russian.

After injecting some potential uncertainties into the story of the past, I would now like to add one of my experiences with the use of nuclear energy together with a closely-related outlook on the not-so-uncertain future.

Technetium discovered with the help of neutron bombardment by Segrè has found its important diagnostic use by which I personally benefited. In 1984, I had open-heart surgery, and a few years later on a visit to Washington, I was dragged by one of the younger men who participated in that operation to Georgetown University in order to check on my heart. That was done by injecting a non-negligible amount of technetium into my blood and then placing counters pointing to my heart to find out how many decay processes of technetium occurred in my heart as it expanded and contracted. I passed the test not quite with flying colors. After all that was done, I went out for lunch with Jay Keyworth, the President's Science Advisor.

No sooner did we sit down, here came the guard running, "Which one of you gentlemen carried in some radioactivity?" Fortunately, I had told Jay about my experience so he raised his eyebrows and said to the guard, "Don't you know, this is the radioactive Dr. Teller!"

I am telling you this story because it is one of the instances of the useful medical applications of radioactivity which is being slowed down by exaggerated fears of such activity. But I want to continue and conclude telling you of the probable way how similar experiments will be carried out in the future. The suggestion I am going to discuss is due to my friend, Lowell Wood, and this suggestion has been followed up by his wife, Muriel Ishikawa.

Instead of technetium that emits one gamma ray, one should use an appropriate isotope of some element that emits at least two gamma rays in extremely rapid sequence so that they are practically simultaneous. From the intersection of the two lines of observation, one would then get a quite precise location of the emitter. All one would have to do is to administer the relevant non-radioactive isotope, irradiate by slow neutrons and look for the double event. This would result in less irradiation and much more information. Indeed, the presence or absence of

appropriate chemicals containing the isotope in question could give us a wealth of information about normal and abnormal tissues.

The great changes due to the development and application of nuclear energy have produced widespread fears. Application of neutrons in biology and solid state physics could proceed much faster if we were not hampered by the fear of anything nuclear. I believe that a hundred years from now, the fear of neutrons will have disappeared the same way as the fear of witches. Our visitors in Hungary may not know that the Hungarians were practically never afraid of witches since in the year 1100 when Könyves Kálmán (Bookish Kálmán) issued his important edict, "De strigis, quidem, quae non sunt, Nulla questio fiat." Please do not misunderstand me. Neutrons do exist, but when used with a little care, they are as harmless as the non-existent witches.

Acta Physica Hungarica 75 (1–4), pp. 13–24 (1994)

BUDAPEST NEUTRON CENTRE USER FACILITIES AT THE MODERNIZED RESEARCH REACTOR

L. ROSTA

KFKI Research Institute for Solid State Physics
P.O.B. 49, 1525 Budapest, Hungary

The Budapest Research Reactor (BRR) was recently restarted after a major upgrading and operates at 10 megawatt nominal power from November 1993. The reactor built in 1958, has been fully reconstructed and upgraded according to modern scientific, technological and safety requirements. This unique important neutron source in Central Europe serves various purposes, such as basic and applied research in physics, chemistry, biology, materials science, as well as commercial utilization. It is also meant for an educational centre. An instrumentation project, supported by national funding agencies, allowed to install a basic set of experimental stations. Considerable effort is being made to install a liquid hydrogen cold neutron source to widen the beam line research capacity. From 1994 the following experimental stations will be available on neutron beams and guides: a two-axis powder diffractometer, a dynamic neutron/gamma radiography station, a small angle neutron scattering device, a three axis spectrometer and a prompt gamma activation analysis spectrometer, as well as a fast-rabbit irradiation tube system with adjoining activation analysis equipment and hot atom chemistry laboratory.

The Budapest Research Reactor

History. The nuclear research rector at the Central Research Institute for Physics (KFKI), Budapest was first started as a Soviet construction, in 1959. A first upgrading from 2 to 4.5 MW was carried out in 1967. In 1986 the reactor was stopped for a complete reconstruction. During the 27 years of exploitation no incident occurred, an extremely hard discipline and careful regime of operation was kept. In this period the research reactor played an essential role in establishing neutron-based research and technology in Hungary. It served as a basic facility for neutron scattering in condensed matter, nuclear physics, radio chemistry and radiation protection investigations, for establishing nuclear medical applications providing radioisotopes, and for starting a nuclear energetics programme through reactor operation and safety studies. It was an important center of university, postgraduate and professional training. Many fruitful, international co-operations were established and the reactor laboratories served as home bases for activity at international organisations like IAEA and JINR Dubna.

In 1983 the government made a decision to reconstruct and upgrade the reactor considering new trends in nuclear research and applications, as well as following modern reactor safety requirements. The upgrading programme prepared the reactor for multipurpose utilisation according to the main objectives: basic and applied

research with neutron beams as well as by means of complex irradiation; technological and commercial applications; education and training. The definition of the reactor parameters and the instrumentation programme was co-ordinated by a user committee, headed by N. Kroó. The neutron scattering project — the main research field — was led by F. Mezei [1].

Upgrading. The full scale reconstruction and upgrading was designed and implemented essentially by Hungarian companies. The modernisation aimed at the following tasks: the substitution of the corroded components; the enhancement of reactor safety; the increase of reactor power. As a result, most of the technological elements (core, tank, cooling circuits, ventilation, electronic control, etc.) were replaced and the complete infrastructure renewed. The reactor safety has been enhanced according to the relevant recommendations of IAEA. The actual core with VVR-SM fuel elements (stored for several years of operation) may provide an average power of 10 MW. The new cooling capacity will allow a further increase of the power up to 20 MW, this will, however, require a new type of fuel element [2].

Recommissioning. The reconstruction was technically finished in 1990, the recommissioning, however, took quite a long time. Because of the reorganisation of the KFKI and the need for a very careful investigation of the scientific community's opinion as well as the complex procedure for the public acceptance, the KFKI-Atomic Energy Research Institute, as a legally independent establishment, responsible for the reactor operation, applied for licensing only in 1992. The reactor became critical the 12 December 1992. The licensing and testing took nearly one year, the regular operation was started the 15th November 1993. The recommissioning was favoured by the following circumstances: evaluations and positive recommendations by different bodies of the Academy; user meetings, demonstrating considerable interest in this "new" facility; an important grant for instrumentation improvement by the National Fund for Scientific Research (OTKA); the programme of internationalisation in the framework of the Central European Initiative (CEI), namely BRR was opened to the international user community [3]; positive balance of the public opinion, i.e. a harmonic dialog with the local authorities and population and openness to the public (e.g. the reactor is open to visitors — as in the past — on the last Friday of every month).

Reactor specifications. BRR is a light water moderated and cooled, tank type nuclear reactor [2]. Its central object, the heavy concrete reactor block surrounding the core, is situated in a hall which represents a semi-hermetically sealed, individually ventilated, rectangular structure with approximately 600 m^2 area. The top of the reactor can be reached by means of a bridge on the second floor, which is the level of the control room situated in the attached building. The first level of the reactor hall allows access to the experimental facilities at the horizontal beam tubes, while the primary pump room and the hot cells can be found in the basement. Fig. 1 shows a schematic vertical cut of the reactor block.

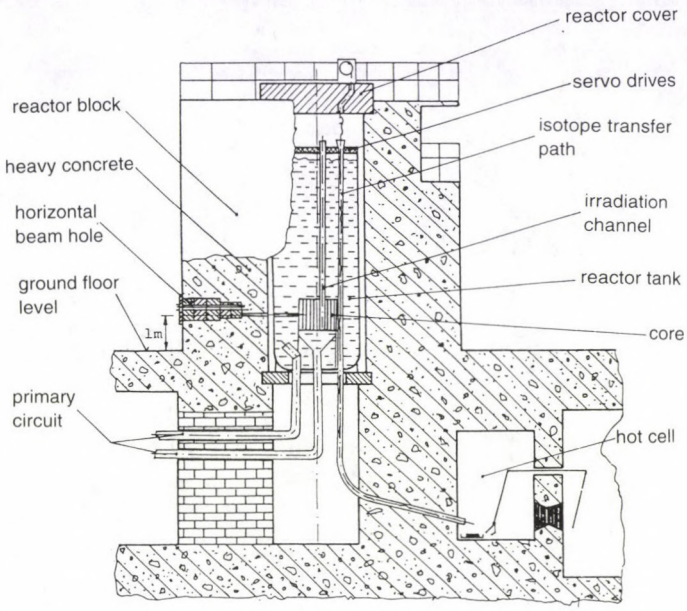

Fig. 1. Schematic view of the vertical section of the reactor block

The cylindrical reactor tank is made of aluminum alloy (R-AlMg 2,5). Its diameter is 2300 mm, with the height of 5685 mm. The base of the reactor core is a hexagonal grid plate with 397 identically formed holes. Into these holes can be placed the fuel elements, the beryllium and aluminum elements, and the guide tubes of the absorber rods.

The standard VVR-SM type fuel is an Al-UAl_4 alloy with 36 % enrichment, aluminum cladding. The average U235 content is 39 g/fuel. The fuel elements are of hexagonal shape, the active length of a fuel is 600 mm. The equilibrium core contains 223 fuel elements.

There are 3 safety, 14 shim and 1 automatic rods which can be positioned by means of ropes, driven by servo motors. All the absorber rods are of boron-carbide, except the stainless steel automatic control rod. Depending on their depth of insertion they absorb a certain amount of neutrons — the simple way to suppress (or increase) the chain reaction. To improve the neutron economy, the core is surrounded by beryllium in order to reflect neutrons escaping from the core back to the fission process.

The water volume of the reactor pool serves for radiation shielding, core cooling and moderation or slowing down the fast neutrons. To cool the fuel elements a continuous flow of water passes through the core raising the water temperature from 50 °C to 60 °C. The outlet water is pumped through heat exchangers. The

heat released by the primary system is transferred from the heat exchangers to the Heller–Forgó type cooling towers. The secondary cooling circuit is also a closed loop and it has higher pressure than the primary one.

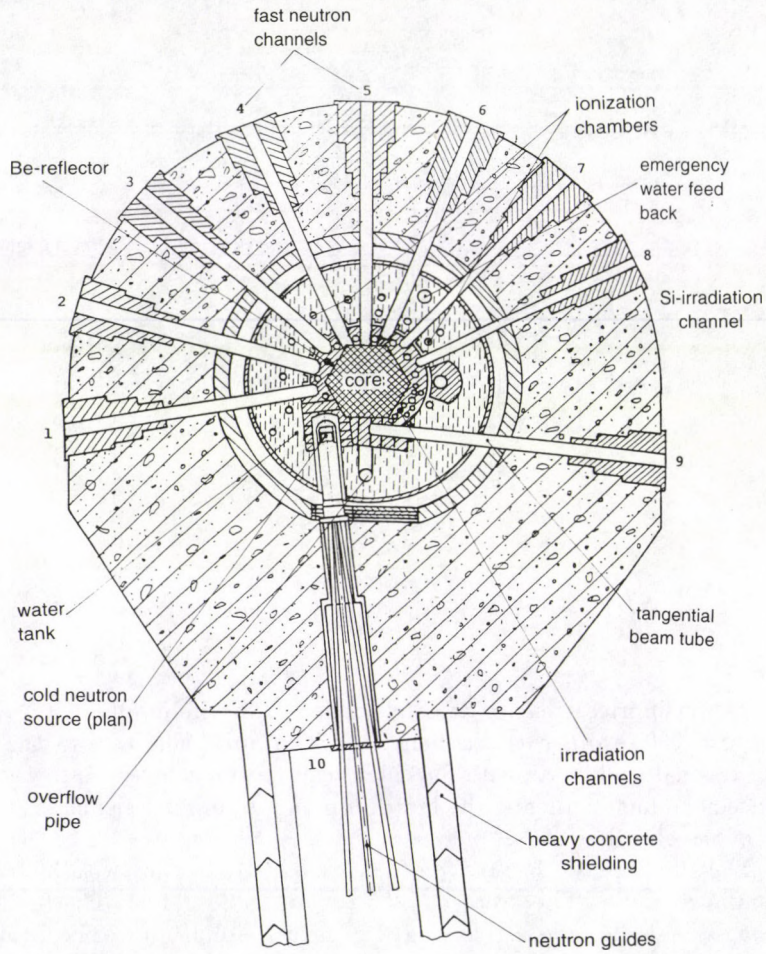

Fig. 2. Horizontal section of the reactor block at 1 m level with the neutron beam tube arrangement

The utilisation of the reactor is provided by means of different irradiation holes and beam tubes with the adjoining auxiliary equipment. A detailed map of the reactor is shown in Fig. 2. 51 vertical irradiation channels with various geometrical and spectral parameters are available in the reactor core and vessel. For the neutron beam measurements different types of horizontal channels have been implemented. Besides the six radial thermal and two fast (looking directly at the core) neutron channels, a new tangential beam tube has been installed. The former

Table I
Main parameters of the VVR-SM Budapest Research Reactor

Power	10 MWatt
Peak Thermal Neutron Flux	
Flux trap	$1.6 \cdot 10^{14}$ n/s cm^2
Reflector	$1.2 \cdot 10^{14}$ n/s cm^2
Peak Fast Neutron Flux	$1 \cdot 10^{14}$ n/s cm^2
Core:	
Radius	1 m
Height	0.6 m
Loading	220 fuel element (equilibrium)
Life	40 days
Moderator/coolant	H_2O (H/U=2.35)
Fuel Elements:	
Type	VVR
Enrichment	36 % ^{235}U
Shielding:	
Thermal	Water–heavy concrete
Biological	concrete
Neutron Ports Beam tubes:	
Radial	8
Tangential	2
Vertical	6
Neutron guides	3 (thermal neutrons)
Cryogenic Facility	H_2 cold source (under construction)
Vertical Thimbles:	
In-core	16
In reflector	19
Rabbit tubes:	
Near-core	1
In reflector	1 (under construction)

thermal column hole is used to take off neutrons tangentially for the neutron guide system and later to install a liquid hydrogen cold neutron source. The horizontal channels are equipped with shutters and proper physical and biological shields. The neutron guide system [4] consists of three glass-mirror guide tubes. The 1.65 m in-pile section is coated with ^{58}Ni while the outer section, which continues into the guide hall, has natural Ni coating. The first tube is straight, the second is curved, and the curved third guide is to be installed. A new 15 x 27 m guide hall extends from the reactor hall, housing the guide instruments.

The reactor cycle is about 40 effective days (for the equilibrium core) which is followed by a reshuffling period of one week. The operation regime is the following: from Mondays 5 or 11 days of continuous operation, as a total $\sim$ 3600 hours per year. The reactor at KFKI has had a good reputation to keep very tight the exploitation schedule. According to different kinds of experimental requirements, however, the timetable can be planned (or modified) in a flexible manner. The reactor staff is well experienced in assisting physical experiments and radioisotope production.The principal reactor characteristics are summarized in Table I.

Neutron research and applications

The Budapest Research Reactor is a unique neutron source in Central Europe. It will provide attractive possibilities in many fields of basic and applied research, in particular when equipped with a cold neutron source. The utilization of the reactor for basic and applied research is considered by the following means [5]:

1. Neutrons produced in the reactor core with an important flux can be guided to the measuring instruments for investigation of elastic and inelastic scattering phenomena, i.e. neutrons can probe in condensed matter structural properties in the 0.01–1000 Å size range and particle interaction behaviours in the 10^{-9}–1 eV energy range.

2. Investigations related to nuclear reactions based on neutron capture (fundamental physical problems, nuclear astrophysics, activation analysis, etc.).

3. The reactor provides experimental basis — as complex irradiation source (neutrons, alpha, beta, and gamma rays) — for materials testing, hot atom chemistry, irradiation damage, biological irradiation, dosimetrical, nuclear safety investigations.

The research activity at BNC is classified into the following areas:

Nuclear and fundamental physics. Polarized and unpolarized neutron-induced nuclear reactions, namely radiative neutron capture, can be utilized in the studies of problems related to nuclear and fundamental physics, nuclear astrophysics and in the development on unique analytical methods [6].

The nuclear physics programme is mainly based on the study of radiative neutron capture. The high neutron flux and extremely low background expected at the end of neutron guide No.1 will provide unique possibilities for gamma-spectroscopic studies of nuclei. Special emphasis is made on measurements of nuclear level lifetimes using novel fast $\gamma_n\gamma\gamma(t)$ coincidence and Doppler-shift timing techniques. The (n,γ) station and the Compton-suppression/pair spectrometer will alternatively be used for neutron-capture prompt-gamma activation analysis (PGAA).

For nuclear astrophysics, to investigate stellar nucleo-synthesis, neutron-capture cross-section measurements in the energy range relevant for the astrophysical s-process are planned using a filtered beam device, to be constructed at one of the radial fast neutron beam ports. The study of fundamental problems — such as time reversal and parity violation in polarized neutron capture, or a measurement of the neutron lifetime — is another field of interest. It will be exploited as soon as a polarized neutron guide becomes available. Activities in nuclear solid state physics and chemistry are also envisaged (e.g. super source-based Mössbauer spectroscopy).

Neutron scattering in condensed matter. The main research activity at the upgraded reactor is the neutron scattering for condensed matter and materials science investigations. Thermal neutrons have proved to be a very useful tool for investigation of condensed matters, since they have energy in the range of the kinetic energy of atoms, molecules and particle aggregates, and wavelengths comparable with the atomic distances. These are the basic conditions to obtain maximum information on positions as well as motions and interactions of structural units in condensed

matters such as solids, liquids, gases, chemical, biological and technological systems. Some examples describing the scope of interest in condensed matter research at BNC are given below [7]:

– Studies on the short and medium range order of amorphous semiconductors and alloys (the isotope sensitive scattering factor is used to investigate the structure factors). Refinement of structural models.

– Investigations of any kind of inhomogeneities (segregation, aggregation, precipitation, spinodal decomposition, etc.) in various (from alloys to biological) systems.

– Combined — structural and dynamic — investigations of molecular fluids with anisotropic features (e.g. liquid crystals, ferrofluids).

– Determination of oxygen sites, magnetic and phonon structure in high temperature superconductors.

Materials science. The growing interest for industrial applications calls for a special programme. The high penetrability of neutrons into materials is the key property in many industrial applications of neutron-based methods. In contrast to many alternative techniques (e.g. X-rays), neutron probes are not affected by the properties of surface layers. Consequently, samples (even complex objects in an "unfinished" stage) or confined objects can be investigated routinely and in-situ.

The main interest is to study segregation processes, e.g. determining inhomogeneities as well as identify preferred orientation of crystallites by texture analysis or carrying out internal stress analysis by high resolution lattice parameter measurements. A few examples we have gained experience for [1,8] are listed below: Texture analysis of ball bearing and carbon fibers; aging calibration of turbine blades by small angle scattering, diffraction and radiography; internal strain analysis of stretched alloys; optimization of pipelines, compressor elements, etc. by neutron radiography.

Activation analysis. Classic (n, γ) reactor-neutron activation analysis (NAA) is still preserving its role as a "workhorse" for the vast amount of analytical work. Combined with computerized high resolution gamma-ray spectroscopy, NAA offers mostly non-destructive, multi-element routine analysis needed in such areas as environmental control, geology, medicine and technological processes. For about 75 elements less than 0.01 pg can be determined.

Simplification of the standardization procedure is of paramount importance in routine activation analysis. A new method using compound nuclear constants (i.e. so called k_0-factors determined experimentally with high accuracy) was developed to eliminate standard preparation and errors originating from published nuclear data [9].

Prompt-gamma neutron activation analysis replaces conventional activation analysis when no suitable radioactive daughter products are available, e. g. light elements (H, C, Si, P, S,) as well as toxic trace elements (Hg, Cd, etc.). Using clean, guided cold neutron beams to increase capture cross-sections, this method will be fully developed and exploited through implementation of the k_0-method.

Practical applications. The production of radioisotopes for medical diagnostics and therapy as well as for industrial purposes is one of the main fields of applications at BRR. The production will be focused on ^{125}I in a special loop (under construction) providing irradiation possibility of $\sim$ 180 Gbq per week. In smaller quantities ^{51}Cr, ^{65}Zn, ^{141}Ce, ^{170}Tm, ^{82}Br, ^{203}Hg are also foreseen to be produced. For industrial purposes ^{192}Ir and ^{60}Co may also be produced, it will, however, require a modified reactor operation schedule for long irradiation times.

Silicon doping for the semiconductor industry will become an important application. For the uniform transmutation an irradiation channel in the Be-reflector will be installed with a thermal neutron flux of $\sim 10^{13}$ ncm^{-2}s^{-1}. The maximum size of an ingot to be treated is of 500 mm length and 4 inch diameter.

Pressure vessel surveillance for nuclear power plants is an important task. The high flux of the research reactor enables to study in a short time the neutron induced embrittlement of NPPs components for many years in advance [2].

Instrumentation

The Budapest Neutron Centre offers experimental possibilities by means of the following instruments (a layout of the reactor and the neutron guide halls with the horizontal beam devices is shown in Fig. 3):

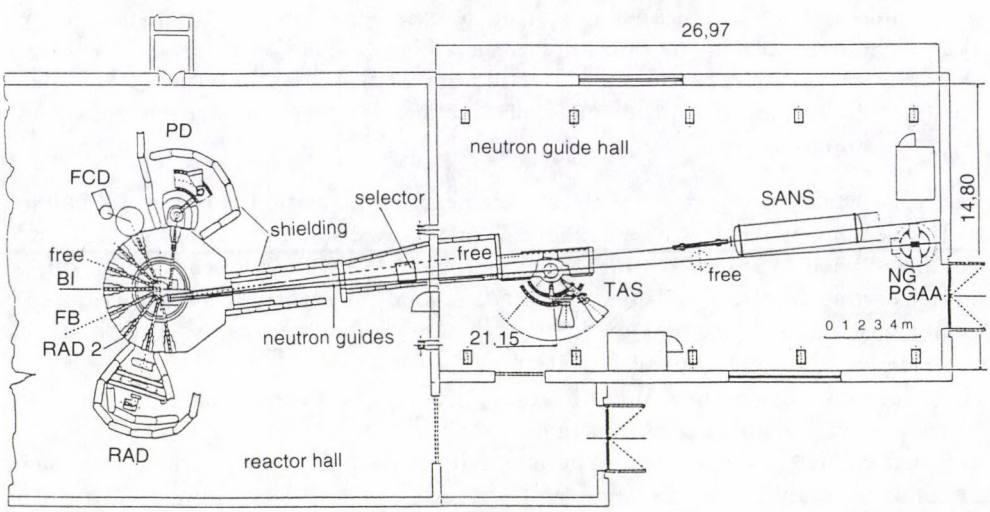

Fig. 3. Layout of horizontal experimental channels and equipment in the Reactor and Neutron Guide Halls of the Budapest Researh Reactor. RAD – neutron-gamma radiography, FB – filtered beam (planned), BI – biological irradiation channel (planned), PD – powder diffractometer, TAS – triple-axis spectrometer, NG – n-capture gamma-ray spectroscopy, PGAA – prompt-gamma activation analysis, SANS – small-angle scattering spectrometer, FCD – four-circle diffractometer (under construction), RAD2 – radiography (planned)

1. Two-axis powder diffractometer. It is located on the new tangential beam port (No. 9). Plane or focusing, Cu or Zn monochromators, 10–30 minutes thin film collimators are used. The wavelength can be varied step by step by rearranging fix positions of the monochromator shielding. A detector bank is assembled of 5 position sensitive ^{3}He-counters with 620 mm length and 25 mm diameter each. The PSD system covers a range of 28°, while moving the detector arm the scattering angle can be extended up to 150°. The diffractometer is controlled by a PC equipped by a multichannel analyser card for the detector electronics [10]. In Fig. 4 Ni-powder calibration spectra clearly demonstrate the advantage of using PSD.

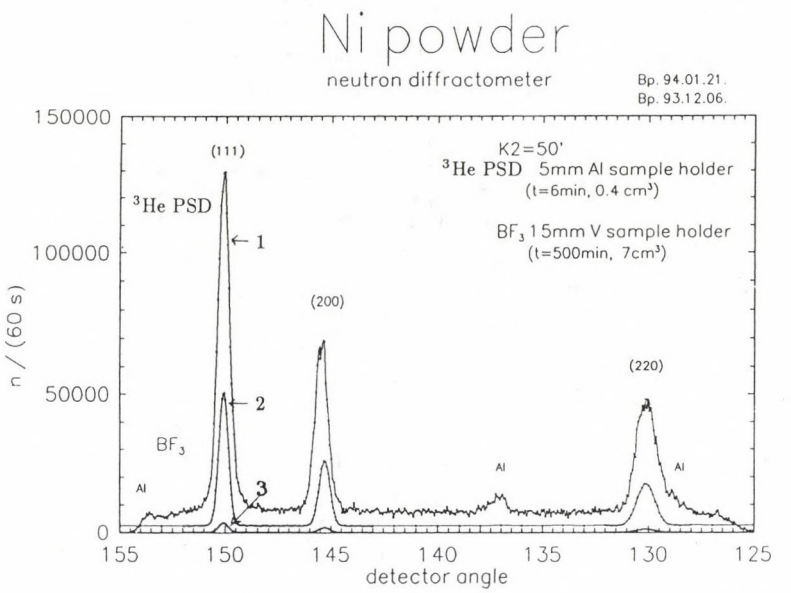

Fig. 4. Comparison of detection efficiency of ^{3}He PSD and that of BF_3 single detector. 1. spectrum: ^{3}He PSD, 2. spectrum: BF_3 scaled to 1. spectrum for equal time, 3. spectrum: BF_3 scaled to 1. spectrum for equal time and equal sample amount. $I(^3\text{He PSD})/I(BF_3) = 40, \Rightarrow$ small amount of samples can be measured: 0.1 g–2 g

2. Neutron and gamma radiography. The horizontal thermal neutron channel No.2 is used for dynamic radiography. The reactor acts as an effective simultaneous neutron and gamma source. Movements or processes of confined objects can be recorded by this equipment consisting of the following main elements: collimator for 150 mm beam diameter, fluorescent converters, high sensitivity TV camera, video-tape recorder (S-VHS), data processing electronics (e.g. image digitizer). XY-scanning in the beam of objects with mass up to 300 kg can be provided, external parameters (temperature, flow velocity, etc.) can also be simultaneously recorded [10,11].

3. Three-axis spectrometer. It is installed in the guide hall at the 21 m position of the neutron guide No.1. The monochromatic beam is provided by a focusing assembly of pyrolytic graphite blades. The wavelength is continuously variable due to the chain type monochromator shielding. The components in the beam path are as follows from the monochromator: shutter, fission chamber monitor, multidisc velocity selector for harmonic filtering, sample environment (cryostat, magnet, etc.), PG-analyser, ^{3}He-counter. Thin film collimators are used throughout. The neutron specifications are given in [10].

4. Small-angle scattering spectrometer. This conventional type SANS device occupies the curved ($R \sim 2000$ m) neutron guide No. 2. The beam path is as follows: multidisc velocity selector with adjustable wavelength and resolution; guide section and pin-hole collimator; chopper for TOF analysis; sample environment (e.g. automatic exchanger); 64×64 cm^2 BF_3 co-ordinate detector in a flight path chamber with motorized displacement (5 m); PC-control and initial data treatment (see details in [10]).

5. Nuclear instruments. A twin station for (n, γ) spectroscopy and prompt gamma activation analysis is under construction at the end of guide No.1, which has from the TAS a 17 m curved section made of borosilicate glass. Both narrow and wide beam collimation may accommodate various sample requirements for simultaneous nuclear physics and PGAA measurements. A Compton suppression γ-ray spectrometer serves as the main detector consisting of a BGO shield (split into 8 parts) and a HPGe detector. Various Ge and BaF scintillator detectors for $\gamma - \gamma$ coincidence, angular correlation and timing measurements complete the device [6].

6. In-pile irradiation. A fast rabbit tube system is used for irradiation at a near-core position neutron activation analysis which — combined with computerized high resolution γ-ray spectroscopy — offers non-destructive, multi-element analysis for about 75 elements with less than 0.01 pg accuracy. Also a laboratory for hot atom chemistry investigations has been equipped.

Instrumentation under development and future plans. The most important extension of BRR facilities is the construction of a cold neutron source (CNS). The moderator cell filled with ~ 450 cm^3 of liquid hydrogen will be placed at the Be-reflector site of the horizontal tangential channel No.10. The direct cooling and condensation of hydrogen in the moderator cell by cold helium gas provides a novel technical solution with enhanced cold neutron output as well as improved safety characteristics [12]. An optimized supermirror neutron guide system bunching 3 beam lines is foreseen. It is hoped that the CNS will be operational in 1996–97.

The following instruments are under way of installation, or construction will soon start (equipment funded): – Four-circle diffractometer at thermal beam port No.8 for single crystal, texture and strain analysis; – A second radiography station at channel No.3; – A filtered beam facility will be constructed using the radial beam channel No.4, looking directly at the core, where scandium and iron filters will be installed externally to provide monochromatic neutrons with energies 2 and 24 keV, respectively. The cross-section will be measured using the activation method. – The fast neutron beam port No.5 will be used to install a biological irradiation station.

A few beam line positions are free (see Fig. 3), and it is considered that the number of instruments at BNC can be increased up to 13–15.

Infrastructure. Most of the laboratories and offices are connected to an area computer network and all experimental stations may be linked to UNIX workstations. For sample conditioning He and Ni cryostats, a closed cycle refrigerator, furnaces, magnets, etc. are available. A small mechanical workshop and chemical laboratory may serve for sample preparation.

Organization

Establishment and location. The KFKI Atomic Energy Research Institute, the KFKI Research Institute for Solid State Physics and the Institute of Isotopes have signed an agreement to establish a Scientific Centre for research reactor users. This assembly of the neutron-based laboratories has been named Budapest Neutron Centre (BNC). The KFKI Atomic Energy Research Institute is in charge of the operation of the reactor, and the management of BNC (via the Directors' Board). An International Scientific Advisory Committee, led by F. Mezei (HMI Berlin), was formed to co-ordinate research activities. BRR is located at KFKI — the largest science and innovation park in Hungary — in a pleasant mountain forest about 10 km distance from the centre of Budapest, easily accessible by city transportation. With its nearly 2500 staff, infrastructure, and a broad spectrum of activities, KFKI provides an ideal basis for BNC [13].

BNC services. 1) Provision of a neutron beam together with technical support, as agreed upon on a case by case basis, to research groups who wish to operate their own instruments. 2) Provision of neutron beams and BNC neutron scattering facilities, together with technical help, for long-term research projects of external groups. 3) Provision of a neutron beam, an appropriate scattering instrument or an irradiation facility and scientific as well as technical support (including data evaluation) for single experiments to be performed by short-term visitors on the basis of individual proposals [1].

Summary

After major reconstruction and upgrading the Budapest Research Reactor is in operation again since November 1993. For a wide range of research and application activities, horizontal and vertical irradiation channels with various parameters are available. A cold neutron source is under construction, the adjoining neutron guide system is actually used with thermal neutrons. Six high-performance experimental stations are available (and some others are under construction) for research and development programs in condensed matter physics, material science, nuclear physics, radiography, activation analysis and other fields. The Budapest Neutron Centre is a new regional/international centre of excellence that hopes to attract wide interest of users in science and technology.

Acknowledgements

The Hungarian Academy of Sciences (MTA), the National Fund for Scientific Research (OTKA) and the National Committee for Technological Development (OMFB) are acknowledged for financial support of BNC. Special thanks should be expressed for the elaboration of the research and application programs as well as for co-operation in writing and editing of various BNC documents to L. Cser, T. Grósz, T. Hargitai, G. Molnár, A. Simonits and I. Vidovszky. The author is indebted to S. Sváb, Gy. Mészáros and F. Deák for providing Fig. 4.

References

1. Neutron Scattering Facilities at Budapest's Modernized Reactor. eds: L.Rosta, L.Fragnoud, Gy.Török, KFKI-91-193, 1991; Applied Research at the Budapest Neutron Centre, Proc. Workshop of CEI: International Use of Centers of Excellence, 26–27 April 1993, Budapest, ELFT, pp.36–41, 1993.
2. F. Gillemot, T. Hargitai, I. Vidovszky, Interregional Seminar on Research Reactor Centers, 22–26 November 1993, Budapest, TECDOC IAEA/SR-183/23.
3. Budapest Neutron Centre. Doc. CEI-SCCE-pro-02, 1992.
4. L. Cser, L.Rosta, Gy.Török: Report KFKI-1989-42/I, 1989.
5. L. Rosta, Interregional Seminar on Research Reactor Centers, 22–26 November 1993, Budapest, TECDOC IAEA/SR-183/27.
6. G. Molnár, T. Belgya, I. Diószegi, F. Fazekas, Zs. Németh, Zs. Révai, Á. Veres, Interregional Seminar on Research Reactor Centers, 22–26 November 1993, Budapest, TECDOC IAEA/SR-183/25.
7. L. Rosta, Physica B, *174*, 566, 1991.
8. T.Grósz, L. Rosta, Materials Research at the Budapest Research Reactor (in Hungarian). Preprint RISP, SzFKI-1993/5, 1993.
9. F. De Corte, A. Simonits, J.Rad.Nucl.Chem. Articles, *133*, 43, 1989.
10. L. Cser, L. Rosta, Gy. Török, Neutron News, *4*, 9, 1993.
11. M. Balaskó, E. Sváb, L. Cser, NDT International, *20*, 157, 1987.
12. T. Grósz, L. Cser, L. Rosta, M. Szalók, Gy. Zsigmond, Physica B, *180–181*, 932, 1992.
13. G. Molnár, L. Rosta, A. Simonits, Introduction of the Budapest Neutron Centre. IAEA Technical Committee Meeting, 4–7 May 1993, Vienna, TECDOC IAEA/SR-177/28.

Acta Physica Hungarica 75 (1–4), pp. 25–30 (1994)

FUNDAMENTAL PHYSICS WITH SLOW NEUTRONS

K. SCHRECKENBACH

Fakultät für Physik, Technische Universität München
D-85748 Garching, Germany

The research field of fundamental physics with slow neutrons is presented. Future experiments are suggested which could be carried out also at a medium flux neutron source.

1. Introduction

When we talk about fundamental physics in neutron research we deal with the fundamental properties and interactions of the neutron itself. This field has rapidly developed in the recent years due to the availability of intense neutron sources and the development of polarization techniques, cold and ultracold neutron sources and neutron optic devices. The stop of the ILL High Flux Reactor since 1991 has seriously slowed down this activity and we can hope for a revival when the facility comes again into operation in 1994. For a neutron source as the research reactor here in Budapest, the intensity in neutron flux is a too big constraint for some of the fundamental physics experiments. But many experiments need more the quality of the neutron beam and a careful design. They should be also feasible here, when the cold neutron source is operational.

The research field can be classified in the following topics:

- neutron particle properties (beta decay, electric dipole moment, $n\bar{n}$ oscillation, neutron rest charge, etc.)
- neutron wave properties (neutron optics, quantum mechanics, interferometry)
- symmetries in neutron interactions (PNC and TRI tests in neutron scattering and nuclear reactions)
- fundamental physics with radiation produced by neutron reactions.

In the present talk I can only give a brief idea on some topics in this field and give some examples with preference to experiments which should be feasible at the Budapest reactor. Many more details could be found in recent books, conference proceedings and review articles [1–4].

2. Free neutron beta decay

The decay of the free neutron is a fundamental process of the weak interaction in the first generation of elementary particles. The dominant decay branch leads to a proton, a free electron and an antineutrino

$$n \rightarrow p + e^- + \overline{\nu}_e + 782 \text{ keV},$$

$$d = V_{ud}d' + V_{us}s' + V_{ub}b',$$

$$d' \to u + W^-; \quad W^- \to e^- + \overline{\nu}_e.$$

In the quark picture the weak interaction eigenstate d' of the d quark transforms into the u quark under emission of a W^- boson. The weak and strong interaction eigenstates are connected by the Kobayashi–Maskawa mixing matrix V. The universal weak interaction coupling constant connects the weak interaction eigenstates, while for the neutron decay the coupling constant is reduced by the factor $V_{ud} = \cos\theta_c = 0.975$, θ_c Cabbibo angle.

Neutron decay properties have been investigated in many aspects. Recently several neutron storage experiments with ultra cold neutrons (UCN) yielded the most precise value for the free neutron lifetime [5]. Combining these results with angular correlation experiments for the decay products the fundamental coupling constants g_V and g_A could be deduced from the neutron decay alone and compared with the data from ft values for superallowed beta transitions and the muon decay. There remains a discrepancy at the level of more than 2σ which is not yet understood [5, 6]. To clarify the situation more neutron decay experiments are needed. But for that an intense UCN source and a very intense source of polarized neutrons are needed. This seems not to be available here. Also for time reversal tests in triple correlation experiments (D and R coefficients) the statistical accuracy is a serious limitation although methodical developments could be also carried out at weaker neutron sources.

There are several effects in the decay of the neutron which have not been studied. This includes the bremsstrahlung spectrum in the free neutron decay and the decay of the neutron into a hydrogen bound state.

The bremsstrahlung spectrum is related to the radiative correction in the beta decay. In the case of the free neutron this spectrum could be studied as a function of the electron energy without the influence of surrounding nucleons and compared with calculations as given for instance by Sirlin [7].

The experiment would certainly be difficult but feasible. A low gamma background neutron beam would be necessary, such as cold neutrons emerging from a neutron guide. The electron spectrum in neutron decay could be measured almost background free by detecting decay protons and electrons in coincidence. This has been already achieved in 1950 by Robson [8]. Adding a detector for the bremsstrahlung (UV radiation and harder) in coincidence should allow a clean measurement.

A further decay mode of interest is the decay to a hydrogen bound state. The antineutrino spectrum is monoenergetic in this decay. The decay branch relative to the normal one is predicted as $\sim 10^{-5}$ [9]. It is not evident how the produced hydrogen atoms could be discriminated from the background. A possibility would be an asymmetry measurement relative to the neutron spin. Due to parity non-conservation the emission of the monoenergetic antineutrinos is asymmetric in respect to the neutron spin and hence also the recoil momentum distribution of the formed hydrogen atoms. It depends also on the populated state in the atomic shell. A pioneering experiment of this kind could be done also at a weaker neutron source,

since a suitable method must be developed first. The next step would be to look for the population of the atomic shells of the hydrogen in this decay mode. It would give us constraints on the occurrence of right handed currents.

3. Interaction of neutrons with nuclei

At first I like to mention an early measurement on the neutron capture on a proton. In [10] the probability of the two gamma decay to the one gamma decay was measured. The result was found to be too high by an order of magnitude compared to theory. But the angular distribution shown in this paper seems not to be correct. It would be interesting to repeat this work.

The polarization and spin flip techniques developed in recent years are an excellent base for a variety of asymmetry experiments. For slow neutrons a degree of polarization of better than 95 % is easily achievable with bent supermirrors. A spin flip device for neutrons does not alter the spectrum or intensity of the neutron beam besides the very weak magnetic interaction on the neutrons magnetic moment. The principle of an asymmetry measurement with polarized neutrons is shown in Fig. 1. A precision of the order of 10^{-6} is readily possible for the asymmetry $(N_+ - N_-)/(N_+ + N_-)$; N_+ and N_- rates for opposite neutron spin directions. In neutron capture reactions the neutron polarization is transferred to the capture state of the nucleus. For the best case of a spin 0^+ target and s-wave capture the polarization of the capture state is equal to that of the neutrons. By this means polarized excited nuclei can be produced in an easy way.

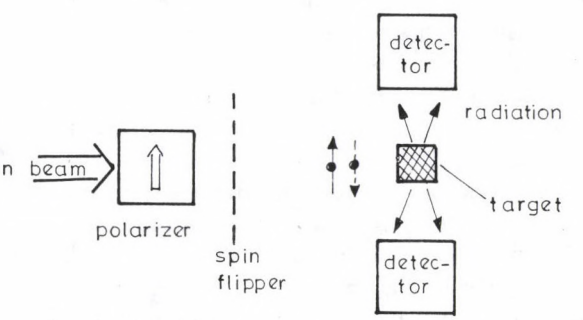

Fig. 1. Principle of an asymmetry measurement in polarized neutron capture reactions. The counting rates in a detector are compared for the two neutron spin directions

A number of experiments have been performed in the past on reactions such as $(\mathbf{n}, \gamma)$, $(\mathbf{n}, f)$. The most interesting target for $(\mathbf{n}, \gamma)$ would be protons. One would learn about fundamental quantities in the weak pion exchange and the weak neutral current. But the expected asymmetry is as small as -5×10^{-8} [11] and the best precision achieved by an ISN/ILL collaboration was $(-4.7 + 4.7)10^{-8}$ [12]. For heavier nuclei there is an enhancement due to the weak interaction mixing of close

nuclear levels with opposite parity. But the particle physics aspect is then lost and nuclear level structure plays the dominant role. For favorable cases the asymmetry can reach a high level such as 0.07 for ^{139}La at the 0.75 eV p-wave resonance.

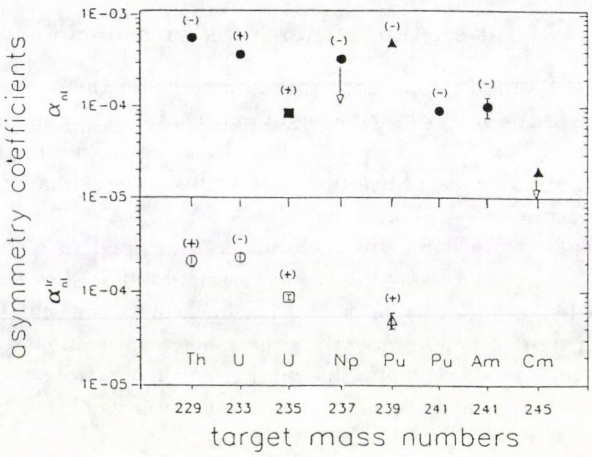

Fig. 2. Absolute values of P-odd (top) and P-even left-right (bottom) asymmetry coefficients for light-fission-fragment emission in the cold-polarized-neutron-induced fission of heavy nuclei [13]

Astonishing are the results on the $(\mathbf{n}, f)$ reaction. The measured asymmetry of the fission fragments seems to be rather similar for fissile nuclei and is of the order of 10^{-4} (Fig. 2 [13]). For a level mixing model there should be more fluctuation in the data. More experiments are necessary to clarify the role of weak interaction in the neutron induced fission process.

It would be extremely interesting to observe a violation of the time reversal invariance (TRI) in any system, since it has been detected via CP violation only in the K^0 system. Triple correlation experiments similar to the D or R coefficient for the free neutron could be considered. But care must be taken of final state effects, i.e. interference effects between the exit channels of the reaction, which could simulate TRI violation. For the case of the neutron the final state effects are calculated as $< 10^{-4}$. For heavier nuclei or for fission the final state effects are in general more important but if measured they may have their own interest. As an example Lobov et al predicted the final state effect in the triple correlation between the spin of an excited nucleus and the momenta of the e^+ and e^- in the following internal pair production process at a level of $Z/137$, Z nuclear charge [14]. This prevents a sensitive TRI test in this reaction but could check the calculation of final state effects, which may be worthwhile if the experimental effort is reasonable.

4. Neutron spin rotation

The parity non-conservation (PNC) of the weak interaction causes neutron spin rotation in matter. Experiments are reviewed by Heckel [15], theoretical aspects

are given by Desplanques [11]. This effect was first observed by Heckel et al in heavier muclei by an experimental method illustrated in Fig. 3. The size of this PNC effect could be explained by nuclear level interference in the neutron scattering process, similar to the above neutron capture PNC effect. Large effects were found for ^{117}Sn and for ^{139}La. An even more interesting case would be a neutron spin rotation experiment on very light nuclei such as protons or deuterons, since the result would be related to the fundamental weak pion exchange mechanism. But the expected size of the effect would be only 10^{-8} rad/cm for a liquid hydrogen target. The group in Seattle (Heckel et al) is planning such an experiment for several years. An experiment on liquid ^{4}He seems to be easier and also feasible at a weaker neutron source, The small neutron scattering and zero neutron capture cross section of ^{4}He would allow a target of substantial thickness. The PNC effect is calculated as 10^{-8} rad/cm. The liquid He has to be pumped between the two sample positions (Fig. 3). The interpretation of the result is complicated in the four nucleon system of ^{4}He but should not be out of the present possibilities.

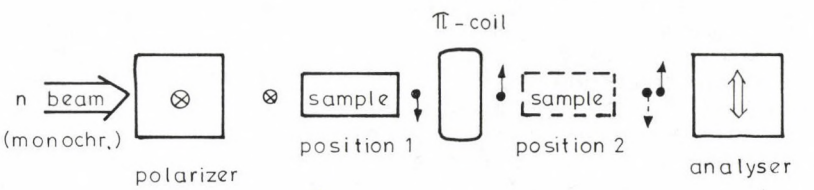

Fig. 3. PNC spin rotation experiment by Heckel et al. The analyser measures the polarization component perpendicular to the main neutron spin direction. By changing the sample position the spin turns into the opposite direction.

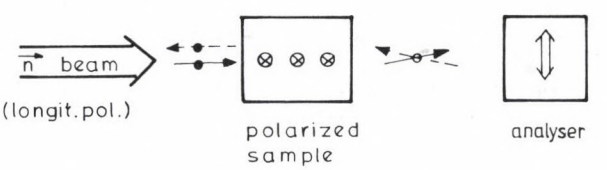

Fig. 4. Possible lay-out for a TRI experiment in neutron scattering

Many discussions came up how to measure a time reversal violating spin rotation in matter (see [16]). Again a nuclear level enhancement is expected and could yield a measurable effect. The principle of the measurement is shown in Fig. 4. The main problem lies in a polarized target without presence of a magnetic field. Recently at LNPI, Russia, and at KEK, Japan, methods were proposed how to polarize a La target and how to control spin rotations not caused by time reversal violation.

5. Conclusion

In conclusion a large variety of experiments are of interest in the field of fundamental physics. Several could be carried out also at a medium flux neutron source like here in Budapest.

References

1. P. A. Krupchitsky, Fundamental Physics Research with Polarized Slow Neutrons, Springer Verlag, Berlin, 1987.
   Yu. A. A. Alexandrov, Fundamental Properties of the Neutron, Oxford Science, 1992.
   D. Dubbers, Prog. Part. Nucl. Phys., *26*, 173, 1991.
2. B. Desplanques, F. Gönnenwein and W. Mampe (eds), Workshop on Reactor Based Fundamental Physics, Grenoble, 1983, J. de Physique, *C3*, 1, 1984.
3. D. Dubbers, W. Mampe and K. Schreckenbach (eds), Workshop on Fundamental Physics with Slow Neutrons, Grenoble, 1989, Nucl. Instr. Meth., *A284*, 1, 1989.
4. G. L. Greene (ed), Workshop on Investigations with Cold Neutrons, Washington, 1986, NBS Special Publication.
5. K. Schreckenbach and W. Mampe, J. Phys., *G18*, 1, 1992.
6. B. G. Erozolimski et al, Phys. Lett., *263B*, 33, 1991.
   A. S. Carnoy et al, J. Phys., *G18*, 823, 1992.
7. A. Sirlin, Phys. Rev., *164*, 1767, 1967.
8. J. M. Robson, Phys. Rev., *83*, 349, 1951.
9. K. Green and D. Thompson, J. Phys., *G16*, L75, 1990.
10. W. B. Dress et al, Phys. Rev. Lett., *34*, 752, 1975.
11. B. Desplanques, Workshop on Reactor Based Fundamental Physics, Grenoble, 1983, J. de Physique, *C3*, 55, 1984.
12. R. Wilson et al, Workshop on the Investigations with Cold Neutrons, Washington, 1986, NBS Special Publication, 85.
13. A. Ya. Alexandrovich et al, Nucl. Phys., *A567*, 541, 1994.
14. G. A. Lobov and A. A. Truchan, Izvestia Akad. Nauk USSR, *35*, 859, 1971.
15. B. Heckel, Workshop on Fundamental Physics with Slow Neutrons, Grenoble, 1989, Nucl. Instr. Meth., *A284*, 66, 1989.
16. P. K. Kabir, Workshop on Fundamental Physics with Slow Neutrons, Grenoble, 1989, Nucl. Instr. Meth., *A284*, 1989 and references cited therein.

Acta Physica Hungarica 75 (1–4), pp. 31–39 (1994)

NEUTRON DEPOLARIZATION IN MAGNETIC MEDIA

M. TH. REKVELDT

Interfacultair Reactor Instituut, University of Technology Delft
2629 JB Delft, The Netherlands

The neutron depolarization technique is based on the change of polarization of a polarized neutron beam in three dimensions after transmission through magnetic substances. This change yields the mean domain size, the mean square direction cosines of the domain magnetizations and the mean magnetization. The method is complementary to other neutron scattering techniques with respect to the size of the inhomogeneities to be studied as well as the dynamic range accessible. As examples will be treated, fluxlines in high temperature superconductors, magnetic correlation lengths in dispersions of magnetic recording particles as a function of milling time and as a special case of overlap between ND and small angle scattering, the magnetic domain structure in thin Co-Cr films.

Introduction

The application of neutron depolarization starts already in 1941 by Halpern and Holstein [1] theoretically and Burgy et al in 1950 experimentally [2]. Contrary to neutron scattering and small angle neutron scattering (SANS) the method has never developed into a widespread application. At present, neutron depolarization is exploited at a few places in the world. Without aiming to be all-embracing, I like to mention the work by Drabkin, Okorokov et al [3] and the theoretical work by Maleyev, Toperverg et al [4] in Leningrad and also by Rauch [5] and Badurek et al [6] in Vienna and all references therein. The range of sizes probed by neutron depolarization is between 0.02 μm and macroscopic dimensions, i.e. complementary to and overlapping SANS. In the range above 0.1 μm the application of SANS fails by a lack of sufficient resolution. However, the application of the neutron depolarization technique is confined to magnetic phenomena and enables one to determine magnetic inhomogeneities as domain size or correlation length of the local magnetization, the mean square direction cosines of the domain magnetization directions and the mean magnetization vector [7,8] and their time dependence. Further it should be noted that in a ND experiment one single intensity measurement determines a correlation length while in a SANS experiment the whole momentum dependence is needed for this information.

In thin magnetic films neutron depolarization can be applied in studying the domain structure perpendicular as well as parallel to the film [9]. In this respect neutron depolarization is also complementary to neutron reflectometry which studies the atomic and magnetic structure of the film perpendicular to the surface [10]. The application range of the reflection technique is typically from atomic dimensions up to 0.1 μm perpendicular to the film, while the range of the neutron depolarization starts above 0.01 μm, however in all directions.

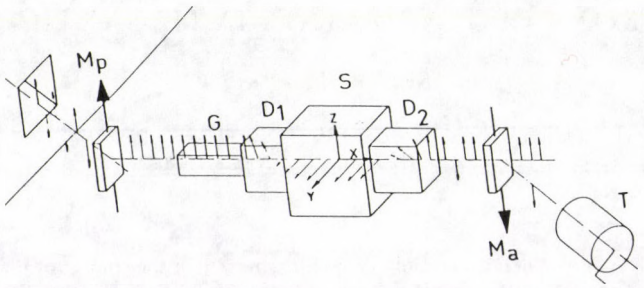

Fig. 1. Schematic overview of depolarization set-up. $M_p - M_a$ = magnetization direction, polarizator-analysator crystal, G = guide field, $D_1 - D_2$ = polarization turners, S = sample holder, T = counter

Also in the dynamics of materials, neutron depolarization is complementary with inelastic neutron scattering, However, the dynamics studied with neutron depolarization are measured in real time in contrast with the scattering techniques. Dynamic experiments are carried out by applying a periodic action to the sample such as a magnetic field or a tension and studying the response of the domain structure on this action by measuring the neutron intensity in periodically triggered time channels [11]. With this technique a time resolution of about 5 μs can be obtained, Because of the limitation in time scale at short times time dependent neutron depolarization has up to now only been applied successfully to eddy current limited domain wall movements and to time dependent rotation of induction in high T superconductors and flux creep.

In the next Sections the neutron depolarization technique will be treated briefly in a number of applications in materials research.

Neutron depolarization technique

The principal set-up is sketched in Fig. 1. It consists of a polarizer (P) and an analyzer (A) with two polarization rotators D1 and D2 and a magnetically shielded sample box in the centre. The devices P and A may be polarizing crystals (e.g. Fe_3Si, Cu_2MnAl) or polarizing mirrors. The device D1 serves to adjust the polarization of the neutron beam along one of the three orthogonal x, y or z axes. The beam passes through a sample, which is positioned in a box of soft iron and μ-metal in order to shield against external magnetic fields. The magnetic induction B, measured by a fluxmeter, is less than 1×10^{-5} T inside the box. Subsequently, the beam passes through a second polarization rotator by means of which each component x, y or z of the polarization vector **P** can be rotated parallel to the axis of magnetization of the analyser (similar to the polarizer). After reflection at the analyser the neutrons are counted by a detector. The set of measured intensities I_{ij} determines the so-called depolarization matrix

$$D_{ij} = \frac{I_s - I_{ij}}{I_s - I_m}, \tag{1}$$

where i, j refer to the adjustment directions of the two polarization rotators and I_s and I_m are the intensities of the fully depolarized and maximum polarized beam, respectively.

Time dependent phenomena can be studied by repeating the process (e.g. a magnetization reversal) periodically in time. In one period the intensity is measured in successive time channels of predefined length Δt. The number of measuring cycles is determined by the desired counting statistics. The time resolution is about 5 μs and results from the wavelength spread $\delta\lambda/\lambda$ of the beam and the time resolution of the detector [11].

The spatial sensitivity of the depolarization set-up of the order of 0.01 μm depends on the acceptance angle of the polarization analyser. This is a direct consequence of the equality of ND and SANS with spin flip, which was shown first in a quantum-mechanical treatment by Maleyev et al [4]. Rosman [14, 15] made a quantitative estimation for this sensitivity for different depolarization set-ups.

In case of zero magnetization ($< \mathbf{B} >= 0$), the diagonal elements of the depolarization matrix can be identified by [7, 14, 15]

$$D_{ii} = \exp[cL_s(\xi^0 - \alpha_{ii}^0)], \tag{2}$$

with $c = c_1^2$ and $c_1 = 4.67 \times 10^{14}\ \lambda\ \mathrm{mT}^{-2}$. Here λ is the wavelength of the neutron beam. Further L_s is the transmission length of the neutrons through the sample,

$$\alpha_{ij}^0 = \frac{8\pi^4}{W} \int_S \Delta B_i(\mathbf{s}) \Delta B_j(-\mathbf{s}) d^2\mathbf{s},$$
$$\xi^0 = \frac{8\pi^4}{W} \int_S \Delta \mathbf{B}(\mathbf{s}) \Delta \mathbf{B}(-\mathbf{s}) d^2\mathbf{s}, \tag{3}$$

and $\gamma_i = \alpha_{ii}/\xi^0$. Here, the integrations extend over the reciprocal plane perpendicular to the neutron transmission direction. The fluctuations $\Delta B(s)$ are connected with the fluctuations $\Delta \mathbf{M}(\mathbf{r})$ as seen in real space, by the Fourier transformation:

$$\Delta \mathbf{B}(\mathbf{s}) = \frac{\mu_0}{(2\pi)^3} \int_W [\mathbf{s}_u \times [\Delta \mathbf{M}(\mathbf{r}) \times \mathbf{s}_u]] e^{i\mathbf{s}\cdot r} d^3\mathbf{r}. \tag{4}$$

The vector $\mathbf{s}_u$ is a unit vector of $\mathbf{s}$. The volume W corresponds to the part of the sample illuminated by the neutron beam. The quantity ξ^0 in Eq. (3) is a magnetic correlation length in product with the square of the amplitude of the fluctuating local magnetic induction. The quantity γ_i is a direct measure of the direction cosines of the local magnetization. In the formulation of Eq. (4) the double vector product accounts for Maxwell's laws $\mathrm{curl}\mathbf{H} = 0$ and $\mathrm{div}\mathbf{B} = 0$. When applied to e.g. particulate systems this formulation in terms of M has the advantage that one

does not need to bother about the strayfields between particles. Equations (3) and (4) show very nicely that the measured correlation length components are in fact the integrated scattering components obtained in SANS, when the Fourier vector s is read as the momentum transfer in neutron scattering which appears to be the case in a thorough derivation of the formulae [4, 15].

For non-vanishing $< \mathbf{B} >$ parallel to the y-axis and moreover, $\alpha_{ij} = 0$ for $i \neq j$, the depolarization matrix D can easily be expressed in the quantities α_{ij} and the mean rotation angle ϕ of the polarization vector in the mean magnetic induction of the sample. In general a theoretical D can be simulated using a model for the magnetic inhomogeneities. By comparison with the experimental D, a maximum of 9 model parameters can be determined simultaneously.

Applications

Neutron depolarization has been applied to a great variety of problems. For example: the direction cosines of local magnetizations in ferrites and ferromagnetic foils under tension [7, 12], magnetization distribution in thin CoCr films with perpendicular anisotropy [9], dynamics of magnetization and domain walls in FeSi crystals [11] and polycrystalline Fe and Ni close to the Curie temperature [17]. Also very accurate critical exponents in Fe and Ni could be determined [18]. A few recent applications on magnetic recording materials and superconductors will be treated in more detail below.

Temperature dependence of ND in high T superconductor YBACU

Experiments were carried out by Roest and Rekveldt [18] on a sintered $YBa_2Cu_3O_x$ sample of size 5.35 × 20.55 × 11 mm^3 with a grain size between 1 and 10 μm. The sample positioned inside a coil is clamped between a magnetic short cirquit to prevent emerging flux from the sample and coil to affect the polarization of the beam outside the sample. The whole is positioned in a cryostat. At low temperature (4 K) a pulsed magnetic field of $\sim$ 0.7 T with 0.1 ms duration was applied after which the depolarization matrix was measured with rising temperature. Figure 2 gives the results of the average magnetic induction components B_x, B_y and B_z and the correlation parameters $\alpha_\perp$ and $\alpha_\parallel$ which show the correlations in the magnetic components perpendicular and parallel to the applied field direction.

The different temperature dependence of $\alpha_\perp$ and $\alpha_\parallel$ is striking and is interpreted as follows. Direct after the field pulse the fluxlines are randomly directed in the half sphere with some remanence in the initial field direction, but in bundles of $\sim$ 20 μm sizes of the same order as the crystallite size. With increasing temperature the fluxlines start to stretch themselves in the average fluxline direction. Above 20 K all fluxlines are parallel but still inhomogeneously distributed. Above 40 K no measurable depolarization is present and the fluxlines are distributed homogeneously over the sample. Above this temperature the linear T dependence of $< B >$ indicates a $(T - T_c)^{1/2}$ dependence of the fluxline spacing.

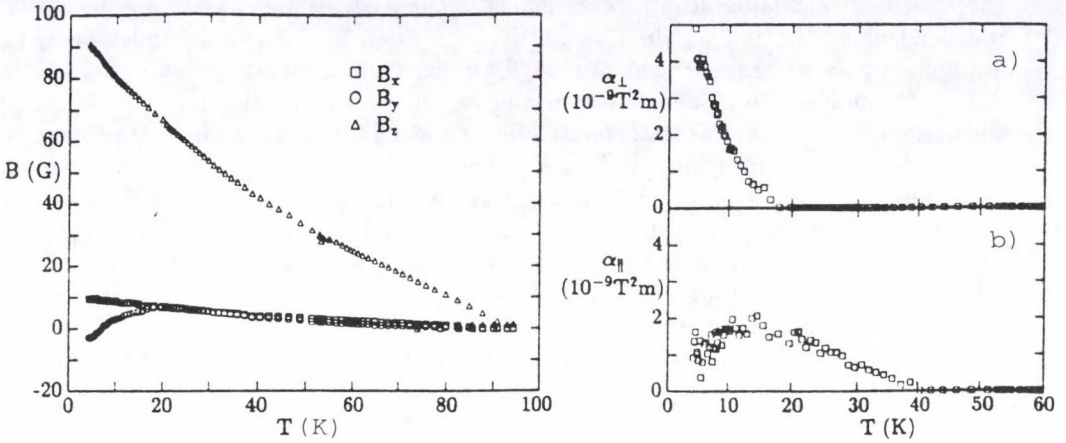

Fig. 2. (Left) Remanent magnetic induction as a function of temperature, after zero-field cooling and a field pulse at 4.2 K. (Right) Average of the squared induction fluctuations perpendicular (a) and parallel (b) to the initial applied field, plotted as a function of temperature

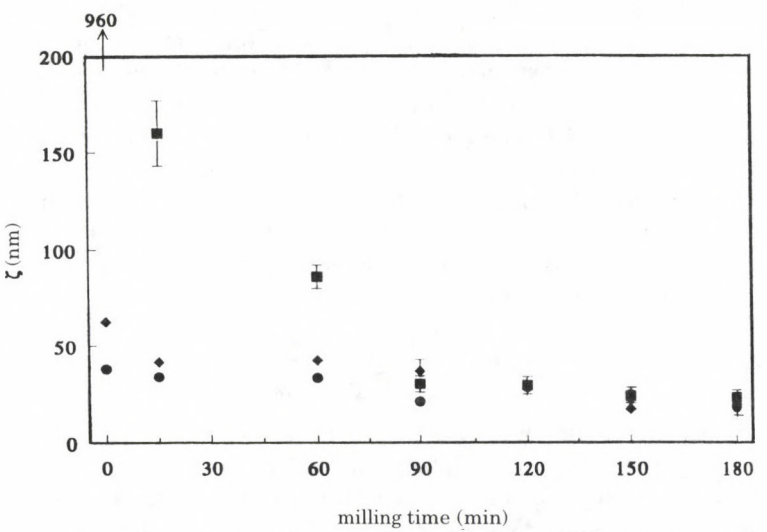

Fig. 3. Correlation length in dispersion as a function of milling time in different magnetic conditions, virginal (full circles), after short pulse of 0.7 T and 0.1 ms duration (full diamonds) and after longer pulse of 0.04 T and several seconds duration (full squares)

Neutron depolarization in dispersions of magnetorecording particles

Dispersions of small ferromagnetic γFe_2O_3 particles were studied in various magnetic conditions as a function of milling time in a ball mill. In first instance

the measured correlation length corresponds to the particle size of ~ 40 nm, nearly independent of the milling time as can be seen from Fig. 3 (black circles). By applying a pulsed magnetic field of 0.25 T, the particles are magnetized uniformly during the pulse of 0.15 ms. After the pulse, clusters of particles will manifest themselves with an increased correlation length as can be seen from Fig. 3 (black diamonds). When during milling the clusters are broken down the correlation length decreases according to the initial particle size. A pulse duration of seconds causes the growth of much larger clusters (black squares) which are stable as long as the particle surfaces are not covered by a surfactant which reduces the magnetic interaction. This covering with surfactant improves with milling time with the result that the measured correlation length decreases with milling time. After 2 hours of milling time only the particle size is still reducing, the clusters have fully disappeared.

Neutron depolarization and SANS in thin CoCr films with perpendicular anisotropy

The magnetic state of the CoCr sample can be described by a domain structure with easy axis of magnetization nearly perpendicular to the film plane. ND experiments were carried out by Kraan et al [20] as a function of transmission angle through the film with a thickness of 0.8 μm with different magnetic history. To increase the depolarization effect a stacking of 50 films was used. Figure 4 shows the measuring set-up and results of the diagonal matrix elements $D_{ii} (i = x, y$ and $z)$ as a function of θ. The change in D_{zz} can directly be understood from the precession of the polarization around the local induction. At $\theta = 0$ the precession angle delivers directly the product of local induction times the domain height h perpendicular to the film. The θ dependence of D_{zz} follows from the partly compensation of the precession angle in one domain by the opposite precession in the neighbouring domain. In formula:

$$D_{zz} = 1 - \frac{\varphi^2}{2}\left(1 - \frac{2\theta h}{3\delta}\right). \tag{5}$$

From the linear extrapolation of D_{zz} at small θ values to $D_{zz} = 1$ the domain size δ in plane is obtained. In general it appears that in these films the domain height h covers only 0.7 of the film thickness and the domain width is dependent on the direction of the last applied field in plane. The absence of θ dependence in D_{xx} is because in this case the polarization is parallel to the local magnetization in the perpendicular domains and is essentially not affected by this local field. The small depolarization in D_{xx} is probably caused by a layer magnetized in the z-direction on the substrate side of the sample, which supports the missing fraction of 30 % in perpendicular domains.

Small angle scattering on a single CoCr film of 2 μm thickness on Si single crystal has been carried out in various magnetic states of the film as demagnetized in different directions. The experiments were carried out at D11 of ILL in 1987 [21] with a momentum resolution of $\Delta Q = 2.5 \times 10^{-5}$ nm^{-1}. The sample was positioned

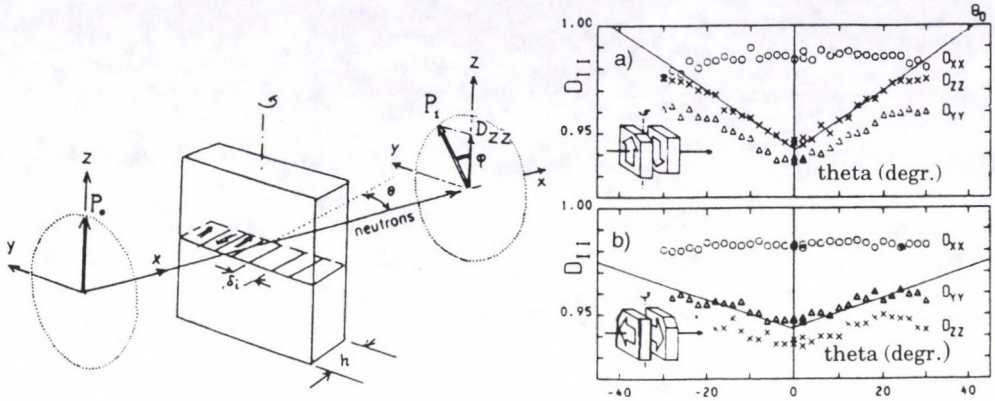

Fig. 4. (Left) Schematic view of measuring set-up. (Right) The elements D_{ii} as a function of transmission angle θ measured with the remanence of the films parallel to $\pm z$ (a) and $\pm y$ (b)

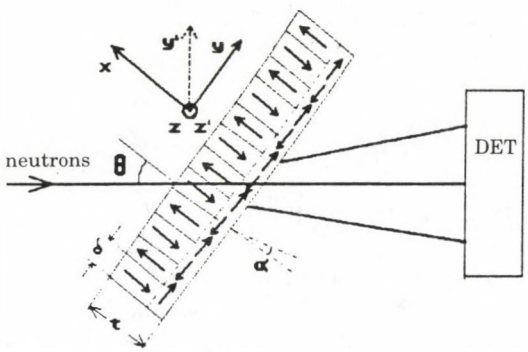

Fig. 5. Scattering geometry of the film rotated around the z-axis in the SANS instrument D11 of the ILL

in the neutron beam according to Fig. 6. The normal on the film makes an angle θ with the neutron beam direction. For this particular domain structure with domain height h and domain width δ the master equation for elastic scattering is given by

$$\frac{d\sigma}{d\Omega} = \left| \int_h dx e^{iQ_x x} \int\int_S d\mathbf{R}\, Np(\mathbf{R}) \mu_P e^{i(Q\cdot\mathbf{R})} \right|^2, \tag{6}$$

with

$$Q_x = Q_y \tan\theta,$$

$$\mu_P = (1 - k_y^2 \sin^2\theta)^{1/2},$$

where the system of axes has been fixed on the sample. For $\theta \neq 0$, anisotropy in the scattering occurs as a function of Q_x given by

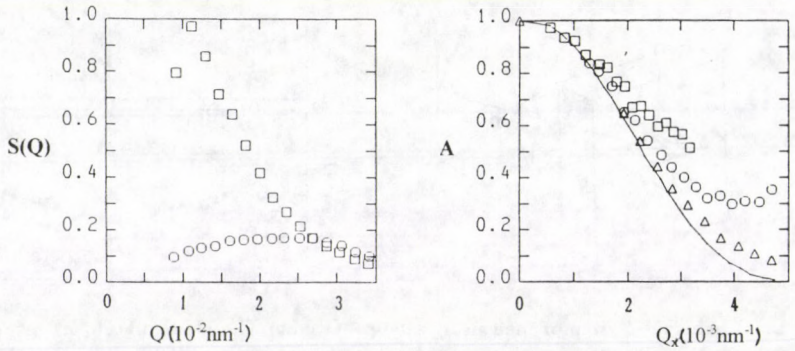

Fig. 6. (Left) Isotropic scattering $S(Q)$ as a function of Q. (Right) Anisotropy in the scattering $A(Q_x)$ at different angular settings of the film, $\theta = 5°$ (□), 10° (o) and 15° (△)

$$A = \frac{\sin^2(Q_x h/2)}{(Q_x h/2)^2}(1 - k_y^2 \sin^2\theta)^{1/2}\frac{S(Q_y)}{S(Q_z)}. \tag{7}$$

Here $S(Q)$ represents the scattering function describing the structure of domain widths in the plane of the film and contains also the anisotropy herein. Further is $p(\mathbf{R})$ in Eq. (6) the magnetic scattering amplitude of each atom dependent on the sign of magnetization at position $\mathbf{R}$. Figure 6 shows the results for one film in the demagnetized and magnetized state for the isotropic part of the scattering $S(Q_z)$ and the anisotropy $A(Q_x)$ for various values of θ of the film one time magnetized perpendicular to the film. The maximum in the scattering $S(Q_z)$ is a measure for the domain width δ and the distribution of domain widths in the plane. The Q_x dependence of A gives directly the domain height h. However, from the different $A(Q_x)$ curves at various θ values information about the angular variation of the magnetization orientations of the domains can be obtained by comparing the results with computer simulations.

Conclusions

ND is complementary to SANS in the range of correlations but is confined to magnetic systems. In general ND is faster than SANS which makes the study using various external parameters easier and leads to a wide-spread application in micro-magnetic studies of materials.

Acknowledgement

The author acknowledges W. H. Kraan, F. J. van Schaik, R. Rosman, W. Roest and P. T. Por who contributed in the course of the years to the work presented in this paper.

References

1. O. Halpern and T. Holstein, Phys. Rev., *59*, 960, 1941.
2. M. Burgy et al, Phys. Rev., *80*, 953, 1950.
3. G. H. Drabkin et al, Sov. Phys. JETP, *20*, 1548, 1965.
4. S. V. Maleyev, J. de Physique, *43*, C7-23, 1982; B. P. Toperverg and J. Weniger, Z. Phys. B – Cond. Mat., *74*, 105, 1989.
5. H. Rauch und E. Löffler, Z. Physik, *210*, 265, 1968.
6. G. Badurek et al, J. de Physique, *43*, C7-57, 1982.
7. M. Th. Rekveldt, Textures and Microstructures, *11*, 127, 1989.
8. A. I. Okorokov et al, Nucl. Instr. and Methods, *157*, 487, 1978.
9. W. H. Kraan et al, IEEE Transactions on Magnetics, Mag. *23*, 65, 1987.
10. G. P. Felcher et al, Rev. Sci. Instr., *58*, 609, 1987.
11. F. J. van Schaik et al, J. Appl. Phys., *52*, 352, 1981.
12. N. Stüsser et al, J. Magn. Magn. Mat., *67*, 207, 1987;
    M. de Jong et al, Key Engineering Materials, *81–83*, 431, 1993;
    M. de Jong et al, this Workshop, Acta Phys. Hung., *75*, 91, 1994.
13. M. Th. Rekveldt, J. de Physique, *38*, CI-23, 1977.
14. R. Rosman and M. Th. Rekveldt, Z. Physik B: Condens. Matter, *79*, 61, 1990; *81*, 149, 1990; Thesis Delft, 1991, ISBN 90-73861-02-0.
15. R. Rosman and M. Th. Rekveldt, J. Magn. Mat., *95*, 319, 1991.
16. N. Stüsser and M. Th. Rekveldt, J. Appl. Phys., *63*, 2065, 1988.
17. N. Stüsser et al, Phys. Rev., *B33*, 6423, 1986.
18. W. Roest and M. Th. Rekveldt, Phys. Rev. B., *48*, 6420, 1993; Proc. International Workshop on Critical Currents, Alpbach, Austria, Jan. 1994.
19. P. I. Mayo et al, J. Magn. Magn. Mat., 1994, in press.
20. W. H. Kraan et al, J. de Physique, Colloque *C8*, 49, *C8*-1981, 1988.
21. M. Th. Rekveldt et al, J. Magn. Magn. Mat., *78*, 110, 1989.

Acta Physica Hungarica 75 (1-4), pp. 41-45 (1994)

ASTROPHYSICS AT NUCLEAR REACTORS

F. KÄPPELER

Kernforschungszentrum Karlsruhe, Institut für Kernphysik
Postfach 3640, D76021 Karlsruhe, Germany

The role of neutron reactions for element synthesis is outlined with emphasis on the mass region $A > 60$, where this reaction type is most important. A brief survey of the various scenarios for neutron dominated nucleosynthesis is followed by a discussion of related nuclear physics data, which can be determined in reactor based experiments. The particular features of such experiments are illustrated by two examples — a determination of the thermally enhanced β-decay of ^{79}Se under stellar conditions, and a possible cross-section measurement on ^{84}Kr.

1. Neutrons in astrophysics

The big bang is the first astrophysical scenario where neutron reactions play a role. Practically all of the presently observed helium in the universe has been produced in a series of reactions including $^1\mathrm{H}(n,\gamma)^2\mathrm{H}$ and $^3\mathrm{He}(n,\gamma)^4\mathrm{He}$. However, primordial nucleosynthesis did not produce sizeable quantities of heavier elements because of the instability gaps at $A = 5$ and $A = 8$. Recently, the discussion of density fluctuations in the early universe has raised the question, whether these gaps could have been bridged by a series of rapid neutron captures in order to explain the composition of the oldest stars in our galaxy. This problem has been addressed by several groups and is still under debate. For a review see Rauscher et al [1].

While neutron reactions among the lightest isotopes were important during the big bang, all of the heavy elements beyond iron have been produced by neutron capture reactions in stars. Fusion of charged particles does no longer contribute to the mass range beyond $A \sim 60$, since the Coulomb barriers are becoming too high and the binding energies per nucleon are decreasing. For explaining the observed abundance distribution between iron and the actinides (Anders and Grevesse [2]) essentially three processes must be invoked. The dominating mechanisms are the slow and the rapid neutron capture processes (s- and r-process), which both account for approximately 50 % of the abundances in the mass range $A > 60$. A minor part of the resulting abundance distribution is modified by the p-process at very high temperatures, which accounts for the rare proton rich nuclei.

The s-process associated with stellar helium burning is characterized by comparably low neutron densities. This implies neutron capture times of the order of several months, much longer than typical beta decay half-lives. Therefore, the s-process path follows the stability valley. The developing s-abundances are determined by the respective (n,γ) cross-sections averaged over the stellar neutron spectrum, such that isotopes with small cross-sections are built up to large abundances. This holds in particular for nuclei with closed neutron shells $N = 50$, 82 and 126, giving

rise to the sharp s-process maxima in the abundance distribution around $A = 88$, 140 and 208.

The r-process counterparts of these maxima are caused by the effect of neutron shell closure on the beta decay half-lives. Since the r-process occurs during stellar explosions (presumably in supernovae) on time scales of a few seconds, neutron captures are much faster than beta decays. This drives the r-process path off the stability valley to where the neutron separation energies are only $\sim$ 2 MeV. There, (n, γ) and (γ, n) reactions are in equilibrium, and the reaction flow has to wait for beta decay to the next higher element. Accordingly, the r-process abundances are proportional to the half-lives of these waiting point nuclei. This means that abundance peaks accumulate again at magic neutron numbers, but at lower mass numbers compared to the related s-process maxima. The separation of the abundance peaks indicates the intersection of the r-process path with the magic neutron numbers.

2. Nuclear physics input

2.1. Experimental data for the s-process

The s-process can be investigated in great detail because the involved isotopes are stable or close enough to stability that the required nuclear physics data are accessible to laboratory experiments.

2.1.1. (n, γ) *rates.* The stellar neutron capture cross-sections are the main information required for s-process studies. Similar to the burn-up in a nuclear reactor, the abundances produced by subsequent (n, γ) reactions and β-decays are inversely proportional to the respective cross-sections. Typical s-process temperatures range from 200 to 300 million K. Accordingly, the proper Maxwellian average cross-sections in the stellar environment have to be determined either by folding the differential cross-section $\sigma(E_n)$, with the thermal neutron spectrum for $kT \sim 30$ keV, or to simulate such a spectrum in the laboratory for a direct determination of the stellar cross-section.

The experimental techniques for the measurement of (n, γ) cross-sections in conjunction with accelerator based neutron sources are discussed in the review of Käppeler et al [3]. At reactors, these studies can be complemented by using filtered neutron beams. Such filters, which are built from isotopes with deep interference minima in the total cross-sections, can provide monoenergetic neutrons in the keV region. The standard examples are filters made from elemental Sc, Fe and Si, which provide neutrons of 2, 24 and 144 keV, respectively. Astrophysically motivated measurements with a 24 keV beam have been reported, for example, by Bradley et al [4]. More recently, the number of monoenergetic beams has been considerably enlarged by the Kiev group (Murzin et al [5]). This extension became possible by the use of separated isotopes, which allows for a more flexible combination of suited materials. About 15 new filtered beams could be established in the energy range between 2 and 400 keV, forming a sufficiently dense grid of energy bins in the astrophysically important range.

Cross-section measurements with monoenergetic neutrons are complementary to experiments at accelerators, because the origin of systematic uncertainties can be quite different. Furthermore, monoenergetic neutrons offer the possibility to study the population probability of isomeric states as a function of neutron energy. Knowledge of these partial cross-sections can be important for the discussion of s-process branchings as outlined at the example of ^{85}Kr in §3.

2.1.2. β-decay rates. The interpretation of the abundance pattern in s-process branchings must account for the fact that the β-decay rates of some branch point isotopes can be influenced by the high temperatures and densities in the stellar plasma. Such changes of the β-decay rates may have different reasons:

– Thermally induced transitions via the stellar photon bath result in a finite population probability of excited nuclear states. If these states decay faster than the ground state, the overall rate will be enhanced. A corresponding example is the decay of ^{79}Se as discussed by Klay and Käppeler [6].

– Since the ionization is almost complete at 300 million K, electron captures are hampered but β-decay in unoccupied electron orbits becomes an important effect in cases where the Q_β values are comparable to the electron binding energies (bound state β-decay).

– The electron gas in the stellar plasma is partly degenerate due to the high density. Therefore, electron captures from the continuum can compensate to some extent the reduced EC probabilities, while β^+-decay is enhanced and β^--decay is hampered.

Generally speaking, there are two groups of s-process branchings, one where the decay rates of the branch point isotope are not affected by temperature and density and another where the corresponding decay rates can be strongly modified under stellar conditions. A comprehensive compilation of the stellar weak interaction rates is given by Takahashi and Yokoi [7].

2.2. Experimental data for the r-process

The difficulty with the nuclear physics data for the r-process is obvious: The r-process path runs so close to the neutron drip line that it is extremely difficult to produce and observe the involved nuclei in the laboratory. Only at magic neutron numbers, where the r-path is closest to stability, two isotopes, ^{80}Zn (Gill et al [8]; Lund et al [9]) and ^{130}Cd (Kratz et al [10]) could be studied so far. This means that practically all the important information has to be obtained by theoretical extrapolation from the region of known isotopes.

Most of what we know about half-lives, masses and P_n values of neutron rich isotopes comes from the spectroscopy of fission fragments, work that has been carried out at reactors, where fission fragments can be isolated via mass separators. In this field, reactor experiments continue to be important for further improvement of the data base for r-process studies.

3. The *s*-process branching at ^{85}Kr

The *s*-process flow in the mass region between Se and Kr is characterized by branchings in the synthesis path at ^{79}Se and ^{85}Kr. The isomer in ^{79}Se can be populated by thermally induced transitions, resulting in a strong temperature effect. In case of the isomer in ^{85}Kr, the excitation energy of the isomer is too high to be efficiently reached by thermal transitions. Consequently, ground state and isomer behave like different isotopes. This means that the branching depends significantly on the partial (n,γ) cross-sections of ^{84}Kr feeding these states, since the short-lived isomer decays always to ^{85}Rb.

Model calculations for different *s*-process scenarios (Käppeler et al [11]; Beer et al [12]; Raiteri et al [13]) find a puzzling situation for the ^{85}Kr branching: there is always a significant uncertainty related to an overproduction of ^{86}Kr. In other words, this behaviour may indicate a tendency in the existing data to overestimate the isomeric ratio, IR = partial cross-section to ^{85m}Kr/total (n,γ) cross-section of ^{84}Kr.

One reason for this unsatisfactory situation is that experimental IR-values are scarce. While the differential (n,γ) cross-section of ^{84}Kr has been measured over most of the relevant energy range (Walter et al [14]), partial cross-sections to the isomer have been measured only for thermal neutrons and for quasi Maxwellian spectra at $kT = 25$ and $kT = 52$ keV (Käppeler et al [15]). The corresponding results for the isomeric ratio are summarized in Table I, which also lists the thermal energies for different *s*-process scenarios.

Table I
Experimental data for the isomeric ratio of ^{84}Kr and typical thermal energies for different stellar scenarios

Thermal energy (keV)	Isomeric ratio	Stellar scenarios
$2.5 \cdot 10^{-6}$ (thermal)	0.67	–
12	?	He shell burning in low mass stars, neutron production via $^{13}C(\alpha,n)^{16}O$
25	0.49	He shell burning in low mass stars and He core burning in massive stars, neutron production via $^{22}Ne(\alpha,n)^{25}Mg$
52	0.42	–
~ 90	?	Shell C burning in massive stars, neutron production via $^{22}Ne(\alpha,n)^{25}Mg$

The IR values of Table I show a clear trend, which implies that the ^{86}Kr production increases with energy. In comparing the ^{86}Kr abundances from different scenarios it turns out that the contribution from low mass stars depends significantly on the – yet unknown – isomeric ratio at $kT = 12$ keV (Raiteri et al [13]). The lack of data around 10 keV and above 50 keV as well as the persisting uncertainties of typically 10 % require additional experimental efforts before the ^{86}Kr yields

obtained from stellar models can be compared in any quantitative way with the actually observed abundances.

A promising possibility to fill in these gaps were to use the monoenergetic neutrons from filtered reactor beams in combination with the activation method used with the quasi Maxwellian spectra at $kT = 25$ and 52 keV (Käppeler et al, [15]). This problem represents a good example, where reactor experiments can provide missing cross-section data for astrophysical applications.

4. Summary

Astrophysical studies at reactors concentrate on three areas:

– The investigation of stellar weak interaction rates is complicated by the fact that large effects in stars are often tiny in laboratory experiments. Therefore, such experiments require the highest possible neutron fluxes and/or sophisticated equipment, e.g. high resolution γ- and β-spectrometers.

– The use of mass separators for the spectroscopy of fission fragments remains important for the determination of nuclear physics data for the r-process.

–The measurement of stellar (n, γ) cross-sections with filtered beams represents a technique complementary to accelerator experiments, since monoenergetic neutrons below 120 keV are not available elsewhere. The combination with the activation method provides sufficient sensitivity to compensate for the limitations in neutron flux.

All these aspects continue to play an important role in experimental nuclear astrophysics.

References

1. T. Rauscher, J. H. Applegate, J. J. Cowan, F.-K. Thielemann and M. Wiescher, Astrophys. J., in press, 1994.
2. E. Anders and N. Grevesse, Geochim. Cosmochim. Acta, *53*, 197, 1989.
3. F. Käppeler, H. Beer and K. Wisshak, Rep. Prog. Phys., *52*, 945, 1989.
4. T. Bradley, Z. Parsa, M. L. Stelts and R. E. Chrien, in: Nuclear Cross-Sections for Technology, eds J. L. Fowler and C. D. Bowman, Washington DC, NBS, NBS Spec. Publ., *594*, 344, 1979.
5. A. V. Murzin, 1993 (private communication).
6. N. Klay and F. Käppeler, Phys. Rev., *C38*, 295, 1988.
7. K. Takahashi and K. Yokoi, Atomic Data and Nuclear Data Tables, *36*, 375, 1987.
8. R. L. Gill et al, Phys. Rev. Lett., *56*, 1874, 1986.
9. E. Lund, K. Aleklett, B. Fogelberg and A. Sangariyavanish, Physica Scripta, *34*, 614, 1986.
10. K. L. Kratz et al, Z. Phys., *A325*, 489, 1986.
11. F. Käppeler, R. Gallino, M. Busso, G. Picchio and C. M. Raiteri, Astrophys. J., *354*, 630, 1990.
12. H. Beer, G. Walter and F. Käppeler, Astrophys. J., *389*, 784, 1992.
13. C. M. Raiteri, R. Gallino, M. Busso, D. Neuberger and F. Käppeler, Astrophys. J., *419*, 207, 1993.
14. G. Walter, B. Leugers, F. Käppeler, Z. Y. Bao, G. Reffo and F. Fabbri, Nucl. Sci. Eng., *93*, 357, 1986.
15. F. Käppeler, A. A. Naqvi and M. Al-Ohali, Phys. Rev., *C35*, 936, 1987.

Acta Physica Hungarica 75 (1–4), pp. 47–54 (1994)

FAST TIMING $\gamma_n\gamma\gamma(t)$ — A NEW TOOL IN NUCLEAR SPECTROSCOPY

H. MACH

Department of Neutron Research, Uppsala University
S-61182 Nyköping, Sweden

Recently introduced fast timing $\beta\gamma\gamma(t)$ method has revitalized the field of dynamic moment measurements with a strong impact in the area of neutron-rich nuclei. The basic concepts of this method and its proposed extension into the neutron capture reactions, $\gamma_n\gamma\gamma(t)$, are discussed. These methods strongly benefit from the new technical developments driven by the very active applied fields where the fast time-delayed techniques are utilized.

Introduction

In general, a nuclear system at a specific level of excitation may decay by α, β or γ emission, or via more exotic processes like fission or emission of a cluster of particles. A probability of a decay of a nuclear level, its lifetime, as well as the intensity ratios between available decay channels, represent important experimental observables that critically constraint nuclear structure models. Many of the excited states exhibit sufficiently long lifetimes that can be measured directly via fast time-delayed spectroscopy. In such measurement a clock is started with a detection of feeding transition and stopped with a detection of transition deexciting a level. In order to measure very short lifetimes the time-delayed technology is put to its limit. In the $\beta\gamma\gamma(t)$ method [1–3] discussed here, the precision of the time measurement is typically $\pm 1 - 2$ ps, but in very special cases it can be as low as ± 0.4 ps. These are demanding limits if one considers that on a scale of 1 ps the speed of β or γ rays (the speed of light) is quite slow at only 0.3 mm/ps in comparison to the dimensions of the timing detectors ($\sim 10 - 25$ mm), and furthermore, that the picosecond time information is extracted from the scintillation pulses (formed when a β or γ ray interacts in a scintillation detector) which themselves are 3 orders of magnitude longer and on the ~ 1 ns scale. However, the art of fast timing measurements has developed slowly over many years.

In the nuclear structure studies in 1960's and early 1970's the fast time-delayed measurements played a major role. Many new and now basic concepts were then tested and developed including fast scintillators, phototubes, Constant Fraction Discriminators (CFD), and sophisticated Time-to-Amplitude-Converters (TAC). However, with a proliferation of accelerator based physics, other techniques, like Coulomb excitations and Doppler shift measurements, dominated the field as the range of applications for simple coincidence time-delayed measurements was rather limited. More importantly, the new techniques were characterized by high precision and reliability in the time domain below ~ 100 ps unmatched by simple time-delayed techniques. Furthermore, the cross-check of results obtained from

the time-delayed and other techniques revealed several cases when results from the time-delayed measurements were off the true values by an unacceptable margin. The origin of these discrepancies can now be understood as discussed in the next Section.

In the mean time, fast time-delayed techniques were utilized in a variety of applied fields with a strong activity in the material sciences, e.g.: studies of hyperfine interactions and positronium annihilation spectroscopy, and also in the field of time-correlated photon counting. Nowadays, it is the applied fields that drive a strong development program in the domain of fast timing detectors and electronics, that in turn affect the methods discussed here: the $\beta\gamma\gamma(t)$ method for the nuclei far from stability and the newly proposed $\gamma_n\gamma\gamma(t)$ method for the neutron capture studies. The opportunities for the fast time-delayed techniques are far from exhausted, and particularly in the "old" domain of nuclear structure physics exciting opportunities for the fast time-delayed studies were, in fact, just created.

General considerations

The recently introduced $\beta\gamma\gamma(t)$ method [1–3] is quite different from simple time-delayed techniques used previously in the nuclear structure physics. In general, it can be characterized by high versatility and precision. However, it also involves a complex and time consuming process of calibration, measurement and data analysis on a level never attempted before. In any case, it is quite surprising that the first concept of such a method was formulated [4] as late as 1986, even though the critical need for such measurements was long recognized and the basic hardware tools were already available since early 1970's.

The time resolution of a pair of timing detectors is a critical parameter in the time-delayed measurement. If a lifetime is sufficiently long in comparison with the Full-Width-at-Half-Maximum (FWHM) resolution, then one can measure it directly from a slope visible on the delayed part of the time spectrum formed by coincidences recorded by a pair of feeding (start) and deexciting (stop) transitions to an isomeric level. For example, in the case of a FWHM resolution of 100 ps one can use shape deconvolution or slope fitting [1] already for lifetimes $T_{1/2} \geq 35$ ps. Such measurements require only a simple time calibration of the TAC unit — now a routine procedure using standard calibrators based on quartz oscillators. Lifetime measurements in the applied fields are generally limited to this case.

The situation is considerably more complicated when the lifetime is shorter and one has to use a centroid shift technique. In this case, from the centroid position of the time-delayed spectrum one subtracts the centroid position of the prompt time spectrum recorded under identical conditions. The difference is the mean life, τ, of the level of interest ($T_{1/2} = \tau \times \ln 2$).

These measurements have specific requirements. In the slope fitting one has to ensure that the slope is due to the level lifetime and not due to a spurious electronic effect. This condition is easy to fulfil if the slope is well defined. In the centroid shift measurement, a requirement that the time-delayed and the reference (prompt) spectra are recorded under identical conditions, is particularly difficult (if not generally impossible) to fulfil. It is thus easy to see the problems of early measurements. Since

the decay of interest and the time calibration sources were measured separately, it was difficult to ensure uniformity of experimental conditions in both runs. Important changes could be caused by differences in the size and strength (count rate) of the sources and their position vis-à-vis timing detectors, and further compounded by drifts and instabilities of electronics. Even if those conditions were met, there is only a handful of cases known in nature where the energies of the feeding and deexciting transitions for the level of interest could be even approximately matched by the energies of the reference (prompt) transitions in the calibration sources. Furthermore, in both cases, one has to ensure that the time spectra do not contain impurity components. In the case of double coincidence measurements that condition is generally violated, although in many cases the main impurity components can be properly accounted for. On the other hand, a high purity of the time-delayed spectrum is assured in the triple coincidence $\beta\gamma\gamma(t)$ measurement discussed below.

Basic concepts of the $\beta\gamma\gamma(t)$ method

The fast timing $\beta\gamma\gamma(t)$ method [1–3] is best suitable for studies of nuclei far from stability line and characterized by a relatively rich decay scheme populated in the β decay. The experimental set-up involves three detectors. Fast timing information is derived from coincidences recorded in two fast scintillators: a small NE111A plastic as β detector and a small BaF_2 crystal for γ rays. The first scintillator has a small volume to ensure a negligible γ efficiency, and it is also thin, 2–3 mm, to ensure a ΔE character for energetic β rays (with the energies about 2–8 MeV) typical for decays far off stability line.

The use of ΔE β detector is critical to the whole concept of $\beta\gamma\gamma(t)$ measurement. One should keep in mind, that the fast timing detectors (plus the associated electronics) are not ideal, thus when two prompt transitions of different energy are recorded in a scintillator, the scintillation signals will be of different intensity. These signals after amplification in a fast photomultiplier and extraction in a CFD unit are presented to the time comparator (TAC) generally at different times. A function expressing relative time differences from recording prompt transitions of different energies is called walk-curve or prompt curve and represents a crucial characteristics of a scintillator+phototube+CFD unit. The point of using a ΔE detector is to ensure that energetic β rays deposit the same energy after passing through such a scintillator and create time response largely independent of the initial β energy. This feature eliminates a need for a walk-curve determination for the β detector and strongly simplifies the process of data analysis.

On the other hand, prompt curve calibration has to be performed for the fast timing γ detector. However, a precise calibration on the level of 1–2 ps is a tedious process. One difficulty is the large energy range, typically from 30 to 3000 keV, that is covered simultaneously during an experimental run and has to be calibrated. Since it is not possible to achieve an optimum efficiency, time resolution, and a flat prompt curve over such dynamic range (2 orders of magnitude) compromises have to be made. A second problem, related to the first one, is that there is no ideal radioactive source for such prompt calibration. We are still searching for the best

sources, and thus for the most precise and efficient procedure of prompt calibration. Note that in the "old" double coincidence measurement one had to use prompt (or reference) calibration sources with transitions of exactly the same energy as those in the decay of interest. The $\beta\gamma\gamma(t)$ method does not have such requirement since the prompt curve defined by a series of calibration transitions is smooth and thus a prompt position can be obtained at any energy by interpolation. Furthermore, at a fission-product mass separator like OSIRIS at Studsvik, hundreds of radioactive beams are available for cross-check or calibration procedures with the activities delivered exactly to the same spot. That creates enormous opportunities for a precise time calibration.

Fast scintillators provide good time resolution (typically of $\sim$ 100 ps FWHM at $E_\gamma = 1.3$ MeV) yet their energy resolution is poor. Although BaF_2 crystal represents a strong improvement over fast plastics both in γ efficiency and energy resolution, yet its energy resolution (typically $\sim$ 9 % FWHM at $E_\gamma = 661$ keV) is insufficient to resolve complex decay spectra. This is why a high resolution Ge detector is added to the system. The combined energy resolution of Ge ($\sim 10^{-3}$) and BaF_2 detectors ($\sim 10^{-1}$) creates a highly selective system with about 10^{-4} resolution. Thus the essential strength of the triple coincidence system is to combine high energy and excellent time resolutions.

In the triple coincidence measurement up to five parameters are collected per coincident event. These are the energies of transitions recorded in the ΔE β, BaF_2 and Ge detectors, and two time delays: between β ray and γ ray from BaF_2 (fast timing spectra) and between β ray and γ ray from the Ge detector. The latter parameter is used to correct for the random events in the system, but occasionally it also provides an additional selection criterion when μs isomers are present in the decay. The data is stored on a hard disk or an optical disk of a PC computer and analysed off-line. With the help of efficient and specialized software a complete data analysis is performed on a PC computer of the 486 DX-33 class. For example sorting involving 150 gates and 100 Mb of data is performed in $\sim$ 6 min. The use of inexpensive PC computers for both data acquisition and analysis gives the fast timing $\beta\gamma\gamma(t)$ system a great portability to perform measurements at various experimental facilities.

In the first stage of the off-line analysis one divides the whole data set into smaller batches and checks each batch for the long-term stability of electronics. Typically a single measurement lasts about 3-5 days; although in a selective case of crucial yet weak activity, it can last up to 8 weeks. Furthermore, since the timing measurements on nuclei of interest and several calibration runs are intermingled and together last up to a few months, one must ensure good stability of electronics over that period of time. Our experience from the $\beta\gamma\gamma(t)$ measurements performed since 1986, first at the TRISTAN separator at Brookhaven National Laboratory in USA and now also at the OSIRIS separator at Studsvik in Sweden, indicates that although the very sensitive timing electronics is in a constant state of fluctuation, yet the effects of such fluctuations are quite manageable. As for the timing stability in particular, the absolute position of the prompt curve fluctuates by a few picoseconds from measurement to measurement, yet the shape of the curve remains

unaffected within the precision of a measurement. This effect has been repeatedly tested and remains a cornerstone of the method. In other words, the relative prompt curve, which is deduced in a set of calibration runs, becomes an absolutely calibrated prompt curve if it is shifted (up or down) to overlap with at least one prompt point internal to the decay (i.e. a reference transition which is part of the decay). This point can be at any E_γ energy.

Energy signal from the BaF_2 crystal represents another critical parameter susceptible to fluctuations. The scintillation light from BaF_2 has a weak fast component and a strong slow component. The fast component is used to define the excellent fast timing property of this crystal, while the slow one defines the energy signal. However, while the fast component remains unaffected, the yield of the slow one is strongly dependent on the crystal temperature. Consequently, a good temperature stability is required not only due to the temperature sensitive electronics (like the CFD and TAC units) but also due to the properties of BaF_2. The quality of the fast timing signal also depends on the condition of the photocathode in the fast photomultiplier as it slowly deteriorates with time.

Although the efficiency of the triple coincidence system is quite low, yet it provides very pure timing spectra (a judicious selection of a γ ray in the Ge detector can result in a single transition in the BaF_2 crystal) and a large number of combinations of gates to select from. The latter leads to lifetime measurements of many levels in the same decay and frequently to the same lifetime measurement but via different decay paths. Consequently a cross-check of results and procedures is always present. Furthermore, since within the same decay all the results are equally affected by fluctuations of the electronics, the problem of instability of electronics is eliminated down to the level of $\sim$ 1 ps. In addition, the off line analysis offers an opportunity to identify and eliminate a batch of data strongly affected by such fluctuations. Our experience shows that a carefully selected and tested electronics offers a remarkable long-term stability.

The following example illustrates a few possible ways to analyse timing data from triple coincidence measurement (for a more complete discussion see [1,3]). In this example we have four excited states (A–D) characterized by the respective mean lives, $\tau_A - \tau_B$, and five deexciting transitions (a–e). The first step would be to measure the mean life of the level B, τ_B, given by the difference between centroid shifts of two time spectra — each involving coincidences between β ray (in the β detector) and the same transition "a" in BaF_2. The first spectrum is generated by coincidence with transition "c" in the Ge detector, thus its time delay is: $\tau_C + \tau_B + \tau_A$. The second spectrum is in coincidence with transition "d" in the Ge detector, thus its time shift is only: $\tau_C + \tau_A$. In this case the same β feeding is responsible for both time spectra, and by the virtue of selecting exactly the same transition in BaF_2 there is no need for a prompt curve determination.

In the second step, we determine the mean life of level "A" by subtracting from the time spectrum where transition "e" is selected in the Ge detector and transition "a" in BaF_2, a reversed time spectrum: where transition "a" is selected in the Ge detector while transition "e" in BaF_2. The first gives a time delay $\tau_D + \tau_A$, while the second gives only τ_D. Similarly in this case, the same β feeding is responsible

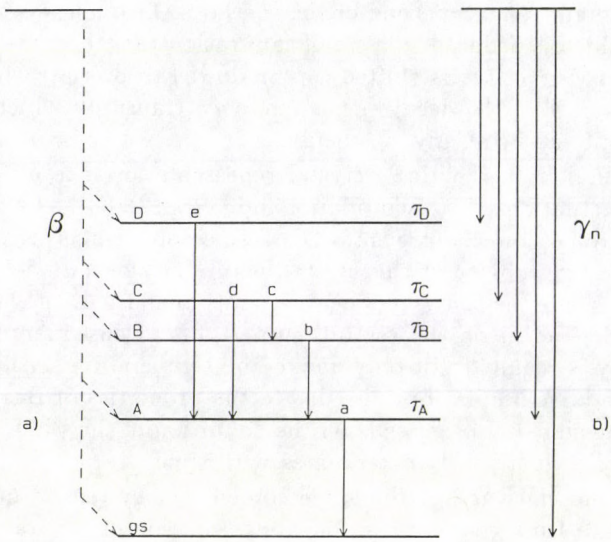

Fig. 1. Schematic decay scheme for (a) β^- decay and (b) (n,γ) capture

for both time spectra, but now we need the prompt curve to correlate the time shifts at energies "e" and "a". Note, however, that only their relative shift is used. Thus only the shape of the prompt curve (relative prompt) is needed and not its absolute position. In other words, the lifetime of level "A" was measured relatively to the lifetime of level "D", which exact value is not relevant in this case.

Similarly, one can deduce the lifetime of level "A" by using a pair of transitions "d" and "a" instead of "e" and "a". Since different time spectra are used in this process it provides a cross-check of results. This case is not as simple as the previous one. Note, that gates are set on the full energy peaks in both: the Ge and BaF_2 detectors. Such procedure is always simple in the auxiliary Ge detector, but not in the fast timing BaF_2. For example: in the BaF_2 spectrum gated by transition "a" in the Ge detector, the full energy peak of transition "d" will sit on a relatively flat background defined by a Compton tail of transition "e" which is of much higher energy. If the ratio of the peak intensity to the background contribution is large, we can reliably correct the timing peak for the background impurity. Otherwise one gets a large uncertainty. This example only illustrated some opportunities given by the triple coincidence timing measurement.

Research opportunities

The $\beta\gamma\gamma(t)$ measurement covers more than 4 orders of magnitude in the lifetime regime from about 1 ps to about 30 ns. The lower limit is defined by the precision of the measurement (typically $\pm 1 - 2$ ps, occasionally ± 0.4 ps), while the upper limit is given by the range of the TAC unit which is usually set to 100 ns.

So far the $\beta\gamma\gamma(t)$ method is the only one capable of systematic studies of level lifetimes down to a few picosecond range for a vast range of neutron-rich nuclei. This situation will change when the radioactive beams and Coulomb excitation in the inverse kinematics will become a standard measurement. However, this latter method will be complementary, since even for the stable nuclei, which can be probed by a variety of techniques, the $\beta\gamma\gamma(t)$ method provides simple means to measure lifetimes for a range of levels strongly populated in the β decay that are otherwise difficult to probe.

Another advantage offered by this time-delayed method is that a level lifetime is measured directly and often with high precision. In particular, if a lifetime is obtained by fitting a well-defined slope then the precision can reach a level of 0.3–0.4 %, thus setting standards for other methods to match. (In principle even better precision is possible, say $\sim$ 0.1 %, but it requires a time consuming calibration of TAC and a very high level of statistics that is not possible within typical limits of the in-beam runs.)

So far a few hundred level lifetimes have been measured with the $\beta\gamma\gamma(t)$ method at the fission product mass separators TRISTAN at BNL/USA and OSIRIS at Studsvik/Sweden, as well as at the JOSEF facility at Jülich/Germany. These results, mainly from the neutron-rich $A = 100$ and $A = 140$ regions, provide crucial information on several local regions of special interest and challenge theoretical interpretation of nuclear structure. A review of some of these results is given in [5].

So far a complete run, that involved the decay of interest and the calibration sources, was performed at one facility. However, special calibration procedures were recently established, which allow to perform fast timing measurements at the PSB-ISOLDE/CERN and at the IGISOL separator at Jyväskylä/Finland while time calibrating the system at the OSIRIS separator. Thus new opportunities have been created by expanding the timing measurements to the $A < 70$, $A = 120$ and $A > 160$ regions, as well as to the proton-rich side by using the β^+ decay.

Fast timing $\gamma_n\gamma\gamma(t)$ method

It is quite natural that the $\beta\gamma\gamma(t)$ method is being modified for use with the (n,γ) spectroscopy which itself represents a powerful tool of research for nuclei along the line of stability. The modified method, labelled here $\gamma_n\gamma\gamma(t)$, is based on some similarity of the β decay and the decay following thermal neutron capture. In the first case, the β particle feeding one of the low-lying states triggers unambiguously the starting timing detector while the cascading γ rays trigger the stopping timing detector. In the second case (see Fig. 1), the high energy of the γ rays deexciting the neutron capture states to the low-lying levels (typically $E_\gamma \approx 5 - 10$ MeV) provides a natural selection mechanism for the starting signal since the transitions deexciting the low-lying states have energy below 3 MeV.

The main problem of this system is a drop in efficiency since the detection of high-energy γ rays is much less efficient than the detection of β rays. Thus, one or more BaF_2 crystals have to be used with an expected size of about 3–4 cm in diameter and height. In order to avoid energy summing effects from the low-energy transitions, these crystals must be well shielded by a thick layer of Pb.

The fast timing $\gamma_n\gamma\gamma(t)$ method as sister to the established $\beta\gamma\gamma(t)$ method will inherit the general features of the calibration and data analysis procedures. Importantly, it would fill a critical gap in the lifetime techniques used in the (n,γ) spectroscopy since the Doppler Shift Attenuation Method is limited to lifetimes below 1 picosecond, while a standard coincidence technique using a set of Ge detectors is capable of lifetime measurements of the order of 1 nanosecond or longer. The $\gamma_n\gamma\gamma(t)$ measurements are expected to cover the same energy range, 30–3000 keV, and time domain, $\sim$ 1 ps – 30 ns, as the $\beta\gamma\gamma(t)$ ones.

Conclusion

The basic features of the $\beta\gamma\gamma(t)$ method have been discussed with the emphasis on the inherited reliability and precision, as well as build in procedures of cross-checking the results. The $\beta\gamma\gamma(t)$ method represents the first sophisticated and versatile time-delay method and thus, naturally, it has opened new and exciting opportunities for the systematic lifetime measurements for the far off stability nuclei.

It is proposed to modify this method for use with the powerful (n,γ) spectroscopy. The modified method, labelled $\gamma_n\gamma\gamma(t)$, will be based on some similarity of the β decay and the decay following thermal neutron capture and naturally it will inherit the general features of the calibration and data analysis procedures. Importantly, it would fill a critical gap in the lifetime techniques used in the (n,γ) spectroscopy.

A Pilot Project is being pursued by a Studsvik–Budapest collaboration with the aim to test the proposed $\gamma_n\gamma\gamma(t)$ method. If successfully tested it should become a standard tool at the international centre for neutron-based scientific research at the KFKI reactor in Budapest.

Acknowledgements

The contribution from other co-authors of the $\gamma_n\gamma\gamma(t)$ project, namely: T. Belgya, G. Molnár, (both of whom introduced the idea of this modified method and initiated the project) and B. Fogelberg are gratefully acknowledged. The authors thank the organizers of this Workshop for creating an excellent environment for scientific discussion and an exchange of ideas. This work was supported in part by the Swedish Natural Science Research Council.

References

1. H. Mach, R. L. Gill and M. Moszyński, Nucl. Instr. Meth., *A280*, 49, 1989.
2. M. Moszyński and H. Mach, Nucl. Instr. Meth., *A277*, 407, 1989.
3. H. Mach, F. K. Wohn, G. Molnár, K. Sistemich, John C. Hill, M. Moszyński, R. L. Gill, W. Krips and D. S. Brenner, Nucl. Phys., *A523*, 197, 1991.
4. H. Mach, Bull. Am. Phys. Soc., *31*, 1235, 1986.
5. H. Mach, B. Fogelberg, M. Hellström, D. Jerrestam and L. Spanier, in Proc. of the XXVII Zakopane School of Physics, eds. R. Broda, W. Meczyński and J. Styczeń, Acta Physica Polonica, *B24*, 71, 1993.

Acta Physica Hungarica 75 (1–4), pp. 55–60 (1994)

NUCLEAR SPECTROSCOPY WITH SLOW NEUTRONS

H. G. BÖRNER

Institut Laue-Langevin
BP 156, 38042 Grenoble Cedex, France

The aim of nuclear spectroscopy is to study nuclear excitations with a view to improving our knowledge of the forces play within the nucleus. Many complementary techniques have been developed to unravel the complex interplay of these forces and it is usually the combination of several experimental approaches such as the study of radioactive decay, transfer reactions, neutron capture, inelastic scattering, Coulomb excitation and other charged particle reactions which allows us to construct detailed level schemes and interpret them. We will concentrate, within the frame of this Workshop on the advanced instrumentation of the neutron capture gamma-ray spectroscopy, which plays an important and specific role in the comprehensive testing of nuclear models. Neutron capture gamma-ray spectroscopy now employs very sophisticated techniques to study nucear structure. The combination of precise measurements of primary gamma transitions with the precision obtained to date with curved and flat crystal and conversion electron spectrometers has considerably extended the possibilities in the study of nuclear structure. The nearly perfect resolution obtained with the most modern double flat crystal spectrometers allows the measurement of lifetimes of excited nuclear states in the range $< 10^{-12}$ s via the observation of the Doppler broadening of gamma rays due to the recoil of the nucleus following emission of a primary gamma ray.

Introduction

Neutron capture gamma ray spectroscopy is by now a classical tool within the rich variety of different approaches used to elucidate nuclear structure. The (n, γ)-reaction is — in contrast to most other approaches — non-selective in terms of nuclear structure and thus offers the possibility of studying very comprehensive sets of low lying nuclear states, as long as their spins are not too far away from those of the capture states. In neutron capture the product nucleus is formed at an excitation energy equal to the binding energy of the captured neutron. Energies, intensities, multipolarities and branching ratios of the subsequent successive deexcitations between the nuclear states are important quantities which then help us to understand the nature of the states involved.

1. Neutron capture

As neutral particles even very slow neutrons are able to approach the atomic nucleus. Within the range of the strong interaction ($\sim$ 1 fm) the neutron may be captured by a nucleus A, forming an excited nucleus $(A+1)^*$.

Neutron capture can be studied in laboratory experiments — where it has become an important tool for nuclear structure studies — but we all know that it plays also a very important role in astrophysics, where it is responsible for specific

processes in stellar nucleosynthesis: Heavier elements (see for instance [1,2] and references therein) are produced essentially by neutron capture during the so-called r-process ("rapid") and s-process ("slow").

It is evident that to date the strongest available laboratory neutron sources are high flux beam reactors. In the following the discussion of neutron capture reactions will be limited to the capture process of slow neutrons (as obtained with a reactor) followed by the emission of gamma rays or internal conversion electrons.

2. Gamma ray measurements following neutron capture

Thermal neutrons are generally captured as s waves. In a typical reactor neutron energy distribution p-wave capture for keV neutrons is also of some importance. The capture state will decay — among others — via the emission of gamma rays. In the decay discrete, low lying, states are populated either directly from the capture state (primary gamma rays of mostly dipole character) or via gamma ray cascades (secondary gamma rays of which the overall majority has dipole or quadrupole character), involving many different routes of population, each consisting of a multiplicity of typically 3 to 4.

2.1. Measurement of primary gamma rays

The energy of primary gamma rays is given by $E_\gamma = (S_n + E_n - E_x - E_{recoil})$ whereby a nucleus of mass M recoils with an energy of $E_{recoil} = E^2_{\gamma/2Mc^2}$. Knowing the neutron binding energy S_n and the neutron energy E_n, and measuring E_γ, one can directly deduce the energies E_x of the populated excited states. This is an attractive feature of primary gamma transitions. Additionally, on the basis of the known capture spin, spin/parity assignments of the levels populated can be made. In thermal or single resonance capture due to the statistical fluctuations in the primary intensities [3,4] those are limited, based mainly on the assumption that the primary transitions are essentially of dipole character. This problem can be overcome by applying the technique of average resonance capture [5] (ARC). Here the fluctuations are considerably attenuated as a function of the number of resonances which contribute to the capture and the intensities can be grouped according to the multipolarities of the primary γ-rays and the possible capture spins. In certain cases (averaging over a great number of resonances, good measuring statistics) it is hence possible to identify complete sets of excited states in certain ranges of spins and energies of excitation. This possible aspect of completeness for a given set of levels has proven to be an extremely powerful tool [6,7] when comparing the experimental results with theoretical predictions [7].

The applicability of the ARC method depends on the number of resonances available for averaging making it less suitable for medium heavy and not at all for light nuclei. Therefore it is not astonishing that to date the most extensive level schemes of light and medium mass nuclei have been obtained through thermal capture studies at high flux reactors. The completeness obtained in these studies was such that sensitive tests of statistical models of nuclear levels and electromagnetic transitions became possible [8].

2.2. Measurement of secondary gamma rays

As has been discussed above the measurement of primary gamma rays yields important information on the existence of excited states up to an excitation energy of 1.5 to 2.5 MeV. However, as primary transitions have dipole character in their large majority, only a relatively small "window" around the capture spin will be populated. Also, it has to be kept in mind that, from the pure fact that a level is populated, one learns only little about its structure (nonselectivity). Such insight and the knowledge of a more extended range of spins must come from a detailed study of the secondary transitions populating and depopulating a specific level.

It is evident that the spectra obtained for secondary gamma rays, following the (n,γ)-reaction, are extremely complex and rich (nonselectivity). The resolving power of classical Ge or Ge(Li) arrangements is suitable for very light nuclei which exhibit a not too high level density. In semi-conductor measurements external target arrangements or in-pile target arrangements yield comparable sensitivity. Compton suppressed systems are widely used. Count rates are in both cases essentially limited by dead time problems. The in-pile arrangement yields the additional possibility for the study of multiple neutron capture.

Detailed and comprehensive level schemes — also for medium heavy and heavy nuclei — can be constructed when advantage is taken of high resolution gamma spectrometers. The simultaneous demands for both, high resolution and high efficiency, are ideally met by employing crystal diffraction spectrometers at in-pile target facilities installed at high flux reactors. Different types of such instruments using curved and flat crystal geometries, respectively, have been used in the past. An overview of those may be found in [9].

The energy resolution of a crystal diffraction spectrometer is obtained from Bragg's law: $\Delta E_\gamma = (2d/nhc)E_\gamma^2 \cos\theta_B \Delta\theta$, where n is the order of reflection, d is the lattice constant, θ_B is the Bragg angle, and $\Delta\theta$ is the angular width of the reflection of a γ line with energy E_γ. $\Delta\theta$ results from the convolution of various functions [10,11] describing the source geometry and crystal size, the regularity of crystal and curvature, and the diffraction pattern which depends on the crystal structure and which is described by the Dynamical Diffraction Theory [12].

The crystals (Si and Ge) available to date for spectroscopy with flat crystals show excellent agreement between theoretically and experimentally determined lineshape and are very close to being "perfect". The measured lineshape can be described by the diffraction pattern folded with a very small amount of extra-broadening (the so-called excess width, for more details see for instance [13]). This allowed to obtain a FWHM of ~ 3 eV for photons of 1 MeV.

The situation for bent crystal spectrometers is more complicated as the dominating contributions to the linewidth $\Delta\theta$ are the source width itself in the direction of the dispersion of the spectrometer and the crystal bending width. Nevertheless a resolution of $\Delta E/E \approx 3 \cdot 10^{-5}$ has already been obtained.

Curved and flat crystal modes are complementary. The first one allows very complete spectroscopy accompanied by high resolving power, the second one allows a detailed study of specific transitions by pushing the experimentally achieved

resolving power close to theoretical limits.

Many (n,γ) facilities are available at a big variety of research reactors. At most of these reactors, classical Ge-gamma spectrometers, using internal or external target geometries, are installed. For those who use crystal spectrometers the ILL Grenoble is currently the only one where access to the complementary flat [14] and bent crystal [15] modes exists.

2.3. Conversion electron spectroscopy

Complementary to (n,γ)-studies the investigation of the (n,e^-) reaction on internal conversion electrons yields crucial information for the interpretation of excited nuclear states. Due to the high sensitivity achieved with modern beta spectrometers the conversion electron spectra are of a complexity comparable to (n,γ) spectra. The high resolution required to disentangle these often very dense spectra is commonly achieved by magnetic spectrometers. An example for such a spectrometer is the BILL electron spectrometer which was previously installed at the ILL [16].

Both gamma rays and conversion electrons are a consequence of the electromagnetical interaction and the conversion coefficient $\alpha = I_e/I\gamma$ is in the majority of cases independent of the nuclear structure. Only for strongly hindered transitions may the emission probability depend significantly on the nuclear structure "penetration effect". The knowledge of the multipolarity of transitions allows to determine spin and parities of levels deduced from secondary transitions and is absolutely necessary to deduce the respective transition strength, the quantity which allows for a most crucial comparison of different theoretical models.

2.4. Coincidence and gamma–gamma correlation experiments

Coincidence data are extremely useful in combination with and as a complement to high resolution measurements. Whereas the high energy resolution and the extremely large dynamical intensity range (five orders of magnitude) of crystal spectrometer data are indispensable for the successful application of the energy combination method, only the observation of coincident transitions allows a definite level assignment, especially at high excitation energy (high level density) where the probability of incorrect energy combinations increases rapidly.

Angular correlation measurements are another useful method for assigning spins and parities to nuclear levels produced after thermal neutron capture. The technique requires an extremal target arrangement and is especially powerful when applied at neutron guides which allow to combine a relatively high incident neutron flux with low gamma background. Such positions use an integrated neutron flux of typically $\sim 10^8$ n/cm^{2}s.

The angular distribution function depends on the spin sequence of the levels and the multipolarities of the deexciting transitions involved. A very typical correlation is observed for 0-2-0 cascades and it is therefore not astonishing that angular correlation measurements have been especially successful in the identification of spin 0 states.

3. Lifetime measurements of nuclear excited states following thermal neutron capture

The knowledge of the lifetimes of excited nuclear levels is known to be of vital importance for the elucidation of nuclear structure phenomena. In the case of gamma decay the range of observed lifetimes spans over many orders of magnitude from $\sim 10^{-18}$ s to days. Many different lifetime measuring methods have been developed, each particularly well suited for a specific range of lifetimes and/or nuclei. However, there exist only a few methods which can be applied directly after neutron capture. Up to date most of such measurements consisted in the determination of delayed gamma–gamma coincidences. Such techniques allow for a search of isomeric states with halflives > 0.5 ns. Especially well known is the so-called "centroid shift method" which has been applied in many experiments with thermal neutrons [17]. Most of the nuclear excited states display, however, lifetimes in the picosecond to femtosecond range. The lifetime-measuring technique GRID (Gamma Ray Induced Doppler broadening [13,18]) gives access to exactly that critical range.

This method is based on the fact that each gamma ray emitted by a nucleus induces a recoil. Any gamma rays emitted successively during the time the nucleus is recoiling are then subject to Doppler shifts. Depending on the lifetime of the intermediate nuclear state involved, the nucleus may have more or less slowed down when the gamma ray, following the recoil, is emitted. The measured Doppler broadened lineshape cames information on the relation between the lifetime and the slowing down time. The latter in effect serves as the clock allowing the determination of the lifetime. The Doppler shifts following gamma recoil are in the order of eV rather than keV and therefore an instrumental resolution of up to 3 orders of magnitude better than the one available with solid state detectors is needed. This is the case for Two Axes Flat Crystal Spectrometers.

4. Example for a very complete neutron capture gamma ray study

When going to higher excitation energies the level schemes extracted from the (n, γ)-reaction become more and more "incomplete". This behaviour is amplified with increasing level density, e.g. with increasing mass of the nucleus.

Nevertheless, up to a certain excitation energy, decay schemes can be produced which are complete in a given spin range which will depend on the capture spin.

The nucleus ^{168}Er is an ideal experimental choice for such a study. The target nucleus, ^{167}Er, has a large thermal cross-section of 650 b and an advantageously high spin of 7/2. As a result a very broad range of levels with spins reaching from 0 up to 10 can be populated in the gamma ray cascade process and has been observed [19]. Precision measurements of the gamma spectrum with curved crystal spectrometers have revealed more than 700 transitions up to an energy of 2.5 MeV with intensities spanning five orders of magnitude. Close to 150 levels have been identified below 3 MeV. Many lifetimes of excited states above 1.5 MeV have been

measured [20] using the GRID method. As a consequence of this study the nucleus ^{168}Er has become the most complete and extensive test of the limits of applicability of models describing low-lying collective excitations (e.g. the geometrical model of Bohr and Mottelson [21], the IBM [22] and the quasiparticle-phonon nuclear model (QPNM) [23]). Additional gamma–gamma coincidence data [24] gave direct evidence for the existence of states proposed by the Ritz combination method and allowed to further extend the level scheme in the region above 2 MeV. These results lead to an interest beyond the detailed level assignments as they affect conclusions concerning the quality of the K quantum number.

References

1. W. A. Fowler, Rev. Mod. Phys., *56*, 149, 1984.
2. H. V. Klapdor et al, Z. Phys., *A299*, 213, 1981.
3. L. M. Bollinger and G. E. Thomas, Phys. Rev., *C2*, 1951, 1970.
4. L. M. Bollinger, Phys. Rev., *C3*, 2071, 1971.
5. L. M. Bollinger, Proc. Conf. Slow Neutron Capture Gamma-Ray Spectroscopy, *ANL-7282*, 523, 1968.
6. R. E. Chrien, N. Y. Acad. Sci., *44*, 40, 1980.
7. R. F. Casten, D. D. Warner, M. L. Stelts, W. F. Davidson, Phys. Rev. Lett., *45*, 1077, 1980.
8. T. v. Egidy et al., AIP Conf. Proc. No.125, 1985, 305, ed. S. Raman.
9. T. v. Egidy, Proc. 3rd Int. Symp. on Neutron Capture γ-Ray Spectroscopy and Related Topics, Brookhaven 1978, eds R. E. Chrien and W. Kane, Plenum Press, New York, 1979, p. 37.
10. O. Schult, Z. Phys., *158*, 444, 1960.
11. O. W. B. Schult, Kerntechnik *7*, 444, 1960.
12. W. H. Zachariasen, Theory of X-ray Diffraction in Crystals, John Wiley and Sons, Inc. New York, p. 145.
13. H. G. Börner and J. Jolie, J.Phys. G, *19*, 217, 1993.
14. E. G. Kessler, G. L. Greene, M. S. Dewey, R. D. Deslattes, H. G. Börner, F. Hoyler, J.Phys. G, *14*, 167, 1988.
15. H. R. Koch, H. G. Börner, J. A. Pinston, W. F. Davidson, J. Faudou, R. Roussille, O. W. B. Schult, Nucl. Inst. Meth., *175*,401, 1980.
16. W. Mampe et al., Nucl. Instr. Meth., *128*, 585, 1975.
17. P. Petkov et al., Nucl. Instr. Meth., *A271*, 617, 1988.
18. H. G. Börner et al., Phys. Lett., *215B*, 45, 1988.
19. W. F. Davidson et al., J. Phys., *67*, 455, 1981.
20. H. G. Börner et al., Phys. Rev. Lett., *66*, 691, 2837, 1991.
21. A. Bohr and B. R. Mottelson, Nucl. Structure, Vol. 2, 1975.
22. A. Arima and F. Iachello, Ann. Phys. NY, *111*, 201, 1978.
23. V. G. Soloview, Z. Phys. *A324*, 393, 1986.
24. A. Jungclaus et al., Phys. Rev. *C49*, 88, 1994.

Acta Physica Hungarica 75 (1–4), pp. 61–69 (1994)

INTENSE SOURCES FOR POSITRON RESEARCH

W. TRIFTSHÄUSER

Institut für Nukleare Festkörperphysik
Universität der Bundeswehr München
85577 Neubiberg, Germany

Positron annihilation is a well-established method in solid state physics and material science. The positron being a very sensitive probe, can give very precise information on the momentum distribution of electrons in metals and alloys as well as on lattice defects in crystals. Starting with the energy distribution of positrons from a radioactive decay, the current development is directed more to monoenergetic positrons of variable energy and of high intensity. The impact of intense positron beams is straightforward: a decrease of the counting time. There are various possibilities and approaches to realize intense positron beams. The aim is to obtain a beam intensity in the order of $\sim 10^{10}$ positrons/s. Parallel to the instalment of intense positron beams, the development of positron microscopes is pursued.

1. Introduction

Experiments in physics involving the interaction of matter with antimatter are fascinating. Positron annihilation has advanced to a standard method for studies of microscopic properties in condensed matter [1]. The field of low energy positron physics has expanded significantly in recent years. This includes not only particle and atomic physics but most extensively the areas associated with condensed matter and material science. The interaction of a positron with solids shows a wide variety [2]. The use of positrons as very sensitive probes in solid state physics can be roughly divided into various categories: as electronic structure probes, as lattice defect probes, as surface and interface probes and as microbeam probes. The advances in positron annihilation methodology from the use of a broad inhomogeneous beam of high–energy positrons from radioactive nuclei to a narrow homogeneous beam of monoenergetic positrons of variable energy, expanded the object of studies from only bulk properties to surfaces and depth specified near surface layers and interfaces, and even further to three-dimensionally specified microscopic regions. In the following Sections I will primarily discuss these very recent and current developments involving positron beams as well as intense positron sources.

2. High intense positron beams

2.1. LINAC based beams

The first intense positron sources were based on the pair production from bremsstrahlung resulting from an electron linear accelerator (LINAC) [3]. It has been established that one electron in the energy range of 50–120 MeV can produce

$10^{-7} - 10^{-6}$ positrons. The operation mode of most LINACs is a pulsed one with a repetition rate dependent on the particular accelerator used ($\sim$ 50–1000 Hz).

Therefore, the produced positrons possess also a pulsed structure, but for many experiments a continuous beam would be preferable. At the university of Gent, Belgium, a Penning trap is used to create a quasi-continuous beam from the 300 Hz pulses with a pulse length of 3 μs (Fig.1).

The typical intensity obtained is 4×10^7 slow positrons per second with 1.3×10^5 positrons per pulse [4]. A real continuous beam could be obtained only with a continuous operating LINAC. Such a device of a superconducting LINAC is being considered at the Research Centre at Rossendorf, Germany. A very serious problem, however, remains with all LINAC based beams: the heating and the cooling of the target.

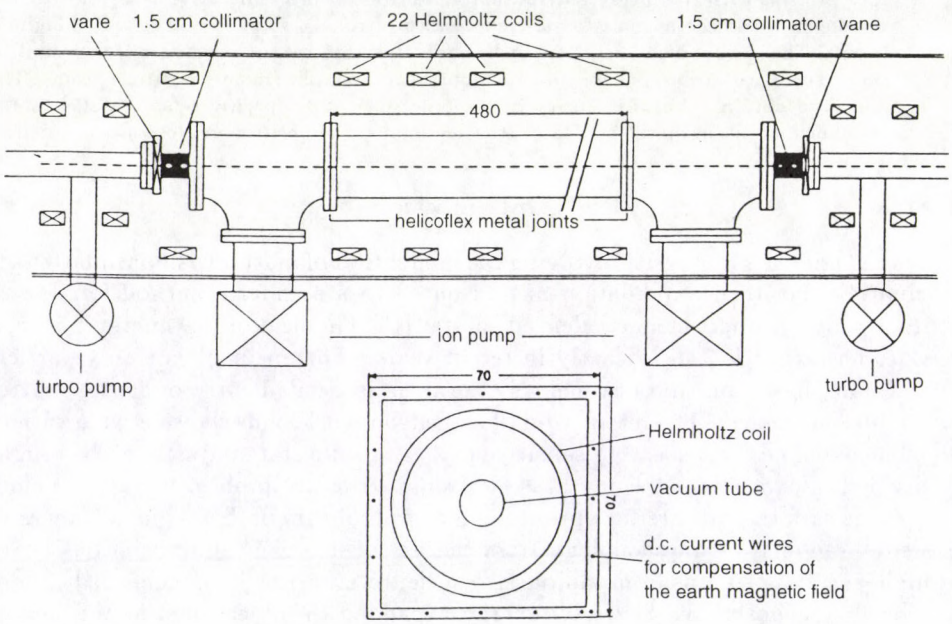

Fig. 1. Lay-out of the installation of the Penning trap [4]

2.2. Reactor based beams

In contrast to the LINAC based beams, a reactor based beam will deliver a constant intensity of positrons. Two different approaches are being pursued: activation of a short-lived positron emitting isotopes, i.e. ^{64}Cu, by thermal neutrons near the reactor core or pair production from high energy gamma rays after capture of thermal neutrons in ^{113}Cd. The first method is being used by Van Veen and his group at the reactor at Delft. The set-up is shown in Fig. 2. ^{64}Cu is produced by

neutron capture of ^{63}Cu and decays with a half-life of 12.8 hours. After a certain time, depending on the neutron flux, an equilibrium positron intensity is obtained. The details of the copper source arrangement are given in Fig. 3. For a thermal neutron flux of 8×10^{12} $cm^{-2}s^{-1}$ the group at Delft estimate a positron yield of about 10^6 positrons per cm^2 and second. With an emitting area of 1000 cm^2 the total intensity would then be 10^9 positrons per second, and after remoderation a positron beam of 1 cm diameter and $2 \times 10^8 e^+$ s^{-1} is being expected [5].

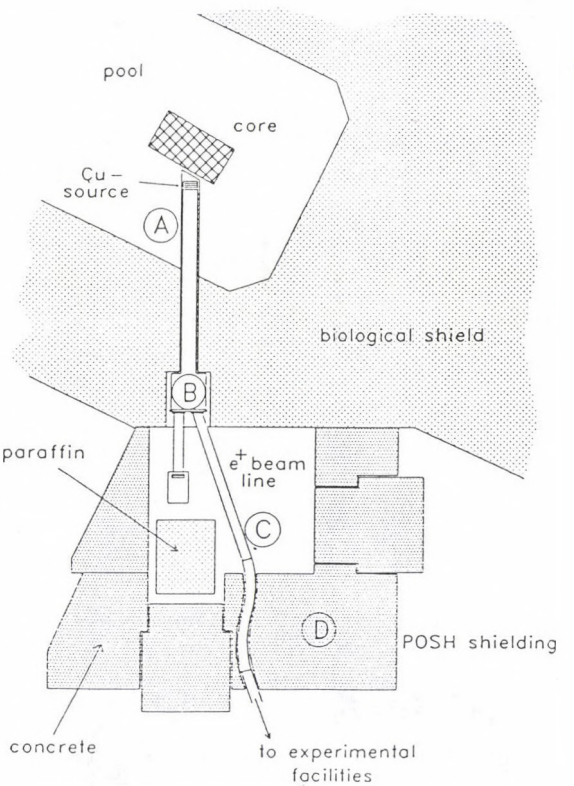

Fig. 2. Schematic setup of the Delft positron beam facility. A: vacuum tube with copper source and magnetic guiding system. B: deflection part of positron beam and neutron beam stop. C: positron beam guiding, bending and monitoring. D: shielding of neutron and gamma radiation

The alternative method is being applied by my group in Munich. The basic principle is shown in Fig. 4. Tungsten foils annealed at about 2800 K in ultra high vacuum ($\sim 10^{-9}$ mbar) are simultaneously used as converters for the pair production as well as moderators to obtain low energy positrons. The arrangement, as shown schematically in Fig. 5, consists of an array of concentric double rings surrounded by a one end closed cylinder of cadmium ($\sim$ 1 mm thick). The device will be placed in a beam tube parallel to the reactor core. For a thermal neutron

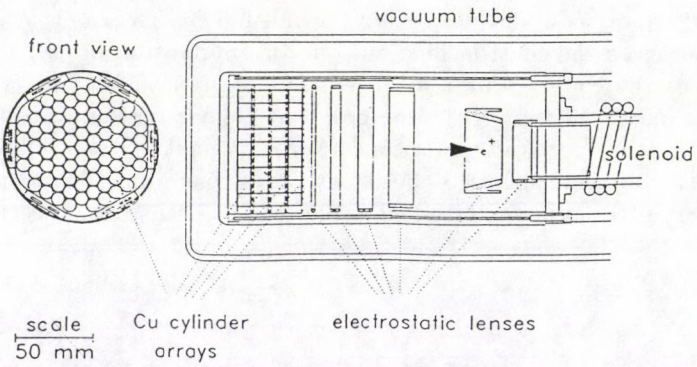

Fig. 3. Details of the Delft source configuration

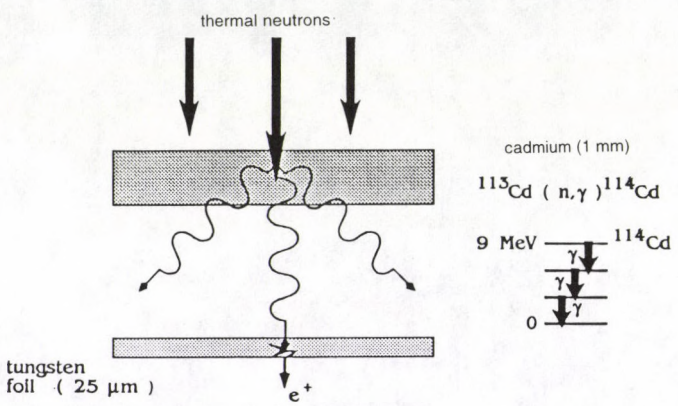

Fig. 4. Principle of the reactor based positron production

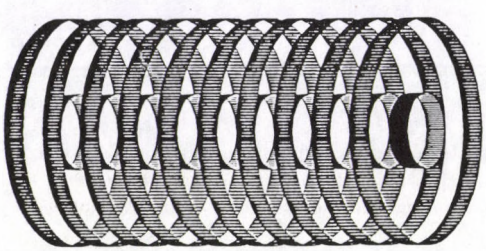

Fig. 5. Schematic array of the tungsten foils

flux of 10^{12} $cm^{-2}s^{-1}$ and the given geometry of the foils, a positron intensity of $10^{10}e^+$ s^{-1} is expected, and after remoderation a positron beam of about 5 mm diameter and 10^9e^+ s^{-1} will result. This device will be the prototype for a similar but more intense beam system at the high flux reactor at the ILL at Grenoble, France [6].

2.3. Radioactive isotope based beam

A new concept for obtaining an intense positron beam has been proposed by Taqqu and collaborators at the Paul Scherrer Institute at Villingen, Switzerland [7-9]. An intense primary positron source (i.e. ^{18}F with half-life 109 min) is deposited as a thin layer on a very thin foil. The schematics are shown in Fig. 6. Confining electric and magnetic fields force the high energy positrons to return towards the foil and are slowed down by passing through the foil. Just before they reach an energy to be completely stopped in the foil, they are directed away from the confinement onto a moderator, and the slow emitted positrons are extracted from the confining field and form a slow positron beam. In a first step it is reported that a confinement efficiency of 82 % was obtained, and with a solid neon moderator, an overall conversion efficiency of 41 % is quoted [10]. This work is still in progress and may result in a high intense low energy positron beam with various user facilities.

3. Pulsed positron beam

During recent years radio frequency pulsed slow positron beams have proved to be a very valuable tool for positron lifetime spectroscopy in the near surface region [11]. The underlying principle is to compress a continuous beam of monoenergetic positrons to pulses of about 150 ps or less at the target by means of special radio frequency components. The timing signals for the lifetime measurements are derived from the corresponding clock signal of the radio-frequency system and the annihilation photons, respectively. The Munich Pulsed Low Energy Positron System was the first such operating system [12]. Later a similar device was installed in Japan [13]. During the last year the Munich beam has been upgraded in order to improve the quality of the lifetime spectra, to achieve a higher efficiency and to enable temperature dependent measurements [14]. This improved version is shown in Fig. 7. An additional preparation chamber has been added for in situ annealing of the single crystalline tungsten moderator. A pre-buncher was installed right after the moderator. This pre-buncher compresses the DC beam to pulses of about 1.7 ns width by applying a saw-tooth voltage of frequency of 50 MHz to a drift tube. About 45 % of all moderated positrons are thus shifted into a time interval of 2 ns. With a 16 mCi ^{22}Na source the count rate is 130 counts per second and the measured beam diameter at the target is 4 mm for beam energies up to 15 keV and increases to about 5 mm for the maximum energy of 28 keV. Apart from the possibility to perform lifetime measurements as a function of the positron energy and hence of the penetration depth of the positron into the specimen, there is another important advantage compared to conventional lifetime measurements: no restriction of the positron intensity because of accidental coincidences. Since one of the timing signals is taken from the radio-frequency system, the final coincidence rate is equivalent to the counting rate of the detector for the annihilation photons (singles rate). This count rate can then be increased almost unlimited if an appropriate intense primary positron source can be used (Section 2.2).

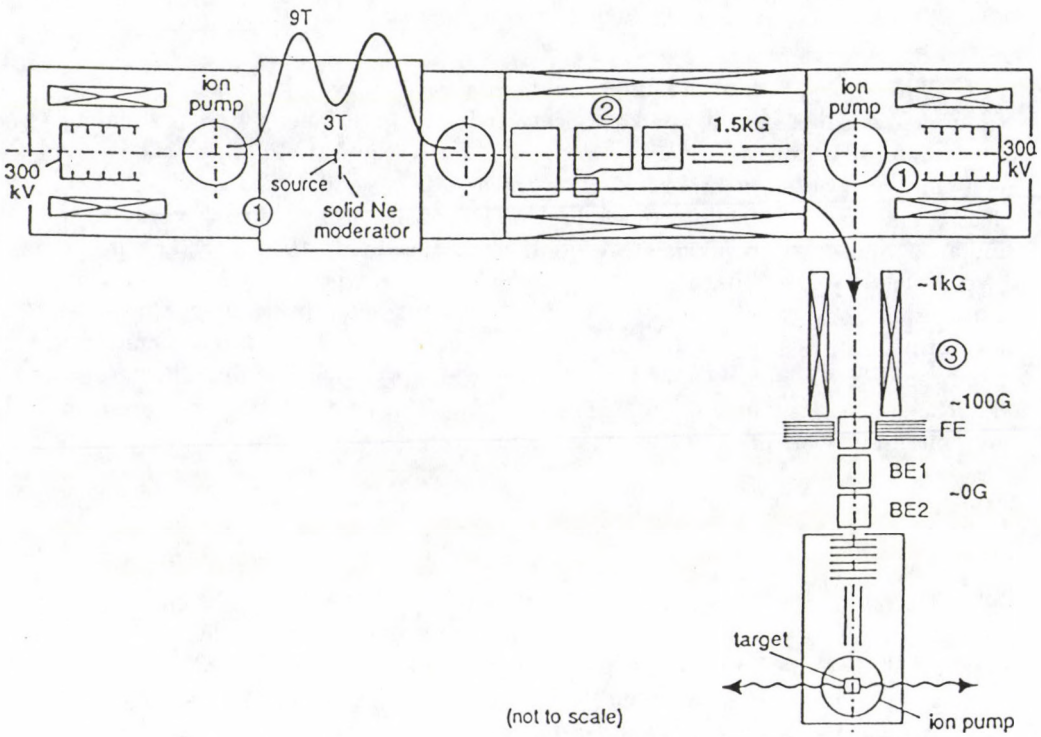

Fig. 6. Layout of the beam production stages (300 kV – 300 kV distance ~ 10 m, 300 kV – target distance ~ 6m). 1 = premoderation stage (~ 5 – 10 keV) and 2 = extraction/final moderation stage (~ eV). They produce the high intensity slow positrons. 3 = field extraction/microbeam formation stage. It is forming the slow positrons into a usable microbeam in field free space. FE = field extraction, BE = brightness enhancement

4. Scanning positron microscope

A logical advancement of a pulsed positron beam of several mm diameter and of variable energy [12] leads to a scanning beam but of microscopic dimensions. About two years ago we started in Munich and Trento, financially supported by the European Community, the project of a scanning positron microscope (SPM). Based on our pulsed beam system [14], a second and cooled moderator is added, so that the final beam diameter at the target will be 1 μm. The schematic set-up is shown in Fig. 8. Integrated in the system is an electron beam which is focussed and scanned with the same electron optics as the positron beam. The electron beam will give a topological picture of the specimen surface whereas the positron beam will give depth profiles of near surface microscopic regions. From the characteristic positron lifetimes, defects as well as defect structures can be distinguished from defect-free regions. We see applications of the scanning positron microscope in various areas of material science and for microelectronic devices.

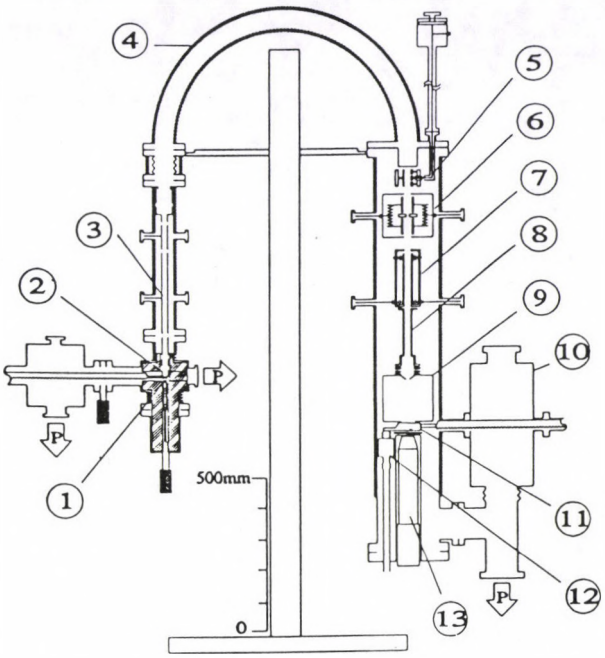

Fig. 7. Schematic layout of the upgraded pulsed positron beam system; 1: ^{22}Na source with tungsten shielding, 2: tungsten single crystal (1 μm) transmission moderator, 3: pre-buncher (saw tooth), 4: magnetic guiding field (7 mT), 5: pre-chopper, 6: main chopper (sine wave), 7: main buncher (sine wave), 8: drift tube, 9: Faraday cage, 10: preparation chamber, 11: specimen holder (cooling and heating), 12: cryostat for liquid N_2, 13: scintillator (BaF_2) and photomultiplier

5. Positron annihilation angular correlation

In metals and alloys, the measurement of the angular correlation of positron annihilation radiation gives detailed information on the electron–positron momentum density especially if positron sensitive detectors are used [15]. Facilities with such devices are in Europe at the Universities in Geneva, Bristol and Munich. Because of the almost negligible contribution of the positron to the total momentum, the electron momentum density can be determined and the Fermi surface can be deduced [16]. Single crystals are required to investigate the electron momentum distributions. Size and quality of the crystals are very important parameters. For some compounds, i.e. high T_c superconductors, it is difficult to grow high quality single crystals of appropriate dimensions in order to be measured with conventional positron sources from radioactive isotopes. Positrons from such sources penetrate on the average 100–200 μm into the specimen before they annihilate. This means that the thickness of the single crystals has to be of the same order of magnitude. Intense and narrow positron beams would be an obvious advantage for the investi-

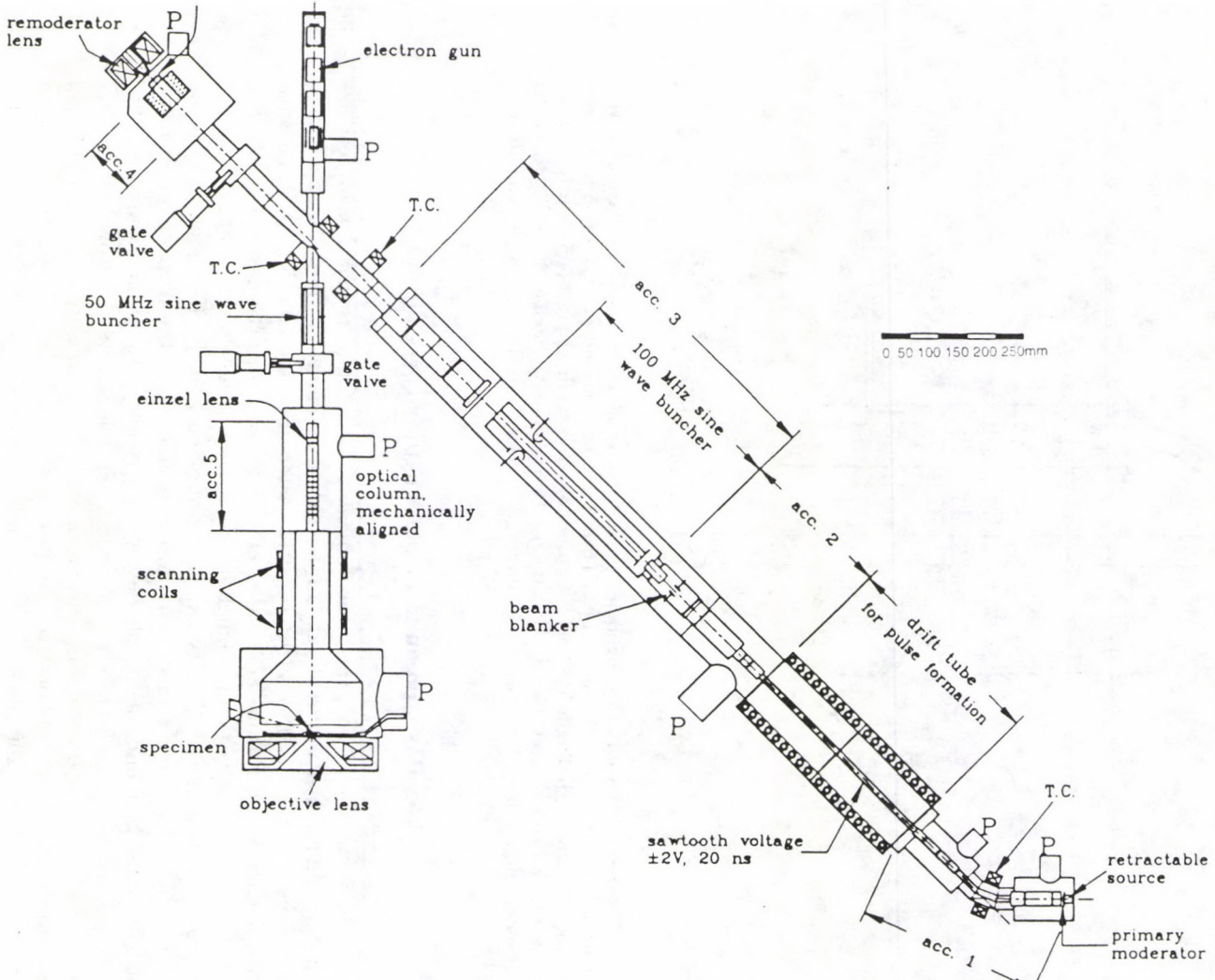

Fig. 8. Schematic layout of the scanning positron microscope. P – pumping port, T. C. – toroidal coils (quadrupole coils for correction and alignment coils will be added if necessary)

gation of solids. In some materials it is difficult or even impossible to prepare large enough single crystals of good quality and with stable homogeneous composition. Monoenergetic positrons of variable energy (up to 50 keV) would allow selection of penetration depth and hence angular correlation measurements in samples made of films grown by epitaxy on substrates.

6. Conclusions and outlook

It is quite obvious that the future direction of positron research is towards intense positron beams of variable energy and micrometer dimensions. The current efforts are following the trend of this development. In not too far away time such systems will come into operation and will open up a new kind of experiments and exciting applications to solid state physics and materials science. Many fascinating experiments with positrons remain to be done.

References

1. W. Triftshäuser, Microscopic Methods in Metals, Topics in Current Physics, *40*, Springer, Berlin–Heidelberg–New York, 1986, pp. 249–295.
2. P. J. Schultz and K. G. Lynn, Rev. Mod. Phys., *60*, 701, 1988.
3. R. H. Howell, R. A. Alvarez and M. Stanek, Positron Annihilation, Arlington, 3–7 April 1982, North-Holland Publishing Company, Amsterdam, 1982, pp. 860–862.
4. D. Segers, J. Paridaens, M. Dorikens and L. Dorikens-Vanpraet, Nucl. Instr. Meth. A, 1993.
5. A. Van Veen, H. Schut, P. E. Mijnarends, L. Seijbel and P. Kruit, Slow Positron Beam Techniques for Solids and Surfaces, Conference Proceedings 303, American Institute of Physics, New York, 1994, pp. 354–364.
6. W. Triftshäuser, G. Kögel, K. Schreckenbach and B. Krusche, Helv. Phys. Acta, *63*, 378, 1990.
7. D. Taqqu, Helv. Phys. Acta, *63*, 442, 1990.
8. U. Zimmermann, Helv. Phys. Acta, *63*, 435, 1990.
9. W. B. Waeber, Helv. Phys. Acta, *63*, 448, 1990.
10. W. B. Waeber, M. Shi, D. Gerola, U. Zimmermann and D. Taqqu, PSI Annual Progress Report 1993, Annex IIIA, pp. 19–22, Würenlingen 1994.
11. G. Kögel, D. Schödlbauer, W. Triftshäuser and J. Winter, Phys. Rev. Lett., *60*, 1550, 1988.
12. D. Schödlbauer, P. Sperr, G. Kögel and W. Triftshäuser, Nucl. Instr. Meth. in Phys. Res., *B34*, 258, 1988.
13. R. Suzuki, Y. Kobayashi, T. Mikado, H. Ohgaki, M. Chiwaki, T. Yamazaki and T. Tomimasu, Japan J. Appl. Phys., *303B*, 532, 1991.
14. P. Willutzki, J. Störmer, G. Kögel, P. Sperr, D. T. Britton, R. Steindl and W. Triftshäuser, Meas. Sci. Technol., *5*, 1, 1994.
15. A. A. Manuel and M. Peter, Helv. Phys. Acta, *63*, 397, 1990.
16. S. S. Rajput, P. Pradsad, R. M. Singru, W. Triftshäuser, A. Eckert, G. Kögel, S. Kaprzyk and A. Bansil, J. Phys.: Condens. Matter, *5*, 6419, 1993.

Acta Physica Hungarica 75 (1–4), pp. 71–76 (1994)

PROMPT-GAMMA ACTIVATION ANALYSIS AND APPLICATIONS IN INDUSTRY, ENVIRONMENT AND MEDICINE

RICHARD M. LINDSTROM

Inorganic Analytical Research Division, National Institute of Standards and Technology Gaithersburg, MD 20899, USA

Neutron capture reactions are in use for chemical analysis at nearly every research reactor. The (n,γ) reaction involves simple physics and penetrating radiations, and for that reason is free of systematic errors common to analytical methods which rely on dissolving the sample. A number of elements not easily determined by conventional neutron activation analysis can be measured through the gamma rays emitted promptly on neutron capture. New applications are being found, especially with recent advances in instrumentation and neutron beam shaping.

Introduction

Chemical analysis by means of the gamma rays emitted promptly upon neutron capture was first performed by Fermi in 1934. Since the late 1970s, prompt-gamma activation analysis (PGAA) has become a routine tool at several reactor centers worldwide for the nondestructive measurement of a number of elements of importance to science, engineering, and medicine. The measurement is performed by inserting a sample into a neutron field (most successfully, an external neutron beam from a research reactor) and measuring the gamma-ray emissions with a germanium detector. Neutrons from ^{252}Cf, other isotopic sources, or neutron generators have been valuable in field applications such as on-line analysis of coal and ores and in explosives detection. Gamma spectra of impressive quality have been collected in deep boreholes in exploring for mineral resources. These field applications have been surveyed [1] and will not be discussed in this paper. Useful reviews of the PGAA technique have been published in the proceedings of the symposium series on capture gamma rays and related topics [2–6].

History and uses of PGAA

PGAA was investigated by a number of pioneers in the late 1960 and early 1970s, using low-powered reactors and NaI or small Ge gamma detectors [7–11]. It was used for the analysis of metals in alloys and ores with modest neutron beams [12,13]. The technique reached its modern form with high neutron flux and large high-resolution detectors at Los Alamos (with the sample inside the reactor) [14], by the University of Maryland group at the National Bureau of Standards [15,16], at the University of Missouri [17] and at McMaster University [18].

PGAA has been applied to the analysis of major and trace elements in standard rocks [19–21], oceanic sediments [22], and construction materials [23], boron in borosilicate glass [24], essential and toxic elements in foods [25,26] and dietary supplements [27]; boron, cadmium, and other elements in environmental materials [28–30]; rare earths in airborne particulates [31]; boron in tissue for neutron capture cancer therapy [32,33]; and many other materials. A bibliography compiled in 1984 listed 522 papers using PGAA in the literature [34].

PGAA with guided neutron beams

Even with neutron beams from 5–20 MW reactors, quantitative multielement PGAA measurements usually require many-hour irradiations because of the large distance, typically 50 cm, between the sample and the detector and therefore a low efficiency (< 0.001 from geometry alone) for detecting the gamma rays from the sample. The utility of the technique is further limited by high background for a number of elements. Even with filtration, reactor neutron beams which are nominally thermal contain substantial fluxes of epithermal and fast neutrons, which must be slowed before they are stopped in the shielding. This almost inevitably calls for hydrogenous materials surrounding the samples, and hence a high background count rate for the H capture line at 2223 keV. Stray neutrons also interact with other elements commonly used in the apparatus such as B, C, N, Al, Fe, and Pb, raising the background for these elements. Neutron scattering from hydrogenous samples can make the variability of this background an important systematic error in PGAA [35].

In the past few years, advances in neutron transport have made intense beams of purely slow neutrons, either thermal or cold, available for analytical purposes at several reactor laboratories: Grenoble [11–21], Kyoto [32], Jülich [36], NIST [37], JAERI [38, 39] and Texas [40]. These facilities will soon be joined by systems at Budapest [41], Cornell [42], and BARC [43]. Guided beams are well suited to PGAA because they are entirely free of fast neutrons and gamma rays. For this reason, a compact, lightweight assembly made with ^{6}Li (which emits no gamma rays on neutron capture) can be used, with no need for thermalizing material, to shape and stop the beam [32,36]. As a result the capture-gamma background is lower and the detector can be closer to the sample, and hence guided beams give much better signal:noise ratios in PGAA than conventional collimated beams. The detectability of hydrogen, in particular, has been improved from milligrams to micrograms [44].

The ability to measure small quantities of hydrogen nondestructively has had numerous applications. Information from PGAA has been essential in interpreting neutron scattering measurements of C_{60} and derivatives [45]. The largest number of future applications may be in metallurgy and other branches of materials science. As a part of a larger program, we have spatially mapped the hydrogen content of a compressor blade from a jet engine which had failed in service [46].The detection limit for hydrogen in metals is now below 10 μg [39], and incremental improvements in prospect can be expected to reduce it to 1 μg or better. An important application will be the determination of H and D in polymers in support of neutron scattering.

Future developments

Much research remains to be done in order to fully exploit the opportunities of PGAA. Recent experiments have made clear that the analytical signal depends on the details of the neutrons' interactions with the sample, notably on the scattering power [47, 48] and even on the temperature of the sample [49]. Neglect of scattering can lead to errors of more than a factor of two in the analytical results. Because cross-sections are larger at low velocity, the magnitude of the effect is larger for cold neutrons than thermal [50]. This is of course especially important for the analysis of polymers and biological materials.

A barrier to the widespread application of PGAA is the need for each laboratory to prepare its own table of sensitivities, by irradiating standards of each element to be determined in that individual system. This problem has been eased for conventional (delayed) neutron activation by employing a composite, dimensionless nuclear constant called k_0, the value of which can be measured and transferred between laboratories much more accurately than the conventionally tabulated cross-sections [51]. The same approach can be applied to PGAA, especially with cold neutrons [52, 53], providing that the effects of neutron scattering within the sample can be controlled, compensated, or corrected for.

Interpretation of capture gamma-ray spectra from complex matrices is not straightforward. The spectra often contain several hundred significant peaks ranging in energy up to the nitrogen capture line at 10.829 MeV. Baselines under the peaks are not smooth because of this complexity, and often also because the number of counts in each channel is small. Unlike the case of radioactive decay, which involves only the lowest few nuclear levels, published tables of capture gamma-ray signatures of the elements [54] are not and never can be complete because of the very large number of levels populated by neutron capture [55,56]. Several analytical laboratories have prepared tables of the most useful capture gamma rays and their most important interferences [16,57,58].

Advances in instrumentation are opening new areas of application of neutron capture gamma rays. It has been appreciated for many years that the complexity of capture spectra can be greatly simplified by Ge–Ge coincidence counting [59]. Although coincidence methods are commonly used in nuclear structure studies, they have not yet found application in PGAA (except for Compton suppression and pair spectrometry [16,38]). There is good reason for this: with 15 % detectors spaced 50 cm from the sample the coincidence efficiency has not been high enough for chemical analysis. Furthermore, acquiring and processing data at a useful rate in a 16384 × 1684-channel coincidence measurement requires a fast computer, large memory and mass storage, and well-designed algorithms for storage, display, and extraction of compositional information. The rapid growth in computer capabilities, the production of high-quality neutron beams, and the availability of efficient gamma detectors now makes Ge–Ge coincidence PGAA appear feasible.

Another paper in this symposium discusses recent progress in forming small-diameter neutron beams with high flux [60-62]. A gain in neutron flux of more than an order of magnitude within a spot 0.5 mm diameter has been demonstrated.

With such small beams, the analysis of much smaller samples or the mapping of heterogeneous samples on a millimeter scale become possible.

Very recently PGAA has been combined with neutron reflectometry [63]. In this measurement, resonantly amplified neutron standing waves were set up in a sandwich of 150 nm polymer films with a 5 nm Gd layer in the center. At appropriate incident angles below the critical angle for reflection from the Ni substrate the neutrons were absorbed by the Gd, with a corresponding drop in the reflectivity. Because of this resonance and because the gamma detector is less than 1 cm from the sample, the sensitivity for generation and detection of the 182 keV Gd capture gamma was very high: 0.02 photopeak counts per neutron. This phenomenon is analogous to total-reflection X ray fluorescence (TXRF), and is likely to have similar applications in the study of films and surfaces.

Conclusion

Chemical analysis through prompt neutron-capture gamma rays has found numerous uses in science and technology. Recent advances in engineering neutron beams give promise of new and unique applications.

Acknowledgments

I am indebted to numerous colleagues at NIST and elsewhere for continual stimulation, and for performing most of the work mentioned here. In addition to those cited in the References, I thank R. F. Fleming, G. P. Lamaze, and J. J. Rush for many essential discussions about the properties and uses of neutrons.

References

1. R. J. Rosenberg, Prompt Gamma Neutron Activation Analysis in Borehole Logging and Industrial Process Control, IAEA-TECDOC-537, IAEA, Vienna, 1990.
2. R. C. Greenwood, in Proc. 3rd Internat. Symp. Neutron-Capture Gamma Ray Spectroscopy and Related Topics, eds R. E. Chrien, W. R. Kane, Plenum, New York, 1979, p. 441.
3. D. L. Anderson, W. H. Zoller, G. E. Gordon, W. B. Walters, R. M. Lindstrom, in Neutron-Capture Gamma-Ray Spectroscopy and Related Topics, Inst. Phys. Ser. 62, eds T. von Egidy, F. Gonnenwein, B. Maier, Inst. Physics, London, 1982, p. 655.
4. M. D. Glascock, in Neutron-Capture Gamma-Ray Spectroscopy and Related Topics, eds T. von Egidy, F. Gonnenwein, B. Maier, Inst. Physics, London, 1982, p. 641.
5. R. E. Chrien, in Neutron Radiative Capture, eds B. J. Allen et al, Pergamon, Oxford, 1984, p. 187.
6. R. M. Lindstrom, D. L. Anderson, in Capture Gamma-Ray Spectroscopy and Related Topics – 1984, AIP Conf. Proc. 125, ed. S. Raman, Am. Inst. Physics, New York, 1985, p. 810.
7. W. G. Lussie, J. J. L. Brownlee, in Proc. Conf. Modern Trends in Activation Analysis, Texas A & M, College Station, 1965, p. 194.
8. T. L. Isenhour, G. H. Morrison, Anal. Chem. *38*, 162, 1966.
9. T. L. Isenhour, G. H. Morrison, Anal. Chem. *38*, 167, 1966.
10. R. C. Greenwood, Trans. Am. Nucl. Soc. *10*, 28, 1967.
11. R. Henkelmann, H. J. Born, J. Radioanal. Chem., *16*, 473, 1973.
12. M. R. Najam, M. Anwar-ul-Islam, A. F. M. Ishaq, J. A. Mirza, A. M. Khan, I. H. Qureshi, J. Radioanal. Chem., *27*, 115, 1975.

13. M. Heurtebise, J. A. Lubkowitz, J. Radioanal. Chem., *31*, 503, 1976.
14. E. S. Gladney, D. B. Curtis, E. T. Jurney, J. Radioanal. Chem., *46*, 299, 1978.
15. M. P. Failey, D. L. Anderson, W. H. Zoller, G. E. Gordon, R. M. Lindstrom, Anal. Chem., *51*, 2209, 1979.
16. D. L. Anderson, M. P. Failey, W. H. Zoller, W. B. Walters, G. E. Gordon, R. M. Lindstrom, J. Radioanal Chem., *63*, 97, 1981.
17. A. G. Hanna, R. M. Brugger, M. D. Glascock, Nucl. Instrum. Methods, *188*, 619, 1981.
18. M. D. Higgins, M. G. Truscott, D. M. Shaw, M. Bergeron, G. H. Buffet, J. R. D. Copley, W. V. Prestwich, in Use and Development of Low and Medium Flux Research Reactors, eds O. K. Harling, L. Clark, P. von der Hardt, MIT Press, Cambridge, 1983, p. 690.
19. M. D. Higgins, Geostand. Newslett., *8*, 31, 1984.
20. D. L. Anderson, Y. Sun, M. P. Failey, W. H. Zoller, Geostand. Newslett., *9*, 219, 1985.
21. S. A. Kerr, R. A. Oliver, P. Vittoz, G. Vivier, F. Hoyler, T. D. MacMahon, N. I. Ward, J. Radioanal. Nucl. Chem., *113*, 249, 1987.
22. Y. Minai, C. Yonezawa, M. Hoshi, Y. Ito, T. Tominaga, in Proc. 5th Internat. Symp. Advanced Nucl. Energy Res., JAERI, Tokai, 1993, p. 818.
23. D. L. Anderson, G. E. Gordon, E. A. Lepel, Canad. J. Chem., *61*, 724, 1983.
24. J. E. Riley, Jr., R. M. Lindstrom, J. Radioanal. Nucl. Chem., *109*, 109, 1987.
25. D. L. Anderson, W. A. Cunningham, E. A. Mackey, Biol. Trace Elem. Res., *27*, 613, 1990.
26. D. L. Anderson, W. A. Cunningham, G. H. Alvarez, J. Radioanal. Nucl. Chem., *167*, 139, 1993.
27. S. C. Hight, D. L. Anderson, W. C. Cunningham, S. C. Capar, W. H. Lamont, S. A. Sinex, J. Food Composit, Anal., *6*, 121, 1993.
28. J. M. Ondov, W. H. Zoller, I. Olmez, N. K. Aras, G. E. Gordon, L. A. Ranticelli, K. H. Abel, R. H. Filby, K. R. Shah, R. C. Ragaini, Anal. Chem., *47*, 1102, 1975.
29. E. S. Gladney, E. T. Jurney, D. B. Curtis, Anal. Chem., *48*, 2139, 1976.
30. M. S. Germani, I. Gokmen, A. C. Sigleo, G. S. Kowalczyk, I. Olmez, A. M. Small, D. L. Anderson, M. P. Failey, M. C. Gulovali, C. E. Choquette, E. A. Lepel, G. E. Gordon, W. H. Zoller, Anal. Chem. *52*, 240, 1980.
31. M. E. Kitto, D. L. Anderson, G. E. Gordon, I. Olmez, Environ. Sci. Technol., *26*, 1992.
32. T. Kobayashi, K. Kanda, Nucl. Instrum. Methods, *204*, 525, 1983.
33. T. Matsumoto, O. Aizawa, T. Nozaki, T. Sato, Atomkernenergie, *44*, (Suppl.) 566, 1984.
34. M. D. Glascock, A Literature Survey of Elemental Analysis by Neutron-Induced Prompt Gamma-Ray Spectroscopy and Related Topics, Univ. of Mo, Columbia, 1984.
35. D. L. Anderson, E. A. Mackey, J. Radioanal. Nucl. Chem., *167*, 145, 1993.
36. R. M. Lindstrom, R. Zeisler, M. Rossbach, J. Radioanal. Nucl. Chem., *112*, 321, 1987.
37. R. M. Lindstrom, R. Zeisler, D. H. Vincent, R. R. Greenberg, C. A. Stone, D. L. Anderson, D. D. Clark, E. A. Mackey, J. Radioanal. Nucl. Chem., *167*, 121, 1993.
38. C. Yonezawa, A. K. H. Wood, M. Hoshi, Y. Ito, E. Tachikawa, Nucl. Instrum. Methods, *A329*, 207, 1993.
39. C. Yonezawa, Anal. Sci., *9*, 185, 1993.
40. B. W. Wehring, K. Ünlü, J.-Y. Kim, C. Rios-Martinez, Trans. Am. Nucl. Soc., *68*, 161, 1993.
41. G. Molnár, Zs. Révay, Á. Veres, A. Simonits, H. Rausch, J. Radioanal. Nucl. Chem., *167*, 133, 1993.
42. D. D. Clark, C. G. Oullet, A. G. Atwood, Trans. Am. Nucl. Soc., *64*, 227, 1991.
43. S. Gangadharan, pers. comm., 1988.
44. R. M. Lindstrom, R. L. Paul, D. H. Vincent, R. R. Greenberg, J. Radioanal. Nucl. Chem., *180*, 275, 1994.
45. D. A. Neumann, J. R. D. Copley, R. L. Cappelletti, W. A. Kamitakahara, R. M. Lindstrom, K. M. Creegan, D. M. Cox, W. J. Romanow, N. Coustel, J. P. McCauley, Jr., N. C. Maliszewskyj, J. E. Fischer, A. B. Smith III, Phys. Rev. Lett., *67*, 3808, 1991.
46. R. L. Paul, R. M. Lindstrom, Rev. Progr. Quant. Nondestr. Eval., *13*, 1619, 1994.
47. J. R. D. Copley, C. A. Stone, Nucl. Instrum. Methods, *A281*, 593, 1989.
48. E. A. Mackey, J. R. D. Copley, J. Radioanal. Nucl. Chem. *167*, 127, 1993.

49. E. A. Mackey, Biol. Trace Elem. Res., 1994 (in press).
50. R. L. Paul, E. A. Mackey, J. Radioanal. Nucl. Chem., *181*, 321, 1994.
51. F. De Corte, A. Simonits, A. De Wispelaere, J. Hoste, J. Radioanal. Nucl. Chem., *113*, 145, 1987.
52. R. M. Lindstrom, R. F. Fleming, R. L. Paul, E. A. Mackey, in Proc. Internat. k_0 Users Workshop, ed. F. De Corte, Univ. Gent, 1992, p. 121.
53. M. Rossbach, F. De Corte, in Proc. Internat. k_0 Users Workshop, ed. F. De Corte, Univ. Gent, 1992, p. 125.
54. M. A. Lone, R. A. Leavitt, D. A. Harrison, Atom. Nucl. Data Tables, *26*, 511, 1981.
55. S. Raman, T. A. Walkiewicz, S. Kahane, E. T. Jurney, J. Sa, S. Gácsi, J. L. Weil, K. Allaart, G. Bonsignori, J. F. Shriner Jr., Phys. Rev. C, *43*, 521, 1991.
56. A. V. Ignatyuk, J. L. Weil, S. Raman, S. Kahane, Phys. Rev. C, *47*, 1504, 1993.
57. M. E. Kitto, Ph. D. Thesis, Univ. of Md., College Park, 1987.
58. M. D. Glascock, Tables for Neutron Activation Analysis, 2nd ed., Univ. of Mo, Columbia, 1989.
59. H. H. Bolotin, in Neutron-Capture Gamma-Ray Spectroscopy, ed. N. Ryde, IAEA, Vienna, 1969, p. 15.
60. D. Mildner, H. Chen, G. Downing, V. Sharov, J. Neutron Res., *1*, 1, 1993.
61. Q. F. Xiao, H. Chen, D. F. R. Mildner, R. G. Downing, R. E. Benenson, Rev. Sci. Instr., *64*, 3252, 1993.
62. D. F. R. Mildner, H. Chen, R. G. Downing, V. A. Sharov, Q. F. Xiao, this Workshop, Acta Phys. Hung., *75*, 177, 1994.
63. H. Zhang, P. D. Gallagher, S. K. Satija, R. M. Lindstrom, R. L. Paul, T. P. Russel, P. Lambooy, E. J. Kramer, F. S. Bates, Phys. Rev. Lett., 1994 (in press).

Acta Physica Hungarica 75 (1–4), pp. 77–89 (1994)

STUDY OF LIQUIDS AND SOLUTIONS

M.-C. BELLISSENT-FUNEL

Laboratoire Léon Brillouin (CEA-CNRS)
CE-Saclay
91191 Gif-sur-Yvette Cedex, France

The aim of this contribution is to present a critical review of what has been achieved on the structure of liquids and solutions and to highlight the capabilities and developments of neutron scattering in this field of research. A great variety of simple to complex systems has been investigated with the aim of obtaining a full microscopic description of the structure. Selected examples of high precision experiments demonstrate the performance of the neutron scattering determination of interaction potentials, intermolecular structures, and partial structure factors of complex systems. The isotopic substitution method is illustrated by the application to the study of the solvation of ions in aqueous and non aqueous solutions.

Introduction

There have been numerous structural studies of liquids and solutions with increasing degree of accuracy due to the high performance of spectrometers available at the steady neutron sources like the Reactor Orphée (LLB-Saclay) and the High Flux Reactor (ILL-Grenoble).

Much progress has been performed in the experimental results obtained at the neutron spallation sources such as ISIS (RAL, Didcot) and IPNS (Argonne, USA). In the case of studies of liquids, coherent neutron scattering gives information about the relative positions and motions of different particles in the liquid,. From this scattering, we determine the structure factor $S(Q)$ of the liquid which leads to the static pair-correlation function $g(r)$. From measurements of the coherent neutron scattering at low values of momentum transfer, we can observe effects due to excitations of cooperative modes in the liquid. Incoherent neutron scattering depends on the motion of a single particle; this allows to study diffusive motions and vibrational density of states and, in this field of investigations, neutrons appear as a unique probe.

The purpose of this short review is not to give a catalogue of liquids which have been investigated during the past years because there are many recent reviews and books about this subject [1–8]. I will present here only selected examples where neutron scattering is particularly powerful and I will give some fields of interest which need to be developed during the next years.

Basic theory

The differential scattering cross-section [9] per unit solid angle and unit interval of outgoing energy E' of the scattered neutron by an assembly of particles is given in the first Born approximation by the following equation:

$$\frac{d^2\sigma}{d\Omega dE'} = AS(Q,\omega), \tag{1}$$

where $\hbar\omega = (k_0^2 - k_1^2)/2m$ is the energy transfer, and m, $\mathbf{k}_0$, $\mathbf{k}_1 = \mathbf{k}_0 - \mathbf{Q}$ are respectively the mass, the initial and final wavevectors of the scattered neutrons, $\hbar\mathbf{Q}$ is the momentum transfer. A depends only on the properties of the particles of the system.

$S(Q,\omega)$ is the dynamic structure factor which is the Fourier transform (FT) over $\mathbf{r}$ and t of the Van Hove pair distribution in space and time $G(\mathbf{r},t)$ which describes the correlation between the presence of a particle in position $\mathbf{r}' + \mathbf{r}$ at time $t' + t$ and the presence of a particle in position $\mathbf{r}'$ at time t', averaged over r'.

We consider scattering due to the nuclear interaction between neutrons and the nuclei of the scattering system.

• If b is the scattering length of the N nuclei assumed all identical, the cross-section is written as:

$$\frac{d^2\sigma}{d\Omega dE'} = \frac{b^2 N k_1}{2\pi\hbar k_0} \int \exp[i(\mathbf{Q}\cdot\mathbf{r} - \omega t)] G(\mathbf{r},t) d\mathbf{r}dt. \tag{2}$$

If the nuclei of the scattering system have a nonvanishing spin, the equation (2) assumes b to be spin-independent.

The G function splits into the G_s and G_d parts

$$G(\mathbf{r},t) = G_s(\mathbf{r},t) + G_d(\mathbf{r},t). \tag{3}$$

G_s describes the correlation between positions of one and the same particle at different times. G_d refers to pairs of distinct particles (the subscripts s and d stand for "self" and "distinct", respectively).

• For nuclei with a spin-dependent scattering length, or for nuclei belonging to different isotopes.

Equation (2) is replaced by

$$\frac{d^2\sigma}{d\Omega dE'} = \frac{N}{2\pi\hbar}\frac{k_1}{k_0} \int \exp[i(\mathbf{Q}\cdot\mathbf{r} - \omega t)] \Gamma(\mathbf{r},t) d\mathbf{r}dt \tag{4}$$

with the spin- or isotope-dependent scattering lengths used in the definition of $\Gamma(\mathbf{r},t)$ which is written as:

$$\Gamma(\mathbf{r},t) = \overline{b^2} G_s(\mathbf{r},t) + (\overline{b})^2 G_d(\mathbf{r},t),$$

where b is any of the b_j's of the system and the average is taken over the spin states of the corresponding particle.

From $G = G_s + G_d$, the differential scattering cross-section is written as:

$$\frac{d^2\sigma}{d\Omega dE'} = \frac{d^2\sigma_{\text{coh}}}{d\Omega dE'} + \frac{d^2\sigma_{\text{incoh}}}{d\Omega dE'}, \tag{5}$$

$$\frac{d^2\sigma_{\text{coh}}}{d\Omega dE'} = \frac{(\bar{b})^2 N}{2\pi\hbar}\frac{k_1}{k_0}\int \exp[i(\mathbf{Q}\cdot\mathbf{r} - \omega t)]G(\mathbf{r},t)d\mathbf{r}dt, \tag{6}$$

$$\frac{d^2\sigma_{\text{incoh}}}{d\Omega dE'} = \frac{\{\overline{b^2} - (\bar{b})^2\}N}{2\pi\hbar}\frac{k_1}{k_0}\int \exp[i(\mathbf{Q}\cdot\mathbf{r} - \omega t)]G_s(\mathbf{r},t)d\mathbf{r}dt. \tag{7}$$

Equations (6) and (7) are the so-called coherent and incoherent scattering cross-sections. The separation of elastic and inelastic scattering which applies to Eq. (6) can be performed for Eq. (7) by considering the limit of G_s for $|t| \to \infty$. In the static approximation, $|\mathbf{Q}| = \frac{4\pi}{\lambda}\sin\theta$ with λ the neutron wavelength and 2θ the diffraction angle, (see Fig. 1) and integrating with respect to E', the differential coherent and incoherent cross-sections per unit solid angle are respectively:

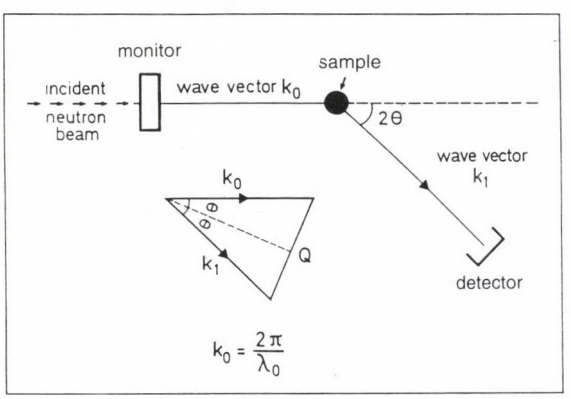

Fig. 1. General scheme of neutron scattering studies

$$\frac{d^2\sigma_{\text{coh}}}{d\Omega} = (\bar{b})^2 N\left\{1 + \int \exp(i\mathbf{Q}\cdot\mathbf{r})g(\mathbf{r})d\mathbf{r}\right\} = (\bar{b})^2 N S(\mathbf{Q}), \tag{8}$$

where $S(\mathbf{Q})$ is the structure factor of the system

$$\frac{d^2\sigma_{\text{incoh}}}{d\Omega} = \{\overline{b^2} - (\bar{b})^2\}N. \tag{9}$$

The incoherent cross-section no longer depends on the structure of the system.

If the diffusion is isotropic which is normally the case for disordered systems as liquids:

$$S(Q) = 1 + \rho_0 \int_0^\infty [g(r) - 1] \frac{\sin Qr}{Qr} 4\pi r^2 dr, \tag{10}$$

where $\rho_0 = N/V$, the number density

$$g(r) = 1 + \frac{1}{2\pi^2 r \rho_0} \int_0^\infty Q[S(Q) - 1] \sin Qr dQ, \tag{11}$$

where $g(r)$ gives the probability of finding an atom at a distance r from a reference atom at the origin.

From the determination of $S(Q)$, the instantaneous distribution (within 10^{-13} to 10^{-15} s) of the pairs of atoms in the system is obtained by Fourier transform; this definition applied to the local order of the first neighbours and next-nearest neighbours in the system.

In the case of polyatomic systems (molecular liquids, aqueous solutions, liquid alloys, it is customary to introduce the partial structure factors $S_{\alpha\beta}(Q)$ and the partial pair correlation functions $g_{\alpha\beta}(r)$, relative to all the pairs of atoms of the system, and the total pair correlation function is written as:

$$g(r) = \sum_{\alpha\beta} c_\alpha c_\beta b_\alpha b_\beta g_{\alpha\beta}(r), \tag{12}$$

where c_α, c_β are the atomic concentrations and b_α, b_β the neutron coherent scattering lengths of the various pairs of atoms.

A change of isotope, if it affects significantly the scattering length, will change the weight of the partials and provide a way of identifying them. Since isotopic substitution alters only very weakly the physico-chemical properties and pair interactions, it will be a powerful tool to mark an atom and study its environment.

In the following we give examples of structure factor determinations and we will focus on the more recent results proper to neutron scattering using a specialized and adapted sample environment equipment (high and low temperature devices, pressure cells, etc ...) and using the isotopic substitution method, allowing to reach the local environment around an identified atom.

Selected examples of $S(Q)$ determinations

Monoatomic liquids

Liquid argon [10]. An example of the $S(Q)$ structure factor for an atomic liquid, obtained with high accuracy is given in Fig. 2a for liquid argon (^{36}Ar), near its triple point at 85 K. $S(Q)$ has a simple shape: a large peak at $Q = 2$ Å^{-1} followed by an oscillating function which decreases in amplitude with increasing Q. Figure 2b displays the pair correlation function $g(r)$ for liquid ^{36}Ar at 85 K. This experiment gave rise to molecular dynamics and Monte Carlo simulations. An early calculation

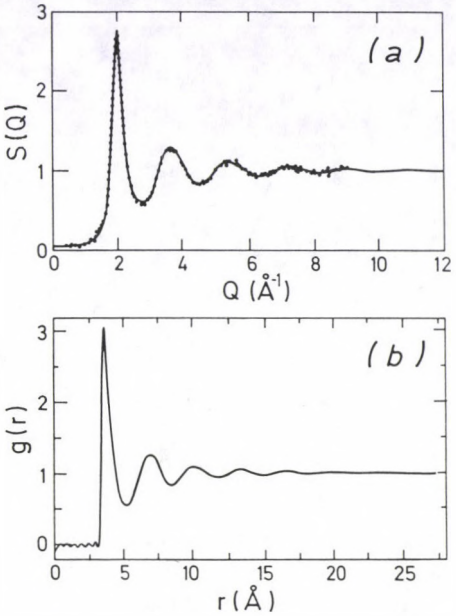

Fig. 2. a) Structure factor $S(Q)$ for liquid argon ^{36}Ar near its triple point. . . . . Experimental data $T = 85$ K, $\rho_0 = 0.0213$ atoms/Å^3; ——— Molecular dynamics $T = 86.56$ K, $\rho_0 = 0.02138$ atoms/Å^3; b) Pair correlation function $g(r)$ for liquid argon ^{36}Ar at 85 K

has been performed by Verlet [11] and a comparison with $S(Q)$ for a Lennard Jones fluid in the same state using molecular dynamics is displayed in Fig. 2a. Some recent Monte Carlo calculation using a very accurate two body potential [12] and including three-body and quantum corrections led to an excellent description of the properties of solid, liquid and gaseous argon.

Liquid gallium [13]. Very accurate measurements of the structure factor $S(Q)$ of liquid gallium at temperatures 326 and 959 K allowed the determination of an effective pair potential $v_{\text{eff}}(r)$ between the gallium atoms at these two thermodynamic states. Figure 3 displays the structure factor $S_{\text{expt}}(Q)$ at 326 K which has been measured over a wide range of wavevectors (0.26–16 Å^{-1}) with a high degree of precision which provides new information on the behaviour of the structure factor for $Q < 2$ Å^{-1}. We have attempted to determine $v_{\text{eff}}(r)$ by inversion of $S_{\text{expt}}(Q)$. The so-called iterative inversion scheme of Masserini and Reatto [14] is then followed to obtain the effective pair potential from the experimental data. It has been shown [14] that the iterative process converges and the pair potential $\phi(r)$ or $\beta v_{\text{eff}}(r)$ obtained after nine iterations within an accuracy of ± 0.04 to 0.07 is displayed in Fig. 4 (as computed on the basis of statistical errors only).

The corresponding $g(r)$ is given in Fig. 4. It agrees within 0.5 % to 1 % with $g_{\text{exp}}(r)$, i.e. the accuracy of the simulation procedure.

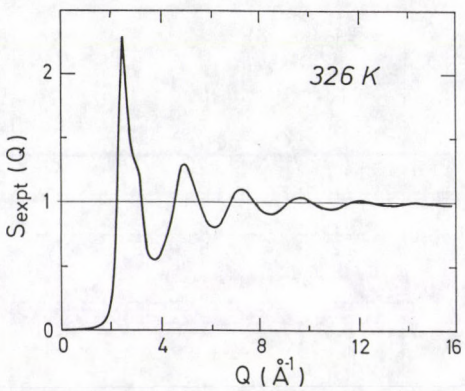

Fig. 3. Structure factor $S_{expt}(Q)$ for liquid gallium at 326 K ($\rho_0 = 0.02138$ atoms/Å^3).

The inversion procedure $S_{expt}(Q)$ establishes that the effective potential is positive and repulsive at distances corresponding to the nearest neighbours and it has a long period of about 8 Å for the oscillations. Temperature dependence was investigated and found to be significant. The inversion method of Masserini and Reatto involves no adjustable parameter and no assumption on the theoretical form of the effective pair potential. It turns out to be quite adequate to take account of $S_{expt}(Q)$ and $g_{expt}(r)$ of liquid metals, but that needs precise measurements of $S_{expt}(Q)$ over a large range of Q wave vectors. It could be interesting to extend the inversion method to other liquid metals or monoatomic liquids which has not yet been performed up to now.

Molecular liquids

Water under extreme conditions of temperature and pressure. Recent structural studies of liquid D_2O [15] have been performed by neutron diffraction. The results cover a large temperature range from 95 °C down to −31.5 °C close to the temperature of homogeneous nucleation and particularly in the low temperature range where liquid water exhibits an abnormal behaviour. At low temperature, that has been achieved by using emulsions [16] which cannot be performed by other techniques than neutron scattering.

In Fig. 5, the pair correlation function of low density amorphous ice [17] is plotted together with that of water at 27 °C and that of supercooled water at −10.5 °C and −31.5 °C.

The measurements, at low temperature confirm the increasing spatial correlations in deeply supercooled liquid water as the temperature is decreased and the tendency to evolve towards the structure of low density amorphous ice. These data should provide an important basis for a comparison with predictions based on different forms of the interaction potential between water molecules.

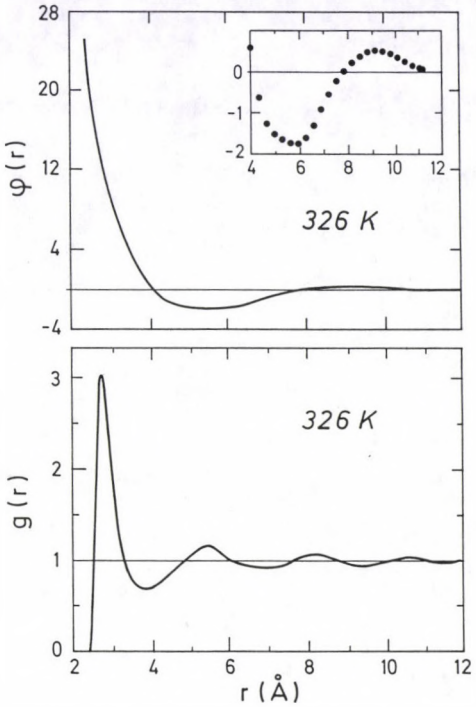

Fig. 4. Pair correlation function $g(r)$ and interaction $\phi(r) = \beta v_{\text{eff}}(r)$ at 326 K. The insert gives the long range part of $\phi(r)$

Method of isotopic substitution

As mentioned in the introduction, the method of isotopic substitution is a powerful tool to study the environment of an atom.

This method has been widely applied to liquid alloys [18], molten salts [6,19], molecular liquids and their mixtures [6,20]. Other liquids such as aqueous solutions [3,4,21,22] and recently non-aqueous solutions [23–25] have been also investigated. I only present here some results obtained in the field of aqueous and non-aqueous solutions which could be extended to the biological solutions and for which some attempts have already been realized [26].

Aqueous ionic solutions: Influence of the counterion [21]. The local coordination of Zn^{2+} depends strongly on counterion, temperature and concentration. Neutron diffraction studies were carried out on solutions of 2 molal zinc triflate $Zn(CF_3SO_3)_2$ and 4 molal zinc chloride $ZnCl_2$ in heavy water. An isotopic difference study of Zn^{2+} based on isotopes of $^{\text{nat}}Zn$ and ^{67}Zn led to the total pair correlation function $G_{Zn}^{D_2O}$ and thus provided direct information regarding the Zn^{2+} hydration.

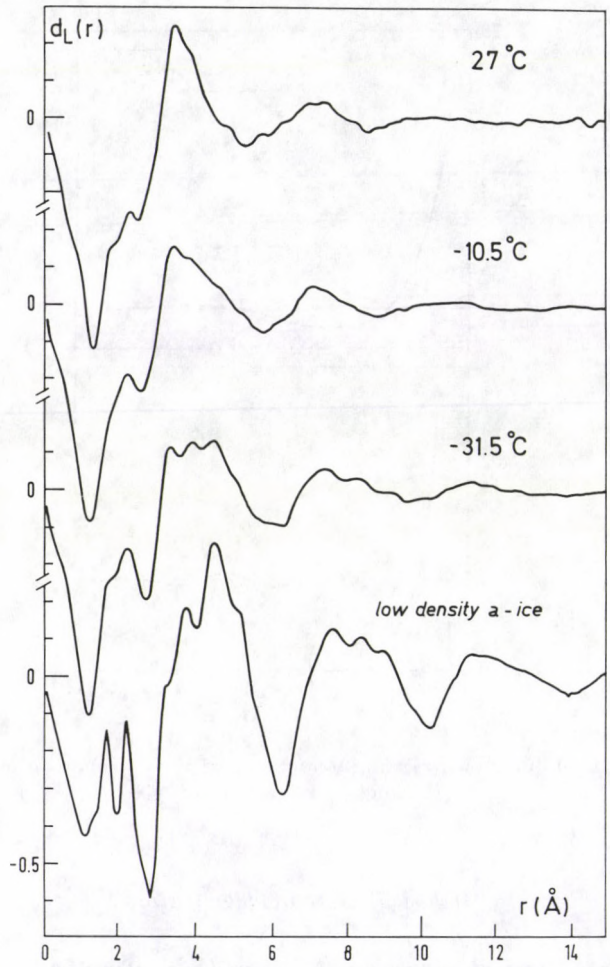

Fig. 5. Pair correlation functions $d_L(r)$ of D_2O obtained respectively at 27 °C, −10.5 °C and −31.5 °C, compared with that of the low density amorphous ice. $d_L(r) = \frac{2}{\pi}\int_0^\infty QD_M(Q)\sin Qr dQ$ for the intermolecular terms only; $S_M(Q) = f_1(Q) + D_M(Q)$ where $f_1(Q)$ is the form factor of the molecule

Figure 6a shows the function $G_{Zn}^{D_2O}(r)$ relative to a 2 molal $Zn(CF_3SO_3)_2$ in D_2O. The coordination numbers $\overline{n}_{Zn}^0$ and $\overline{n}_{Zn}^D$ are consistent with two D atoms per O atom; the hydration number is $n = 5.3(2)$. This demonstrates that there is no significant penetration of the triflate ion into Zn^{2+} hydration shell.

In the case of the zinc chloride, as shown in Fig. 6b, Zn^{2+} has not a hydration shell as well defined as for Zn^{2+} in zinc triflate solution. The analysis of $G_{Zn}^{D_2O}(r)$ leads to the conclusion that the partial pair correlation function $g_{ZnCl}(r)$ contributes

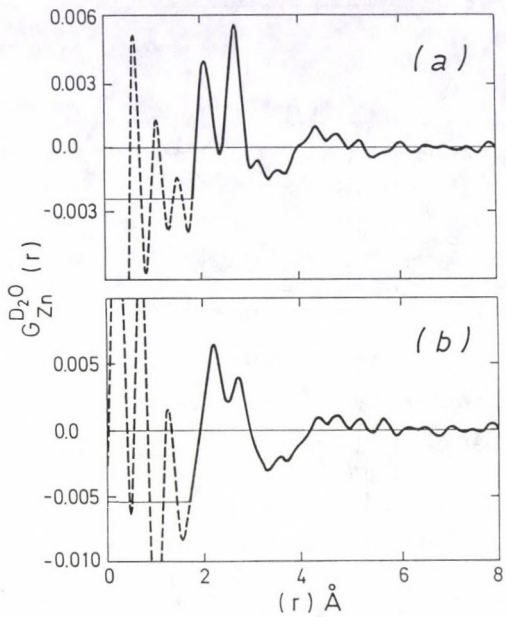

Fig. 6. a) 2 molal $Zn(CF_3SO_3)_2$ solution in D_2O. Total pair correlation function $G_{Zn}^{D_2O}$. The two peaks at 2.09 and 2.69 Å can be identified with the nearest neighbour $Zn^{2+}-O$ and $Zn^{2+}-D$ correlations. b) 4 molal $ZnCl_2$ solution in D_2O. Total pair correlation function $G_{Zn}^{D_2O}$; Zn^{2+} is coordinated to 4.1(5) water molecules and 1.4(5) chloride ions

significantly to $G_{Zn}^{D_2O}(r)$ in the hydration region and provides clear evidence for $Zn^{2+}-Cl^-$ complexation.

Non-aqueous ionic solutions: Influence of the solvent. Neutron scattering techniques begin to be applied to non-aqueous ionic solutions [23–25].

The structure around lithium ions in solutions of lithium bromide in acetonitrile and water has been studied [24]. The isotopic difference method has been applied to lithium ions. Figures 7a and 7b show respectively the total pair correlation function $G_{Li}^{D_2O}(r)$ for a 1.88 M aqueous solution and $G_{Li}^{AN}(r)$ for a 0.58 M acetonitrile solution. In the case of the acetonitrile solution it has been found that the bromide anion enters into the first solvation shell around the lithium ion, whereas in the case of the aqueous solution the first hydration shell of the cation is not disturbed by the anion. The solvation number is approximately 3 in the case of acetonitrile and approximately 4.5 in the case of water.

Liquids in confined geometry [27–29]

More recently there has been interest in the way proximity to an interface leads to modification of the overall molecular behaviour. Several types of experimental

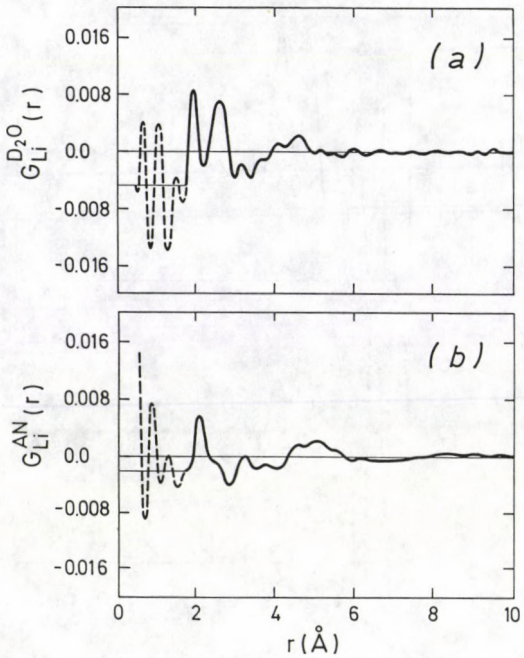

Fig. 7. a) 1.88 M LiBr solution in D_2O. Total pair correlation function $G_{Li}^{D_2O}$. The two peaks at 1.94 and 2.58 Å can be identified with the nearest neighbour Li^+-O and Li^+-D correlations. b) 0.58 M LiBr solution in CD_3CN. Total pair correlation function G_{Li}^{AN}. The decomposition of G_{Li}^{AN} with three Gaussian peaks leads to Li–N (2.05 Å), LiBr (2.46 Å) and Li–C_1 (3.17 Å) correlations

approach of the problem of interfacial structure have been adopted; the methods involve the study of D_2O in microporous silica of varying pores [27], in clay systems [27] or inside interconnected pores of Vycor glass [28]. In this last system, when decreasing the temperature, it is possible to supercool water but not to the extent expected for such a small confining space. In fact the presence of large hydrophilic silica interface enhances the nucleation of ice. The observed phase of ice is the cubic ice I_c which appears at about -18 °C, in the full hydrated Vycor, instead of the expected hexagonal (I_h) form (Fig. 8). The neutron scattering experiments of cyclohexane C_6D_{12} [27] in microporous silica show that the resulting plastic crystal phase is strongly influenced by the thermal history of the sample — the nucleation point is depressed by ~ 40 °C.

A novel experiment by neutron scattering led to the first determination of the structure factor of an amorphous protein, the C-phycocyanin [29]. The effects of hydration and temperature on the total function $d(r)$ have been studied explicitly. The changes in $d(r)$ functions observed in hydrated samples depend strongly on the level of hydration and most of these changes are due to water–protein interactions.

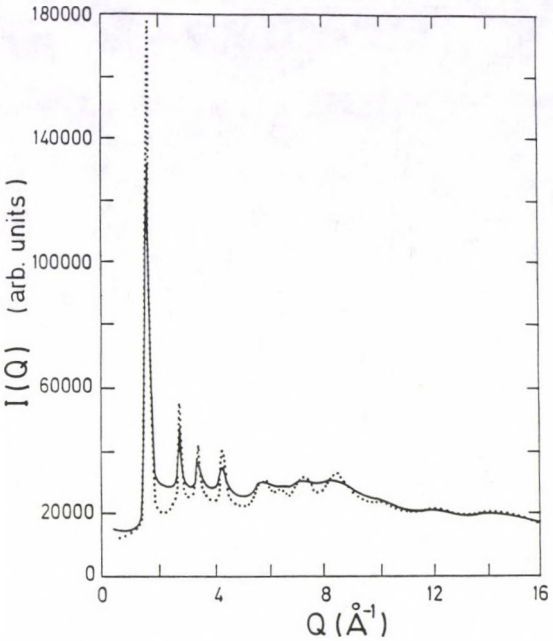

Fig. 8. Spectra of cubic ice (dotted line) (−198 °C) and confined D_2O from fully hydrated Vycor (full line) at −41.5 °C; there is ∼ 27 % liquid water still present below the Bragg peaks of cubic ice

At 0.365 g D_2O per g of protein, the water crystallized into hexagonal ice at 200 K and below, but at 0.175 g D_2O per g of protein, no crystallization of water was observed.

At the higher hydration a peak appears in the $d(r)$ function (Fig. 9) which indicates that the average distance of the water molecule in the hydration shell from the amino acid residues is 3.5 Å. This effect is clearly evident in the computer simulations [30] which show an increase in the clustering of water molecules close to the protein surface within distances of 3–4.25 Å (mainly away from the nonpolar atoms in the protein).

Conclusion

In this review, we have presented the more recent results obtained about the structural study of liquids and solutions. Some examples of recent accurate work have been given and demonstrate the capability of neutron scattering in the description of the structure of a liquid and the possibility of the determination of an effective pair potential.

The isotopic substitution method has now been extended to the knowledge of the detailed arrangement about a chosen ion in polyelectrolyte solutions, which

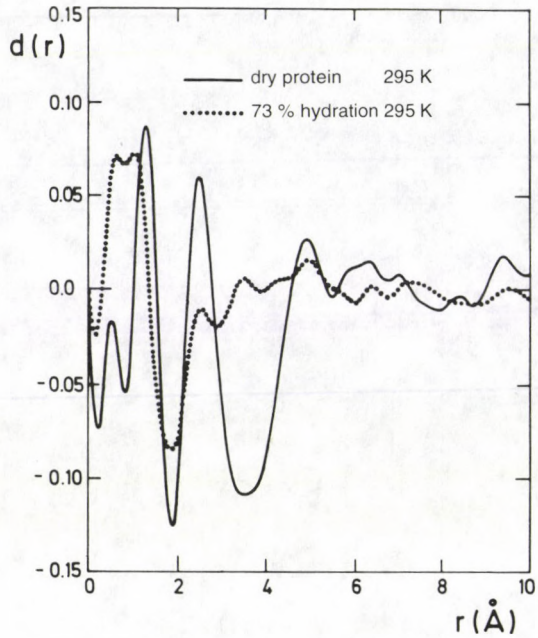

Fig. 9. $d(r)$ function for a dry deuterated protein C-phycocyanin and for a 73 % (0.365 g D_2O/g-protein) hydrated protein C-phycocyanin at 295 K. ($d(r) = 4\pi r \rho_0[g(r) - 1]$)

opened the field to the biological solutions.

A novel field of interest concerns the study of liquids at interfaces. The first results about water close to hydrophilic surface (Vycor surface) or close to protein results are presented. Much work must now involve the hydrophobic hydration.

The performance of neutron scattering has also been used to study liquids as function of pressure and temperature [31–32] and an important field of research which needs to be developed concerns the liquids and solutions under supercritical conditions.

Acknowledgements

I would like to thank colleagues, researchers, students, secretaries and technicians who help to make this work so enjoyable.

References

1. J. P. Hansen and I. R. Mc Donald, Theory of Simple Liquids, Second Edition, Academic Press, London, 1986.
2. P. A. Egelstaff, An Introduction to the Liquid State, Second Ed. Oxford University Press, Oxford, 1992.

3. G. W. Neilson and J. E. Enderby, Water and Aqueous Solutions, Adam Hilger, Bristol, 1986.
4. M.-C. Bellissent-Funel and G. W. Neilson, The Physics and Chemistry of Aqueous Ionic Solutions, NATO ASI Series C, Vol. 205, D. Reidel Publisher, Dordrecht, 1987.
5. J. C. Dore and J. Teixeira, Hydrogen Bonded Liquids, NATO ASI Series C, Vol. 329, Kluwer Academic Publishers, Dordrecht, 1991.
6. J. J. C. Teixeira-Dias, Molecular Liquids: New Perspectives in Physics and Chemistry, NATO ASI Series C, Vol. 379, Kluwer Academic Publishers, Dordrecht, 1992.
7. W. S. Howells and A. K. Soper, Recent Developments in the Physics of Fluids, Adam Hilger, Bristol, 1992.
8. J. Teixeira, F. Wanderlingh, R. Giordano, A. J. Dianoux and A. J. Barnes, J. of Molecular Structure, Special Issue, *296*, 177, 1993.
9. L. van Hove, Phys. Rev., *95*, 249, 1954.
10. J. L. Yarnell, M. J. Katz, R. G. Wenzel and S. H. Koenig, Phys. Rev., *A7*, 2130, 1973.
11. L. Verlet, Phys. Rev., *165*, 201, 1968.
12. J. Barker, R. A. Fisher and R. O. Watts, Mol. Phys., *21*, 657, 1971.
13. M.-C. Bellissent-Funel, P. Chieux, D. Levesque and J. J. Weis, Phys. Rev., *A39*, 6310, 1989.
14. G. L. Masserini and L. Reatto, Phys. Rev., *B30*, 5367, 1984.
15. M.-C. Bellissent-Funel, in: Hydrogen-Bonded Liquids, eds J. C. Dore and J. Teixeira, 117, Kluwer Academic Publishers, Dordrecht, 1991.
16. M.-C. Bellissent-Funel, J. Teixeira, L. Bosio and J. C. Dore, J. Phys.: Condens. Matter, *1*, 7123, 1989.
17. M.-C. Bellissent-Funel, J. Teixeira and L. Bosio, J. Chem. Phys., *87*, 2231, 1987.
18. M.-C. Bellissent-Funel, P. J. Desre, R. Bellissent and G. Tourand, J. Phys. F: Metal Phys., *7*, 2485, 1977; P. Chieux and H. Ruppersberg, J. Phys. (Paris) Colloq. C8, *41*, C8-145, 1980.
19. R. L. Mc Greevy, Solid State Phys., *40*, 247, 1987; R. L. Mc Greevy and L. Pusztai, Proc. Roy. Soc. Lond., *A430*, 241, 1990.
20. J.-F. Jal, C. Mathieu, P. Chieux and J. Dupuy, Phil. Mag., *B62*, 351, 1990; P. Damay, F. Leclercq and P. Chieux, Phys. Rev., B, *40*, 4696, 1989; P. Chieux, J.-F. Jal, L. Hily, J. Dupuy, F. Leclercq and P. Damay, J. Phys. (Paris) IV, Colloq. C5, C5-3, 1991.
21. D. H. Powell, P. M. N. Gullidge, G. W. Neilson and M.-C. Bellissent-Funel, Mol. Phys., *71*, 1107, 1990.
22. J. R. C. van der Maarel, D. H. Powell, A. K. Jawahier, L. H. Leyte-Zuiderweg, G. W. Neilson and M.-C. Bellissent-Funel, J. Chem. Phys., *90*, 6709, 1989.
23. D. H. Powell and G. W. Neilson, J. Phys.: Condens. Matter, *2*, 5867, 1990.
24. T. Cartailler, W. Kunz, P. Turo and M.-C. Bellissent-Funel, J. Phys.: Condens. Matter, *3*, 9511, 1991.
25. P. B. Lond, P. S. Salmon and D. C. Champeney, J. Am. Chem. Soc., *113*, 6420, 1991; P. S. Salmon and P. B. Lond, J. Phys.: Condens. Matter, *4*, 5249, 1992.
26. J. L. Finney, in: Water and Aqueous Solutions, eds G. W. Neilson and J. E. Enderby, 227, Adam Hilger, Bristol, 1986.
27. J. C. Dore, F. Coveney and M.-C. Bellissent-Funel, in: Recent Developments in the Physics of Fluids, eds S. W. Howells and A. K. Soper, F299, Adam Hilger, Bristol, 1992.
28. M.-C. Bellissent-Funel, L. Bosio and J. Lal, J. Chem. Phys., *98*, 4246, 1993.
29. M.-C. Bellissent-Funel, J. Lal, K. F. Bradley and S. H. Chen, Biophys. J., *64*, 1542, 1993.
30. P. J. Rossky and M. Karplus, J. Am. Chem. Soc., *101*, 1913, 1979; M. Levitt and R. Sharon, Proc. Natl. Acad. Sci. USA (Biophys.), *85*, 7557, 1988.
31. G. W. Neilson, Chem. Phys. Lett., *68*, 247, 1979; R. Winter, F. Hensel, T. Bodensteiner and W. Glaser, Ber. Bunsenges. Phys. Chem., *91*, 1327, 1987; A. Y. Wu, E. Whalley and G. Dolling, Mol. Phys., *47*, 603, 1982; P. Postorino, R. H. Tromp, M. A. Ricci, A. K. Soper and G. W. Neilson, Nature, *366*, 668, 1993.
32. M.-C. Bellissent-Funel and L. Bosio, to be published, J. Chem. Phys., 1995.

Acta Physica Hungarica 75 (1-4), pp. 91-100 (1994)

INTERNAL STRESSES IN AMORPHOUS $Fe_{40}Ni_{40}B_{20}$ STUDIED WITH NEUTRON DEPOLARIZATION

M. DE JONG[1,2], A. VAN OUDENAARDEN[2], J. SIETSMA[2], M. TH. REKVELDT[1] and A. VAN DEN BEUKEL[2]

[1] *Interfaculty Reactor Institute,* [2] *Laboratory of Materials Science*
Delft University of Technology
Mekelweg 15, 2629 JB Delft, The Netherlands

The magnetic domain structure of amorphous materials is, because of the magneto-elastic coupling, mainly determined by the internal stress state. The stress and field dependence of the domain structure contains important information on the internal stress distribution in the material. The three-dimensional Neutron Depolarization technique has been used to study the stress and field dependence of the bulk domain structures in as-quenched and annealed $Fe_{40}Ni_{40}B_{20}$. A three-layer domain structure model corresponding to compressive and tensile internal stresses is presented to explain the measured data. The influence of surface roughness on the interpretation of ND measurements in amorphous ribbons is discussed.

Introduction

Amorphous materials are metastable by nature. This is clearly demonstrated by the fact that bulk properties like resistivity, Young's modulus and viscosity change when the material is subjected to annealing treatments. Small structural changes in the amorphous system are the cause of the observed changes of the physical properties. A number of models has been developed to describe this structural relaxation (e.g. [1]).

Another important feature of as-quenched amorphous ribbons is the presence of internal stresses. These stresses are caused by the large thermal gradients occurring during production of the ribbons by the melt-spinning process. The aim of the present investigation is to study the internal stress distribution in the as-quenched material and the relaxation of internal stresses during heat treatments. In as-quenched amorphous magnetic materials, with non-zero magnetostriction, the local magnetization direction is coupled to the local stress state by the mechanism of magnetoelastic coupling. In fact, the magnetoelastic energy is the most important contribution to the magnetic anisotropy in as-quenched materials [2]. In materials with a positive magnetostriction, tensile stresses cause the magnetization directions within domains to be parallel to the axis of principle stress, while compressive stresses in such materials lead to local magnetizations perpendicular to this axis. So, the magnetization orientation by itself delivers information about the *sign* of the internal stresses. Furthermore, the way in which the domain structure changes under the application of tensile stress reveals the *distribution* of the internal stresses.

In tensile stress regions, the magnetization process is mainly governed by domain wall movements, whereas in compressive stress regions magnetization rotation is the most important magnetization process. The application of a magnetic field to the sample, by which the magnetization state is changed, therefore provides an alternative means to study the internal stresses through the magnetic anisotropy.

Three-dimensional Neutron Depolarization has been used by various authors to study the domain structure in amorphous materials as a function of the applied tensile stress and of the magnetic field [3,4]. This paper will present neutron depolarization measurements as a function of the applied stress and of the magnetic field in two relaxation states of $Fe_{40}Ni_{40}B_{20}$. A domain structure model will be used to interpret the measurements in terms of the internal stress distribution.

Experimental

In a three-dimensional neutron depolarization experiment the polarization vector $\mathbf{P}$ of a polarized beam is analysed after transmission through a magnetic sample. The time dependence of the polarization vector subjected to an induction $\mathbf{B}$ is described by the Larmor equation

$$\frac{d\mathbf{P}}{dt} = \gamma(\mathbf{P} \times \mathbf{B}), \tag{1}$$

with $\gamma = 1.83 \times 10^8\ \mathrm{s^{-1}T^{-1}}$ the gyromagnetic ratio of the neutron. In the Larmor approach [5], which can be used in ferromagnetic materials with large domains, the polarization vector will precess around the domain magnetization directions that the neutron passes during transmission. The relation between the polarization vector before and after transmission, $\mathbf{P}^0$ and $\mathbf{P}^1$, respectively, is given by $\mathbf{P}^1 = \hat{D}\mathbf{P}^0$. Here $\hat{D}$ is called the depolarization matrix, the elements of which can be experimentally determined through

$$D_{ij} = \frac{I_s - I_{ij}}{I_s - I_m}, \tag{2}$$

with I_{ij}, the measured intensity and i, j $(= x, y, z)$ the polarizing and analysing directions. I_s and I_m are the intensities of the fully depolarized and polarized beam, respectively. The depolarization matrix $\hat{D}_1$ for a beam of polarized neutrons passing a single domain can be written as:

$$\hat{D}_1 = \hat{U} + \hat{A}_1 \sin(\phi) + \hat{A}_1^2(1 - \cos(\phi)), \tag{3}$$

where $\hat{U}$ is the unity matrix, $\phi = c_1 B_s \delta$, with $c_1 = 7.47 \times 10^4\ \mathrm{T^{-1}m^{-1}}$, a set-up constant, B_s, the spontaneous induction and δ, the domain thickness. Matrix $\hat{A}_1$ is given by

$$\hat{A}_1 = \begin{pmatrix} 0 & -m_z & m_y \\ m_z & 0 & -m_x \\ -m_y & m_x & 0 \end{pmatrix}, \tag{4}$$

with m_i, the i-component of the reduced magnetization vector $\mathbf{m}$ (relative to the saturation magnetization). If the sample is uniformly magnetized, the polarization vector will only precess around the magnetization direction. In the case of a magnetization distribution over the area of the beam, in addition to precession also shortening of the polarization vector due to deviations from the average magnetization will occur.

Two kinds of measurements have been performed. In the first kind, depolarization matrices have been measured in zero applied field as a function of applied tensile stress for both as-quenched and annealed (600 K, 10 s) $Fe_{40}Ni_{40}B_{20}$ ribbon (width 2.5 mm, thickness 30 μm, $B_s = 1.0$ T [6], from Vacuumschmelze GmbH). The samples were stressed by an electro pull-magnet, which was controlled by a feed-back system containing a strain-gauge transducer to measure the applied force. All samples were magnetized in a field of 4800 A/m before starting the stress dependent measurements in zero applied field. In the second kind of measurements, we varied the applied magnetic field stepwise, bringing the samples from negative to positive saturation and back, while applying a constant value of tensile stress. Both low field (less than 40 A/m) and high field (up to 4800 A/m) measurements have been done.

The three-layer model

In order to obtain domain structure characteristics from the measured depolarization matrices, it is necessary to model the domain structure. It is assumed that, because of geometric reasons, all internal stresses act in the ribbon plane. The production of the ribbons by melt-spinning gives rise to a structure consisting of layers with in-plane compressive and tensile stresses. In the model that is proposed here, the internal stresses occur in a three-layer structure. The two outer layers contain, because of the higher cooling rates at the surfaces, compressive stresses. The inner layer contains tensile stresses. In a material with a positive magnetostriction constant ($\lambda_s = 1.35 \times 10^{-6}$ [7] for $Fe_{40}Ni_{40}B_{20}$), such an internal stress state leads to a domain structure as drawn in Fig. 1. The tensile stresses in the inner layer give rise to domains with their magnetization in the yz-plane, oriented in the direction of the principal stress component. These domains will be referred to as "yz-domains". Compressive stresses will cause regions of domains with their magnetization oriented in the $+x$ or $-x$ direction. These domains will be referred to as "x-domains". As a first approximation the outer layers are assumed to have equal thicknesses. In principle the theoretical matrix for the three-layer model should be derived by averaging the matrix over all possible neutron paths. In the present case, the averaging can be carried out independently for each layer. The theoretical matrix $\hat{D}^{(x)}$ for each of the outer layers follows from (3) and (4) by setting m_y equal to zero and assuming that, because of otherwise large demagnetization fields, the average $\langle m_x \rangle$ equals zero:

$$\hat{D}^{(x)} = \begin{pmatrix} 1-(1-\cos(\phi_x))(1-\gamma_x^0) & -\langle m_z^0\rangle \sin(\phi_x) & 0 \\ \langle m_z^0\rangle \sin(\phi_x) & \cos(\phi_x) & 0 \\ 0 & 0 & 1-(1-\cos(\phi_x))(1-\gamma_z^0) \end{pmatrix}, \tag{5}$$

with $\phi_x = c_1 B_s \delta_x$ and δ_x the average thickness of each outer layer. The orientation parameter γ_z^0 equals $\langle \cos^2 \alpha_z^0 \rangle$ with α_z^0, the angle between the local magnetization in the two outer layers and the z-axis, $\gamma_x^0 = 1 - \gamma_z^0$ because $\sum_i \gamma_i = 1$ and $\gamma_y^0 = 0$. In the low field region the assumption is made that the magnetizations in the surface layers all are directed along the x-direction ($\gamma_z^0 = 0$).

In case of a uni-axial anisotropy $\langle m_z^0 \rangle = \sqrt{\gamma_z^0}$, representing the uniform rotation of magnetizations in the outer layers under application of a high external field. The depolarization matrix for the yz-domains $\hat{D}^{(yz)}$ follows from the Eqs (3) and (4) by setting m_x equal to zero and assuming that $\langle m_i m_j \rangle = \langle m_i \rangle \langle m_j \rangle$ and $\langle m_y \rangle = 0$:

$$\hat{D}^{(yz)} = \begin{pmatrix} \cos(\phi_z) & -\langle m_z\rangle \sin(\phi_z) & 0 \\ \langle m_z\rangle \sin(\phi_z) & 1-(1-\cos(\phi_z))(1-\gamma_y^i) & 0 \\ 0 & 0 & 1-(1-\cos(\phi_z))(1-\gamma_z^i) \end{pmatrix}, \tag{6}$$

with $\phi_z = c_1 B_s \delta_z$ and $\delta_z = \delta_{\text{tot}} - 2\delta_x$, the average thickness of the inner layer. The value of the total thickness δ_{tot} has been determined to be 29.5 μm by applying a high field (4800 A/m) and a large external stress (300 MPa) to the sample. It is assumed that in this case the domain structure is formed by just one domain with magnetization parallel to the ribbon plane. This value of the total thickness is in agreement with the one obtained from weighing the sample. The orientation parameter γ_z^i for the inner layer, is defined in a similar way as γ_z^0, $\gamma_y^i = 1 - \gamma_z^i$. The parameter $\langle m_z \rangle$ represents the z-component of the average reduced magnetization in the inner layer.

The theoretical model matrix is the product of the three contributions:

$$\hat{D}^{\text{model}} = \hat{D}^{(x)} \hat{D}^{(yz)} \hat{D}^{(x)}. \tag{7}$$

The parameters δ_x, γ_z^i, γ_z^0 and $\langle m_z \rangle$ can be determined from a fit of the model to the measured matrix.

Results and discussion

As mentioned before, we performed two kinds of experiments. First, the results of the stress dependent measurements at zero applied field will be discussed, followed by those of the field dependent measurements.

In Fig. 3 a typical example of measured depolarization matrices in the low field regime is plotted together with the model fits for the as-quenched ribbon. The

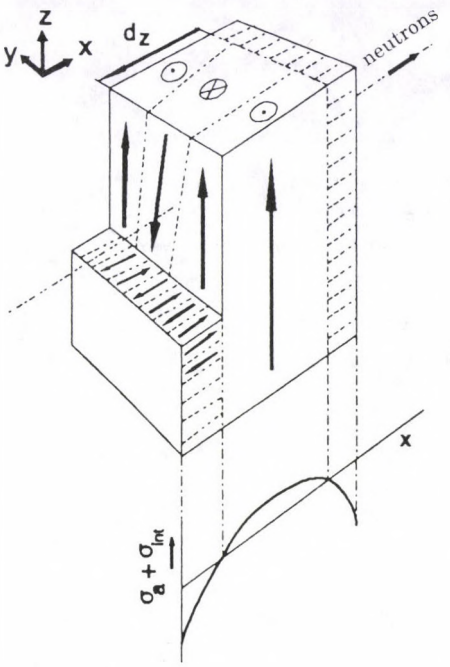

Fig. 1. The three-layer domain structure. Note the connection between the magnetization direction in the domains and the sign of the resultant of internal stress (σ_{int}) and applied stress (σ_a).

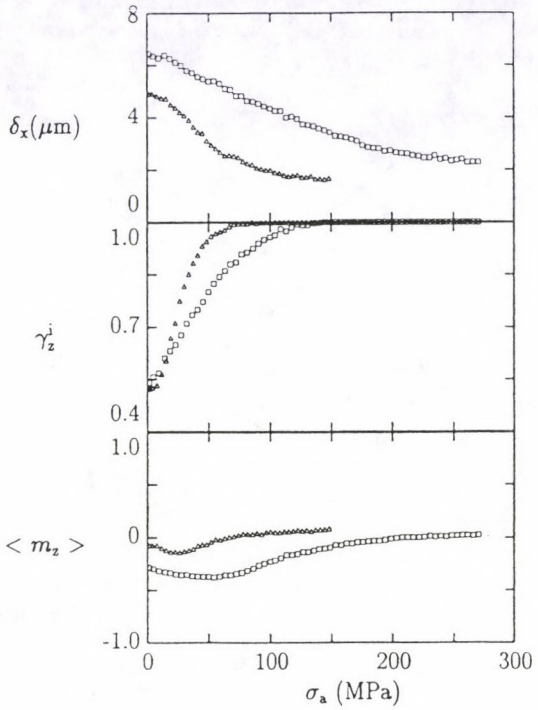

Fig. 2. The model parameters δ_x, γ_z^i and $\langle m_z \rangle$ as a function of the applied stress σ_a, shown for the as-quenched (□) ribbon and the ribbon annealed at 600 K for 10 s (△).

fact that all non-diagonal elements other than D_{xy} and D_{yx} equal zero, supports the thought behind the three-layer model that the z-axis is the principal axis of the mean magnetization. The shift of the hysteresis loops in D_{xy} and D_{yx} with respect to zero applied field is probably caused by stray fields in the sample chamber.

The results of the model fits of the stress dependent measurements are plotted in Fig. 2 for both the as-quenched and the annealed ribbon ($H = 0 \Rightarrow \gamma_z^0 = 0$). The application of tensile stress has two consequences for the internal stresses. One is the compensation of the *compressive* stresses, which results in a decrease of the thickness δ_x of the outer layers. The other consequence is that the direction of the resultant stress in the inner layer of initially randomly directed, but in-plane, *tensile* stresses will rotate towards the axis of the applied stress. This results in an increase of the mean square direction cosine γ_z^i of the magnetization directions in the inner layer. The changes in the parameters δ_x and γ_z^i, for the annealed ribbon occur at smaller values of the applied stress than in the case of the as-quenched

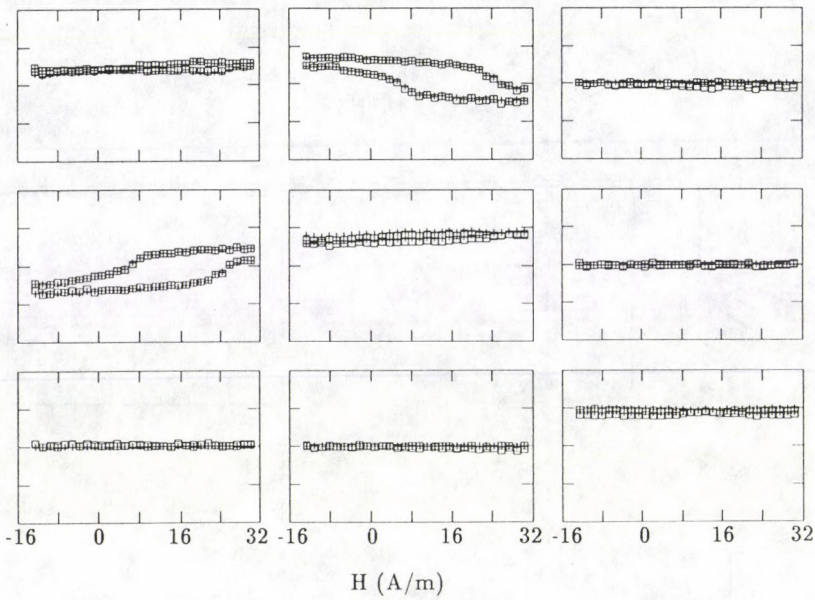

Fig. 3. The depolarization matrix for the as-quenched (□) ribbon as a fucntion of the applied field H in the low field region. The model fits are denoted by (+)

ribbon. This reflects the relaxation of both compressive and tensile stresses by the applied heat treatment. The parameter $\langle m_z \rangle$ represents the remanent magnetization after application of the field of 4800 A/m prior to the measurements. The changes in $\langle m_z \rangle$ with applied stress are due to the displacement of domain walls in the material. From Fig. 2 it must be concluded that the thickness δ_x at zero applied field does not become zero at 300 MPa. Although already successful in explaining the stress dependent measurements, the three-layer model gains further support by the second type of experiments, in which we varied the applied magnetic field stepwise at constant external stress. In the Figs 4 and 5 the fit results are shown for respectively the as-quenched and the annealed ribbon at zero applied stress and at an applied stress of 120 MPa. The parameter δ_x is almost constant, which supports the assumption of $\gamma_z^0 = 0$. At these low fields only displacements of the 180° walls in the inner layer will occur, leading to the hysteresis behaviour of the mean reduced magnetization in the inner layer $\langle m_z \rangle$. Note that both the squareness of the hysteresis loop and the value of $\langle m_z \rangle$ at the extremes of the low field region increase when an external stress is applied. These results support the idea, reflected by the increase of the orientation parameter γ_z^i, that the z-direction becomes the axis of resultant anisotropy as the applied stress increases. The annealed samples show an even higher $\langle m_z \rangle$ at 120 MPa than the as-quenched samples. This is obviously

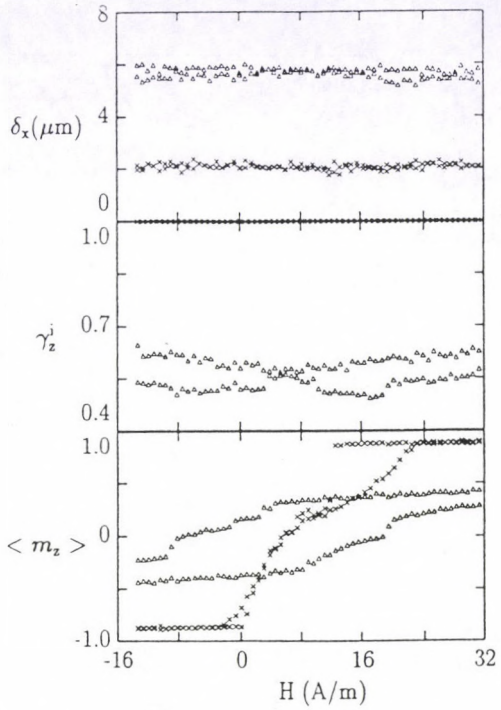

Fig. 4. The model parameters δ_x, γ_z^i and $\langle m_z \rangle$ as a function of the applied field H, shown for the as-quenched ribbon at 0 MPa (□) and at 120 MPa (+)

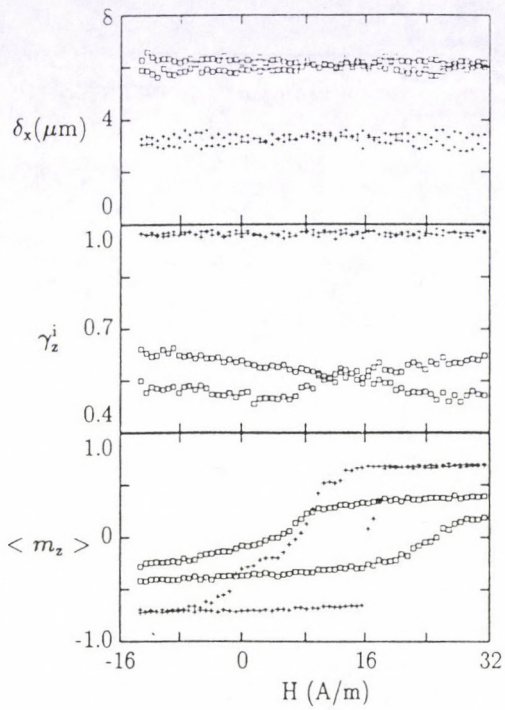

Fig. 5. The model parameters δ_x, γ_z^i and $\langle m_z \rangle$ as a function of the applied field H, shown for the ribbon annealed at 600 K for 10 s at 0 MPa (△) and at 120 MPa (×)

caused by the relaxation of internal stresses by the heat treatment, since in this case the anisotropy caused by the external stress overrules the anisotropy caused by the internal stresses more easily.

The rotation of the magnetizations in the outer layers can be studied when fields up to 4800 A/m are applied. A similar fitting procedure as for the low field measurements leads to the results plotted in Fig. 6, keeping δ_x fixed at the values given in Figs 4 and 5. For the annealed ribbon at 120 MPa the parameter γ_z^0 has no clear meaning, since in this case the thickness of the outer layers is practically zero. The behaviour of $\langle m_z \rangle$ is a logical extension of its low field behaviour, $\langle m_z \rangle$ increases with increasing applied field. When an external stress is applied, the increase of $\langle m_z \rangle$ is steeper and the rotation of the magnetizations in the inner layer by the magnetic field is easier. The latter follows from the behaviour of γ_z^i for the stressed and unstressed as-quenched ribbon. The increase and approach to unity of the orientation parameter γ_z^0 as a function of applied field shows the rotation of magnetizations in the outer layer. The average anisotropy in these layers, as determined by the resultant of internal compressive stresses and external

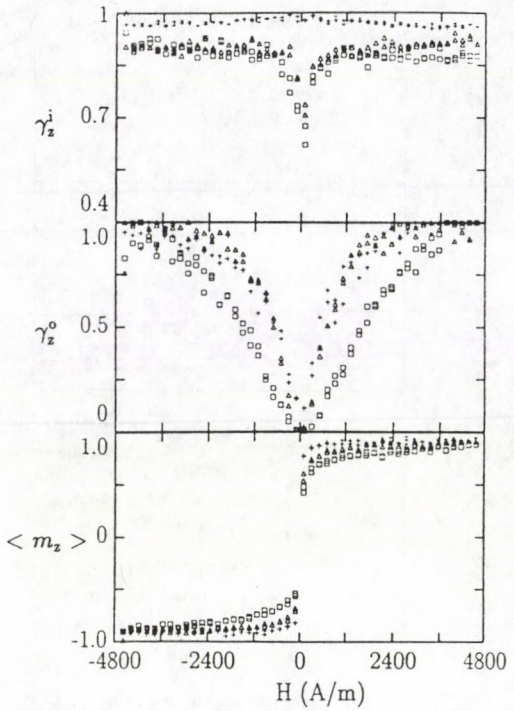

Fig. 6. The model parameters γ_z^i, γ_z^0 and $\langle m_z \rangle$ as a function of the applied field H, shown for the as-quenched ribbon at 0 MPa (□), the as-quenched ribbon at 120 MPa (+) and the ribbon annealed 600 K for 10 s at 0 MPa (△).

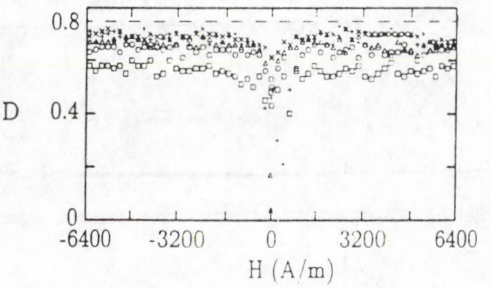

Fig. 7. The determinant D as a function of the applied field H at 300 MPa. Unpolished ribbon (□), polished with resp. 10 % (o), 20 % (△), 30 % (+) and 40 % (×) of thickness reduction. The dashed line is the value of D without a sample

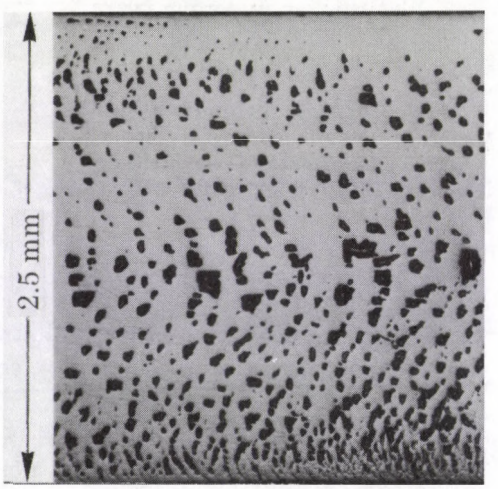

Fig. 8. A photograph of a polished ribbon after 10 % thickness reduction (magnification 36 times). Black spots are irregularities (craters)

tensile stress, decreases as the external stress increases. The external stress causes the magnetizations in the outer layers to be rotated in the z-direction at smaller applied fields. Comparing the results for the as-quenched and annealed ribbon at

zero applied stress, the faster increase with applied field of all parameters, in case of the latter ribbon, proves once again the reduction of internal stresses by the heat treatment.

Although the results of fitting the stress and field dependent measurements by the three-layer model yield an overall consistent picture of the distribution of internal stresses, in details some problems remain. In contrast to the low field region, where the applied stress could not reduce the thickness of the outer layers δ_x completely to zero, the large applied fields can rotate the magnetizations in the outer layers almost fully in the z-direction. Furthermore, looking at Fig. 6, the question arises why $\langle m_z \rangle$ seems to saturate at somewhat lower values than unity. The cause of the latter two phenomena is the remaining depolarization at high applied fields and large external stress. In Fig. 7, the determinant of the depolarization matrix, which is a measure of the depolarization, is plotted as a function of the applied field at large applied stress (300 MPa) for an as-quenched ribbon. The value of the determinant at the highest field is considerably lower than in an experiment without sample. This means that the magnetization is still not homogeneous over the area of the neutron beam. In the same Figure, the determinants are plotted for as-quenched ribbons whose dull sides were polished to obtain a reduction in surface roughness. It is clear that the determinant at the highest applied field increases as the surface roughness of the ribbons is decreased. From Fig. 8, which shows a photograph of the polished ribbon with 10 % thickness reduction, it is clear that surface roughness is huge. The conlusion seems valid that surface roughness is the main cause for the remaining depolarization at high applied fields and high applied stress. This remaining depolarization is the cause of $\langle m_z \rangle$ not completely reaching its saturation level. Obviously, the surface roughness was not taken into account in the three-layer model. Hence, we need not be surprised that mere application of external stress cannot create a homogeneous anisotropy throughout the whole volume.

Conclusions

The influence of heat treatments on the stress and field dependence of the measured depolarization matrices is large. The stress and field dependent depolarization matrices can be explained fairly well by a three-layer domain structure model with the outer layers corresponding to compressive stresses and the inner layer to tensile stresses. The surface roughness of the ribbons causes depolarization that cannot be removed by applying an external field or stress.

References

1. F. Spaepen, Acta Metall., *25*, 407, 1977.
2. H. Fujimori, in Amorphous Metallic Alloys, ed. F. E. Luborsky, Butterworth, London, 1983, p. 300.
3. M. de Jong, J. Sietsma, M. Th. Rekveldt and A. van den Beukel, Key Engineering Materials, *81–83*, 431, 1993.
4. A. Veider, G. Badurek, R. Grössinger and H. Kronmüller, J. Magn. Magn. Mat., *60*, 182, 1986.
5. M. Th. Rekveldt, Textures and Microstructures, *11*, 127, 1989.
6. F. E. Luborsky, in Ferromagnetic Materials, Vol. 1, ed. E. P. Wolfarth, North Holland, Amsterdam, 1980, p. 451.
7. L. Köszegi and H. Kronmüller, Appl. Phys., *A34*, 95, 1984.

Acta Physica Hungarica 75 (1–4), pp. 101–106 (1994)

INTEREST OF NEUTRON SCATTERING FOR THE INVESTIGATION OF LIQUID-CRYSTALLINE POLYMERS

L. NOIREZ

Laboratoire Léon Brillouin (CEA-CNRS)
CE-Saclay
91191 Gif-sur-Yvette Cedex, France

Small-Angle Neutron Scattering is the unique method which allows the determination of the polymer conformation in the bulk. This method has been applied to several kinds of liquid crystalline polymers. We report here general results obtained on side-chain liquid-crystal polymer, main-chain liquid-crystal polymer and finally combined liquid-crystal polymers. It is shown that the polymer conformation is largely dependent on the insertion site of the liquid crystal molecule and on the structure of the mesophase.

The conformation of a polymer in the bulk is an isotropic coil for which characteristic size is proportional to the root mean square of its length. The liquid crystal molecules have rod-like shapes and are able to align their long axis parallel to each other in the nematic phase (N), while in the smectic phase (SA), they are in addition stacked in layers of well-defined thickness. When the liquid-crystalline molecules are inserted in a polymer chain via a small chain (usually an alkyl chain) called "spacer", the mesomorphic properties of the liquid crystal molecules are not lost. The introduction of "flexible spacer concept" [1] has enabled the synthesis of a broad variety of liquid crystal polymers using all the possible combinations to include the liquid crystal in a polymer chain. These new polymers have obviously generated much interest the last years, not only because of the understanding challenge, but because of the technological interest for optical data storage, high molecules fibers easily processable with extrusion, moulding methods.

Neutron Scattering is a particularly well-adapted method to investigate these systems. The dimensions and the anisotropy of the polymer chain in the bulk are provided by Small-Angle Neutron Scattering (SANS), whereas several informations concerning the mesophase structure are obtained by Neutron Diffraction. In addition, the layers in the smectic A phase are broad enough to allow the observation of the first Bragg reflections (and usually liquid crystal polymers do not possess high reflection orders) with the same SANS device. The simultaneous study of the polymer conformation and of the mesophase structure is then possible.

We propose to compare the main-chain conformation of different liquid crystal polymers in the following situations:

– when the liquid crystal molecule is grafted on the side of a polymer chain, obtaining the side-chain liquid crystal polymers;

– when the liquid crystal molecule is inserted along the polymer chain giving the main-chain liquid-crystal polymer;

– when the polymer possesses at the same time a liquid crystal molecule on the side part and along the polymer chain, one obtains the combined liquid-crystal polymer.

These polymers have various degrees of polymerization included between 10 and 300, measured by using Gel Permeation Chromatography-Light Scattering on line [2].

Neutron scattering experiments

The scattering cross-section $S(q)$ at small q values (where $q = \frac{4\pi}{\lambda} \sin \frac{\theta}{2}$ with θ, the scattering angle, and λ, the wavelength) gives information on the macroscopic aspect of the sample. An artificial means to create heterogeneities in polymers in bulk, is to prepare samples of hydrogenated polymers mixed with selectively deuterated polymers. It has been demonstrated [3,4] that the scattering function of a mixture containing X_H hydrogenated polymers and X_D deuterated polymers ($X_H + X_D = 1$) is given by:

$$S(\mathbf{q}) = N \cdot X_H \cdot X_D (a_D - a_H)^2 P(\mathbf{q}),$$

where N is the total number of polymer chains, a_H, a_D are the coherent scattering lengths of the protonated and deuterated monomers, respectively (at small q values, each monomer can be considered as a scatterer of coherent scattering length a) and $P(\mathbf{q})$ is the Form Factor of a single chain. $P(\mathbf{q})$ is directly related to the square of the radius of gyration R_g^2 or to its component R_x^2, R_y^2, R_z^2 following the Ox, Oy, Oz axis. At small q values, the Guinier domain defined by $q \leq 1/R_g$ is reached and the Zimm approximation can be applied; $P(\mathbf{q})$ becomes:

$$P(q_x, q_y, q_z) \propto n^2 (1 - q_x^2 \cdot R_x^2 - q_y^2 R_y^2 - q_z^2 R_z^2).$$

q_x, q_y, q_z are the projections of the scattering vector along Qx, Oy, Oz axis. In the case of liquid-crystal polymers, the direction of the magnetic field which aligns the liquid crystal molecules is a symmetry axis of the polymer. If Ox is parallel to the direction of the magnetic field, R_x^2 is called $R_\parallel^2$. The two other components are then perpendicular to the magnetic field:

$$R_y^2 = R_z^2 = R_\perp^2.$$

The radius of gyration is then given by:

$$R_g^2 = 2R_\perp^2 + R_\parallel^2.$$

So, when the magnetic field and the scattering plane are placed perpendicular to the incident beam, we measure the scattering intensity in the planes containing the parallel and the perpendicular directions to the magnetic field:

$$\frac{1}{I} = \frac{1}{I(0)} \cdot (1 + q_\parallel^2 \cdot R_\parallel^2 + q_\perp^2 \cdot R_\perp^2).$$

The polymer anisotropy is then calculated in terms of components of radius of gyration ($R_{\|}$) and perpendicular ($R_{\perp}$) to the magnetic field.

In most cases, the liquid-crystal polymers are only partially deuterated. It is indeed difficult from a chemical point of view to substitute all the protons. Moreover, the partial labeling presents the advantage that we can choose the part of the macromolecule to be observed.

Indeed, the intensity scattered by a mixture of hydrogenated polymers with partially deuterated polymers is associated to the form factor of the labelled part of the macromolecule. This can be experimentally demonstrated using the expression of the scattering function of a polymer chain with several scatterers (a_H or a_D for the labelled part, $a_2 \ldots, a_n$):

$$S(\mathbf{q}, (a_H, a_D), a_2, \ldots a_n) = NX_H X_D (a_H, a_D)^2 P(\mathbf{q}) + S_0(\mathbf{q}, a_H, a_D), a_2, \ldots, a_n),$$

where $P(\mathbf{q})$ is the partial form factor of the labelled part of the polymer. Experimentally, we show by taking either hydrogenated sample ($X_H = 1$) or a fully partially deuterated sample ($X_D = 1$), that there is no coherent scattering contribution from S_0 in the small q-range (Fig. 1.) S_0 is then negligible compared to the first term.

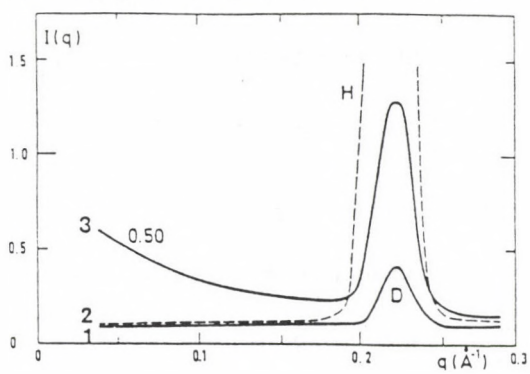

Fig. 1. Intensity scattered by a sample containing X_H of hydrogenated polymers and X_D of polymer deuterated on the main-chain only.
1. obtained with $X_D = 1$.
2. obtained with $X_H = 1$.
3. obtained with $X_D = X_H = 0.5$.

In the case of side-chain liquid-crystal polymers and combined liquid-crystal polymers, we were interested in the main-chain conformation, so only the main-chain has been deuterated, whereas only the spacer of the main-chain is deuterated in the case of main-chain liquid-crystal polymers [5].

Experimental results

The neutron experiments presented here have been carried out on the SANS spectrometer PAXY of the Lab. Léon Brillouin. The experimental conditions are described in details in two PhD theses which subjects were respectively the study of side-chain liquid-crystal polymer [6] and the study of main-chain liquid-crystal polymer [7]. Let us just recall that the q-range used for these studies is typically 0.01 Å$^{-1} < q < 0.3$ Å^{-1} and that the samples are monodomains oriented by a magnetic field of 1.4 T by decreasing the temperature from the isotropic phase down to the glassy state.

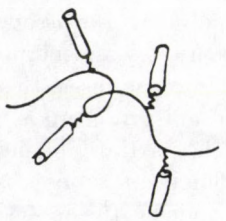

Side-chain liquid-crystal polymers. Side-chain liquid-crystal polymers are deuterated on the main-chain only, in order to study the main-chain conformation of the polymer in the different mesophases. The main-chain is usually a polyacrylate or polymethacrylate chain with a spacer of six methyl, a biphenyl or a phenyl benzoate group as a hard core ended by a small alkyl chain of variable length. The series of liquid-crystal polymer studied presents, following the nature of the hard core or the length of the terminal chain, two types of succession of phases by decreasing the temperature:

I (isotropic phase)$-N - S_A - T_g$ (glassy state)

or

I (isotropic phase)$-N - T_g$.

For example, the polymethacrylate PMA-OC_4H_9:

$$\sim [CH_2 - C(CH_3)(CO_2-(CH_2)_6- O - \phi - CO_2 - \phi - OC_4H_9)] \sim$$

corresponds to these transition temperatures:

$$I - N(108\ ^\circ\mathrm{C}) - S_A(98\ ^\circ\mathrm{C}) - T_g(35\ ^\circ\mathrm{C}).$$

Excepted in the isotropic phase, the conformation of the polymer backbone is no more an isotropic coil in the different phases:

– when the liquid-crystal polymer presents only a nematic phase, the polymer backbone adopts a prolate conformation in which the average direction of the backbone is that of the liquid crystal axis. This situation is sterically convenient since the packing is fulfilled simultaneously for the side-chain part and the backbone.

– when the liquid-crystal polymer presents the $S_A - N - I$ phase succession, the anisotropy of the polymer backbone is always such that the backbone is mostly oriented perpendicular to the direction of the liquid-crystal molecules ($R_{\|} < R_{\perp}$). This anisotropy corresponding to an oblate backbone shape is small in the nematic phase. It increases in the S_A phase reaching anisotropy ratios of $R_{\perp}/R_{\|} = 4$. It has been experimentally ascertained by neutron diffraction [8] that the polymer backbone is mostly localized between the liquid crystal molecules layers in the S_A phase. The stronger the smectic order is, the more the polymer backbone is excluded from the liquid crystal molecules zones. Even in the nematic phase, it remains some fluctuations (corresponding to a smectic order of short range but still comparable to the polymer dimension (100 Å)). These fluctuations could be sufficient to induce the oblate anisotropy observed in the nematic phase.

Main-chain liquid-crystal polymers. The only experimental observations of the conformation of a main-chain liquid-crystal polymer concern a nematic polyester synthesized by Blumstein [9], and

successively studied by SANS by d'Allest et al [10] and Li et al [5]. This polymer presents the advantages of a broad nematic phase with a relatively low temperature for the isotropic–nematic transition. The SANS results indicate in the nematic phase that the chain is extremely stretched in the direction of the applied magnetic field. The anisotropy is also so large that the Zimm approximation can no more be used to obtain the component $R_{\|}$. Using the cylinder model for the scattering function, they show that the ratio (cylinder radius/cylinder length) can reach a value greater than thirty! On the other hand, this polymer has the behaviour of a random coil in the isotropic phase with a size proportional to the root mean square of its length (Gaussian coil). The flexibility of the chain is then totally recovered in this phase [7].

Combined liquid-crystal polymers. The combined liquid-crystal polymer is a combination of a main-chain and a side-chain polymer. What will be the resulting polymer conformation? Is there a competition between the liquid crystal molecules or a reinforcement of the liquid crystal effect (cooperative effect)?

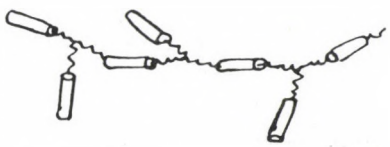

The only combined liquid-crystal polymer studied by SANS until now presents a main-chain liquid-crystal molecule of length 32 Å and a shorter side-chain liquid-crystal molecule of 23 Å [10]. It corresponds to the following formula:

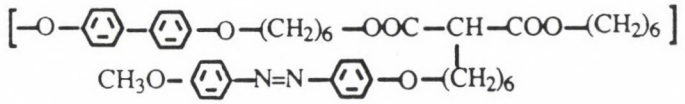

and shows the following phase succession by decreasing the temperature:

$I(153\ °C) - N(136\ °C) - S_A(130\ °C) - S_C(109\ °C)$ (tilted smectic phase).

By labeling the biphenyl group of the main-chain, one obtains by SANS the conformation of the main-chain alone. This study shows that the main-chain is only slightly oriented in the direction of the magnetic field in the nematic and the S_C phases (30 % of deformation $R_{\|}/R_{\perp}$). This prolate anisotropy increases in the S_A phase without reaching the extreme stretching found for the linear polymer [5]. The smectic layer thickness corresponds moreover to the length of the side-chain. All these results seem to indicate that the main-chain does not contribute to the mesomorphic character of the phase which is then dominated by the side-chain contribution.

In this sense, there is neither competition, nor cooperative effect between these two liquid crystal molecules. This polymer can be considered as a very "diluted" side-chain polymer. Indeed, the distance between two side-chain neighbours is large (30 Å) compared to the case of the preceding side-chain polymers which possess lateral liquid crystal molecules, e.g. in every (meth)acrylate bond. In this case, the interactions occur no more between side-chains of a same polymer (which provides $R_{\|} \ll R_{\perp}$) but also and perhaps mainly between side-chains belonging to other polymers. The slight stretching ($R_{\|} \geq R_{\perp}$) can even be understood as the result of the packing effect similar to what was found for nematic side-chain

polymers. However, it can be hazardous to generalize these results since several other combined liquid-crystal polymers present the smectic phases for which the layer thickness is very different from the length of both liquid crystal parts.

Concluding remarks

General features of three large families representative of the liquid crystalline polymers have been drawn here. In all the cases we have shown, using the SANS technique associated to the labelling method, that the polymer chain is always affected by the liquid crystal order. Although the spacer plays a decoupling role between the rigid part of the liquid crystal and the polymer itself, the main-chain can be extremely deformed in the mesophases. It is the case of the main-chain liquid-crystal polymer, in which even the spacer is itself stretched in the nematic phase, or the case of side-chain polymer confined between liquid crystal layers in the smectic phase. On the other hand, adding supplementary liquid crystal molecules on the side of a main-chain liquid crystal polymer does not necessarily procure a supplementary ordering. Obviously, the behaviour of the combined liquid-crystal polymer is more complicated and needs other studies in order to generalize these results. A selective deuteration of either the main-chain or the side-chain, could be a good solution to identify by neutron diffraction as it has been done in [8], the role of each liquid-crystal molecule. This method can be particularly interesting when the layer thickness is not commensurable with the length of the liquid-crystal molecules.

References

1. H. Finhelmann, H. Ringsdorf and J. H. Wendorff, Makromol. Chem., *179*, 273, 1978.
2. a) L. Beltzung, C. Strazielle, J. Zinn-Justin, Phys. Rev. Lett., *39*, 95, 1984; b) A. Lapp, J. Herz, C. Strazielle, Makromol. Chem., *186*, 1919, 1985.
3. P. G. de Gennes, Scaling Concept in Polymer Physics, Cornell Univ. Press, 1979.
4. J. P. Cotton, D. Decker, H. Benoit, B. Farnoux, J. Higgins, G. Jannink, J. des Cloizeaux, R. Ober and C. Picot, Macromolecules, *7*, 863, 1974.
5. M. H. Li, A. Brulet, P. Davidson, P. Keller and J. P. Cotton, Phys. Rev. Lett., *70*, 2297, 1993.
6. L. Noirez, Ph. D. Thesis, Univ. of Orsay, 1989.
7. M. H. Li, Ph. D. Thesis, Univ. of Orsay, 1993.
8. L. Noirez, P. Davidson, W. Schwarz and G. Pepy, Liq. Cryst., *16*, 1081, 1994.
9. A. Blumstein and S. Vilasagar, Mol. Cryst. Liq. Cryst., *72*, 1, 1981.
   R. B. Blumstein and A. Blumstein, Mol. Cryst. Liq. Cryst. (Lett.), *165*, 361, 1988.
10. J. S. d'Allest, P. Sixou, A. Blumstein, R. B. Blumstein, J. Teixeira and L. Noirez, Phys. Rev. Lett., *61*, 2562, 1980.
11. a) B. Reck, Ph. D. Thesis, Univ. of Mainz, 1988; b) L. Noirez, H. Poths, R. Strazielle and R. Zentel, to be published in Liq. Cryst.

Acta Physica Hungarica 75 (1–4), pp. 107–116 (1994)

NEUTRON SCATTERING FROM AMORPHOUS METALS

P. LAMPARTER

Max-Planck-Institut für Metallforschung
Seestrasse 92, 70174 Stuttgart, Germany

Detailed information about the structure of amorphous metallic alloys, the so-called metallic glasses, is obtained from neutron diffraction in combination with the isotopic substitution technique. In many cases neutron diffraction and X-ray diffraction are complementary techniques. The atomic structure of these materials is characterized by distinctive topological and chemical ordering effects.

The establishment of theoretical models on the basis of accurate structural data provides a deeper insight into the 3-dimensional arrangement of the atoms in amorphous metals.

Neutron diffraction is particularly suited for the investigation of the distribution of hydrogen atoms in amorphous alloys.

Small angle scattering presents a means for the characterization of the inhomogeneous structure of metallic glasses.

1. Introduction

The structure of amorphous alloys is described by means of their partial structure factors and partial pair correlation functions. From the pair correlation functions the atomic distances and the coordination numbers are obtained. Neutron diffraction presents a very powerful tool for the establishment of these partial functions because of the possibility to achieve a strong contrast variation by adoption of the isotopic substitution technique. In favourable cases the combination of neutron and X-ray diffraction as complementary methods is very useful.

During the last years a shift of the main activities in the field of structural investigations of amorphous alloys from the experimental side to the modelling side could be observed.

A special topic of increasing interest is the incorporation of hydrogen in amorphous metals. Here the merit of neutron diffraction in combination with hydrogen-deuterium substitution is obvious.

Small angle scattering experiments are essential for the investigation of metallic glasses beyond their atomic scale structure.

2. Theoretical

In the following the basic definitions and equations needed for the characterization of the structure of amorphous alloys are summarized. For a detailed description see e.g. the reviews by Wagner [1] and by Lamparter and Steeb [2].

The total structure factor according to the definition by Faber and Ziman [3] is obtained from the coherent cross-section per atom $d\sigma/d\Omega|_{\text{coh}}$ as:

$$S^{FZ}(Q) = \left[d\sigma/d\Omega|_{\text{coh}}(Q) - (<b^2> - <b>^2)\right] / <b>^2, \tag{1}$$

where $Q = 4\pi \sin\Theta/\lambda$ = scattering vector, 2Θ = scattering angle, λ = wavelength, b = scattering length (which depends on Q for X-rays), and $< \ldots >$ = compositional average.

In an alternative definition of the structure factor by Ashcroft and Langreth [4] the Laue monotonic term $<b^2> - <b>^2$ is not subtracted:

$$S^{\text{AL}}(Q) = d\sigma/d\Omega|_{\text{coh}}(Q)/ <b^2>. \tag{2}$$

For a n-component system the total structure factor $S(Q)$ is composed of $n(n+1)/2$ partial structure factors $S_{ij}(Q)$, each of them describing the structural correlations of $i-j$ atomic pairs ($S_{ij}(Q) = S_{ji}(Q)$). For a binary system with concentrations c_1 and c_2 the total $S^{FZ}(Q)$ is:

$$S^{\text{FZ}}(Q) = \left[c_1^2 b_1^2 S_{11}(Q) + c_2^2 b_2^2 S_{22}(Q) + 2c_1 c_2 b_1 b_2 S_{12}(Q)\right] / <b>^2. \tag{3}$$

The partial pair correlation functions $G_{ij}(R)$ are obtained from the structure factors by Fourier transformation:

$$G_{\text{ij}}(R) = \frac{2}{\pi} \int_0^\infty Q\,[S_{ij}(Q) - 1] \sin QR\, dQ. \tag{4}$$

Fourier transformation of the total structure factor $S^{FZ}(Q)$ yields the total pair correlation function $G^{FZ}(R)$, which is composed of the $G_{ij}(R)$ functions as:

$$G^{FZ}(R) = \left[c_1^2 b_1^2 G_{11}(R) + c_2^2 b_2^2 G_{22}(R) + 2c_1 c_2 b_1 b_2 G_{12}(R)\right] / <b>^2. \tag{5}$$

Note that $G^{AL}(R) = G^{FZ}(R) <b>^2 / <b^2>$.

The $G_{ij}(R)$ are related to the partial pair density distribution functions $\rho_{ij}(R)$ by:

$$G_{ij}(R) = 4\pi R\,[\rho_{ij}(R)/c_j - \rho_0], \tag{6}$$

where ρ_0 is the mean atomic number-density of the system. The $\rho_{ij}(R)$ represent the number of j-atoms per unit volume at distance R from an i-atom at the origin.

The interatomic distances R_{ij} are given by the positions of the maxima of the $G_{ij}(R)$ or $\rho_{ij}(R)$, and the partial coordination numbers Z_{ij} are obtained from integration over the first maxima of the radial distribution functions $4\pi R^2 \rho_{ij}(R)$.

The widths ΔR_{ij} of the peaks of the distribution functions are a measure for the widths of bond-lengths distributions, resulting from structural and thermal disorder.

We note that besides the description of the structure in terms of atomic pairs there is an alternative formalism, introduced by Bhatia and Thornton [5], in terms of density and concentration fluctuations. This formalism, however is out of the scope of the present paper.

3. Determination of partial pair correlation functions

A detailed investigation of the structure of an amorphous system means the evaluation of the complete set of the partial structure factors using one of the different contrast variation methods. For a binary alloy three total $S(Q)$ have to be measured with chemically identical samples, but where the ratio of the scattering lengths b_1 and b_2 is different in each case. This provides a set of three equations according to Eq. (3) with different weighting factors w_{ij} which can be solved for the three partial $S_{ij}(Q)$. The determinant of the w_{ij} is a measure of the reliability of the results to be expected. In the following examples for contrast variation are given which involve neutron diffraction.

3.1. Combination of neutrons and X-rays for $Ti_{84}Si_{16}$

The combination of neutron scattering and X-ray scattering is suitable in those cases where the scattering lengths for the two radiations are sufficiently different for at least one of the components, in particular for elements with a negative neutron scattering length. Figures 1a,b show the total correlation functions $G_x(R)$ and $G_n(R)$ for the metallic glass $Ti_{84}Si_{16}$, produced by melt spinning (Lamparter et al [6]). Due to the negative scattering length of Ti ($b_{Ti} = -0.3438$, $b_{Si} = +0.4149$, in 10^{-12}cm) the Ti–Si correlation appears as a distinct negative peak in $G_n(R)$ at $R_{TiSi} = 2.64$ Å, followed by the positive Ti–Ti peak at $R_{TiTi} = 2.9$ Å. The total $G^{FZ}(R)$ in terms of the partial $G_{ij}(R)$ are:

$$G_x(R) = 0.80G_{TiTi}(R) + 0.01G_{SiSi}(R) + 0.19G_{TiSi}(R),$$

$$G_n(R) = 1.69G_{TiTi}(R) + 0.09G_{SiSi}(R) - 0.78G_{TiSi}(R).$$

Neglecting the small contribution of the Si–Si pairs the two equations were solved for the partial functions $G_{TiSi}(R)$ and $G_{TiTi}(R)$ (Fig. 1c). The first peak of G_{TiSi} is quite sharp, $\Delta R_{TiSi} = 0.33$ Å, and drops down again to the $-4\pi\rho_0 R$ line between the first and the second peak.

This well defined Ti–Si coordination sphere reflects the chemical bonding between the metal atoms and the metalloid atoms. The metal–metal correlation is less distinct, $\Delta R_{TiTi} = 0.45$ Å. It has been found generally with metal-metalloid glasses that their short range order is characterized by a chemical ordering effect between the unlike constituents.

3.2. Isotopic substitution for $Ni_{80}P_{20}$ and $Ni_{81}B_{19}$

The most reliable partial structure factors were obtained with the isotopic substitution technique. As an example the results from a neutron diffraction experiment with amorphous melt spun $Ni_{80}P_{20}$ (Lamparter and Steeb [7]) are presented. Figure 2 shows the total structure factors of three $Ni_{80}P_{20}$ samples which were prepared using different Ni isotopes (^{nat}Ni,$b = 1.03$; ^{62}Ni,$b = -0.87$; ^{0}Ni,$b = 0$).

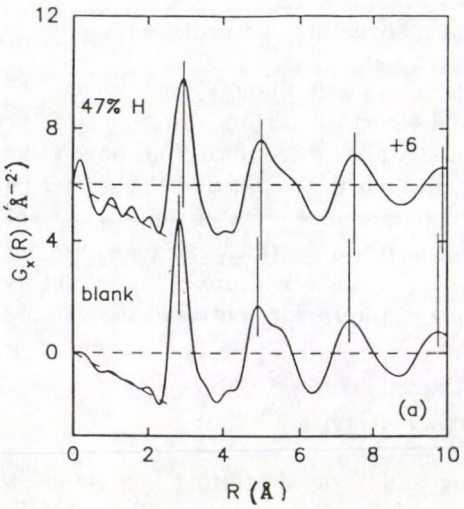

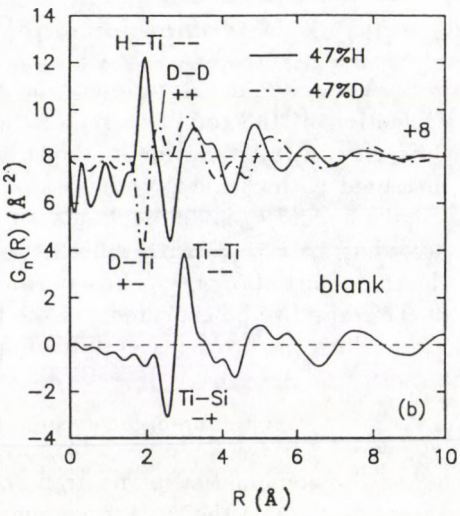

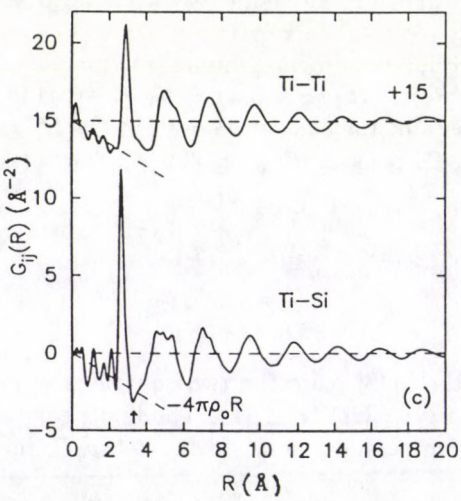

Fig. 1a. $Ti_{84}Si_{16}$ blank and with 47 % H: total pair correlation functions $G^{AL}(R)$ from X-ray diffraction.
Fig. 1b. $Ti_{84}Si_{16}$ blank and with 47 % $H(D)$: total pair correlation functions $G^{AL}(R)$ from neutron diffraction.
Fig. 1c. $Ti_{84}Si_{16}$: partial pair correlation functions. The arrow marks the point where $G_{TiSi}(R)$ drops down to $-4\pi\rho_0 R$, corresponding to $\rho_{TiSi}(R) = 0$.

The zero-scattering isotopic mixture ^{0}Ni was produced by alloying ^{62}Ni and ^{60}Ni ($b = 0.28$). The latter sample was designed in such a way that the weighting factors of the Ni–Ni and the Ni–P correlations become zero and thus it became possible to observe directly the metalloid-metalloid correlations in a metallic glass.

The very different weighting factors and accordingly the very different shapes of the total $S(Q)$ in Fig. 2 show the strong variation of contrast in the present case. The three corresponding equations yield the partial structure factors $S_{ij}(Q)$ in Fig. 3, and by Fourier transformation the partial pair correlation functions $G_{ij}(R)$ in Fig. 4 (dotted curves). In Fig. 5 the $G_{ij}(R)$ of the metallic glass $Ni_{81}B_{19}$, derived in the same way by Lamparter et al. [8], are plotted. The structural parameters, taken from the partial $G_{ij}(R)$ are listed in the Figures.

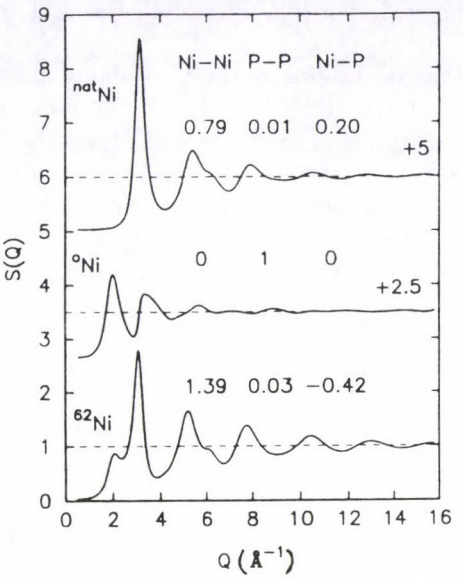

Fig. 2. $Ni_{80}P_{20}$: total structure factors $S^{AL}(Q)$. The numbers are the coefficients of the $S_{ij}(Q)$ in Eq. (3)

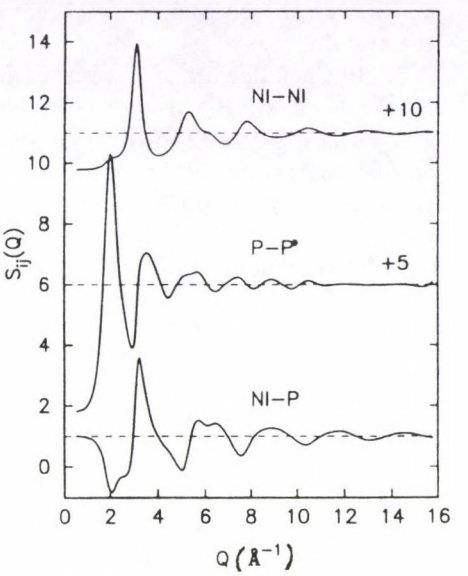

Fig. 3. $Ni_{80}P_{20}$: partial Faber–Ziman structure factors

The results show that the atomic structure in this type of amorphous alloys is well organized: The metal–metalloid correlation, compared with the metal–metal correlation, is characterized by a smaller distance and by a sharper bond-length distribution. After the main peak the metal–metalloid function again drops down to the $-4\pi\rho_0 R$ line. These pronounced features are due to the chemical interaction between the metal and the metalloid atoms. The smaller metalloid atoms, P and B, do not appear as direct neighbours, but exhibit as a double peak a distinct distance correlation at two distances between 3 and 4 Å followed by extended oscillations. The structure of both metallic glasses seems to be quite similar, but the correlation functions $G_{PP}(R)$ and $G_{BB}(R)$ show that there are also differences in detail.

For the metallic glass $Ni_{65}B_{35}$ accurate partial functions have been established by Ishmaev et al [9] using also Ni-isotopes.

4. Structural models

The body of structural information provided by pair correlation functions of amorphous systems is generally limited for two reasons: First, they present a statistical description in terms of average values of the structural parameters which may vary from site to site of a selected reference atom. Secondly, they present a one-dimensional projection of the three-dimensional atomic arrangement. By construction of models, using the experimental results as a guideline, information beyond pair correlations can be obtained, such as information about bond angles

and about the question whether or not preferred coordination polyhedra exist in the system.

In the following some results from model calculations for the amorphous alloys $Ni_{80}P_{20}$ and $Ni_{81}B_{19}$ using the Reverse Monte Carlo (RMC) method by Mc Greevy and Pusztai [10] are shown. As starting configuration in each case a cluster of 1500 atoms was generated by a molecular dynamics calculation, where the attractive potential between unlike atoms was the strongest one. Then the configuration was refined by RMC. The agreement between the experimental $G_{ij}(R)$ and those calculated from the model clusters in Figs. 4, 5 is excellent.

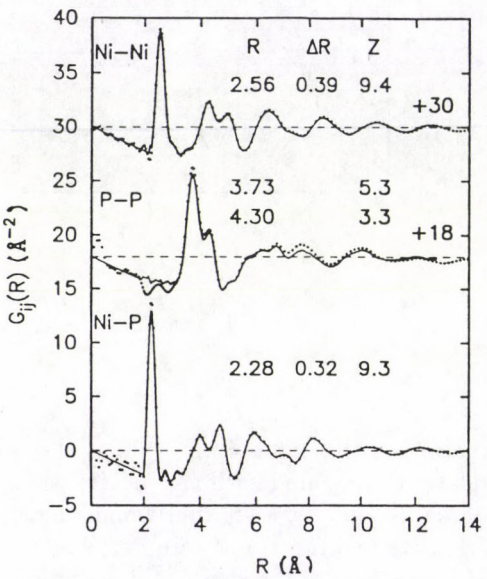

Fig. 4. $Ni_{80}P_{20}$: partial pair correlation functions. ··· experimental, — RMC model

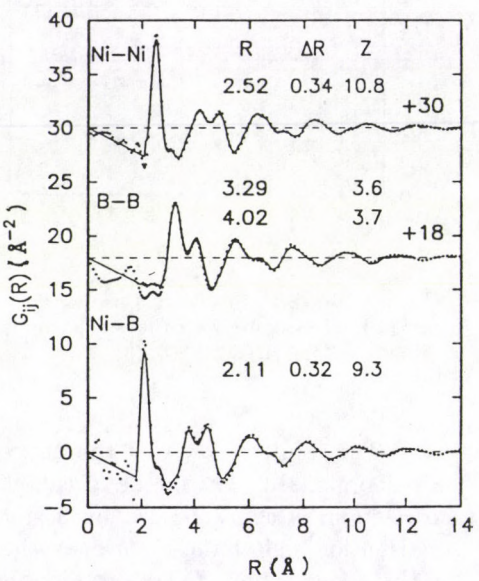

Fig. 5. $Ni_{81}B_{19}$: partial pair correlation functions. ··· experimental, — RMC model

From the coordinates of the three-dimensional model clusters further structural properties can be calculated, which are not accessible from the 1-dimensional experimental pair correlation functions. The histograms of the coordination numbers of Ni-atoms around P or B in Fig. 6 show that the value of about 9 atoms, as deduced from neutron diffraction, represents an average value of a rather broad distribution between 6 and 11 Ni-atoms, which appears to be sharper for the $Ni_{81}B_{19}$ alloy.

As preferred coordination polyhedra around the metalloid atoms in amorphous metal–metalloid alloys trigonal prisms of 6 metal atoms with 3 further metal atoms on the square faces of the prisms have been proposed (see e.g. Dubois et al, [11]). This structural unit occurs in the related crystalline phases, e.g. in Ni_3P and Ni_3B. An analysis concerning this feature was performed with the present RMC

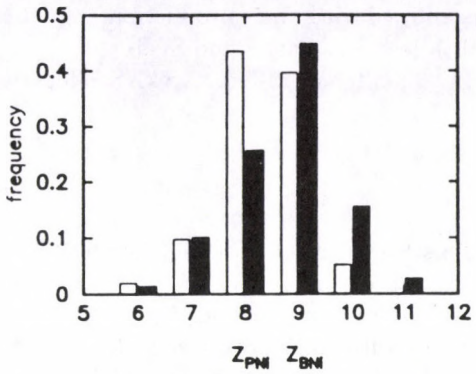

Fig. 6. $Ni_{80}P_{20}$, $Ni_{81}B_{19}$: partial coordination numbers of Ni-atoms around P and B. Histograms from RMC model (full bars for P)

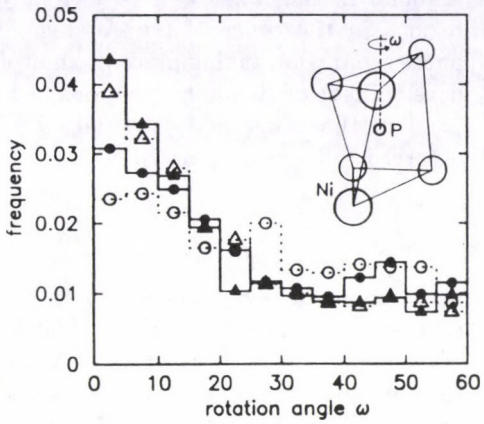

Fig. 7. $Ni_{80}P_{20}$ (•), $Ni_{81}B_{19}$ (▲): Histograms of rotation angle ω. Full symbols with RMC model, open symbols for random distribution

clusters (Fig. 7): The angles ω of rotation of 3 Ni-atoms, being mutual neighbours, against 3 further Ni-atoms, placed at the opposite side of a central P-atom, were recorded. Opposite means that the angle of inclination between the two tetrahedra, having a P-atom as common vertex, has to be within a certain limit (30° was chosen in the present case). Fig. 7 shows the histograms of ω. Those double-tetrahedra where ω is not too far from zero may be regarded as more or less distorted trigonal prisms, whereas those where ω is large may not. In fact, a certain preference of trigonal prisms is observed, however, the distribution is smeared out over the whole range between 0° and 60°.

The dashed line in Fig. 7 shows the histogram for 750 statistical reference clusters, where Z_{PNi} Ni-atoms were placed randomly, i.e. without any packing rule, around a central P-atom. The frequencies of Z_{PNi} were taken from Fig. 6. Again a preference of prismatic arrangements is observed. From this we have to conclude that we do not need stereochemical concepts with reference to crystalline counterparts to explain the occurrence of trigonal prisms in the metallic Ni–P glass, but simply statistical packing. The same behaviour is stated for the Ni–B glass.

5. Small angle scattering

Small angle neutron scattering (SANS) experiments revealed that many metallic glasses are not homogeneous, but contain structural fluctuations, which often occur on two different length scales (see e.g. Lamparter and Steeb [12]).

Frequently a scattering behaviour according to the Guinier law (Guinier and Fournet [13])

$$I(Q) = \text{const} \cdot \exp(-R_G^2 Q^2/3) \tag{7}$$

is found in the range $Q > 0.1$ Å^{-1}, yielding Guinier radii R_G of the scattering regions in the order of ten Å (Fig. 8). These regions have been attributed to phase separation taking place in amorphous alloys during their production, e.g. the development of B-enriched regions in $Fe_{80}Bi_{20}$ (see e.g. Faigel and Sváb [14]).

In the range of very small $Q < 0.1$ Å^{-1} often a different SANS effect is observed following a power law

$$I(Q) = \text{const} \cdot Q^{-S} \tag{8}$$

with exponents $-S$ between -3 and -4. This SANS effect reflects extended fluctuations on length scales up to 1000 Å or more, the source of it being still subject of ongoing research work. Fig. 9 shows SANS curves of amorphous $Ni_{30}Ti_{60}Si_{10}$ in the melt spun blank state as well as after loading with 16 % hydrogen or deuterium, respectively (Lamparter and Boucher [15]). The scattering was explained by the existence of inner surfaces in the as prepared glass, giving rise to a power law scattering ($-S = -2.8$). The absorbed H(D)-atoms tend to segregate at these inner surfaces. This causes an enhancement of the scattering contrast, which is larger with deuterium than with hydrogen due to its larger scattering length.

Coming back to the atomic structure of phase separated amorphous alloys it should be noted that the structural parameters deduced from wide angle diffraction represent average values of the two phases, which complicates their interpretation considerably.

Furthermore, it is evident that a detailed study of an amorphous system may require a very extended Q-range to be covered, e.g. from 10^{-4} Å^{-1} up to 30 Å^{-1}.

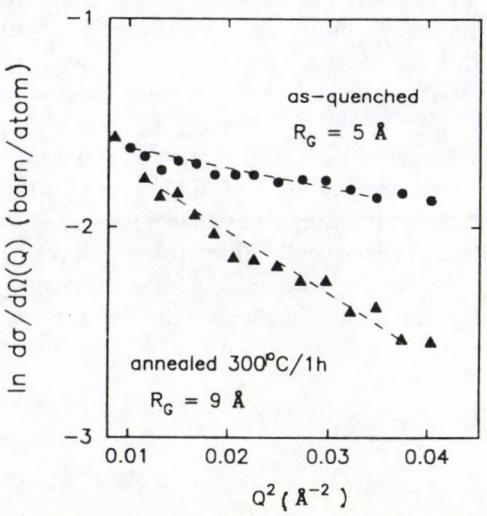

Fig 8. $Fe_{80}B_{20}$: Guinier plot of small angle neutron scattering. --- linear fit

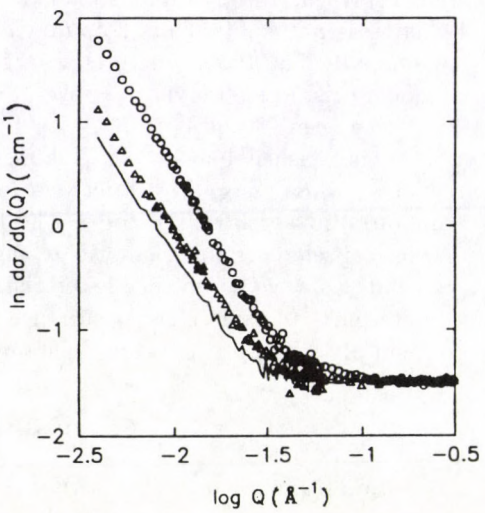

Fig. 9. $Ni_{30}Ti_{60}Si_{10}$: small angle scattering. — blank, △ with 16 at% H, o with 16 at% D

6. Hydrogen in amorphous $Ti_{84}Si_{16}$

Neutron diffraction, in contrast to X-ray diffraction, is particularly suited for the investigation of hydrogen in amorphous alloys. In addition, isotopic substitution of hydrogen ($b = -0.374$) by deuterium ($b = 0.667$) yields information about partial correlation functions. As an illustrative example some results on hydrogenated amorphous $Ti_{84}Si_{16}$ are presented in Figs. 1a,b (Lamparter and Steeb [16]). The total pair correlation functions $G(R)$ in Fig. 1a, as determined by X-ray diffraction, provide no information about the hydrogen itself, but they show how the amorphous host matrix is modified by the absorption of hydrogen atoms. The shift of the maxima towards larger distances reveals an expansion of the structure by about 5 %.

The neutron $G(R)$ functions in Fig. 1b show very strong changes after hydrogen loading due to the contributions of the partial correlation functions which involve H(D). The opposite signs of the scattering lengths of H and D enable the identification of the individual peaks in the total $G(R)$, as marked in Fig. 1b, and the determination of structural parameters, though the complete set of 6 partial correlation functions of the 3-component system is not known. Partial coordination numbers were determined by fitting Gaussian functions to the individual peaks. The H(D)-Ti peak at 1.93 Å is positive with H and negative with D. The coordination number $Z_{H(D)-Ti} = 4$ means that the hydrogen atoms occupy tetrahedral Ti_4 sites in the Ti–Si glass. The H(D)–H(D) correlation appears as a positive peak at 2.25 Å with D, but only as a shoulder with H because of the smaller scattering length of H. The coordination number is $Z_{H(D)-H(D)} = 2$. As the H–H distance of 2.25 Å is distinctly larger than the distance between the centres of two adjacent Ti-tetrahedra (1.25 Å) the H-atoms do not occupy neighbouring tetrahedral sites in the structure.

References

1. C. N. J. Wagner, J. Non-Cryst. Sol., *31*, 1, 1978.
2. P. Lamparter, S. Steeb, Structure of Amorphous and Molten Alloys, in: Material Science and Technology, Vol. 1, VCH, Weinheim, 1993, pp. 217–228.
3. T. E. Faber and J. M. Ziman, Phil. Mag., *11*, 153, 1965.
4. N. W. Ashcroft and D. C. Langreth, Phys. Rev., *156*, 685, 1967.
5. A. B. Bhatia and D. E. Thornton, Phys. Rev., *B2*, 3004, 1970.
6. P. Lamparter, A. Habenschuss and A. H. Narten, J. Non-Cryst. Sol., *86*, 109, 1986.
7. P. Lamparter and S. Steeb, Proc. 5th Int. Conf. on Rapidly Quenched Metals, 459, 1985.
8. P. Lamparter, W. Sperl, S. Steeb and J. Blétry, Z. Naturforsch., *37a*, 1223, 1982.
9. S. N. Ishmaev, S. L. Isakov, I. P. Sadikov, E. Sváb, L. Kőszegi, A. Lovas and Gy. Mészáros, J. Non.-Cryst. Sol., *94*, 11, 1987.
10. R. L. McGreevy and L. Pusztai, Molecular Simulation, *1*, 359, 1988. The RMC-program was kindly supplied by R. L. McGreevy.
11. J. M. Dubois, P. H. Gaskell and G. LeCaer, Proc. Roy. Soc. Lond., *A402*, 323, 1985.
12. P. Lamparter and E. Steeb, Proc. 4th Int. Conf. on Non-Crystalline Materials, NCM4, 137, 1988.
13. A. Guinier and G. Fournet, Small Angle Scattering of X-Rays, Wiley and Sons, London, 1955.
14. Gy. Faigel and E. Sváb, Proc. 5th Int. Conf. on Rapidly Quenched Metals, 487, 1985.
15. P. Lamparter and B. Boucher, Z. Naturforsch., *48a*, 1086, 1993.
16. P. Lamparter and S. Steeb, Physica, *B180*, 782, 1992.

Acta Physica Hungarica 75 (1-4), pp. 117-122 (1994)

STATIC AND DYNAMIC ATOMIC CORRELATIONS IN AMORPHOUS SYSTEMS

S. N. ISHMAEV and E. SVÁB[1]

Kurchatov Institute
123182 Moscow, Russia
[1] *KFKI Research Institute for Solid State Physics*
P.O.B. 49, 1525 Budapest, Hungary

Short-range order, medium-range structure and dynamics of metallic glasses Zr–Be, Ni–Nb and Ni–B were investigated by high r-space resolution pulsed neutron diffraction, small-angle and inelastic neutron scattering methods on isotopic substituted samples. The experimental data regarding partial atomic correlations were analysed by Monte Carlo and recursion methods. In Zr–Be system the structure is dominated by atomic sizes and composition, and the phonon spectrum splits into regions corresponding to the predominant vibrations of the heavy and light atoms. In Ni–Nb system the chemical short range order was determined and inhomogeneities of about 180 Å were detected. In Ni–B system Ni–Ni and B–Ni local arrangements are ordered, whereas Ni–B and B–B arrangements are more disordered.

Introduction

Short-range order and atomic vibrations, as well as the relationship between the structure, phonon and electron spectra of metallic glasses are attracting major interest, because of the unusual properties of these metastable systems. In studies of structural and dynamic correlations at the level of partial atomic distributions the most detailed information can be obtained by neutron scattering methods employing isotopic contrast of samples.

In this paper a brief review is given on our recent results on amorphous Zr–Be, Ni–Nb and Ni–B systems. Neutron diffraction, neutron inelastic scattering, small-angle neutron scattering and specific heat measurements were performed and computer modelling was applied using the experimental data. This work was done in the frame of scientific collaboration between Russian Research Centre Kurchatov Institute (KI) and Research Institute for Solid State Physics, Hungary (RISP).

Results and discussion

Zr–Be system

Amorphous Zr–Be is interesting because of the large difference in atom sizes and masses, thus this system can become amorphous in a wide range of composition. So, it is possible to identify the structure and dynamic characteristics of the individual components.

The structure factor $S(Q)$ was measured by the time-of-flight neutron diffractometer at the Linac "Fakel" pulsed source (KI) up to a momentum transfer of $Q_{max} = 41.5$ Å^{-1} [1]. As a result, the reduced radial atomic distribution function, $G(r)$ was determined by Fourier transformation with high spatial resolution: $\Delta r = 0.13$ Å. Figure 1 shows $G(r)$ functions for amorphous alloys of $Zr_{1-c}Be_c$ ($c = 0.3$, 0.4 and 0.5). The total $G(r)$ function represents the contributions of all three partial distributions in the first coordination shell:

$$r_{BeBe} = 2.25 \text{ Å}, \quad r_{ZrBe} = 2.71 \text{ Å} \quad \text{and} \quad r_{ZrZr} = 3.12 \text{ Å}.$$

In order to obtain reliable interpretation of the partial distributions A. Bratkovsky and A. Smirnov have used the direct Monte Carlo method with Morse type potential to construct the atomic structure model of amorphous Zr–Be system [1]. Calculations have provided a satisfactory description of experimental $G(r)$ functions as is shown in Fig. 1. The same parameters for interatomic potentials were used in a wide range of composition.

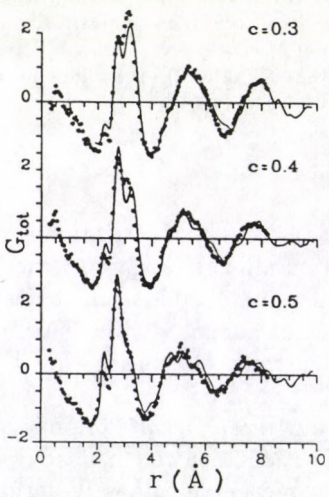

Fig. 1. Total reduced atomic distribution functions, $G_{tot}(r)$ of amorphous $Zr_{1-c}Be_c$ alloys. Experiment (dots) and direct Monte Carlo model calculation with Morse potential (solid line) [1]

The same samples were used by G. Syrykh and M. Khlopkin in a study [1] of the generalized phonon spectrum, $g(E)$ by inelastic neutron scattering (IR-8 reactor in KI) and by specific heat measurements in the temperature range of 1.6–40 K (KI), respectively. Using the obtained structure model A. Bratkovsky and A. Smirnov calculated the vibrational spectra by recursion method [1]. Figure 2 shows the experimental and calculated $g(E)$ spectra.

The density of vibrations splits into two clearly separated regions: 0–28 and 28–80 meV, corresponding to the predominant vibrations of the heavy (Zr) and light (Be) atoms. On the whole, the calculations have reproduced well the main features of experimental $g(E)$ curves and the composition dependence.

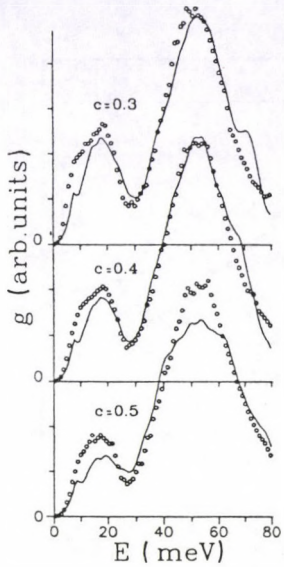

Fig. 2. Experimental (circle) and calculated by recursion method (solid line) generalized vibrational spectra of atoms, $g(E)$ in amorphous $Zr_{1-c}Be_c$ alloys [1]

Analysis of the partial distributions obtained by direct Monte Carlo modelling has indicated that the atomic structure of amorphous Zr–Be alloy is dominated by geometrical factors (atomic sizes and composition) and chemical ordering does not have a significant role. An increase in the Be concentration reduces the nearest distances between identical atoms, shifts and broadens the high-energy part of the vibrational spectrum, increases the Debye temperature, lowers the density of electron states and the superconducting transition temperature.

Ni–Nb system

In the $^{i}Ni_cNb_{1-c}$ system ($c = 0.62$ and 0.44) the partial structure correlations in the short- and medium-range order were investigated using isotopic substituted samples (i = nat, 58, 60, 62), neutron diffraction (KI, RISP) [2] and small-angle neutron scattering (LLB, Saclay) [3] methods.

For both concentrations the first neighbour distances between unlike atoms (Ni–Nb) are less than the mean value of the corresponding Ni–Ni and Nb–Nb distances, and concentration–concentration correlation function $G_{CC}(r)$ has minimum at this distance. This means that chemical short range order (CSRO) exists in these transition metal–transition metal type amorphous alloys and it is stronger in the Ni-rich composition.

Inhomogeneities in the amorphous isotopic Ni–Nb system have been investigated by small angle neutron scattering in the momentum transfer from 0.007 to 0.45 $Å^{-1}$ [3]. A strong increase in the structure factors is observed below 0.04 $Å^{-1}$, whereas above 0.06 $Å^{-1}$ they smoothly become constant. In order to clarify the

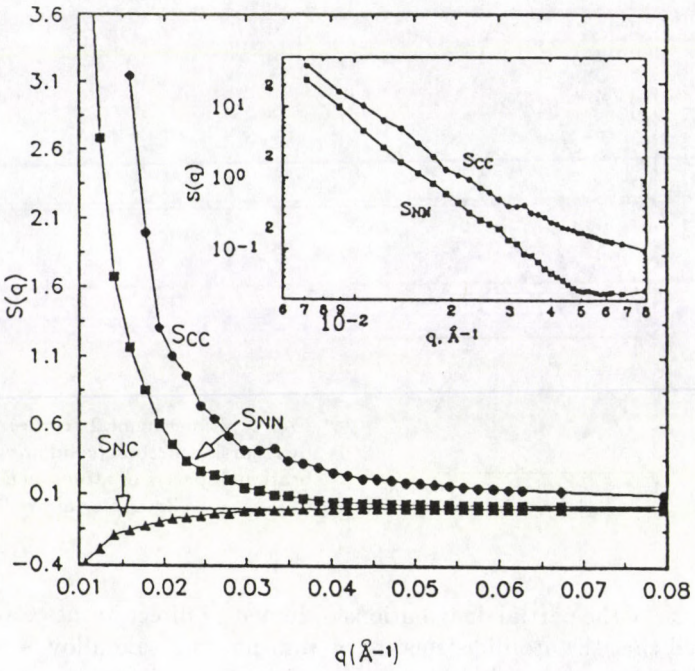

Fig. 3. Partial N–C structure factors at low Q values for $Ni_{44}Nb_{56}$ amorphous alloy [3]. The insert shows the curves in log-log representation

origin of this effect the total structure factors are separated into partial density-concentration (N–C) structure functions, as it is shown in Fig. 3.

It can be seen that inhomogeneities originate from both topological and chemical fluctuations. A characteristic correlation length of 180 Å was obtained from random two phase model.

Ni–B system

In our previous neutron studies of the partial structure [6] and dynamics [7] in isotopic $^{i}Ni_{65}B_{35}$ (i = nat, 60 and $\langle b \rangle_{Ni} = 0$) amorphous alloys it was shown that the local atomic order and vibrational spectrum differ significantly from the crystalline analog of Ni_2B. Existence of first neighbour B–B contact has been established [6]. On amorphisation a significant part of the density vibration states of the light metalloid atoms change over from the high- to the low-energy region [7]. Reverse Monte Carlo (RMC) simulation (L. Pusztai) [4] and Force Algorithm (FA) (M. Mendelev and D. Belashchenko) [5] were applied for modelling the atomic level structure of amorphous $Ni_{65}B_{35}$ using neutron diffraction measurements [6] as input data. From these calculations new information on local orientational ordering, i.e.

three particle first neighbour bond angle correlations $B(\cos\theta)$ were obtained, as it is shown in Fig. 4. Good qualitative agreement is obtained between the results by RMC and FA modelling.

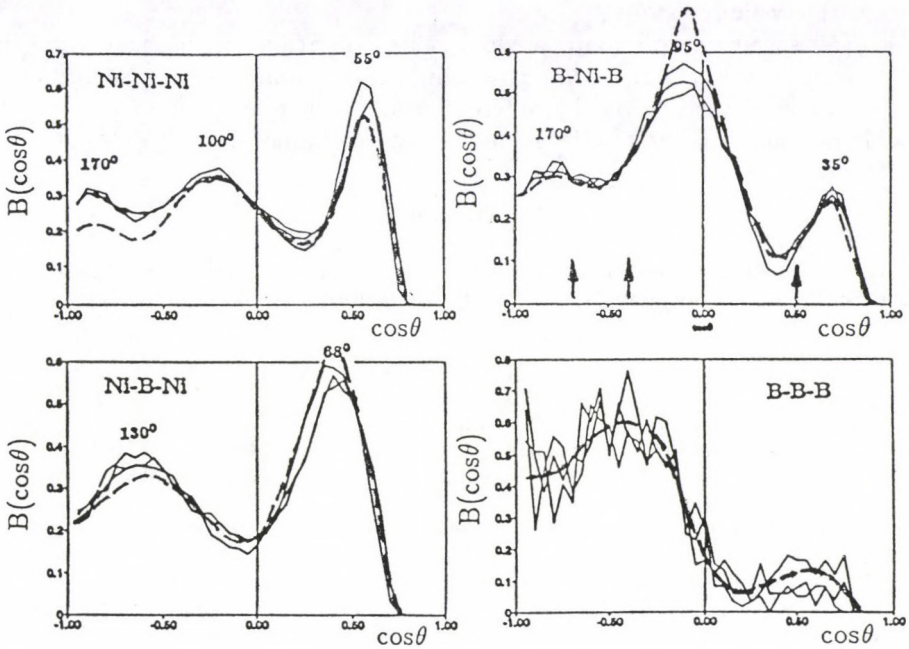

Fig. 4. Comparison of cosine distribution of bond angles in amorphous $Ni_{65}B_{35}$ obtained by RMC (three runs) [4] (solid line) and FA [5] (dashed line) calculations. The arrows note the angles in crystalline Ni_2B

RMC and FA model calculations confirm the experimental result of boron–boron contact at 1.9 Å with a coordination number of one. It is obtained that Ni–Ni and B–Ni local arrangements are ordered, whereas Ni–B and B–B arrangements are more disordered. Local symmetry does not imply close connection between glassy $Ni_{65}B_{35}$ and its crystalline counterpart Ni_2B.

Conclusions

Static correlations are different in amorphous systems of various types:

- in simple metal–metal amorphous alloys (Zr–Be) the short-range structure is dominated by geometrical factors, i.e. atom sizes and concentrations;
- in transition metal–metal type systems (Ni–Nb) weak CSRO is present;
- in transition metal–metalloid systems (Ni–B) strong CSRO exists between unlike atoms;
- in medium-range scale inhomogeneities may exist and they have both topological and chemical origin.

Dynamic correlations in amorphous systems with different atom masses have the following specific features:

- singularities in the density of vibrational states become indistinct and a long tail in the $g(E)$ spectrum appears at the high-energy region in comparison with crystalline state;
- $g(E)$ spectrum splits into predominantly vibrations of the heavy and light atoms, however, light atoms give some contribution to the low-energy region.

Complex investigations by different methods including computer modelling provide new and general knowledge on the nature of amorphous state.

Acknowledgements

We are grateful to all our co-authors [1–7]. This work was supported by the Russian Fundamental Science Foundation grant No. 93-02-2580 and by Hungarian OTKA grant No. 2934.

References

1. A. M. Bratkovsky, S. L. Isakov, S. N. Ishmaev, I. P. Sadikov, A. V. Smirnov, G. F. Syrykh, M. N. Khlopkin and N. S. Chernoplekov, J. Non-Cryst. Solids, *156–158*, 72, 1993.
2. E. Sváb, Gy. Mészáros, J. Takács, S. N. Ishmaev, S. L. Isakov and I. P. Sadikov, J. Non-Cryst. Solids, *144*, 99, 1992.
3. E. Sváb, S. Borbély, Gy. Mészáros, S. N. Ishmaev and R. Glas, Journal de Physique IV–C8, *3*, 291, 1993.
4. L. Pusztai and E. Sváb, J. Phys.: Condens. Matter, *5*, 8815, 1993.
5. M. I. Mendelev, D. K. Belashchenko and S. N. Ishmaev, Inorganic Materials, *29* (11), 1483, 1993.
6. S. N. Ishmaev, S. L. Isakov, I. P. Sadikov, E. Sváb, L. Kőszegi, A. Lovas and Gy. Mészáros, J. Non-Cryst. Solids, *94*, 11, 1987.
7. M. G. Zemlyanov, G. F. Syrykh, N. A. Chernoplekov and E. Sváb, J. Exp. Theor. Phys., *94* (11), 365, 1988.

Acta Physica Hungarica 75 (1–4), pp. 123–130 (1994)

SURFACES AND INTERFACES USING NEUTRON REFLECTIVITY

A. MENELLE

Laboratoire Léon Brillouin (CEA-CNRS)
CE-Saclay
91191 Gif-sur-Yvette Cedex, France

During the past ten years, neutron reflectivity has proved to be a very useful tool for the investigation of surfaces and interfaces. At Laboratoire Léon Brillouin in Saclay, we have developed a vast program of research centred on four different fields. Concentration profiles of polymers in the vicinity of the surface of solvent have been studied. Interdiffusion between polymer layers has also been investigated. Metallic multilayers which are now commonly used in many neutron optics devices like neutron guides, monochromators and supermirrors have received our interest.

Introduction

The understanding of surface and interfacial phenomena is of considerable interest, both for fundamental physics and technological applications. Many experimental techniques have been developed to study interfaces. One is neutron reflectivity that is now used for nearly ten years. Owing to their wave-like character, neutrons can be reflected and refracted at a boundary between two media. The angular or wavelength dependence of the reflectivity has been shown to be correlated to the scattering length density profile perpendicular to the surface. This provides us with a method for studying physical phenomena arising near the interfaces.

The purpose of this short paper is to give a rapid presentation of this relatively new technique. Using some selected examples, I will try to show which type of systems can be measured, and which type of information can be obtained from the experiments. I will also present the various limitations of this technique. More detailed information on the neutron reflectivity can be found in recent review papers [1–2].

Principles of neutron reflectivity

Neutron incident on an interface will undergo refraction and reflection provided the refractive indices of the media on the two sides of the interface are different. For non-magnetic material, neglecting the absorption, the refractive index n is given by the expression [3]:

$$n = 1 - \frac{Nb}{2\pi}\lambda^2, \tag{1}$$

where λ is the neutron wavelength, N is the number density, and b is the average coherent scattering length. For a magnetic material magnetised in the plane of the

surface there is an additional term. We have a spin dependent refractive index $n_\pm$ for the neutron polarized parallel (+) and antiparallel (-) to the applied field. It is given by:

$$n_\pm = 1 - \frac{N}{2\pi}\lambda^2(b \pm C\mu), \tag{2}$$

where μ is the average magnetic moment per atom and C is a constant equal to $0.2645 \cdot 10^{-12}$ cmμB^{-1}. At an interface separating two media 1 and 2, with refractive index n_1 and n_2, the relation between the angle of incidence θ_1 and refraction θ_2 will be given by Snell's law:

$$n_1 \cos\theta_1 = n_2 \cos\theta_2. \tag{3}$$

If, for example, medium 1 is vacuum (or the air) then $n_1 = 1$. If medium 2 is a non magnetic material with a positive scattering length, then n_2 is lower than 1. Expanding the cosine for small θ, we have total reflection for incident angles and wavelength that verify:

$$\frac{\theta_1}{\lambda} \leq \sqrt{\frac{N_2 b_2}{\pi}}. \tag{4}$$

For angles and wavelength where you have not total reflection, the reflectivity R can be calculated using the Fresnel's law, and is a function of the wavevectors k_i in medium i. Since the geometry of the reflectivity measurements is such that the angle of incidence and reflection are equal, only the component normal to the surface has to be considered. Then k_1, k_2 and R are given by:

$$k_1 = \frac{2\pi}{\lambda} \cdot \sin\theta_1, \tag{5}$$

$$k_2 = \sqrt{k_1^2 - 4\pi N_2 b_2}, \tag{6}$$

$$R = \left|\frac{k_1 - k_2}{k_1 + k_2}\right|^2. \tag{7}$$

In the case of a complex system composed of many layers deposited on a substrate, the reflection coefficient has to be calculated recursively from the substrate interface to the air. If the interface is not perfectly flat, and presents some imperfections, Névot and Croce [4] have shown that in the case of a Gaussian distributed height–height correlation function, the reflectivity R is modified by a Debye–Waller-like factor to obtain the corrected reflectivity R:

$$R_c = R \cdot \exp(-k_1 k_2 \langle\sigma\rangle), \tag{8}$$

where $\langle\sigma\rangle$ is the root mean square roughness of the interface.

As it has been seen in the preceding equations, the reflectivity is a function of the wavevector. In a neutron experiment, you have two different ways to change your wavevector. The most common method is to use an incident fixed wavelength and vary the reflection angle. But you can also work at fixed angle. and vary the wavelength. This last method is called the time-of-flight method.

A neutron time-of-flight reflectometer

At Saclay, on the ORPHEE reactor, we have installed two neutron reflectometers DESIR and EROS that use the time-of-flight method. In order to allow the measurements of liquid–air interfaces, they use a horizontal geometry. They are built under the same experimental set-up which is represented in Fig. 1. They are installed at the end of two different cold neutron guide benders that deliver a wavelength range from 4 Å to 20 Å. Neutron pulses are produced by a rotating disk chopper covered with absorbing material. The repetition rate is of the order of 15 Hz; the transmission can be varied from 0.5 % to 5 %. This defines the time resolution of the experiment. The angular resolution is given by two collimating slits F1 and F2 (see Fig. 1) situated at each end of an evacuated collimator 3 m long on DESIR and 4 m long on EROS. The horizontal size of the slits is 2 cm, and their vertical width can be varied from 0.5 mm to 4 mm. The deviation of the horizontal incoming beam toward the surface of liquid samples is done by three successive reflections on mirrors installed between the two slits. The use of neutron supermirrors enables to obtain incident angles up to five degrees without important flux losses. The beam is then reflected by the sample. In order to obtain a good angular resolution, the detector is located at the end of a long evacuated tube. The total time-of-flight path L is 7 m long. A He^3 X-Y multidetector of 128 x 128 cells with horizontal and vertical step of 1.5 mm is used for the detection of the reflected beam. Generally, the detector is not moved when changing the incident angle. The multidetector allows rapid alignment and sample quality checking. Time-of-flight acquisition can be performed simultaneously on 16 different areas of the detector. This enables very fast and convenient measurements of non-specular diffused intensity (intensity at outgoing angle different from the incident angle). A single He^3 counter is also available on EROS, and is used when angles higher than two degrees are needed for the measurements. The minimum reflectivity that can be measured with our reflectometers is of the order of 10^{-5}. A typical counting time is twelve hours for a low reflectivity measurement.

Neutron reflectivity enables the measurements of three main parameters with a precision of a few per cent. One is the layer thickness in a range from 10 Å to 5000 Å. From Eq. (1) one obtains also the coherent scattering length density (Nb), and with Eq. (8) interface roughness varying from 5 Å to 100 Å can also be investigated. The principal limitation comes from the minimum measurable reflectivity. Due to the decaying form of the reflectivity curves we have access to only a limited wavevector range that does not allow to obtain information on a short distance.

The main advantage of the time-of-flight configuration is that once the alignment is done, everything stays fixed during the acquisition and the whole reflectivity curve is recorded continuously. This is very interesting in the case of measurements on liquid samples, since during the whole acquisition, no vibrations coming from the various movements can induce perturbation of the liquid surface. For example, our reflectometers have been used to measure the concentration profile of a linear flexible polymer (poly-dimethylsiloxane) adsorbed from a good solvent (toluene) at

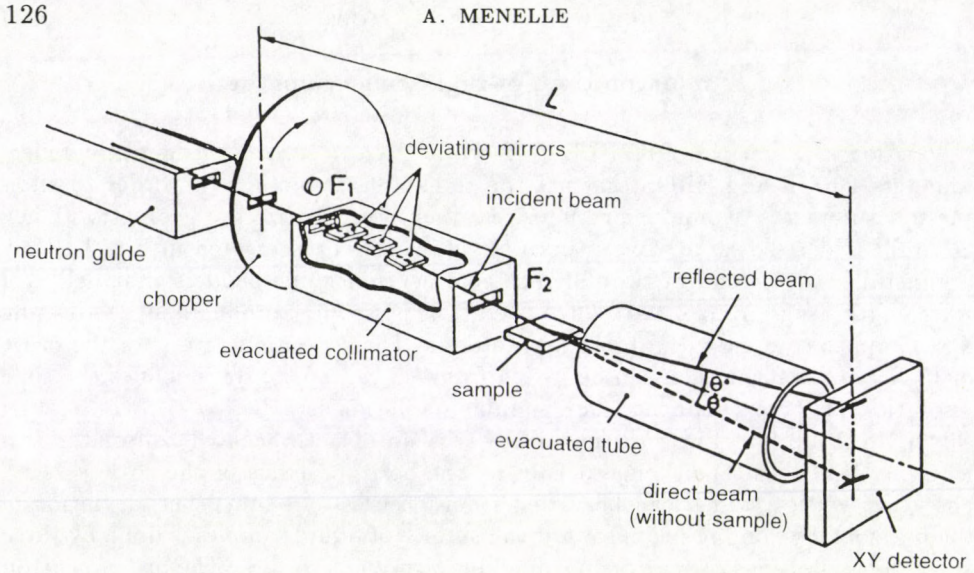

Fig. 1. General scheme of the Saclay time-of-flight reflectometers EROS and DESIR

the liquid–air interface [5]. It has been shown to conform to scaling laws proposed by de Gennes [6]. Depletion layers at the vicinity of the surface of a semidilute solution of polystyrene in toluene have also been measured [7]. The oil–water interfaces with and without surfactant layer have also been studied [8].

Polymer interdiffusion measurements

Due to the lengths of the order of 100 Å that can be measured, neutron reflectivity is well adapted to the measurements on polymer systems which generally have movements on this length scale. In addition, due to the large difference of scattering length between hydrogen and deuterium, one has a very good contrast between polymers if one is deuterated and not the other. Using the spin coating technique, one can prepare bilayers of polymers on silicon wafers up to a size of 5 cm in diameter [9] with an initial thickness of the interface of the order of 10 Å. In polymer layers below the glass transition, everything is frozen. If the temperature is increased above the transition, the molecules start to move. In a bilayer system as described before, the width of the interface will increase. This variation can be followed as a function of time, temperature and molecular weight. This enables to check the reptation model of de Gennes [10]. This has been done by Karim et al [11] using annealed and then quenched samples, the measurements have been done at room temperature.

As we have seen one of the advantages of the time-of-flight technique is that during the acquisition everything is fixed, and one obtains the whole reflectivity curve in one measurement. By decreasing slightly the resolution that is used, and carefully choosing the angle of the experiment, one can diminish the acquisition time

to one or two hours. This time scale is well suited for the study of interdiffusion problem and so in-situ measurements can be performed. We have done such type of measurements on bilayers systems of around 500 Å hydrogenated polystyrene on top of 1200 Å of deuterated polystyrene deposited on a silicon wafer.

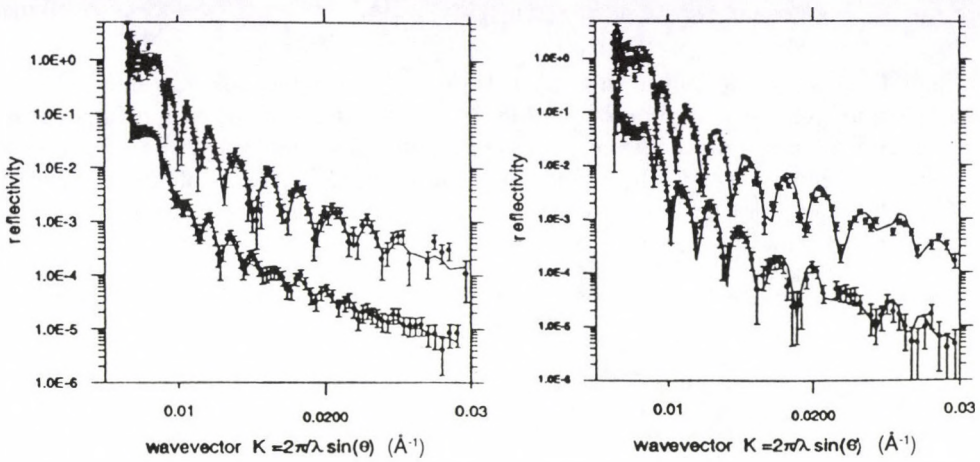

Fig. 2. Reflectivity measured on the non-cross-linked sample (left), and on the cross-linked sample (right), after one hour annealing at 115 °C (top curves), and the end of the annealing (lower curves). The lower curves have been shifted by a factor 0.05 for clarity

Our interest is to understand what will be the behaviour of the polymer molecules if their movements are reduced. One way to decrease the mobility of the polymers is to create crosslinks between the molecules. So we have performed in-situ reflectivity measurements on a cross-linked and a non-cross-linked sample. Acquisitions were done each hour and the annealing times were first 26 h at 115 °C, followed by 20 h at 130 °C, and then 15 additional hours at 145 °C for the cross-linked sample. The reflectivity curves obtained have been adjusted using a two layer model. The parameters of this model were the thickness of each layer and the roughness of the interface. The roughness at the silicon interface and at the surface were kept constant as well as the scattering length densities. The measured reflectivity adjustments after one hour annealing at 115 °C, and the end of the annealing for the two samples are represented in Fig. 2. The frequency of the large oscillations is due to the thickness of the deuterated polystyrene layer which stays nearly constant. Their amplitude depends on the width of the interface between the two polymers. A large interface is a poorly defined interface, and so the amplitude of the characteristic oscillations corresponding to this layer will be low. So from Fig. 2, we can see that, as expected, interdiffusion occurs in the non-cross-linked sample (left) since the amplitude of the oscillations is nearly completely damped after annealing. It is not the case for the cross-linked sample.

All the experimental curves have been adjusted. Using Eq. (8), we have obtained the variation of the characteristic roughness of the interface $\langle\sigma\rangle$ with the

time. In order to compare properly different measurements done at different temperatures, we have used a reduced time as proposed by William, Landel and Ferry [12]. The normalisation factor a_T to calculate this reduced time for the polystyrene is given by:

$$\log(a_T) = 13.7 \frac{T - T_g}{50 + T - T_g}, \tag{9}$$

where T_g is the glass transition temperature of polystyrene (100 °C) and T is the temperature of the experiment. In Fig. 3 the variation of $\langle\sigma\rangle$ is represented as a function of this reduced time. The completely different behaviour of the two systems is shown clearly, since when you have a large increase of the roughness of the interface for the non-cross-linked sample, the cross-linked sample remains unperturbed on a much larger time scale.

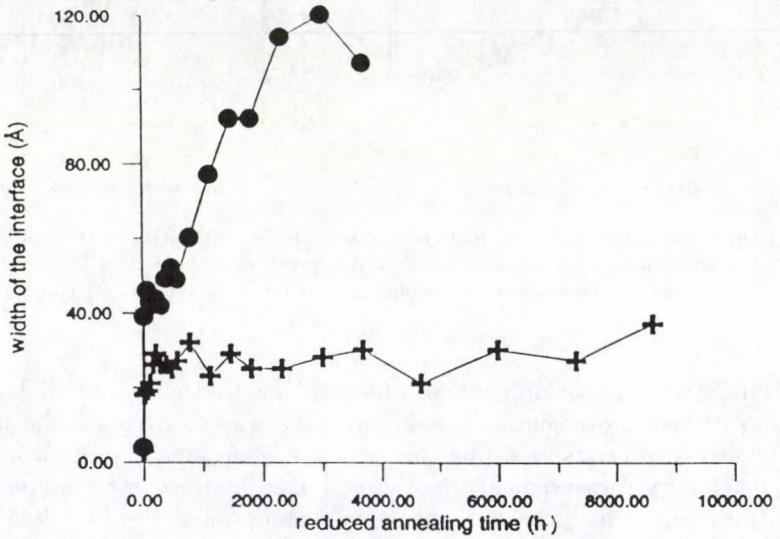

Fig. 3. Variation of the width of the interface between the deuterated polystyrene and the protonated polystyrene as a function of the reduced time for the cross-linked sample (+) and the non-cross-linked sample (•)

Neutron supermirrors development

Neutron reflectivity can also be used for technological applications like neutron optic devices. They are usually made of metallic multilayers, and can be used to improve the performances of neutron guides. In cooperation with the CILAS company, we have an important program of development of neutron supermirrors. They are made of aperiodic layers of alternately deposited low index (reflecting) and high index (spacer) layers [13]. Compared to classical nickel coated mirrors, supermirrors allow to extend the total reflection plateau. This extension is created by a succession of Bragg peaks that correspond to the different thickness of the

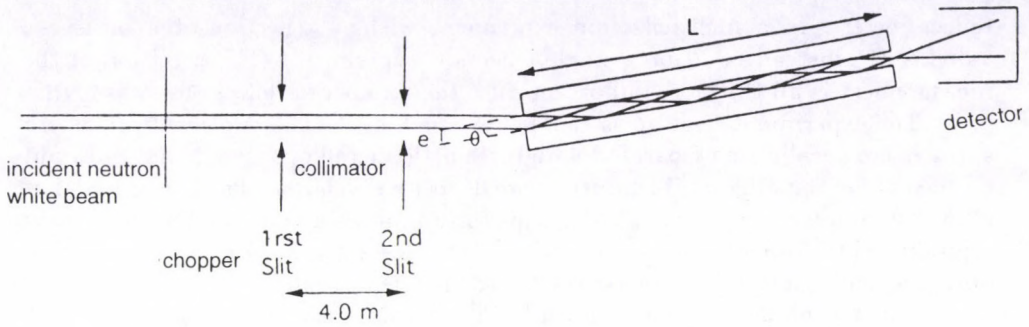

Fig. 4. Experiment set-up used for multireflection experiment. $L = 500$ mm: mirrors length; $e = 1$ mm: distance between the mirrors; θ: incident angle

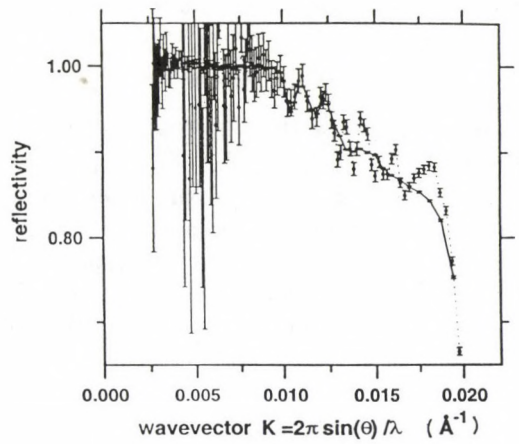

Fig. 5. Reflectivity measurement R by classical single reflection (dotted line) and calculated $\sqrt[7]{R'}$ (solid line) from multireflection measurement R' for 7 reflections on supermirror NiC/Ti

bilayers present in the aperiodic multilayers. They are made with NiC/Ti layers where nickel carbide is the reflecting material and titanium is the spacer. Supermirrors were used when building a new neutron guide at the LLB. They enable a spectacular increase of the transmitted flux [14].

For this particular application, the most interesting part of the reflectivity curve is situated in regions where the reflectivity value is close to one, that is on the extended plateau, just before the apparent cut off of the mirror. Using a standard single reflection experiment, a very long counting time is required in order to obtain the statistical accuracy needed to measure variations of reflectivity less than 1 %. In order to improve the precision of the measurements on the extended plateau, we have installed a time-of-flight neutron multireflection experiment on the EROS

reflectometer. In a multireflection experiment with N reflections the measured value is R^N instead of R for a single reflection experiment. The precision of the measurement is all the more important since the number of reflections N is high.

The experimental set-up is represented in Fig. 4. The two identical mirror surfaces are parallel and separated with three little metallic spacers 1 mm thick put on the edge of the mirrors. The mirrors are deposited on boron glass substrates that allows us to use the mirrors as slits. This set-up allows a very good measurement reproducibility. Mirrors are inclined with the angles $+\theta$ and $-\theta$ chosen in order to obtain an entire number of reflections N. The incident beam is measured for $\theta = 0$.

This technique has been applied to the characterization of a supermirror. A number of reflections of 7 and an angle of θ of 0.8 degree were used. Figure 5 displays the experimental reflectivity curve $R(k)$ of the classical single reflection measurement, and also the seventh root ($\sqrt[7]{R'}$) of the measured reflectivity R' obtained with multireflection. One can see that, using a similar counting time, the experimental error is decreased by the use of multireflection. The precision of the reflectivity measurement in the region of the plateau is thus markedly increased.

Conclusion

I have presented in this paper the two time-of-flight reflectometers installed at Saclay on the ORPHEE reactor. They enable measurements of reflectivity down to 10^{-5}. They have been used to perform measurements on liquid–air interfaces to characterise adsorption and depletion layers of polymer near the surface of a solvent. I have described an example of application to in situ measurement of polymer interdiffusion. Multireflection is an improvement of this technique that increases the precision of the measurements in a region where the reflection coefficient is close to unity.

References

1. J. Penfold and R. K. Thomas, J. Phys.: Condens. Matter, *2*, 1369, 1990.
2. T. P. Russell, Materials Science Reports, *5*, 173, 1990.
3. S. A. Werner and A. G. Klein, Neutron Scattering, eds K. Skold and D. Price, Academic Press, New York, 1986.
4. L. Nevot and P. Croce, Phys. Appl., *15*, 761, 1980.
5. L. T. Lee, O. Guiselin, B. Farnoux and A. Lapp, Macromolecules, *24*, 2518, 1991.
6. P. G. de Gennes, Macromolecules, *14*, 1637, 1981.
7. L. T. Lee, O. Guiselin, A. Lapp and B. Farnoux, Phys. Rev. Lett., *67*, 2838, 1991.
8. L. T. Lee, D. Langevin, and B. Farnoux, Phys. Rev. Lett., *67*, 2678, 1991.
9. T. P. Russell, S. H. Anastasiadis, A. Menelle, G. P. Felcher and S. K. Satija, Macromolecules, *24*, 1575, 1991.
10. P. G. de Gennes, Scaling Concepts in Polymer Physics, Cornell Univ. Press, Ithaca, NY, 1979.
11. A. Karim, A. Mansour, G. P. Felcher and T. P. Russell, Phys. Rev., B, *42*, 6846, 1990.
12. M. L. Williams, R. F. Landel and J. D. Ferry, J. Chem. Phys., 3161, 1955.
13. J. B. Hayter and H. A. Mook, J. Appl. Cryst., *22*, 35, 1989.
14. B. Ballot, F. Samuel and B. Farnoux, SPIE Proc., San Diego, *1738*, 159, 1992.

Acta Physica Hungarica 75 (1–4), pp. 131–140 (1994)

INELASTIC NEUTRON SCATTERING STUDIES OF CATALYSTS

PHILIP C. H. MITCHELL

Department of Chemistry, The University of Reading
Reading RG6 2AD, UK

Inelastic neutron scattering is a spectroscopic technique which enables one to observe vibrational and rotational spectra of catalysts and sorbed species. The spectrum is due to energy transfer from the incident neutrons to the scatterer. Since hydrogen is the strongest scatterer the INS technique is especially useful for investigating motions involving hydrogen atoms. I shall review applications of neutron scattering in catalytic studies and describe our INS studies of molybdenum-containing catalysts using the time focused crystal analyzer spectrometer (TFXA) at the ISIS pulsed neutron source at the Rutherford Appleton Laboratory. Particular topics will include chemisorbed hydrogen, the nature and binding of water in alumina-supported molybdenum oxide catalysts, the search for metal-hydrogen and sulfur-hydrogen species in molybdenum disulfide catalysts, and the interaction of benzene and thiophene with the catalyst, species in zeolites, and surface reactions of hydrogen.

Introduction

In this paper I provide an overview of applications of neutron scattering spectroscopy in studies of catalysts and adsorbed species. The emphasis will be on how neutron spectroscopy is complementary to photon spectroscopy and how in some circumstances neutron scattering can provide a vibrational spectrum which is difficult or impossible to obtain by other methods. The use of neutrons requires well planned experiments at a central facility and I shall have something to say about the practical aspects of such experiments.

Principles of neutron scattering

The neutron is a particle of mass number 1, zero charge, and spin 1/2. It interacts with matter by collisions and magnetically [1,2,3]. Neutrons because they are uncharged particles penetrate the electron clouds of atoms exposed to a neutron beam and are scattered by the atomic nuclei. A fraction of the neutrons lose energy by exciting vibrational modes of the material. In incoherent scattering (which is the only type of scattering considered here) the scattering is from a single scattering centre and so interference of scattered neutron waves (coherent scattering, neutron diffraction) is not included.

The neutron scattering spectrum is a plot of neutron scattering intensity vs neutron energy loss. It looks like an infrared or Raman spectrum (Fig. 1). The

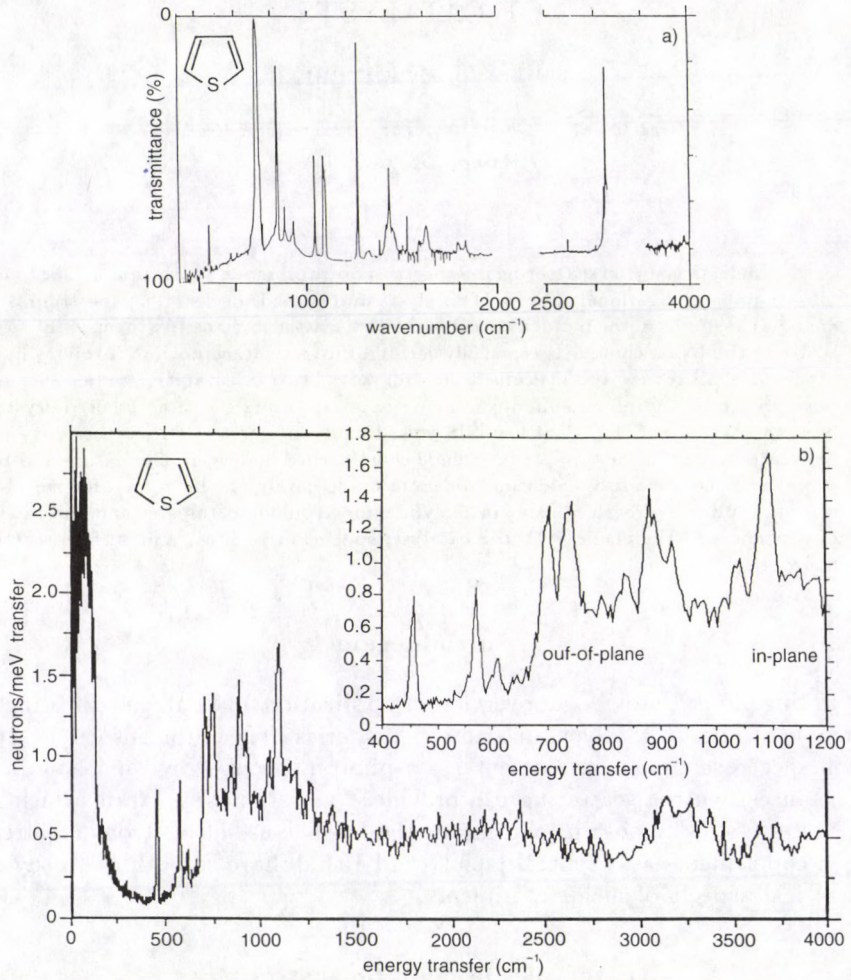

Fig. 1. Thiophene (a) infrared spectrum of the solid at 77 K (recorded by L. Sheridan) (b) inelastic neutron scattering spectrum of the solid at 20 K (recorded on the TFXA spectrometer at the Rutherford Appleton Laboratory). The inset is the expanded INS spectrum of thiophene between 400 and 1400 cm^{-1}. Assignments refer to the C–H bending modes

scattering law connects scattering intensity (S) with momentum transfer (Q) and the root mean square displacement (U) of the scatterer [4]

$$S_n(Q, n\omega_0) = (1/n!)(Q^2U^2)^n \exp(-Q^2U^2). \tag{1}$$

Here n is an integer (1, for the fundamental, 2 for the first overtone, etc.) ω_0 is the oscillator frequency; U^2 equals $h/2\mu\omega_0$ where μ is the oscillator reduced mass. The INS spectrum is thus the amplitude-weighted vibrational density of states averaged over all Q space.

All molecular vibrations are neutron-active. This is because the nuclear interactions are independent of dipole or polarizability selection rules. Accordingly the scattering intensity is straightforwardly related to the concentration of the scatterer. In neutron spectroscopy more emphasis is placed on band intensities than in photon spectroscopy [2]. Neutrons are much more penetrating than photons and electrons and pass through material in the beam. The ability of a nucleus to scatter a neutron is given by its scattering cross-section, σ. The value of σ is 80 barns for hydrogen and ca 5 barns for most other elements and for deuterium. Therefore motions involving hydrogen are strongly emphasized in neutron spectroscopy: stretching, bending and rotational modes of H–X bonds (where X is H or another element) and modes where hydrogen rides on another atom, for example a X–O vibration of a X–OH bond.

Because the scattering cross-section of deuterium is so much less than that of hydrogen selective substitution of hydrogen by deuterium in a scatterer can help with assignments, those modes involving deuterium becoming very weak. Of course the oscillator frequency also falls as a result of the mass change as in photon spectroscopy.

In the INS spectra of catalysts and adsorbed species scattering due to species other than hydrogen (metal atoms, oxygen, sulfur) is weak whereas infrared and Raman bands from modes involving other atoms as well as hydrogen may be strong and so add to the complexity of the spectra. Neutron spectroscopy, as we shall see, is especially useful for studying the spectra of hydrogenic species uncomplicated by other species.

Experimental procedure

My experience is mainly with pulsed neutrons from the spallation source at the Isis facility at the Rutherford Appleton Laboratory (RAL) in the UK [3,5,6] but much of what I have to say is applicable to neutrons from a reactor [7]. Here I describe a typical inelastic scattering neutron experiment on the Time-of-Flight Crystal Analyser (TFXA) spectrometer at the RAL.

Sample masses and data accumulation times are large for neutron spectra because the intensities are weak compared with photon and electron spectra. To measure the spectrum of an adsorbed species which comprises a few per cent of the total material (for example, thiophene on a molybdenum disulfide catalyst) we would use 5–10 g of material and accumulate the spectrum for 12 h. However, with a pure substance excellent spectra may be obtained with less than a gram of material.

For an air stable compound the sample container is an aluminium foil sachet. Air sensitive compounds are contained in a stainless steel or aluminium cell located

in the neutron beam. The beam area is 5 x 25 cm. The spectrum is measured with the material at 20 K to minimise thermal broadening.

In the TFXA spectrometer the energies of the scattered neutrons are measured by a time-of-flight method. The data analysis with instrument-based computer programs is an important part of the neutron scattering experiment. Background scattering from the instrument and the sample container is subtracted from the spectrum. The resulting spectrum may be integrated to obtain the number of hydrogen atoms in the beam. The scattering intensities of a series of samples may be normalised on the sample masses (assuming all of each sample is in the neutron beam) or by integration of the intensities in selected regions of the spectrum. To obtain the spectrum of an adsorbed species one subtracts the spectrum of the support determined separately. Manipulation of the neutron scattering intensities in this way is successful because the intensities are proportional to the mass of the scatterer — an attractive feature of neutron scattering. The result is a complete vibrational spectrum of a substance over the range 16 to 8000 cm^{-1} with a resolution of 1–2 %. Using these techniques significant structural information is extracted from what, at first sight, may seem unpromising spectra (Fig. 2).

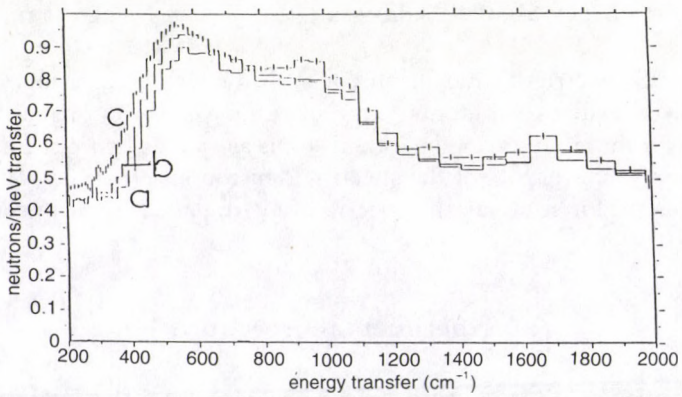

Fig. 2. Inelastic neutron scattering spectra of γ-alumina and molybdate on alumina: (a) alumina, (b) 7 % MoO_3/alumina, (c) 14 % MoO_3/alumina

Modelling the spectra

The final stage of interpretation is to fit the experimental spectrum and a theoretical spectrum generated by a molecular force field model. Computer fitting of observed and calculated INS spectra can be achieved with, for example, the CLIMAX program [8]. Vibrational frequencies and amplitudes are calculated from the masses and dispositions of the constituent atoms and the forces operating between them. The force constants are refined to give the best fit to the position and intensities of the INS bands. The program then minimises the residual difference between

the observed spectra and those calculated from the model. Using this or equivalent procedures we can, for example, test the validity of proposed adsorbate-site geometries.

Chemisorbed hydrogen. The INS spectrum of hydrogen chemisorbed on Raney Ni can be modelled with hydrogen atoms in three-fold sites of Ni (111) [9] (944 cm^{-1}, symmetric stretch, E; 1137 cm^{-1}, A_1 asymmetric stretch). Solving the harmonic model gives the force constant and bond length k(H–Ni) 0.58 mdyn $Å^{-1}$, d(Ni–H) 1.88 Å. Similarly the INS spectrum of hydrogen on Pd black [10,11] can be modelled with hydrogen in 3-fold sites (823 cm^{-1} symmetric stretch, 916 cm^{-1} asymmetric stretch giving k(H–Pd) 0.4617 mdyn $Å^{-1}$ and d(H–Pd) 1.881 Å. However, on Pt black saturated with hydrogen at 80 K the INS spectra are best modelled for H in a 2-fold site [12,13] (532 cm^{-1}, asymmetric stretch along $2\bar{1}\bar{1}$; 927, 1339 H in 2-fold site asymmetric stretch along $0\bar{1}\bar{1}$ and symmetric stretch along 111) giving k(H–Pt) 0.86 mdyn $Å^{-1}$, d(H–Pt) 1.90 Å.

Adsorbed benzene. In a classic study of benzene on nickel and platinum the height of the benzene molecule above the nickel surface was calculated from changes in the spectrum of benzene due to distortion of the adsorbed benzene molecule [7,14,15]. From valence force field analysis of the spring constants of the adsorbed benzene it was found that benzene is ca 2–2.5 Å above the metal surface.

Adsorbed thiophene. Currently we are using INS to determine the orientation of thiophene molecules on the surface of a molybdenum disulfide catalyst [16]. We use INS because scattering from adsorbed thiophene, which is hydrogenic, is stronger than scattering from the catalyst and therefore the thiophene spectrum is not obscured by the spectrum of the catalyst. The INS spectrum is measured at 20 K and is therefore the spectrum of solid thiophene. The spectra (internal modes at > 400 cm^{-1}) are shown in Fig. 3. For thiophene adsorbed on a fully sulfided molybdenum/alumina catalyst the C–H out-of-plane modes of thiophene are changed in position and intensity compared with solid thiophene. This suggests that thiophene lies flat on the surface. On a reduced molybdenum sulfide/alumina catalyst, where there are anion vacancies at molybdenum, changes are observed in the in-plane modes suggesting that the orientation of the thiophene molecule has changed, possibly by binding at a molybdenum site.

Species characterisation by INS fingerprinting

Just like photon spectra, neutron spectra can be used for fingerprinting molecules — assigning bands to characteristic modes and hence to molecular species [17]. For hydrogenic species the neutron scattering spectra will often provide more information than infrared, Raman and electron energy loss spectra [1, 3]. The possibility of overtones in the neutron spectra may also be exploited (see below). In making assignments it is desirable to have also the infrared and Raman spectra. I describe a number of examples in the catalyst area.

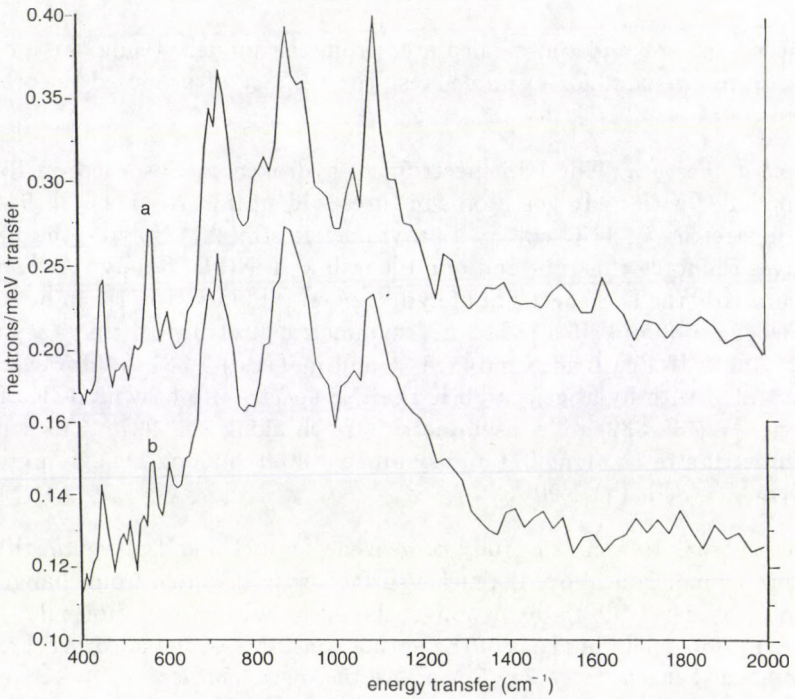

Fig. 3. Inelastic neutron scattering spectra of adsorbed thiophene (ca 1 monolayer) on alumina-supported molybdenum disulfide catalysts (a) catalyst sulfided but not reduced in hydrogen, (b) catalyst sulfided and reduced. Notice the band shifts and intensity changes in the C–H out-of-plane modes (cf. Fig. 1(b)) in (a) and in the in-plane modes in (b)

Oxides and sulfides. In neutron scattering spectra bands due to metal–oxygen and metal–sulfur vibrations are inherently weak. The INS spectra reveal features of the spectra of hydrogenic species in particular M–H and H–O and H–S modes, arising from the chemisorption of hydrogen

$$M - X + H_2 \rightarrow M - H + H - X.$$

The INS of zinc oxide having hydrogen chemisorbed at room temperature and measured at 77 K shows Zn–H bending (829 cm^{-1}) and stretching (1665 cm^{-1}) and a H–O bend (1125 cm^{-1}). Hydrogen motions associated with lattice phonon modes were observed below 600 cm^{-1} [18].

There is much interest in the interaction of hydrogen with sulfide catalysts used as hydrogenation and hydrodesulfurisation catalysts [19]. On sulfides hydrogen chemisorbs dissociatively as on oxides. H–S modes have been identified on MoS_2 (662 S–H bend) and WS2 [20–25] (694 cm^{-1} S–H bend, 1380 cm^{-1} and 2074 cm^{-1} first and second harmonics, 2500 cm^{-1} S–H stretch). But Mo–H and W–H species have not been identified. Possibly protons migrate to sulfide groups after dissociation of H_2.

In contrast on a reduced RuS_2 catalyst both H–S species (654 and 720 cm^{-1}) and Ru–H species (540 and 823 cm^{-1}, bending modes of two different Ru–H species) have been identified by INS [26].

Zeolites. Zeolites are acidic aluminosilicates with an internal structure of linked channels and cages of molecular dimensions. INS has been used extensively to probe the acidity and internal space of zeolites. There have been a number of force field calculations which enable one to compare calculated frequencies and intensities of the INS spectra with experimental spectra and so model the atomic motions of the zeolite. For example, the band assignments for dehydrated zeolite rho (where T is tetrahedral Al^{3+} or Si^{4+}) are T–OH torsion of planar symmetric AlO(H)Si units (360 cm^{-1}), H motion associated with symmetrical T–O stretch (750 cm^{-1}), out-of-plane T–O–H bend (1060 cm^{-1}), in plane T–O–H bend (1150 cm^{-1}) [27].

INS studies of ammonia and ammonium ions in zeolites have been used to probe the acidity and internal space of zeolites. The INS of ammonium ions in zeolite Y shows species in the supercages [28] (240–400 cm^{-1} hindered librations) and in smaller sodalite cages (64 cm^{-1} NH_4^+).

We have used INS to demonstrate that a metal complex encapsulated in the zeolite cage and acting as a well-defined catalytic centre is distorted compared with the free complex (Fig. 4).

Water in a hydrated molybdenum oxide/alumina catalyst — overtones. The librational modes of water in a hydrated molybdenum oxide/alumina catalyst appear as a broad peak with maxima near 450 cm^{-1} and the first overtone near 900 cm^{-1}. The peak intensity is proportional to the molybdenum in the catalyst; therefore the 450 cm^{-1} peak is assigned to water associated with molybdenum. The reduced mass, μ, of water was calculated from the ratio of the intensities of the fundamental and first overtone using Eq. (1) (with $n = 1, 2$; $U^2 = h/2\pi\omega_0$. The value (4) indicates water coordinated to molybdenum [29].

Surface species and reactions

Changes of neutron scattering intensity of hydrogen on surfaces have been used to study interactions between hydrogen atoms and reaction with other species of catalytic interest.

Dilution of chemisorbed hydrogen with deuterium — lateral interactions between surface hydrogen atoms. Deuterium is heavier than hydrogen and a weaker scatterer. Partial substitution of hydrogen with deuterium has an effect which helps us to understand the hydrogen interactions. On Pt black isotopic dilution of adsorbed H with D causes narrowing of the INS band shapes and a shift of energies due to reduction of coupling between H oscillators on the surface [30,31].

Surface reaction of CO with hydrogen. Reactions involving hydrogen have been monitored using INS. When a hydrogenated raney nickel catalyst was dosed with carbon monoxide the scattering intensity of hydrogen in three-fold sites decreased as the temperature was raised from 80 to 300 K. At the same time features in

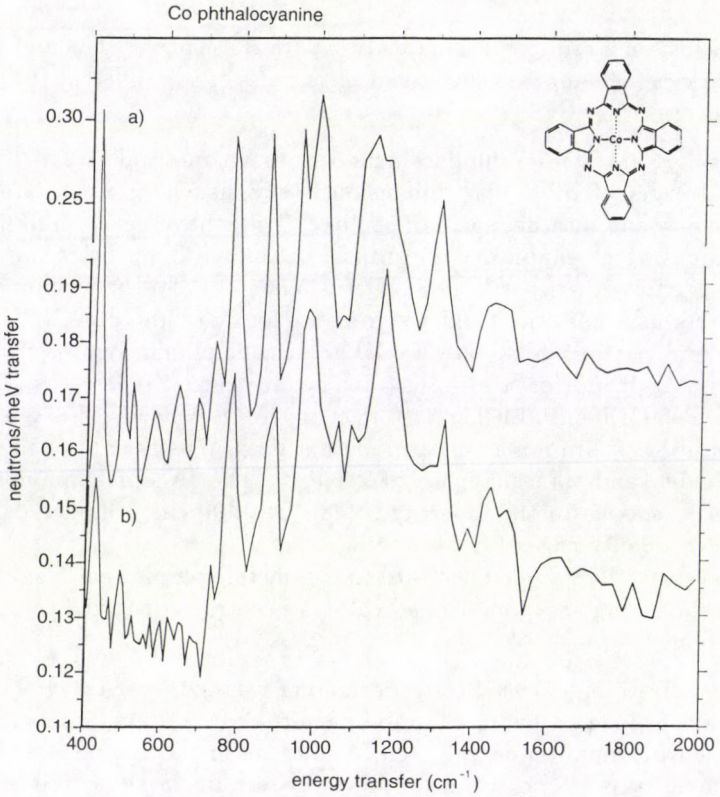

Fig. 4. Inelastic neutron scattering spectra of cobalt phthalocyanine (CoPc) (a) solid, (b) encapsulated in zeolite Y. Notice changes in the band positions and intensities of encapsulated CoPc showing distortion of the structure due to encapsulation

the spectrum assigned to C–H modes appeared. Thus the three-fold hydrogen was reacting with adsorbed CO [32,33].

Surface reaction of hydrogen with oxygen. On platinum reaction of adsorbed hydrogen with oxygen has been followed by the decrease of intensity of the hydrogen scattering and development of H–O modes (1032 cm^{-1}, bending mode of HO/Pt (111) [34]).

Quasielastic neutron scattering. Quasielastic neutron scattering (QUENS) [3] is not strictly part of the subject matter of this paper but it should be mentioned as an important application of neutron scattering in catalysis. In the QENS technique we exploit the broadening of the incoherent elastically scattered peak due to translation and rotation of scattering nuclei to investigate diffusion in solids and liquids. The elastic peak width is analysed as a function of momentum transfer. We thus obtain atomic-scale information on the motions of hydrogen and hydrogenic species on catalysts. The technique has been especially useful in studying the dynamics of molecules in zeolites: methane [35], benzene [36–39], xylene [40].

Conclusions

Many catalysed reactions involve hydrogen and hydrogen-containing molecules. My aim in this paper has been to illustrate how inelastic neutron scattering can be exploited to provide information on the structures of catalysts and adsorbed and reacting molecules. With the development of neutron sources we expect to see increased use of neutron scattering in catalytic research but, inevitably, with the proviso that in proposing experiments we are clear what it is we can get from neutron scattering that we cannot get — or only with great difficulty — from another technique.

Acknowledgements

I thank the UK Science and Engineering Research Council for support, Dr John Tomkinson of the Rutherford Laboratory for many stimulating discussions, and the catalyst group at Lille France (Professor Grimblot and Dr Payen) for a productive collaboration.

References

1. C. M. Mate, B. E. Bent and G. A. Somorjai, in: Hydrogen Effects in Catalysis, eds Z. Paal and P. G. Menon, Marcel Dekker, New York, 1988, p. 57.
2. J. Tomkinson, in: Recent Experimental and Computational Advances in Molecular Spectroscopy, ed. R. Fausto, Kluwer Academic Publishers, London, 1993, p. 229.
3. T. J. Udovic and R. D. Kelley, in: Hydrogen Effects in Catalysis, eds Z. Paal and P. G. Menon, Marcel Dekker, New York, 1988, p. 167.
4. D. Graham, J. Howard, T. C. Waddington and J. Tomkinson, J. Chem. Soc. Faraday Trans., *1*, 79, 1713, 1983.
5. J. Penfold and J. Tomkinson, The ISIS Time Focussed Crystal Analyser Spectrometer, TFXA, Rutherford Appleton Laboratory, 1986.
6. J. Tomkinson, in: Neutron Scattering at a Pulsed Source, eds R. J. Newport, B. D. Rainford and R. Cywinski, Adam Hilger, Bristol, 1988, p. 36.
7. R. K. Thomas, in: R. F. Barrow, D. A. Long and J. Sheridan, Molecular Spectroscopy, The Chemical Society, London, 1978, p. 232.
8. G. J. Kearley and J. Tomkinson, Inst. Phys. Conf. Ser. No. 107, p. 245, 1990.
9. P. R. Cavanagh, R. D. Kelley and J. J. Rush, J. Chem. Phys., *77*, 1540, 1982.
10. C. M. Sayers and C. J. Wright, J. Chem. Soc. Faraday Trans., *1*, 80, 1217, 1984.
11. I. J. Braid, J. Howard and J. Tomkinson, J. Chem. Soc. Faraday Trans., *2*, 79, 253, 1983.
12. C. M. Sayers, Surf. Sci., *143*, 411, 1984.
13. J. Howard, T. C. Waddington and C. J. Wright, in: Neutron Inelastic Scattering, Vol. 2, IAEA, Vienna, 1978, p. 499.
14. H. Jobic, Surf. Sci., *95*, 496, 1980.
15. H. Jobic and A. Renouprez, Surf. Sci., *111*, 53, 1981.
16. P. C. H. Mitchell, J. Grimblot, E. Payen and J. Tomkinson, in: T. J. Dines, C. H. Rochester and J. Thomson, Catalysis and Surface Characterisation, Royal Society of Chemistry, 1990, p. 68.
17. R. R. Cavanagh, J. J. Rush and R. D. Kelley, in: Vibrational Spectroscopy of Molecules on Surfaces, Vol. 4, Methods of Surface Characterisation, eds J. T. Yates and T. E. Made, Plenum Press, New York, 1987.
18. J. Howard, I. J. Braid and J. Tomkinson, J. Chem. Soc. Faraday Trans. *1*, 80, 225, 1984.
19. P. C. H. Mitchell, in: Catalysis (Specialist Periodical Report) ed. C. Kemball, The Chemical Society, London, 1977, Vol. 1, p. 204; P. C. H. Mitchell, in: Catalysis (Special Periodical

Report), eds C. Kemball and D. A. Dowden, The Chemical Society, London, 1982, Vol. 4, p. 175; M. Zdrazil, Catalysis Today, *3*, 269, 1988; B. C. Wiegand and C. M. Friend, Chem. Rev., *92*, 492, 1992; C. M. Friend, Scientific American, *268*, (4), 42, 1993.
20. C. J. Wright, C. Sampson, D. Fraser, R. B. Moyes, P. B. Wells and C. Riekel, J. Chem. Soc. Faraday Trans., *1*, 76, 1585, 1980.
21. C. Sampson, J. M. Thomas, S. Vasudevan and C. J. Wright, Bull. Soc. Chim. Belg., *90*, 1215, 1981.
22. C. J. Wright, Catalysis, *7*, 46, 1985.
23. P. Sunberg, R. B. Moyes and J. Tomkinson, Bull. Soc. Chim. Belg., 967, 1991.
24. R. B. Moyes, in: Hydrogen Effects in Catalysis, eds Z. Paal and P. G. Menon, Marcel Dekker, New York, 1988, p. 583.
25. C. J. Wright, D. Fraser, R. B. Moyes and P. B. Wells, Appl. Catal., *1*, 49, 1981.
26. H. Jobic, G. Glugnet, M. Lacroix, S. Yuan, C. Mirodatos and M. Breyesse, J. Amer. Chem. Soc., *115*, 3654, 1993.
27. M. J. Wax, R. R. Cavanagh, J. J. Rush, G. D. Stucky, L. Abrams and D. R. Corbin, J. Phys. Chem., *90*, 532, 1986.
28. W. P. J. H. Jacobs, R. van Santen and H. Jobic, J. Chem. Soc. Faraday Trans., 1191, 1994.
29. P. C. H. Mitchell, J. Tomkinson, J. G. Grimblot and E. Payen, J. Chem. Soc. Faraday Trans., *89*, 1805, 1993.
30. J. J Rush, R. R. Cavanagh, R. D. Kelley and J. M. Rowe, J. Chem. Phys., *83*, 5339, 1985.
31. R. J. Elliott and A. A. Maradudin, in: Inelastic Scattering of Neutrons, Vol. 1, IAEA, Vienna, 1965, p. 231.
32. R. D. Kelley, J. J. Rush and T. E. Madey, Chem. Phys. Lett., *66*, 159, 1979.
33. R. D. Kelley, R. R. Cavanagh and J. J. Rush, J. Catal., *83*, 464, 1983.
34. G. B. Fisher and B. A. Sexton, Phys. Rev. Lett., *44*, 683, 1980.
35. H. Jobic, Chem. Phys. Lett., *170*, 217, 1990.
36. H. Jobic, M. Bee and G. J. Kearley, Zeolites, *9*, 312, 1989.
37. F. Vignemaeder and H. Jobic, Chem. Phys. Lett., *169*, 31, 1990.
38. H. Jobic, M. Bee and A. J. Dianoux, J. Chem. Soc. Faraday Trans., *1*, 85, 2525, 1989.
39. H. Jobic, M. Bee, J. Karger, H. Pfeifer and J. Caro, J. Chem. Soc. Chem. Comm., *4*, 341, 1990.
40. M. Czjzek, H. Jobic and M. Bee, J. Chem. Soc. Faraday Trans., *87*, 3455, 1991.

Acta Physica Hungarica 75 (1–4), pp. 141–148 (1994)

NEUTRON RADIOLOGY — AN OVERVIEW

JOHN P. BARTON

NRE, Inc. (Consultant)
1422 Vue Du Bay Ct, San Diego, CA 92109 USA

Neutron radiation can be used like X-rays to penetrate materials for inspection. The information obtained can be quite different from that obtained by X-rays because only neutrons respond to the nuclear properties of materials. The simplest technology provides static imaging of the transmitted neutron beam (neutron radiography), but dynamic imaging (neutron radioscopy) is becoming increasingly powerful. High flux reactor sources offer important advantages over alternative lower flux sources (reactors, accelerators and isotopes) especially through the use of high beam collimation, high beam intensity, or selected neutron energy. Complementary neutron probe techniques for materials evaluation include neutron elastic scattering, thermal neutron analysis, fast neutron analysis, pulsed fast neutron analysis, neutron resonance attenuation and associated particle time-of-flight techniques. Neutron radiology and supporting neutron probe methods have applications for macroscopic materials evaluation, engineering studies, or nondestructive testing in fields such as nuclear fuels, pyrotechnics, aircraft inspection, forensic science, agriculture, medical–dental research, and international verification of nuclear non-proliferation agreements.

1. Introduction

This paper provides a brief review of the present status of neutron radiology activities worldwide. It is hoped that this independent perspective may assist in the future development of neutron activities at the Budapest Neutron Centre (BNC). The modernized 10 MW KFKI research reactor has several features that are obvious candidates for neutron radiology uses: radial beams, tangential beams, and eventually a cold source with neutron guide. The BNC might also consider accelerator and isotopic source potential using complementary Neutron Inspection for Location and Composition (NILC).

The staff of the Budapest KFKI centre, including M. Balaskó and E. Sváb, have reported neutron radioscopy research performed since 1984 using the 4.4 MW WWR-SM reactor at Budapest and the 9 MW ASTRA reactor at Seibersdorf, Austria. This research features dynamic studies with simultaneous neutron and gamma ray analysis applied to important engineering development of refrigerator design, and visco clutch design [1].

2. Complementary methods for macroscopic inspection with neutrons

The review will cover several different macroscopic inspection techniques that use neutron sources and nuclear radiation detection expertise. Other papers in this workshop will cover neutron activation analysis and microscopic neutron techniques such as neutron scattering and neutron interferometry.

Methods for neutron radiology and related macroscopic inspections are divided below into eight groups. The activity in each group can fall into three categories: (1) research into new or improved neutron based inspection techniques; (2) use of the neutron inspection method for product quality control or monitoring; and (3) use of the neutron inspection method for research in other fields including engineering development.

2.1. Neutron radiography – Thermal neutrons

In this group of methods a collimated neutron beam is extracted from a neutron moderator and passed through the object being inspected where a still picture is obtained, normally using X-radiography transparency film. There are numerous variables such as neutron source type, collimator design, and method of obtaining the photographic image. This is the simplest method of neutron radiography. It has a wide variety of applications, and it is the most widely applied method [2].

2.2. Neutron radiography — Epithermal, resonance energy, fast neutrons

In these methods the neutron energy is selected. For example, a reactor neutron beam may be filtered by cadmium. An alternative filter, steel, can provide a window at a special energy which penetrates the object. Also a crystal spectrometer may be used to provide a monochromatic beam at a particular resonance peak. The methods can provide advantages over standard neutron radiography especially where the item of interest has high neutron resonance cross-section peaks [3].

2.3. Neutron radiography — Subthermal neutrons

These methods use either a filter (such as beryllium–bismuth) or a guide tube with a cold neutron source (refrigerated moderator) to enhance the subthermal neutron intensity. The method offers the advantage that, for certain crystalline materials, cold neutron penetration can be high. Also cold neutrons can increase the opacity of other materials that may need to be distinguished [4].

2.4. Neutron radioscopy

These methods use electronic imaging in place of the film. Radioscopy is used widely for studies of dynamic situations, such as fluid flow. Also neutron radioscopy is useful for imaging static situations, where image integration and electronic image processing are important. Neutron radioscopy is being developed for thermal and cold neutrons [5].

2.5. Neutron computed tomography

Typically the object is rotated in a fixed neutron beam and image information is extracted at multiple angles of projection. The data is then processed in a computer to provide tomographic axial slice images. The method has been developed

computer to provide tomographic axial slice images. The method has been developed using film data input [6] or electronic imaging [7]. The method can provide sensitivities much improved over methods 1–4. Dramatic progress is being reported. In one recent research program neutron computed tomography using a moderately powered reactor beam (250 kW) was able to show fine details of hydride buildup in titanium-alloy aircraft jet engine fan blades.

2.6. Neutron induced autoradiography

In these methods the object is exposed to a field of neutrons and the capture gamma forms an image of either prompt or delayed activity. The applications range from study of ancient paintings to medical research [8].

2.7. Neutron gauging

Neutron attenuation can be determined using a neutron flux counter in place of a film or video detection system. This quantitative method, known as neutron gauging, can provide superior precision for some applications. The AEROTEST reactor facility in the USA has a permanently installed narrow neutron beam specially designed for neutron gauging [9].

2.8. Neutron inspection for location and composition (NILC)

In *thermal neutron analysis* a beam of thermal neutrons is directed at the item to be inspected and the emergent gamma ray pattern, detected with an array of detectors, enables information about the internal geometry and composition to be reconstructed. The techniques are being developed so that non-reactor neutron sources can be used to identify hidden narcotics, explosives, or fissile materials. The material identification relies on multi-dimensional data analysis of ratios of elements such as N, C, O and H. Primary signatures are from nitrogen (10.8 MeV), and hydrogen (2.2 MeV). For airport security baggage inspection, performances of 100 % sensitivity with 20 % false positive readings, and 90 % sensitivity with 2 % false positive readings have been reported [10].

Fast Neutron Analysis is similar to the thermal neutron analysis discussed above, except that the signals are from interactions of fast neutrons, mostly inelastic scattering. The method provides high penetration for large objects [11].

In the *Neutron Elastic Scattering* a beam of neutrons is directed at the object and the neutrons scattered back from the object are measured.

In the *Neutron Resonance Attenuation* method the incident neutron beam is typically in the range 0.5 MeV to 5 MeV. The resonances in the total cross-sections enable a two dimensional projection to be reconstructed [12].

The *Associated Particle Neutron Imaging* method uses neutrons generated by a reaction such as deuteron on tritium, where an alpha particle is associated with each emisson of a 14 MeV neutron. Detection of the alpha particle enables the time

and direction of the neutron emission to be registered. The method permits either 2-dimensional or 3-dimensional fast neutron transmission images to be reconstructed [13].

The *Pulsed Thermal Neutron Analysis* method is similar to thermal neutron analysis except that the neutron source is pulsed (accelerator or beam chopper), and the gamma rays are measured when the source is off. The method is best used in conjunction with other methods, as by itself it has poor imaging and sensitivity properties [12].

The *Pulsed Fast Neutron Analysis* method is similar to fast neutron analysis but uses time-of-flight technologies to obtain spatial distribution of the signal. It is claimed to be more promising than many of the alternative methods. It should provide both 2-dimensional and 3-dimensional imaging of small and large objects.

In many cases a particular inspection is best performed using a combination of methods. This can apply equally to small neutron source methods (e.g. pulsed fast thermal neutron interrogation) [12], or to reactor beam methods (e.g. neutron radioscopy and neutron gauging).

3. Sources, collimators and imagers trends

3.1. Sources

Reactor types in use worldwide for neutron radiology range from the high flux reactors at Petten (HFR), Saclay (ORPHEE), and Japan (JRR-3) to low power reactors of which the extreme may be the 1 watt UTR reactor at Kinki University in Japan. About 30 different countries have at least one reactor-based neutron radiology research project. Japan has neutron projects on nine reactors [14].

Accelerators are in use widely, for example in Japan six neutron radiology centers rely on accelerators (3 cyclotrons and 3 Van de Graaff). In the USA there are neutron radiology projects using the MF Physics D-T type sealed tube generator, and the Radio Frequency Quadrupole (RFQ) accelerator. In France the SODERN sealed tube DT generator is being developed with increased yield. In the United Kingdom, Oxford Instruments and Rolls Royce have announced a neutron radiology system based on a supercooled transportable cyclotron [15].

Isotopic sources are also in use for neutron radiology. Examples include a mobile system for underwater inspection at nuclear power plants [16], a maneuverable system for inspection of intact aircraft for corrosion [17], and a stationary system planned to produce one high quality exposure each day [18].

3.2. Collimators

Collimators need to be custom designed for each particular situation. Typical options include underwater or dry, horizontal or vertical, radial or tangential, divergent or parallel. Other important features include filters, beam scrapers, and variable apertures. Recent designs include a very wide angle collimator at Pantex in USA which will expose up to nine films simultaneously [18].

3.3. Imagers

The most widely used imaging methods for non-radioactive objects are (1) gadolinium metal converter with fine grain, single coated, X-ray transparency film; (2) scintillator screen with spectrally matched light sensitive film; (3) electric imaging using either an image intensifier with an optimized gadolinium oxy-sulphide input screen, or a changeable scintillator viewed by a TV camera. The video chain invariably includes an image processing system.

For neutron radiology inspection of nuclear fuel or other highly radioactive objects the two most useful imager processes are: (1) activation transfer and (2) track etch. The track etch is mostly used when precise dimensional changes are being investigated.

4. Discussion of NR equipment possible at BNC

4.1. Cold beam from reactor

The cold neutron guide will be particularly attractive for neutron radiology. There are only three comparable guide tube neutron radiology facilities; ORPHEE 14 MW reactor, France; KUR 5 MW reactor and JRR-3 20 MW reactor, Japan [19]. The beams have exceptionally high intensity cold neutron flux, and they have low interference radiation. This is offset by lack of collimation. In addition to the cold guide narrow beam and the radial narrow beam designed for simultaneous neutron and gamma radioscopy, consideration may be given to a third beam optimized to compete for the international market in turbine blade and other film type neutron radiography. A broad beam design using beryllium–bismuth filters cooled by liquid nitrogen could be cost effective if sufficient workload can be won. Reports from other cold beam facilities should be noted. There are operating broad beam cold neutron facilities at Petten HFR reactor. In addition past work with cold beams at the Aldermaston HERALD reactor, Harwell DIDO reactor, and General Atomics TRIGA reactor should be noted [20].

4.2. Thermal beam from reactor

Consideration might be given to shared use of a thermal neutron beam in addition to the cold beam. By use of helium flight paths it may be possible to provide a thermal neutron radiology beam with field of view larger than the cold beam without displacing other beam users. A study of collimator designs for reactors. such as SAPHIR (Switzerland) could be helpful on this matter [21].

4.3. Complementary neutron source methods

In addition to reactor based neutron radiology systems there is an expanding future for custom built neutron inspection systems for applications such as aircraft maintenance [17], airport security [12], and process control [9]. Circumstances could arise in which the BNC could consider development of a transportable or custom designed stationary neutron system for general or specific applications.

5. Discussion of NR activities possible at BNC

5.1. Nondestructive testing services

There is an international market for neutron radiography services. In some cases those needing neutron radiographic inspections will look for the most convenient service, but in others they may shop worldwide for the least expensive service. For example, large numbers of jet engine turbine blades have to be inspected with neutron radiography. In some cases blades made by Rolls Royce in England have been shipped to such places as Australia, Canada or the USA for routine inspection. A first step in preparing a new business plan for the KFKI reactor could be to hold discussions with the current users of neutron radiography services worldwide.

The most common applications requiring neutron radiography include nuclear fuel, jet engine blades, and pyrotechnics. However, there are other potential applications. For example in recent months the manufacturers of automobile air bag safety systems in the USA have decided to inspect, using X-ray, every one of the million or more bag detonator systems manufactured each year. If neutron radiology could be pioneered to include automatic defect recognition and to be available at an acceptable price this could be a future high throughput service to complement the X-ray inspection.

5.2. NR for Research Projects

Recently centers in 4 countries reported on NR research progress for composites and ceramics [22]. Also a KFKI electronic imaging capability could complement recent progress on fluid flow particularly in Japan and USA [23]. The work done in nearby Vienna and Prague on inspection of building materials (concrete) should be noted [24]. There has been a tendency for certain countries to focus on high technology applications and weapons. Low technology but potentially very important work, in fields such as agriculture research could be very rewarding [25]. Initial work has been done in applications of NR for dental or medical research [26]. Much of this work appears suitable for expanded interdisciplinary studies, possibly low in budget but high in value. One study area that is suggested would evaluate techniques for radiography of human extremities high in bone content such as wrist and ankles, elbows and knees. By use of thermal or epithermal neutrons combined with thin slice neutron computer tomography techniques it should be possible to obtain radiographs at acceptably low radiation doses.

5.3. Neutron inspection for location and composition (NILC) development

Important probe (NILC) techniques are rapidly progressing. One important application is nuclear materials assay. The International Atomic Energy Agency (IAEA) headquartered in Vienna, near Budapest, monitors the Non-Proliferation Treaty. They might also help to monitor the storage of dismantled nuclear warhead material. In addition to IAEA activity by nuclear powers there appears to be a

case for a non-nuclear power participation. In this way a non-nuclear power might maintain the independent expertise to verify the verifiers of nuclear Non-Proliferation Treaties to which it may be a signatory. The needs for neutron inspection methods are complex and could include methods to determine the quantity of fissile material in a sealed container without revealing the owners design details [27].

6. Conclusions

Firstly, the facilities at the new Budapest Neutron Centre (BNC) might provide for research projects leading to more sophisticated and more powerful methods for macroscopic inspections using neutrons. Also the complementary nature of reactor and accelerator neutron sources appears to open many avenues for research into new techniques.

Secondly, the BNC could consider providing neutron radiology services to meet the needs of national or international industries and to provide some financial income.

Thirdly, neutron techniques used as a tool for research in other areas (such as the refrigerator and clutch engineering research already under way) could be expanded to other areas of research. Examples given include composites, construction materials, fluid flow problems, agriculture research, medical–dental research, and international verification of nuclear non-proliferation or disarmament [28–32].

References

1. M. Balaskó, E. Sváb, A. Nedelik, Fourth World Conference on Neutron Radiography (WCNR-4), 31–38, ed. J. P. Barton, Gordon & Breach Publishers, 1993. Also Regional Meeting, Nuclear Energy in Central Europe, 590–597, ed. Joze Rant, European Nuclear Society Publisher, 1993.
2. M. R. Hawksworth, J. Walker, Proceedings First World Conf. on Neutron Radiography (WCNR-1), 5–21, ed. J. P. Barton et al, D. Reidel Publishers, 1982.
3. W. L. Whittemore, H. Berger, 23–33, WCNR-1.
4. J. P. Barton, Brit. J. App. Phys., *16*, 1833, 1965.
5. Y. Murata, 35–46, Proceedings Third World Conf. on Neutron Radiography (WCNR-3), ed. S. Fugine et al, Kluwer Publishers, 1990. Also WCNR-1, 601–673, 8 papers; WCNR-3, 431–548, 13 papers; WCNR-4, 309–374, 481–544, 16 papers.
6. WCNR-1, 403–418, 2 papers.
7. Proceedings Second World Conf. on Neutron Radiography (WCNR-2), ed. J. P. Barton et al, D. Reidel Publishers, 1987, 695–782, 10 papers. Also WCNR-4, 545–638, 10 papers.
8. Capture Gamma: WCNR-2, 519–526; WCNR-3, 781–88; WCNR-4, 279–298, 5 papers.
9. Neutron Gauging: WCNR-2, 821–828. Also Proceedings Nuclear Techniques for Analytical and Industrial Applications, 1–68, ed. G. Vourvopoulos, Western Kentucky Univ. Publisher, 1993.
10. A. J. Caffrey et al, Idaho National Engineering Lab. USA, unpublished.
11. T. Gozani, US Patent No. 5,098,640, awarded March 1992.
12. Review of Neutron Probe Methods; report for Los Alamos National Laboratory prepared by NRE Inc. under contract 1994, unpublished (39 papers).
13. E. Rhodes et al, WCNR-4, 827–836.
14. Reactor NR: WCNR-1, 85–290, 24 papers; WCNR-4, 375–446, 10 papers.
15. Small Source Systems NR: WCNR-1, 672–726, 7 papers; WCNR-4, 447–480, 6 papers.

16. Underwater Inspection NR: WCNR-2, 359–366.
17. Maneuverable NR System: WCNR-4, 133–142, 153–160.
18. Pantex Divergent Beam NR: WCNR-4, 707.
19. Cold Guide Tubes: WCNR-2, 106, WCNR-4, 395–402 and 415–422, 3 papers.
20. Proceedings Radiography with Neutrons Conf. ed. M. R. Hawksworth, Brit. Nuc. Energy. Soc. Publishers, 1975, 31–38, 129–132.
21. SAPHIR Reactor Beam NR: R. J. Hammer et al, WCNR-4, 383.
22. Composites NR: WCNR-4, 45–50, 173–186, 187–194, 237–248 (4 papers).
23. Fluid Flow NR: WCNR-4, 309–374, (7 papers).
24. Concrete NR: WCNR-4, 74–94, (2 papers).
25. Agriculture NR: WCNR-4, 57–64; WCNR-3, 731–737; WCNR-1, 580–590.
26. Medical and Dental NR: WCNR-1, 533–580 (4 papers); WCNR-2, 481–488, 497–518 (3 papers); WCNR-3, 687–730 (5 papers); WCNR-4, 299–308 (1 paper).
27. US Congressional Office of Technology Assessment Report. Dismantling the Bomb and Managing the Nuclear Materials, 200 pages, available from Code 7170, P.O. Box 371954, Pittsburgh, PA.
28. I. Czoch et al, Hungarian Possibilities in Support of International Safeguards. IAEA Symposium on International Safeguards, Vienna, March 14, 1994.
29. H. Böck, The Role of a Small Research Reactor Center for the Development of Safeguards Techniques, IAEA 3–14–194.
30. F. Lévai, Institute of Nuclear Techniques, University of Budapest, unpublished.
31. J. Safar, Institute of Isotopes, Hungarian Academy of Sciences, Budapest, unpublished.
32. E. Szőllősi, Hungarian Atomic Energy Commission, Budapest, unpublished.

Acta Physica Hungarica 75 (1–4), pp. 149–159 (1994)

STRESS MEASUREMENT FOR PLEASURE AND PROFIT

M. T. HUTCHINGS

NDT Department, AEA Industrial Technology
521.1 Harwell, Didcot, OX11 0RA, UK

Neutron diffraction is the best available technique to measure non-destructively the absolute stress tensor as a function of depth within components or weldments of crystalline materials. The technique has been used extensively, often on commercial contract, to examine the stress field in components which are small enough to be taken to an intense neutron source. It has also been used to calibrate the more limited, but portable, techniques which can be used *in situ* on plant, and to validate computer codes using model samples. The data often provide new insights into the behaviour of materials of importance to physicists, materials scientists and engineers. This paper gives a short description of the technique and illustrates its use with examples of the measurement of the stress in weldments, metallic components, and composite materials.

Introduction

Almost all neutron source institutes now have a diffractometer which is either dedicated to, or is available for, stress measurement. In an era when the value of science to society must be increasingly emphasized, stress measurement provides an excellent example of the application of neutron scattering to industry-related problems. This is substantiated by the fact that industry is willing to pay the full commercial cost of measurements if they help to solve an urgent and expensive problem. This additional contribution to the funding of an institute is often welcomed to supplement that from the more conventional sources.

The detailed measurement of residual stress fields within components and weldments, which are formed by inhomogeneous plastic deformation or heat treatment such as welding, has been a challenge set by engineers for many years (Mordfin [1]). Macrostress or Type I stress, which varies over distances which are relatively large compared to the grain size, is of prime concern to the engineer. However, microstress or Type II stress, which varies on a spatial scale of the order of the grain size can also give information relevant to the mechanical behaviour of many materials.

The neutron diffraction method of stress measurement (Hutchings and Krawitz [2]) closely parallels and complements the X-ray diffraction method (Noyan and Cohen [3]). However, it enables in-depth measurements to be made on account of the much deeper penetration, by a factor of 10^2–10^4, of the neutron into most materials. In contrast the X-ray method examines near-surface stress fields to a maximum depth of $\sim 100\ \mu$m. Absolute macrostress tensors, macrostress gradients, stresses due to applied loading, and microstress can be measured in-depth uniquely using neutron diffraction. The technique was first developed in 1980, with parallel

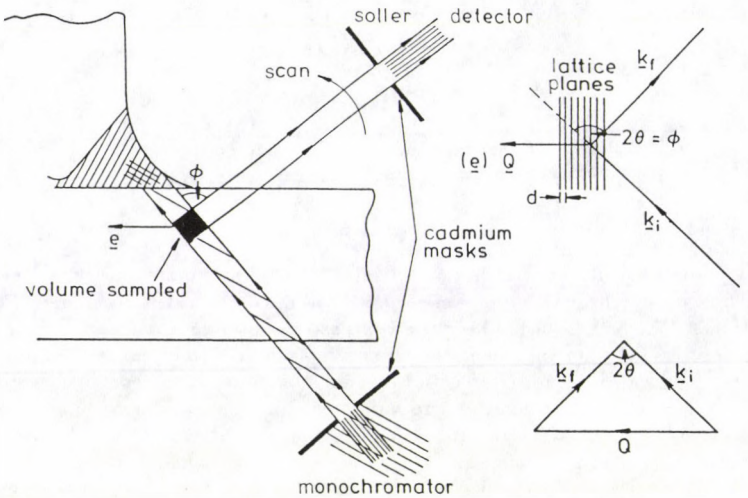

Fig. 1. The principles of strain measurement, showing the definition of gauge volume sampled and the direction of strain measured

work being carried out in the UK (Allen et al [4]), in Germany (Pintschovius et al [5]) and in the USA (Krawitz et al [6]). It is now used with confidence world-wide as a non-destructive technique, providing new information for the engineer in an increasing number of applications. The major drawback of the neutron diffraction method to the engineer is its need of intense neutron beams, available only at medium or high-flux reactor or at an accelerator-based, usually time-pulsed, neutron source. This limits its use to relatively small portable components, with typical maximum dimension $\sim 50 - 100$ cm. However, it can also be used to test computer codes using model samples, to test assumptions made in the use of portable, but usually much more limited, techniques, and to calibrate these techniques for use in the factory or field. The exploration of the finer points of the neutron diffraction technique is providing materials scientists with new insights into the fundamental behaviour of materials under stress, as well as providing neutron experimentalists with a new instrumental challenge to improve the speed of measurement (see Vrana et al [7] for example).

Principles of the diffraction technique

The basic principle of the method lies in the use of the lattice plane spacing of grains to act as an internal strain gauge throughout the component. Full details are given by Allen et al [8]. The diffraction method is illustrated in Fig. 1 and is discussed here primarily in terms of a reactor-based instrument, where modified standard high-resolution powder neutron diffractometers are often quite suitable.

The white neutron beam from the reactor is first monochromated to a chosen wavelength λ by Bragg reflection from a large single-crystal monochromator. This monochromated beam is defined in direction by a soller slit collimator, or by apertures, to pass over the 'sample axis' about which the detector rotates. The detector counts neutrons scattered through an angle ϕ, with the scattered beam again defined in direction by a soller slit assembly. Both the beam incident on the sample and the beam entering the detector are defined in area by horizontal and vertical apertures in a neutron absorbing mask, made of cadmium for example. The 'gauge volume' or 'volume sampled' by the diffractometer is defined by the intersection of the incident and scattered beam, as shown in Fig. 1. A sample placed wholly within this volume will have its average property measured, whereas a large sample may be moved through the gauge volume in order to obtain a profile of a property such as strain.

Polycrystalline materials give rise to cones of diffracted neutrons at angles $\phi_{hkl} = 2\theta_{hkl}$ about the incident beam on the sample. These angles are given by Bragg's Law:

$$2d_{hkl} \sin \theta_{hkl} = \lambda, \tag{1}$$

where d_{hkl} is the lattice spacing of planes with Miller incides hkl. The cone of scattering arises from a subset of crystallites or grains in the sample, just those which satisfy Bragg's Law and which are oriented so that the planes are at an angle θ to the incident beam. It is usual to define a scattering vector $\mathbf{Q} = \mathbf{k}_i - \mathbf{k}_f$, where $\mathbf{k}_i$ and $\mathbf{k}_f$ are the incident and scattered neutron wavevector, of magnitude $|k| = 2\pi/\lambda$, as shown in Fig. 1. For Bragg reflection $\mathbf{Q}$ is normal to the planes giving the diffracted beam, and of magnitude equal to that of the reciprocal lattice vector τ of the planes, $|Q| = |\tau_{hkl}|$.

The detector is scanned through ϕ_{hkl} to determine the peak-count angle, which, in the case of a large component, corresponds to the average d_{hkl} of the grains in the gauge volume sampled. Usually a fitting routine using least-squares minimisation is used to determine the angle and angular width of the peak. The average lattice macrostrain in the volume sampled is then given by

$$e_{hkl} = (d_{hkl} - d_{ohkl})/d_{ohkl} = -(\cot \theta_{ohkl}) \cdot (\phi_{hkl} - \phi_{ohkl})/2, \tag{2}$$

where d_{ohkl} is the lattice spacing of a 'stress free' sample of the same material composition, and $\phi_{ohkl} = 2\theta_{ohkl}$ the corresponding diffraction angle. The direction in which the strain $\mathbf{e}_{hkl}$ is measured is that of the scattering vector $\mathbf{Q}$. The mean lattice microstrain in the volume sampled is related to the angular peak width, although there may be other contributions.

As the lattice spacing can only change elastically it is an elastic strain which is always measured, but this may be a result of intergranular strains arising from a plastic deformation or thermal treatment of the sample. If an accurate value of d_0, or ϕ_0, can be measured, the strain determined is absolute. However, obtaining a true ϕ_0 may prove difficult in practice. A small annealed sample with measurements made in several orientations and averaged, or an extreme part of a component, may

be taken to be in zero strain. Alternatively a sum rule or boundary conditions, after conversion to stress, may be used.

In order to determine the strain in different directions in the sample, the sample must be rotated accurately about the centre of the gauge volume so that each direction lies along **Q**. This is often quite difficult to do in practice, and requires very careful alignment and centering of the sample. Large samples may hit the spectrometer hardware, or path lengths of the beam in the sample may become excessive, preventing some orientations. It should be noted that the volume sampled is independent of the vertical height of the aperture in the scattered beam, so in order to increase intensity this can be as large as possible consistent with the definition in direction of **e** required. At $\phi = 90°$ the cone becomes a plane of scattering, and this is usually also the optimum scattering angle for definition of the gauge volume. Although the resolution in strain increases with ϕ and is best at $\phi \sim 180°$, using $\phi \sim 90°$ scattering at both monochromator and sample is often a good compromise. The gauge volume shape and size must be chosen with due consideration paid to the direction and magnitude of the strain gradient, the intensity of scattering and consequent measurement time, and the size of the grains in the sample. Typically, gauge volumes are between 1 and 27 mm^3.

The use of a horizontal position sensitive detector (PSD) can speed up data collection by effectively performing the scan of ϕ at one setting. However, care must be taken as the definition of the gauge volume becomes difficult, masks must be placed very close to the sample and these may well prevent rotation of the sample to give strains in different directions. It should be noted that, in contrast to normal powder diffraction, higher wavelength orders, $\lambda/2$, $\lambda/3$, etc., from the monochromator can often be used with advantage in strain measurement. In order to obtain diffraction angles of $\phi \sim 90°$ neutron wavelengths in the region $\lambda = 1.5 - 3.0$ Å must usually be used.

An alternative to a steady reactor source of neutrons is the pulsed white beam of neutrons given by a spallation source. In this case polycrystalline diffraction is observed at a fixed ϕ, and time-of-flight t is used to scan the different lattice planes. The strain is now given by $e = \Delta t/t = \Delta\lambda/\lambda$, where $t = L/v = (\lambda m/h)L$ is the time taken for a neutron with mass m and velocity v to travel a path length L, and h is Planck's constant. The advantage of this method is that strains may be measured from many lattice planes $\{hkl\}$ at once. As for the reactor instrument counters at 90° must be used to give measurement of the full strain tensor, and such instruments are currently under development. The positioning of the sample is even more critical here as it may effect L and hence t.

Conversion of strain to stress

In most cases the strain and stress are triaxial and can be represented by a strain tensor $\boldsymbol{\varepsilon}$ and stress tensor $\boldsymbol{\sigma}$. If we define axes $Oxyz$ within the sample, and define $\boldsymbol{\varepsilon}$ at a point with respect to these axes, then the strain measured in a direction specified by direction cosines $(l'm'n')$ relative to $Oxyz$ is given by:

$$e(l'm'n') = l'^2\varepsilon_{xx} + m'^2\varepsilon_{yy} + n'^2\varepsilon_{zz} + 2l'm'\varepsilon_{xy} + 2m'n'\varepsilon_{yz} + 2n'l'\varepsilon_{zx}. \quad (3)$$

At least six measurements of $e(l'm'n')$ are therefore necessary to determine the six terms in $\boldsymbol{\varepsilon}$, but clearly the accuracy can be improved if more are made. The simplest directions are those along, and at 45° to the axes $Oxyz$. Having determined $\boldsymbol{\varepsilon}$, the principal strain axes OXYZ and the principal strains $\boldsymbol{\varepsilon}^D$ along them may be found by diagonalization. The principal internal stresses along these axes are then related, assuming an elastically isotropic model with macroscopic Young's modulus E and Poisson's ratio ν, by

$$\sigma_{ii}^D = [E/(1+\nu)]\varepsilon_{ii}^D + \{\nu E/[(1-2\nu)(1+\nu)]\}\cdot(\varepsilon_{XX}^D + \varepsilon_{YY}^D + \varepsilon_{ZZ}^D), \quad i = X, Y, Z. \tag{4}$$

Plane strain or plane stress are special cases of these general expressions. Typically, for steel a shift in ϕ from that of a stress-free sample of 0.01° at 90° indicates a strain of $\sim 100\ \mu\varepsilon$ or a stress of ~ 20 MPa. Accuracy in measurement of 0.005°–0.010° is usually obtained by peak profile fitting using a computer. Practical path lengths, that is of the total incident plus diffracted beams, in steel and in aluminium are typically 50 and 100 mm, respectively, for volumes sampled of 27 mm^3. This means that one can measure to a depth of ~ 2.5 cm into steel from a flat surface. Longer paths in the material, for deeper penetration, can be realised by sampling larger gauge volumes, but absorption effects may then become important and these can give rise to anomalous shifts in peak angle. In principle all crystalline materials can be examined, but some materials, such as nickel, scatter neutrons incoherently, and others, such as titanium alloy, have small Bragg intensities making measurements at depth correspondingly more difficult.

Anisotropy of the elastic constants

In most materials, the values of E and ν in Eq. (4) are dependent on the lattice planes (hkl) used as the 'strain gauge', since the elastic response of each grain to an applied stress is anisotropic. Indeed one needs to determine the 'neutron elastic constants' by calibration, using for example a compact stress rig which can be accommodated on a neutron diffractometer (see Allen et al [9]). Such a rig allows a known uniaxial stress to be applied in tension or compression to a sample of material, and the strain to be measured either along the direction of stress ($\|$) or perpendicular to it ($\perp$). The intensity of the reflection, related to its multiplicity and the effects of any texture present, has also to be considered when making a choice of (hkl).

For a single crystal the effective elastic modulus can readily be calculated, and, for example, is found to vary by over a factor of two between reflections in ferritic steel, showing that inclusion of the effects of elastic anisotropy is of paramount importance in interpreting neutron diffraction stress data. The calculation of the response of polycrystalline material to an applied uniaxial stress in not straightforward, and assumptions as to continuity at grain boundaries must be made to simplify the procedure. The two simplest approximations give extreme bounds to the actual response. These are the Voigt and Reuss models in which strain or stress is respectively assumed continuous across grain boundaries. A more realistic model

is given by Kröner (Sayers [10], Allen et al [8]), which approximates to the mean of the Voigt and Reuss bounds (Allen et al [9]). If stresses beyond the yield point are applied, slip will tend to occur in the grains but will be constrained by the surroundings. The theory for such effects is not yet fully developed (Leffers [11]). Results obtained from measurements using stress rigs should provide key data for a better understanding of plastic strain at the grain interaction level. Measurements show that the use of the 211 Bragg reflection is a good practical choice for steels.

Examples of strain and stress field measurement

A selection of examples of measurements is briefly given to illustrate the range of application of the technique. Full details can be found in the references given.

Stress in weldments

One of the the key uses of the neutron diffraction method of stress measurement has been to investigate in-depth stresses in and around the weld in a variety of weldments. These measurements can now actually test the assumptions and theories which had hitherto been used to estimate the stress levels. Another typical use is in the validation of a new portable magnetic stress measurement technique developed for the Harwell Offshore Inspection Service (HOIS). A series of neutron diffraction measurements were made on a single-V manual metal arc weldment of 50D steel (Allen et al [12]). The triaxial stress was determined from a series of strain measurements using a gauge volume of $3 \times 3 \times 3$ mm^3, at positions along a line perpendicular to the weld line at an average depth of 1.5 mm below the surface. The principle axes were found to lie close to the symmetry axes of the weldment. Using the magnetic techniques of magnetoacoustic emission (MAE) and stress-induced magnetic anisotropy (SMA), measurements were also made along the same line. The magnetic data were converted into biaxial stress levels, with errors, using dedicated software together with biaxial calibration maps made from similar material under known applied stress. The comparison of the two sets of stress values shows excellent agreement as seen from Figs 2a and 2b (Buttle and Hutchings [13]).

Near-surface residual stresses caused by shot peening

Shot peening is a cold-working process in which the surface is plastically deformed by bombardment with fine shot. It is used to produce compressive stress at the surface layer of components in order to inhibit the propagation of surface cracks. The components of residual strain as a function of depth beneath the surface of a heavily peened block of nickel based superalloy have been measured by Ezeilo et al [14] using a gauge volume of dimension ~ 0.5 mm perpendicular to the surface. The triaxial strain data, corrected for partially filled gauge volume effects, were converted into the stress values, shown in Fig. 3. The compressive surface stress rapidly diminishes and a significant tensile region is observed between depths of 0.6 and 2 mm. The nature of this tensile region was first revealed by such neutron diffraction measurements.

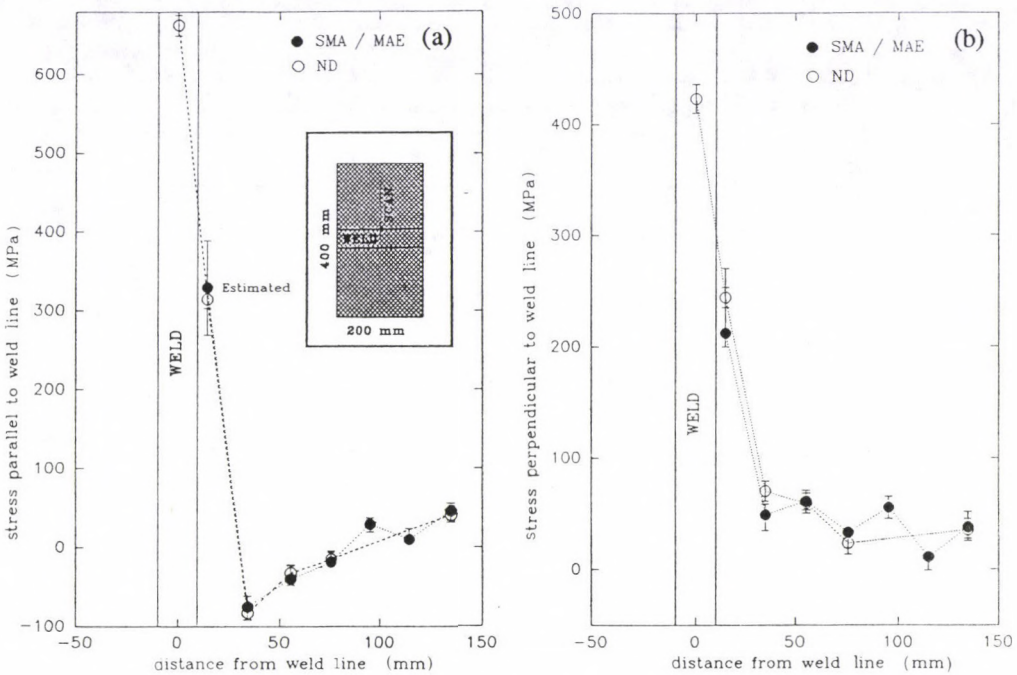

Fig. 2. Biaxial stress along the symmetry axis perpendicular to the weld line determined from combination of MAE and SMA measurements and from neutron diffraction on mild steel plate containing single-V manual metal arc weld (inset). (a) Stress component parallel, and (b) stress component perpendicular, to the weld line

Residual stress in composite materials

The stress in each component of a crystalline composite material can be measured separately from its distinct Bragg reflections. This unique ability of the neutron diffraction technique to measure the through-thickness strain in each phase of a two phase material is illustrated by recent work, carried out for the UK Department of Trade and Industry (DTI), on quenching induced stresses in an Al/particulate-SiC composite. Of specific interest is the effect of macroscopic residual stress on the crack front propagation during fracture toughness tests, when crack front curvature might invalidate the test. A 15 mm thick plate of BP217 Al/SiCp was studied at Risø National Laboratory.

This plate had been subjected to a 'T4' heat treatment which entails a rapid quench from 505 °C. The measured principal strain and stress represented as vectors (T) in each phase i, Al or SiC, averaged over the gauge volume, may be taken to

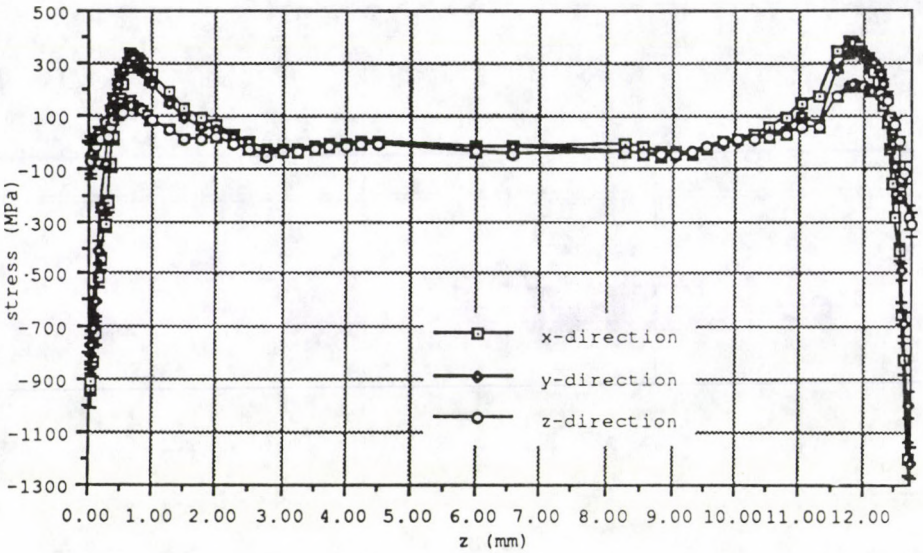

Fig. 3. Residual stress components as a function of depth (z) from the surface of a shot peened nickel superalloy block. The x and y axes lie in the surface plane of the block (Ezeilo et al [14])

comprise two types of contribution (see Allen et al [15] for example):

$$\mathbf{e}_i^T(\mathbf{r}) = \mathbf{e}^M(\mathbf{r}) + \mathbf{e}_i^m(\mathbf{r}), \tag{5}$$

and

$$\boldsymbol{\sigma}_i^T(\mathbf{r}) = \boldsymbol{\sigma}^M(\mathbf{r}) + \boldsymbol{\sigma}_i^m(\mathbf{r}). \tag{6}$$

The first contribution is a macrostrain (M) component, independent of phase, which will arise from uneven or constrained cooling of the component during manufacture or heat treatment. The second contribution (m), is sometimes referred to as a 'microstrain/stress', but is better described as a mean 'mismatch' strain/stress, in each phase. The mismatch contribution has two parts. Firstly, a mismatch elastic term, proportional to the macroscopic contribution, due to the elastic constant mismatch between the reinforcing particles and the matrix. This gives the elastic transfer of the load from the matrix to the inclusions. Secondly, a mismatch thermal term, due to the different expansion coefficients and elastic constants of the two phases. This arises from cooling in production, and is tensile in the matrix and compressive in the reinforcement. The equilibrium condition for the mismatch strains over the gauge volume gives

$$f_1\boldsymbol{\sigma}_1^m + (1 - f_1)\boldsymbol{\sigma}_2^m = 0, \tag{7}$$

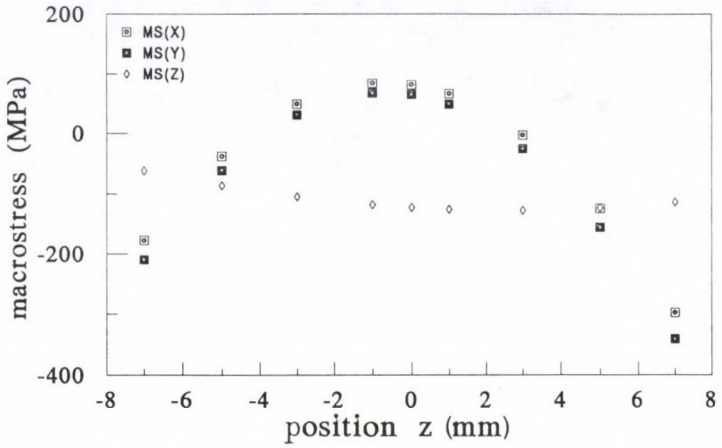

Fig. 4. The variation of three principal macrostress components, as calculated from the measured Al matrix and SiC reinforcement strains, through the thickness (z) of a quenched Al/SiC MMC plate. The x and y axes lie in the plane of the plate

where f_1 is the volume fraction of the reinforcing phase (SiC). Thus if the *stresses* in the two phases and the volume fractions of each phase are known, the macroscopic stress may be readily deduced from

$$\boldsymbol{\sigma}^M(r) = f_1 \boldsymbol{\sigma}_1^T(\mathbf{r}) + (1 - f_1)\boldsymbol{\sigma}_2^T(\mathbf{r}). \tag{8}$$

The three strain components, e_x, e_y and e_z were measured in each phase using the Al(111), Al(002), and SiC(111) Bragg reflections. These data were then converted to stress neglecting the small anisotropy in the elastic constants. The resulting stresses in each phase show the same general trend through the thickness, z, but with the Al phase more tensile than the SiC phase. Using Eq. (8) and the volume fraction of SiC, $f_1 = 0.17$, the macroscopic stress was calculated and is shown in Fig. 4. It is seen that the components have a parabolic variation through the plate, but that σ_z does not approach zero at the surfaces as expected, probably reflecting the accumulative uncertainties in the calculation, particularly in the reference zero stress values used. The parabolic form of stress is as expected from thermal quenching, and will cause curvature of a crack front propagating in directions where it affects the crack opening.

Stress during fatigue cycling of a compact tension specimen

The maximum triaxial stress levels along the line of cracking of a small ($31.5 \times 49.6 \times 13.1$ mm^3) compact tension specimen of BS 4360 steel have been measured by bolting the specimen at the peak stress level (Hutchings et al [16]). The specimen

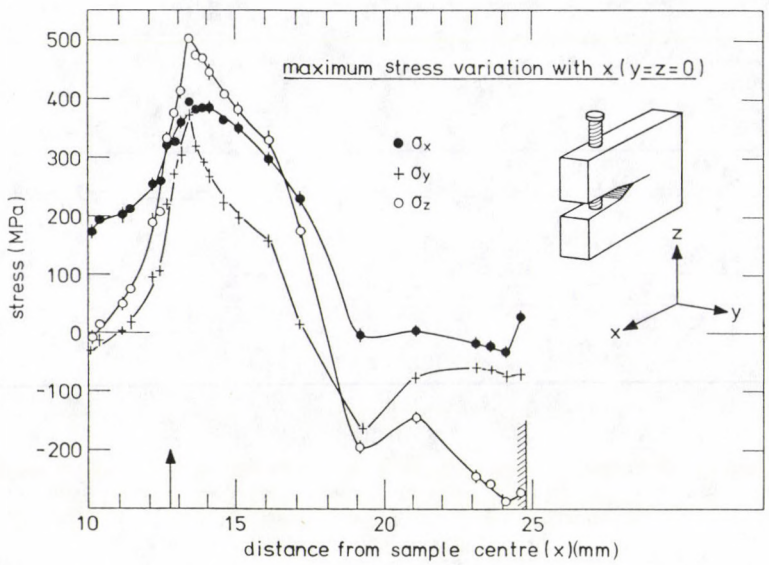

Fig. 5. Triaxial stress variation with position x in a cracked fatigue test specimen bolted in the maximum crack-tip stress configuration. The arrow denotes the position of the crack tip on the specimen centre line, and the shaded line the outer edge of the specimen (Hutchings et al [16])

had been subjected to 20 000 cycles of fatigue loading, with a stress intensity level varying between a minimum of $K = 3$ and maximum of $K = 34$ MPa mm$^{1/2}$, in order to produce a small crack of 3.6 mm length. The data were taken with a gauge volume of 1 mm^3, and are shown in Fig. 5. The stress field was found to be neither plane strain nor plane stress, states often assumed in theoretical calculations, and the peak stress levels are spatially broader and less in magnitude than expected from theory assuming plane strain. Instrumental gauge volume resolution could have contributed to this reduction. On removal of the bolt to give the minimum load situation, it was found that the peak level moved away from the crack tip with consequences for hydrogen or sulphur embrittlement.

Summary

Neutron diffraction provides a non-destructive absolute method of measurement of residual stress at depths of up to ~ 2.5 cm in steel and ~ 7 cm in aluminium. Its unique nature is particularly important for addressing safety related industrial problems. The technique is also becoming increasingly valuable to the fundamental materials science field, in the understanding of the stress distribution in new materials to be used by engineers such as metal matrix composites, and also in shedding light on the strain response at the average grain level of metals stressed into the plastic regime.

Acknowledgements

I would like to thank my colleagues at AEA Harwell who collaborated in much of the work cited. The work was supported in part by the Corporate Research Programme of AEA Technology, by the HOIS, and by the UK DTI.

References

1. L. Mordfin, in: Encyclopedia of Materials Science and Engineering, ed. R. W. Cahn, Pergamon, Oxford, 1986.
2. M. T. Hutchings and A. D. Krawitz (eds), Measurement of Residual and Applied Stress using Neutron Diffraction, Kluwer, Dordrecht, 1992.
3. I. C. Noyan and J. B. Cohen, Residual Stress — Measured by Diffraction and Interpretation, Springer, New York, 1987.
4. A. J. Allen, C. Andreani, M. T. Hutchings and C. G. Windsor, NDT International, 249, October, 1981.
5. L. Pintschovius, V. Jung, E. Macherauch, R. Schäfer and O. Vöhringer, in: Residual Stress and Stress Relaxation, eds E. Kula and V. Weiss, Plenum, New York, 1982, pp. 467–482.
6. A. D. Krawitz, J. E. Brune and M. J. Schmank, in: Residual Stress and Stress Relaxation, eds E. Kula and V. Weiss, Plenum, New York, 1982, pp. 139–155.
7. M. Vrana, P. Lukas, P. Mikula and J. Kulda, Nucl. Instr. and Methods, *A338*, 125, 1994.
8. A. J. Allen, M. T. Hutchings, C. G. Windsor and C. Andreani, Adv. in Phys., *34*, 445, 1985.
9. A. J. Allen, M. Bourke, W. I. F. David, S. Dawes, M. T. Hutchings, A. D. Krawitz and C. G. Windsor, in: International Conference on Residual Stress ICRS2, eds G. Beck, S. Denis and A. Simon, Elsevier, London, 1989, pp. 78–83.
10. C. M. Sayers, Phil. Mag., *A49*, 243, 1984.
11. T. Leffers, in: Deformation of Polycrystals: Mechanisms and Microstructures, eds N. Hansen, A. Horsewell, T. Leffers and H. Lilholt, Risø Nat. Lab., Roskilde, 1981, pp. 55–71.
12. A. J. Allen, M. T. Hutchings and M. Kocsis, private communication.
13. D. J. Buttle and M. T. Hutchings, British J. Non-Destructive Testing, *34*, 175, 1992.
14. A. N. Ezeilo, P. S. Webster, G. A. Webster and P. J. Webster, in: Measurement of Residual and Applied Stress using Neutron Diffraction, eds M. T. Hutchings, A. D. Krawitz, Kluwer, Dordrecht, 1992, pp. 535–543.
15. A. J. Allen, M. A. M. Bourke, S. Dawes, M. T. Hutchings and P. J. Withers, Acta Metall. Mater., *40*, 2361, 1992.
16. M. T. Hutchings, C. Hipplsey and V. Rainey, Mat. Res. Soc. Symp. Proc., *166*, 317, 1990.

Acta Physica Hungarica 75 (1–4), pp. 161–168 (1994)

DIFFUSE NEUTRON SCATTERING FOR INVESTIGATION OF ORDERING PHENOMENA IN SOLIDS: $YBa_2Cu_3O_{6+x}$ AND METAL-HYDRIDES

O. BLASCHKO

Institut für Experimentalphysik, Universität Wien
Strudlhofgasse 4, A-1090 Wien, Austria

The elastic diffuse neutron scattering technique allows the investigation of ordering phenomena in solids. Recent results on oxygen ordering in $YBa_2Cu_3O_{6+x}$ and some peculiar features of hydrogen ordering in metal–hydrogen systems are discussed.

1. Introduction

In perfect crystals the elastic intensity is essentially confined to Bragg points in reciprocal space. If the perfect long-range ordered structure is deteriorated by defects, lattice distortions, imperfect and short-range order, then elastic scattering is observed outside the fundamental Bragg reflections. This elastic scattering which generally appears as broad intensity distributions in reciprocal space gives valuable information on the state of imperfect order and short-range order present in the crystal. Despite its low intensity elastic diffuse neutron scattering can reveal very peculiar structural features in solids. In the present paper we will shortly describe the possibilities of diffuse neutron scattering experiments by giving a review on experimental results recently obtained in two systems, i.e. $YBa_2Cu_3O_{6+x}$ and hexagonal rare-earth hydrides.

2. Oxygen order in the High-Tc $YBa_2Cu_3O_{6+x}$ compound

In $YBa_2Cu_3O_{6+x}$ compound oxygen atoms form chains for $x > 0.4$ within the basal plane inducing a symmetry change from a tetragonal to an orthorhombic structure [1]. This orthorhombic structure represents the well-known high temperature superconductor and is stoichiometric at $x = 1$.

At lower concentrations $0.4 < x < 1$ the presence of oxygen vacancies gives the possibility of vacancy ordering. This ordering process procedes by the formation of superstructures consisting of filled and empty oxygen chains. For $x = 0.5$ a $(1/2, 0, 0)$ superlattice reflection was found indicating a sequence of alternating filled and vacant oxygen chains and corresponding to the OII phase [2–5]. Other superstructures were obtained by electron microscopy methods showing locally different ordering sequences [6], [7]. Theoretical models suggest for $x > 0.5$ an oxygen ordering according to the Magneli series, i.e. $(\square\bullet)n\bullet$ (where $\square$ and $\bullet$ represent empty and filled oxygen chains and n a parameter related to oxygen stoichiometry).

The occurrence of a Magneli-type ordering should induce with increasing x a broadening of the $(1/2, 0, 0)$ peak giving finally satellites at $(1/3, 0, 0)$ and $(2/3, 0, 0)$ for $x = 2/3$ [8]. Diffuse neutron scattering experiments were performed in a $YBa_2Cu_3O_{6+x}$ single crystal for a series of different oxygen concentrations. The region in reciprocal space near the $(1/2, 0, 0)$ reciprocal lattice point was investigated as a function of temperature [9]. The results are shown in Figs 1 and 2.

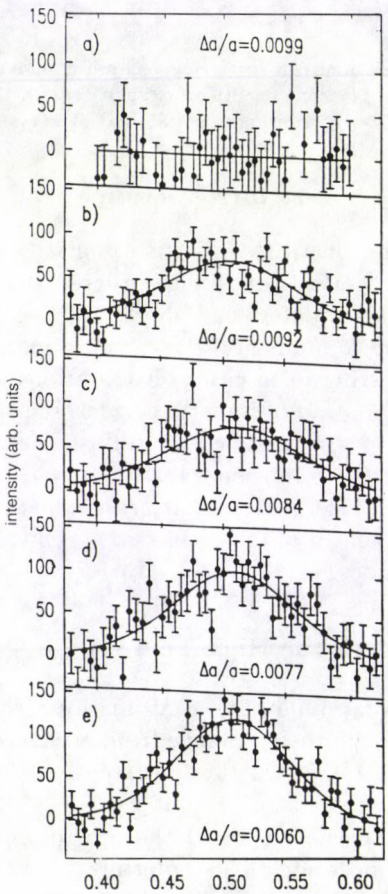

Fig. 1. Diffuse intensity in $YBa_2Cu_3O_{6+x}$ around the $(1/2, 0, 0)$ superlattice position along the [100] direction for different values of the orthorhombic splitting $\Delta a/a$ at 50 °C. The corresponding oxygen concentrations are (a) $x = 0.68$, (b) $x = 0.64$, (c) $x = 0.60$, (d) $x = 0.57$ and (e) $x = 0.50$

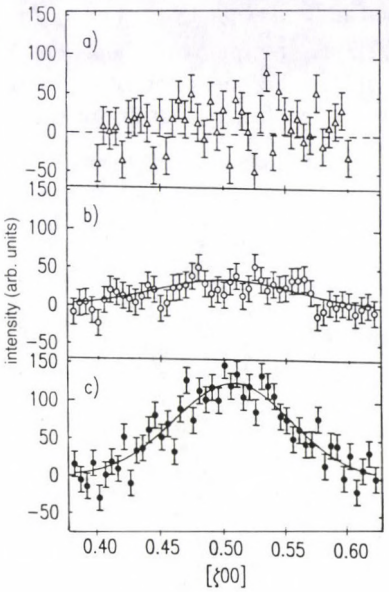

Fig. 2. Temperature dependence in $YBa_2Cu_3O_{6+x}$ of the diffuse intensity around the $(1/2, 0, 0)$ superlattice position for different temperatures at a fixed concentration of $x = 0.50$. (a) $T = 150$ °C, (b) $T = 100$ °C and (c) $T = 50$ °C

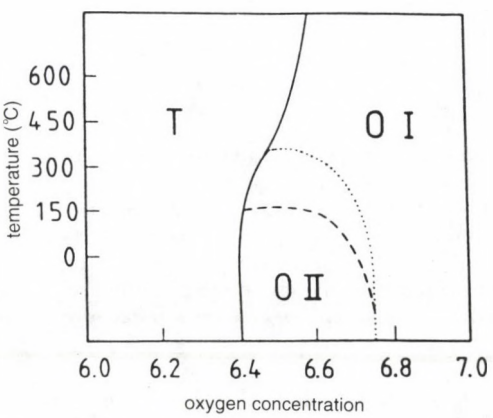

Fig. 3. Schematic representation of the observed stability limit (dashed line) of the $[1/2, 0, 0]$ ordered structure in $YBa_2Cu_3O_{6+x}$ in comparison to a theoretical phase diagram of [10]. The different phases are the tetragonal (T), the orthorhombic (OI), and the orthorhombic superstructure (OII). The solid line indicates the T–OII phase boundary, the dotted line the theoretical stability limit of the OII phase

In Fig. 1 for concentrations $0.5 < x < 0.64$ a broad elastic intensity distribution centered at the $(1/2, 0, 0)$ point is observed. The width of the intensity distribution may increase by a few per cent with concentration, but no drastic broadening is observed when $x \to 2/3$. Moreover, for $x > 0.64$ no diffuse intensity at all is found. In Fig. 2 the temperature dependence of the short-range order intensity is shown for a typical concentration of $x = 0.5$. Figure 2 shows that the intensity decreases at 100 °C and finally has disappeared at 150 °C.

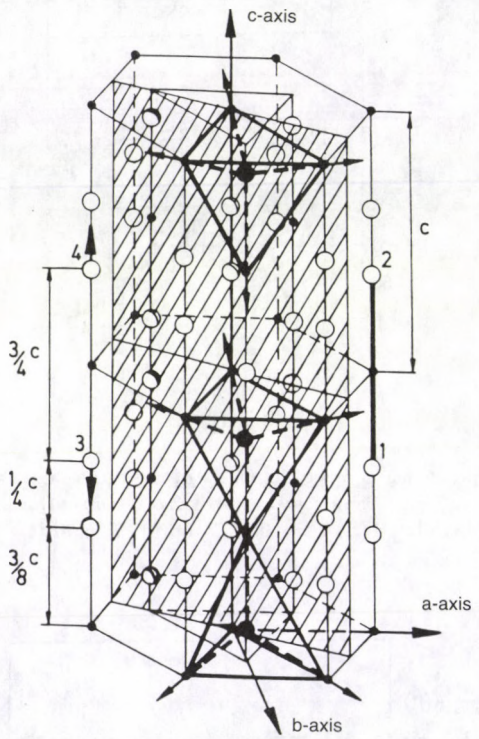

Fig. 4. Two adjacent unit cells of the hexagonal lutetium lattice aligned along the c-axis: • lutetium atoms; o interstitial sites; • hydrogens. In the upper half of the Figure a lutetium tetrahedron is shown. The arrows indicate displacements of the metal atoms. In the lower part, the occupation of two second-neighbour tetrahedral interstitial sites along the c direction is shown with the undisplaced central lutetium atom common to both tetrahedra. The hatched section marks the $c^* - a^*$ scattering plane. As indicated on the left-hand side, second-nearest neighbours forming the hydrogen pair are separated by $(3/4)c$.

From these investigations a phase diagram could be established and is shown in Fig. 3. The experimentally determined phase diagram confirms the stability of the OII phase within a similar concentration range as predicted by theory [10]. On the other hand, the experiments showed that the stability of the OII is significantly lower in temperature (150 °C) as proposed in the theoretical work [10].

Finally, no indication for a Magneli-type ordering was found in this work [9].

3. Hydrogen ordering in hexagonal rare-earth–hydrogen systems

The phase diagram of some hexagonal rare-earth–hydrogen systems such as ScH_x, YH_x, HoH_x, ErH_x, TmH_x and LuH_x is characterized by a solid solution phase extending to rather high hydrogen concentrations and stable down to 0 K [11]. An anomaly in resistivity found about 20 years ago was the only indication for some structural change occurring within the solid solution phase at lower temperatures [12].

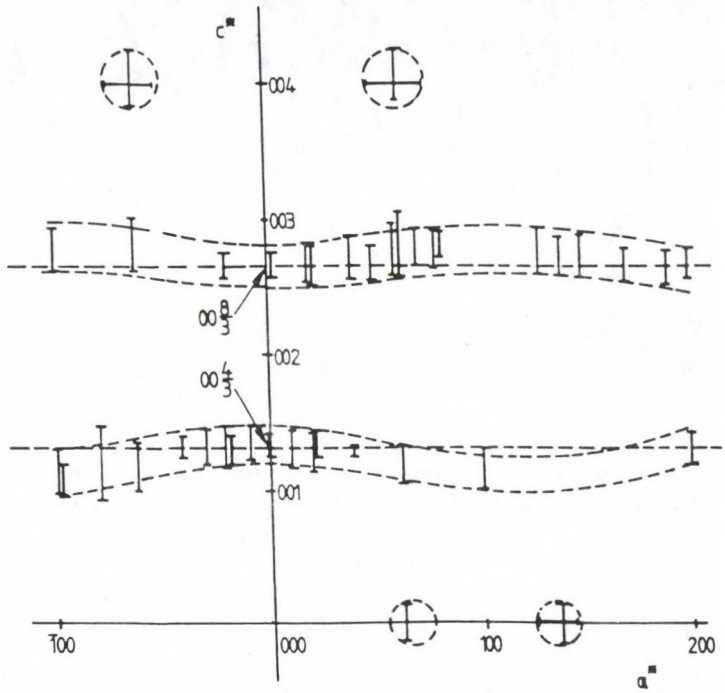

Fig. 5. Difference between the diffuse scattering intensities observed at 150 and 300 K within (c^*, a^*) plane in $LuD_{0.19}$. The bars indicate the full width at half-maximum in individual scans

In recent years a peculiar hydrogen ordering tendency was discovered by a series of diffuse neutron scattering experiments [13–16]. In these rare-earth systems the hydrogen atom is located on a tetrahedral interstitial site. The diffuse neutron scattering experiments have shown that with decreasing temperature the hydrogen atoms form chains along the hexagonal c-direction. The basic structural entity of the chains is a hydrogen pair bridged by a central metal atom (Fig. 4).

This peculiar structural state was deduced from elastic diffuse scattering results as shown in Fig. 5 for LuD_x. Fig. 5 shows a complex intensity pattern in reciprocal space characterized by diffuse intensity ridges perpendicular to the hexagonal c-direction.

The ridges shown as isointensity contours within the (c^*, a^*) reciprocal lattice plane in Fig. 5 were also observed in (c^*, b^*) reciprocal lattice planes and indicate

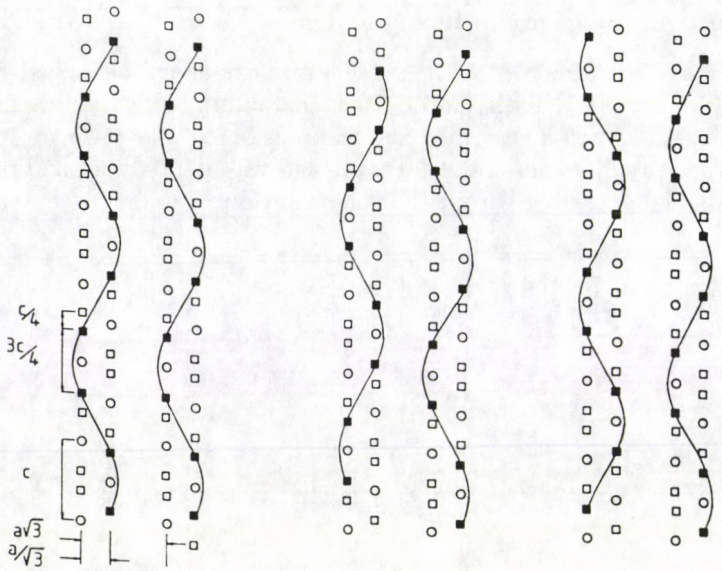

Fig. 6. Three different two-chain arrangements on adjacent c axes along the b direction

a two-dimensional intensity distribution in reciprocal space. From fundamental arguments of scattering theory it follows that the corresponding H order should consist of one-dimensional H structures. The intersection points of the ridges with the c-axis, i.e. $(0, 0, 4/3)$ for the first order position and $(0, 0, 8/3)$ for the second position indicate the presence of an atomic correlation over a distance of $(3/4)c$ in real space. The $(3/4)c$ distance corresponds to the distance between the hydrogen atoms in the pair (as shown in Fig. 4).

However, an arrangement of individual H pairs is not able to explain the scattering pattern experimentally observed. From the width of the diffuse ridges along c^* it follows that the $(3/4)c$ correlations should extend over several atomic distances. This means that hydrogen chains consisting of H pairs should be formed.

Furthermore, in addition to the diffuse ridges Fig. 5 shows localized intensities represented by closed intensity contours. These localized intensities cannot be understood by a random arrangement of hydrogen chains but indicate the presence of interchain correlations. Therefore, in order to take into account the interchain correlations two chain arrangements as shown in Fig. 6 have been proposed. The calculated scattering pattern obtained from a statistical average of the three possible two-chain arrangements, taking into account all symmetry operations of the hexagonal lattice, is in quite good agreement with the experimental results (Fig. 7).

4. Conclusion

In this review I have presented two recent examples of elastic diffuse neutron scattering experiments revealing significant information on partially ordered struc-

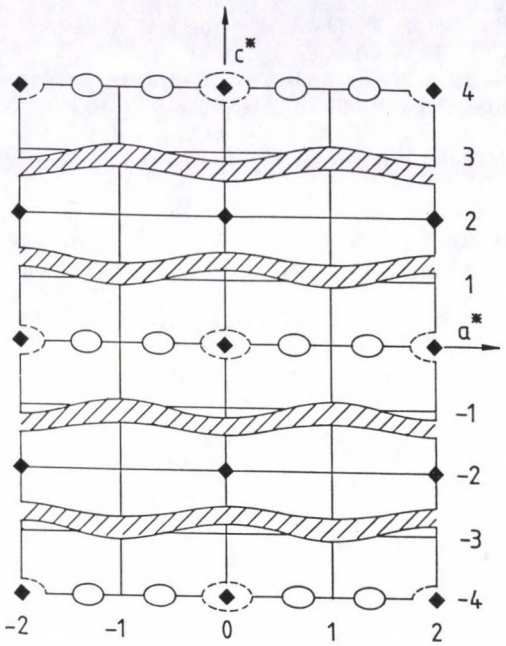

Fig. 7. Calculated full width at half maximum contours of the scattered intensity within the (c^*, a^*) plane in LuD_x obtained from a statistical average of the three structures shown, taking into account all symmetry operations of the hexagonal matrix. For the regions of increased intensity marked by dashed contours, no reliable experimental data are available for comparison due to the nearby Bragg peaks

tures. Elastic diffuse neutron scattering is a valuable tool for the investigation of microscopic structural features in solid state systems.

Acknowledgement

This work was partly supported by the Fonds zur Förderung der wissenschaftlichen Forschung, Austria.

References

1. J. D. Jorgensen, M. A. Beno, D. G. Hinks, L. Soderholm, K. J. Volin, R. L. Hittermann, J. D. Grace, I. K. Schuller, C. U. Segre, K. Zhang and M. S. Kleefish, Phys. Rev. B, *36*, 3608, 1987.
2. G. van Tendeleo, H. W. Zandbergen and S. Amelinckx, Solid State Commun., *63*, 389, 1987; *63*, 603, 1987.
3. R. M. Fleming, L. F. Schneemeyer, P. K. Gallagher, B. Batlogg, L. W. Rupp and J. V. Waszczack, Phys. Rev. B, *37*, 7920, 1988.
4. T. Zeiske, R. Sonntag, D. Hohlwein, N. H. Andersen and T. Wolf, Nature, *353*, 542, 1991.
5. J. Reyes-Gasga, T. Krekels, G. van Tendeloo, J. van Landuyt, S. Amelinckx, W. H. M. Bruggink and H. Verweij, Physica C, *159*, 831, 1989.
6. D. J. Werder, C. H. Chen, R. J. Cava and B. Batlogg, Phys. Rev. B, *37*, 2317, 1988.

7. R. J. Cava, A. W. Hewat, E. A. Hewat, B. Batlogg, M. Marezio, K. M. Rabe, J. J. Krajewski, W. F. Peck and L. W. Rupp, Physica C, *165*, 419, 1990.
8. A. G. Khachaturyan and J. W. Morris, Phys. Rev. Lett., *61*, 215, 1988; *64*, 76, 1990.
9. W. Schwarz, O. Blaschko, G. Collin, F. Marucco, Phys. Rev. B, *48*, 6513, 1993.
10. D. de Fontaine, G. Ceder and M. Asta, Nature *343*, 544, 1990.
11. J. P. Burger, J. N. Daou, A. Lucasson, P. Lucasson and P. Vajda, Z. Phys. Chemie, *143*, 111, 1985.
12. J. N. Daou, A. Lucasson and P. Lucasson, Solid State Comm., *19*, 895, 1976.
13. O. Blaschko, G. Krexner, J. N. Daou and P. Vajda, Phys. Rev. Letter, *55*, 2876, 1985.
14. O. Blaschko, G. Krexner, J. Pleschiutschnig, G. Ernst, J. N. Daou and P. Wajda, Phys. Rev. B, *39*, 5605, 1989.
15. M. W. McKergow, D. K. Ross, J. E. Bonnet, I. S. Anderson and O. Schaerpf, J. Phys. C, *20*, 1909, 1987.
16. O. Blaschko, J. Pleschiutschnig, P. Vajda, J. P. Burger and J. N. Daou, Phys. Rev. B, *40*, 5344, 1989.

Acta Physica Hungarica 75 (1–4), pp. 169–175 (1994)

IS IT POSSIBLE TO PRODUCE THE NEXT GENERATION OF UCN SOURCES WITH DENSITY 10^3–10^4 cm^{-3}?

A. SEREBROV

St. Petersburg Nuclear Physics Institute
188350 Gatchina, Russia

The analysis of the evolution of UCN sources is presented. It is shown that the gain factor of about 10^4 and the UCN density about 10^3–10^4 cm^{-3} can be obtained by means of solid D_2 at 4 K.

For the first time ultracold neutrons (UCN) were obtained 25 years ago in the experiments, which were carried out by F. Shapiro with colleagues in Dubna (Russia) [1] and by Steyerl in Munich (Germany) [2]. From that time the density of UCN has been increased by eight orders of magnitude and now it accounts for around 10–10^2 n/cm^3. Figure 1 shows UCN source evolution from 1968 up to now. Here only those experiments are presented which demonstrated the best UCN densities every time, the total number of experiments related to this problem is considerably higher. The highest densities of UCN were obtained in Gatchina (PNPI) [3] and Grenoble (ILL) [4]. It was reached with high thermal neutron fluxes, with liquid hydrogen and deuterium sources. The dependence in Fig. 1 looks like a saturation function. It seems that the future progress is problematic, Actually, the most intensive fluxes of thermal neutrons were used already.

Nevertheless, the question is the following: is it possible to produce the alternative version of UCN sources at very low temperature, but with moderate neutron fluxes? More detailed consideration shows that such approach is possible to apply and it allows to obtain considerable UCN density up to 10^3–10^4 n·cm^{-3} and to create a new generation of UCN sources. Therefore, the slack development of UCN sources in the past is a temporary phenomenon. A new sudden change of UCN density is possible. The talk is devoted to this question.

As it is well known, the gain factor for the yield of very cold neutrons is proportional to $1/T_n^2$, where T_n is the temperature of neutron flux. For example, the thermalization of neutron flux down to 30 K gives the gain factor about 100. Since the thermalization of neutron spectrum below 30 K is a very difficult experimental task, it seems that the temperature gain factor about 100 is the upper limit for the method of low temperature UCN sources. However, this conclusion is correct for the thermodynamical equilibrium between neutron flux and medium. It could be shown that for nonequilibrium systems the considerable gain factor of UCN yield is

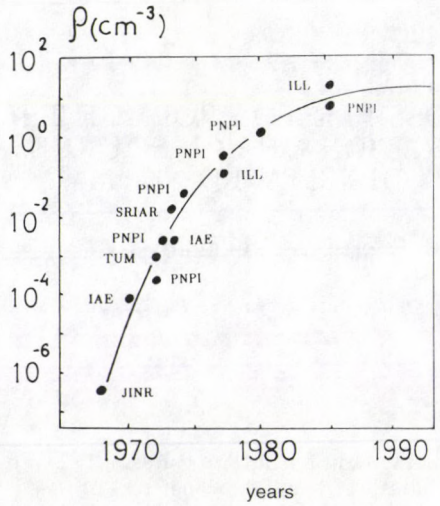

Fig. 1. Evolution of UCN sources. JINR – Joint Institute of Nuclear Research (Dubna, Russia); IAE – Kurchatov Institute of Atomic Energy (Moscow, Russia); TUM – Technical University Munich (Garching, Germany); PNPI – St. Petersburg Nuclear Physics Institute (Gatchina, Russia); SRIAR – Scientific Research Institute of Atomic Reactors (Dimitrovgrad, Russia); ILL – Institute Max von Laue – Paul Langevin (Grenoble, France)

possible. For example, for D_2 UCN source at the temperature 4 K and the neutron temperature 40 K the gain factor accounts for $2.5 \cdot 10^4$.

Let us consider the yield of UCN from a substance at the temperature T with neutron flux at the temperature T_n. The probability of UCN production is:

$$P(E_{UCN}) = n \int \Phi(T_n, E_0) \cdot \sigma(T, E_0 \to E_{UCN}) dE_0, \tag{1}$$

where $\Phi(T_n, E_0) = \Phi_0 \cdot E_0/T_n^2 \exp(-E_0/T_n)$ is the neutron flux, $\sigma(T, E_0 \to E_{UCN})$ is the differential cross-section for UCN production from energy E_0, n is the number of nucleus per volume unit. The yield of UCN or the flux of UCN will be:

$$\Phi_{UCN}(E) = \frac{\nu}{4\pi} P(E_{UCN}) \int \exp(-n\sigma_{UCN} l/\cos\theta) \sin\theta d\theta dl d\varphi, \tag{2}$$

l is depth, where UCN was produced, θ is the angle of escape; $\sigma(E_{UCN}) = \sigma_a(E_{UCN}) + \int \sigma(T, E_{UCN} \to E_0) dE_0$ is the total UCN cross-section, which is the sum of the capture cross-section and the scattering cross-section. After integration we have:

$$\Phi(E_{UCN}, T, T_n) = \frac{\nu}{4} \cdot \frac{\int \Phi(T_n, E_0) \sigma(T, E_0 \to E_{UCN}) dE_0}{\sigma_a(E_{UCN}) + \int \sigma(T, E_{UCN} \to E_0) dE_0}. \tag{3}$$

Let us define the temperature gain factor as:

$$G(T, T_n) = \frac{\Phi_{UCN}(T, T_n)}{\Phi_{UCN}(T = 300\ \mathrm{K}, T_n = 300\ \mathrm{K})}, \tag{4}$$

then

$$G(T, T_n) = \frac{300^2}{T_n^2} \cdot \frac{\int E_0/E_{UCN} \exp(-E_0/T_n) \cdot \sigma(T, E_0 \to E_{UCN}) dE_0}{\sigma_a(E_{UCN}) + \int \sigma(T, E_{UCN} \to E_0) dE_0}. \tag{5}$$

The cross-section of inelastic scattering can be calculated in the frames of Debye model by means of three parameters θ, σ_0, μ [5], where θ is the Debye temperature, σ_0 the nuclear cross section, μ reduced mass ($\theta_{D_2} = 110$ K).

$$\sigma(E_i \to E_f) = \sum_1^\infty \sigma_n(T, E_i \to E_f)$$

is the sum of multiphonon processes

$$\sigma(E_i \to E_f) = \sigma_0 \left(1 + \frac{1}{\mu}\right)^2 \cdot \sqrt{\frac{E_f}{E_i}} \cdot e^{-\frac{E_i + E_f}{\mu\epsilon}} \left(\frac{E_i + E_f}{\mu}\right)^n \cdot \frac{f_n(E_i - E_f)}{n!}, \tag{6}$$

where

$$f_n(\varepsilon) = \int f_{n-1}(\varepsilon') \cdot f(\varepsilon - \varepsilon') d\varepsilon';$$

$$f(\varepsilon) = \frac{g(|\varepsilon|)}{\varepsilon(1 - e^{-\varepsilon/T})}; \quad g(\varepsilon) = \frac{3}{\theta^3} \cdot \varepsilon^2; \quad |\varepsilon| < \theta;$$

$$\frac{\ni}{\theta} = \frac{1}{2} \cdot \left(\frac{\theta}{T}\right)^2 \cdot \left(\int_0^{\theta/2T} x \coth x dx\right)^{-1}.$$

The results of the $G(T, T_n)$ calculations for D_2 UCN source are presented in Fig. 2 and Fig. 3. Here the experimental results of measurements for the source with volume 150 cm^3 for the temperature range 10–19 K [6] and for the UCN source with the volume 1 liter for the temperature range 19–25 K [7] are presented also. The dotted line in Fig. 2 is the extrapolation to the temperature range 10–19 K for the 1 liter source on the basis of experimental data for the 150 cm^3 source. Rather good agreement between the experimental and theoretical parameter $\partial G/\partial T$ is seen. This allows us to hope that these calculations will hold true for the temperature range down to 4 K. Figure 3 shows the UCN yield dependence on the effective temperature of the neutron spectrum. The calculations have been carried out taking into account multiphonon processes. Optimal temperature of neutron spectrum 40 K corresponds to the maximum of UCN rate production, which depends rather weakly on the source temperature. The decreasing of source temperature

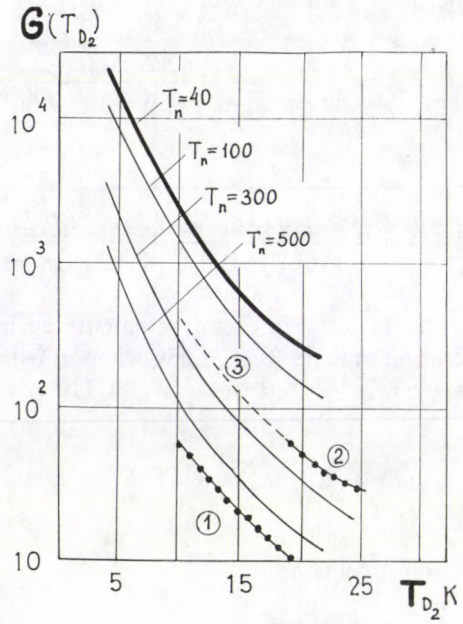

Fig. 2. The calculated dependences of gain factor in UCN yield on the temperature of D_2. Different curves correspond to the different temperatures of the neutron flux. 1. experimental dependence of gain factor in UCN yield on the temperature of the D_2 UCN source with volume 150 cm^3; 2. with volume 1 liter; 3. extrapolation of experimental data (2) to the temperature range 10–19 K by means of experimental data (1)

provides the increasing of the depth of UCN yield. This process provides mainly the temperature dependence of gain factor, as it is shown in Fig. 2.

For these calculations the source temperature and the effective temperature of neutron spectrum were considered as independent parameters. However, they are connected closely and an effective temperature of neutron flux inside the source depends on the source volume and its temperature. The necessary source size is defined also by the depth of UCN yield, which grows up with the decreasing of the source temperature reaching its limit because of the capture cross-section. The inelastic scattering cross-section and the capture cross-section for D_2 are compared at 4 K, therefore the decreasing of source temperature below 4 K is not so effective. The exponential depth of UCN yield at this temperature amounts to 54 cm for UCN with a velocity 7 m/s. The dependence of UCN yield as a function of the source size can be calculated with the formula:

$$\Phi(E_{UCN}) = \frac{1}{4} \cdot P \cdot L_0 \left[1 - e^{-L/L_0} \left(1 - \frac{L}{L_0} \right) + \left(\frac{L}{L_0} \right)^2 \cdot Ei \left(-\frac{L}{L_0} \right) \right], \qquad (7)$$

where $L_0 = (n \cdot \sigma)^{-1}$, Ei is the Eiri function.

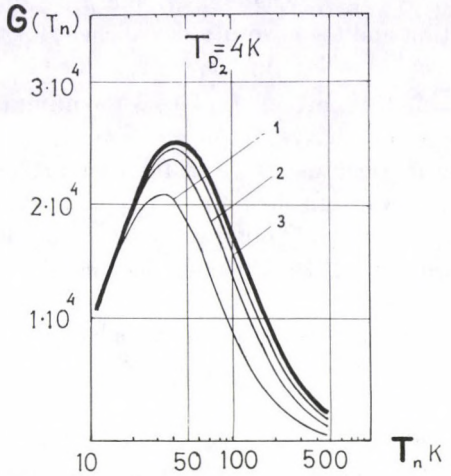

Fig. 3. The calculated dependence of UCN gain factor on the temperature of neutron flux. 1. one-phonon approximation; 2. two-phonon approximation; 3. three-phonon approximation

For instance, when $L/L_0 = 1$ the UCN yield amounts to 78 %, when $L/L_0 = 2$ the UCN yield will be 93 %. For the source with ^{58}Ni coating on the internal surface of its walls besides the window the source size can be reduced by the factor of two. Therefore, in practical case the source size 30 cm should be sufficient. At the same time the D_2 source with this size can thermalize the flux of thermal neutron down to the temperature 60–100 K. This is rather close to optimal conditions for this task and can give a gain factor $(1 \div 2) \cdot 10^4$.

The density of UCN in the source is:

$$\rho = \frac{2\Phi_0}{3} \cdot \left(\frac{E_{lim}}{T_n = 300 \text{ K}} \right)^2 \cdot \frac{G(T, T_n)}{v_{lim}}, \tag{8}$$

where Φ_0 is the total neutron flux, E_{lim}, v_{lim} are limit energy and limit velocity of UCN spectrum. Taking into account that $v_{lim}^{D_2} = 4.4$ m/s and $v_{lim}^{^{58}Ni} = 8.2$ m/s we have: $\rho = 8.9 \cdot 10^{-14} \Phi_0 G(T, T_n)$. Thus for $\Phi_0 = 2 \cdot 10^{14}$ n/cm^2·s and $G = (1 \div 2) \cdot 10^4$, $\rho = (2 \div 4) \cdot 10^5$ cm^{-3}.

The next principal question is: could the source of this type be placed in the neutron flux $2 \cdot 10^{14}$ n/cm^2 · s? Sure, the allocation of this source close to the reactor core is impossible because of the heating by fast neutrons and γ-rays from the fuel elements, but at the distance 1 m from the reactor core inside D_2O reflector the γ-field is decreased by a factor of 100, while the flux of thermal neutrons is decreased not more than six times. For instance, at the edge of D_2O reflector of HF ILL reactor the γ-heating is $4 \cdot 10^{-2}$ W/g at the flux of thermal neutrons $2 \cdot 10^{14}$ n/cm^2 · s. The heavy water is a good shielding from γ-rays of core and it almost completely restricts the flux of fast neutrons.

The minimal limit for the ratio of γ-field and the field of thermal neutrons is formed by $\Phi_\gamma = \Phi_{th}\Sigma_{D_2O} \cdot \mu^{-1}_{D_2O}$, where Σ_{D_2O} and μ_{D_2O} are the macroscopic neutron capture cross-section and the absorption coefficient for the γ-rays, respectively. Thus the γ-heating is: $q(\frac{W}{g}) = \Phi_\gamma \cdot \mu_{D_2} \cdot \rho^{-1}_{D_2} \cdot E_\gamma = 2.8 \cdot 10^{-17} \cdot \Phi_{th}$ ($cm^{-2} \cdot s^{-1}$) or $5.5 \cdot 10^{-3}(\frac{W}{g})$ for $\Phi_{th} = 2 \cdot 10^{14}$ $cm^{-2} \cdot s^{-1}$. This is the minimal limit. Unfortunately, any shell which provides the cavity in D_2O medium will give a considerably higher contribution for the source heating. One of the best materials for this purpose is zirconium. For the 3 mm vacuum shell and 1 mm cold shell the γ-heating will be: $q_\gamma(\frac{W}{g}) = 0.92 \cdot 10^{-16}\Phi_{th}$ ($cm^{-2} \cdot s^{-1}$) or $1.8 \cdot 10^{-2}(\frac{W}{g})$ for $\Phi_{th} = 2 \cdot 10^{14}$. This estimate should be increased by 30 % because of the partial thermalization of neutron flux. Thus for the practical case the total γ-heating for D_2 of UCN source will be about $(6 \div 7) \cdot 10^{-2}(\frac{W}{g})$ at the edge of the D_2O reflector. This level of heating can be reduced by the factor of 2 or 3 by means of interchannel Bi shield if it will be necessary.

The next principal question is: what temperature will be inside the solid D_2 source at this level of radiation? The temperature difference between the wall and center of source: $\Delta T = q\frac{\rho}{6\lambda} \cdot R^2$ for the spherical form or $\Delta T = q \cdot \frac{\rho}{4\lambda} \cdot R^2$ for cylindrical form, where λ is the coefficient of thermal conductivity, R is the radius. The thermal conductivity of the solid deuterium considerably depends on its ortho-para modification. For 98 % ortho-deuterium (equilibrium concentration at 4 K) $\lambda = 0.12$ $W \cdot cm^{-1} \cdot K^{-1}$. For the UCN source the most close to practical realization (cylinder with 150–180 mm diameter and 300 mm length, see Fig. 4) the temperature in the center of source will differ from the wall temperature by 1.2 K. The possibility to keep 98 % concentration of ortho-deuterium under radiation must be checked experimentally. In the worst case, if it will be impossible, the problem of thermal conductivity may be solved by the sectionalization of the source with the size of cylindrical cell with 50 mm diameter.

When the source is cooled with liquid helium and the thermal flux is about $6 \cdot 10^{-2}$ $W \cdot cm^{-2}$ then the difference of wall and helium temperatures could amount to 0.1–0.2 K. Thus the average source temperature of about 5 K can be provided. When the effective neutron temperature is about 100 K then the gain factor will be about 10^4. Then $\rho_{UCN} = 8.9 \cdot 10^{-10} \cdot \Phi_{th}$ or $\rho = 1.8 \cdot 10^5$ cm^{-3} for $\Phi_{th} = 2 \cdot 10^{14}$ $cm^{-2} \cdot s^{-1}$. Taking into account the losses of UCN in the source walls and the transmission factor through UCN guide one should expect the UCN density about $(1 \div 2) \cdot 10^4$ cm^{-3} for the experiment.

The thermal power released in the solid deuterium will be about 60–70 W, the same power will be released in zirconium source walls. To cool this source the refrigerator with power 150–200 W will be required. This task may be solved using available cryogenic equipment.

Thus the next generation of UCN sources with UCN density 10^3–10^4 cm^{-3} for experimental researches is possible. The increasing of UCN density by two orders of magnitude will allow to improve considerably the accuracy of measurements in the field of fundamental physics (neutron electric dipole moment, neutron lifetime, asymmetry of the neutron decay and so on). Apparently, applied researches for

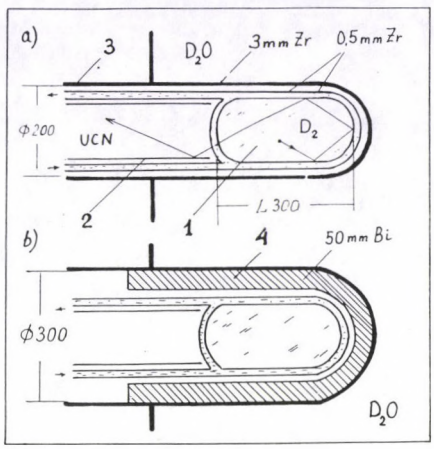

Fig. 4. Simplest layout of solid D_2 UCN source at the edge of D_2O reflector. 1. UCN source; 2. UCN guide; 3. Reactor channel; 4. Bi shield

the solid state and surface physics will be possible if this density of UCN will be obtained.

The UCN source of this type may be realized at high flux reactors with heavy water reflector like HFR at ILL (Grenoble, France), also at the reactor PIK, being constructed at PNPI (Gatchina, Russia) and at the reactor ANS under construction at ORNL (Oak-Ridge, USA).

Acknowledgements

The author is thankful to the colleagues V. Mityukhlyaev, A. Zakharov, V. Nesvizhevsky, A. Kharitonov for useful discussions, also to G. Greene, C. West, T. Bowles, M. Pendlebury and R. Golub for contacts which stimulated the development of this proposal.

References

1. F. L. Shapiro et al, Preprint P3-4127, Joint Institute of Nuclear Research, Dubna, USSR, 1968; Sov. Phys. JETP Lett., *9*, 23, 1969.
2. A. Steyerl, Phys. Lett., *29B*, 33, 1969.
3. A. P. Serebrov et al, Sov. Phys. JETP Lett., *44*, 344, 1986.
4. A. Steyerl et al, Phys. Lett., *116A*, 347, 1986.
5. V. F. Turchin, Slow Neutrons, Moscow, 1963.
6. A. P. Serebrov et al, Phys. Lett., *80A*, 413, 1980.
7. A. P. Serebrov et al, Journal of Neutron Res., *1* (4), 71, 1993.

Acta Physica Hungarica 75 (1–4), pp. 177–188 (1994)

COLD NEUTRON GUIDING AND FOCUSING

D. F. R. MILDNER, H. CHEN, R. G. DOWNING, V. A. SHAROV[1] and Q. F. XIAO[1]

National Institute of Standards and Technology
Gaithersburg MD 20899, USA
[1] *X-Ray Optical Systems, Inc.,*
Albany NY 12205, USA

Neutron guides using reflective optics are used to transport thermal neutron beams. Narrow channels enable the neutron beam to be bent more sharply than with wide guides. Recent developments in polycapillary fibers with thousands of channels having sizes of a few microns have allowed cold neutrons to be guided and focused. A neutron focusing lens can enable an increased lateral resolution of the measurement and an improvement in the detection limits for specific elements for neutron absorption techniques in analytical and materials research. Over an order of magnitude increase in neutron intensity within a submillimeter focal spot has been achieved. Beam benders can also provide more end-positions for experimental stations.

Introduction

The principle of multiple mirror reflection from smooth surfaces at small grazing angles enables the transport of high intensity slow neutron beams to locations of low background for neutron scattering experiments and to provide facilities for multiple instruments. These neutron guides are now commonplace at research reactors, particularly those with cold sources. The transmission depends on the critical angle of the guide coating. Originally coatings of nickel with a critical angle $\gamma_c = 17.3$ mrad nm^{-1} were used. Now ^{58}Ni guides with $\gamma_c = 20.4$ mrad nm^{-1} are preferred with a 40 % increase in transmission. Further increase in transmission is obtained with nickel-titanium supermirror coatings. The limitations of the reflectivity of the earlier supermirrors coatings are probably now overcome, and guides with a critical angle of twice that of ordinary nickel are shortly expected [1]. Some guides are curved to take the beam away from the fast neutrons and gammas, and have good transmission for slow neutrons above a characteristic wavelength; others are straight and require filters to obtain good transmission characteristics without the unwanted radiation.

A new concept proposed by Hayter [2] is the neutron optical filter in which the beam may be deflected by a small angle with a high transmission above a cut-off wavelength, without the spatial asymmetry of the curved guide. An initial long nickel guide is followed by a short length of supermirror guide offset by a small angle ξ, after which the nickel guide continues at a further small angle ξ. The length of the intermediate supermirror guide is such that there is no direct line of sight through the entire system. The advantage of such geometry is that it has the property that

a parallel beam is transported unchanged, unlike the case of a curved guide. The supermirror critical angle must be at least twice that of nickel. This concept has been extended by Copley [3] who has calculated the transmission properties of such filters, with either parallel-sided or tapered central sections having different critical angles. A filter of this type can therefore be designed for the particular experimental arrangements.

Converging guides

The ability to transport cold neutrons with high efficiency using highly reflecting surfaces provides the opportunity to focus the neutron beam. However, Liouville's theorem requires that an increase in neutron current density given by focusing is obtained with a necessary increase in beam divergence. This theorem can be satisfied by placing a converging guide at the end of a long straight guide. The gain of converging systems depends on three factors: the convergence angle for the converging guide, the ratio of the critical angles of the converging and straight guides, and the neutron wavelength λ. Intensity gains for the two-dimensional converging guide [4] are limited to perhaps an order of magnitude on account of the increase in the absolute angle that a neutron trajectory makes with the device axis upon successive reflections. This increase occurs until either the neutron is transmitted by the system, or the glancing angle is greater than the critical angle for reflection at that particular wavelength, in which case the neutron is lost. The greatest gains are achieved when the critical angle θ_c of the converging guide is much greater than the divergence of the incoming beam defined by the critical angle of the straight guide.

Measurements have been performed by Copley and Majkrzak [5] at a wavelength $\lambda = 0.41$ nm, using two converging glass plates, with a surface of one of three different materials, float glass ($\gamma_c = 10.8$ mrad nm^{-1}), nickel-coated float glass, and float glass with Ni–Ti supermirror coating. The converging plates are placed after a straight guide consisting of two float glass plates that define the incident beam, and are of sufficient length that the spatial distribution at the exit is uniform. They find that their experimental results agree well with calculations, except in the case of the supermirror. This is because the high reflectivity for the supermirror is not maintained at large values of θ_c/λ. A two-dimensional focusing system using nickel-titanium supermirrors is in operation at Jülich [6]. The square conical guide is placed at the end of a straight guide with a surface coating of ^{58}Ni, and increases of 2.5 and 3.0 in intensity have been obtained at wavelengths of 0.6 and 1.0 nm respectively.

No doubt higher gains can now be achieved with the current technology in the manufacture of supermirror coatings. However, the maximum intensity gain possible from a converging guide system is about an order of magnitude [4]. The reason is that many trajectories are lost after multiple reflections. A much better method is to use many narrow guides. This allows the possibility of a greater curvature than for macroguides for a given wavelength, for the transmission characteristics of a curved guide depend on the ratio of the transverse to longitudinal dimension of the guide [7].

Polycapillary fibers

Miniature versions of neutron guides can be used to transport, bend and focus thermal neutron beams. Recent developments in glass polycapillary fibers with thousands of channels having sizes of a few microns have enabled cold neutrons to be guided and focused on a scale suitable for laboratory needs [8]. Neutron absorption techniques in analytical and materials research (such as neutron depth profiling [9] and prompt gamma activation analysis [10]) do not require a monochromatic incident beam nor a small angular divergence. A neutron focusing lens can enable an increased spatial resolution of the measurement and an improvement in the detection limits for individual elements. This might allow such techniques to complement other means for non-destructive analysis of trace elements in materials. For example, a large specimen, such as a weld, might be scanned across a focused neutron beam to obtain spatially resolved elemental compositions at selected areas. This allows the two-dimensional prompt radiation analysis with submillimeter resolution of certain elements such as H, B, Li, N and Na. Applications to neutron scattering instrumentation, such as small-angle scattering, may also become possible. In addition, beam benders constructed in a similar manner can also provide more end-positions for other instrumentation.

The cross-section of a typical polycapillary fiber is shown in Fig. 1. The advantage of narrow ($\sim$ 10 μm) channels is that the neutron beam can be bent through a smaller radius of curvature than with wide ($\sim$ 50 mm) guides. The neutron trajectories have more reflections per unit length through the narrow channels, and the coefficient of reflection must be high for reasonable transmission through the channels. The transmission properties of the capillaries depend on the internal diameter and the bending radius of the channels, the glass composition, and the surface smoothness. These properties need to be understood if the capillaries are to be used efficiently to construct a high gain focusing device. We have performed experimental measurements, computer simulations and analytic calculations to support the design of neutron focusing lenses.

We have studied the properties of individual polycapillary fibers of various compositions, and have performed cold neutron transmission measurements on both straight and bent fibers of different lengths. An example of the transmission measurement through a straight fiber as a function of fiber length is shown in Fig. 2. These transmission and divergence measurements have been aided by the development of video radiation detector [11] (VRD), which consists of a charge injection device imaging chip with a ^{6}LiF (n, α) converter film, as a position detector. Typically the active area of the silicon chip is 7×9 mm^2, with pixel sizes as small as 12×13.7 μm^2. The average intensity is evaluated by integrating the number of counts in the pixels within the area of interest.

The transmission efficiencies depend strongly on the divergence of the incident beam. Provided that the reflectivity of the inner surface is close to unity, the transmission loss is linearly proportional to the average number of reflections that neutrons make travelling along the channel. The transmission through bent polycapillaries is important because the bending of the fibers makes the redirecting of

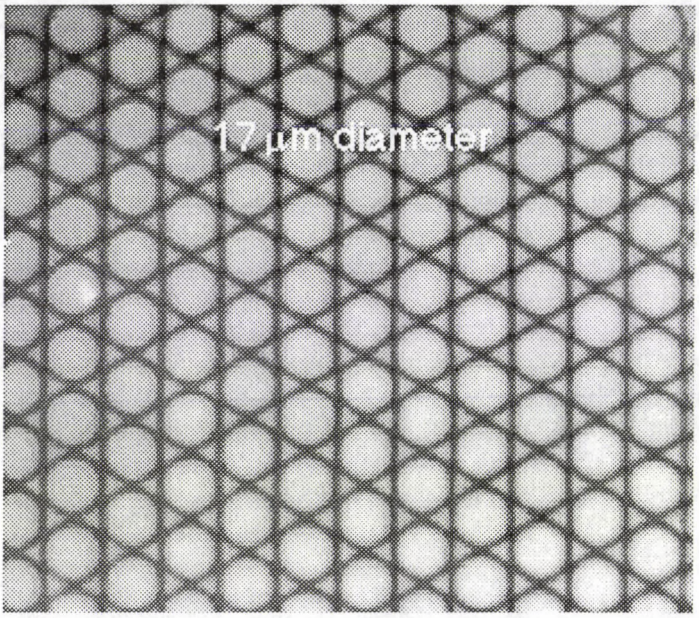

Fig. 1. An optical micrograph of a polycapillary fiber with 17 μm diameter capillaries

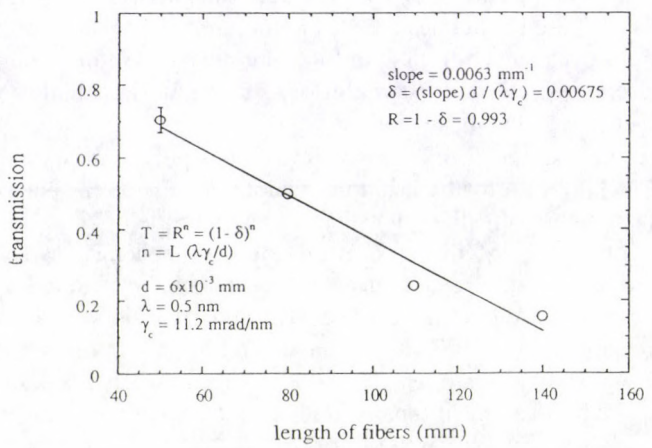

Fig. 2. Transmission of straight fibers as a function of the fiber length for evaluating the reflectivity

neutron beams possible. We have also performed divergence measurements [12,13] on the transmitted beam for both straight and bent polycapillaries.

In our earliest measurements [14] we measured the transmission of a white beam of cold neutrons through polycapillary fibers made of a lead-silica glass with an outer diameter of 0.4 mm and hexagonal cross-section. Each fiber had an open area of 36 % and contained 1261 parallel channels each of a hexagonal cross-section. Each capillary channel had an internal diameter of 6 μm. Measurements have been performed both on straight and bent fibers. As the curvature is increased, the transport efficiency decreases, but even with a bending radius of 0.38 m, $\sim$ 50 % of those neutrons which enter the fiber are transmitted. For this case, the neutron beam is deflected by 18.5° over a distance of 130 mm.

A relatively crude demonstration of the possible focusing action was shown by placing nine such fibers around a cylindrical surface and forcing their exit to point towards a common focus. A series of images of the emerging neutron beam at 10 mm intervals from the end of the fibers demonstrated the focusing effect. In a practical instrument, more than a thousand such fibers are required to achieve intensity gains which could be as high as a couple of orders of magnitude.

Neutron focusing lens

The prototype neutron focusing lens [15] with lead-silica capillary fiber optics used a technology developed originally for X-rays using boron-silica glass. The lens was constructed with 721 fibers (described above) held in place by four membranes with an array of holes made by chemical etching. The holes are spaced so that the first two meshes hold all the fibers parallel to the lens axis, and the last two meshes maintain the fibers all pointing towards a common focal spot on the axis. The bending radius of the outermost fiber is 1327 mm. The entrance diameter of the lens is 29 mm, and the exit diameter is 15 mm. The lens has been thoroughly examined with both thermal and cold neutron beam of various spectral and spatial distributions. The focal spot is 104 mm from the exit of the lens, and we have shown that a cold neutron beam can be focused to a size of 1 mm with a gain of order three. The actual characteristics depend on the divergence and spectrum of the incident beam. The neutron transmission of the fibers, and consequently the gain of the lens, depends on the neutron wavelength. In practice, the lens must be designed for a given application. When the incident beam divergence is high relative to the critical angle of the glass of the fibers, a lower proportion of the incident beam is captured by the lens, so that the gain is reduced.

More recently we have tested a second lens [16] (shown schematically in Fig. 3) of focal length 57 mm which contains fibers of borosilicate glass (γ_c = 11.3 mrad nm^{-1}). The original purpose of the lens was for producing a quasiparallel beam of soft X-rays from a point source, but we have obtained excellent results using the lens in the reverse direction, taking a broad cold neutron beam to a focus of less than 1 mm. This lens has a total length of 100 mm and a focal distance of 57 mm from the end of the fibers. The entrance of the lens (of hexagonal cross-section with a corner-to-corner distance of 29.4 mm) was placed about 150 mm from

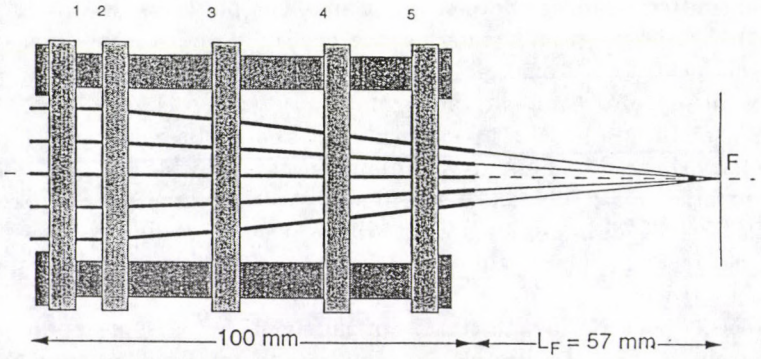

Fig. 3. A schematic diagram showing the arrangement of the lens, indicating the location of the fine meshes which hold in place the 919 fibers, all of which point to the focus F

the exit of a 50×50 mm^2 ^{58}Ni guide which views the cold source through a beryllium filter cooled to 77 K and has a nominal current density of 1×10^8 cm^{-2} s^{-1}. Hence only neutrons of wavelengths longer than 0.4 nm are incident on the lens, and with a divergence of 20.4 mrad nm^{-1} characteristic of the guide surface material.

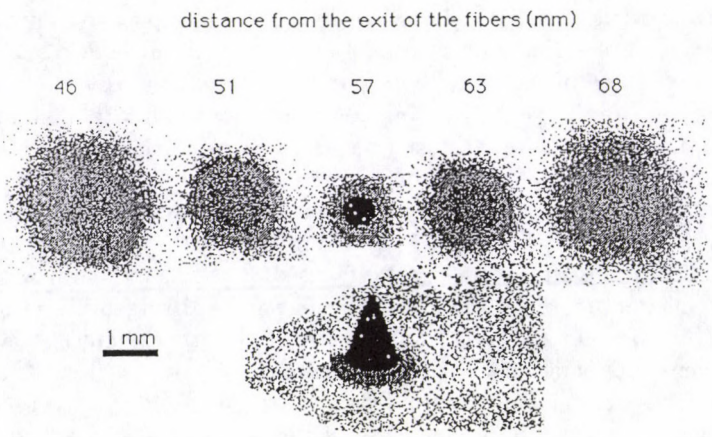

Fig. 4. The images of the transmitted neutron flux taken by a real-time neutron camera at different distances from the exit of the lens, indicating the convergence of the outputs of the fibers, and their subsequent divergence beyond the focus. A three dimensional image at the focus of the lens shows the focused beam intensity

The intensity distribution of the images taken by the VRD at different distances around the focus indicates that the focused intensity has a conical distribution rising above the surrounding background (see Fig. 4). From this image the

spatial distribution or intensity profile of the beam at the focus is obtained (see Fig. 5). The results show that this focus is symmetric in azimuth, and the profile is nearly triangular in shape, with a FWHM of 0.49 mm, and with some further intensity in the wings. The base width of the intensity profile is about 1.2 mm. The narrow (compared to lead-silica fibers) FWHM of the profile is caused by absorption, consistent with previous experimental observation for borosilicate fibers [13].

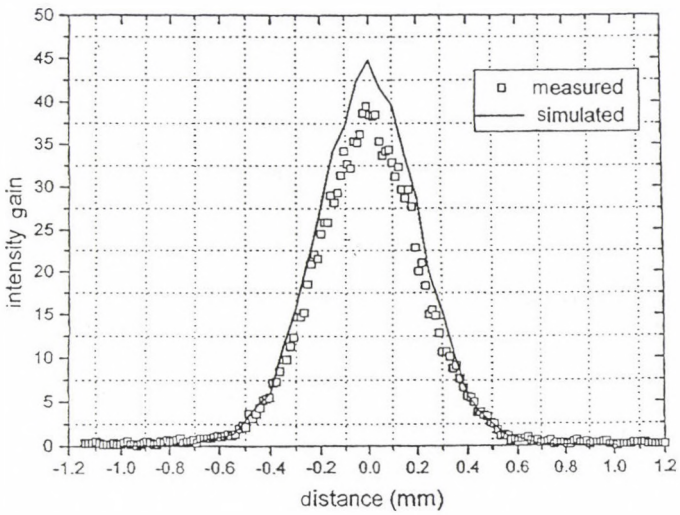

Fig. 5. The spatial distribution or intensity profile of the beam at the focus. The results from the computer simulation are superimposed on the experimentally determined data points

An important characteristic of a focusing lens is its gain in neutron current density at the focus; this depends on the divergence of the incident neutron beam. The design of a focusing lens does not allow all neutrons incident on the entrance to be focused. For this lens there are 919 capillary fibers, each of radius 0.22 mm, arranged in a hexagonal pattern around the central straight fiber. Although all the fibers are close-packed at the exit, the filled fraction f_L at the entrance of the lens is 0.27. Similarly, each fiber has a hexagonal arrangement of 547 channels, each with a diameter of 14 μm, and a fractional open area $f_F = 0.55$. The lens therefore takes only a fraction of the neutron beam of area $\sim$ 680 mm^2 at the lens entrance and focuses it into an area of less than 1 mm^2. Hence the gain obtained by a reduction in effective area is about 100. This ignores the diminished transmission through the outer curved fibers (the maximum bending angle is 0.134 rad). In addition, the incident beam divergence θ_d from the ^{58}Ni guide tube is greater than the critical angle θ_c of the capillaries, so that the gain of a lens modified [17] by the factor $(\theta_c/\theta_d)^2$, which is independent of wavelength. From this analysis the expected

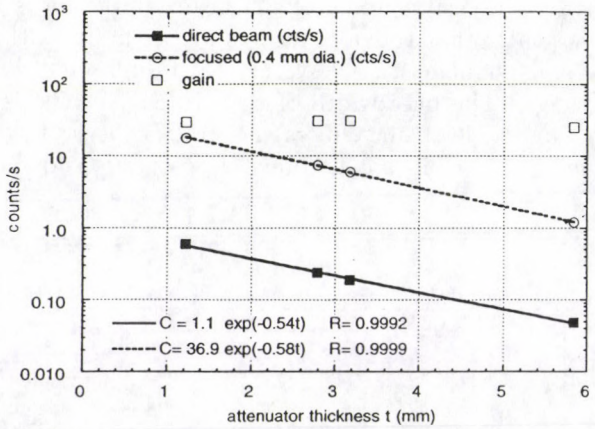

Fig. 6. The beam intensity measured with and without the focusing lens as a function of the thickness of the acrylic attenuator

intensity gain [16] averaged over the area corresponding to the expected FWHM (0.77 mm) is 37. The results show that the maximum gain of the focused beam is about 40, though the gain averaged over the observed FWHM (0.49 mm) is 25. The gain averaged over an area corresponding to the rms value of the radial distribution of the intensity at the focus (0.71 mm) is 19. These experimental results agree well with those obtained by computer simulation [18] (see Fig. 5).

Spectrum shift of the focused beam

One property of a capillary lens is the shifting of the spectrum transmitted through the lens. Measurements were performed with a spectrum approximating a 65 K Maxwellian distribution, with a 0.4 nm cut-off by a beryllium–bismuth filter. Four acrylic attenuators of different thickness t are placed upstream of the lens and the intensity at the focal point was recorded for each thickness (see Fig. 6). Similarly, the direct beam intensity as a function of the attenuator thickness was also recorded after removing the lens. No data were collected without the attenuators because the detector count rate had saturated.

Both curves show the characteristic exponential decrease of intensity as a function of t, as expected in any transmission measurements. The fit using $I = I_0 \exp(-\mu t)$ gives an attenuation coefficient $\mu = 0.54$ mm^{-1} for the direct beam, and 0.58 mm^{-1} for the focused beam. Here, μ represents the removal cross-section for the polychromatic beam by the attenuator, which is determined by the composition of the acrylic, averaged over the incident spectrum and modified by the wavelength dependence of the efficiency of the detector. If the neutron spectrum were not altered by the presence of the lens, the two attenuation coefficients would be the same. Though these measurements are only qualitative, the difference in attenuation demonstrates that the spectrum transmitted through the lens

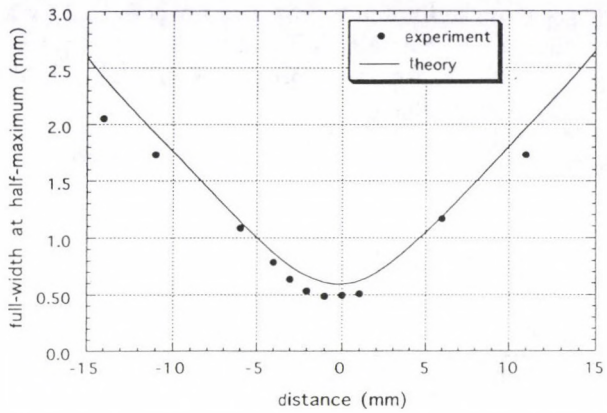

Fig. 7. The full width at half-maximum of the beam profile around the focus at 57 mm for the lens with fibers of radius 0.22 mm, using a Maxwellian beam of neutrons with a short wavelength cut-off at 0.4 nm. Also indicated is the theoretical width

is weighted to longer wavelengths, as expected. However, this difference is comparable to the margin of error in the measurements, so that the spectrum shift is not easily detectable using the current technique. Also shown is the ratio of these two measurements, that is, the intensity gain at the focus averaged over a circle of diameter 0.4 mm, as a function of attenuator thickness. Extrapolation of these data to zero attenuation gives a gain of 33.

Analytic calculations

We have characterized the properties of a polycapillary neutron lens. The beam width as a function of the distance from the exit of the lens is expressed [17] in terms of the transverse variance of the spatial distribution of neutrons leaving the fibers. From these expressions the intensity gain of the lens may be defined. The size of the beam at the focus for a given wavelength depends on the focal length of the lens, the critical angle of the fibers, the radius of the polycapillary fibers, and numerical aperture of the lens. We obtain an optimum focal length [19] of the lens by maximizing the current density at the focus for a given size of the focal spot. This length depends on the critical angle averaged over the spectrum transmitted by the lens. In addition, we may define a depth of focus as a measure of the range of distance over which the focus is reasonably constant. We have related these values both to the prototype lens and the second lens on which we have made measurements. The results shown in Fig. 7 indicate that these considerations describe the characteristics of the lens remarkably well.

We have also calculated the distribution of polar angles for trajectories which may be propagated through a cylindrical channel [20]. We can then determine the transmission and the beam profile at a given distance from the end of the channel as a function of polar angle. In our experimental work, we measure the transmission through cylindrical channels illuminated by a beam delivered by a square guide of much larger area (shown schematically in Fig. 8). We have determined a reasonable approximation [21] for the transmission properties and compared the results with those generated using a computer simulation.

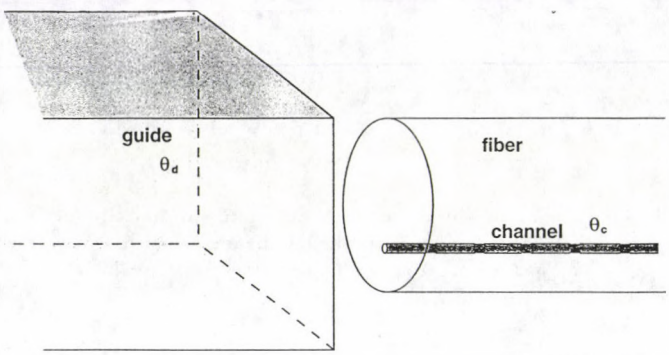

Fig. 8. A schematic diagram indicating a neutron guide of rectangular cross-section and critical angle θ_d illuminating a fiber of smaller cross-section containing many cylindrical channels or capillaries with critical angle θ_c

Computer simulation

These experimental results are compared with a ray-tracing simulation [18]. The program selects trajectories randomly from the spectral, spatial and angular distributions of the output of the guide, calculates the reflection probabilities for each reflection for the trajectory through the curved channel, and determines the transmission and exit divergence through the lens. Good agreement with experimental results has been obtained (see Fig. 5) by considering in the simulation only reflectivity losses caused by absorption. We conclude that the influence of other loss mechanisms on reflectivity, such as surface roughness and waviness, are not significant compared with the absorption loss for the borosilicate fibers. This program has enabled us to characterize the expected performance of a neutron focusing lens placed at the end of a ^{58}Ni guide tube. Over an order of magnitude increase in neutron intensity within a submillimeter focal spot is predicted.

We have reported the results of a simulation which models the performance of a neutron focusing lens which uses polycapillary fibers with channel diameters

of 17 μm. While these two studies are not directly comparable, we find that decreasing only the channel diameters, but keeping the other parameters exactly the same, increases the gain by about 20–30 %. Further gains might be achievable by even narrower channels, though we find that the optimum is about 10 μm diameter channels. With the smaller channel widths the number of reflections increases further and therefore reflection losses increase. In addition, the spacing of the meshes which hold the polycapillaries in position determines the accuracy with which the fibers point to the focus.

Conclusions

The principle of multiple mirror reflection from smooth surfaces at small grazing angles enables the transport of neutron beams through polycapillary fibers of narrow hollow channels ($\sim$ 10 μm). These miniature neutron guides can be used in a focusing lens for neutron absorption techniques in analytical and materials research for increasing the spatial resolution of the measurement and improving the detection limits for individual elements. The transmission efficiency and exit divergence of cold neutrons guided through both straight and bent polycapillary fibers made of borosilicate glass have been measured, and experimental results have been compared with ray-tracing simulations. The good agreement suggests that surface roughness and waviness are not significant compared with absorption losses.

The performance of a neutron focusing lens placed at the end of a ^{58}Ni guide tube has been characterized and optimized for a neutron spectrum from a cold source. We have shown that significant gains in neutron current density within a submillimeter focal spot are achieved using a focusing lens of polycapillary fibers. The results of focusing a polychromatic cold neutron beam using a compact lens of borosilicate fibers with a focal distance of 57 mm show an intensity profile at the focus which is approximately conical in shape with a full-width at half- maximum of 0.5 mm, and with an average gain in intensity of about 20. These results which are also confirmed by a simulation with excellent agreement are considerably better than our earlier results on a prototype lens using lead silica glass polycapillary fibers. The potential for high gains is substantially better for such lenses than for converging guides. We expect intensity gains of two orders of magnitude within a submillimeter focal spot should be achievable in the near future.

Acknowledgements

We acknowledge many fruitful discussions with colleagues at NIST, X-Ray Optical Systems, Inc. of Albany, NY, the Center for X-Ray Optics at the State University of New York at Albany, and the Institute for Roentgen Optical Systems at the Russian Scientific Center, Kurchatov Institute in Moscow, Russia. The U.S. Department of Commerce, Department of Energy, and National Science Foundation have supported this work. V. A. Sharov has been supported partially by a grant under the Cooperation in Applied Science and Technology (CAST) program of the Agency for International Development, administered by the National Research Council.

References

1. B. Vidal, Z. Jiang and F. Samuel, in: Neutron Optical Devices and Applications, eds C. F. Majkrzak and J. L. Wood, Proc. SPIE, *1738*, 30, 1992.
2. J. B. Hayter, in: Neutron Optical Devices and Applications, eds C. F. Majkrzak and J. L. Wood, Proc. SPIE, *1738*, 2, 1992.
3. J. R. D. Copley, J. Neut. Res., *2*, 21, 1994.
4. D. F. R. Mildner, Nucl. Instrum. and Meth. *A301*, 395, 1991.
5. J. R. D. Copley and C. F. Majkrzak, in: Thin-Film Neutron Optical Devices: Mirrors, Supermirrors, Multilayer Monochromators, Polarizers and Beam Guides, ed. C. F. Majkrzak, Proc. SPIE, *983*, 93, 1989.
6. M. Rossbach, O. Schärpf, W. Kaiser, W. Graf, A. Schirmer, W. Faber, J. Duppich and R. Zeisler, Nucl. Instrum. Meth. *B35*, 181, 1988.
7. D. F. R. Mildner, Nucl. Instrum., *A290*, 189, 1990.
8. D. F. R. Mildner, H. Chen, R. G. Downing and V. A. Sharov, J. Neut. Res., *1*, 1, 1993.
9. R. G. Downing, G. P. Lamaze and J. K. Langland, J. Res. NIST, *98*, 109, 1993.
10. R. M. Lindstrom, J. Res. NIST, *98*, 127, 1993.
11. R. G. Downing, C. J. Zeissler and H. Chen, in: Neutrons, X-Rays and Gamma Rays: Imaging Detectors, Material Characterization Techniques and Applications, eds J. M. Carpenter, D. B. Cline, R. Lanza and D. F. R. Mildner, Proc. SPIE, *1737*, 308, 1993.
12. H. Chen, R. G. Downing, D. F. R. Mildner and V. A. Sharov, in: Neutron Optical Devices and Applications, eds C. F. Majkrzak and J. L. Wood, Proc. SPIE, *1738*, 395, 1992.
13. H. Chen, D. F. R. Mildner, R. G. Downing, R. E. Benenson, Q. F. Xiao and V. A. Sharov, Nucl. Instrum. and Meth., *B*, *89*, 411, 1994.
14. H. Chen, R. G. Downing, D. F. R. Mildner, W. M. Gibson, M. A. Kumakhov, I. Yu. Ponomarev and M. V. Gubarev, Nature (London), *357*, 391, 1992.
15. M. A. Kumakhov and V. A. Sharov, Nature (London) *357*, 390, 1992.
16. H. Chen, D. F. R. Mildner and Q. F. Xiao, Appl. Phys. Lett., *64*, 2068, 1994.
17. D. F. R. Mildner and H. Chen, J. Appl. Cryst., *27*, 943, 1994.
18. Q. F. Xiao, H. Chen, D. F. R. Mildner, R. G. Downing and R. E. Benenson, Rev. Sci. Instrum., *64*, 3252, 1993.
19. D. F. R. Mildner, J. Appl. Cryst., *26*, 721, 1993.
20. D. F. R. Mildner and H. Chen, J. Appl. Cryst., *27*, 316, 1994.
21. D. F. R. Mildner, V. A. Sharov and H. Chen, J. Appl. Cryst., *28*, in press, 1995.

Acta Physica Hungarica 75 (1–4), pp. 189–197 (1994)

NEUTRON ACTIVATION ANALYSIS: AN OLD FAITHFUL TO CHERISH

F. DE CORTE

The National Fund for Scientific Research
and
Laboratory of Analytical Chemistry, Institute for Nuclear Sciences, University of Gent
Proeftuinstraat 86, B-9000 Gent, Belgium

Neutron activation analysis (NAA) was launched in 1936, and has since then undergone a dramatic evolution with respect to instrumentation and applications. From a few selected examples throughout these years, it is concluded that NAA exhibits a number of outstanding features which are of lasting value up to the present day. This should also be seen in the light of recent developments which are paving the way to more effective, new and specific applications.

Introduction

At the 7th International Conference on Modern Trends in Activation Analysis, held in Copenhagen/Denmark, June 1986, Hilde Levi presented a semicentennial lecture [1] describing the experiments she carried out in 1935–1936 together with George von Hevesy at the Copenhagen Institute of Theoretical Physics (nowadays known as the Niels Bohr Institute) and which were leading to the launching of neutron activation analysis [2]. These experiments were linked to a topic of the day which even at present is a challenging analytical task: the determination of a rare earth in one of the other elements of the RE series. Apart from Levi's story of how it was found out that one "should be able to detect even the smallest trace of dysprosium in any other of the rare earths, even if it is only present as a slight impurity", and how this was followed by the really decisive analytical experiment which concerned the determination of europium in gadolinium samples, a description was given of the equipment used. This consisted of a Ra–Be source, a Geiger counter and an amplifier — all home made — combined with a commercial phone call register as the recorder, an equipment of which she said to "have a notion that it would amuse you very much to learn how primitive the tools and the means were at that time, especially in comparison with what you use in machinery and gadgetry nowadays".

Today, in 1994, the analyst would make use of a pneumatic rabbit transfer system for short and long irradiations in reactor sites with a suitable neutron thermalisation, whereby the sample could be surrounded by a cadmium cover in order to improve the sensitivity for elements activating well with epithermal neutrons. Then, gamma-spectrometry would be performed using high-resolution HPGe and LEPD detectors served with an automatic sample changer and connected via spectroscopy-grade electronics to a PC-based spectrum analyzer for storage and

processing. If still needed, computer-steered post-irradiation chemical separations would be carried out so as to avoid insurmountable spectral interferences and thus to significantly lower the limit of detection. All this is the result of an evolution where isotopic neutron sources were replaced by research reactors, where GM counters were replaced by NaI(Tl) and next by lithium-drifted Ge detectors, and where recorders were replaced by single- and multi-channel analyzers first off- and then on-line with mainframes and later on with personal computers.

Sustained by these dramatic instrumental developments, during this time span of 58 years — from 1936 up to the present date — NAA proved to be of vital importance when it came to the trace and ultratrace quantification in a wide variety of sample types, related to applications in such areas as geochemistry and cosmochemistry, biomedicine, archaeometry and authenticity control of art objects, production and processing of high-purity materials, forensics, and environmental monitoring. This is illustrated in the present paper by means of four selected topics, namely radiochemical NAA of semiconductor-grade silicon (as developed in the mid 1960s), radiochemical and instrumental NAA of lunar samples collected by Apollo missions (late 1960s and 1970s), instrumental NAA of sewage sludges of municipal or industrial origin (early 1980s) and radiochemical k_0-standardised NAA of human blood serum (second half of the 1980s). From these and other applications conclusions can be drawn regarding the usefulness of reactor neutron activation analysis and its possible role in the future. As emphasised, this role should be considered in the light of new insights into the power of NAA, e.g. as a reference determination method with a physically different basis compared to other techniques, and in the light of new developments such as the design of automated NAA labs, the introduction of software-supported k_0-NAA, and the extension to prompt-γ cold-neutron activation analysis, paving the way to more effective, new and specific applications.

Radiochemical NAA of semiconductor-grade silicon

The first application shown here deals with a topic that was quite actual in the 1960s, namely the analysis of semiconductor materials such as silicon, germanium, selenium, gallium arsenide, etc., the properties of which are very dependent on the presence of impurity atoms at a concentration level as low as the nanogram per gram. The example given is the radiochemical NAA of silicon as developed and applied in our laboratory in the period 1964–1969 [3,4]. Samples of about 1 gram were irradiated for periods of a few days up to two weeks in the BR-2 reactor of the Nuclear Study Centre, Mol/Belgium, at a thermal neutron flux of $\sim 10^{14}$ cm^{-2}s^{-1}. The post-irradiation separation scheme, worked out for the determination of 21 elements, involved extraction, ion exchange, distillation and precipitation techniques. It may be curious to see in [3] that the analysis scheme included measurements both with a NaI(Tl) and with a Ge(Li) detector (apart from plastic scintillation counting used for the ^{204}Tl pure β^--emitter). This perfectly reflects, however, the quite drastic instrumental evolution in those years, when the first, home made, Ge(Li) detector (18 cm^3 volume, 4 keV resolution) was put into operation in our lab (in fact, just after the elaboration of the separation scheme

Table I
Analysis results of semiconductor-grade Si, $ng \cdot g^{-1}$

B content, ppb	Si D1	Si D3	Si C3	Si B3	Si A3
Si-type	< 1	< 1	< 0.5	< 0.25	< 0.12
Specific resistance	p > 250 Ω · cm	n > 25 Ω · cm	n > 50 Ω · cm	n > 150 Ω · cm	n > 200 Ω · cm
Au	0.00074	0.00028	< 0.0001	0.00017	0.00048
Sb	0.0093	0.0032	< 0.003	< 0.002	< 0.006
Ga	< 0.03	< 0.003	< 0.003	< 0.004	< 0.01
Fe	< 20	< 30	< 40	< 40	< 100
K	< 5	< 1	< 1	< 2	< 5
Cr	< 0.5	< 0.4	< 0.6	< 0.5	< 1
Mo	< 0.2	< 0.06	< 0.08	< 0.07	< 0.2
Sn	< 9	< 6	< 8	< 7	< 20
As	< 0.02	0.81	< 0.008	0.007	< 0.02
Co	< 0.2	< 0.2	< 0.2	< 0.2	< 0.6
In	< 3	< 2	< 3	< 2	< 7
Zn	< 6	< 3	< 3	< 3	< 9
Cu	< 0.1	< 0.06	< 0.07	2.62	< 0.56
W	< 0.01	< 0.005	< 0.006	< 0.005	< 0.02
Ta	1.6	< 0.03	< 0.04	< 0.03	< 0.09
Na	0.30	1.53	0.34	0.24	0.51
Eu	< 0.01	< 0.006	< 0.002	< 0.008	< 0.02
Sm	< 0.003	< 0.002	< 0.002	< 0.002	< 0.006
La	< 0.01	< 0.01	< 0.01	< 0.01	< 0.04
Sc	0.15	< 0.02	< 0.04	< 0.03	< 0.09
Tl	< 2	< 2	< 2	< 2	< 9

was nearly completed).

An important feature of the analysis scheme was that the standardisation was performed by means of the so-called triple-comparator method [4], which was especially developed for this purpose in order to solve the problem of multi-element standardisation in the actual circumstances, where the samples had to be packed in small containers for irradiation in reactor sites with ever changing neutron spectrum characteristics. Therefore, Girardi's well-known single-comparator method [5] was made flexible with respect to the irradiation conditions by using a minimum of two (or better, three) monitors thus allowing the in-situ determination of the thermal to epithermal neutron flux ratio. In fact, this was one of the developments leading later on to the k_0-method [6].

The analysis results of some types of semiconductor-grade silicon are shown in Table I. Apart from giving an idea of the sensitivity of the method, one striking result concerns the Na content, which seems to be rather constant in all samples, between 0.2 and 1.5 $ng \cdot g^{-1}$. Instead of this being due to a rather reproducible contamination, as believed at that moment, it is caused by the matrix interference $^{28}Si(n, \alpha p)^{24}Na$ with a very high Q-value of 14.7 MeV, as published by Niese in 1977 [7].

Radiochemical and instrumental NAA of lunar samples

The earliest applications of NAA were in the areas of geochemistry and cosmochemistry, many of them being concerned with the determination of the rare earth elements in terrestrial rocks, meteorites and sediments. In order to improve the detection limits, it was often necessary to make use of dedicated single-element or group separations, or to apply special techniques for irradiation and counting, such as epicadmium NAA or low-energy counting with an LEPD, respectively.

NAA applications in the geosciences were significantly stimulated by the Apollo Lunar Sample Analysis Program in the late 1960s and 1970s. With these valuable and unique materials, the emphasis was put on the determination of as many elements as possible in a single small aliquot of the sample. Illustrative for this is, among others, the work of Wänke and collaborators of the Max-Planck-Institut für Chemie at Mainz/Germany, an example of which can be found in the Proceedings of the Second Lunar Science Conference, 1971 [8]. Their paper reports on the concentration determination of 47 major and trace elements in 14 samples of lunar igneous rocks, soils and breccias, collected by the Apollo 12 mission. For the determination of 43 elements on one and the same sample of 0.5 g, the samples were processed as follows:

- 1st and 2nd irradiation: with neutrons from a 14 MeV neutron generator;
  1. five times 10 s each for the determination of O and Si;
  2. three times 5 min each for the determination of Fe, Mg and Al;
- 3rd and 4th irradiation: in the Mainz TRIGA research reactor, for 6 h at 7×10^{11} $cm^{-2}s^{-1}$;
  3. instrumentally, with several countings during a cooling period of 3 weeks, using a large volume Ge(Li) detector, for the determination of Na, K, Sc, Ti, Ca, Cr, Mn, Fe, Co, La, Ce, Nd, Sm, Tb, Yb, Lu, Hf and Ta;
  4. radiochemically, after decomposition under vacuum with Na_2O_2, for the determination of Ni, Cu, Ga, Ge, Rb, Sr, Pd, In, Cs, Ba, Pr, Gd, Dy, Ho, Er, W, Ir, Au, Th and U.

Without going into detail, it can be stated that the results of these activation analysis procedures enabled to draw highly relevant conclusions with respect to i) the chemical composition of the igneous rocks and its relation to sample locations and cosmic ray exposure ages, ii) the two component origin (local basaltic and granitic) of the various soil samples, and iii) the classification into two groups of metallic iron particles separated from the fines of a sample. With respect to the latter it should be noted that analyses were performed on individual metal grain masses at the sub-mg level.

Instrumental NAA of sewage sludges

It goes without saying that elemental concentration determination has always been one of the corner stones when it came to environmental control and sanitation. Thus, it is not surprising that. as soon as mankind became fully conscious of this problem, NAA was going to play a significant if not pioneering role, in spite of the

fact that for instance such an important element as lead cannot be detected with this technique (unless use is made of special installations for measuring the 800 ms ^{207m}Pb isotope).

Table II
Maximum permissible additions of sludge to agricultural land

Origin of sludge	Addition, ton.ha^{-1}	Limiting element
Dry sludge Koersel	530	Zn
Dry sludge Lommel	68	Zn (Cd)
Dry sludge Bocholt	415	Cu (Zn)
Dry sludge Genk	250	Cr, Zn

As one of the numerous applications of NAA, in the present paper the example is given of a pilot study performed in the early 1980s by Dams and coworkers at the Institute for Nuclear Sciences of the Gent University, dealing with instrumental NAA of sewage sludges originating from municipal or industrial water treatment plants [9]. The relevancy of this study is clear when considering that at that moment the application of sewage sludges (which can be considered as a low-grade fertilizer) as a manure to agriculture land became more and more attractive. Thus, the fear existed that the presence of heavy metals could lead to contamination of the soil, soil or surface waters and food crops. In the paper of Dams et al [9], it was argued that, next to the extractable fraction also the total metal content of the sludge is of interest, not only concerning the most important heavy metals usually determined by AAS (such as Cr, Ni, Co, Cu, Zn, Cd, Pb, Mo and Sn) but also the nutrient elements K, Ca, Mg, Na, etc. and other potentially toxic elements. In view of this, the possibility of applying multielement NAA, with a reasonable expense of manpower, was explored. After solving the serious problem of how to obtain a representative homogeneous sample for the analysis, 50 mg amounts (prepared from 2 kg fractions taken from the sludge drying beds) were wrapped in Whatman 41 filters and pressed into pellets for irradiation in the Gent Thetis reactor. Two irradiations were carried out: one of 2 min at a neutron flux of 2.5×10^{12} cm^{-2}s^{-1} followed by 2 Ge(Li) measurements after decay times of 4 and 22 min, and one of 2 h at 1.5×10^{12} cm^{-2}s^{-1} followed by 3 measurements with decay times up to 15 days. For standardisation, use was made of Girardi's single-comparator method or of multielement standards, for the short or long irradiations, respectively.

From the results obtained in the above mentioned pilot study, it was concluded that, with 40 major elements detectable, the elaborated instrumental NAA procedure turned out to be at least competitive if not superior to most other analytical techniques. It was found that one single irradiation followed by two Ge(Li) measurements after 10 h and 5 days decay times, enabled to trace significant enrichments for the most important metals Cr, Mn, Fe, Co, Ni, Cu, Zn, As, Se, Ag, Cd, Sb, Au and U. Simultaneously, concentration data for elements such as Na, K, Br, Sr, Cs, Ba, rare earths, W, Th, etc. are obtained with no additional costs. As a practical result, Table II shows the maximum permissible additions to agricultural land of the four "domestic" sludges investigated, together with the element(s)

playing a limiting role. The latter was derived from the acceptable metal contents for soils published by the Food Administration Organisation (FAO). On the other hand, the industrial sludge, originating from a water treatment plant connected with a wire-drawing mill, turned out to be so heavily contaminated with metals that it could not be considered for agricultural application at all.

Radiochemical k_0-standardised NAA of human blood serum

Instrumental NAA for trace and ultratrace elements in biological/biomedical matrices is often hampered by the fact that major radioactivities of such radionuclides as ^{24}Na, ^{32}P, ^{82}Br, etc. are induced. Then, post-irradiation separations are required in order to avoid gamma-spectral interferences. The example given here concerns the radiochemical NAA for thirteen trace elements in human blood serum, as performed in the second half of the 1980s by Lin Xilei et al, of the group of Cornelis at Gent [10]. The material investigated was a pooled serum which was prepared a few years earlier by Versieck et al [11] and certified on the authority of several specialists all over the world who analysed it with different analytical techniques [12].

For the determination of Cs, Fe, Hg, Rb, Se and Zn in the here described NAA application about 100 mg of lyophilized serum was irradiated for 13 days at a neutron flux of 10^{13} cm^{-2}s^{-1} in the BR-2 reactor in Mol, Belgium. The determination of Ag, Co, Cr, Sb, Sc, Sn and Sr necessitated working with ashed samples because of the required long irradiation at a high neutron flux (13 days at 10^{14} cm^{-2}s^{-1} in the BR-2 reactor). After irradiation and sample digestion, a radiochemical group separation procedure was applied based on the use of three inorganic ion exchangers: acid aluminium oxide (AAO), hydrated antimony pentoxide (HAP) and hydrated manganese dioxide (HMD). Four separated groups with matched gamma-ray energies and intensities were obtained, leading to reliable and efficient measurements. The standardisation of the analysis was done by means of both the k_0-method, with the use of Zr-foil and Au–Al alloy as flux monitors/comparators [13], and the relative method, with the use of standards which after irradiation underwent the same procedure as the samples.

The results of the analysis, shown in Table III, reveal that the concentrations obtained by the k_0-method and the relative method are consistent and are also in good agreement with the certified values when available. It is interesting to note that Sn was an unexpectedly detected element for which no standard was coirradiated, so that quantification was only possible via the k_0-method. Furthermore, it should be mentioned that significant corrections had to be performed for the interference reactions ^{54}Fe(n,α)^{51}Cr and ^{44}Ca(n,γ;β^-;n,γ)^{46}Sc in the determination of Cr and Sc via the reactions ^{50}Cr(n,γ)^{51}Cr and ^{45}Sc(n,γ)^{46}Sc, respectively. As shown in a separate paper [14] in the k_0-standardisation method these neutron induced reaction interferences can be accurately corrected for by employing the usual neutron flux monitors, namely a Zr-foil and a dilute Au–Al alloy.

Table III
RNAA results for thirteen elements in biological reference material human serum

Element	No. of samples	Mean ± s.d.		Certified values	
		k_0-method	Relative method		
Ag (ng g^{-1})	4	0.93±0.039	0.93±0.084	–	–
Co (ng g^{-1})	10	3.0 ±0.14	2.91±0.039	3.6	(3.0 – 4.2)
Cr (ng g^{-1})	4	1.0 ±0.60	1.0 ±0.43	0.76	(0.67 – 0.87)
Cs (ng g^{-1})	6	9.8 ±0.47	9.3 ±0.24	10.0	(7.7 – 12.3)
Fe (μg g^{-1})	12	26 ±1.4	26 ±1.0	25.9	(24.4 – 27.4)
Hg (ng g^{-1})	6	6.1 ±0.21	6.4 ±0.18	–	–
Rb (μg g^{-1})	12	1.7 ±0.15	1.62±0.089	1.85	(1.52 – 2.18)
Sb (ng g^{-1})	4	0.25±0.15	0.24±0.13	–	–
Sc (pg g^{-1})	3	19 ±2.2	16 ±2.2	–	–
Se (μg g^{-1})	6	1.07±0.034	0.98±0.043	1.05	(1.00 – 1.10)
Sn (ng g^{-1})	4	10 ±2.6	–	–	–
Sr (μg g^{-1})	6	0.35±0.014	0.35±0.016	–	–
Zn (μg g^{-1})	12	9.7 ±0.46	9.4 ±0.37	9.6	(9.4 – 9.8)

Present and future role of NAA

The above given examples represent only four of a myriad of applications reported since the launching of NAA. More information can for instance be found in the series of proceedings of the international conferences on Modern Trends in (Neutron) Activation Analysis [Texas A&M (1961), Texas A&M (1965), NBS Washington D. C. (1968), Saclay, France (1972), München, Germany (1976), Toronto, Canada (1981), Copenhagen, Denmark (1986), Wien, Austria (1991)]. From all this, it is clear that the success of NAA was due to a number of outstanding features. Indeed, its excellent sensitivity for many elements, its experimental versatility leading to a high selectivity, its multielement capability, its contamination- and blank-free character, its matrix independent properties, its non-destructive possibilities and its solid theoretical foundation enabling to identify and predict all sources of systematic or random variation, all these combined features made NAA to a very powerful and reliable analytical tool.

In spite of these top-level performances, it should not be denied that in recent years NAA was seriously waylaid by a number of developments and circumstances, such as the advent of powerful novel determination techniques (optimized AAS, ICP-MS, etc.) and the interest in speciation e.g. in the analysis of biomedical matrices, not to speak about the post-Chernobyl "nuclear doom". However, apart from the latter mania being misplaced from the nuclear-analytical point of view, it would be superficial to conclude that NAA is a thing of the past which simply can be brushed aside. Indeed one should use NAA for what it can do, and one should realize that some of its features are of lasting value and even unique up to the present day.

The present and future role of NAA should be interpreted in the light of new insights into its power. This especially refers to the fact that it is an accurate and

traceable method, with a physically different basis compared to other techniques, and with a built-in possibility of self verification since in many cases results for an element can be obtained via different γ-lines of different isotopes [15, 16]. This makes NAA to a reference method, which is eminently suited for the calibration of other analytical techniques and for the certification of reference materials.

Also, the role of NAA should be seen in the context of new developments. Among these, mention can be made of the installation of automated NAA labs, as done by Erdtmann and Petri at the Research Centre KFA Jülich [13] and of the introduction of prompt-γ cold-neutron activation analysis, as dealt with at the present Workshop by Lindstrom from the NIST, Gaithersburg, USA [17]. In addition, an important recent development is considered to be the release of the software package KAYZERO/SOLCOI (for MS-DOS) by Bossus and Van Sluijs at DSM Research (Geleen, The Netherlands) for use in k_0-based NAA, as reported earlier [18] and also at the present Workshop [19]. As shown in former papers [13, 20, 21] the k_0-method — the principles of which are used nowadays in some 45 labs — significantly increases the manageability of NAA. This is especially so in case of multielement or panoramic analysis where an irradiation of a monitor together with the sample, followed by some 4 measurements after decay times up to 1 month, allows the determination of concentrations or detection limits for about 60 elements. Finally, it is not without importance to remark that, as a contribution to the accuracy and traceability of k_0-NAA, a few years ago the European IRMM (former CBNM) at Geel, Belgium issued an Al – 0.1 % Au alloy with a certified Au content [22].

It is believed that the above sketched modern insights and developments, among others, will lead to a situation where NAA will continue to fulfil its specific and valuable role in the arsenal of the available analytical techniques.

Acknowledgements

Thanks are due to A. De Wispelaere for valuable technical assistance. Grateful acknowledgement is made to the National Fund of Scientific Research (Belgium) for financial support.

References

1. H. Levi, Semicentennial Lecture, Addendum to the Proceedings of the 7th International Conference on Modern Trends in Activation Analysis, Copenhagen, Denmark, June 23–27, 1986.
2. G. von Hevesy, H. Levi, Det Kgl. Danske Videnskab. Selskab. Math-fys. Medd., *14*, 5, 1936; *15*, 11, 1938.
3. F. De Corte, A. Speecke, J. Hoste, J. Radioanal. Chem., *8*, 287, 1971.
4. F. De Corte, A. Speecke, J. Hoste, J. Radioanal. Chem., *9*, 9, 1971.
5. F. Girardi, G. Guzzi, J. Pauly, Anal. Chem., *37*, 1085, 1965.
6. A. Simonits, F. De Corte, J. Hoste, J. Radioanal. Chem., *24*, 31, 1975.
7. S. Niese, J. Radioanal. Chem., *38*, 37, 1977.
8. H. Wänke, F. Wlotzka, H. Baddenhausen, A. Balacescu, B. Spettel, F. Teschke, E. Jagoutz, H. Kruse, M. Quijano-Rico, R. Rieder, Proceedings of the Second Lunar Conference, Vol. 2, M.I.T. Press, p. 1187, 1971.
9. R. Dams, A. M. Buysse, M. Helsen, J. Radioanal. Chem., *68*, 219, 1982.
10. Lin Xilei, D. Van Renterghem, R. Cornelis, L. Mees, Anal. Chim. Acta, *211*, 231, 1988.

11. J. Versieck, J. Hoste, L. Vanballenberghe, A. De Kesel, D. Van Renterghem, J. Radioanal. Nucl. Chem., *113*, 299, 1987.
12. J. Versieck, J. Hoste, L. Vanballenberghe, A. De Kesel, J. Hoste, B. Wallaeys, J. Van Den Haute, N. Baeck, H. Steyaert, A. R. Byrne, F. W. Sunderman, Anal. Chim. Acta, *204*, 63, 1988.
13. F. De Corte, A. Simonits, F. Bellemans, M. C. Freitas, S. Jovanović, B. Smodiš, G. Erdtmann, H. Petri, A. De Wispelaere, J. Radioanal. Nucl. Chem., *169*, 125, 1993.
14. Lin Xilei, D. Van Renterghem, F. De Corte, R. Cornelis, J. Radioanal. Nucl. Chem., *133*, 153, 1989.
15. J. J. M. De Goeij, J. R. W. Woittiez, J. Radioanal. Chem., *168*, 429, 1993.
16. A. R. Byrne, Fresenius J. Anal. Chem., *345*, 144, 1993.
17. R. M. Lindstrom, this Workshop, Acta Phys. Hung., *75*, 71, 1994.
18. R. Van Sluijs, D. Bossus, D. Vervecken, Proceed. Int. k_0 Users Workshop – Gent, ed. F. De Corte, Lab. Anal. Chem., INW, RUG, 1992, p. 15.
19. R. Van Sluijs, D. A. W. Bossus, D. Vervecken, G. Klok, this Workshop, Acta Phys. Hung., *75*, 355, 1994.
20. F. De Corte, A. Simonits, A. De Wispelaere, J. Hoste, J. Radioanal. Nucl. Chem., *113*, 145, 1987.
21. F. De Corte, A. De Wispelaere, M. Van Den Boer, D. Bossus, R. Van Sluijs, Anal. Chim. Acta, *254*, 127, 1991.
22. C. Ingelbrecht, F. Peetermans, F. De Corte, A. De Wispelaere, C. Vandecasteele, E. Courtijn, P. D'hondt, Nucl. Instrum. and Methods, *A303*, 119, 1991.

Acta Physica Hungarica 75 (1–4), pp. 199–201 (1994)

ULTRAFAST RABBIT SYSTEMS AND THEIR APPLICATIONS

F. GRASS

Atominstitut der Österreichischen Universitäten
Schüttelstrasse 115, A-1020 Wien, Austria

Irradiation facilities available for short-time activation analysis at the Atominstitut are described together with their practical use in various fields such as environmental science and geochemistry.

The rabbit systems are installed in the institute's TRIGA Mark II reactor: the horizontal Fast Irradiation and Measurement Systems with a transfer time of 20 ms, leading to a n-flux of 1.3E12 $s^{-1}cm^{-2}$ and a flux ratio of 20; the Vertical Fast Irradiation and Measurement System with a transfer times of 300 ms (with N_2

Table I
Nuclear data of radionuclides used for analyses

Nuclide	Half life	Gamma energy [keV]	Beta energy [MeV]	Nuclide	Half life	Gamma energy [keV]
Li-8	810 ms		12.6	Se-77m	17.7 s	162
B-12	20 ms		13.4	Br-79m	4.8 s	208
F-20	11.1 s	1633	5.4	Br-80	17.6 min	616
Ne-23	37.2 s	439		Sr-87m	2.81 h	388
Na-24m	20 ms	472		Y-89m	15.7 s	909
Mg-27	9.48 min	1014		Ag-108	2.41 min	633
Al-28	2.246 min	1779		Ag-110	24 s	657
Cl-38m	710 ms	671		In-116m_2	2.18 s	162
Cl-38	37.3 min	2168		In-116m_1	54.2 min	417
Sc-46m	18.7 s	142		I-128	25 min	443
Ca-49	8.72 min	3084 or DE		Ba-137m	2.55 min	662
Ti-51	5.76 min	320		Ba-139	83.3 min	166
V-52	3.75 min	1433		La-140	40.2 h	1596
Mn-56	2.56 h	1811		Pr-142	19.2 h	1576
Co-60	10.5 min	59		Sm-155	22.4 min	104
Cu-66	5.10 min	1039		Eu-152m	9.2 h	963
Zn-69m	13.8 h	439		Gd-161	3.6 min	361
Ga-72m	37 ms	97		Er-167	2.6 s	208
Ga-72	14.1 h	834		Dy-165m	13 min	108
Ge-71m	20 ms	175		Dy-165	2.65 h	515
Ge-75m	49 s	140		Pb-207m	840 min	569
As-75m	16 ms	279		Au-197m	7.8 s	279

Table II
Application of short-time activation analysis at the Atominstitute

Sample description	Elements analysed by radionuclides	Irradiation device	Schedule Tirr, Tm1, Tm2, Tm3 [s]	Remarks questions
As-ore "Betalyt"	As-75m	FIMS	1 - 0.1 - -	content
(Al_2O_3,Na_2O,Li_2O)	Na-24m, Li-8, Al-28	FIMS	2 - 6 - 200	Na/Li exchange
Polyaniline	Na-24m, Cl-38m	FIMS	5 - 5 - -	$NaClO_4$?
Polyacetylene	Na-24m, Cl-38m, Li-8, F-20, Ti-51, Al-28	FIMS	20 - 6 - 600 -	$LiClO_4$? $LiBF_4$?
Oil well water, sea water enriched on DOWEX 1 XB	B-12	FIMS	1 -1	BF_4-complex
F in standard materials plants, sea animals, bone, sewage, sediments	F-20, Na-24m	FIMS	22 - 22 - -	correction of Na-23(n,alpha)F-20 reaction by Na-24m
Cl in iron concrete after PVC-fire	Cl-38m	FIMS	5 - 5 - -	depth profile by drilling holes
All halogens in fumarole water	F-20, Cl-38, Br-80, I-128	VFIMS	300-30-300-600	^{6}LiD-converter
Waste water of a waste incineration plant	F-20, Cl-38, Br-79m, I-128	FIMS	20-20-200	single activation
Wet filter cake of a waste incineration plant	F-20, Cl-38, Se-77m Co-60m, Zn-69m, Ag-110, V-52, Ba-139, I-128, Cu-66, Br-80	FIMS	20-20-60-6–	pseudo cyclic 5 samples
Rare earth analysis	La-140, Pr-142, Sm-155 Eu-152m, Gd-161, Er-167 Dy-165m, Y-89m	FIMS	20-20-200	RE-ore
Wet filter cake	O-19, Sn-125, Cd-111m, Hg-199m, V-52, Co-60m, As-76, Sb-122, Ba-137m Cu-66, In-116m(Sn), Sr87m Zn-69m, I-128, Br-80	VFIMS	900, 60, 300, 900	pseudo cyclic 5 samples ^{6}LiD-converter
BCR 176, BCR-146	F-20, Cl-38, Ag-110	VFIMS	20-20-200	single activation
	Cu-66, In-116m (Sn) Cd-111m, In-116, V-52 I-128, Hg-199m	VFIMS	900-600-600	^{6}Li-converter
Oil products	V-52	GAPTS	300-600	up to 10 g samples
Organic chlorine in H_2O	Cl-38	GAPTS	900-900	extract

as transport gas) or 120 ms (with He) leading to a flux position of 2.5E12 $s^{-1}cm^{-2}$ and a flux ratio of 12, and the General Atomic Pneumatic Transfer System with a transfer time of 4 s leading to an equivalent position using pressurized air form the institute's air pressure system.

VFIMS enables a drastic flux hardening by inserting a ^{6}LiD-converter over the irradiation position. It is fully automatized allowing 16 samples to be irradiated and measured according to a preset time table. Decay analyses can be performed

on FIMS and VFIMS simultaneously with the registration of the gamma-spectra. Decay curve analysis and evaluation of peak areas can be performed immediately after their registration. A Cherenkov detector for hard β-emitters and neutron counters for the delayed neutron-emitters together with a 15 % and a 20 % n-type HPGe detector enable the determination of up to 20 elements: B by 20 ms ^{12}B, Li by 840 ms ^{8}Li, and F by 11.3 s ^{20}F using the Cherenkov counter, the fissionable U and Pu isotopes by delayed neutron counting, and Na by 20 ms ^{24m}Na, Ge by 20 ms ^{71m}Ge, Ga by the 37 ms ^{70m}Ga, Yb by 68 ms ^{175m}Yb, Ba by 320 ms ^{136m}Ba, Cl by 715 ms ^{38m}Cl, Pb by 740 ms ^{207m}Pb, and Zr by 760 ms ^{90m}Zr using the HPGe detectors, to list only short lived isotopes with less than 1 s half life. To enable gamma-spectrometry at the high count rates unavoidable when using these short lived nuclides for AA, Westphal's Loss Free Counting system with a Preloaded Filter Amplifier has been used in the latest applications. The PFA system allows an actual throughput of up to 100 kc/s with only moderate peak broadening.

The nuclear data of the short and medium lived radionuclides used in these systems for analysis are listed in Table I.

As seen from Table II fast transfer systems have a broad applicability not only for the radionuclides in the second half life range, but also in the range of hours or even days.

References

1. O. Brandstätter, F. Girsig, F. Grass, R. Klenk, Nucl. Instr., *104*, 45, 1972.
2. A. Salahi, F. Grass, F. Bensch, T. Kasa, E. Seidl, S. Roth, J. Trace & Microprobe Techn., *6*, 229, 1988.
3. J. D. Buchanan, General Atomic GA-2662 Report, 1961.
4. G. P. Westphal, Nucl. Instr. & Methods, *A229*, 261, 1990.
5. F. Grass, American Nuclear Soc., Nov. 1990, TANSAO, *62*, 220, 1990.

Acta Physica Hungarica 75 (1–4), pp. 203–219 (1994)

ACHIEVEMENTS IN NEUTRON INTERFEROMETRY

H. RAUCH

Atominstitut der Österreichischen Universitäten
Schüttelstrasse 115, A-1020 Wien, Austria

Within a perfect crystal interferometer widely separated coherent beams can be produced which can be influenced by nuclear, magnetic and gravitational interaction. The verification of the 4π-symmetry of spinor wave functions and of the spin superposition law at a macroscopic scale and the observation of gravitational effects including the Sagnac effect have been widely debated in literature. The coupling of the neutron magnetic moment to resonator coils permitted the coherent energy exchange between the neutron system and the macroscopic resonator. This phenomenon provided the basis for the observation of the magnetic Josephson effect with an energy sensitivity of 10^{-19} eV. Partial beam path detection experiments are in close connection with the development of quantum mechanical measurement theory. A striking spectral modulation effect has been observed by means of a proper post-selection procedure under conditions where the spatial shift of the wave trains greatly exceeds the coherence length of the neutron beams traversing an interferometer. It is shown that Schrödinger-cat-like states are created by the superposition of two coherent states generated in the interferometer. These entangled states exhibit under certain circumstances characteristic squeezing phenomena indicating a highly non-classical behaviour.

Introduction

Different kinds of neutron interferometers have been tested in the past. The slit interferometer is based on wavefront division and provides long beam paths but only a very small beam separation [1, 2]. The perfect crystal interferometer [3, 4] is based on amplitude division. The interferometer based on grating diffraction is a more recent development and has its main application for very slow neutrons [5]. A schematical comparison is shown in Fig. 1. The perfect crystal interferometer provides highest intensity and highest flexibility for beam handling and is now most frequently used due its wide beam separation and its universal availability for fundamental, nuclear and solid-state physics research.

The perfect crystal interferometer represents a macroscopic quantum device with characteristic dimensions of several centimeters. The basis for this kind of neutron interferometry is provided by the undisturbed arrangement of atoms in a monolithic perfect silicon crystal [3, 6]. An incident beam is split coherently at the first crystal plate, reflected at the middle plate and coherently superposed at the third plate (Fig. 1, middle).

From general symmetry considerations follows immediately that the wave functions in both beam paths, which compose the beam in the forward direction behind the interferometer, are equal ($\psi_0^I = \psi_0^{II}$), because they are transmitted–reflected–reflected (TRR) and reflected–reflected–transmitted (RRT), respectively. The

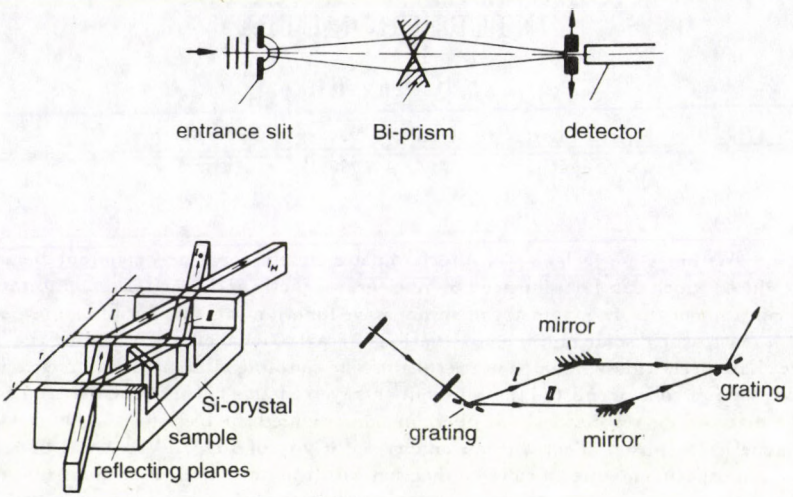

Fig. 1. Scheme of a slit, a perfect crystal and a grating interferometer

de Broglie wavelength of the neutrons diffracted from such crystals is about 1.8 Å and their energy is about 0.025 eV. The theoretical treatment of the diffraction process from the perfect crystal is described by the dynamical diffraction theory, which can also be found in the literature for the neutron case [7, 8, 9, 10]. Inside the perfect crystal two wave fields are excited when the incident beam fulfils the Bragg condition, one of them having its nodes at the position of the atoms and the other in between them. Therefore, their wave vectors are slightly different ($k_1 - k_2 = 10^{-5}k_0$) and due to mutual interference processes, a rather complicated interference pattern is built up, which changes substantially over a characteristic length Δ_0, the so-called Pendellösung length, which is of the order of 50 μm for an ordinary silicon reflection. To preserve the interference properties over the length of the interferometer, the dimensions of the monolithic system have to be accurate on a scale comparable to this quantity. The whole interferometer crystal has to be placed on a stable goniometer table under conditions avoiding temperature gradients and vibrations. A phase shift between the two coherent beams can be produced by nuclear, magnetic or gravitational interactions. In the first case, the phase shift is most easily calculated using the index of refraction [11, 12]:

$$n = \frac{k_{in}}{k_0} = 1 - \frac{\lambda^2 N}{2\pi}\sqrt{b_c^2 - \frac{\sigma_r}{2\lambda}} + i\frac{\sigma_r N \lambda}{4\pi}, \tag{1}$$

which simplifies for weakly absorbing materials ($\sigma_r \to 0$) to

$$n = 1 - \lambda^2 \frac{N b_c}{2\pi}, \tag{2}$$

where b_c is the coherent scattering length and N is the particle density of the phase shifting material. The different k-vector inside the phase shifter causes a spatial shift $\mathbf{\Delta}$ of the wave packet which depends on the orientation of the sample surface $\hat{\mathbf{s}}$

$$\mathbf{\Delta} = \frac{\mathbf{k} - \mathbf{k}_0}{k} D_0 \quad \text{with} \quad \mathbf{k} - \mathbf{k}_0 = \frac{(1-n)k\hat{\mathbf{s}}}{(\hat{\mathbf{k}} \cdot \hat{\mathbf{s}})}. \tag{3}$$

As in ordinary light optics the change of the wave functions is obtained as follows:

$$\psi \to \psi_0 e^{i\mathbf{\Delta}\cdot\mathbf{k}} = \psi_0 e^{-Nb_c\lambda D} = \psi_0 e^{i\chi}. \tag{4}$$

Therefore, the intensity behind the interferometer becomes

$$I_0 \propto |\psi_0^I + \psi_0^{II}|^2 \propto (1 + \cos\chi). \tag{5}$$

The intensity of the beam in the deviated direction follows from particle conservation:

$$I_0 + I_H = \text{const}. \tag{6}$$

Thus, the intensities behind the interferometer vary as a function of the thickness D of the phase shifter, the particle density N or the neutron wavelength λ. A wave-packet description has to be used to define coherence properties in real experiments.

$$\psi(\mathbf{r}) \propto \int a(\mathbf{k}) e^{i\mathbf{k}\cdot\mathbf{r}} d^3k. \tag{7}$$

Standard quantum mechanics defines the momentum distribution of the beam by

$$g(\mathbf{k}) = |\psi(\mathbf{k})|^2 = |a(\mathbf{k})|^2 \tag{8}$$

and, therefore, one gets the real part of the coherence function as the Fourier-transform of the momentum distribution

$$|\Gamma(\mathbf{\Delta})| \propto \left| \int g(\mathbf{k}) e^{i\mathbf{k}\cdot\mathbf{\Delta}} d^3\mathbf{k} \right|, \tag{9}$$

which simplifies for Gaussian momentum distributions

$$g(\mathbf{k}) \propto \exp\left[-(\mathbf{k} - \mathbf{k}_0)^2 / 2\delta\mathbf{k}^2\right], \tag{10}$$

with characteristic widths δk_i to

$$|\Gamma(\mathbf{\Delta}_0)| = \prod_{i=x,y,z} \exp\left[-(\Delta_i \delta k_i)^2/2\right]. \tag{11}$$

The mean square distance related to $|\Gamma(\mathbf{\Delta})|$ defines the coherence length $\mathbf{\Delta}$ which is for Gaussian distribution functions directly related to the minimum uncertainty relation ($\Delta_c^i = 1/(2\delta k_i)$).

Any experimental device deviates form the idealized assumptions made by the theory: the perfect crystal can have slight deviations from its perfectness, and its dimensions may vary slightly; the phase shifter contributes to imperfections by variations in its thickness and inhomogeneities; and even the neutron beam itself contributes to a devation form the idealized situation because of its momentum spread δk. Therefore, the experimental interference patterns have to be described by a generalized relation

$$I \propto A + B\cos(\chi + \Phi_0), \tag{12}$$

where A, B and Φ are characteristic parameters of a certain set-up. It should be mentioned, however, that the idealized behaviour described by Eq. (5) can nearly be approached by a well balanced set-up [13]. The reduction of the contrast at high order results from the longitudinal coherence length which is determined by the momentum spread of the neutron beam ($\Delta_x = (2\delta k_x)^{-1}$. This causes a change in the amplitude factor of Eq. (12) as ($B \to B\exp[-(\Delta_i \delta k_i)^2/2]$). The wavelength dependence of χ in Eq. (4) disappears in a special sample position where the surface of the sample is oriented parallel to the reflecting planes and the path length through the interferometer becomes $D_0/\sin\theta_B$ and, therefore, the phase shift $\chi = -2d_{hkl}Nb_cD_0$ becomes independent of the wavelength and the damping at high interference orders is strongly reduced as compared to the standard position. Related results of a recent experiment where the interference pattern in the 256th interference order has been measured in the dispersive and the nondispersive sample position are shown in Fig. 2 [14]. The much higher visibility of the interferences in the nondispersive sample arrangement is visible and is caused by the much smaller momentum spread perpendicular to the reflecting planes of the perfect crystal.

Various post-selection measurements in neutron interferometry have shown that interference fringes can be restored even in cases when the overall beam does not exhibit any interference fringes due to spatial phase shifts larger than the coherence length of the interfering beams [15, 16, 17, 18]. This indicates that the simple picture which predicts interference only when wave packets spatially overlap is untrue. Interference actually occurs no matter how large the optical path difference may be. From classical optics it has been known for many years that the coherence properties manifest themselves in a spatial intensity variation for phase shifts smaller than the coherence length and in a spectral intensity variation for large phase shifts [19, 20, 21, 22, 23]. This phenomenon becomes more apparent for less monochromatic beams and can cause overall spectral shifts [24, 25] and even squeezing phenomena [26, 27]. The related phenomena for matter waves have been discussed recently [28, 29] and will be elucidated in more detail in this paper.

All the results of interferometric measurements, obtained until now can be explained well in terms of the wave picture of quantum mechanics and the complementarity principle of standard quantum mechanics. Nevertheless, one should bear in mind that the neutron also carries well-defined particle properties, which have to be transferred through the interferometer. These properties are summarized in

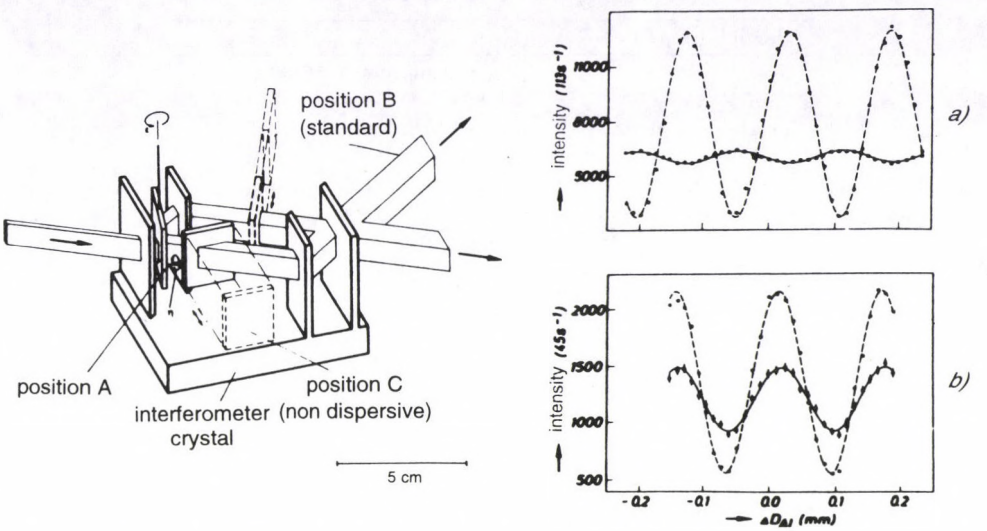

Fig. 2. Interference pattern observed at high order ($m = 256$) with a dispersively (above) and a nondispersively arranged sample [14]. (Dashed lines correspond to measurement at low order.)

Table I together with a formulation in the wave picture. Both particle and wave properties are well established and, therefore, neutrons seem to be a proper tool for testing quantum mechanics with massive particles, where the wave–particle dualism becomes very obvious.

All neutron interferometric experiments pertain to the case of self-interference, where during a certain time interval, only one neutron is inside the interferometer, if at all. Usually, at that time the next neutron has not yet been born and is still contained in the uranium nuclei of the reactor fuel. Although there is no interaction between different neutrons, they have a certain common history within predetermined limits which are defined, e.g., by the neutron moderation process, by their movement along the neutron guide tubes, by the monochromator crystal and by the special interferometer set-up. Therefore, any real interferometer pattern contains single particle and ensemble properties together.

Partial beam path detection experiments

A certain attenuation can be achieved either by a semi-transparent material or a proper chopper system. The transmission probability in the first case is defined by the absorption cross-section σ_a of the material [$a = I/I_0 = \exp(-\sigma_a N D)$] and the change of the wave function is obtained directly form the complex index of refraction (Eq. 1):

$$\psi \to \psi_0 e^{i(n-1)kD} = \psi_0 e^{i\chi} e^{-\sigma_a N D/2} = e^{i\chi}\sqrt{a}\psi. \tag{13}$$

Table I
Properties of the neutrons

Particle properties:	
mass	: $m = 1.6749543(86) \cdot 10^{-24}$ g
spin	: $s = \hbar/2$
magnetic moment	: $m = -1.91304308(54)\mu_K$
half life	: $T_{1/2} = 641(8)$ s
electric charge	: $q < 2.2 \cdot 10^{-20} e$
electric dipol moment	: $d < 4.8 \cdot 10^{-25} e \cdot$ cm
confinement radius	: $R = 0.7$ fm
quark structure	: $n = u - d - d$
Wave properties:	
Compton wavelength	: $\lambda = h/mc = 1.32 \cdot 10^{-13}$ cm
de Broglie wavelength	: $\lambda_B = h/m\nu \simeq 1 \cdot 10^{-8}$ cm*
coherence length	: $\Delta_c = \lambda^2/\Delta\lambda = 1 \cdot 10^{-6}$ cm*
packet length	: $\Delta_p = v \cdot \Delta t = 1.10$ cm*
decay length	: $\Delta_d = v \cdot T_{1/2} = 2 \cdot 10^8$ cm*
phase difference	: $0 \leq \chi \leq 2\pi$

* values belong to thermal neutrons ($\lambda_B = 1.8$ Å, $v = 2200$ m/s)

Therefore, the beam modulation behind the interferometer is obtained in the following form

$$I_0 \propto |\psi_0^I + \psi_0^{II}|^2 \propto [(1+a) + 2\sqrt{a}\cos\chi]. \tag{14}$$

On the other hand, the transmission probability of a chopper wheel or another shutter system is given by the open to closed ratio, $a = t_{open}/(t_{open} + t_{closed})$, and one obtains after straightforward calculations

$$I \propto \left[(1-a)|\psi_0^{II}|^2 + a|\psi_0^1 + \psi_0^{II}|^2\right] \propto [(1+a) + 2a\cos\chi], \tag{15}$$

i.e. the contrast of the interference pattern is proportional to $\sqrt{a}$, in the first case, and proportional to a in the second case, although the same number of neutrons are absorbed in both cases. The absorption represents a measuring process in both cases because a compound nucleus is produced with an excitation energy of several MeV, which is usually de-excited by gamma rays. These can easily be detected by different means.

Figure 3 shows the dependence of the normalized contrast of the measured interference pattern on the transmission probability [30, 31, 32]. The different contrast becomes especially obvious for low transmission probabilities where the interfering part of the interference pattern is distinctly larger than the transmission probability through the semi-transparent absorber sheet. The discrepancy diverges for $a \to 0$ but it has been shown that in this regime the variations of the transmission due to variations of the thickness or of the density of the absorber plate have to be taken into account which shifts the points below the $\sqrt{a}$-curve [33]. This can most easily be understood if the variation of the beam attenuation due to variations of the thickness or density fluctuations are included $a = \overline{a} + \Delta a$, which yields after

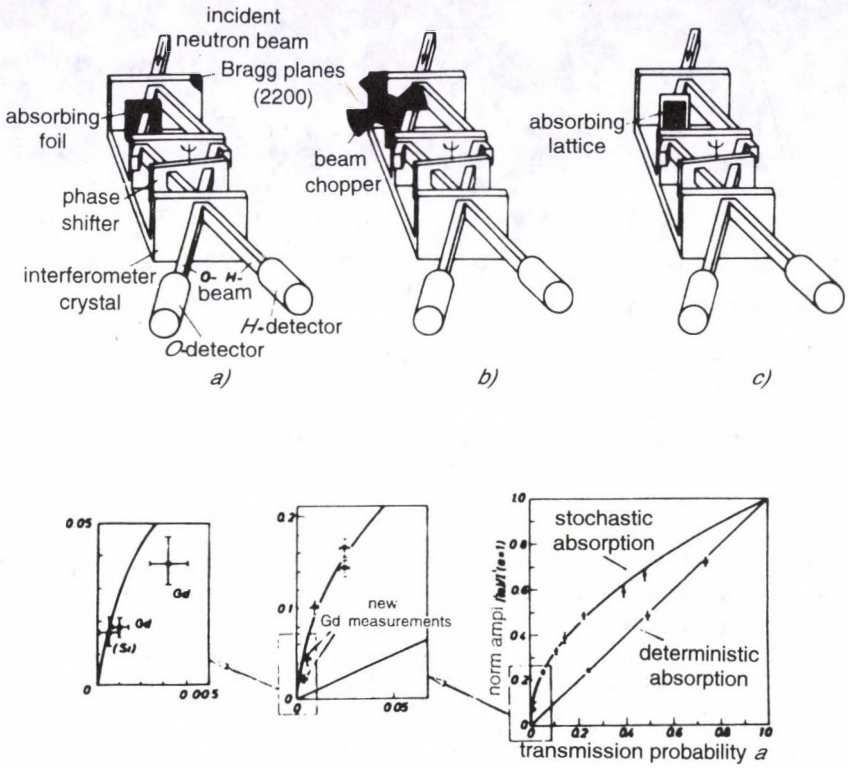

Fig. 3. Sketch of the experimental arrangement for absorber measurements (above). (a) stochastic absorption, (b) deterministic absorption, (c) attenuation by a transmission grating. Reduction of the contrast as a function of beam attenuation for different attenuation methods (below) [31, 32]

averaging

$$\sqrt{a} < \sqrt{\bar{a}} \tag{16}$$

indicating that the points fall below the $\sqrt{a}$-curve.

The region between the linear and the square root behaviour can be reached by very narrow chopper slits or by narrow transmission lattices, where one starts to lose information of through which individual slit the neutron went. This is exactly the region which shows the transition between a deterministic and a stochastic view and, therefore, it can be formulated by a Bell-like [34, 35] inequality

$$\sqrt{a} > x > a. \tag{17}$$

The stochastic limit corresponds to the quantum limit when one does not know any more through which individual slit the neutron went. Which situation exists depends on how the slit widths compare to the coherence lengths ($\Delta_i \approx (2\delta k_i)^{-1}$) in the related direction. In case that the slit widths become smaller than the

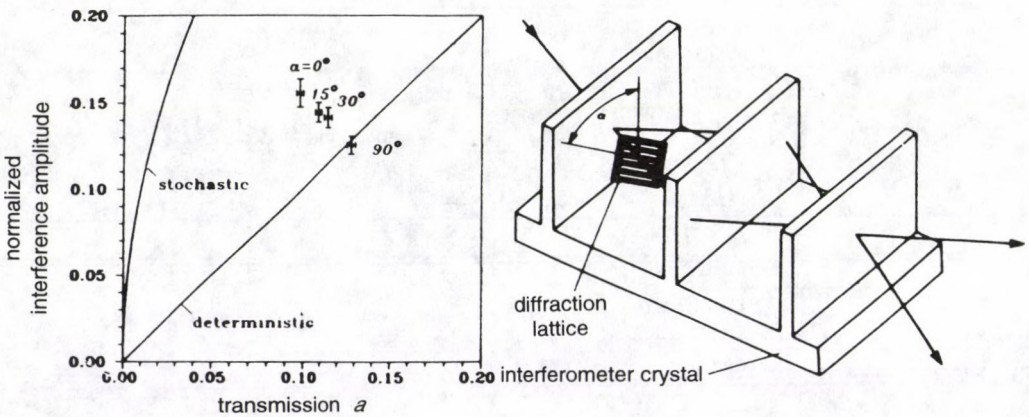

Fig. 4. Lattice absorber in the interferometer approaching the classical limit when the slits are oriented horizontally and the quantum limit when they are oriented vertically [31, 36]

coherence lengths, the wave function behind the slits shows distinct diffraction peaks which correspond to new quantum states ($n \neq 0$), which now do not overlap with the undisturbed reference beam. The creation of the new quantum states means that those labelled neutrons carry information about the chosen beam path and, therefore, do not contribute to the interference amplitude [36]. A related experiment has been carried out by rotating an absorption lattice around the beam axis where one changes from $l \ll \Delta_x$ (vertical slits) to $l \gg \Delta_y$ (horizontal slits), Fig. 4, because the coherence length parallel to the reflecting lattice vector is much larger than in any other directions. Thus, the attenuation factor a has to be generalized including not only nuclear absorption and scattering processes but also lattice diffraction effects if they remove neutrons from the original phase space.

A very similar situation exists if a very fast chopper produces beam bursts (packet lengths) shorter than the coherence time $\Delta t_c = \Delta/v$. In this case, diffraction in time occurs which also removes neutrons out of the original phase space. This limit is very difficult to reach with a mechanical chopper but it can probably be tackled with a high frequency spin flipper.

Neutron Josephson effect

This phenomenon is based on the dipol coupling of the magnetic moment μ of the neutron to a magnetic field $\mathbf{B}(H = -\mu\mathbf{B})$ which causes the famous 4π-symmetry of spinor wave functions, as measured in early neutron interferometer experiments [37, 38]. The change of the wave function reads:

$$\psi \rightarrow \psi_0 e^{-i(Ht/\hbar)} = \psi_0 e^{-i(\mu Bt/\hbar)} = \psi_0 e^{-i\sigma\alpha/2} = \psi(\alpha), \tag{18}$$

where α represents a formal description of the Larmor rotation angle around the field $\mathbf{B}(\alpha = (2\mu/\hbar)\int Bdt = (2\mu/\hbar v)\int Bds)$. This enabled also the realization of the

spin superposition experiments where spin-up ($|\uparrow>$) and spin-down states ($|\downarrow>$) are superposed producing a final state perpendicular to both initial states [39, 40]. It is interesting to mention that in the case of spin reversal by means of a resonance flipper the spin term is accompanied by an energy exchange equal to the Zeeman energy $\hbar\omega_r = 2\mu B$. This provided the basis for the observation of a new quantum beat effect: the magnetic Josephson analog.

A double coil arrangement can be used for the observation of a new quantum beat effect. If the frequencies of the two coils are chosen to be slightly different, the energy transfer becomes different too ($\Delta E = \hbar(\omega_{r1} - \omega_{r2})$). The frequency difference can be made very small, if high quality frequency generators are used for the field generation. The flipping efficiencies for both coils are always very close to unity (better than 0.99). Now, the wave functions change according to

$$\psi \rightarrow e^{i(\omega-\omega_{r1})t}|\downarrow> + e^{i\chi}e^{i(\omega-\omega_{r2})t}|\downarrow> . \tag{19}$$

Therefore, the intensity behind the interferometer exhibits a typical quantum beat effect, given by

$$I \propto 1 + \cos[\chi + (\omega_{r1} - \omega_{r2})t]. \tag{20}$$

Thus, the intensity behind the interferometer oscillates between the forward and deviated beam without any apparent change inside the interferometer [41]. The time constant of this modulation can reach a macroscopic scale which is correlated to an uncertainty relation $\Delta E \Delta t \leq \hbar/2$. Figure 5 shows the result of an experiment, where the periodicity of the intensity modulation, $T = 2\pi/(\omega_{r1} - \omega_{r2})$, amounts to $T = (47.90 \pm 0.15)$ s caused by a frequency difference of about 0.02 Hz. This corresponds to a mean difference of the energy transfer between the two beams, $\Delta E = 8.6 \cdot 10^{-17}$ eV, and to an energy sensitivity of $2.7 \cdot 10^{-19}$ eV, which is better by many orders of magnitude than that of other advanced spectroscopic methods. This high resolution is strongly decoupled from the monochromaticity of the neutron beam, which was $\Delta E = 5.5 \cdot 10^{-4}$ eV around a mean energy of the beam $E_B = 0.023$ eV in this case. It should be mentioned, that the result can also be interpreted as being the effect of a slowly varying phase $\Delta(t)$ between the two flipper fields, but the more physical description is based on the argument of a different energy transfer. The extremely high resolution may be used for fundamental, nuclear and solid-state physics applications.

The quantum beat effect can also be interpreted as a magnetic Josephson effect analog. In this case, the phase difference is driven by the magnetic energy ($\Delta B_0 = B_{02} - B_{01}$)

$$\frac{\delta}{\delta t}(\Delta_2 - \Delta_1) = \omega_{r2} - \omega_{r1} = \frac{2\mu\Delta B_0}{\hbar} \tag{21}$$

and, therefore,

$$\Delta(t) = (\omega_{r2} - \omega_{r1})t = \frac{2\mu\Delta B_0}{\hbar} \cdot t. \tag{22}$$

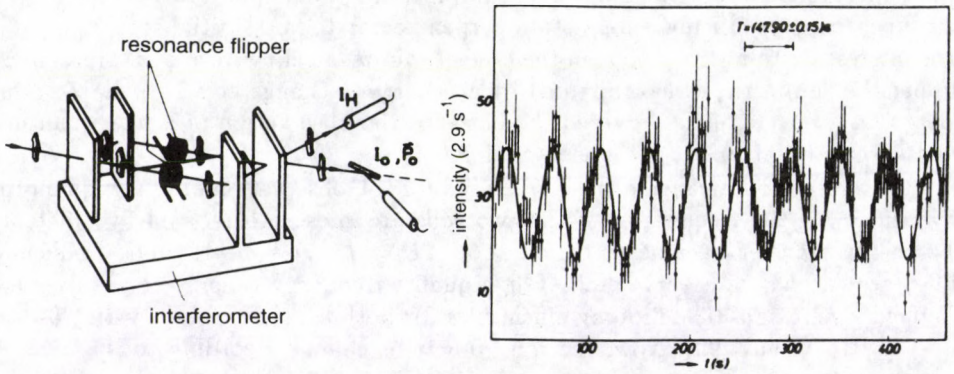

Fig. 5. Quantum beat effect observed when the frequencies of the two flipper coils differ by about 0.02 Hz around 71.89979 kHz [41]

This yields the observed modulation (compare Eq. (20))

$$I \propto (1 + \cos \Delta(t)). \tag{23}$$

This is analogous to the well-known Josephson effect in superconducting tunnel junctions [42], where the phase of the Cooper pairs in both superconductors is related to the electrical energies on both sides of the junction according to

$$\frac{\delta}{\delta t}(\Phi_2 - \Phi_1) = \frac{1}{\hbar}(E_2 - E_1) = \frac{1}{\hbar} 2 \text{ eV} \tag{24}$$

which is driven by the electrical potential V between both superconductors. This gives

$$\Phi(t) = \frac{2eV}{\hbar} \cdot t \tag{25}$$

and a superconducting Josephson current

$$I_S = I_{sMax} \sin \Phi(t). \tag{26}$$

Postselection of states

In the course of several neutron interferometer experiments [15, 16, 17, 18] it has been established that smoothed out interference properties at high interference order can be resored even behind the interferometer when a proper spectral filtering is applied. The experimental arrangement with an indication of the wave packets at different parts of the interference experiment is shown in Fig. 6. An additional

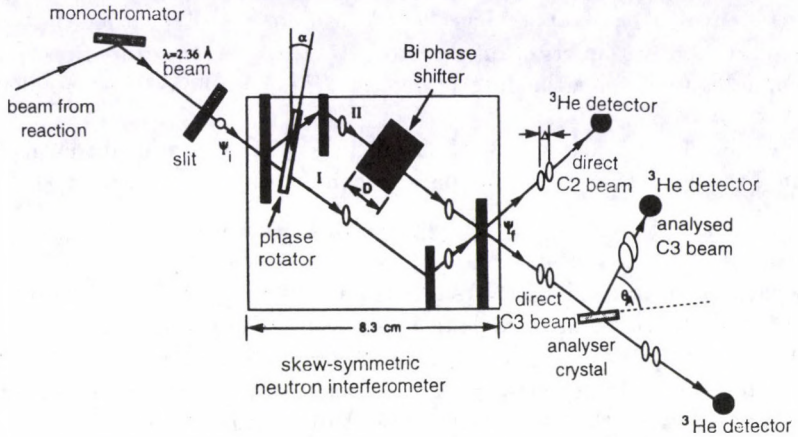

Fig. 6. Scheme of the experimental arrangement with a skew-symmetrically cut perfect crystal interferometer and a post-selection analyser crystal [18, 28]

monochromatization is applied behind the interferometer by means of various single crystals brought into Bragg position.

Using Eqs (5) and (7), the momentum-dependent intensity reads:

$$I_0(\mathbf{r},\mathbf{k}) = |\psi_0^I(\mathbf{r},\mathbf{k}) + \psi_0^{II}(\mathbf{r}+\Delta,\mathbf{k})|^2 \propto |a(\mathbf{k})|^2|1+\cos(\boldsymbol{\Delta}(\mathbf{k})\cdot\mathbf{k})|^2, \tag{27}$$

whereas the overall beam reads

$$I_0(\boldsymbol{\Delta}_0) \propto 1 + |\Gamma(\boldsymbol{\Delta}_0)|\cos\boldsymbol{\Delta}_0\cdot\mathbf{k}, \tag{28}$$

where $\boldsymbol{\Delta}_0$ represents the spatial phase shift for the $\mathbf{k}_0$-component of the packet. Eq. (28) describes the interference fringes when $\boldsymbol{\Delta}_0$ is varied. The formula also shows that the overall interference fringes disappear for spatial phase shifts larger than the coherence lengths $[\Delta_i \geq \Delta_c^i = 1/(2\delta k_i)]$ (see Eq. (11)). This behaviour is shown in Fig. 7 and has been verified experimentally by several investigations for Gaussian and non-Gaussian neutron beams [43, 44, 45].

In our experiment we deal with the coherence properties along the interferometer axis (x), where the (tangential) components of the momentum vectors (and coherence length) do not change due to Bragg diffraction. According to basic quantum mechanical laws, the related momentum distribution follows from Eq. (27) and for Gaussian packets it can be rewritten in the form ($\mathbf{k} = k_x, k_y, k_z$)

$$I_0(k) = \exp[-(k-k_0)^2/2\delta k^2]\left\{1+\cos\left(\chi_0\frac{k_0}{k}\right)\right\}, \tag{29}$$

where the mean phase shift is introduced ($\chi_0 = k_0\Delta_0 = Nb_c\lambda_0 D_{eff}$). The surprising feature is that $I_0(k)$ becomes oscillatory for large phase shifts where the

interference fringes described by Eq. (28) disappear (see Fig. 7). This indicates that interference in phase space has to be considered [46,47] rather than the simple wave function overlap criterion described by the coherence function (Eq. (10)). The second beam behind the interferometer (H) just shows the complementary modulation $I_H = I_{total} - I_0$.

The amplitude function [48] of the packets arising from beam paths I and II determines the spatial shape of the packets behind the interferometer

$$I_0(x) = |\psi(x) + \psi(x + \Delta)|^2, \tag{30}$$

which separates for large phase shifts into two peaks (Fig. 7). For Gaussian packets, δx corresponds to the coherence length Δ_c and fulfils the minimum uncertainty relation $\delta x \delta k = 1/2$. For an appropriately large displacement ($\Delta \gg \Delta_c$), the related state can be interpreted as a superposition state of two macroscopically distinguishable states, that is, a stationary Schrödinger-cat-like state [49, 59], but here first for massive particles. These states — separated in ordinary space and oscillating in momentum space — seem to be notoriously fragile and sensitive to dephasing effects [51, 52, 53, 54].

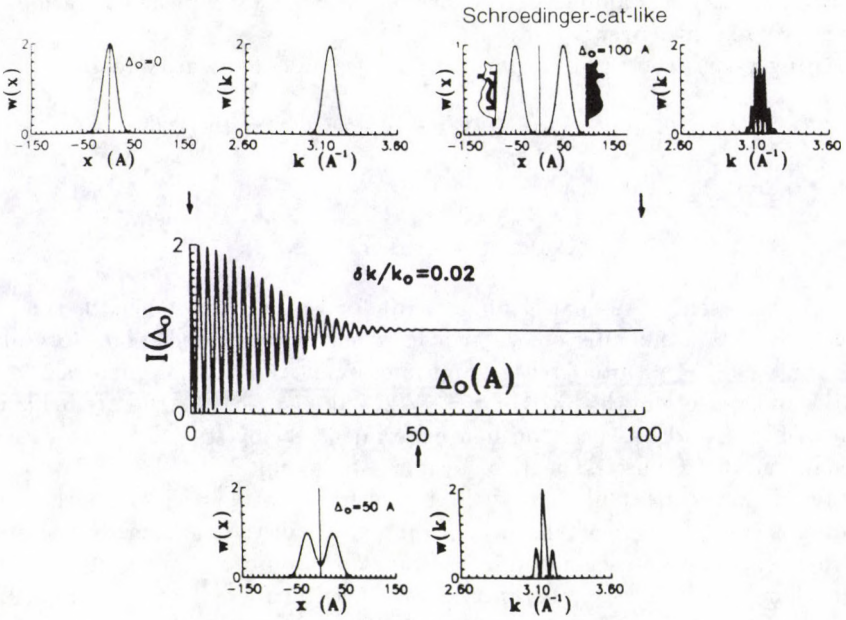

Fig. 7. Interference pattern as a function of the relative phase shift (middle) and related wave packets and momentum spectra behind the interferometer [18]

Measurements of the wavelength spectrum were made with a silicon crystal with a rather narrow mosaic spread which reflects in the parallel position a very

narrow band of neutrons only ($\delta k'/k_0 \approx 0.0003$) causing an enhanced visibility at large phase shifts (Fig. 8). This feature shows that an interference pattern can be restored even behind the interferometer by means of a proper postselection procedure. In this case the overall beam does not show interference fringes anymore and the wave packets originating from the two different beam paths do not overlap.

The momentum distribution has been measured by scanning the analyser crystal through the Bragg position. The related results are shown in Fig. 9 for different phase shifts. These results clearly demonstrate that the predicted spectral modulation (Eq. (29)) appears when the interference fringes of the overall beam disappear. The modulation is somehow smeared out due to averaging processes across the beam due to various imperfections, unavoidably existing in any experimental arrangement. The contrast of the empty interferometer was 60 %.

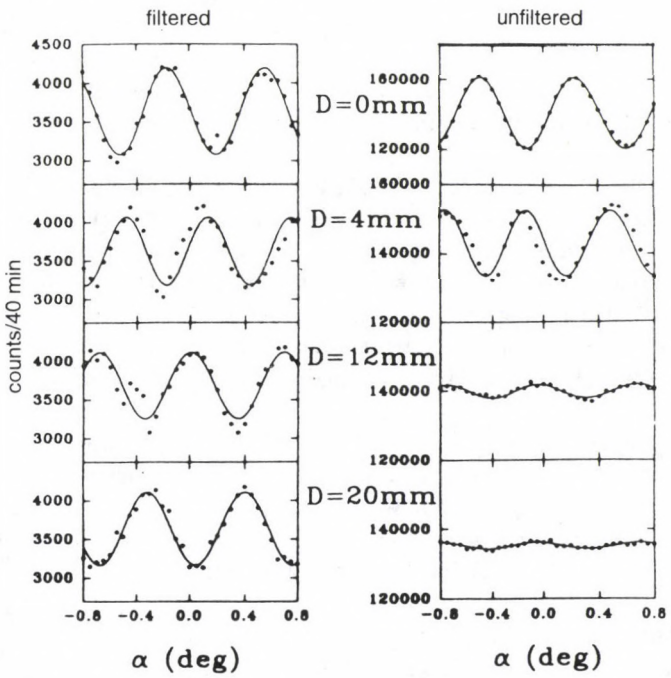

Fig. 8. Interference pattern of the overall beam ($\delta k/k_0 = 0.012$) and the beam reflected from a nearly perfect crystal analyser in the antiparallel position ($\delta k'/k_0 = 0.003$) [18]

Discussion

All the results of the neutron interferometric experiments are well described by the formalism of quantum mechanics. According to the complementarity principle of the Copenhagen interpretation, the wave picture has to be used to describe the observed phenomena. The question how the well-defined particle properties of the

neutron are transferred through the interferometer, is not a meaningful one within this interpretation, but from the physical point of view it should be an allowed one.

The newly discovered persisting phase space coupling in cases of large spatial shifts of the wave packets may bring some attenuation to the action of plane wave components outside the packet, The results clearly demonstrate that a spectral modulation can be observed in neutron interference experiments at high interference order and that interference has to be treated in phase space rather than in ordinary space. It looks like that the plane wave components of the wave packets, i.e. narrow band width components, interact over a much larger distance than the size of the packets. This interaction guides neutrons of certain momentum bands to the O- or H-beam, respectively. These phenomena throw a new light on the discussion on Schrödinger-cat-like situations in quantum mechanics and, therefore, on the discussion about the EPR-experiments, too [28, 56, 57, 58]. Spatially separated packets remain entangled in phase space and nonlocality appears as a result of this entanglement. The analogy with optical experiments performed in the time-frequency domain is striking [23]. An analogue situation exists in neutron spin-echo systems where multiple spin rotation plays an equivalent role as high order interferences discussed here [59].

Each peak in the momentum distribution corresponds to a different number of phase shifts experienced by the neutrons of that wavelength band during its passage through the interferometer. In that sense, the minimum quantum unity of the incident wave packet becomes a new quantity representing different quantum states with distinguishable properties. This kind of labelling shows that constructive interference is restricted to that wavelength band only; a situation similar to that where new states have been created due to lattice diffraction inside the interferometer (Fig. 4) [36].

The new quantum states created behind the interferometer can be analysed with regard to their uncertainty properties. Analogies between a coherent state behaviour and a free but coherently coupled particle motion inside the interferometer have been addressed previously [32]. In such cases, the dynamical conjugate variables x and p minimize the uncertainty product with identical uncertainties $(\Delta x)^2 = (\Delta k)^2 = 1/2$ (in dimensionless units). Using $I_0(k)$ and $I_0(x)$ (Eqs (29) and (30)) as distribution function we get in our case

$$\lim_{\Delta \gg \delta x} < (\Delta x)^2 > = < x^2 > - < x >^2 = (\delta x)^2 + \left(\frac{\Delta}{2}\right)^2 \tag{31}$$

and (for $\delta k/k_0 \ll 1$)

$$\begin{aligned} < (\Delta k)^2 > &= < k^2 > - < k >^2 \\ &= (\delta k)^2 \left\{ 1 - \left(\frac{\Delta_0}{2\delta x}\right) \frac{e^{-(\Delta_0/2\delta x)^2/2} \cos(\Delta_0 k_0) + e^{-(\Delta_0/2\delta x)^2}}{\left[1 + e^{-(\Delta_0/2\delta x)^2/2} \cos(\Delta_0 k_0)\right]^2} \right\}. \end{aligned} \tag{32}$$

These relations are shown in Fig. 10 indicating that for $(\Delta k)^2$ values below the coherent state value can be achieved, which in quantum optic terminology means

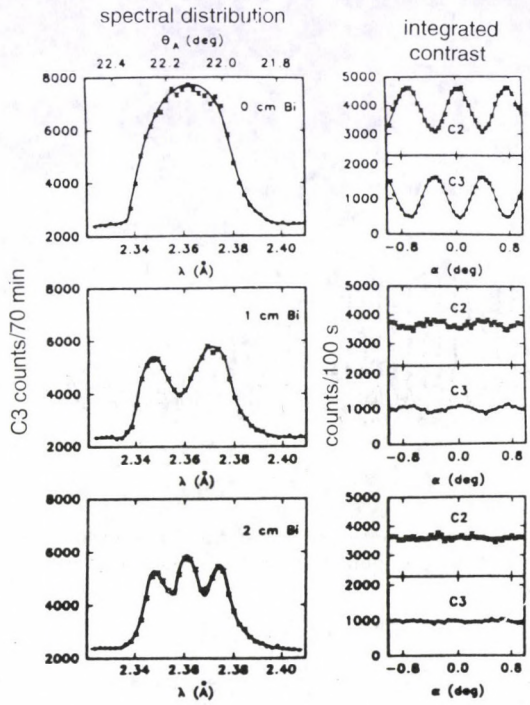

Fig. 9. Measured spectral modulation of the outgoing beam and the residual interference pattern for different bismuth phase shifter thickness. The wavelength resolution of the analyser was 0.002 A [18]

squeezing [35, 60, 61]. One emphasizes that a single coherent state does not exhibit squeezing, but a state created by superposition of two coherent states can exhibit a considerable amount of squeezing. Thus highly nonclassical states are made by the power of the quantum mechanical superposition principle.

Acknowledgements

Most of the experimental results discussed in detail have been obtained by our Dortmund–Grenoble–Vienna interferometer group working at the high flux reactor in Grenoble, and some recent ones stem from our cooperation with the Columbia–Missouri group working at the MURR reactor. The cooperations within these groups and especially the cooperation with colleagues from our Institute, which are cited in the references, are gratefully acknowledged.

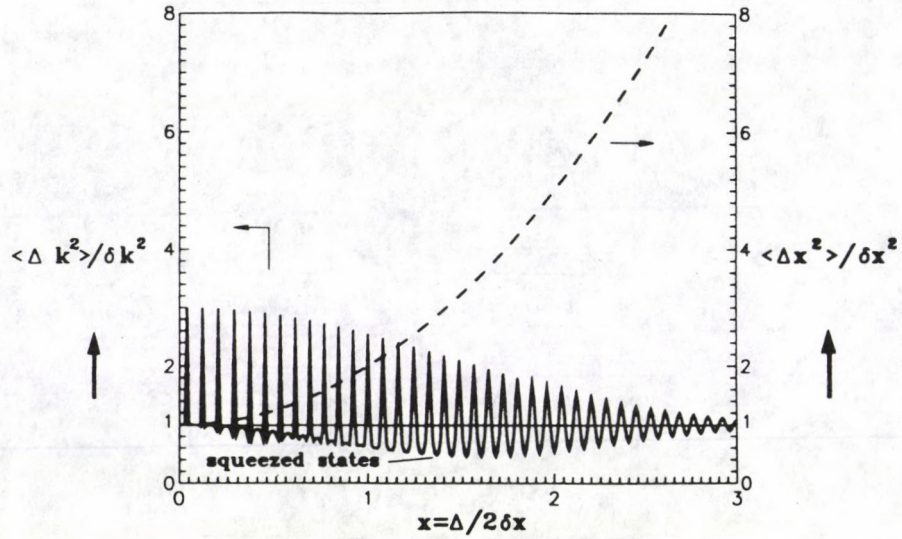

Fig. 10. Spatial and momentum uncertainties of the outgoing beams with the indication of squeezing in the momentum domain [18]

References

1. H. Maier-Leibnitz, T. Springer, Z. Physik, *167*, 386, 1962.
2. R. Gaehler, J. Kalus, W. Mample, J. Phys., *E13*, 546, 1980.
3. H. Rauch, W. Treimer, U. Bonse, Phys. Lett., *A47*, 369, 1974.
4. W. Bauspiess, U. Bonse, H. Rauch, W. Treimer, Z. Physik, *271*, 177, 1974.
5. A. I. Ioffe, V. S. Zabiyankan, G. M. Drabkin, Phys. Lett., *11*, 373, 1985.
6. U. Bonse, M. Hart, Appl. Phys. Lett., *6*, 155, 1965.
7. H. Rauch, D. Petrascheck, Neutron Diffraction, ed. H. Dachs, Springer Verlag, Berlin, 1978, Chap. 9.
8. V. F. Sears, Can. J. Phys., *56*, 1261, 1978.
9. W. Bauspiess, U. Bonse, W. Graeff, J. Appl. Cryst., *9*, 68, 1976.
10. D. Petrascheck, Acta Phys. Austr. *45*, 217, 1976.
11. M. L. Goldberger, F. Seitz, Phys. Rev., *71*, 294, 1947.
12. V. F. Sears, Phys. Rep., *82*, 1, 1982.
13. U. Bonse, H. Rauch eds, Neutron Interferometry, Clarendon Press, Oxford, 1979.
14. H. Rauch, E. Seidl, D. Tuppinger, D. Petrascheck, R. Scherm, Z. Physik, *B69*, 69, 1987.
15. S. A. Werner, R. Clothier, H. Kaiser, H. Rauch, H. Wölwitsch, Phys. Rev. Lett., *67*, 683, 1991.
16. H. Kaiser, R. Clothier, S. A. Werner, H. Rauch, H. Wölwitsch, Phys. Rev., *A45*, 31, 1992.
17. H. Rauch, H. Wölwitsch, R. Clothier, H. Kaiser, S. A. Werner, Phys. Rev., *A46*, 49, 1992.
18. D. L. Jacobson, S. A. Werner, H. Rauch, Phys. Rev., *A 49*, 3196, 1994.
19. L. Mandel, J Opt. Soc. Am., *52*, 1335, 1962.
20. L. Mandel, E. Wolf, Rev. Mod. Phys., *37*, 231, 1965.
21. F. Heineger, A. Herden, T. Tschudi, Opt. Comm., *48*, 237, 1983.
22. D. F. V. James, E. Wolf, Phys. Lett., *A157*, 6, 1991.
23. X. Y. Zou, T. P. Grayson, L. Mandel, Phys. Rev. Lett., *69*, 3041, 1992.
24. E. Wolf, Phys. Rev. Lett., *63*, 2220, 1989.
25. D. Faktis, G. M. Morris, Opt. Lett., *13*, 4, 1988.
26. W. Schleich, M. Pernigo, Fam Le Kien, Phys. Rev., *A44*, 2172, 1991.

27. J. Janski, A. V. Vinogradov, Phys. Rev. Lett., *64*, 2771, 1990.
28. H. Rauch, Phys. Lett., *A173*, 240, 1993.
29. H. Rauch, Proceedings Quantum Measurement & Control, eds E. Ezawa and Y. Murayama, North Holland, 1993, p. 223.
30. H. Rauch, J. Summhammer, Phys. Lett., *104A*, 44, 1984.
31. J. Summhammer, H. Rauch, D. Tuppinger, Phys. Rev., *A36*, 4447, 1987.
32. H. Rauch, J. Summhammer, M. Zawisky, E. Jericha, Phys. Rev., *A42*, 3726, 1990.
33. M. Namiki, S. Pascazio, Phys. Lett., *147*, 430, 1990.
34. J. Bell, Physics, *1*, 195, 1965.
35. D. Home, F. Selleri, Revista del Nuovo Cim., *14*, 1, 1991.
36. H. Rauch, J. Summhammer, Phys. Rev., *46*, 7284, 1992.
37. H. Rauch, A. Zeilinger, G. Badurek, A. Wilfing, W. Bauspiess, U. Bonse, Phys. Lett., *A54*, 425, 1975.
38. S. A. Werner, R. Colella, A. W. Overhauser, C. F. Eagen, Phys. Rev. Lett., *35*, 1053, 1975.
39. J. Summhammer, G. Badurek, H. Rauch, U. Kischko, A. Zeilinger, Phys. Rev., *A27*, 2523, 1983.
40. G. Badurek, H. Rauch, J. Summhammer, Phys. Rev. Lett., *51*, 1015, 1983.
41. G. Badurek, H. Rauch, D. Tuppinger, Phys. Rev., *A34*, 2600, 1986.
42. B. D. Josephson, Rev. Mod. Phys., *46*, 251, 1974.
43. H. Rauch, in: Neutron Interferometry, eds U. Bonse and H. Rauch, Clarendon Press, Oxford, 1979, p. 161.
44. H. Kaiser, S. A. Werner, E. A. George, Phys. Rev. Lett., *50*, 563, 1983.
45. R. Clothier, H. Kaiser, S. A. Werner, H. Rauch, H. Wölwitsch, Phys. Rev., *A44*, 5357, 1991.
46. W. Schleich, J. A. Wheeler, Nature, *326*, 574, 1987.
47. W. Schleich, D. F. Walls, J. A. Wheeler, Phys. Rev., *A38*, 1177, 1988.
48. J.-M. Levy-Leblond, F. Balibar, Quantics, North-Holland, 1990.
49. A. Legett, Proc. Found. Quantum Mechanics, ed. S. Kamefuchi, Phys. Soc. Japan, 1984, p. 74.
50. B. Yurke, W. Schleich, D. F. Walls, Phys. Rev., *A42*, 1703, 1990.
51. D. F. Walls, G. J. Milburn, Phys. Rev., *A31*, 2403, 1985.
52. R. J. Glauber, New Techniques and Ideas in Quantum Measurement Theory, ed. D. M. Greenberger, N. Y. Acad. Sci. 1986, p. 336.
53. M. Namiki, S. Pascazio, Phys. Rev., *A44*, 39, 1991.
54. H. Zurek, Physics Today, Oct. 1991, p. 36.
55. C. Dewdney, Phys. Lett., *A109*, 377, 1985.
56. A. Einstein, B. Podolsky, N. Rosen, Phys. Rev., *47*, 777, 1935.
57. D. M. Greenberger, M. A. Horne, A. Zeilinger, in: Bell's Theorem, Quantum Theory and Conceptions of the Universe, ed. M. Kafatos, Kluwer Publ. Dordrecht, 1989, p. 69.
58. N. D. Mermin, Phys. Rev. Lett., *65*, 1838, 1990.
59. G. Badurek, H. Weinfurter, R. Gähler, A. Kollmar, S. Wehinger, A. Zeilinger, Phys. Rev. Lett., *71*, 307, 1993.
60. D. F. Walls, Nature, *306*, 141, 1983.
61. S. L. Braunstein, R. I. McLachlan, Phys. Rev., *A35*, 1659, 1987.

Acta Physica Hungarica 75 (1-4), pp. 221-225 (1994)

POSTERS (SOLID STATE PHYSICS)

THE ORIGIN OF Sm ION INTERMEDIATE VALENCE STATE IN SmB_6

P. A. ALEKSEEV, V. N. LAZUKOV and I. P. SADIKOV

RRC Kurchatov Institute
123182 Moscow, Russia

The extended inelastic neutron scattering study of SmB_6 single- and polycrystalline samples has been performed to search the effects of intermediate valence state of Sm ions in lattice and magnetic excitation spectra. Several specific features have been discovered in the spectra obtained. The possible structure and properties of the wavefunction of Sm ion ground state are discussed.

Introduction

SmB_6 is a "classical" intermediate valence (IV) system which was extensively studied from the middle of the 60's during two decades. The investigations were concentrated around two main features of its physical properties: homogeneous mixed valence state ($v = 2.56$) of Sm ions and narrow gap of a few meV in the electronic density of states at E_f, which gives rise to semiconductor-like behaviour at low temperatures.

The inelastic neutron scattering is one of the most powerful tools for investigating the IV phenomenon. A serious problem in the realization of this intent is the extremely high capture cross-section of thermal neutrons by the natural Sm and B. The isotopically purified materials are necessary for the preparation of a suitable sample. This paper gives a survey about most of our neutron scattering experiments done since 1989 on SmB_6 [1-8].

Experimental details

The samarium oxide and the pure boron enriched up to 98.6 % of ^{154}Sm and 99.4 % of ^{11}B were used to create the polycrystalline samples. The single crystal (~ 1 cm^3) of SmB_6 was grown by floating zone melting technique from the polycrystalline rod. The diffraction and preliminary inelastic neutron scattering experiments were performed at the IR-8 medium flux reactor of the Kurchatov Institute. The most measurements of the phonon frequencies were done using the IN-8 three-axis spectrometer (TAS) at the Institute Laue-Langevin. The same single crystal was used in the measurements of magnetic excitation spectra at 2T TAS at the Laboratory Leon Brillouin. The study of high energy spin-orbit intermultiplet transitions was performed on the polycrystalline sample of $^{154}Sm^{11}B_6$ and reference sample $La^{11}B_6$ at the time-of-flight spectrometers HET at the ISIS facilities of Rutherford Appleton Laboratory.

Results

1. Phonons (Fig. 1)

One of the remarkable features is the overall softening of the acoustic and the lowest optic phonons in SmB_6 in comparison with that of the isostructural non IV system LaB_6 [7,9]. The softening reaches the value of 20 % in the Γ-point for optic phonon. The pronounced anomalies are observed in SmB_6 contrary to LaB_6 for the longitudinal acoustic branches in the [110] and [111] directions. These anomalies resemble the similar softening of La phonons in the [111] direction in other famous IV semiconductor SmS [10].

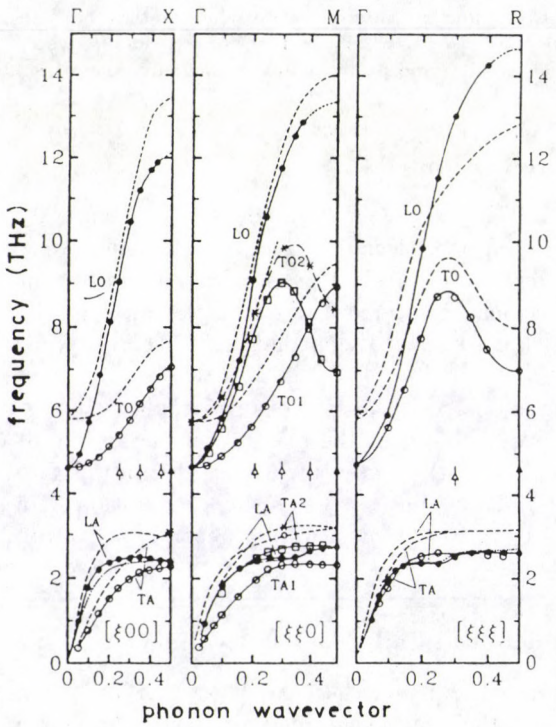

Fig. 1. Phonon dispersion curves for SmB_6 at $T = 300$ K (experimental points are connected by guidelines). Dashed lines are the phonon branches for LaB_6

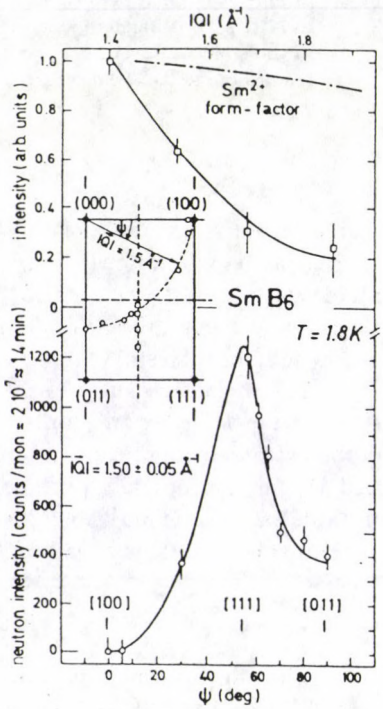

Fig. 2. Radial (upper part) and angular (lower part) variations of the magnetic intensity associated with the magnetic peak at $\hbar\omega_2 \approx 14$ meV in SmB_6; insert: trajectories within the $(0\bar{1}1)$ scattering plane corresponding to these plots

The intriguing experimental result is the observation of two extra phonon modes for SmB_6. The first was obtained at 300 K as a weak signal with a maximum

at about 19 meV in the energy gap between acoustic and optic phonon branches (triangles in Fig. 1). The signal disappears in the background when the temperature goes down below 100 K. Nothing was found in the gap between acoustic and optic branches in our measurements of the LaB_6 single crystal. Another unusual signal was observed in longitudinal geometry in [110] direction near the BZ boundary for large enough values of Q. Its energy is about 15 meV at 1.8 K and strongly depends on temperature: the peak position shifts to the foot of the elastic line with temperature rises to about 100 K.

2. Low energy magnetic excitation ($E \sim 14$ meV)

The intensity of the 14 meV peak drops rapidly with rising of the momentum transfer Q and decreases faster than due to the usual f-electron form factor (see Fig. 2, upper part). The most detailed study of this puzzling excitation has been carried out at several temperatures between 1.8 and 73 K and at a selected point of BZ with $Q \simeq 1.5$ Å^{-1} (Fig. 3). The fast drop of the intensity when temperature rises takes place in the narrow interval 20–40 K. This excitation has been measured at the lowest temperature $T = 1.8$ K at a number of points in plane [110]–[001] of the reciprocal space. The most interesting result is the dependence of the peak intensity not only on the $|Q|$, but the very strong dependence on $Q/|Q|$ obtained from measurements with $|Q| = 1.5$ Å^{-1} (Fig. 2, lower part). At this Q-value the intensity of the 14 meV excitation is near zero for [100], goes through the maximum near [111]-direction and falls to some intermediate value for [110].

3. Spin–orbit (intermultiplet) transitions (Fig. 4)

The two main magnetic peaks with energy positions close to the energies of the intermultiplet transitions for the stable valence Sm^{2+} and Sm^{3+} ions have been identified. The ratio of the intensities for these two peaks is in a reasonable agreement with the ratio of dynamic structure factors for corresponding values of Q. The trial measurements of the polycrystalline sample $^{154}Sm_{0.5}Ba_{0.5}{}^{11}B_6$ were done under the same conditions as SmB_6 (valence $v = 2.7$) (Fig. 4). The obvious rise of the intensity of high energy peak with respect to the low energy one is in accordance with the change of the average valence to more of 3+ when Sm is partly substituted by Ba. The evidence of single site origin of these excitations follows from these data.

The experimental width of the peaks is greater than the instrumental resolution. Experiments with SmB_6 single crystal prove the absence of any detectable dispersion of $J = 0 \Rightarrow J = 1$ excitation, thus its large (≥ 20 meV) width is true intrinsic.

Discussion

The observed anomalies in the phonon dispersion curves at room temperature were analysed successfully in [1] from the standpoint of the generalized charge

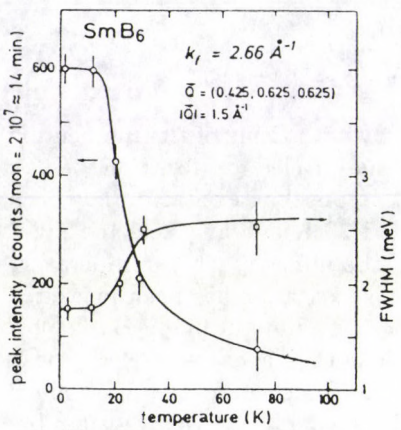

Fig. 3. Temperature dependence of the intensity and linewidth of the magnetic peak at $\hbar\omega_2 \approx 14$ meV in SmB_6

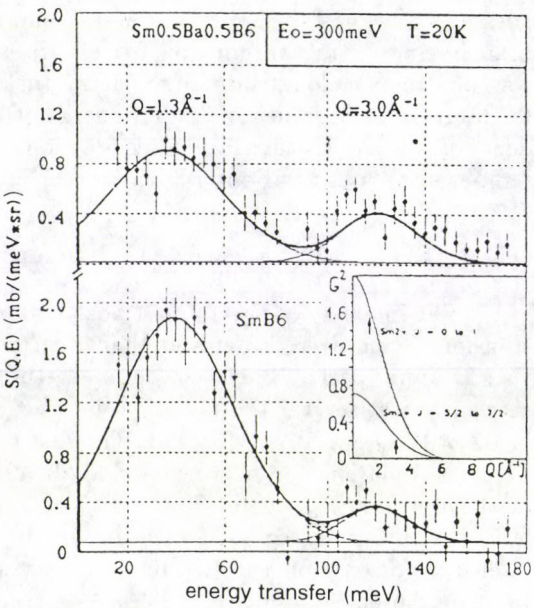

Fig. 4. The magnetic contribution to $S(Q, E)$ for SmB_6 and $Sm_{0.5}Ba_{0.5}B_6$, measured on HET at scattering angle $\langle\phi\rangle = 5°$; Q values are given for $E = 40$ and 120 meV. Lines are the best fits by the two Gaussians. Inset: inelastic structure factor $G^2(Q)$ for intermultiplet transitions of Sm^{2+} and Sm^{3+} ions. Arrows indicate the values of G^2 corresponding to experimental conditions

density distortion model. It was shown that the dipole "distortion shell" mode (Γ_{15}) is responsible for the general softening of phonons, the anomalies (kinks) in LA [110], [111] are well described by the nonlocal monopolar ("breathing") mode (Γ_1) specific for the IV semiconductor. This adiabatic consideration cannot give two extra modes; one of which was observed at room temperature ("gap" mode at $E = 19$ meV) and another one which exists at low temperatures near the LA [110] branch. The energy of the monopolar excitation is supposed to be of the order of a few meV. Therefore, the non- or even anti-adiabaticity have to be considered for the full description of lattice vibration excitation spectrum of SmB_6 to be found. The calculations [11] of the spectrum of such a system give evidence that dispersionless "gap" mode results from anti-adiabatic (phonon energy is higher than electronic) interaction between LO phonon and Γ_1 exciton like some kind of local mode due to defect in the perfect lattice. The low temperature mode corresponds to longitudinal acoustic phonon excitation in the lattice distorted by Γ_1 electronic excitation.

The simultaneous existence of the transitions specific for f^6 and for f^5 configurations in the spectra of SmB_6 gives direct evidence of the mixed nature of Sm ion ground state wavefunction. The large intrinsic line width corresponds to rather short life time (3×10^{-13} s) and proves the homogeneous origin of the IV state. The Q-dependence of intensity of both peaks is in agreement with single-ion calculations [4]. Therefore, the well localized $4f$-electrons are most probably responsible for this part of the excitation spectra.

The experimentally observed sharp Q-dependence of 14 meV excitation intensity corresponds obviously to delocalized electron spin density distribution. The distance from the origin to the maximum in the radial part of the electron density can be estimated as $1.5 - 2$ Å, three times larger than $4f$ shell radius. From the other side, the surprisingly small intrinsic width with respect to intermultiplet transitions, unusual temperature behaviour and anisotropy of the inelastic structure factor may result from non single-ion origin of this excitation. It is some kind of excitation in the "loosely bound" electron state which exists at low temperatures and "disappears" at temperatures enough for the thermal activation of conduction electrons. The particular anisotropy of the inelastic structure factor reflects the anisotropy of radial distribution of the spatially extended wavefunction. Probably it is connected with a topology of an octahedron built on the six Sm ions in simple cubic Sm sublattice, between which the d- and p-electrons are spread forming the wavefunction of the exciton of the intermediate radius.

Acknowledgement

This work was supported by RFFR (Grant 93-02-2582).

References

1. P. A. Alekseev, A. S. Ivanov, B. Dorner, H. Shober, K. A. Kikoin, A. S. Mishchenko, V. N. Lazukov, E. S. Konovalova, Yu. B. Paderno, A. Yu. Rumyantsev, I. P. Sadikov, Europhysics Lett., *10*, 457, 1989.
2. P. A. Alekseev, A. S. Ivanov, V. N. Lazukov, I. P. Sadikov, A. Severing, Physica B, *180/181*, 281, 1992.
3. P. A. Alekseev, J.-M. Mignot, J. Rossat-Mignod, V. N. Lazukov, I. P. Sadikov, Physica B, *186/188*, 384, 1993.
4. P. A. Alekseev, V. N. Lazukov, B. D. Rainford, R. Osborn, I. P. Sadikov, E. S. Konovalova, Yu. B. Paderno, Europhysics Lett., *23*, 247, 1993.
5. P. A. Alekseev, Physica B, *186/188*, 365, 1993.
6. J.-M. Mignot, P. A. Alekseev, J. Rossat-Mignod, V. N. Lazukov, I. P. Sadikov, Proceedings of SCES-93, San Diego.
7. P. A. Alekseev, A. S. Ivanov, V. N. Lazukov, A. Severing, ILL Annual Report, p. 66, 1990.
8. P. A. Alekseev, V. N. Lazukov, R. Osborn, B. D. Rainford, I. P. Sadikov, ISIS Annual Rep., p. 239, 1992.
9. H. G. Smith, G. Dolling, T. Goto, Solid State Comm., *53*, 15, 1985.
10. H. A. Mook, R. M. Nicklov, T. Penney, F. Holtzberg, M. W. Shafer, Phys. Rev., *B18*, 2995, 1978.
11. K. A. Kikoin, A. S. Mishchenko, JETP, *104*, 3810, 1993.

Acta Physica Hungarica 75 (1–4), pp. 227–230 (1994)

APPLICATIONS OF DYNAMIC NEUTRON AND GAMMA RADIOGRAPHY AT THE BUDAPEST RESEARCH REACTOR

M. Balaskó, E. Svab[1], I. Cserháti[2], F. Ozsvári[2] and J. Oláh[2]

KFKI Atomic Energy Research Institute
P.O.B. 49, 1525 Budapest, Hungary
[1] *KFKI Research Institute for Solid State Physics*
P.O.B. 49, 1525 Budapest, Hungary
[2] *Lehel-Electrolux*
P.O.B. 64, 5101 Jászberény, Hungary

Dynamic neutron and gamma radiography equipment (DNGR) has been installed at the Budapest research reactor. DNGR is used as non-destructive testing method for research and development of products for various companies. Investigations have been performed on absorption and compression type refrigerators which provide useful information for engineering and development work.

Introduction

Neutron radiography has proved to be a useful tool in non-destructive testing investigations, and its increasing role may be observed in various applications (see e.g. [1] and therein). Flow of fluids, evaporation and condensation processes in closed metal objects and tube systems are visualized and analysed by DNGR which provide useful information for experts involved in developing work. Among our main applications are investigations of inner processes in various thermodynamical devices like absorption and compression type refrigerators [2,3], heat tubes [4].

In this paper we give a description of our new DNGR experimental facility which has been built out in connection with the refurbishment of the Budapest 10 MW research reactor, which is again in operation since November 1993. Some of our latest results on optimalization of working parameters of absorption and compression type refrigerators are presented.

Experimental facility

A new DNGR installation has been constructed and put into operation at the thermal channel No. 2 of the WWR-SM 10 MW Budapest research reactor.

Both neutron and gamma radiation are obtained simultaneously from the reactor core through a pin-hole type collimator. The collimator is constructed in a very similar way as described in our previous paper [5]. Collimation ratio is $L/D = 170$, diameter of the beam is 150 mm and neutron flux is 5×10^7 n/cm^2 s at the object position. Objects under investigation with a weight of up to 250 kg

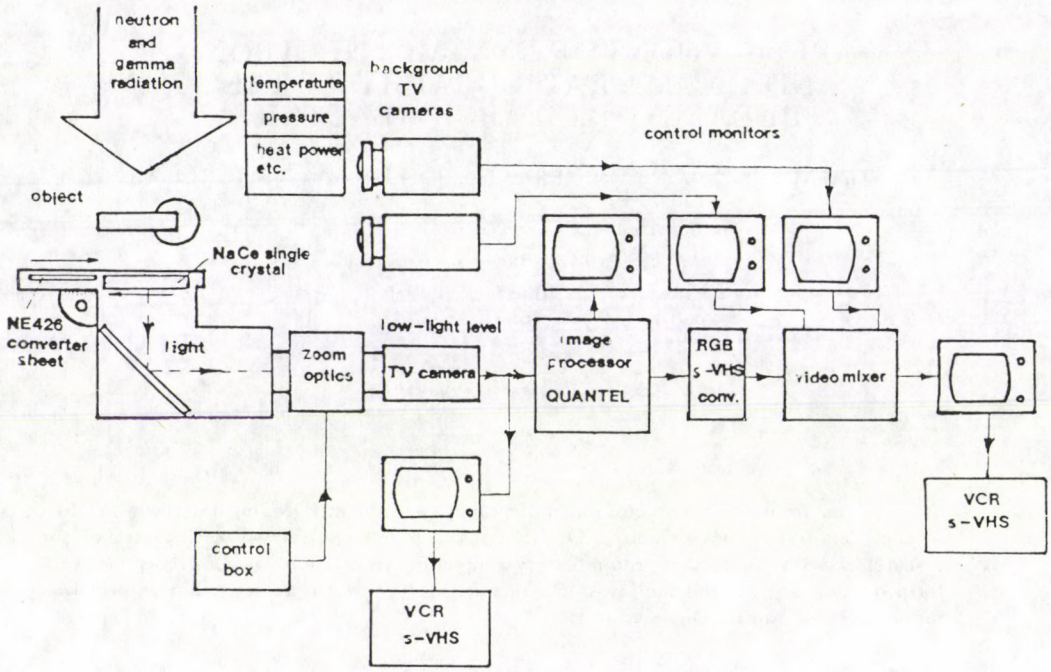

Fig. 1. Imaging system of the DNGR facility

and a surface area of 600 mm × 1000 mm can be moved into the correct position of the beam by means of a remote control mechanism.

Figure 1 shows the schematic arrangement of the imaging system. For neutron radiography imaging NE 426 converter screen, for gamma radiography imaging NaCe single crystal is used. The light image is detected by 10^{-4} lux TV 1122 type television camera. The imaging cycle is 40 ms, thereby providing the possibility for visualizing medium speed movements up to about 2.5 m/s inside the investigated object. Radiography images are displayed on monitor, stored by S-VHS recorder and for further analysis a QUANTEL image processing system is used. In addition to the radiography image other parameters characterizing the operation of the investigated object — such as operating time, pressure, temperature, flow velocity, power consumption — are measured and recorded.

Applications

Compression type refrigerators

Chlorofluoro-carbons CFCs are one of the so-called "greenhouse" gases and so may be relevant to the problem of global warming of the earth, although their significance is likely to be comparatively minor. Many CFCs are used as working

fluids in refrigerators, freezers and air-conditioning units. The development of safe, effective substances is one of the most difficult challenge facing industry throughout the world. Much work has been focused in the last years on finding suitable ozone-benign replacement material.

According to the Montreal Protocol (1986) which was formulated on the International Conference "Saving the ozone layer" the following rates for CFCs products reduction were accepted:

1993 – consumption cut to 80 % of 1986 level

1998 – consumption cut to 50 % of 1986 level, similar cuts in production.

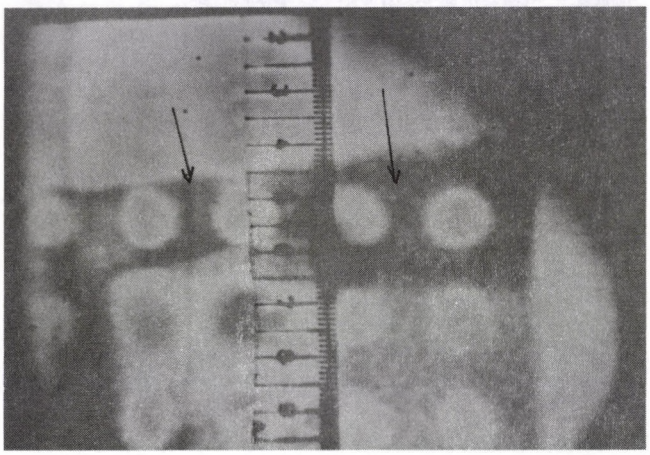

Fig. 2. Segregation of the synthetic lubrication oil on the surface of R-134a organic material in the evaporator after the restart of the compressor

Hungarian refrigerator manufacturers meet with this problem as well, as they are interested in Western-European export. The new cooling material is R-134a freon which does not cause any damage in the ozone layer, but its oil solving capability is smaller than those for previously used ones [7]. This fact causes many problems for designers and producers. It is very important to know the segregation points; these may be visualized by neutron radiography. As an example Fig. 2 shows the segregation of the synthetic lubrication oil on the surface of R-134a organic material in the evaporator after the restart of the compressor. This layer hinders the evaporation of R-134a, and it is missing from the lubrication process of the compressor bearing. Schematic layout of compressor refrigerator and details of its working process were described in our previous work [3].

Absorption type refrigerator

The study of inner processes in absorption type refrigerators is a very favourable task for DNGR investigations, because these units consist of small diameter tubes with thin wall. The operation of an absorption type refrigerator is based on

two fundamental priciples: a) the ability of large quantities of ammonia gas to be absorbed into cold water at low pressure and then at higher temperatures and high pressure to be driven out again, and b) the ability to condense ammonia vapour at a high pressure and high temperature and to evaporate it again at a lower temperature in the presence of an inert gas although even the total pressure remains the same. During this evaporation process large quantities of heat can be taken into the ammonia. Further details and a functional model of an absorption aggregate may be found in [3].

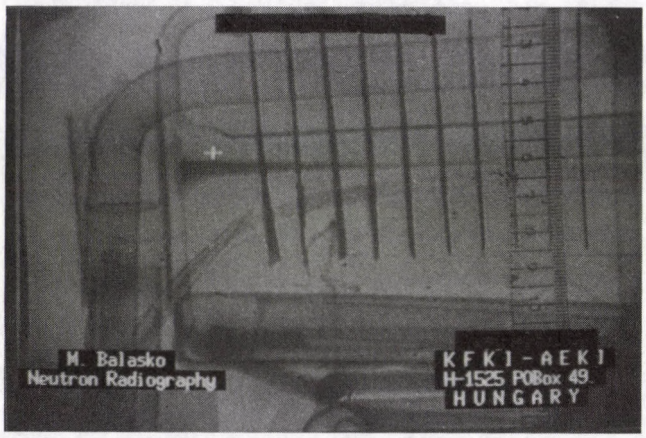

Fig. 3. Liquid ammonia is gathered in the condenser in consequence of the incorrect position of the outlet hole

As far as an absorption refrigerator is working without motor and compressor, the undisturbed stream in the tube system is very important . As an example Fig. 3 shows such kind of defect. Liquid ammonia is gathered in the condenser because the position of the outlet hole is incorrect. In consequence, the cooling material is missing from the evaporator and the efficiency of the unit drastically reduces.

References

1. Proc. Fourth World Conf. on Neutron Radiography (WCNR-4) ed. J.P. Barton, Gordon and Breach Science Publ., New York, 1993.
2. M. Balaskó, E. Sváb, L. Cser, L. Pálvölgyi, J. Oláh, Proc. 3rd European Conference on Nondestructive Testing, Firenze, Vol. 4, 383, 1984.
3. M. Balaskó, E. Sváb, H. Nedelik, Proc. Fourth World Conf. on Neutron Radiography (WCNR-4) ed. J.P. Barton, Gordon and Breach Science Publ., New York, 31, 1993.
4. M. Balaskó, S. Könczöl, E. Sváb, Int. J. Refrig., *9*, 80, 1986.
5. M. Balaskó, E. Sváb, L. Cser, NDT International, *20*, 157, 1987.
6. M. Balaskó, E. Sváb, A. Burtscher, Proc. Conf. Non-Destructive Testing (Elsevier-Science Publishers B.V., Amsterdam, Vol. 1, 96, 1989.
7. J. du Parquet, G. Bayon, Proc. Fourth World Conf. on Neutron Radiography (WCNR-4) ed. J.P. Barton, Gordon and Breach Science Publ., New York, 1993.

Acta Physica Hungarica 75 (1–4), p. 231 (1994)

NEUTRON SCATTERING STUDIES OF PHASE TRANSITIONS IN PROTONATED AND DEUTERATED AMMONIUM HYDROGEN SULPHATE

L. BOBROWICZ and I. NATKANIEC

Frank Laboratory of Neutron Physics, JINR, Dubna, Russia

K. HOLDERNA-NATKANIEC, M. MROZ and W. NAWROCIK

Institute of Physics, A. Mickiewicz University Poznan, Poland

Abstract

Ammonium hydrogen sulphate, $(NH_4)HSO_4$, is ferroelectric [1] in the temperature range between 270 K and 154 K. With increasing hydrostatic pressure the ferroelectric properties of this crystal disappear [2] and proton superionic conductivity is observed at temperatures above 460 K [3]. The results of neutron powder diffraction (NPD) and inelastic incoherent neutron scattering (IINS) studies of normal and deuterated ammonium hydrogen sulphate in different solid phases are presented. The measurements were performed on the NERA inverted geometry time-of-flight spectrometer [4] of the IBR-2 high-flux pulsed reactor of the JINR at Dubna.

No change is found in the NPD and IINS spectra for the I–II phase transition at 270 K, while the II–III phase transition at 154 K is clearly seen. The latter phase transition is marked by a change in structure and proton dynamics. The behaviour of the deuterated ammonium hydrogen sulphate at cooling is analogous to that of a protonated substance. Upon heating at about 230 K a new structural transition was observed. The new phase thus obtained may be overcooled below the temperature of the II–III phase transition. Our investigations show that the NPD spectra of this new phase correspond to the high pressure phase IV of a normal substance. The phase IV below ca. 200 K becomes metastable and exists even at normal pressure within the temperature region of the phases II and III. With increasing temperature the phase IV transforms directly to the phase I at about 270 K. The IINS spectra of the phases I, II and IV indicate disorder of hydrogen bonds in the crystal and fast reorientations of ammonium ions above the temperature of the II–III phase transition. Below this temperature difference in vibrational spectra of the phase III and IV is caused by different crystal structures and the ordering of hydrogen bonds.

References

1. R. Pepinsky, K. Vedam, S. Hoshino and Y. Okava, Phys. Rev., *111*, 1508, 1958.
2. I. N. Polandov, V. P. Mylov and B. A. Strukov, Fiz. Tverdovo Tela, *10*, 2232, 1968.
3. A. N. Baranov, E. G. Ponyatovsky, V. V. Sinitsyn, R. M. Fedosyuk and L. A. Shuvalov, Crystallography, *30*, 1121, 1985.
4. I. Natkaniec, S. I. Bragin, J. Brankowski and J. Mayer, Proc. ICANS XII, Abingdon 1993, RAL (in press).

Acta Physica Hungarica 75 (1-4), pp. 233-237 (1994)

A PACKAGE OF DEDICATED PC SOFTWARE FOR NEUTRON POWDER DIFFRACTION DATA PROCESSING AND ANALYSIS

E. JANSEN, W. SCHÄFER and G. WILL

Mineralogisches Institut, Universität Bonn
Poppelsdorfer Schloss, 53115 Bonn, Germany
and
Forschungszentrum Jülich -MIN/ZFR-
52425 Jülich, Germany

Commonly used powder structure refinement programs and a variety of auxiliary routines for the handling of powder patterns are collected in a software package of individual programs to be run in any laboratory on personal computers. The package contains PC least squares versions of the full pattern refinement Rietveld method and of the two-stage method applying individual peak profile analysis (PROFAN) and using integrated intensities (POWLS). The auxiliary programs represent a comprehensive PC software environment containing tools for scaling and combining data sets, for adding and subtracting different files, for determination of background and peak intensities, for displaying and labelling of diagrams, for hardcopies on printers and plotters and for file outputs to be included in word processing systems.

Introduction

Encouraged by more than 20 years of experience in the operation of two neutron diffractometers as dedicated service instruments for university institutes and other external research groups we have put together a package of software tools, which are needed in the context of crystallographic and magnetic structure analysis, when doing neutron powder diffraction. There are two well-established methods in handling powder diffraction patterns: the full pattern refinement Rietveld method [1, 2] and the two-stage method using integrated intensities. Integrated intensities of individual reflections and/or groups of overlapped reflections are used as observed quantities in the program POWLS (Will [3]) analogous to the procedure in single crystal data analysis. There are programs available (see Jansen et al [4]) to determine the integrated intensities in a first step by profile fitting of the powder diffraction pattern. PROFAN is a program to perform this stepwise on selected peaks or peak clusters to be decomposed.

In order to run these programs independent of large mainframe computer installations and their specific restrictions with respect to hardware and operating systems, we have prepared PC versions of the programs ready to run in any laboratory on an IBM compatible personal computer under DOS. Due to modern compilers and PC developments, it is no problem, nowadays, to transfer even large least squares refinement programs to personal computers. However, working with

those programs on PCs is sometimes cumbersome because of lack of environment. Therefore the program package presented here contains an auxiliary software PC environment to support preparation, processing, exploitation and presentation of powder diffraction patterns. Programs with graphic facilities are designed for an interactive operation by means of a mouse on a graphic screen. The auxiliary programs are written in Turbo Pascal 6.0, the Rietveld and POWLS programs in Fortran 77. When using a PC with coprocessor, the turn around times of the least squares routines are comparable to working conditions on a mainframe computer.

Least squares refinement PC programs

Rietveld PC code

The PC code of the total pattern profile refinement is based on Rietveld's original source code (T418, 419 [5]) containing both nuclear and magnetic structure refinements. Data input and crystallographic model description are analogous to Rietveld's handling. Magnetic structures, inlcusive those of enlarged, but commensurate lattice periodicities, are defined by appropriate translation and rotation matrices of the magnetic moments. Modifications made by several authors with respect to a modified treatment of background or a simplified method to decompose an observed pattern into Bragg intensities, and which caused negative consequences on the validity of R-values, have been avoided. Weighted and expected profile R-values are calculated from background cleaned step intensities. R-Bragg values defined in this Rietveld PC code are comparable to those obtained by integrated intensity refinements (see Jansen et al [6]). Bragg R-values are given for the nuclear, the magnetic and the total reflection intensities.

POWLS-PC

POWLS-PC is the PC version of the established computer program POWLS (POWder Least Squares) for calculation and refinement of X-ray and neutron powder diffraction data (Will [3, 7]). The program combines the calculation of structure model intensities and the adjustment of structural parameters to observed intensities. Observed quantities to be used for a non-diagonal least squares procedure, are integrated intensities of both individual reflection and/or groups of overlapping reflections. Crystallographic and magnetic intensities can be handled either separately or simultaneously. Symmetry informations of all crystallographic space groups, X-ray scattering factor tables, nuclear neutron scattering lengths and tables of magnetic form factors are supplied in separate files. Structural parameters to be refined are occupation numbers, atomic positions, isotropic or anisotropic thermal vibrations and preferred orientation; parameters with respect to magnetic structures are amount and direction of ordered magnetic moments. An extended version of this program comprises also the handling of incommensurate lattice periodicities of magnetic structures. Miller indices of magnetic superlattice or satellite reflections are automatically generated. A final comparative list of observed and

calculated intensities is given together with appropriate R-Bragg values. Additional PC tools are provided to display and plot model diffraction patterns using the POWLS output and selected peak profiles.

PROFAN-PC

PROFAN-PC [8] is the PC version of PROFAN (PROFile ANalysis), which fits preselected profile functions into measured peaks or peak clusters from either neutron, X-ray or synchrotron diffraction patterns. Profile shape functions actually implemented are Gaussian, Lorentzian and Pseudo-Voigt. The profile analysis or refinement can be performed independently of preliminary structural knowledge. Profile parameters like peak positions, halfwidths and heights are refined by least squares methods. Subsequently these parameters can be used for appropriate purposes either in structure determination or refinement (POWLS) or in texture and strain and stress analysis. Halfwidth parameters can also be fixed according to a known 2θ dependence, like that defined by parameters U, V, W in the Rietveld routine. The actual profile analysis of a pattern is performed stepwise on selected peaks or peak clusters after segmenting the pattern manually into suitable sections.

Auxiliary PC programs

This PC environment software comprises a variety of different programs [9], which support preparation and presentation of powder diffraction patterns. The input to be handled is according to the widely used file format, which is defined by a *start/step/stop* declaration in the beginning. There are tools for scaling and combining data sets, for adding and subtracting different files, for determination of background and peak intensities, for displaying and labelling of diagrams, for hardcopies on printers and plotters and for file outputs to be included in word processing systems. The programs written in Turbo Pascal 6.0 are aimed at IBM compatible PCs with a graphic adaptor like VGA, running under DOS. The wide potential of graphic manipulations is used to support the interactive operation at the PC. Graphic input is performed by a mouse and/or cursor keys. The programs are divided into two groups, the non-interactive routines ADD, SUB, OPE and ACC, and the graphic interactive routines SHO, BAC, INT and PAT.

Non-interactive routines

Intensities of patterns with identical *start/step/stop* values can be added or subtracted point by point with the tools ADD and SUB, respectively. Sum patterns are needed for instance, in case of several patterns collected under identical experimental conditions. SUB may be used for instance, to subtract a high temperature pattern without magnetic reflections from a low temperature pattern containing both nuclear and magnetic intensities. Another frequent use of SUB is the generation of a difference pattern of observed and calculated count rates. Arithmetic operations like addition, subtraction, multiplication or division of count rates by

selected offsets or factors are performed with the program OPE. Such operations are useful to normalize or compare data files measured under different experimental conditions. Data files of different *start/step/stop* values can be combined to a common data file of equidistant stepwidth when using the program ACC, which stands for accumulation. ACC may be used for patterns which have been measured for instance under different settings of a position-sensitive detector and which are to be combined to a composed accumulated data file.

Interactive graphic routines

Structure analysis and refinement from powder diffraction measurements starts favourably with a visual inspection of the diffraction patterns. Visual control is also necessary to observe and estimate the progress of data evaluation during successive runs of profile fits. The program SHO displays diffraction data files on a graphic screen. The patterns are placed inside a frame, which is generated automatically. The initial scale is found by a check of the limits of all input patterns. Depending on the actual limits, the axes are provided with appropriate ticks and labels. A zoom facility is provided and can be applied repeatedly, also in sections already zoomed. In case of the existence of a special file containing reflection positions and Miller indices, the program SHO performs a labeling of the diffraction pattern for presentation, documentation and publishing purposes. All structure refinements are connected with the separation of background from the real Bragg intensities. The program BAC, standing for background, generates a background polygon by footing marks to be selected interactively on the screen. The BAC menu offers tools to add, change and delete footings controlled by rubber lines. The determination of integrated Bragg intensities is performed using the program INT. Peak ranges can be defined manually by means of a cursor box to set limits on the abscissa. Integrated intensities and mean peak positions are calculated with estimated deviations. Finally, the program PAT, standing for patching, modifies input files of different scales or zero shifts to match each other in an accumulated data file. All graphic programs use common routines to display files and to interact with the user.

Driver software

The program package includes drivers to perform hardcopies on printers supported by the GRAPHICS command of DOS, on Postscript devices, as well as on HPGL plotters. File outputs are generated for inclusion into common word processing systems, e.g. WordPerfect.

Conclusions

It should be emphasized that the program package is an ad-hoc collection of individual programs, which are aimed to be run independent of each other. This holds especially for the least squares refinement programs, which meet different requirements also with respect to prior structural knowledge. The program collection

concentrates on the needs of structure refinements according to our practical experiences in the operation of powder diffraction service instruments. Nevertheless, there are tools, e.g. PROFAN, which have proven to be helpful in the preparation of data for ab initio structure determinations or for strain and stress or texture analysis. The auxiliary programs can be applied for any purposes, where diffraction patterns have to be handled. Here we take into account today's trends of using modern PCs instead of large mainframe computer systems.

Acknowledgement

This work was supported by the German Federal Minister for Research and Technology (BMFT) under contract no. 03WI3BON.

References

1. H. M. Rietveld, Acta Cryst., *22*, 151, 1967.
2. H. M. Rietveld, J. Appl. Cryst., *2*, 65, 1969.
3. G. Will, J. Appl. Cryst., *12*, 483, 1979.
4. E. Jansen, W. Schäfer and G. Will, J. Appl. Cryst., *21*, 228, 1988.
5. H. M. Rietveld, An Algol Program for Refinement of Nuclear and Magnetic Structures by the Profile Method, RCN-104, 1969, RCN, Petten.
6. E. Jansen, W. Schäfer and G. Will, J. Appl. Cryst., *27*, 492, 1994.
7. G. Will, E. Jansen and W. Schäfer, POWLS-80: Program for Calculation and Refinement of Powder Diffraction Data, Jül-1867, 1983, KFA, Jülich.
8. P. Merz, E. Jansen, W. Schäfer and G. Will, J. Appl. Cryst., *23*, 444, 1990.
9. E. Jansen, W. Schäfer and G. Will, Proceedings of EPDIC-3, Wien, 25.-28.9.1993, Mater. Sci. Forum, *166–169*, 187, 1994.

Acta Physica Hungarica 75 (1–4), pp. 239–242 (1994)

MEDIUM RANGE CORRELATION IN DECOMPOSING BINARY SYSTEMS

L. ROSTA, O. BLASCHKO[1], S. BORBÉLY, A. JÁKLI and L. NOIREZ[2]

KFKI Research Institute for Solid State Physics,
P.O.B. 49, 1525 Budapest, Hungary
[1] *Institut für Experimentalphysik, Universität Wien*
Strudelhofgasse 4, 1090 Wien, Austria
[2] *Laboratoire Léon Brillouin (CEA-CNRS), CE-Saclay*
91191 Gif-sur-Yvette Cedex, France

The evolution of the structure was followed in decomposing binary systems. In Au–Pt and Au–Ni alloys, $TiH(D)_x$ and liquid crystal dispersed polymer mixtures small angle neutron scattering results revealed the common feature for decomposition phenomena of different origin: pattern formation and development of medium range structures.

1. Introduction

In composite systems homogeneous non-equilibrium states can be provided by different treatments, then during a relaxation decomposition may induce a morphology of mesoscopic scale. The formation of the precipitation patterns depends on the volume fraction and the different types of interactions of the components. As a result, isolated clusters within a matrix or an interconnected network of precipitated phases may occur.

In a neutron scattering experiment the measured intensity is proportional to the momentum and time dependent structure function $S(q,t)$, which measures spatial correlations and might show a scaling behaviour indicating the time evolution of the mesoscopic precipitation patterns.

Here we present a systematic neutron scattering investigation of three different binary systems: simple Au-based alloys [1], titanium–hydrogen composites [2] and liquid crystal dispersed polymers [3]. The metastable homogeneous starting phases were produced in different manner, as well as the driving force for the decomposition has different origin.

2. Experimental

The Au–Pt and Au–Ni samples with several concentrations nearly symmetric to the miscibility gap in the phase diagram were prepared by induction melting. Homogenization at a temperature just below the melting point was performed which was followed by a quench to room temperature. The decomposition was monitored step by step by annealing at several temperatures up to 600 °C.

The $TiH(D)_x$ samples were obtained by the following procedure: Titanium loaded with hydrogen (deuterium, for other samples) was compressed to 60 kbar,

heat treated at 620 K and rapidly quenched in liquid nitrogen. The pressure was then released, but the samples were stored in a nitrogen cryostat to preserve the metastable phase.

The liquid crystal–polymer system was composed in the following way: To produce samples with different ordering properties and concentrations, in nematic (5CB) or smectic (8CB) liquid crystals (LC) 1.5–3 wt% of reactive monomers (BAB or BMB) and, in addition, photo initiator (0.7–1.5 wt% benzoin methyl ether) were dissolved at elevated temperatures. Polymerization was induced by UV light. Some samples were prepared with magnetic field alignment [3].

The neutron scattering experiments were performed on spectrometers at the Orphée Reactor (LLB-Saclay, France). The scattered intensity data were analysed in terms of the $S(q)$ structure functions in the framework of those models which were properly adapted to the three different systems [1–3].

3. Results and discussion

For the decomposition in the series of Au–Pt alloys the structure functions were analysed for their shape and width [1] and the scaling behaviour was established for the late stages of the relaxation (annealing up to 600 °C). We have observed a considerable narrowing of the spherically averaged $S(q)$ function near the middle of the miscibility gap (60 at% Pt). For this composition a strong anisotropic scattering was detected (Fig. 1), meaning that the precipitated phases occur as plates on the (200) lattice planes. In both Au–Pt and Au–Ni alloys significant side-band reflections were detected in the diffuse scattering measurements, also supporting the picture of parallel platelets. This morphology induces correlations of longer range typically of 20 nm for the Pt, and 4 nm for the Ni-content alloys, respectively. In the study of the Au–Ni system the formation of parallel plate-like patterns was monitored also by electron microscope imaging in the 0.01 mm–100 nm range.

In the case of $TiH(D)_x$ SANS data were recorded for samples with $x = 0.728$, 0.832 and 0.917. Different $I(q)$ plots were analysed for the 0.007–0.08 A^{-1} q-range. First, the low temperature χ-phase was measured and the signal was detected to be very weak indicating a random distribution of $H(D)$ atoms in the interstitial sites of the fco metal sublattice. By heating the samples the γ- and δ-phases were obtained at above 140 K and 480 K, respectively [4]. These latter are nearly stoichiometric compounds containing — due to the decomposition — finely dispersed α-Ti precipitates. A fractal model was tried to fit the experimental curves, by analogy of TiH_2 fractal precipitates in CuTi(H) [ref. in 2]. Finding values somewhat higher than 3 for the fractal dimension did not prove the fractal behaviour, while the separation of H(D)-free and perfectly ordered $TiH(D)_1$ regions is clearly demonstrated by the intensity variation in accordance with the lower or higher contrast for hydrogenated and deuterated samples, respectively. The best fit was obtained in the framework of a random two phase model, which yields a correlation length of 5–6 nm. Furthermore, in the high temperature δ-phase, a significant increase of the size of the α-Ti precipitates is observed.

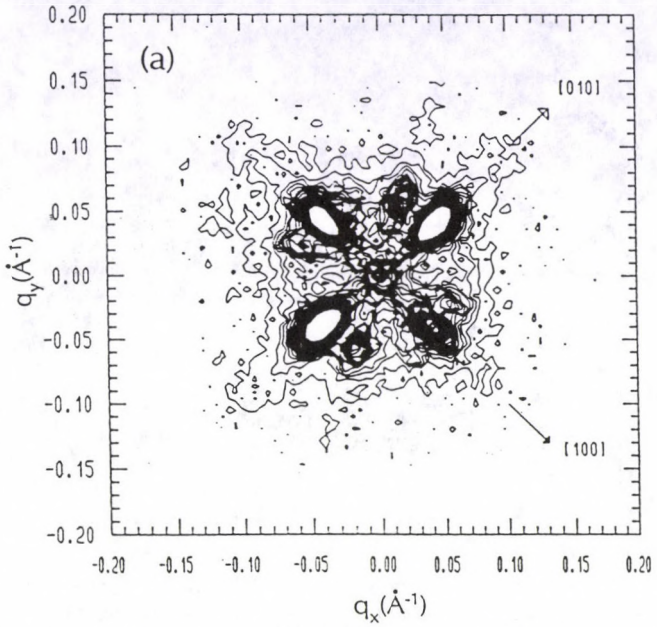

Fig. 1. Two-dimensional SANS intensity distribution represented by isointensity lines for the Au–Pt (60 at%) sample [1]

In the LC-based composite system the polymerization leads to the phase separation of a small amount of non-mesogenic polymer, which forms a physically interconnected fiber network in the continuous liquid crystal matrix. The fibers have rough surface and their cross-section radius is typically 30 nm. In the framework of a surface fractal model [3 and ref. therein] one can describe that on cooling the system, smaller polymers separate out resulting in thicker fibrils with a less smooth surface, while the phase transitions in the LC matrix do not influence the distribution of the rather rigid fibers. A model for the decomposed medium is proposed in Fig. 2.

Regarding the problem of alignment in this system it was found that the polymerization of non-mesogenic monomers in an aligned smectic A matrix induces the anisotropy of the resulting network, which becomes elongated parallel to the LC director. Figure 3 illustrates a sketch of the LC-fibril interface. In this picture one can explain the very stable alignment of the decomposed phase (anisotropy remains even after several thermal cycles without magnet), namely the polymer network freezes the LC alignment, imposed by fuzzes on the diffuse liquid crystal–polymer surface.

4. Conclusion

In the three systems with various origin of decomposition different kinds of morphology were observed. In the Au-based alloys the formation of modulated mesoscopic structures is governed by elastic interactions due to geometrical misfits of the components. In the LC-based system due to the nature of polymerization

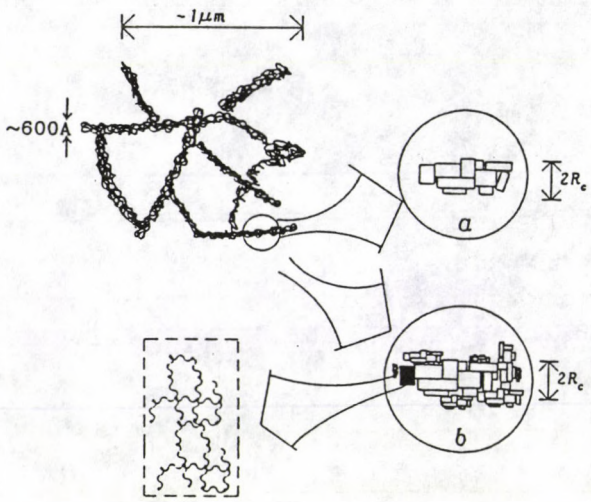

Fig. 2. Schematic representation of the polymer network in the liquid crystal matrix. The structure of the fibres is shown in the encircled part at high (a) and low (b) temperatures. The rectangles represent polymer reticulates and the enlarged sketch is constructed of self similar units, which is characteristic for fractal structures [3]

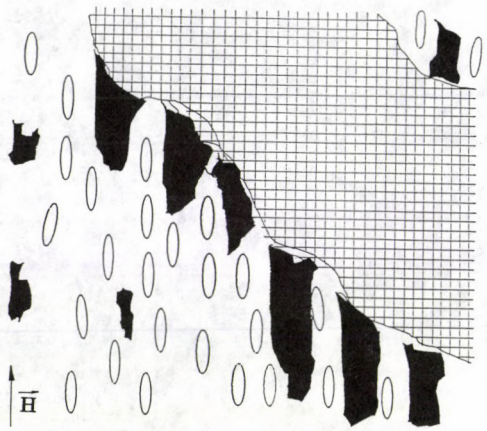

Fig. 3. A sketch of a fragment for the liquid crystal–polymer interface formed after aligning the substance in an external magnetic field. The ellipses represent the LC molecules, the hatched part — the stem of the polymer network and the filled parts — the smaller polymers segregated in the aligned medium

(decomposition driven by a strong chemical reaction) an interconnected network is formed even in the dilute case. The third type of decomposition in titanium–hydrogen can be ascribed to an ordering procedure, when during relaxation the hydrogen atoms arrange into well defined positions and a separation of the ordered phases occurs. The common feature, however, for the above systems is that their morphology can be characterized by correlations in a scale of a few and up to a few tens of nanometers.

Acknowledgements

This work was partly supported by the OTKA grant 2951 in Hungary and the FFwF in Austria.

References

1. R. Glas, O. Blaschko, L. Rosta, Phys. Rev., *B 46*, 5972, 1992.
2. I. O. Bashkin, A. I. Kolesnikov, V. Yu. Malishev, E. G. Ponyatovsky, S. Borbély, L. Rosta, G. Pépy, J. de Physique, C8, 287, 1993.
3. A. Jákli, L. Bata, K. Fodor-Csorba, L. Rosta, L. Noirez, Liquid Crystals, *17*, 227, 1994.
4. A. I. Kolesnikov, A. M. Balagurov, I. O. Bashkin, V. K. Fedotov, V. Yu. Malishev, G. M. Mironova, E. G. Ponyatovsky, J. Phys.: Condens. Matter, *5*, 5045, 1993.

Acta Physica Hungarica 75 (1-4), pp. 243-246 (1994)

NEUTRON DIFFRACTION INVESTIGATION OF THE CATIONIC DISTRIBUTIONS IN $Me_xCo_{3-x}O_4$ (Me = Cu, Mg, Zn) SPINELS

K. KREZHOV and P. KONSTANTINOV

Institute for Nuclear Research and Nuclear Energy, Bulgarian Academy of Sciences
72 Tzarigradsko Chaussee blvd, 1784 Sofia, Bulgaria

Results from neutron powder diffraction investigations of the crystal structure of some binary metal-cobalt oxide spinels with the general formula $Me_xCo_{3-x}O_4$ (Me = Cu, Mg, Zn), $0 < x < 1$ are reported and discussed. The Vegard law for solid state solutions was found to have place. A partly inverse cubic spinel structure was established for all compositions in the systems studied. The behaviour of the structural parameters is discussed on the basis of the cationic formulae accounting for the quantitative distribution of metal ions among the tetrahedral and octahedral lattice sites.

Introduction

The distribution of metal ions among the tetrahedrally coordinated (A) and the octahedrally coordinated (B) interstices in the cubic close packed array of oxygen ions of the crystal structure of spinels is of continuing interest in connection with the general understanding of their electric and magnetic properties. Several types of ordering can take place in this structure. Spinels with divalent cations in only A or only B lattice sites are called 'normal' or 'inverse', respectively. The 'disordered' spinel where different ion species, e.g. divalent and trivalent cations, are divided statistically between the two crystallographic sites is a special case of the most common 'partly inverse' spinels, for which the actual distribution generally deviates from the random one and reflects the preference of some cations to enter a certain site.

In this paper we discuss some results of our recent studies on the cationic distribution in $Me_xCo_{3-x}O_4$ (Me = Cu, Mg, Zn) spinels by neutron diffraction. The virtues of using this technique to locate oxygen and to distinguish site occupancies by nuclei of elements with close atomic number are well known.

Experimental part

These cobalt oxide-based systems have a low thermal stability which prevents the application of conventional ceramic techniques for spinel preparation. Therefore, monophase $Me_xCo_{3-x}O_4$ samples were obtained by an alternative method [1] under 'soft' thermal conditions by using appropriate precursors with a specific layered structure. Details about preparation and characterization of the samples can be found elsewhere [2, 3, 6].

The neutron diffraction data were collected on loosely pressed samples in thin walled vanadium containers by means of two-axis diffractometers at the steady

Table I

Dependence of the lattice cell parameter, a_0, oxygen parameter, u, tetrahedral (A) and octahedral (B) site occupancies of $Me_xCo_{3-x}O_4$ (Me = Cu, Mg, Zn) spinels on the metal (Me) content, x, in the formula unit

				Occupancies A			Occupancies B		
Me	x	a_0, Å	u	Me^{2+}	Co^{3+}	Co^{2+}	Me^{2+}	Co^{3+}	R %
	0.0	8.0835(6)[9]	0.389(1)			1.00		2.00	2.4
	(Co_3O_4)	8.065[10]	0.388			1.00		2.00	4.7
		8.0819(3)[11]	0.388(1)			1.00		2.00	3.1
Mg	0.379(4)	8.1006(6)	0.3880(1)	0.18(2)	0.20(2)	0.62(2)	0.20(2)	1.80(2)	2.5
	0.582(3)	8.1143(5)	0.3875(1)	0.23(2)	0.35(2)	0.42(2)	0.35(2)	1.65(2)	2.5
	0.675(7)	8.1211(7)	0.3870(2)	0.22(3)	0.46(3)	0.32(3)	0.46(3)	1.54(3)	2.8
	0.868(8)	8.134(1)	0.3865(2)	0.19(3)	0.68(3)	0.13(3)	0.68(3)	1.32(3)	2.7
	0.925(6)	8.139(1)	0.3859(3)	0.20(4)	0.73(4)	0.07(4)	0.73(4)	1.27(4)	2.3
Cu	0.15(4)	8.0857(5)	0.3886(1)	0.08(2)	0.07(2)	0.85(4)	0.07(2)	1.92(2)	5.0
	0.27(3)	8.0909(5)	0.3883(1)	0.12(1)	0.15(2)	0.73(3)	0.15(2)	1.85(2)	4.8
	0.37(5)	8.0979(5)	0.3879(1)	0.15(2)	0.22(3)	0.63(5)	0.22(3)	1.78(3)	5.4
	0.56(4)	8.1084(5)	0.3873(1)	0.22(2)	0.34(2)	0.44(4)	0.34(2)	1.66(2)	5.7
	0.75(3)	8.1203(5)	0.3869(1)	0.28(1)	0.47(2)	0.25(3)	0.47(2)	1.53(2)	4.5
	0.95(4)	8.1334(5)	0.3862(1)	0.38(2)	0.57(2)	0.05(4)	0.57(2)	1.43(2)	5.3
Zn	0.576(6)	8.0881(7)	0.3886(1)	0.53(1)	0.04(1)	0.42(1)	0.04(1)	1.96(1)	2.3
	0.686(8)	8.0926(7)	0.3884(1)	0.62(1)	0.06(1)	0.31(1)	0.06(1)	1.94(1)	2.5
	0.79(1)	8.0944(7)	0.3883(1)	0.68(1)	0.11(1)	0.21(1)	0.11(0)	1.89(1)	2.3
	0.964(9)	8.1007(7)	0.3882(1)	0.80(1)	0.16(1)	0.04(1)	0.16(1)	1.84(1)	2.3
	0.99(1)	8.1019(7)	0.3881(1)	0.79(1)	0.20(1)	0.01(1)	0.20(1)	1.80(1)	2.3

Data refined using the following neutron nuclear scattering amplitudes: $b_{Co} = 0.253$, $b_{Mg} = 0.5375$, $b_{Cu} = 0.7718$, $b_{Zn} = 0.5480$, $b_O = 0.5805$ (10^{-12} cm) [7]. For the case of $Zn_xCo_{3-x}O_4$ the most recent value $b_{Co} = 0.249$ [8] was used.
Standard deviations referred to the last significant digit are given in parentheses.
Profile reliability factors $R = (\Sigma_i |I_i^{exp} - I_i^{calc}|)/\Sigma_i I_i^{exp}$.
Space group $Fd3m$, origin at $\bar{3}m$. Positions: O in 32e, Me(A) in 8a, Me(B) in 16d.

state research reactors IRT-Sofia and WWR-Řež near Prague as well as the DN-2 time-of-flight spectrometer at the pulsed reactor IBR-2 at Dubna.

All compositions of the systems studied are paramagnetic at room temperature, so that only nuclear Bragg reflections are revealed in the diffraction pattern. The structural parameters were refined by INVPAR [4] code using the integrated intensities of $Cu_xCo_{3-x}O_4$ [2] or by MRIA [5] code applying the full profile analysis of the TOF diffraction patterns of $Mg_xCo_{3-x}O_4$ [3] and $Zn_xCo_{3-x}O_4$ [6] spinel systems.

Results and discussion

Table I shows the results of the structural analysis and compares it to the structure of Co_3O_4 which is a known representative of normal spinels.

An important feature is that the variation of the quantity of Me-cations in

B-sites and A-sites in dependence on composition x is linear. The amounts Me(B) and Me(A) were calculated from the scattering amplitudes of the effective scatterers in B- and A-sites, denoted by b_B and b_A, respectively, refined as either independent variables or parameters constrained through composition. Using the refined values of b_B and b_A, from the condition for electrical neutrality one comes to the site occupancies given in Table I which satisfy the ionic chemical formula

$$Me^{2+}_{x-\alpha}Co^{2+}_{1-x}Co^{3+}_{\alpha}[Co^{3+}_{2-\alpha}Me^{2+}_{\alpha}]O^{2-}_4,$$

where ions in B lattice sites are enclosed in brackets and formal valences of the cations are taken into account. Thus, all compositions in the systems under study are partly inverse spinels.

The Vegard law for continuous solid state solutions was found to have place. Linear regression analysis shows that a straight line can be safely drawn through the particular set of lattice constants a against Me-content x for each one of the systems studied. Being with different slopes the lines $a = f(x)$ have intercepts close to the ASTM value of the lattice constant of Co_3O_4 ($x = 0$).

With increasing Me-content the oxygen parameter u was found to decrease from the value 0.389 attributed to Co_3O_4 in the literature but remaining ever higher than the ideal value 0.375 calculated in the frames of the hard spheres model of the close packed FCC oxygen lattice. This implies that with increasing x the oxygen anions shift along the cube diagonals ([111] directions) causing the octahedral interstices to enlarge at the expense of the tetrahedral interstices.

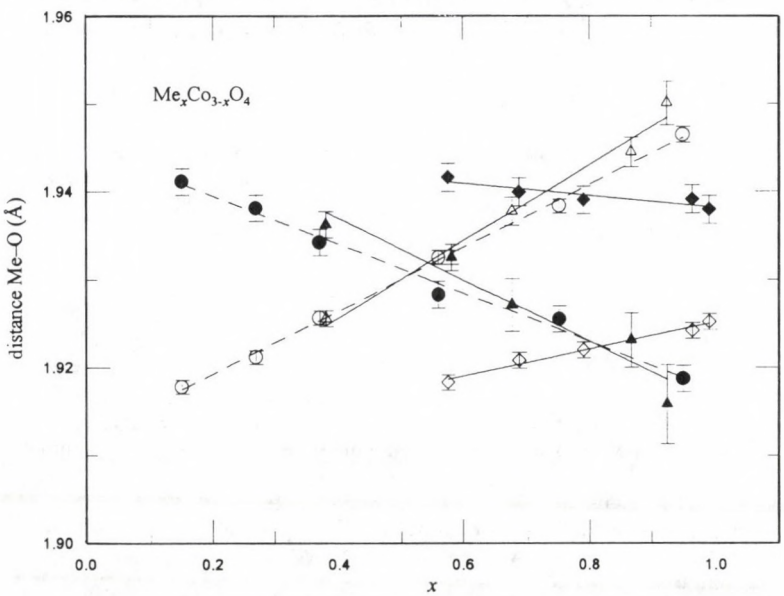

Fig. 1. Dependence of the average distances between oxygen and the metal cation in tetrahedral (black symbols) and octahedral (hollow symbols) sites on composition x. Symbols used: △, ▲ — $Mg_xCo_{3-x}O_4$, ○, ● — $Cu_xCo_{3-x}O_4$, ◇, ◆ — $Zn_xCo_{3-x}O_4$. The lines are drawn only to guide the eye.

The behaviour of the dependence of the tetrahedral and the octahedral bond lengths on composition depicted in Fig. 1 is consistent with the cationic distribution described by the relevant ionic formula of the particular spinel system. Taking into account the effective ionic radii, the smooth decrease of tetrahedral and the increase of the octahedral bond length can be understood as a consequence of the presence of bigger divalent ions in the octahedral interstices. This conclusion is supported by the small effect observed in the case of $Zn_xCo_{3-x}O_4$ compositions, which remain almost normal spinels.

As a matter of fact, the slopes of the straight lines, which describe the dependencies $Me(B) = f(x)$ and $Me(A) = f(x)$, reflect in a direct way the distribution of cobalt and Me-cations. Hence, all compositions from the $Cu_xCo_{3-x}O_4$ system are disordered spinels because a statistical distribution of Cu^{2+} among A- and B-sites is inferred form the line slopes which are very close to 1/3 and 2/3, respectively. The conclusion for a random distribution of copper is in agreement with the observed cubic macrosymmetry of $Cu_xCo_{3-x}O_4$ and helps understand the absence of the cooperative Jahn–Teller effect under the assumption that the static deformations associated with Cu^{2+} ions occupying both A and B sites have opposite directions. On the other hand, the slopes of the dependencies of Zn^{2+} (A) and Zn^{2+} (B) on x point that there is a strong preference of Zn^{2+} to enter A lattice sites. This effect well known for site occupancies of zinc cations in the ferrites, takes place in the cobaltites studied, too. The maximum fraction of Zn in the octahedral sites does not exceed 0.2, so that Zn cobaltites investigated are rather normal than inverse. Finally, the fraction of Mg^{2+} ions occupying A-sites is found to be almost independent of x over the range of compositions studied. Therefore, there is a limit to the occupancy of A-sites by Mg.

Acknowledgements

The authors express their gratitude to Prof. Petrov for kindly providing samples and for illuminating discussions, as well as to Dr. S. Neov and Dr. A. Balagurov for valuable help with the neutron data collection. The partial financial support of the National Fund for Scientific Research of Bulgaria is gratefully acknowledged.

References

1. L. Markov, K. Petrov and R. Ioncheva, Zh. Neorg. Khim., *30*, 3023, 1985.
2. K. Petrov, K. Krezhov, P. Konstantinov, J. Phys. Chem. Solids, *50*, 577, 1989.
3. K. Krezhov and P. Konstantinov, J. Phys.: Cond. Matter, *4*, L543, 1992.
4. K. Krezhov, K. Petrov, T. Karamaneva, J. Sol. St. Chem., *48*, 33, 1983.
5. B. V. Zlokazov and V. V. Chernyshov, Communications of JINR, 1990 P10-90-315 Dubna, Russia.
6. K. Krezhov and P. Konstantinov, J. Phys.: Cond. Matter, *5*, 9287, 1993.
7. L. Koester and H. Rauch, International Atomic Energy Agency, Report 2517/RB, 1981.
8. L. Koester, H. Rauch and E. Seymann, Neutron News, *3*, 38, 1992, Fold-out table of neutron scattering lenghts.
9. O. Knop, K. I. G. Ried, Sutarno and I. Nakagawa, Canad. J. Chem., *46*, 3463, 1968.
10. W. L. Roth, J. Phys. Chem. Solids, *25*, 1, 1964.
11. K. Petrov, I. Karamaneva, S. Angelov and D. Mehandjiev, Mater. Res. Bull., *18*, 637, 1983.

Acta Physica Hungarica 75 (1–4), pp. 247–252 (1994)

WAVELENGTH DEPENDENT NEUTRON DEPOLARIZATION IN SOFT MAGNETIC AMORPHOUS RIBBONS

K. KREZHOV, V. LILKOV[1] and P. KONSTANTINOV

Institute for Nuclear Research and Nuclear Energy, Bulgarian Academy of Sciences
72 Tzarigradsko Chaussee blvd, 1784 Sofia, Bulgaria
[1] *University of Mining and Geology*
Sofia Darvenitza, Bulgaria

Results from bulk domain structure determination by analysing the wavelength dependent depolarization of a polychromatic beam of polarized neutrons transmitted through soft magnetic ribbons are presented and discussed. Information on mean magnetization, static magnetization fluctuations, and magnetic anisotropy was obtained for amorphous ferromagnetic ribbons of composition $Fe_{78}Co_{8.1}B_{13.9}$ and $Fe_{56.2}Co_7Ni_{15.6}Si_4B_{17.2}$ taken as examples. Under favourable circumstances even simple models of the domain structure are found satisfactory as in the case of carefully demagnetized samples. However, more complex modes are shown to be reasonable in describing the change in bulk magnetization state probed by the neutrons.

Introduction

The theories describing the effect of neutron depolarization by a multidomain ferromagnet predict on the basis of procedures for statistical averaging under some restricting assumptions that the logarithmic depolarization is proportional to the square of wavelength λ or remains practically λ-independent [1, 2]. However, the magnetic ribbons are thin enough so that to throw doubts upon such an approach since just a few domains are likely to be crossed along the neutron trajectory. This makes more appropriate to test particular domain structure models by calculating directly the loss in polarization which they invoke and by comparing the results with the experimental data. Recently [3, 4] we have shown the feasibility of using this approach in studying samples of amorphous ribbons based on the 3-d metal-metalloid composition. In particular cases some simple analytical models, e.g. the model of domains penetrating the bulk [4], were found satisfactory in explaining some of the recorded depolarization data. The discussion here is extended towards more complex models which describe the depolarization behaviour over the useful range of wavelengths.

Experimental part

The samples were prepared by planar flow casting [5]. The basic static magnetic characteristics were determined by regular macroscopic magnetic measurements. Some preliminary neutron measurements were performed on the neutron

polarimeter of the reactor IRT-Sofia [5]. The λ-dependent depolarization was determined from flipping ratio measurements using the TOF spectrometer SPN of JINR, Dubna [4]. The data for the D_{zz} component of the depolarization matrix, i.e. $D_{zz} = f(\lambda)$, were recorded for two geometries of the sample orientation with respect to incident polarization vector $\mathbf{P}$ neutron velocity $\mathbf{v}$.

First, the perpendicular transmission at zero applied magnetic field $\mathbf{B}_{\text{ext}}$ was measured on a sample with ribbon axis set parallel to $\mathbf{P}_0$ and the normal of a particular marked surface area pointing along $\mathbf{v}$. Next, the sample was inclined so that $\mathbf{P}_0$ and the normal vector to the sample surface make an angle $\pi/2 - \alpha_0$, and $\mathbf{B}_{\text{ext}}$ parallel to $\mathbf{P}_0$ was applied. From the angular frequency ω_λ of the depolarization oscillations with λ at an applied $\mathbf{B}_{\text{ext}}$ sufficiently high to bring the sample into saturated state, the saturation induction $\mathbf{B}_0$ was estimated.

Theoretical models, results and discussion

The wavelength dependent depolarization of upright samples proved to be very sensitive to the magnetization state of the samples: the λ-dependence changed from the $\exp(-A\lambda^2)$ law to strongly damped or nearly undamped cosine dependencies. It is well known [6] that the planar flow casting used to fabricate amorphous ribbons causes internal stresses and in as-cast material the microscopic domain structure reflects their local distribution. Tensile stresses give rise to regions of wide domains with magnetization oriented in the direction of the principal stress component. Compressive stresses involve domains occupying a fraction of the ribbon volume wherein the magnetization is oriented perpendicular to the ribbon surface. Thus, an out-of-plain anisotropy is created mainly due to the magnetoelastic effect.

In view of the above mentioned experimental facts we tested a theoretical model expressed as the sum of two terms

$$D_{zz} = (1-c)D_{zz}^{(1)} + cD_{zz}^{(2)}, \tag{1}$$

where c denotes the fraction of a particular domain structure type.

The validity of the assumed domain structure was checked by means of a nonlinear least squares fitting procedure. The conventional χ^2 factor was used as one of the possible criteria for goodness-of-fit. Additionally, the consistency of the mean induction derived from the fit and the value obtained from macroscopic magnetic measurements has been checked.

The following models of a particular domain structure were put in combination:

a. the model of penetrating domains [4] which extend throughout the ribbon thickness

$$D_{zz} = \frac{1-\cos^3\alpha}{3(1-\cos\alpha)} + \frac{2-\cos\alpha(3-\cos^2\alpha)}{3(1-\cos\alpha)}\cos\Phi_\lambda \frac{\sin CB_{av}\frac{\Delta d}{2}\lambda}{CB_{av}\frac{\Delta d}{2}\lambda}, \tag{2}$$

where $\Phi_\lambda = CB_{av}\delta\lambda$ is the angle of neutron spin precession within a domain, $C = 4.63 \cdot 10^{-5}$ for B in G, δ in μm, and the wavelength λ in nm, Δd is

the uncertainty in sample thickness d, or in domain size δ, since $\delta = d$. The magnetic induction of individual domains B_i is approximately equal to the mean induction of the medium ($B_i \approx \langle B \rangle = B_{av}$). Here α is the maximum angular deviation of local $\mathbf{B}_i$ from $\mathbf{P}_0$.

b. the model of a sandwich-like domain structure of Landau–Lifschitz type, with closure domains at opposite faces of the specimen magnetized either parallel or antiparallel [9,10].

$$D_{zz} \approx \frac{2}{3}(\Delta\Theta)\frac{d}{\delta'}\left[\frac{\sin\Phi_\lambda}{\Phi_\lambda} - \cos\Phi_\lambda\right] + \cos\Phi_\lambda, \tag{3}$$

where $\Delta\Theta$ is a parameter describing the disorientation of main domains and δ' is the closure domain height.

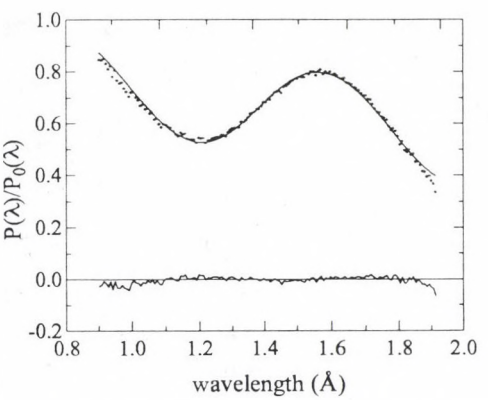

Fig. 1. D_{zz} vs neutron wavelength for a sample $Fe_{56.2}Co_7Ni_{15.6}Si_4B_{17.2}$ in $B_{ext} = 345\ G$, $\alpha_0 = 30°$; points: measured intensities, full line: calculated curve, reduced $\chi^2 = 1.08$. The difference (measured minus calculated) curve is also shown. Best fit parameters: $\langle B \rangle = (8412 \pm 6)G$, $B_0 = (8100 \pm 7)G$, $\alpha = 25°12' \pm 11'$, $\alpha_1 = 3°52' \pm 39'$, $\langle \Delta B \rangle = 533 \pm 49)G$, $(\langle \Delta B_\perp^2 \rangle \delta)^{1/2} = (3973 \pm 110)G \cdot \mu m^{1/2}$

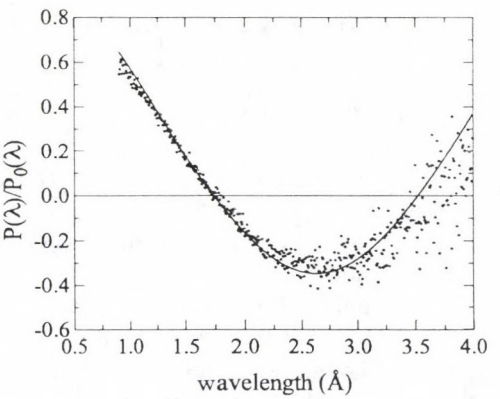

Fig. 2. D_{zz} vs neutron wavelength for a carefully demagnetized sample $Fe_{78}Co_{8.1}B_{13.9}$ in $B_{ext} = 0\ G$, $\alpha_0 = 0°$: points: measured intensities, full line: calculated curve, reduced $\chi^2 = 0.7$. Best fit parameters for the model of penetrating domains: $B_{av} = (5760 \pm 16)G$, $\alpha = 167°48' \pm 1°48'$

c. a model of a specimen magnetized along z-axis ($B_z = \text{const} \neq 0$) for which the other two components of magnetization remain uncorrelated, i.e. B_x and B_y are randomly distributed in the plane perpendicular to z-direction. The

z-component of magnetic domain induction may originate from an applied magnetic field or a single axis magnetic anisotropy present [12,11].

$$D_{zz}\left[1-(1-\cos\Phi_\lambda)\left(1-\frac{\langle B_z^2\rangle}{\langle B\rangle^2}\right)\right]^{d/\langle\delta\rangle}, \tag{4}$$

where $\Phi_\lambda = C\langle B\rangle\langle\delta\rangle\lambda$ is the net rotation angle of the neutron spin within a single magnetic domain of an average size $\langle\delta\rangle$ along the neutron flightpath, d is the sample thickness, and λ is the neutron wavelength.

The oscillation of the measured depolarization $D(\lambda) = P(\lambda)/P_0(\lambda)$ with wavelength in the case of inclined samples in applied $\mathbf{B}_{ext}$ has been approximated using a least squares fitting procedure by

$$P(\lambda)/P_0(\lambda) = e^{-A_1\lambda^2}\cos^2\alpha + e^{-A_2\lambda^2}\sin^2\alpha\frac{\cos(\omega_\lambda\lambda - \arctan\omega_0\tau_0)}{\sqrt{(\omega_0\tau_0)^2+1}},$$

or

$$= P(\lambda)/P_0(\lambda) = e^{-A}\left\{\cos^2\alpha + e^{-A_3\lambda^2}\sin^2\alpha\frac{\cos(\omega_\lambda\lambda - \arctan\omega_0\tau_0)}{\sqrt{(\omega_0\tau_0)^2+1}}\right\}, \tag{5}$$

according to the theoretically derived formulae [4], wherein $\omega_\lambda = C\langle B\rangle d_{eff}$, $d_{eff} = d/\cos\alpha_0$, $\omega_0 = 1.83\cdot 10^4\langle B\rangle(d_{eff}/L)$, L is in meters, and $\arctan\omega_0\tau_0$ is added to describe the phase shift due to the uncertainty in the precession angle caused by the actual width of neutron pulses τ_0. The mean induction of the sample is $\langle\mathbf{B}\rangle = \mathbf{B}_0 + \mathbf{B}_{ext}$. The explicit form of the quantities A, A_1, A_2 and A_3 reflects the domain model in a given magnetization state and depends on the magnitude of the angle of polarization vector precession within a domain.

Figure 1 shows an example of the measured oscillation curves in applied magnetic field and the fitted curves using the parameters given in Table I. The calculated small values of the angle α_1 imply that in state of complete saturation the magnetic induction of the samples of both compositions is oriented slightly out of the sample surface. This means that there is a magnetic anisotropy whose axis essentially lies in the ribbon plane and a small contribution of a term perpendicular to the surface as it should be expected [6].

As a matter of fact, Fig. 1 displays the results obtained on a stack of three ribbon pieces rather than on a single piece as Figs. 2, 3 and 4 show. The best fit parameters are given in the captions of the Figures.

Insofar as the case of $Fe_{78}Co_{8.1}B_{13.9}$ has been discussed earlier [4], here we shall summarize briefly the results of fitting formula (1) to the oscillation curves $D_{zz} = f(\lambda)$ of $Fe_{56.2}Co_7Ni_{15.6}Si_4B_{17.2}$ in different magnetization states as follows:

1. $Fe_{56.2}Co_7Ni_{15.6}Si_4B_{17.2}$ in remanent state of known history
   - the limit cases by using only individual domain structure models described by formulae (2), (3), and (4) gave high χ^2 values, namely 8.25, 29, and 8.3, respectively;

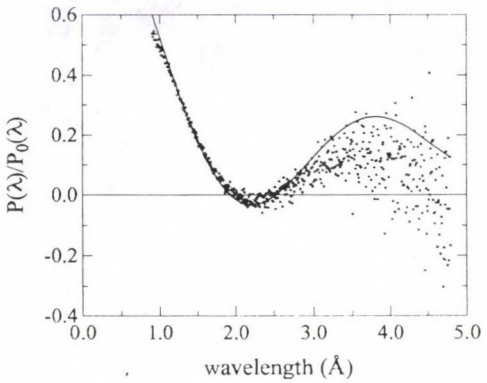

Fig. 3. Wavelength dependence of the depolarization by a not completely demagnetized sample $Fe_{56.2}Co_7Ni_{15.6}Si_4B_{17.2}$ in zero field: points – measured intensities, line – calculated curve using the model combinations between sandwich-like LL domains: $\langle B \rangle = (7530 \pm 20)G$, $\Delta\Theta/\delta' = (30.27 \pm 0.08) \cdot 10^{-3}$ rad $\cdot\, \mu m^{-1}$ and a fraction $(1 - c) = 0.28$ of penetrating domains: $B_{av} = \langle B \rangle$, $\alpha = 63°54' \pm 24'$. Reduced $\chi^2 = 1.5$

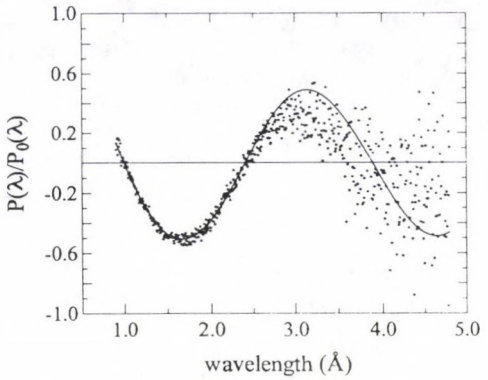

Fig. 4. Wavelength dependence of the depolarization by a carefully demagnetized sample $Fe_{56.2}Co_7Ni_{15.6}Si_4B_{17.2}$ in zero field: points – measured intensities, line – calculated curve using the model of Landau–Lifschitz sandwich-like domains: $\langle B \rangle = (7610 \pm 15)G$, $\Delta\Theta/\delta' = (13.30 \pm 0.07) \cdot 10^{-3}$ rad $\cdot\, \mu m^{-1}$. Reduced $\chi^2 = 0.92$

- the combination of models (2) and (4) improved the χ^2 value ($\chi^2 = 1.3$). The domain size was estimated as $\delta \approx 0.5d$. However, the estimate of $\langle B \rangle = 6280$ G remained well below the values $B_S = 7700$ G from magnetization measurements and $B_0 = 8100$ G from the angular frequency ω_λ of the oscillations in applied field;
- the best fit in terms of both $\langle B \rangle$ and χ^2 is presented in Fig. 3. As it is to be expected, the estimated angle $\alpha \approx 64°$, which measures the deviations of individual domain induction vectors B_i from the direction of incident polarization $\mathbf{P}_0$, is much lower than $\alpha = 180°$ which should correspond to orientations of local $\mathbf{B}_i$ fully at random.

2. $Fe_{56.2}Co_7Ni_{15.6}Si_4B_{17.2}$ in demagnetized state

   The demagnetization was carried out on the in-beam sample placed within a magnetizing coil by decreasing gradually the amplitude of the alternate magnetic field from 1600 A$\cdot$m^{-1} to zero. The three possible combinations have been checked. To a certain extent the combination of formulae (2) and (4) produced a satisfactory result in case of fixed low fraction of penetrating domains (less than 5 %), but when taken as an independent parameter

the fraction of penetrating domains became zero and the fitting procedure converged to the result displayed in Fig. 4.

Table I

Depolarization parameters derived from $D_{zz} = f(\lambda)$ curve fitting: α – angle between $\mathbf{P}_0$ and $\langle \mathbf{B} \rangle$, $|\langle \mathbf{B} \rangle| = |\mathbf{B}_0 + \mathbf{B}_{ext}|$, α_1 – angle between $\mathbf{B}_0$ and sample surface, $\langle \Delta \mathbf{B}_\perp^2 \rangle$ – perpendicular component of mean square induction fluctuations, $\langle \Delta \mathbf{B} \rangle$ – estimate of the mean induction inhomogeneity. $B_{ext} = 345$ G, d – full thickness, B_S – saturation induction measured with magnetometer. The sample surface is inclined under an angle $\alpha_0 = 30°$ with respect to $\mathbf{P}_0 \parallel \mathbf{B}_{ext}$

Composition	d	B_S	$\langle B \rangle$	B_0	α	α_1	$\langle \Delta B \rangle$	$\left(\frac{\langle \Delta B_\perp^2 \rangle}{\delta}\right)^{1/2}$	$(\langle \Delta B_\perp^2 \rangle \delta)^{1/2}$
	μm	G	G	G			G	G/μm$^{1/2}$	G/μm$^{1/2}$
$Fe_{78}Co_{8.1}B_{13.9}$	45	5600	6150	5834	23°24′	5°12′	176	78.6	–
$Fe_{56.2}Co_7Ni_{15.6}Si_4B_{17.2}$	58.3	7700	8412	8100	25°12′	3°52′	533	–	3973

Finally, it can be noticed that the dispersion in depolarization data is rather high for $\lambda > 3.5$ Å, at present. This is due to the lower incident neutron intensity which requires longer measurement time in the long wavelength region and this is going to be done in future experiments.

In conclusion, it is worth mentioning again that Figs 3 and 4 clearly illustrate the high sensitivity to magnetization state of the wavelength dependent depolarization technique which can be utilized in many fields, e.g. stress dependent domain structure studies we plan to carry out in near future.

Acknowledgement

This work has been financially supported in part by the National Fund for Scientific Research of Bulgaria.

References

1. O. Halpern and T. Holstein, Phys. Rev., *59*, 960, 1941.
2. B. Toperverg and T. Weniger, Z. Phys. *B74*, 105, 1989.
3. K. Krezhov and V. Lilkov, Proc. of 7-th ISCMP, Varna, 1992, World Sci. Publ. Comp., Singapore, 410, 1993.
4. K. Krezhov, V. Lilkov, P. Konstantinov and D. Korneev, J. Phys.: Cond. Matter, *5*, 9277, 1993.
5. K. Krezhov, V. Lilkov, V. Mikhailova, A. Okorokov and V. Runov, Compt. Rend. Acad. Bulg. Sci., *45*, 17, 1992.
6. H. Kronmüller, Phil. Mag. B, *48*, 125, 1983; Phys. Stat. Sol., (b), *127*, 531, 1985.
7. H. Kronmüller and B. Gröger, J. Physique (Paris), *42*, 1285, 1981.
8. W. Fernengel and H. Kronmüller, JMMM, *37*, 167, 1983.
9. W. Kraan and M. Rekveldt, JMMM, *8*, 168, 1978.
10. N. Stüsser, H. Builtjes and M. Rekveldt, JMMM, *67*, 207, 1987.
11. S. Mitsuda and Y. Endoh, J. Phys. Soc. Japan, *54*, 1570, 1985.
12. M. Rekveldt, Z. Physik, *259*, 391, 1973; Textures and Microtextures, *11*, 127, 1989.

Acta Physica Hungarica 75 (1–4), pp. 253–256 (1994)

NEUTRON DIFFRACTION STUDY OF THE SHORT-RANGE ORDER IN TeO_2–M_2O (M = Li, Na, K, Rb) GLASSES

S. NEOV, I. GERASIMOVA, V. KOZHUKHAROV,[1] P. MIKULA[2] and P. LUKÁŠ[2]

Institute for Nuclear Research and Nuclear Energy, Bulgarian Academy of Sciences
72 Tzarigradsko Chaussee blvd, 1784 Sofia, Bulgaria
[1] *Higher Institute of Chemical Technology*
1756 Sofia, Bulgaria
[2] *Nuclear Physics Institute*
25068 Řež near Prague, Czech Republic

The changes of the short-range order in tellurite glasses due to the increasing dimensions of the modifier cations have been studied by neutron diffraction method. To identify the contribution of the different partial RDFs a crystal-like model approach was undertaken.

1. Introduction

New multicomponent tellurite glasses belong to the superheavy flints with refraction indexes of 2.15–2.25 and good transmittance in visible and near IR regions. Intensive investigations of glass forming area [1,2], macroscopic properties [3] and short-range order [4,5] are accomplished. Due to the presence of heavy (Te) and light (O) atoms in these glasses, the neutron scattering [6,7] has a definite advantage over the X-ray and electron diffraction methods.

Detailed structural investigations of alkaline–tellurite glasses are not published. The short-range order in glassy TeO_2–Li_2O system is studied by X-ray [4,8] and neutron diffraction [9]. By EPR method [10] a 4-fold coordination of Te atom in TeO_2–Na_2O glasses is established. The presence of Na^+ ions in the glassy matrix causes the formation of non bridging O atoms and additional trigonal deformation of the TeO_4 complex. During the synthesis process, the kinetic factors influence the atomic arrangement, as well as the chemical properties and atomic dimensions ratio of the glassformer and modifier atoms. The aim of the present study is to follow up the structural evolution of tellurium-oxygen matrix, due to the increasing dimensions of the modifier cations ($R_{Rb} > R_K > R_{Na} > R_{Li}$) in tellurite glasses, containing 15 mol % alkaline oxides as modifier.

2. Experimental procedure

2.1. Materials and glass synthesis

The raw materials: TeO_2 and M_2CO_3 (M= Li, Na, K, Rb) are p.a. purity. Four tellurite glasses containing equal molar quantity (15 mol %) modifying oxide – Li_2O, Na_2O, K_2O and Rb_2O are synthesized. Batches of 30 g quantity were melted in Pt crucibles for 40 min. The syntheses were made in an atmosphere of dry air at 800 °C. The melt was cooled on massive Cu plate. The samples were not annealed following their preparation.

2.2. Neutron diffraction measurements

The neutron structure factors $S(Q)$were measured on TKSN-400 spectrometer, installed on the LVR-15 reactor at the Nuclear Physics Institute, Řež, Prague. The maximal value of the scattering vector is $Q_{max} = 10.8$ Å^{-1}. The obtained $S(Q)$ of studied compositions are presented in Fig. 1.

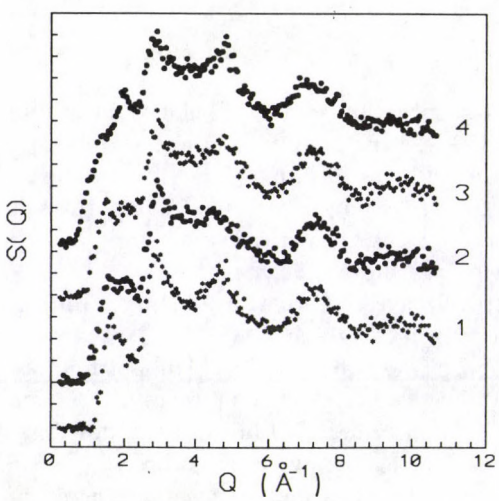

Fig. 1. Neutron structure factors of $85TeO_2+15M_2O$ glasses: M = Li(1), Na(2), K(3), Rb(4)

3. Results and discussion

Because of the dominant TeO_2 content in the glasses, $S(Q)$ are very similar to the structure factor of pure tellurite glass [11]. The increase of the modifier cation dimensions corresponds to the changes of the first interference maximum, which is

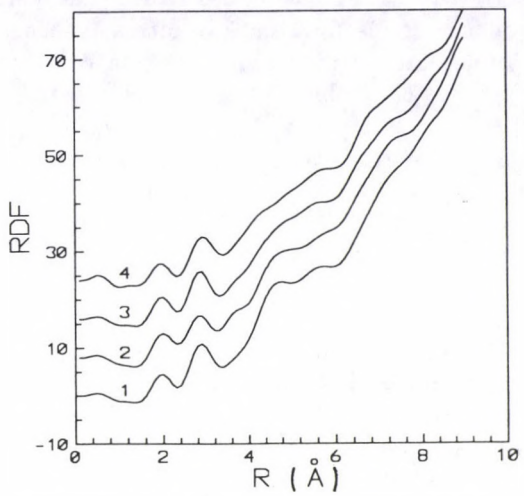

Fig. 2. RDFs of the studied glasses. Curves 1 to 4 denote the same compositions as in Fig.1

divided into two components. The sub peak situated at 1.8 $Å^{-1}$ coincides with the first $S(Q)$peak of pure TeO_2 glass [11] and correspond to the diffraction maxima of α-TeO_2 structure. The second component correlates with the position of (100) reflection of Li_2O, Na_2O, K_2O and Rb_2O crystal structures, respectively. The presence of these interference maxima can be an indication that at low modifier content (< 15–20 mol %) the short-range order (SRO) of the glass-former and modifier persists in the glasses. For reliable interpretation, the experimental RDFs were compared with model RDFs. Because of the absence of compounds in the studied concentration region the model RDFs were calculated starting from the experimental RDF of pure TeO_2 glass and the structures of alkaline oxides (Li_2O, Na_2O, K_2O, Rb_2O). The crystal-like RDFs describe well the first two coordination spheres of the experimental RDFs. For TeO_2–Li_2O system this good correlation is extended to the fourth RDF maximum. The shortest O-alkaline ion distances in the crystal state are R_{Li-O} = 2.00 Å, R_{Na-O} = 2.403 Å, R_{K-O} = 2.787 Å and R_{Rb-O} = 2.802 Å. From these values it follows that the first coordination maximum, situated at 1.88–1.95 Å is due to Te–O arrangement and only in the case of TeO_2–Li_2O glass is it influenced from the shortest Li-O distances (about 6 % from the peak area). The Na–O distances from the first coordination sphere get into the minimum between the P1 and P2 maxima and this is clearly observed in the experimental RDF curves. For K_2O and Rb_2O modifiers the values of O-alkaline ion distances get into the region of the characteristic of α-TeO_2 O-O coordination peak at 2.8 Å. In TeO_2–Rb_2O glass the first RDF's maximum is displaced by $\approx$0.08 Å versus the shorter values and its area diminishes by 20–25 %. At the same time a new maximum at R ~2.3 Å appears. The most probable cause of these changes are

the special features of the basic structural units of the glassformer – TeO_4 trigonal bipyramids. It is established that one of the Te–O axial bonds is not equivalent of the rest three bonds in TeO_4 unit and exhibits a tendency to elongation and breaking off during the glass forming process. At a concentration of 15 mol % Rb_2O we observe the first step of this process, namely the transition from 4 to 3+1 coordination state of the Te atom with respect to oxygen. When Na_2O, K_2O and Li_2O modifiers are used this transition is not registered and the area of the first maximum corresponds to fourfold Te–O coordination.

4. Conclusion

By analogy of alkaline–silicate systems [12,13], the decreasing of the modifier cation dimensions decreases the tendency towards phase separation. The incorporation of the alkaline oxides leads to breaking down of the bonds between TeO_4 bipyramids and localization of the alkaline ions near the deformed TeO_4 groups. In the common case the coordination state of Te atoms remains fourfold.

Acknowledgement

This work was supported by the Bulgarian National Science Fund, Contract No F98.

References

1. W. Vogel and H. Bürger, Silikattechnik, *25*, 205, 1974.
2. A. Yahkin, in: Struktura i Fiziko-Chim. Svoistva Neorg. Stekol., Chimia, Leningrad, 1974, p. 290 (in Russian).
3. O. Breusov, T. Revzina and N. Druz, J. Inorg.Chem., *10*, 1990, 1965 (in Russian).
4. G. Brady, J. Chem. Phys., *24*, 447, 1956.
5. K. Suzuki, Methods of Experimental Physics 23, Part B, Neutron Scattering, 243, 1987.
6. S. Neov, I. Gerasimova, K. Krezhov, B. Sidzhimov and V. Kozhukharov, Phys. Stat. Sol. (a), *47*, 743, 1978.
7. A. C. Wright, C. A. Yarker, P. A. V. Johnson and F. A. Wedgwood, Proc. IVth Int. Conf. Phys. Non-Cryst. Solids, Clausthal-Zellerfeld, 1976, pp. 118–123.
8. G. Brady, J. Chem. Phys., *27*, 300, 1957.
9. S. Neov, V. Kozhukharov, I. Gerasimova, K. Krezhov and B. Sidzhimov, J. Phys. C (Solid State Phys.), *12*, 2475, 1979.
10. D. Galimov, A. Sherstjuk, D. Judin and A. Yahkin, J. Struct. Chem. *12* (3), 408, 1971.
11. S. Ishmaev, S. Neov and V. Kozhukharov, unpublished results.
12. A. F. Andersen and S. Urnes, Phys. and Chem. of Glasses, *1*, 399, 1975 (in Russian).
13. W. Vogel, Phys. Stat. Sol., *14*, 255, 1966.

Acta Physica Hungarica 75 (1-4), pp. 257-260 (1994)

PAIR CORRELATION FUNCTIONS OBTAINED FROM VERY SHORT STRUCTURE FACTORS, USING REVERSE MONTE CARLO

L. PUSZTAI and O. GEREBEN

Laboratory of Theoretical Chemistry, Roland Eötvös University
P.O.B. 32, 1518 Budapest, Hungary

It is shown that the Reverse Monte Carlo method [5] is able to provide the correct pair correlation function even if the structure factor is available over only very limited momentum transfer range. The Q range can be as short as 0.5–3 Å^{-1}. In case of a perfect data decreasing the particle diameters (distances of closest approaches) has no effect on the efficiency of the method.

It is widely accepted that if a precise pair correlation function (pcf), $g(r)$, is to be obtained then the diffraction measurement has to be carried out over as large a momentum transfer, Q, range as possible. In order to meet this requirement huge efforts have been, and are currently put in developing new experimental techniques (for a review see e.g. [1]). There are a number of instances, however, where there are severe practical obstacles to making such achievements. For systems of colloidal particles, for example, it is not in general possible to obtain structure factors (sf), $S(Q)$, further than the first (or sometimes part of the second) peak [2]. This limitation makes it impossible to carry out the usual analysis, that is, to obtain $g(r)$ by direct Fourier transformation of $S(Q)$. It is also well known that the shorter the available Q range the more difficult is to obtain details of the structure by the direct transform [3].

It has recently been shown [4] that it is possible to derive the pcf of a dilute polymer latex, even if the structure factor is available over only very limited Q range. In the cited work the Reverse Monte Carlo (RMC) simulation [5] was used for obtaining the pcf.

The basic RMC algorithm has been described elsewhere in detail [5–7], therefore only the relevant parts are mentioned here. In short, RMC moves particles around randomly in the simulation box in order to reproduce a given set of diffraction data within the experimental uncertainties. If the structure factor (or the total coherent scattering function, $F(Q)$) is used as input data then first the pcf for the simulation box, $g^C(r)$, is calculated. From $g^C(r)$ the calculated structure factor, $S^C(Q)$ is obtained by inverse Fourier transformation, and then this $S^C(Q)$ is compared to the experimental structure factor, $S^E(Q)$. In this way truncation errors can only stem from the inadequate system size, i.e. from using too short r, but not too short Q range.

The problem of limited Q space information can be present in other cases, as well, due to, for example, the lack of the most up-to-date equipment. This gives

the issue considerable practical importance. On the other hand, it is also intriguing how much the ($Q \to \infty$) structure factor of infinite in principle is really needed for obtaining precise pair correlation functions. In order to clarify this problem the following model calculations, involving the Reverse Monte Carlo technique, have been performed.

The general strategy of our approach was to take experimental (or model) structure factors initially and then to generate shorter and shorter versions of them. This has mostly been done by chopping off roughly 2 $Å^{-1}$ parts from the high Q end of the sf's. Resulting structure factors from every stage of the above shortening have been handled as independent 'experimental' results, and have been modelled by RMC. The calculations were started from identical initial configurations. Pair correlation functions obtained by RMC from the structure factors of the same system, but of different Q ranges have then been compared to the original $g(r)$. The shortening procedure has continued until substantial deviations were observed in these comparisons.

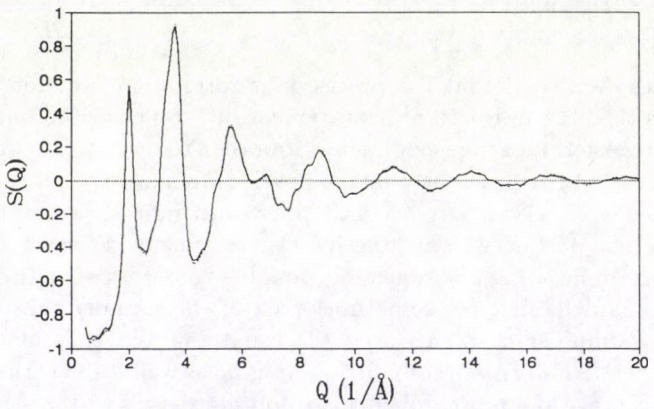

Fig. 1. 'Experimental' (dotted line) and calculated (solid line) structure factors of the system (amorphous silicon) over the Q range between 0.4 and 20 $Å^{-1}$

The data set taken as start was the neutron diffraction (ND) measurement of Kugler et al on amorphous silicon [8]. The data have been analysed by RMC previously (see [8]). In order to assure total independence of problems of technical nature, corresponding to the evaluation of experiments, hereafter not the original data but the RMC fits to the data will be considered as model data set. In this way the presence of particle configurations, that are consistent with the data, is also guaranteed.

The use of $N = 1728$ particles with the number density of $\varrho_0 = 0.050$ $Å^{-3}$ resulted in a box length, L, of about 30 Å. This system size proved sufficient for modelling in Q space. In all the calculations 500000 accepted moves were completed, starting from an identical initial configuration, which was a diamond lattice.

The original structure factor of a-Si [8] was measured between 0.4 $Å^{-1} \geq Q \geq 23$ $Å^{-1}$. The structure factor used in this study, which is a result of an RMC calculation, can be seen in Fig. 1. Within the above region 9 more stages were generated, with structure factors between 0.4 $Å^{-1}$ and 20, 17, 14, 11, 8, 6, 4.35, 3.8

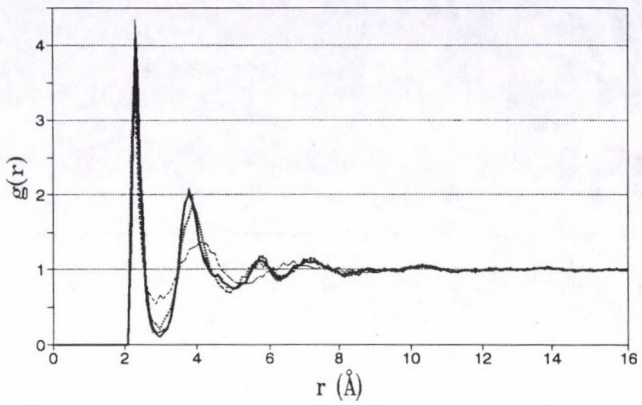

Fig. 2. Pair correlation functions of the system obtained over the Q range between 0.4 and 23 (solid), 11 (dotted line), 6 (heavy solid line), 4.35 (heavy dotted line) and 2.6 (dashed line) $Å^{-1}$

and 2.6 $Å^{-1}$. As it is evident from Fig. 2, differences between pcf's based on short and the original sf's become visible only when the upper limit decreases down to 4.35 $Å^{-1}$ (!). The two $g(r)$'s are clearly different when the upper limit is 2.6 $Å^{-1}$. This effectively means that using RMC the first two peaks of the structure factor are sufficient for reproducing the correct pair correlation function. This is most surprising in this highly ordered system, where a substantial amount of information seems to hide at higher Q values (see Fig. 1).

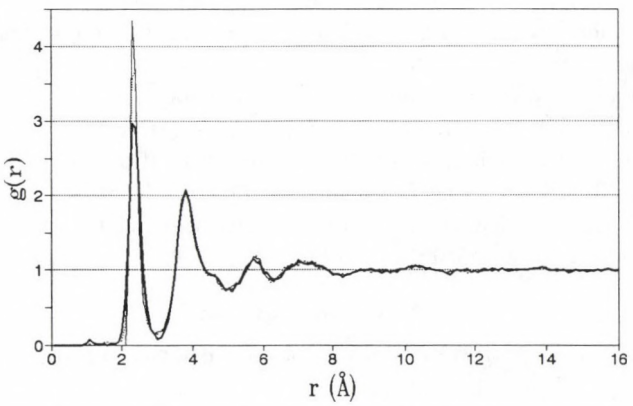

Fig. 3. Pair correlation functions of the one system obtained over the Q range between 0.4 and 23 (solid), 11 (dotted line), 6 (heavy solid line). The particle diameter was $\Delta = 2.2$ Å in the first case, whereas in the latter two cases it was $\Delta = 1.0$ Å

In order to demonstrate that a good quality ('perfect' in our case) data contains the first neighbour distance uniquely, further calculations have been performed with reduced particle diameters. Results from this series can be seen in Fig. 3. It is evident that using data between 0.4-6.0 $Å^{-1}$ the correct $g(r)$ is not influenced. This is a strong indication that even this important piece of information, the correct first neighbour distance, is incorporated in shorter parts of the full structure factor.

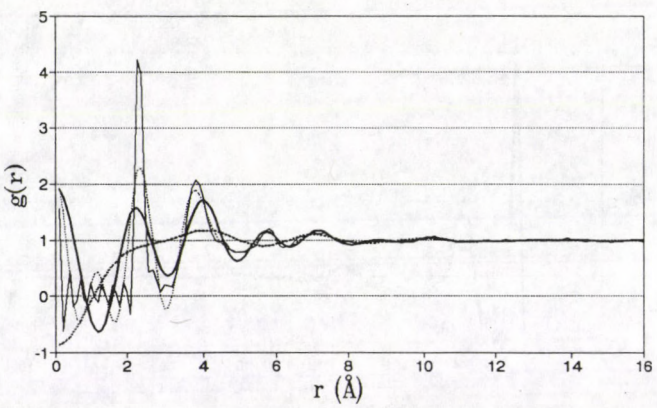

Fig. 4. Pair correlation functions of the system obtained by the direct Fourier transformation of structure factors over the Q range between 0.4 and 23 (solid), 6 (dotted line), 4.35 (heavy solid line) and 2.6 (heavy dots) $Å^{-1}$

We have also calculated the pair correlation functions as direct Fourier transforms of the corresponding ('shortened') structure factors. Some of these pcf's are shown in Fig. 4. Already when using 6 $Å^{-1}$ as upper limit the ratio of the first two peaks has drastically altered. It should be noted that no smoothing was applied: it would have flattened the curve further, although the low r parts would have become more reliable.

It seems that in principle short parts of the full (i.e. extending up to $Q = \infty$) structure factor are sufficient for reproducing the correct r space information. It has been established here, using a rather difficult model system, that the first two peaks of the structure factor define the basic features of the pair correlation function. This evidence reflects the well known fact that *each* point of the structure factor contains contributions from the *full* pair correlation function.

The work described here might have some impact on the trends of analysing and measuring diffraction data from disordered materials. It has clearly been shown that RMC is more reliable than the direct Fourier transform method when the momentum transfer range is limited.

Acknowledgment

This work has been supported by OTKA Grants No. F 4320 and F 7218.

References

1. J. C. Dore, IOP Conference Series, *101*, 1, 1989.
2. See e.g. R. H. Ottewil, Progr. Colloid Polym. Sci., *67*, 71, 1980.
3. E. Sváb, N. Kroó, S. N. Ishmaev, I. P. Sadikov and A. A. Chernyshov, Solid State Comm., *44*, 1151, 1982.
4. G. Tóth and L. Pusztai, J. Phys. Chem., *96*, 7150, 1992.
5. R. L. McGreevy and L. Pusztai, Molec. Sim., *1*, 359, 1988.
6. R. L. McGreevy and L. Pusztai, Proc. Roy. Soc. A, *430*, 241, 1990.
7. R. L. McGreevy, M. A. Howe, D. A. Keen and K. Clausen, IOP Conference Series, *107*, 165, 1990.
8. S. Kugler, L. Pusztai, L. Rosta, P. Chieux and R. Bellisent, Phys. Rev. B, *48*, 7685, 1993.

Acta Physica Hungarica 75 (1–4), pp. 261–265 (1994)

INVESTIGATIONS ON THE STRUCTURE OF EVAPORATED PURE AMORPHOUS SILICON

S. KUGLER

Quantum Theory Group, Institute of Physics, Technical University of Budapest
H-1521 Budapest, Hungary

and

L. PUSZTAI

Laboratory of Theoretical Chemistry, Roland Eötvös University
P.O.B. 32, 1518 Budapest, Hungary

Some search on the Cambridge Structural Database and Reverse Monte Carlo calculations were performed for pure amorphous Si. On the basis of diffraction data three dimensional models were constructed for determining the disordered structure of a–Si. The pair correlation function was derived directly from the large scale models.

Introduction

Reverse Monte Carlo (RMC) simulation [1], a method for diffraction data analysis and/or structural modelling of amorphous materials was used for generating three dimensional particle configurations that are consistent with the experimental structure factor. The basic algorithm has been described elsewhere [1,2] in detail. It was demonstrated that RMC results are sufficiently unique at higher packing fraction values and in the absence of directional forces [3,4], but this is far from guaranteed for covalent systems of relatively low packing fraction. In the latter case it is possible in principle that a range of structural models are consistent with a given diffraction data, instead of a single model. In these instances it is desirable that experimental evidences other than the diffraction result, or even theoretical models, be present in order to manifest them as *constraints* for the steric configurations (see [5]). Instead of using constraints it would also be possible to consider every possibility of a local arrangement that has so far been found experimentally. In this work this approach will be used.

The 0.45 g nearly pure evaporated amorphous Si sample has been prepared in the Central Research Institute for Physics, Budapest. A preliminary neutron diffraction experiment [6] was performed at the 7C2 spectrometer installed on the hot source of the reactor Orphee at Saclay. A new neutron diffraction measurement was performed using the D4 twin-axis diffractometer at the high flux reactor in the Institut Laue-Langevin [5]. The angular range covered by the two multidetectors $1.5° - 65°$ and $46° - 131°$ provide us with a momentum transfer range from 0.33 to 23.0 $Å^{-1}$.

Preliminary analysis of local order

Information on the possible local arrangements in amorphous silicon might be gained by analysing embedded silicon fragments inside different kinds of compounds (molecules). The environment of silicon atoms might be considered as a "white noise" which is supposed to be similar to an amorphous arrangement.

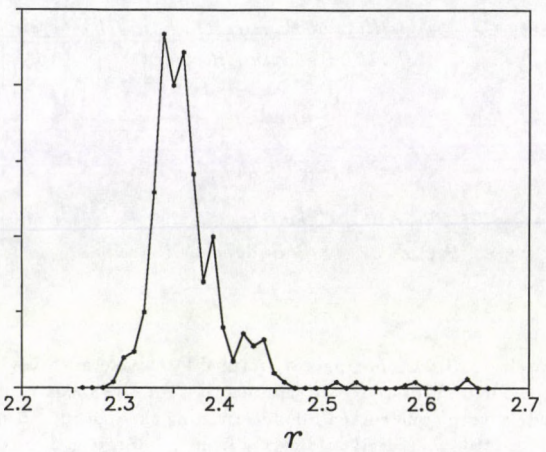

Fig. 1. The histogram of Si–Si bond lengths (Å) distribution using the CSD

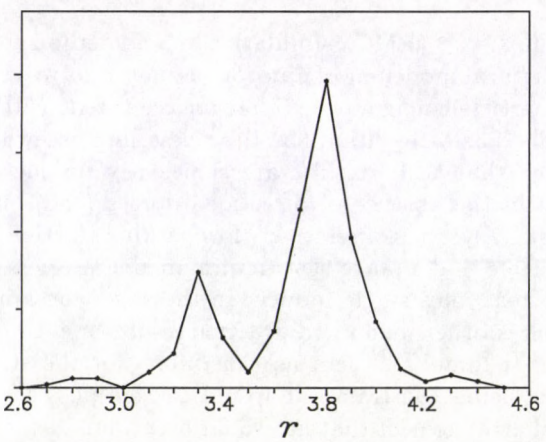

Fig. 2. The histogram of second neighbours (Å) distribution using the CSD

A systematic analysis of structural data has been carried out by means of Cambridge Structural Database [7] (CSD). This database contains results of different diffraction studies. We have collected the experimentally determined structural data on molecules containing at least one Si–Si–Si fragment. Searching the CSD 384 targets have been found. The R factor of these data showing the accuracy of the

measurements has been checked. Some of them were greater than 0.1. We cancelled such data, because the accuracy of these measurements was found not to be satisfactory. 346 Si–Si–Si fragments remained after this process. The first conclusion of bond angle analysis is that the Si_3 triangle is present among the fragments. The bond angles are about 60°, i.e. a nearly equilateral triangle can be found. Most of the a–Si theoretical models do not contain such a feature of the structure. There are angles around 90°, too. It belongs to the nearly planar square arrangement. The last conclusion is that a greater than 130° Si–Si–Si bond angle has never been measured. The histogram of bond length distribution is shown in Fig. 1. The bond length analysis shows that the lower limit is 2.29 Å. The upper limit is 2.65 Å but there are very few bond lengths over 2.46 Å. The second neighbour distances are shown in Fig. 2.

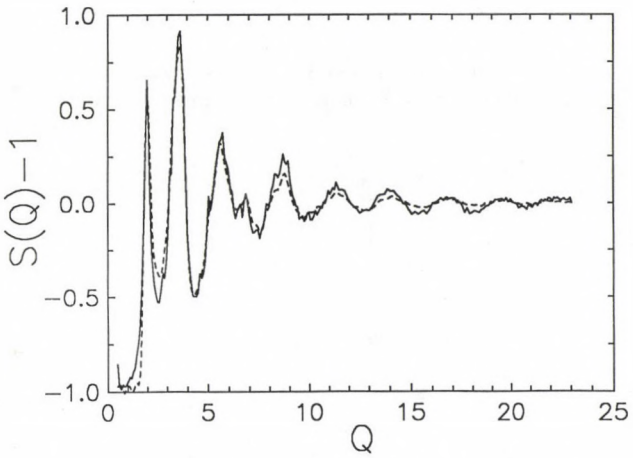

Fig. 3. Measured structure factor (solid line) compared to RMC model (dotted lines) in the range of 0 – 23 $Å^{-1}$

Simulation details

For the structural model which is going to be discussed in this work (see below) $N = 1728$ particles (i.e. points) were confined in a cubic box of sides $L = 32$ Å. This setup gave the experimental microscopic number density of ϱ=0.0505 $Å^{-3}$. The experimentally measured and corrected structure factor was used as input data for the RMC calculation. A hard core diameter (lowest limit of bond length) of 2.20 Å was also applied in order to efficiently avoid physically meaningless configuration. The run lasts for about 1 million accepted steps.

Figure 3 shows the comparison of the RMC solution for the Model and the experimental $S(Q)$. The overall agreement is good, so that the case is worthwhile for further considerations.

On the one hand, the correlation function was derived from the models and, on the other hand, it was calculated by a Fourier transformation procedure from

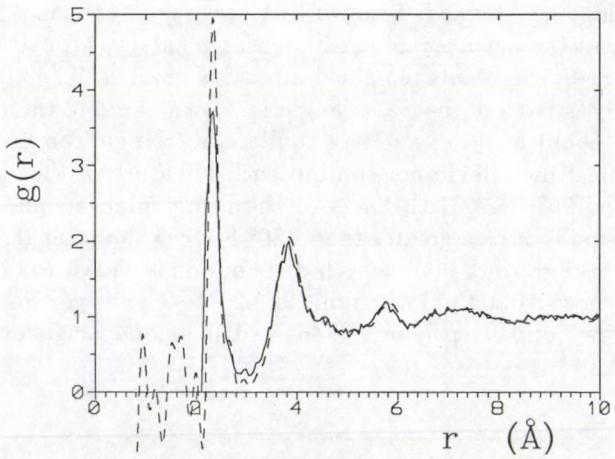

Fig. 4. The pair correlation function as it was derived directly from the model (solid line) and as it was calculated by a Fourier transformation procedure of measured $S(Q)$ (dashed line)

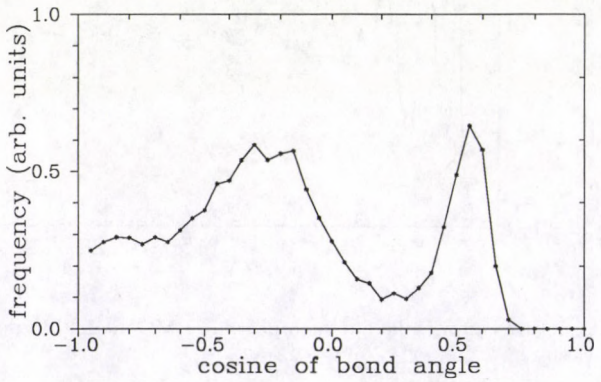

Fig. 5. Cosine distribution of bond angles calculated from unconstrained RMC

the measured $S(Q)$. The RDF's are displayed in Fig. 4. The maximum positions of first and second neighbour peaks are 2.34 Å and 3.85 Å, respectively. The full widths of the first neighbour peaks are different at half maximum.

If one looks at the cosine distribution of bond angles (Fig. 5), the unexpected large peak at $\cos\Theta = 0.5$ ($\Theta = 60°$) is dominating the picture. Remembering that the CSD contains quite a few examples of such bond angle, the existence of 60 degree angles cannot be excluded, although their demonstrated high proportion is unlikely. Note that the RMC Model contains a significant amount of tetrahedral angles (around $\cos\Theta = -0.33$), which indicates that without them it is not possible to build a reliable structural model.

Acknowledgements

We are indebted to Gy. Argay (Central Research Institute for Chemistry, Budapest) for his technical assistance. This work was supported by Országos Tudományos Kutatási Alap (OTKA), Grants No. 2951, No. F 4320 and No. T 4316 .

References

1. R. L. McGreevy and L. Pusztai, Molec. Sim., *1*, 369, 1988.
2. R. L. McGreevy, M. A. Howe, D. A. Keen and K. Clausen, IOP Conference Series, *107*, 164, 1991.
3. L. Pusztai and G. Tóth, J. Chem. Phys., *94*, 3042, 1991.
4. R. L. McGreevy and M. A. Howe, Phys. Chem. Liq., *24*, 1, 1991.
5. S. Kugler, L. Pusztai, L. Rosta, P. Chieux and R. Bellissent, Phys. Rev. B, *48*, 7685, 1993.
6. S. Kugler, G. Molnár, G. Pető, E. Zsoldos, L. Rosta, A. Menelle and R. Bellissent, Phys. Rev. B, *40*, 8030, 1989.
7. F. H. Allen, O. Kennard and R. Taylor, Acc. Chem. Res. *16*, 146, 1983.

Acta Physica Hungarica 75 (1–4), pp. 267–272 (1994)

SMALL-ANGLE NEUTRON SCATTERING STUDY OF AMORPHOUS ISOTOPIC Ni–Nb SYSTEM

E. Sváb, S. Borbély, Gy. Mészáros, S. N. Ishmaev[1] and R. Glas[2]

KFKI Research Institute for Solid State Physics
P.O.B. 49, 1525 Budapest, Hungary
[1]*Kurchatov Atomic Energy Institute*
123182 Moscow, Russia
[2]*Laboratoire Léon Brillouin, CEN Saclay*
91191 Gif-sur-Yvette, Cedex, France

Inhomogeneities in amorphous Ni–Nb samples prepared from various Ni-isotopes are investigated for two compositions, Ni-44 at% and Ni-62 at% by small-angle neutron scattering (SANS) in the scattering vector range from 0.007 to 0.45 $Å^{-1}$. A strong increase in the structure factors is observed below 0.04 $Å^{-1}$ whereas above 0.06 $Å^{-1}$ they smoothly become constant. In order to clarify the origin of SANS the total structure factors are separated into the Bhatia–Thornton partial structure functions. It is shown that the inhomogeneities are both topological and chemical in character. A characteristic correlation length of about 180 Å is obtained.

Introduction

In most cases, amorphous alloys obtained by different rapid quenching methods are not homogeneous, they contain quenched-in inhomogeneities formed during solidification. The dimension of these inhomogeneities lies in the sensitivity range of small-angle scattering, i.e. from about 10 to some 200 Å [1–6].

In this study small-angle neutron scattering (SANS) measurements are presented on amorphous Ni-Nb isotopic samples. In order to clarify the topological and chemical origin of the observed inhomogeneities the partial structure functions are separated and analysed on the basis of the Bhatia–Thornton formalism [7].

Experimental details and data evaluation

Amorphous $Ni_{44}Nb_{56}$ and $Ni_{62}Nb_{38}$ ribbons [8–10] of 2 mm width and 20 μm thickness were prepared by the melt spinning technique from various Ni-isotope mixtures with different coherent neutron scattering amplitude. For both compositions three Ni-isotopic samples were investigated: from ^{58}Ni(enr. 99.8 %), from ^{60}Ni(enr. 99.7 %), and from ^{0}Ni. The last of these was prepared from a mixture of ^{62}Ni(enr. 99.4 %) and ^{60}Ni in such a way as to give zero average coherent neutron scattering amplitude for Ni. In the case of $Ni_{62}Nb_{38}$, a fourth sample was also prepared from ^{62}Ni and ^{60}Ni to give zero average scattering amplitude for the sample. For simplicity the samples will be denoted as ^{58}Ni, ^{60}Ni, ^{0}Ni and zero alloy.

Table I

Numerical values of weighting factors used in data evaluation of Eqs (2) and (3). Cond(W) is a quantitative measure for the accuracy of partial structure functions (for definition see e.g. [10])

Sample	Weighting factors			Sample	Weighting factors		
	w_{NN}^{BT}	w_{NC}^{BT}	w_{CC}^{BT}		w_{NN}^{BT}	w_{NC}^{BT}	w_{CC}^{BT}
$^{58}Ni_{44}Nb_{56}$	0.899	1.266	0.450	$^{58}Ni_{62}Nb_{38}$	0.915	1.152	0.363
$^{60}Ni_{44}Nb_{56}$	0.848	−1.438	0.610	$^{60}Ni_{62}Nb_{38}$	0.819	−1.585	0.767
$^{0}Ni_{44}Nb_{56}$	0.575	−2.00	1.739	$^{0}Ni_{62}Nb_{38}$	0.383	−2.003	2.618
cond(W)		5.4		cond(W)		4.2	
				$^{Z}Ni_{62}Nb_{38}$	0.003	−0.231	4.231

Measurements were performed at the PAXE spectrometer in LLB Saclay [11]. In order to cover the wide q-range from 0.007 to 0.45 Å^{-1}, scattering curves were measured at two neutron wavelengths, viz. 8 and 4 Å with 5 and 1.2 m sample-to-detector distance, respectively. Small pieces of amorphous ribbons weighing about 5 g were pressed between two vanadium plates of 0.15 mm thickness. Transmission varied from 50 to 80 % dependent on the isotopic content of the sample and on the wavelength used in the measurement. The scattered intensity was corrected for background, absorption, incoherent scattering and was then normalized to incoherent scattering from a 1 mm thick water standard to eliminate the detector efficiency. The coherent scattered intensity was converted to absolute units using the method outlined by Teixeira [12], based on the direct determination of the intensity of the primary beam.

The Bhatia–Thornton total structure function $S_{tot}^{BT}(q)$ was calculated from the coherently scattered intensity $I_{coh}(q)$ as

$$S_{tot}^{BT}(q) = \frac{I_{coh}(q)}{\langle b^2 \rangle}, \tag{1}$$

where $\langle b^2 \rangle = c_a b_a^2 + c_b b_b^2$; b_a, b_b and c_a, c_b are the coherent scattering amplitudes and concentrations of a and b types of atoms, respectively. The total structure factor is represented as a weighted sum of three partial structure functions

$$S_{tot}^{BT}(q) = \frac{\langle b \rangle^2}{\langle b^2 \rangle} S_{NN}(q) + \frac{c_a c_b (b_a - b_b)^2}{\langle b^2 \rangle} S_{CC}(q) + \frac{2\langle b \rangle (b_a - b_b)}{\langle b^2 \rangle} S_{NC}(q), \tag{2}$$

where $\langle b \rangle = c_a b_a + c_b b_b$; $S_{NN}(q)$ represents the contribution from correlation between density fluctuations, $S_{CC}(q)$ correlation between chemical concentration fluctuations, and $S_{NC}(q)$ correlation between density and concentration fluctuations.

The partial Bathia–Thornton structure functions were calculated for both concentrations by solving the equation system

$$[S_{tot,i}^{BT}(q)] = [w_{NC,i}^{BT}][S_{NC}^{BT}(q)], \tag{3}$$

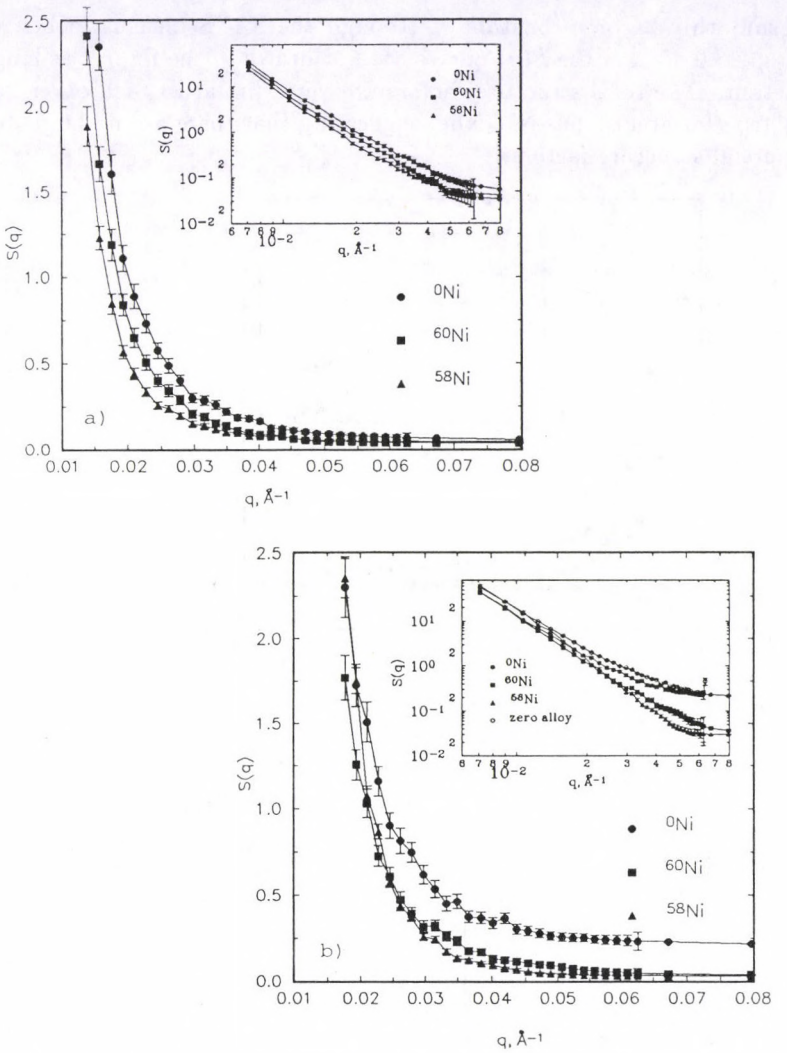

Fig. 1. Total structure factors of amorphous $Ni_{44}Nb_{56}$ (a) and $Ni_{62}Nb_{38}$ (b) for different isotopic samples. The inserts show the curves in log–log representation. The SANS intensity is constant up to 0.45 $Å^{-1}$, thus it is not drawn in the Figure

where $S^{BT}_{tot,i}(q)$ with $i = 1, 2, 3$ are the total structure factors measured on ^{58}Ni, ^{60}Ni and ^{0}Ni, respectively. The numerical values of the weighting factors, $w^{BT}_{NC,i}$ used in the calculation are given in Table I.

Results and discussion

The total structure factors for $Ni_{44}Nb_{56}$ and $Ni_{62}Nb_{38}$ are shown in Fig. 1. A strong increase is observable below 0.04 $Å^{-1}$ whereas above 0.06 $Å^{-1}$ the structure

factors smoothly become constant. Although the SANS measurements were performed up to 0.45 $Å^{-1}$ the $S(q)$ curves are not drawn in the figures as long as they are constant. The total structure factors are very similar to each other; this is especially true for amorphous $Ni_{44}Nb_{56}$ suggesting that there are no large differences in the partial structure factors.

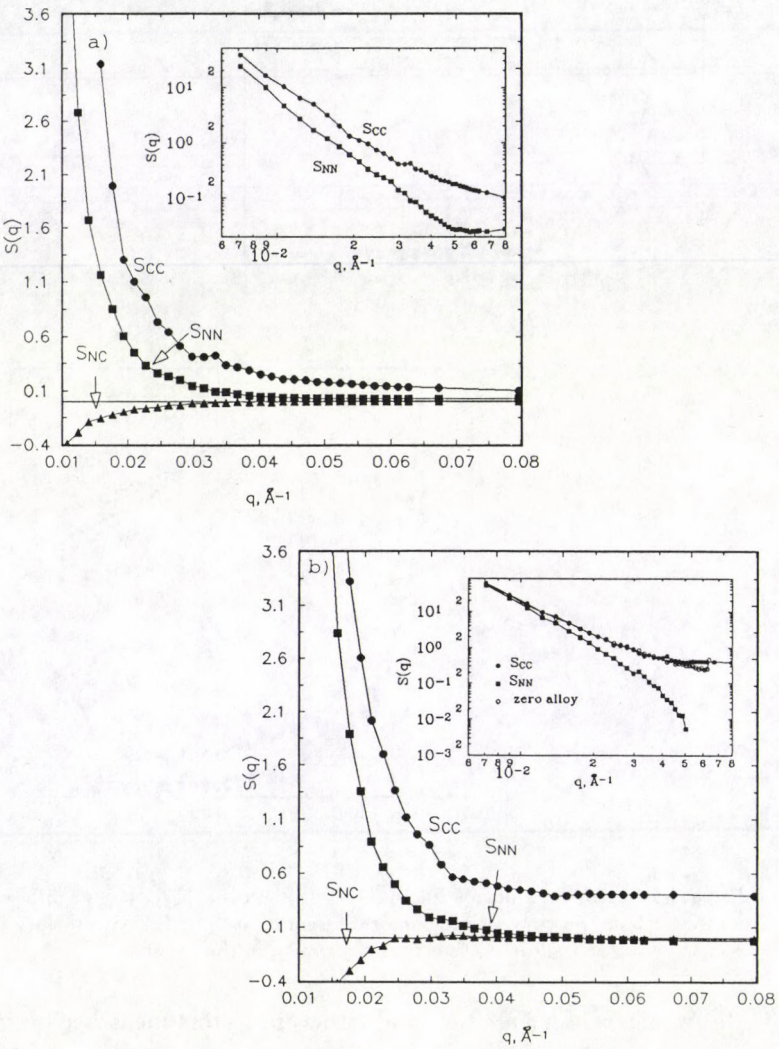

Fig. 2. Bhatia–Thornton partial structure factors for amorphous $Ni_{44}Nb_{56}$ (a) and $Ni_{62}Nb_{38}$ (b). The inserts show the curves in log–log representation

The Bhatia–Thornton partial structure functions are shown in Fig. 2. In the case of $Ni_{62}Nb_{38}$ four different isotopic samples were measured. This gives the unique possibility to compare $S_{CC}(q)$ determined from the three independent measurements on ^{58}Ni, ^{60}Ni ad ^{0}Ni by solving equation system (3) with that obtained

directly from a single measurement on the zero alloy sample. The two curves are practically identical.

For both concentrations the $S_{NN}(q)$ and $S_{CC}(q)$ curves behave in nearly the same way. However, in both cases the level of $S_{CC}(q)$ is higher than that of $S_{NN}(q)$ and the difference between the two partial structure factors is slightly larger for $Ni_{62}Nb_{38}$. This may be seen to be even more pronounced in double logarithmic scale drawn in the inserts to the Figures. In spite of the difference in level, one can conclude that inhomogeneities revealed by small-angle scattering are of both topological and chemical nature.

In order to obtain information on the dimension of the inhomogeneities, various SANS fitting procedures were used for data evaluation. The first part of the curves in log–log plot — see the insert — gives a straight region in the scattering vector range from 0.007 up to about 0.03 $Å^{-1}$, which can be characterized by a slope of about -3.5 independently of the chemical and isotopic compositions. This is in good agreement with the finding in [3] where a slope of -3.6 was given for amorphous $Ni_{63}Nb_{37}$. Attempts have also been made to use the Guinier formalism to fit the experimental total and partial functions without reasonable results. The Guinier curves showed continuous curvature without any distinct straight region. This means that in the Ni–Nb amorphous system there are no inhomogeneities of well-defined dimensions as was established for some metal–metalloid type amorphous materials, e.g. Ni–P [1], Fe–B [2].

The total and partial structure factors were successfully fitted to a random two-phase model described in [13]. The best fit provided a correlation length between 150 and 200 Å for the various curves. Thus, it may be concluded that in the investigated amorphous Ni–Nb system, inhomogeneities originating from both density and chemical fluctuations with a characteristic correlation length of about 180 Å are present.

Acknowledgements

This work was supported by the Hungarian OTKA Grant No 2934 and by the Russian Fundamental Science Foundation No. 93-02-2580.

References

1. S. Steeb and P. Lamparter, J. Phys. France, Colloque *C8, 46*, 247, 1985.
2. E. Sváb, Gy. Faigel, Gy. Mészáros, S. N. Ishmaev, I. P. Sadikov, A. A. Chernyshov, J. Phys. France, Colloque *C8, 46*, 267, 1985.
3. M. Schaal, P. Lamparter and S. Steeb, Z. Naturforschung, *43a*, 1061, 1988.
4. P. Lamparter, S. Steeb, D. M. Kroeger and S. Spooner, Materials Science and Engineering, *97*, 227, 1988.
5. M. Schaal, P. Lamparter and S. Steeb, Z. Naturforschung, *44a*, 4, 1989.
6. H. Trauble, P. Lamparter and S. Steeb, J. Phys. France, *2*, 1029, 1992.
7. A. Bhatia and D. E. Thornton, Phys. Rev., *B2*, 3004, 1970.
8. In the present SANS experiment the same samples were measured as those investigated in refs. 9–10.
9. E. Sváb, Gy. Mészáros, J. Takács, S. N. Ishmaev, S. L. Isakov and I. P. Sadikov, J. Non-Cryst. Solids, *144*, 99, 1992.

10. E. Sváb, Gy. Mészáros, G. Konczos, S. N. Ishmaev, S. L. Isakov and A. A. Chernyshov, J. Non-Cryst. Solids, *104*, 291, 1988.
11. J. Teixeira, in: Equipments Experimentaux, Laboratoire Léon Brillouin, 1987.
12. J. Teixeira, in: Structure and Dynamics of Strongly Interacting Colloids and Supermolecular Aggregates in Solution, ed. S. H. Chen, Kluwer, Amsterdam, 1992, pp. 635–658.
13. P. Debye, H. R. Anderson and H. Brumberger, J. Appl. Phys., *28*, 679, 1957.

Acta Physica Hungarica 75 (1–4), pp. 273–274 (1994)

TRIPLE-AXIS NEUTRON SPECTROMETER AT THE BUDAPEST MODERNIZED REACTOR

L. ROSTA, GY. TÖRÖK, J. JANI and I. V. NAUMOV[1]

KFKI Research Institute for Solid State Physics
P.O.B. 49, 1525 Budapest, Hungary
[1] *Kurchatov Atomic Energy Institute*
D-182 Moscow, Russia

One of the neutron scattering facilities at the restarted research reactor at KFKI Budapest is the triple-axis spectrometer. The structural set-up and the main technical parameters are described.

A triple axis spectrometer has been designed for structural and dynamical studies of condensed matter and installed on a straight neutron guide at a 19 m position from the reactor core (Figs 1–2). The monochromatic beam is provided by a 90 mm high focusing multi blade pyrolithic graphite monochromator. The movable part of the monochromatic shielding has a chain type construction of 3.20 m length along the neutron guide consisting of 16 combined (iron, borated polyethylene) shielding elements. When changing the incident wavelength the hole chain is driven by the monochromator–sample arm, automatically providing the most effective shielding near the detector area. For higher order filtering in the incident monochromatic beam a new type multidisc neutron velocity selector is installed in front of the sample goniometer. The beam divergence is determined by thin film soller collimators.

For the incident beam monitoring a ^{235}U fission chamber and for the detection of the scattered neutrons a ^{3}He counter is used. The program and control of the spectrometer is provided by a PC 386 with interfacing of an LLB-Saclay type driving electronics.

The main parameters of the spectrometer:

Beam tube	thermal (cold) neutron guide 25 × 100 mm
Monochromator, Analyser	pyrolithic graphite 80 × 90 mm
Collimations interchangeable	45′, 30′, 15′
Range of monochromator angle	$38° < 2\Theta < 126°$
Range of scattering angle	$-120° < 2\Phi < +40°$
Range of analyser angle	$-40° < 2\Theta < 120°$
Flux at specimen at 3.35 Å	2×10^5 n/cm^2/s (without cold source)
Beam size at specimen	width: 25 mm, height 60 mm
Momentum transfer	0–2.7 Å
Energy transfer	0–3.2 THz

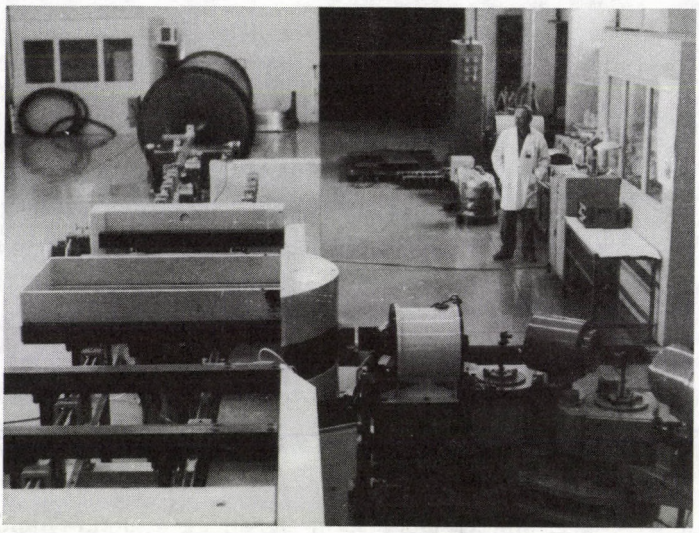

Fig. 1. Triple-axis neutron spectrometer under construction at the Budapest Research Reactor

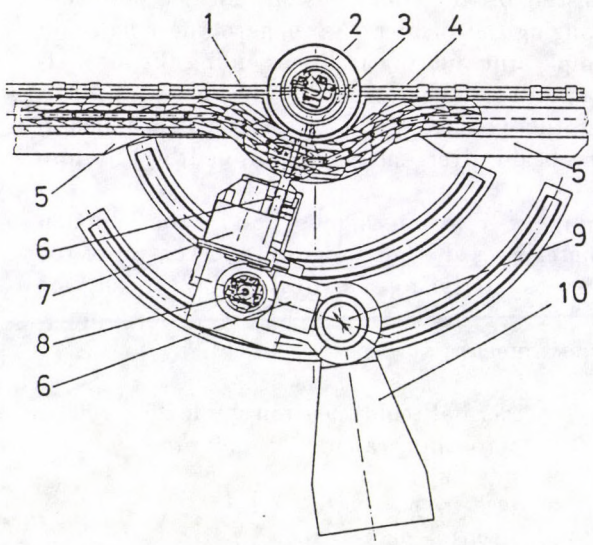

Fig. 2. Schematic arrangement of the triple-axis spectrometer at a neutron guide tube. 1. neutron guide, 2. focussing monochromator, 3. cadmium lock, 4. chain type shielding, 5. shielding, 6. collimator, 7. filtering velocity selector, 8. sample, 9. analyser, 10. detector bank

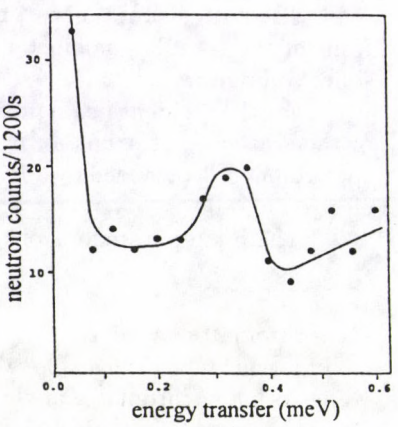

Fig. 3. Example of an inelastic scattering pattern recorded on the triple-axis spectrometer by constant-Q scan at $\lambda = 3.355$ Å incident neutron wavelength. The $(0, 0, 2.03)$ longitudinal acoustic phonon resonance was measured on a 40 mg pyrolithic graphite single crystal

Acta Physica Hungarica 75 (1-4), pp. 275-278 (1994)

NEUTRON DIFFRACTION STUDIES OF LATTICE PARAMETERS AND THE PHASE DIAGRAM OF $K_{1-x}(NH_4)_xSCN$ SOLID SOLUTIONS

L. S. SMIRNOV, I. NATKANIEC, YU. A. SHADRIN and A. I. SOLOV'EV

Frank Laboratory of Neutron Physics, JINR
141980 Dubna, Russia

Results of temperature and concentration dependence investigations of unit cell parameters and volume of $K_{1-x}(NH_4)_xSCN$ mixed crystals by powder neutron diffraction are presented. It is shown that the transformation from monoclinic phase III to orthorhombic phase II starts at low temperatures near $x = 0.75$.

1. Introduction

Previously, P. W. Bridgman noted the strangeness of KSCN and NH_4SCN compounds having different crystal structures at room temperature, "because K and NH_4 usually replace each other isomorphously" [1]. Later, different investigators [2–9] have shown that there are really two isomorphous phases in KSCN and NH_4SCN: the tetragonal phase I and orthorhombic phase II. Transitions from phase I to phase II in KSCN and NH_4SCN occurs at 413 K and 390 K, respectively, but then NH_4SCN transforms into a monoclinic phase III at 360 K. However, the transition from phase I into phase II in KSCN is due to the ordering of SCN ions, but this transition in NH_4SCN is due to the ordering of SCN and only two NH_4 ions, following the ordering of another two NH_4 ions during the phase transition from the orthorhombic to the monoclinic phase [10,11]. The orthorhombic phase II of the $K_{1-x}(NH_4)_xSCN$ mixed crystal must be disordered due to reorientation of the NH_4 ion. The temperature range where orthorhombic phase II exists in NH_4SCN is very narrow, and over that temperature interval, the stochastic reorientations and strong anharmonics of the NH_4 ion hinder measurements of its dynamics. For investigation of the NH_4 ion dynamics in both the orthorhombic and monoclinic phases we have carried out a search for the position of the boundary between phases II and III on an $x - T$ phase diagram of the $K_{1-x}(NH_4)_xSCN$ mixed crystal.

2. Sample preparation and neutron diffraction results

The KSCN and NH_4SCN samples were prepared form a fine-grained powder-like material of high purity. The purity of the main substance was no less than 99.9 %. Because the samples were very hydroscopic, they were dried at 75 °C. The mixed crystals of $K_{1-x}(NH_4)_xSCN$ were prepared by means of evaporation of an aqueous solution of KSCN and NH_4SCN at 75 °C.

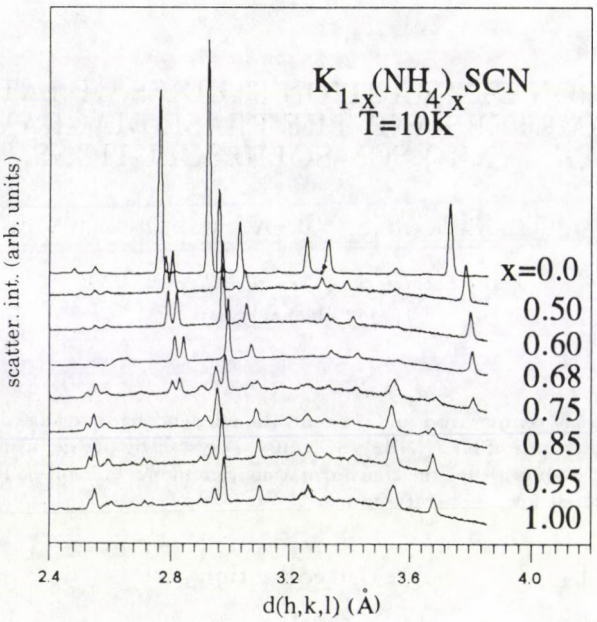

Fig. 1. Neutron diffraction spectra of $K_{1-x}(NH_4)_xSCN$ of varying concentrations at 10 K

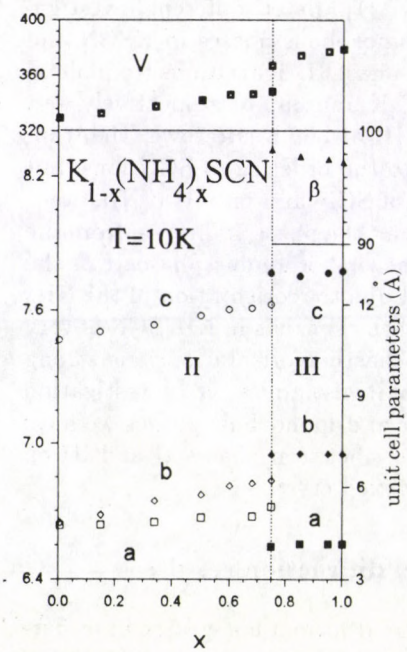

Fig. 2. Concentration dependence of unit cell parameters and volumes of the $K_{1-x}(NH_4)_xSCN$ mixed crystals at 10 K

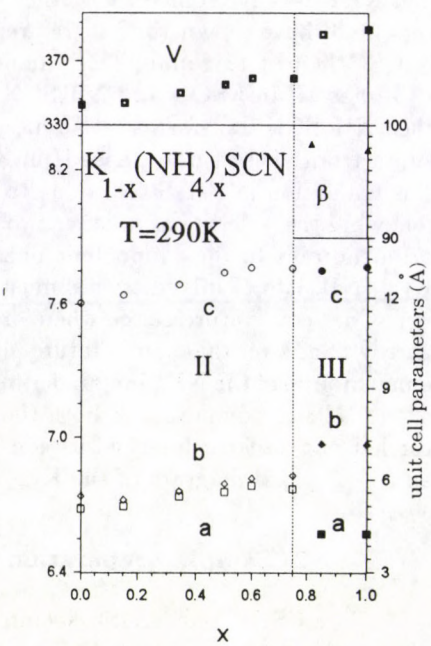

Fig. 3. Concentration dependence of unit cell parameters and volumes of the $K_{1-x}(NH_4)_xSCN$ mixed crystals at 290 K

Measurements with the $K_{1-x}(NH_4)_xSCN$ powder samples for $x = 0$, 0.15, 0.34, 0.50, 0.60, 0.68, 0.75, 0.85, 0.95 and 1 were performed over a wide temperature range on the NERA-PR TOF neutron spectrometer, placed at the IBR-2 reactor at JINR [12]. The neutron diffraction spectra of some $K_{1-x}(NH_4)_xSCN$ mixed crystals measured at a temperature of 10 K are presented in Fig. 1.

The unit cell parameters of phases I, II and II of the mixed crystals were determined with the help of the "MRIAAU"-90 program [13]. The measured spectra of KSCN and NH_4SCN are in full agreement with the known structures of the tetragonal (I) and orthorhombic (II) phases determined in [2–6] and of the monoclinic (III) phase from [4, 7–9]. The character of the changes in unit cell parameters and volumes of KSCN and NH_4SCN at the I–II phase transition is typical for a second order phase transition. The II–III transformation in NH_4SCN is a first order type and is accompanied by an increase in the volume of phase III.

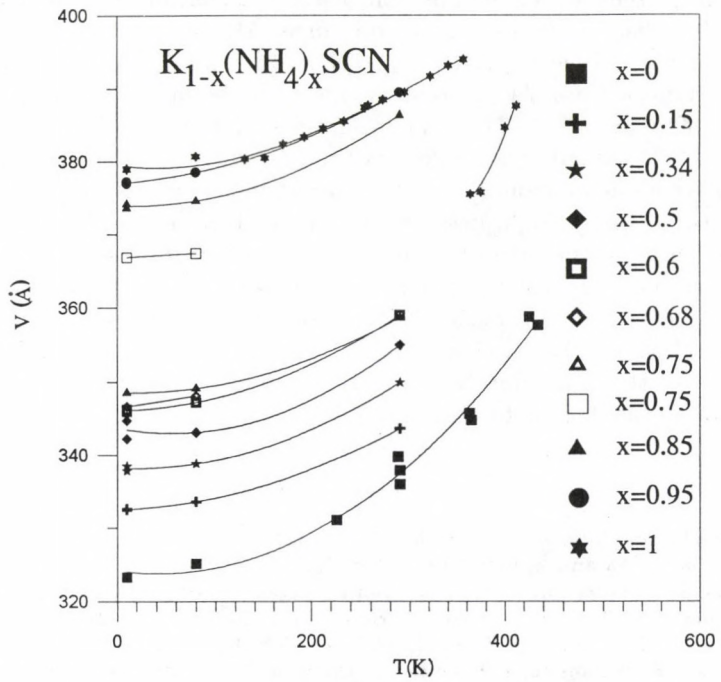

Fig. 4. Temperature dependence of unit cell volumes of $K_{1-x}(NH_4)_xSCN$ mixed crystals

The concentration dependence of unit cell parameters and volumes of the $K_{1-x}(NH_4)_xSCN$ mixed crystals was obtained from diffraction spectra measured at 10, 80 and 290 K. The unit cell parameters and volumes appropriate to 10 and 80 K differed only slightly from those measured at 10 and 290 K and are presented in Figs 2 and 3. The transformation from the orthorhombic to monoclinic phase manifests itself in the $K_{1-x}(NH_4)_xSCN$ mixed crystal at 10 K at a concentration near $x = 0.75$. At this concentration and temperature we observed both of these phases together (see Fig. 1, $x = 0.75$). The investigation of the temperature depen dence of the diffraction spectra for this concentration shows that transformation

has the order (II+III)–II–I with a noticeable hysteresis below the transformation temperature from phase II to phase (II+III).

The unit cell parameters of the monoclinic phase do not show any noticeable dependence on concentration. The unit cell parameters of the orthorhombic phase show different dependences on concentration. The a parameter has a weak concentration dependence, the b and c parameters show a linear concentration dependence up to $x = 0.60$, above which they manifest saturation. The temperature dependence of the unit cell volumes of $K_{1-x}(NH_4)_xSCN$ mixed crystals for different concentrations is presented in Fig. 4. The temperature dependence of the volume of NH_4SCN monoclinic phase III shows an anomaly near 200 K and was discussed in [14].

3. Conclusion

In the present work, the position of the transformation boundary from the orthorhombic phase II to the monoclinic phase III on the $x - T$ phase diagram for mixed crystals of the $K_{1-x}(NH_4)_xSCN$ was determined first by means of neutron powder diffraction. At low temperatures this boundary begins near the concentration of $x = 0.75$. These investigations of the $x - T$ phase diagram of $K_{1-x}(NH_4)_xSCN$ mixed crystals give us the possibility to investigate the influence of the orthorhombic or monoclinic site symmetry on NH_4 ion dynamics [15]. It is also known that under high pressure the temperature of transformation from the monoclinic phase to the orthorhombic phase has a negative slope and the volume change in the first type of transition diminishes with decreasing temperature [1, 12]. The concentration dependence of the unit cell volume of the $K_{1-x}(NH_4)_xSCN$ mixed crystal shows that a change in concentration reflects the influence of the temperature of the transition from the monoclinic to orthorhombic phase on the unit cell volume analogous to that of pressure.

References

1. P. W. Bridgman, Proc. Am. Acad. Sci., *51*, 55, 1915.
2. Y. Yamada, T. Watanabe, Bull. Chem. Soc. Jpn., *36*, 1032, 1963.
3. C. Akers, S. W. Peterson, R. D. Willet, Acta Crystallogr., *B24*, 1125, 1968.
4. W. Klement, Jr., C. W. F. T. Pistorius, Bull. Chem. Soc. Jpn., *49*, 2148, 1976.
5. S. Yamamoto, M. Sakuno, Y. Shinnaka, J. Phys. Soc. Jpn., *56*, 4393, 1987.
6. A. Hamada, S. Yamamoto, Y. Shinnaka, J. Phys. Soc. Jpn., *59*, 954, 1990.
7. Z. V. Zvonkova, G. S. Zhdanov, Zh. Fiz. Chimii, *23*, 1495, 1949.
8. V. E. Zavodnik, Z. V. Zvonkova, G. S. Zhdanov, E. G. Mirevich, Kristallografiya, *17*, 107, 1972.
9. J. W. Bats, P. Coppens, Acta Crystallogr., *B33*, 1542, 1977.
10. O. Blaschko, W. Schwarz, W. Schranz, A. Fuith, Ferroelectrics, *124*, 139, 1991.
11. W. Schranz, A. Fuith, H. Warhanek, R. Blinc, J. Seliger, T. Apih, J. Bolinsek, Ferroelectrics, *125*, 257, 1992.
12. User Guide, Neutron experimental facilities at JINR, Dubna, p. 25, 1991.
13. V. B. Zlokazov, J. Appl. Cryst., *25*, 69, 1992.
14. L. S. Smirnov, I. Natkaniec, S. I. Bragin, J. Brankowski, A. I. Solov'ev, V. A. Goncharova, E. L. Gromnitskaya, G. G. Il'ina, O.V. Stal'gorova, (to be published).
15. I. Natkaniec, L. S. Smirnov, A. I. Solov'ev, S. I. Bragin, Proceedings of LT-20, Aug. 4–11, 1993, Eugene, Oregon, USA.

Acta Physica Hungarica 75 (1-4), pp. 279-284 (1994)

DOUBLE-BENT-CRYSTAL SANS INVESTIGATION OF THE CREEP EXPOSED CMSX2 SINGLE CRYSTAL

P. STRUNZ, P. LUKÁŠ, P. MIKULA, J. ŠAROUN, E. KEILOVÁ[1] and J. KOČÍK[1]

Nuclear Physics Institute
25068 Řež near Prague, Czech Republic
[1]*Nuclear Research Institute*
25068 Řež near Prague, Czech Republic

The single crystal superalloy CMSX2 was studied after a creep exposition at high temperature by small-angle neutron scattering and transmission electron microscopy. The anisotropic character of scattering curves displayed the platelet shape of γ' precipitates. The presence of an interparticle maximum enabled to evaluate the characteristic interparticle distance. Both SANS and TEM results indicate the influence of the creep exposition on the morphology of the precipitates.

Introduction

Mechanical properties of superalloys, especially those based on nickel, predetermine these materials for high temperature applications [1]. High strength creep resistance is one of the most important properties of nickel-based single-crystal superalloys. A basic feature in the mechanical properties of these materials is their diphasic nature, where the ordered γ' precipitates grow in a matrix formed by the γ-phase. The γ' precipitates prevent the gliding of dislocations [2] and their morphology plays an important role in the mechanical properties of the superalloys at high temperatures [1,3].

The earlier studies of CMSX2 have shown that a microstructure with a regular arrangement of cubic γ' precipitates corresponds to an optimal creep resistance [3]. During a tensile deformation of CMSX2 at high temperatures (near 1000 °C), the γ' precipitates coarsen into the form of platelets perpendicular to the stress axis [2]. This transformation ("rafting") leads to a longer lifetime before rupture at high temperatures [4].

The influence of the creep on the morphology of γ' precipitates can be successfully studied, besides the electron microscopy, by means of small-angle neutron scattering (SANS) [5]. Our crept sample of the single-crystal superalloy CMSX2 was investigated in detail by different techniques. In this paper, we report the results of the small-angle neutron scattering and the transmission electron microscopy (TEM) studies. The results of the neutron diffraction topography (NDT) experiment were reported previously [6].

Sample

The cylindrically shaped sample was prepared at Centro Sviluppo Materiali, Roma (Italy), by directional solidification. The crystallographic direction < 100 > was parallel to the rotation axis of the sample. The conditions of the casting led to a dendritic solidification structure [6].

The single crystal was subjected to a strain of 120 MPa at a temperature of 1050 °C for 742 hours. The creep exposition was stopped at the beginning of the tertiary phase of the creep curve. The operating force was parallel to the < 100 > crystallographic direction. We consider three parts of the sample: the fully creep exposed part A, the specimen head (part C) originally fixed in the holder during the creep exposition and the transitional part B. As a significant difference in creep exposition can be supposed between these parts, deformation dependent structural properties were related to the sample head, where a lower deformation degree is expected.

Experimental

SANS experiment was performed on the medium resolution double-bent-crystal diffractometers installed at the reactor LVR-15 in NPI Řež. Scattering curves at lower Q-range ($0.2 \div 2.6 \times 10^{-3}$ Å^{-1}) were measured on the diffractometer SPN-100 step by step [7] whereas the measurement in Q-range $1.35 \div 11.4 \times 10^{-3}$ Å^{-1} was performed on the SANS diffractometer DN-2 equipped with a position sensitive detector (PSD) [8].

The scattering curves were taken in parts A, B and C of the sample and for two orientations. Vertical or horizontal arrangement of the sample corresponds to the measurement of scattering in the plane perpendicular or parallel to the sample axis, respectively. In both cases the axis of the sample was perpendicular to the incident neutron beam. Measured scattering curves obtained from parts A and C of the sample are drawn in Fig. 1 for both orientations. Figure 2 displays two TEM micrographs of the longitudinal sections of the sample.

Results and discussion

An anisotropic character of scattering curves obtained from all parts of the sample, which was found by measurement at two perpendicular orientations (see Fig. 1), revealed that the cubic γ' precipitates coarsened into the precipitates of the platelet form even in the sample head. The presence of an interparticle interference peak on the scattering curves measured in horizontal arrangement of the sample indicated an ordered morphology of platelets; an orientation of γ' precipitates was perpendicular with respect to the stress axis.

The scattering data obtained at horizontal arrangement of the sample can be explained by a simple model of the sample microstructure. We can suppose that the scattered intensity is composed of two parts: the first part is caused by scattering on ordered particles and creates the interference maximum whereas the

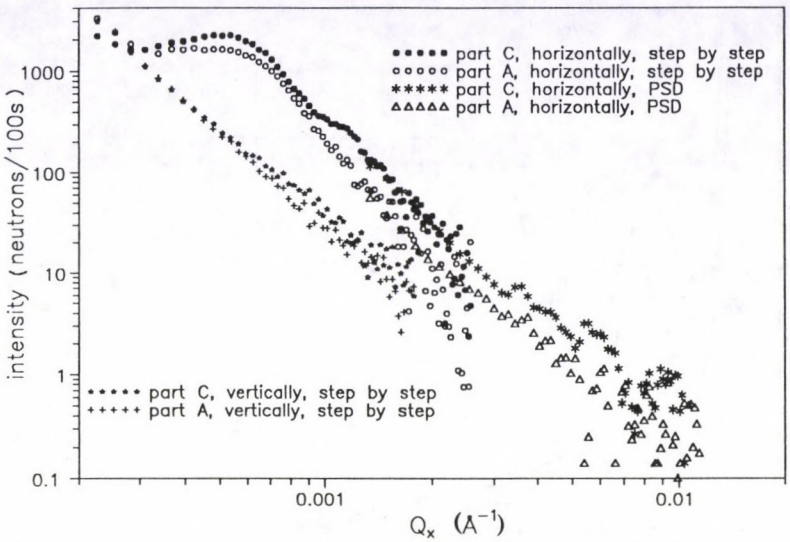

Fig. 1. Scattering curves obtained from parts A and C, normalized to the same irradiated volume (100 mm^3) and time of measurement

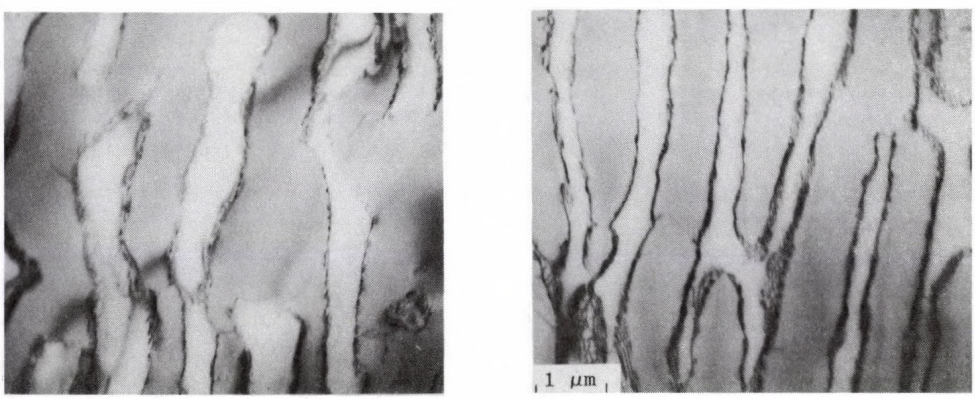

Fig. 2. TEM micrographs of part A (a) and part C (b)

rest of the intensity follows from the scattering on disordered particles and decreases from $Q = 0$ to $Q = \infty$. The shapes of the scattering curves correspond to this morphology because the intensity increases for $Q \to 0$ and it cannot be explained only by the presence of ordered microparticles.

In order to separate these parts from the measured curves, we fitted a dependence composed of two analytical functions on the data measured at Q-range

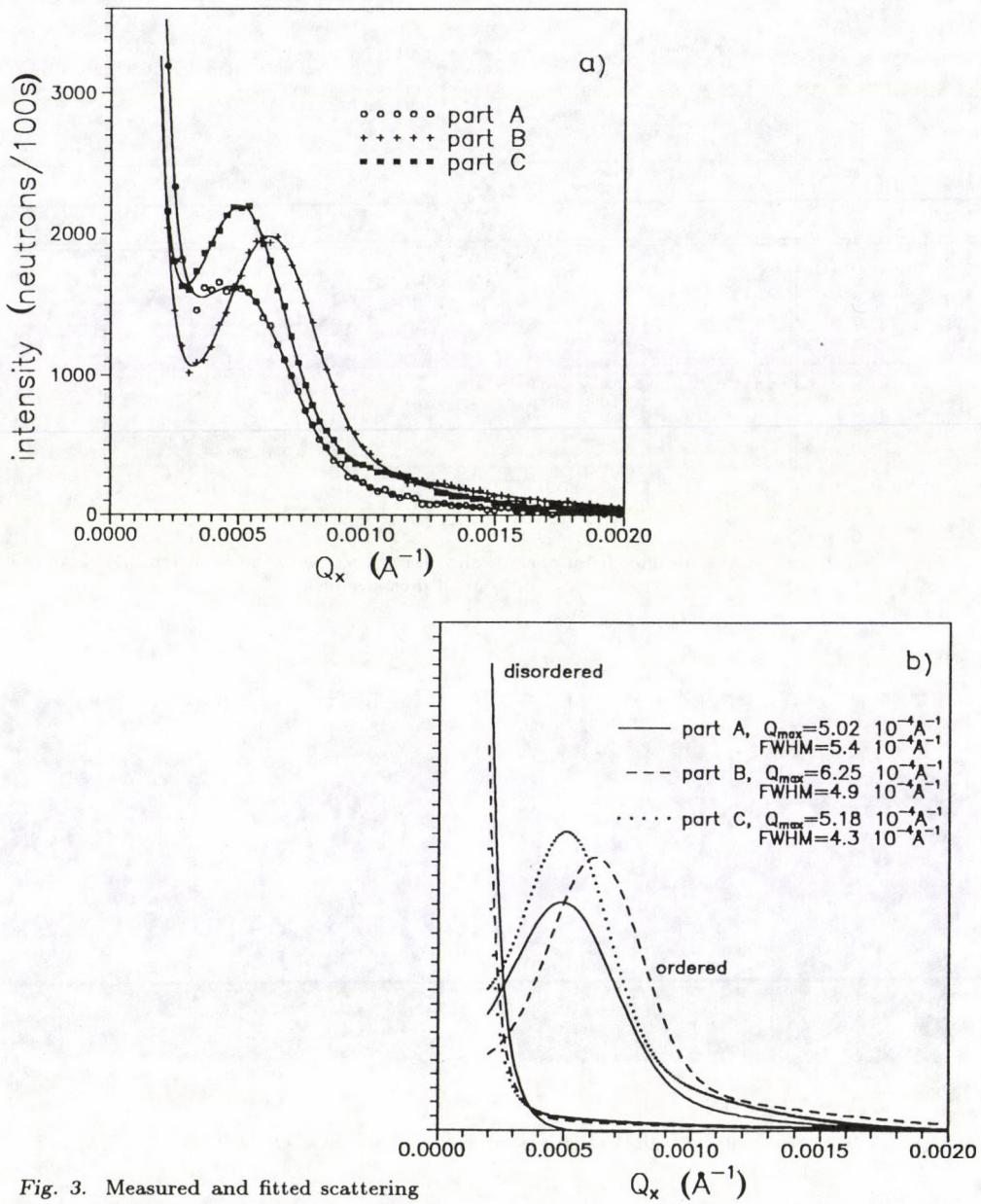

Fig. 3. Measured and fitted scattering curves of horizontally positioned sample (a) and separated parts of the scattered intensity (b)

$0.2 \div 2.6 \times 10^{-3}$ $Å^{-1}$ for a horizontally positioned sample. The first component was a sum of two Gaussian functions where the first one had its maximum fixed at $Q = 0$. The sum describes qualitatively a shape of a scattering curve influenced

by an interparticle interference and in our case it describes the scattering on the ordered precipitates. The second compound of the fitted dependence, which corresponds to the scattering on disordered and relatively larger inhomogeneities, was approximated by the sum $a_1/Q^2 + a_2/Q^3 + a_3/Q^4$, where a_1, a_2, a_3 are the fitted coefficients. The results of the fitting procedure and corresponding separated parts of the scattered intensity are presented in Fig. 3.

The curves corresponding to the ordered particles in Fig. 3b show the decrease of scattering intensity from part C to part A and, simultaneously, the increase of FWHM values of the interference maxima. The relatively largest volume of the second, disordered, compound is in the part A of the sample. It can be estimated by the comparison of intensities of the corresponding curves in Fig. 3b at the lowest Q-values. This behaviour indicates that the creep exposition reduced the ordering of γ' platelets while the growth of larger particles occurred in the sample. However, this simple model cannot explain the origin of larger particles.

The reduction of the ordering of the γ'-precipitates was confirmed by TEM (see Fig. 2). The micrographs also allow to estimate an average distance between the platelets. We found the values 1.3 and 1.1 μm in the parts A and C of the sample, respectively. The more exact value of the characteristic interparticle distance L_c can be deduced from the position of the interference maxima of the scattering curves (see Fig. 3b) by using the formula $L_c = 2\pi/Q_{\max}$, where $Q_{\max}$ is the position of the interparticle interference maximum. The L_c values of 1.28, 1.01 and 1.24 μm were found by means of this formula for the fully (part A), moderately (B) and minimally (C) exposed part of the single crystal, respectively. As the SANS method provides bulk information, the result is a statistical average over the whole irradiated part of the sample.

Conclusion

The investigation specified the morphology of γ' precipitates in all parts of the sample. The SANS measurement revealed the influence of the long creep exposition on the ordering of γ' platelets and this result was confirmed by TEM.

The DBC SANS experiment proved the applicability of this SANS technique for studies of nickel-based single-crystal superalloys at Q-range which is not easily obtainable on collimator-type SANS instruments. This momentum transfer range is particularly interesting for investigation of a γ'-precipitates arrangement.

The results of SANS and TEM measurements —yielding information at the microstructural level — were completed by neutron diffraction topography and neutron diffractometry which characterized the creep exposed CMSX2 sample mainly at the macrostructural level [6]. This combination of different techniques provided rather complex information about the influence of the creep exposition on the CMSX2 superalloy.

Acknowledgements

The authors thank Professor F. Rustichelli and Professor G. Albertini (University of Ancona, Italy) for stimulating discussion and Professor A. di Gianfrancesco (Centro Sviluppo Materiali, Roma, Italy) for providing the sample.

References

1. T. Khan, P. Caron, D. Fournier and K. Harris, Mat. et Techn., *10–11*, 567, 1985.
2. D. W. Chung, M. Chatwwedi and D. J. Lloyd, Acta Met., *24*, 227, 1976.
3. P. Caron and T. Khan, Mat. Sci. Eng., *61*, 173, 1983.
4. R. A. Mackay and M. V. Nathal, Acta Met., *38*, 993, 1990.
5. D. Bellet, P. Bastie, A. Royer, J. Lajzerowicz, J. F. Legrand and R. Bonnet, Journal de Physique I, *2*, 1097, 1992.
6. P. Strunz, P. Lukáš, P. Mikula, J. Šaroun, G. Albertini, F. Rustichelli, G. Cicognani and A. di Gianfrancesco, Czech. J. Phys., *44*, 687, 1994.
7. J. Kulda and P. Mikula, J. Appl. Cryst., *16*, 498, 1983.
8. P. Lukáš, P. Mikula, J. Šaroun and P. Strunz, Nucl. Instr. Meth., *A338*, 111, 1994.

Acta Physica Hungarica 75 (1-4), pp. 285-289 (1994)

DYNAMICS INVESTIGATIONS OF THE PROTON CONDUCTOR 12-TUNGSTOPHOSPHORIC ACID BY NEUTRON SCATTERING

M. DAVIDOVIĆ, N. TJAPKIN, U. B. MIOČ[1] and PH. COLOMBAN[2]

Institute of Nuclear Sciences 'VINČA'
P.O.B. 522, 11001 Belgrade, Yugoslavia
[1] *Faculty of Physical Chemistry, University of Belgrade*
P.O.B. 137, 11001 Belgrade, Yugoslavia
[2] *Laboratoire de Spectrochimie infrarouge et Raman, CNRS*
2, rue Henry Dunant, Thiais, France

Compared with other spectroscopic techniques, the method of inelastic incoherent neutron scattering (IINS), owing to extraordinary large cross-section of hydrogen for incoherent scattering, has great advantages in the investigation of the dynamics of protons in compound where they are surrounded by heavy atoms. For proton conductors, this technique enables the identification of various protonic species, determination of their dynamics, as well as the dynamics of heavy atoms to a measure in which they are bonded to hydrogen. Here we discuss the IINS spectra obtained with a pulsed neutron source, during the dehydration process of 12-tungstophosphoric acid 6-hydrate $(H_5O_2)_3{}^*(PW_{12}O_{40})$.

Introduction

In the last decade, considerable progress has been made in the understanding of the nature of protonic entities in hydrogen bonded solids and solid state superionic protonic conductors, using inelastic incoherent neutron scattering technique [1,2].

Higher hydrates of 12-tungstophosphoric acid belong to a not very large group of compounds that are superionic proton conductors at room temperature [3,4]. At least four stable hydrates $H_3PW_{12}O_{40}nH_2O$ (WPA-n) with $n = 29, 21, 14$ and 6 are known to exist, in certain regions of temperature and relative humidity [5]. They consist of the Keggin anions $(PW_{12}O_{40})^{3-}$ which are interconnected with hydrogen-bonded water molecules [6]. In higher hydrates not all positions of water molecules are determined, some of them being highly disordered. Infrared (IR) and Raman techniques showed the existence of various protonic species ($H_5O_2^+$, H_3O^+, H_2O, OH^-, H^+) and the temperature dependent dynamic equilibrium between them [7,8]. Only for hexahydrate (WPA-6) the position of the acid protons and all water molecules was determined and it was shown that they were in nearly planar dihydroxonium ions ($H_5O_2^+$), connected with four Keggin anions. The higher hydrates have superionic conductivity and the hexahydrate appeared to be poor bulk protonic conductor [9,10]. In spite of intensive investigations by many experimental techniques, it has not been decisively established what protonic species take part in charge transfer and what is the mechanism of superionic conductivity. Our recent investigations [10,11] suggest that some of the mechanism of conductivity in lower hydrates ($n < 6$), and even in anhydrous samples, could be the same as

in higher hydrates — the jumps of individual protons H^+ between proton carriers (H_2O and/or Keggin framework).

In the present paper we want to show that IINS is appropriate for following of the dehydration of WPA-6, i.e. what happens with the protons after the destruction of dihydroxonium ion, which can be important for the determination of the proton transfer mechanism for the whole group of these compounds.

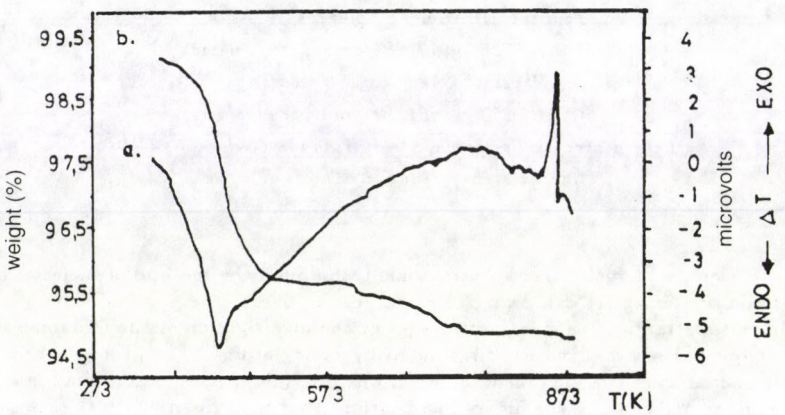

Fig. 1. a) DTA and b) TGA curves of $(H_5O_2)_3(PW_{12}O_{40})$

Experimental procedure

We report here on the study of IINS spectra, using the time-focused crystal analyser spectrometer (TFXA) at the ISIS pulsed neutron source at the Rutherford Appleton Laboratory, during the dehydration of 12-tungstophosphoric acid hexahydrate. TFXA operation is similar to a beryllium-filter instrument at reactor source. The resolution width is only 200 μeV for the incident neutron energies and 2 % of the energy transfer at higher energies. The samples were obtained by heating WPA-29 powder at 373, 473, 573 and 873 K. All IINS spectra of annealed samples [12] were measured at 25 K.

Thermogravimetry (TGA) and differential thermal (DTA) analysis were done by using a TGA Dupont Nemours instrument and a Stanton–Redcroft–STA 1000 thermoanalyser (scanning rate 10 K/min).

"Direct" current conductivity $\sigma(f \to 0)$ was extracted from impedance measurements on an LCR-meter HP 4284A, in the frequency (f) range 1 Hz–1 MHz on the compressed pallets.

Results and discussion

The annealing temperatures of samples for the IINS measurements were selected from the thermogram in Fig. 1.

The sample heated at 373 K is a hexahydrate. For the sample annealed at 473 K nearly one water molecule is left over, and for that annealed at 573 K $n \sim 0$.

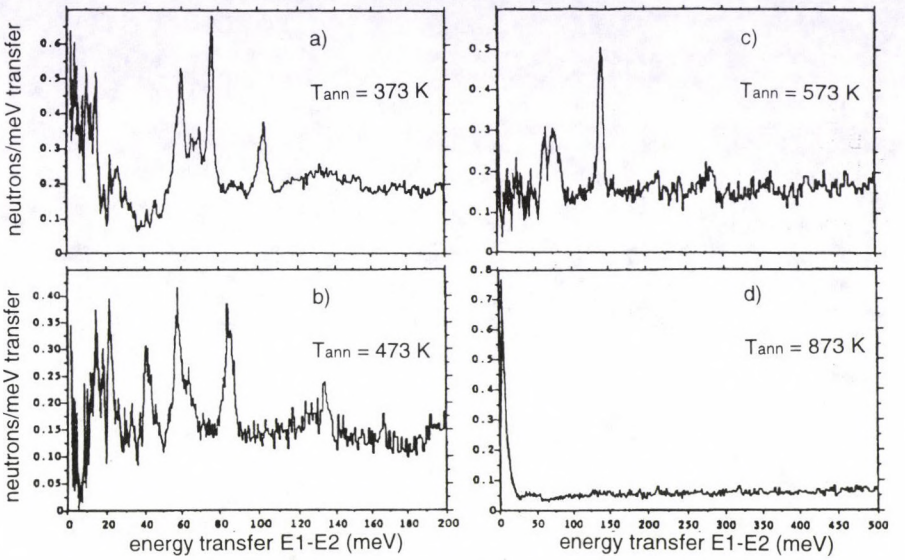

Fig. 2. IINS spectra of WPA-6 annealed at a) 373; b) 473; c)573 and d) 873 K

All the samples were heated in air. X-ray powder diffraction measurements show that Keggin's structure is preserved at these temperatures [13].

The neutron spectrum of the sample annealed at 373 K in Fig. 2a is in agreement with already assigned spectra [14] of WPA-6. It is seen that the peaks in the IR spectrum of $H_5O_2^+$ ions are just in the region which is characteristic for the Keggin anion, so that they are not easy to detect by the optical vibrational spectroscopies. With the use of IINS, however, it is clearly seen that annealing at 470 K leads to the destruction of dioxonium ions. It can be noticed that heating at 570 K leads to the disappearance of the peaks characteristic for the oxonium ion [14,15], e.g. at 134 and 200 meV, (Fig. 2b) and to the formation of a new peak, at about 143 meV, originating from the "free" protons, i.e. the protons trapped in between the cavities of the host lattice (Fig. 2c). For the sample annealed at 870 K, it is clear that there are no protons left over (Fig. 2d).

The behaviour of protons is investigated through temperature dependence of conductivity (σ) for WPA-n, given in Fig. 3.

In the temperature dependence of conductivity for hexahydrate obtained by heating of the WPA-29 at 373 K in air (•), two regions can be noticed. At lower temperatures, surface conductivity is dominant, and at the higher temperature bulk conductivity obeys an Arrhenius law, with an activation energy of 1.07 eV. Measurements in a vacuum of 0.5 Torr on the sample heated for 24 h (o) at 373 K enable obtaining of the values for bulk conductivity at lower temperatures as well. The measurements on samples with lower content of water ($n < 6$); $n \simeq 0$ (1–0.5 water molecule) and $n = 0$, the free proton containing phase, were performed in a vacuum of $\sim$ 0.05 Torr, to prevent rehydration. The sample had been first heated to about 530 K, and after several hours the measurements began, on cooling (x).

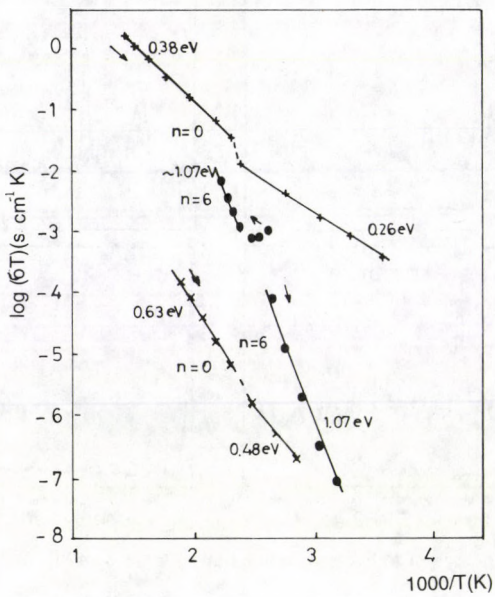

Fig. 3. Temperature dependence of conductivity (σ) for WPA-n. Arrows indicate cooling or heating.

It can be seen that at about 416 K a phase transition occurs, manifesting itself in jump of conductivity and a change of activation energy. The phase transition is more clearly seen on the curve for anhydrous ($n = 0$) heteropolyacid heated for several hours at about 673 K(+). The IINS results (Fig. 2) where the dynamics of proton species, from dioxonium ion to "free" proton is shown, could be correlated with electrical measurements. The low conductivity of WPA-6 is the consequence of proton bonding into the dioxonium ion. As the annealing of the samples at elevated temperature was done under different conditions for IINS and electrical measurements, the comparison of the results of the two methods cannot be done straightaway. However, according to other results [11] the high conductivity of the sample with $n = 0$ could be related to protons.

Conclusion

The IINS spectroscopic technique, combined with IR and Raman spectroscopies, is a method appropriate for following mutual transformations of protonic species in lower hydrates of heteropolyacids. As the conductivity mechanism seems to be the same for the lower and the higher hydrates, individual proton jumps, location of the protons by IINS may have a decisive role in the understanding of details of charge transfer mechanism for this whole group of superionic conductors.

Acknowledgements

This paper was partly supported by the Serbian Research Fund. Dr. U. B. Mioč and Dr. M. Davidović acknowledge the support of the British Council during the measurements at RAL (UK). They also thank the SERC (ISIS Service) and Dr. J. Tomkinson.

References

1. J. Tomkinson, Spectrochim. Acta, *48A*, 329, 1992.
2. G. J. Kearley, R. P. White, C. Forano and R. C. T. Slade, Spectrochim. Acta, *46A*, 419, 1990.
3. O. Nakamura, T. Kodam, I. Ogino and Y. Miyaka, Chem. Letters, 17, 1979.
4. R. C. T. Slade, J. Barker, H. A. Pressman and J. H. Strange, Solid State Ionics, *28–30*, 594, 1988 (and references therein).
5. O. Nakamura, I. Ogino and T. Kadama, Solid State Ionics, *3/4*, 397, 1981.
6. M. R. Noe-Spirlet, G. M. Brown, W. R. Busing and H. A. Levy, Acta Crystallogr., *A31* 980, 1975 (and references therein).
7. U. B. Mioč, Ph. Colomban and A. Novak, J. Mol. Structure, *218*, 123, 1990.
8. U. Mioč, M. Davidović, N. Tjapkin, Ph. Colomban and A. Novak, Solid State Ionics, *46*, 103, 1991.
9. R. C. T. Slade, H. A. Pressman and E. Skou, Solid State Ionics, *26*, 219, 1988.
10. N. Tjapkin, M. Davidović, Ph. Colomban and U. B. Mioč, Solid State Ionics, *61*, 179, 1993.
11. N. Tjapkin, M. Davidović, U. Mioč and Ph. Colomban, submitted for publication.
12. U. B. Mioč, M. Davidović, N. Tjapkin and J. Tomkinson, Annual Report, ISIS, Vol.II, RAL-92-052, A331, p.122.
13. U. B. Mioč, R. Dimitrijević, M. Davidović, Z. Nedić, M. Mitrović and Ph. Colomban, J. Mater. Sci., *29*, 3705, 1994.
14. D. J. Jones, J. Penfold, J. Tomkinson and J. Roziere, J. Mol. Struct., *197*, 113, 1989.
15. U. B. Mioč, Ph. Colomban, M. Davidović and J. Tomkinson, J. Mol. Struct., *326*, 99, 1994.

Acta Physica Hungarica 75 (1–4), pp. 291–299 (1994)

NEUTRON TOMOGRAPHY: PRINCIPLES AND REALIZATION

B. P. Toperverg, G. P. Gordeev, V. T. Lebedev, Gy. Török,[1]
L. Cser[1], L. Rosta[1], M. Th. Rekveldt[2] and W. Roest[2]

St. Petersburg Nuclear Physics Institute
188350 Gatchina, Russia
[1] *KFKI Research Institute for Solid State Physics*
P.O.B. 49, 1525 Budapest, Hungary
[2] *IRI Delft, The Netherlands*

A new method of neutron tomography is used for the determination of the internal magnetic flux distribution in high-Tc ceramics.

Introduction

The determination of magnetic flux distribution in various condensed media has a general interest with respect to different fundamental and applied researches. Recently, this problem has attracted further attention in connection with the research on high-T_c superconducting ceramics. New superconductors possess the hierarchy of scales of the inhomogeneities, such as grains, twin boundaries, fluctuations of the oxygen concentration or stacking faults, etc. Most of the irregularities described above could act as sources of flux line pinning with different effectivity depending on the temperature and magnetic field. The microscopic picture of the field distribution inside the high-T_c superconducting materials should be rather complicated. Such kind of ceramics could be considered as multi-connected systems of superconducting grains coupled with each other by weak random Josephson junctions [1,2]. The resulting network is an effective superconducting medium resembling the behaviour of an ordinary type II superconductor but in the low field region the flux does not penetrate into the grains.

The low field distribution in high-T_c superconducting ceramics La–Sr–Cu–O has been studied [3] by the method of three dimensional neutron polarization analysis. The temperature and field dependence of the remanent inductance of the magnetic field trapped by La–Sr–Cu–O ceramics (T_c = 40 K) and the long-time relaxation of trapped field have been examined. Recently the patterns of internal field distribution of the ceramic sample Y–Ba–Cu–O were obtained by means of the neutron polarized beam scanning [4]. The information about the Josephson screening currents was extracted from these patterns at the magnetic field less than a low critical field of grains. These experiments yield the unique data on the high-T_c ceramics possessing a number of anomalous properties distinguishing them from conventional hard low temperature superconductors type II.

Nevertheless, the abilities of the aforesaid direct methods are strongly limited because of low intensities of narrow scanning beams. Therefore, the spatial resolution of this differential scanner could not be better than 100 μm. The luminosity is also depressed by monochromatization. At least three-dimensional analysis should be used for low fields ($H < 100$ Oe) only to avoid the aberrations in polarization caused by undefined fields near the sample. These circumstances stimulate to develop new more powerful methods for the investigation of magnetic flux structure. It seems to be appropriate to use Larmor precession of neutron spins within the sample for a broad neutron wavelength spectrum similarly in the well-known Neutron Spin Echo Method [5]. The basic idea of this method presented here was proposed by B. T. Toperverg. The aim of this report is the demonstration of first results on the field of neutron tomography developed in co-operation of IRI, PNPI and KFKI.

Principle of neutron tomography

The neutron beam is passing through the region of magnetic field in which neutron polarization for a given wavelength λ undergoes some precessions (Fig. 1). Here $\mathbf{P}_0$ is the initial vector of polarization settled perpendicular to the field B and L is the path. Neutron are flying along the field direction. Installing a sample with an internal field distribution $\mathbf{B}(r)$ with axial symmetry, the resulting phase of spin rotation is defined by

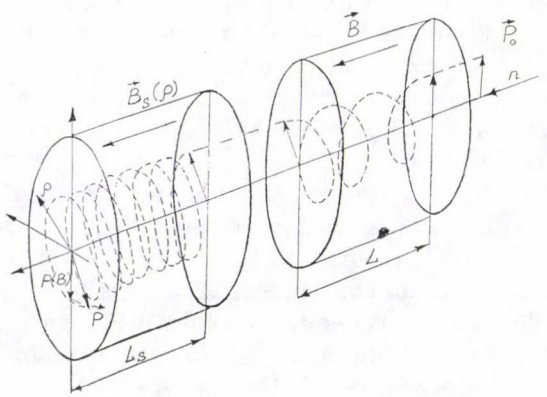

Fig. 1. The neutron polarization vector $\mathbf{P}_0$ precessing about fields $\mathbf{B}$ and $\mathbf{B}_s$

$$\varphi = \varphi_s + \varphi_0 = (\gamma m/\hbar)(B_s(\rho)L_s\lambda + BL\lambda) \tag{1}$$

with neutron gyromagnetic ratio γ, mass m and the length of the specimen L_s. So the integral of the polarization contains the information about the internal field B_s:

$$P(B) = P_0\pi \iint W(\lambda)\cos[\varphi(\rho) + \varphi_0]\rho d\rho d\lambda. \tag{2}$$

Here P is the projection of polarization vector to the initial direction and $W(\lambda)$ characterizes the beam spectrum. In order to extract the field distribution from the integral of the polarization we need to carry out the Fourier transform of the function $P(B)$. We assume the experimental procedure as the measurement of polarization versus field B. The normalized Fourier transform depends on the internal field distribution $B_s(\rho)$:

$$F(\lambda) = f(\lambda)/f_0(\lambda) = (1/\pi\rho_m^2) \int_0^{\rho_m} \cos(\alpha L_s B)(\rho)\lambda)\rho d\rho, \tag{3}$$

$$f(\lambda) = \int P(B)\cos(\alpha BL\lambda)dB,$$

$f_0(\lambda)$ obtained when $\varphi_m = 0$, where $\alpha = \gamma/m\hbar$, ρ_m is the radius of the sample. The determination of $B_s(\rho)$ is possible by using the inverse function $\rho^2(B)$. When we have the integral:

$$F(\lambda) = (1/\pi\rho_m^2) \int [d\rho^2/dB] \cos[\alpha BL_s\lambda]d\lambda. \tag{4}$$

Thus neutrons are powerful tools in the study of internal local fields which could be evaluated individually carrying out separated experiments. The testing of abilities of the method was performed for radial geometry in Delft (IRI) in 1993. This research work is continued at PNPI (Gatchina) using another version arisen from Neutron Spin Echo.

Tomography and NSE

The aim of the authors at this step was the search of a new way to graft the "tomography virus" to NSE machine and transform it to an instrument making aforesaid data. That would be attractive as it promises the development of these researches at all NSE spectrometers available for users. This has been done at PNPI's Neutron Spin Echo spectrometer (Fig. 2), operating at present as a spectrometer of quasielastic scattering with spectrum modulation by spin phase precession [5–8]. This scattering technique has a special character when measuring neutron energy transfer and performing analysis of scattered neutron polarization at the same time. Usually the combination of the full polarization analysis and the spin echo technique is impossible, but this difficulty can be overcome due to the modulation of neutron spectrum. We have to point out that in this modified version of NSE we have a fully polarized neutron beam at the sample but the information on spin rotation in precession field is saved in the structure of spectrum. In that case we can install spin turn devices before and behind the sample and create in this way a new precession field region. So we separate in space the NSE and the sample's cell with its own local field to be investigated. This "three field" version of NSE has been realized for the continuation of tomography experiments. The experimental procedure is

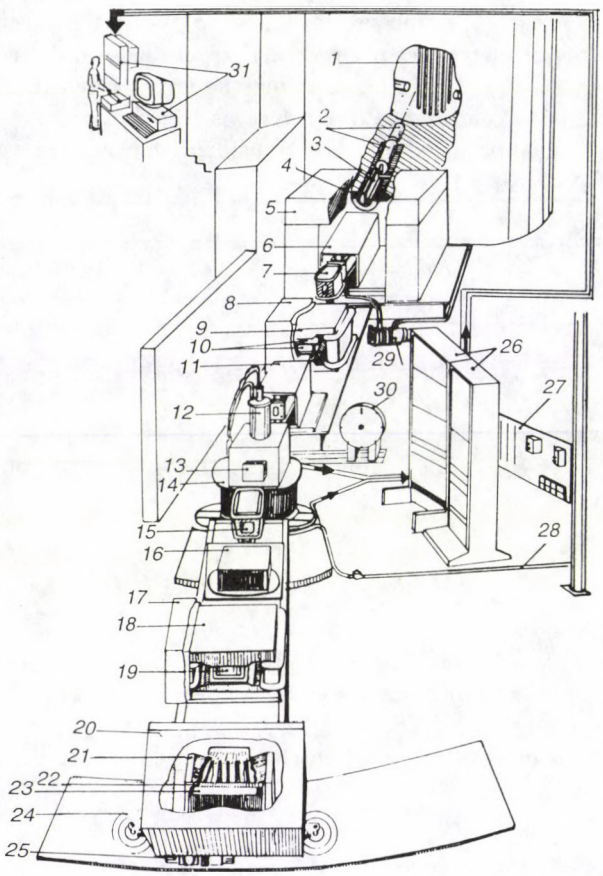

Fig. 2. The Spin Echo Spectrometer of PNPI: 1 – the reactor zone, 2 – collimators, 3 – the mirror covered by ^{58}Ni, 4 – plug, 5 – the shield of polarizer, 6 – the first polarizer; 7, 15 – spin flippers; 8, 17 – screens, 9 and 18 precession magnets; 10, 19 – spin turn devices of $\pi/2$; 11 – the second polarizer; 12 – sample unit; 13 – units for vector analysis of polarization; 14 – transport module; 16, 21 – analysers; 20 – detector's shield; 22 – 20-channel collimator; 23 – detector (20-counters); 24 – air support; 25 – basic frame's power driver; 26 – CAMAC modules; 27 – power supply; 28 – compressed air; 29 – vacuum pumping; mechanical chopper; 30 – system for control and data collection

described as follows: The passing of neutron polarization through the spectrometer is illustrated in Fig. 3. The detailed description of PNPI's NSE spectrometer can be found in [8].

The precession in the first region and reflection from the second polarizer create a special structure of neutron wavelength spectrum:

$$I_s = (1/2)[1 \pm P_0 \cos(\Lambda N 1)]W(\Lambda), \tag{5}$$

where $\Lambda = 2\pi\lambda/ < \lambda >$ and $< \lambda >$ is the mean wavelength. The number of precessions for $< \lambda >$ is proportional to the field strength in first and second region,

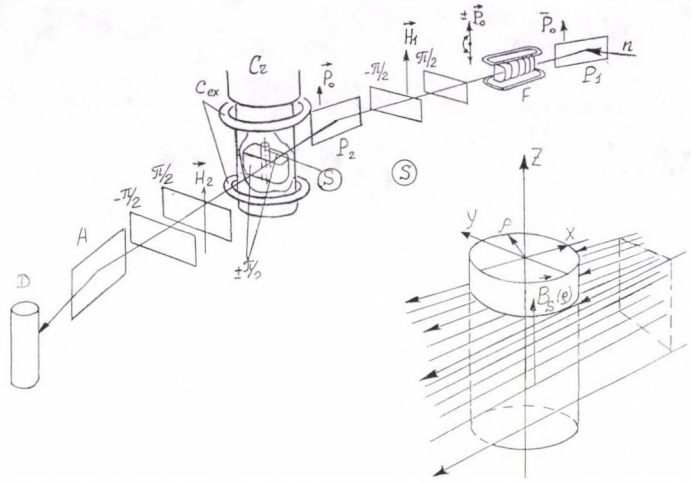

Fig. 3. Layout of the instrument for tomography based on NSE spectrometer: P_1 – the first polarizer; F – spin flipper; $\mathbf{H}_1$ – the first precession field; $\pm\pi/2$ – spin turn devices; P_2 – the second polarizer; Cr – cryostat; S – sample; C_{ex} – coils producing the field at the sample; $\mathbf{H}_2$ – the second precession field; A – analyser; D – detector

$N1 \propto H1$ and $N2 \propto H2$. The reversing of polarization before precession causes the phase shift of π which corresponds to the change of sign $\pm$. In the third region (sample cell) the outcoming polarization should oscillate that reflects local fields distribution:

$$P_{s_x} = P_0 \cos[\Lambda(N3 + n_s(y))]. \tag{6}$$

We assume that the sample has an axial symmetry of the local field distribution. All initial polarizations are vertical and spin rotation will be in a horizontal plane. The sample's axis is also directed vertically. So the local polarization for a given point at beam's section depends on the single variable y. In absence of sample we could observe the rotation of polarization caused by a weak guide field (number of rotations $N3$). The internal fields add some number of rotations $n(y)$. The detected spectral intensity of transmitted beam at any point of beam's section may be written as

$$i_D = W(\Lambda)[1 \pm P_0 \cos(\Lambda N1)[1 + P\cos(\Lambda N2)\cos[\Lambda(N3 + n(y))]]/4. \tag{7}$$

In expression (7) we have taken into account the evolution of polarization in the second precession region and in the last part of the expression the reflection from the analyser. The experimental intensities $I^{\pm}$ correspond to spectral ones integrated over beam area and wavelength interval. In terms of an effective "polarization" we see the NSE signal:

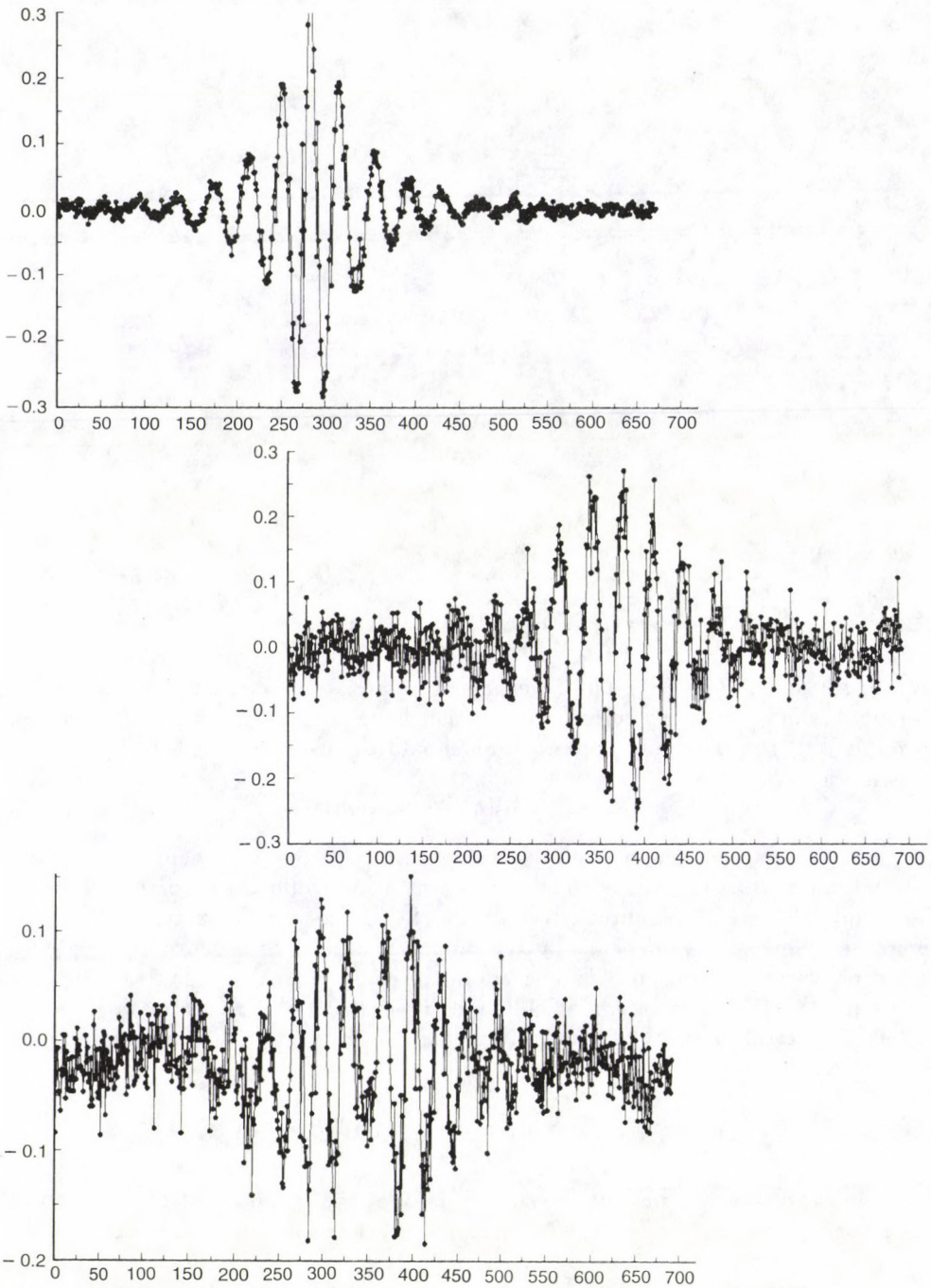

Fig. 4. Patterns of echo groups: effective polarization vs current in correcting coil (proportional to the difference of precessions, i.e. N2–N1). The two field group is shown in a). The three field echo groups are: b) the group split by trapped flux (field cooled sample at 30 K in external field of 43 Oe); c) warm sample $T = 100$ K $> T_c$

$$P_e = (I^+ - I^-)/(I^+ + I^-),$$

$$P = (P_0^2/2) \int W(\Lambda) \cos[\Lambda(N3 + n(y))] \cos(\Lambda \Delta N) d\Lambda dy/y_0 \int W(\Lambda) d\Lambda, \quad (8)$$

$$\Delta N = N2 - N1.$$

This definition will be correct when $N1, N2 \gg 1$ and $N2 - (N3 + n) \gg 1$, which are ordinary conditions for NSE measurements validity. Our calculation shows the splitting of a "normal" echo group caused by the third field. As a result we have the superposition of NSE signals

$$P_e(\Delta N) = (P_0^2/4)[P_e^+(\Delta N) + P_e^-(\Delta N)], \quad (9)$$

$$P_e^{\pm} = \int W(\Lambda) \cos[\Lambda[\Delta N \pm (N3 + n(y))]] d\Lambda dy/y_0 \int W(\Lambda) d\Lambda.$$

A single echo group should be observed by zero third field, i.e. if $N3 + n = 0$. First the proposed experimental procedure was tested by computer simulation. We have obtained these effects of echo group splitting indeed. The second step was carried out as a neutron experiment on an "artificial" specimen. We have used a long solenoid with thick walls for testing the method (internal diameter = 1.5 mm and external one = 4.5 mm). This "sample" has a well defined flux distribution (B homogeneous inside and decreases linearly with a radius up to zero on external boundary). The experimental improvements of the method's validity stimulated the beginning of preliminary measurements on high-T_c superconductors.

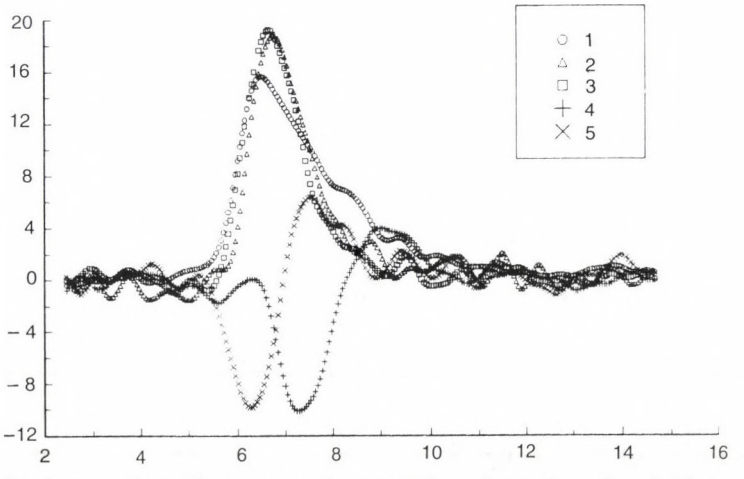

Fig. 5. The Fourier transform of echo signal: 1 – rebuilt beam's spectrum (two field measurement); 2, 3 – correspond to a warm sample at $T > T_c$ (no trapped flux, all changes of spectral polarization caused by the weak guide field $H_g = 10$ Oe); 4, 5 – reveal the influence of trapped flux on spectral polarization for applied fields of 43 and 86 Oe, respectively

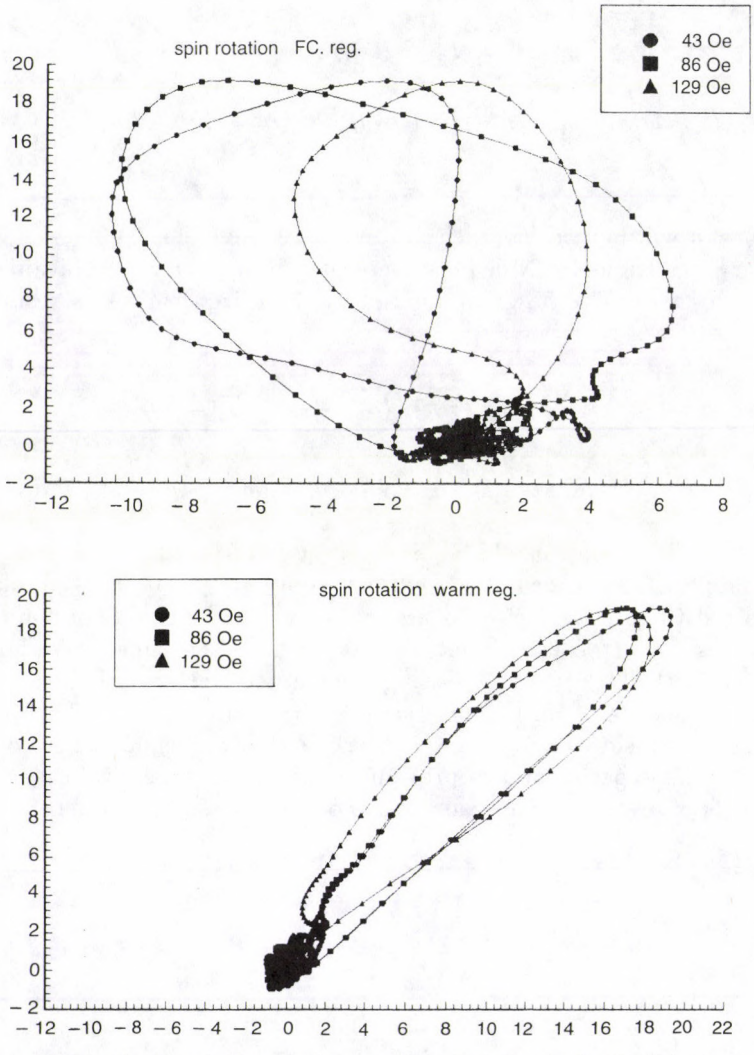

Fig. 6. The effects of spin rotation in the sample: spectral polarization for superconducting sample obtained at temperature $T > T_c$ for three different applied fields, i.e. 43, 86 and 129 Oe. The pictures are drawn by the "running" of wave length along the curve that corresponds to a variation of neutron's time-of-flight through the sample

Experiments on high-T_c ceramics

The experiment on Y–Ba–Cu–O ceramics ($T_c \approx 90$ K) concern the observation of magnetic flux trapping in low field region when the field does not penetrate into grains [1–4]. The cylindrical sample with a diameter of 8 mm and a height of 16 mm has been installed into the box filled with helium gas. This box was equipped with a ring-shaped special spin turn device. This ring was made of a hard magnetic foil and magnetized up to saturation which served for the creation of the boundaries of the

third precession field (Fig. 3). This $\pi/2$ turner, designed for use at low temperature conditions, was placed into the cryostat. We have used the field cooled regime (F.C.): i.e. the sample was cooling down from $T > T_c$ to a given temperature in the field ($H_{ex} = 0 \div 100$ Oe). The following measurements were done after switching off the field. It remains only weak guide field $H = 10$ Oe. The external field was directed along the axis of the sample, i.e. vertically. We have observed the effects of trapped flux in ceramic at 30 K for three fields of 43 Oe, 86 Oe and 129 Oe.

In order to evaluate spin rotation effects in the sample we performed two sets of measurements of echo group on the NSE spectrometer of PNPI for "three field" mode: cold sample ($T = 30$ K); hot sample ($T > T_c$). Also the initial echo group was determined for "two field" regime which corresponds to a normal operation of spin echo machine. Figure 4 shows the patterns for these experiments. One can see the evolution of NSE signal by variation of the third field. A non-split group in the absence of the third field possesses of a high amplitude as compared with signals for the split echo group in accordance with (9) as well as the spreading is more expressed for a higher applied field. That indicates the presence of the trapped flux at the low temperature and expresses its dissipation by warming the sample above T_c.

Much clearer evidence for trapped flux phenomena can be found by comparing Fourier-transformed spectra (Fig. 5). Here we observed a direct phase shift at various wavelengths induced by internal field. An obvious picture of the action of internal field is shown in Fig. 6 where the "plane" of Fourier-transformed polarization is presented: "cold" polarization vs "hot" one. The moving along the line means the viewing by changing wavelength or neutron time-of-flight.

Thus, the presented results reveal the experimental abilities of tomography method which should be advantageous for a really "white" wavelength spectrum. For such a situation it will be possible to obtain full information on local fields using Fourier transform secondly for the function (3). For a broad but finite spectrum (Fig. 5) we must solve an integral equation or use some models for fitting. The simple model of homogeneous field distribution inside the sample was used for data of Fig. 5.

As a result we have obtained parameters which correspond to the values of external field but the behaviour of the experimental curve deviates from the calculated one. The treatment of observed trapped flux behaviour should be based on much more information which we hope to obtain in the future experiment at KFKI's rebuilt reactor.

References

1. K. A. Muller, M. Takashige and J. C. Bednorz, Phys. Rev. Lett., *58*, 11, 1987.
2. C. P. Bean, Rev. Mod. Phys., *36*, 31, 1964.
3. L. A. Akselrod et al, Preprint of LNPI-1523, Leningrad, 1989.
4. L. A. Akselrod et al, Preprint of PNPI, 1804, St. Petersburg, 1993.
5. F. Mezei, Z. Physik, *255*, 146, 1972.
6. V. T. Lebedev, G. P. Gordeev, Pisma v. Zh. Teh. Fiz., *11*, 820, 1985.
7. B. Farago and F. Mezei, Study of Magnon Dynamics in Fe near T_c by Modified NSE-technique, Intern. Conf. on Neutron Scatt. in Santa Fé, August 19–23, 1985.
8. G. P. Gordeev and V. T. Lebedev, Preprint on LNPI-1633, Leningrad, 1990.

Acta Physica Hungarica 75 (1–4), pp. 301–304 (1994)

RIETVELD REFINEMENT TO DETERMINE MOLECULAR CONFORMATION USING MODIFIED CHEMICAL CONSTRAINTS

GY. TÖRÖK, L. V. GOLOSOVSKY[1], R. M. IBBERSON[2] and L. ROSTA

KFKI Research Institute for Solid State Physics
P.O.B. 49, 1525 Budapest, Hungary
[1] *St. Petersburg Nuclear Physics Institute*
188350 Gatchina, Russia
[2] *ISIS, Rutherford Appleton Laboratory*
Chilton, Didcot, OX11 OQX, UK

A novel combination of molecular modelling and full profile refinement with chemical constraints has been used to detemine the low-temperature crsytalline C5 phase structure of MBBA.

Neutron powder diffraction data were recorded on a 95 % deuterated sample of MBBA using the High Resolution Powder Diffractometer, HRPD, at the pulsed spallation source ISIS, Rutherford Appleton Laboratory, U.K. The diffraction data were recorded in fixed angle detector banks at backscattering ($2\theta_{ave} = 168°$) and at 90° over a time-of-flight range of 85–230 ms. The measurement was performed on the $C5$ phase [1,2] at 5 K.

The size $Vc = 1513$ Å^3, and structural complexity of the MBBA $C5$ phase is beyond the scope of the traditional Rietveld profile analysis method. It was, therefore, necessary to make extensive use of chemically derived geometric slack constraints within the profile refinement procedure and, more importantly, develop a method of model optimisation in order to establish the correct conformation of the molecule within the unit cell.

Structure solution and refinement was achieved through the following steps:

(i) The MBBA molecular geometry is established using known chemical bond distances and angles.

(ii) The molecule is positioned in the elementary cell, following sequential translation along and rotation around the principal cell directions. The best starting position was calculated minimising the residual:

$$\min = |Fcalc(hkl)^2| - |Fobs(hkl)^2|.$$

(iii) The molecular conformation is established. Consideration of calculated rotational barriers and potentials for the free molecule are used to establish characteristic axes of rotation in the crystalline phase [3, 4]. Sequential rotation of these molecular components around these axes establishes the optimum conformation by again minimising the function given by (ii).

(iv) Full profile refinement including geometric slack constraints and using the structural model determined above as starting parameters.

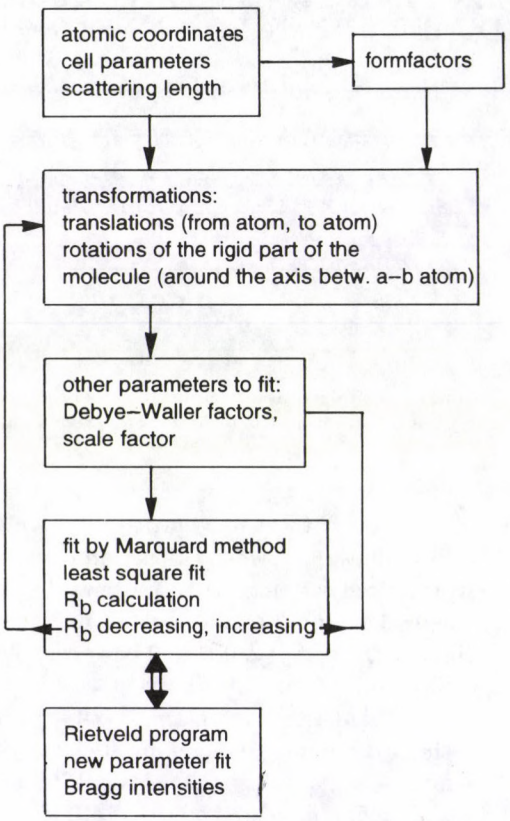

Fig. 1. Flow chart for the conformation fit program

Despite the high intrinsic peak overlap and sample dependent line broadening the highest resolution backscattering diffraction data showed the structure to be triclinic with space group P-1 of lattice parameters

$$a = 7.9776, \quad b = 5.7224, \quad c = 31.1119, \quad \alpha = 90.730, \quad \beta = 91.950, \quad \gamma = 91.243.$$

This is the variance with a monoclinic structure previously reported [1,2]. Since in the elementary cell $Z = 4$, a structure where two molecules have different conformations was assumed. The data recorded at 90° were used for profile refinement in combination with 218 geometric slack constraints for the 82 atoms in the refinement. For all atoms the displacement parameters and site occupation factors were fixed because of the limited nature of diffraction data. Using the flow chart depicted

in Fig. 1 the best fit for $C5$ phase diffraction data is shown in Fig. 2. Rwp= 0.195 and a χ^2 value 1.99 obtained thus permit a reliable molecular packing scheme to be proposed for the crystalline $C5$ phase of MBBA. The molecular packing is shown in Fig. 3. The two independent molecules in the unit cell have different conformations. In one molecule the benzene rings are coplanar whereas in the second molecule there is an angle of 60° between the benzene ring planes. Such a structure is consistent with Raman data that indicates non-Debye behaviour for the low frequency range of vibrational states [5].

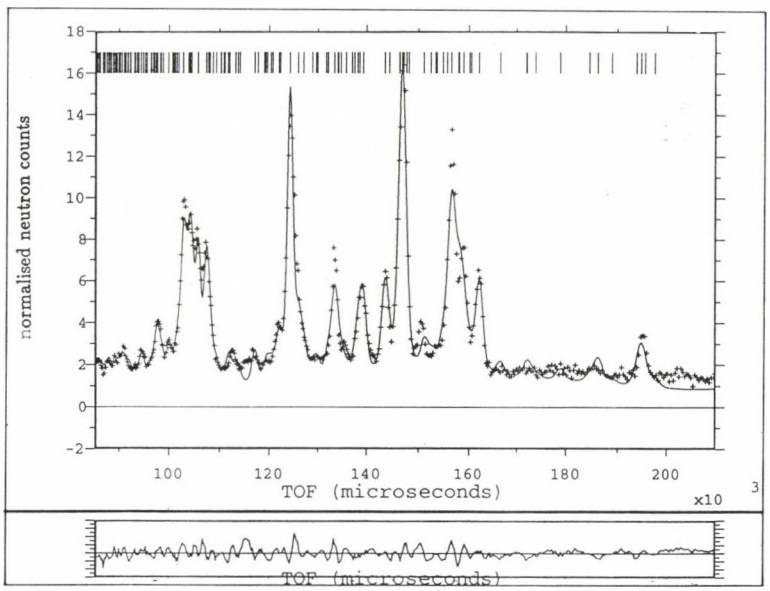

Fig. 2. The best fit for HRPD pattern for MBBA $C5$ phase

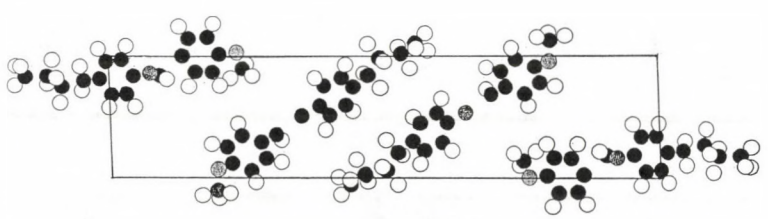

Fig. 3. The molecular packing scheme for $C5$ phase of MBBA

References

1. L. Rosta, N. Kroó, V. K. Dolganov, P. Pacher, V. G. Simkin, Gy. Török and G. Pépy, Mol. Cryst. Liq. Cryst., *144*, 197, 1987.
2. G. Pépy, R. Fouret, M. More and L. Rosta, Physica Scripta, *39*, 485, 1989.
3. J. Berges, H. Perrin and M. Jaffrain, C. R. Acad. Sc. Paris, *281*, Sep. 22, 1975.
4. J. Berges and H. Perrin, Journal de Chimie Physique, *78*(7/8), 1981.
5. A. V. Belushkin, V. K. Dolganov, W. Zaleski, I. Navrotznik, I. Natkaniec and E. F. Shaka, Comm. of JINR Dubna, P14–414, 1984.

Acta Physica Hungarica 75 (1-4), pp. 305-310 (1994)

HIGH RESOLUTION NEUTRON DIFFRACTION TECHNIQUES FOR STRAIN/STRESS MEASUREMENTS AT A STEADY STATE REACTOR

M. VRÁNA, P. MIKULA, P. LUKÁŠ, J. ŠAROUN and P. STRUNZ

Nuclear Physics Institute
25068 Řež near Prague, Czech Republic

Two high-resolution neutron diffraction techniques: three-axis nondispersive setup and two-axis energy dispersive transmission arrangement for nondestructive strain/stress measurements are described. Both techniques, mutually complementary provide sensitivity in relative difference between lattice spacings $\Delta d/d$ down to 10^{-5} and FWHM of 10^{-3} rad permitting profile broadening analysis for reasonable sample volumes and counting times even at a medium power research reactor.

Introduction

Residual stresses are determined form the measurement of residual strains, which are then converted to stresses using appropriate moduli. Neutrons, similarly to X-rays, are used to measure lattice strain but because absorption constraints in most engineering materials are much smaller than for X-rays, rather large volume samples may be investigated nondestructively [1,2]. The lattice strain is defined as $\varepsilon = \Delta d/d$, where Δd is the change in lattice spacing due to strain and d is the unstrained spacing. Differentiating of Bragg's equation, $2d\sin\theta = \lambda$, where θ is the diffraction angle, gives $\varepsilon = -\cot\theta \cdot \Delta\theta$ at a fixed wavelength λ. For the measurements conventional high resolution powder diffractometers are usually used. The investigated volume element of the sample is precisely defined by absorbing masks in the input and output beams. Measurements related to the strains are made by recording the peak position and the peak profile with respect to the chosen gauge volume. As neutron counts are related to the size of the gauge volume (tens of mm^3) and good instrumental resolution is required (peak shifts are of the order of 10^{-4}–10^{-3} rad) experiments of this type are usually performed at high flux reactors.

Using cylindrically bent perfect crystals as neutron monochromator and analyser and thanks to focusing in real and momentum space our dedicated three axis spectrometer and double crystal diffractometer permit us high resolution strain measurements even at our medium power reactor for reasonable sample volumes and counting times.

Three-axis setup

A schematic three-axis arrangement for the study of polycrystalline materials is shown in Fig. 1. Its favourable properties consist basically of the following steps:

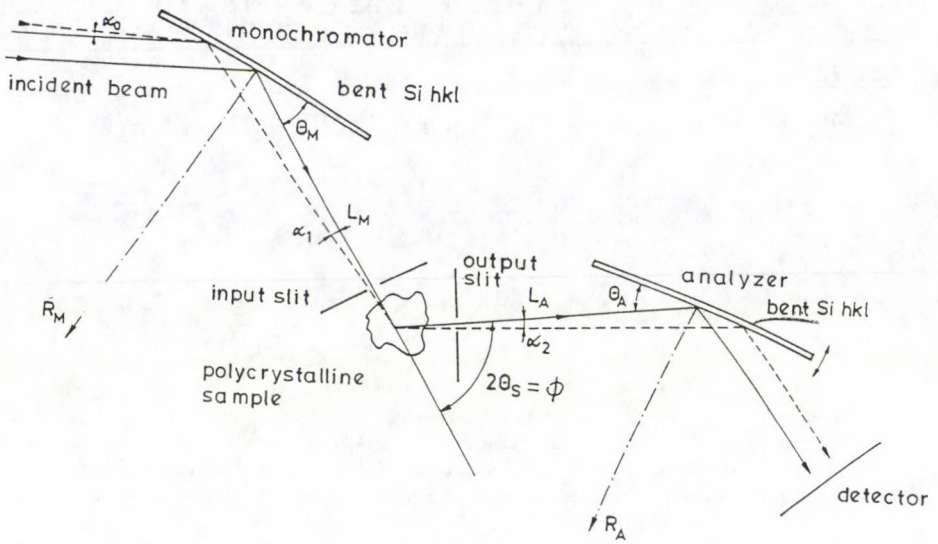

Fig. 1. Schematic sketch of the three-axis setup equipped with a bent Si single-crystal monochromator and analyser for high-resolution strain/stress measurements

1. Neutrons diffracted by a bent perfect crystal monochromator are focused on a polycrystalline sample (focusing in real space).

2. The beam diffracted at an angle ϕ by a volume element selected by a pair of input and output slits is analysed by a bent perfect crystal analyser optimized for maximum resolution (focusing in momentum space).

Contrary to the arrangement employing conventional mosaic crystals, in our case of bent perfect crystals there is a strong angular-wavelength correlation in the beams incident on the sample and also on the analyser. This fact permits the whole three axis arrangements to be optimized for a maximum resolution, of course, limited to a rather short Q-range. The general condition of focusing in momentum space minimizing the dispersion between all elements of the described system has been derived in the following form [3]

$$2\tan\theta_s = \frac{\tan\theta_M}{1 - \frac{L_M}{R_M \sin\theta_M}} + \frac{\tan\theta_A}{1 - \frac{L_A}{R_A \sin\theta_A}}. \tag{1}$$

Inspection of the relation (1) reveals that by setting the suitable bending radii R_M, R_A (eventually the distance L_M, L_A) the "dispersion-free" diffractometer arrangement may be achieved even in a general case of different lattice spacings

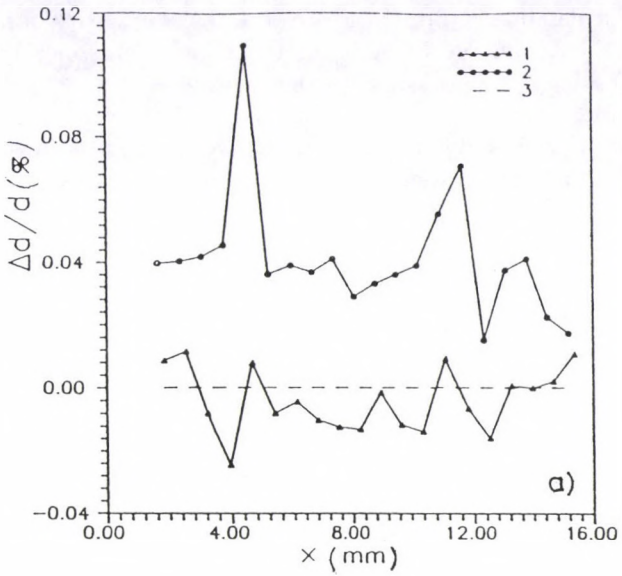

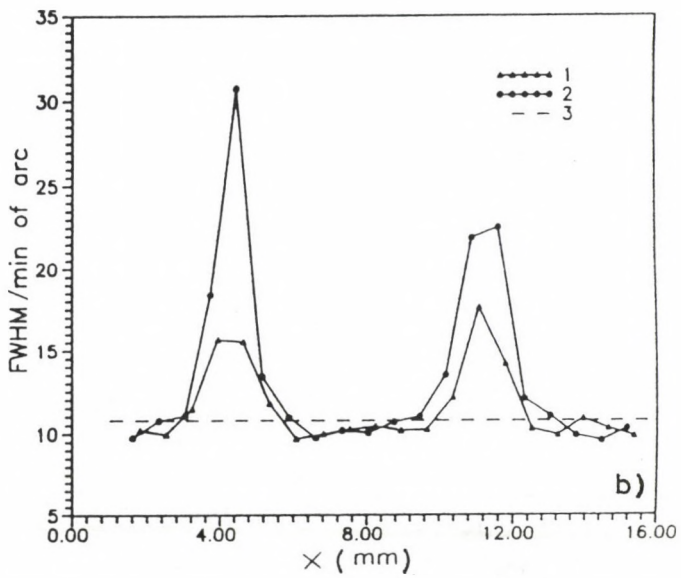

Fig. 2. Scans of residual strain through $\Delta d/d$ (a) and FWHM (b) measurements along the longest edge of a steel bar (10× 10 mm cross-section) consisting of three pieces welded by the use of an electron beam at positions $x = 4$ mm and $x = 12$ mm. 1 and 2 correspond to measurement from the 2 mm layer in the depth of 5 mm and 1 mm, respectively, 3 – a free piece of the steel bar

of monochromator (analyser) with respect to the spacing of the sample. This fact permits to fulfil the above mentioned two requirements and consequently, to increase the luminosity and the resolution of the setup simultaneously. The properties of different combinations of reflections on the monochromator, sample and analyser

were experimentally tested. For details see [3]. The FWHM and the intensity of a diffraction profile obtained by the ϕ-scan and being of the Gaussian form is mainly influenced by the effective mosaicity (proportional to the thickness) of the bent monochromator. In practical measurements we usually use FWHM of 7′ (it refers to standard samples of Fe(110), Al(200) and Cu(111)) and an investigation sampled volume of about 30–100 mm^3 permitting reasonable counting times at our medium power reactor.

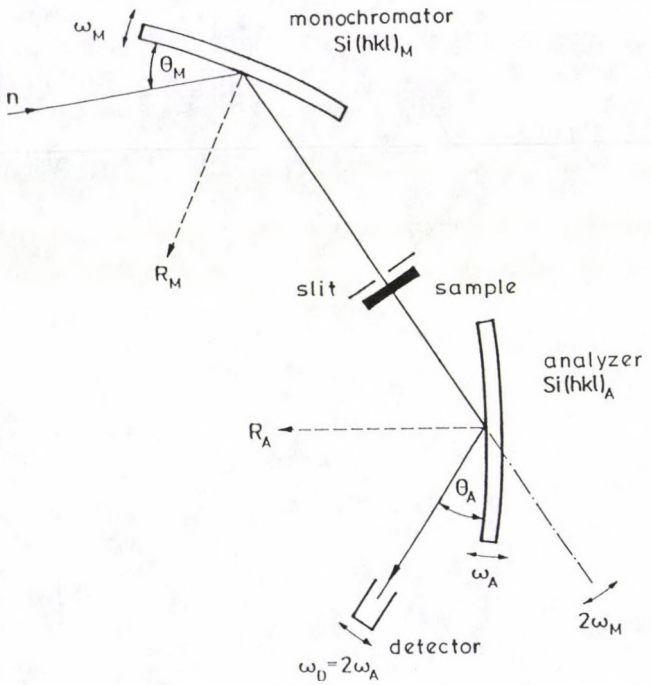

Fig. 3. Schematic sketch of the double-axis arrangement used for energy-dispersive neutron-transmission strain measurements

Figure 2 demonstrates the scan of residual strain along the longest edge of a steel bar consisting of three individual parts welded by an electron beam.

Energy-dispersive neutron transmission diffraction

This method is particularly used at pulsed neutron sources, where the intensity wavelength dependence is analysed by the time-of-flight (TOF) technique [4]. It is well known that in case of diffraction by a polycrystalline sample there is a limiting value of λ ($\lambda_0 = 2d_{hkl}$) for each Bragg reflection where the backscattering is reached. Consequently, neutrons of $\lambda > \lambda_0$ cannot be reflected by the corresponding system of the lattice planes (hkl). On the other hand, when going down with λ,

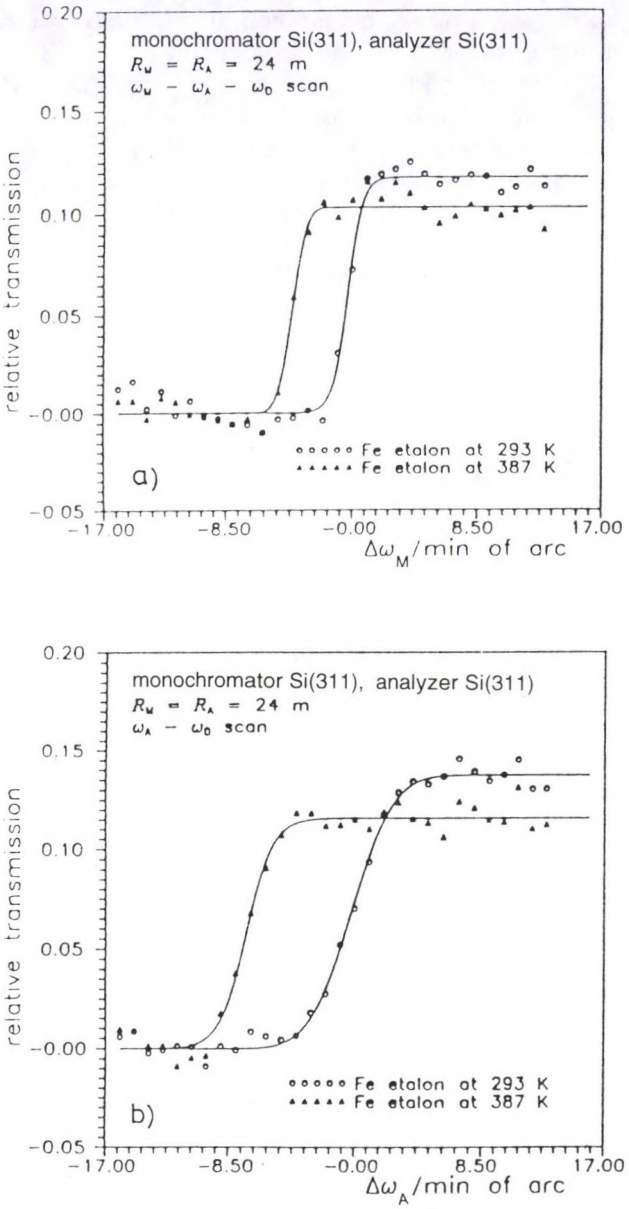

Fig. 4. Relative transmission function vs $\Delta\omega_M$ ($\omega_M - \omega_A - \omega_D$ scan) (a) and $\Delta\omega_A$ ($\omega_A - \omega_D$ scan) (b) of a Fe(321) standard sample for two different temperatures

at this critical value of λ_0 the intensity of neutrons transmitted through the polycrystalline sample decreases steeply. Thus Bragg edges corresponding to individual reflections can be observed in the transmission TOF spectra. The most important

advantage of using this method at the pulsed source consists in the possibility of using the full white spectrum and studying many Bragg edges simultaneously.

However, for residual strain/stress studies in many cases there are sufficient strain measurements on one or several chosen reflections. For such a case in analogy to the TOF technique we have proposed and tested this energy dispersive transmission diffraction at our steady state reactor when using a conventional double-crystal diffractometer equipped with bent perfect crystals (monochromator and analyser) with an investigated sample placed in between. To keep the neutron wavelength with a sufficiently high precision we used the dispersive double-crystal (+,+) setting (see Fig. 3). It is clear that the $\Delta\lambda$-resolution is in this case tunable and determined by a crystal curvature according to the relation

$$\Delta\lambda/\lambda = \cot\theta\,\delta\theta, \tag{2}$$

where $\delta\theta$ means the "effective mosaicity" of the bent perfect crystal which in the limiting case of the flat crystal is equal to the width of the so-called Darwin box. We tested the following two scans:

$$1.\ \omega_M - \omega_A - \omega_D\ (\Delta\omega_D = 2\Delta\omega_A)\ scan$$

It permits to measure $I(\lambda)$ dependence (with and without the sample) in steps of λ chosen by the monochromator when rocking in the incident polychromatic beam in the vicinity of the diffraction edge λ_0.

$$2.\ \omega_A - \omega_D\ (\Delta\omega_D = 2\Delta\omega_A)\ scan$$

Contrary to the former case, within this scan the angular position of the monochromator is fixed and set for the reflection of λ_0-neutrons. Then the second crystal analyses $I(\lambda)$ distribution within the range $(\lambda_0 - \Delta\lambda/2, \lambda_0 + \Delta\lambda/2)$ of neutrons coming from the monochromator as selected form the polychromatic beam and passed through the slits determining a sample gauge volume. If the monochromator–analyser distance coincides with the focal length of the bent monochromator the sensitivity to peak shifts increases twice with respect to the former scan.

Fig. 4 demonstrates the ability of this energy-dispersive transmission technique on a Fe(321) standard sample when instead of mechanical stress we used a homogeneous heating of the whole sample volume.

References

1. A. J. Allen, M. T. Hutchings, C. G. Windsor and C. Andreani, Adv. in Physics, *34*, 445, 1985.
2. M. T. Hutchings and A. D. Krawitz (eds): Measurement of Residual and Applied Stress Using Neutron Diffraction, NATO ASI Series: Applied Sciences, *26*, Kluwer, Acad. Publ. Amsterdam, 1992.
3. M. Vrána, P. Lukáš, P. Mikula and J. Kulda, Nucl. Instrum. and Methods in Phys. Research, *A338*, 125, 1994.
4. H. G. Priesmeyer, J. Larsen and K. Meggers, J. Neutron Research, *2*, 31, 1994.

Acta Physica Hungarica 75 (1–4), pp. 311–316 (1994)

INTERMOLECULAR INTERACTION IN AQUEOUS SOLUTIONS OF TETRAMETHYLUREA

L. Cser, T. Grósz and Yu. M. Ostanevich[1]

KFKI Research Institute for Solid State Physics
P.O.B. 49, 1525 Budapest, Hungary
[1] *Joint Institute for Nuclear Research*
141980 Dubna, Russia

The intermolecular interaction in aqueous solutions of tetramethylurea was studied at low concentrations by carrying out a series of concentration dependent SANS measurements.

The behaviour of the concentration dependence of the forward scattering cross-section and the squared value of the apparent radius of gyration suggests the presence of attractive forces between the TMU molecules while the increase of the radius of gyration can be interpreted in terms of formation of aggregates. The model calculation performed is based on the assumption that the aggregates can be represented by dimers. The theory of chemical equilibrium is used for connecting the number of monomers and dimers. The set of parameters obtained by the least mean squares fit of model to the observed data is presented.

Over its entire concentration range tetramethylurea (TMU) is miscible with water despite the fact that the TMU molecule is nonionic and contains four hydrophobic methyl groups.

Our previous small-angle neutron scattering (SANS) investigations revealed a number of interesting features of the structure of aqueous TMU solutions. By using a wide variety of the contrast variation method (both normal and deuterated TMU molecules were dissolved in heavy and light water) we were able to show that some structural changes take place in the aqueous TMU solution at an aquamolality of about 0.7; that the hydrophobic interaction between the TMU molecules becomes more attractive at higher temperature; that contact pairs are present in the relatively dilute solutions; that there is preferential orientation of water molecules in the hydration sphere.

It seems plausible that in the solution at least two types of interactions between the TMU molecules exist: a direct dipole-dipole and dispersion interaction between the solute molecules, and hydrophobic interaction which can lead to formation of solvent–separated and contact pairs. In addition to this two water molecules can form direct hydrogen bonds with the carbonyl group of TMU.

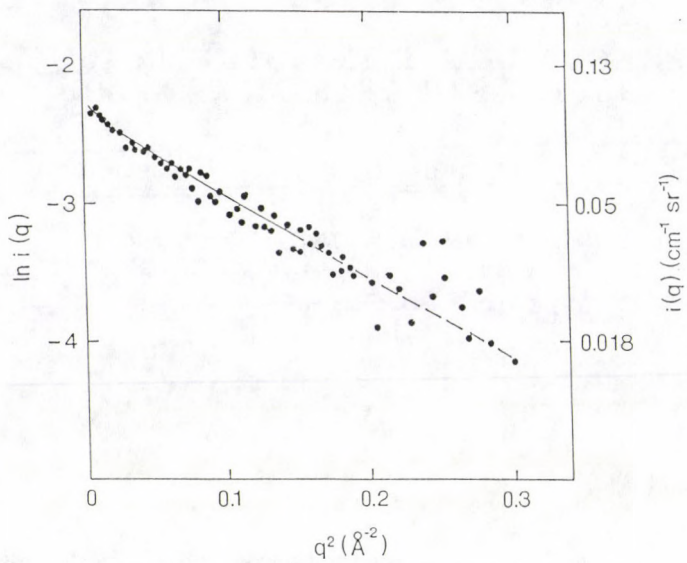

Fig. 1. Guinier plot for a 1 m solution of H-TMU in D_2O, ($i(q)$: scattering cross-section, q: transferred momentum)

The present work aims to study these interactions at low concentrations by carrying out a series of concentration dependent SANS measurements. A typical scattering pattern in Guinier coordinates is given in Fig 1. It is seen that the data can be well approximated by a straight line, thus there are two parameters to be evaluated: the slope of the straight line and the scattered intensity at zero momentum transfer $(q = 0), i(0)$.

The first parameter gives the so-called apparent value of the radius of gyration $(R_{g,app})$ while the second one, due to the use of a standard vanadium scatterer, can be transformed into the absolute scattering cross-section of the molecule.

These parameters are shown in Figs 2 and 3. From these figures it can be seen that there is a very slight concentration dependence in the forward scattering cross-section and that the squared value of the apparent radius of gyration shows a nonlinear increase with increasing TMU concentration.

Such behaviour hints at the presence of attractive forces between the TMU molecules since a hard sphere repulsion force, which is of very short range, would give rise to a steep decrease in the forward scattering cross-section. On the other hand, the increase of the radius of gyration can be interpreted in terms of formation of aggregates. The simplest assumption would be that the aggregates can be represented by dimers; on the basis of this assumption, we perform a model calculation . The observed values of $i(0)$ and $R^2_{g,app}$ are averages which for two types of non-interacting particles can approximately be written as

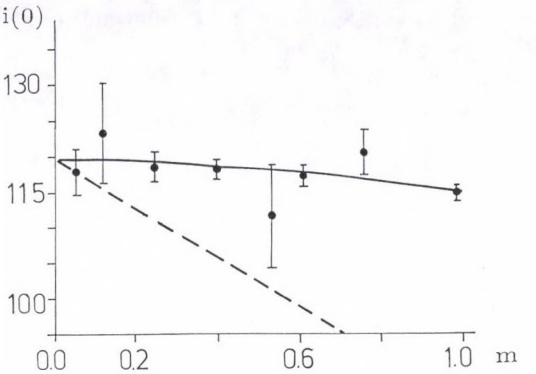

Fig. 2. The forward scattering intensity cross-section of one TMU molecule (in barns) as the function of the TMU concentration (m, aquamolality). Full circles with error bars: experimental points, full line: the result of the least square fit, broken line shows the hard-sphere calculation for dependence

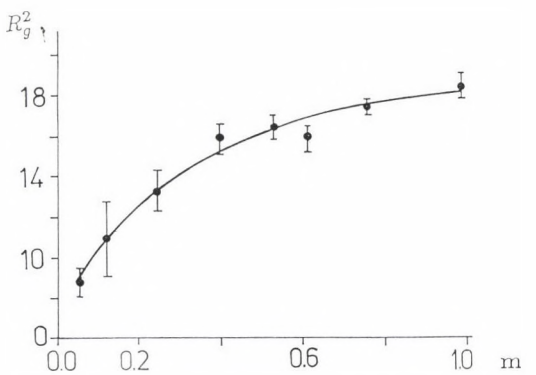

Fig. 3. The squared value of the radius of gyration (in Å^2) as the function of the concentration (m, aquamolality). Full circles with error bars: experimental points, the full line is the result of the least square fit

$$i(0) \equiv d\sigma/d\Omega = i_1(0) + i_2(0) \tag{1}$$

and

$$R^2_{g,app} = -(1/3)i(0)^{-1}di/d(q^2) \equiv$$

$$R^2_{g,1}i_1(0)/[i_1(0) + i_2(0)] + R^2_{g,2}i_2(0)/[i_1(0) + i_2(0)]. \tag{2}$$

For interacting particles the whole effect of the interaction can be described by the coefficients appearing as integrals in the expression of the scattered intensity

distribution. These integrals contain the pair correlation functions and the number of different interacting particles [2]

$$i(q) = i_0(0)n \sum p_k < F_k^2(q) > +$$

$$+ \sum \sum p_k p_j (1/v_1) \int_0^\infty [P_{kj}(r) - 1](sin(qr)/qr) 4\pi r^2 dr. \tag{3}$$

Here $P_{kj}(r)$ gives the probabilities that the k-th and j-th type particles are separated by distance r, and v_1 is the volume offered to each particle, p_k is the relative abundance of the k-th particle. The forward scattering intensity $i(q = 0)$ for the system consisting of hard spheres can be easily calculated and the result of the calculation can be expressed as a linear function of the partial volumes (Φ) of the particles. For example for uniform spheres $i(0) = n[1 - 8\Phi]$.

So far as the interacting particles are concerned the coefficients of the partial volumes stemming from the integrals in Eq. (3) appear to be less simple, and for a mixture of aggregates one has to utilize some modelling approach. These coefficients — B_{ik} — reflect the type of interaction appearing between the i-th and k-th types of particle.

For simplicity, here we restricted ourselves to the consideration of pair correlation, in which case there are two main approaches to the model description of aggregate formation. According to the first one we can consider the aggregates as relatively stable dimers in which two TMU monomers are bound via interaction the nature of which should be elucidated later. The theory of chemical equilibrium can be used for connecting the number of monomers and dimers, in the equilibrium

$$TMU + TMU \overset{\mathrm{K}}{\rightleftharpoons} [TMU - TMU]. \tag{4}$$

Then

$$n = n_m + 2n_d$$

and

$$K = n_d / n_m^2. \tag{5}$$

In addition, $B_{mm} = 8 - 2K$ [3] and B_{dd} and B_{md} are expected to have values close to those of the hard sphere. The concentration dependence of the forward scattering intensity can be written as

$$i(0) = i_0\{(n_m/n)[1 - B_{mm}\Phi(n_m/n)] + 4(n_d/n)[1 - B_{dd}\Phi(n_d/n)] -$$

$$-2(n_m/n)(n_d/n)B_{md}\Phi\}. \tag{6}$$

In the same approximation the concentration dependence of the apparent value of the radius of gyration may then be expressed as

$$R_{app}^2 = (n_m/n)[R_{gm} - B_{mm}\Phi(n_m/n)^2(R_{gm}^2 + D_{mm})] +$$

$$+4(n_d/n)[R_{gd}^2 - B_{dd}\Phi(n_d/n)(R_{gd}^2 + D_{dd}^2)]-$$

$$-2(n_m/n)(n_d/n)B_{nm}\Phi[(1/2)(R_{gm}^2 + R_{gd}^2) + D_{md}^2], \tag{7}$$

where

$$R_{gd}^2 = R_{gm}^2 + \frac{1}{4}(2R + L)^2. \tag{8}$$

Here $R = 3.6$ Å is the equivalent radius of the TMU molecules and L is the distance between the TMU molecules. The indices m and d stand for the monomers and dimers, respectively. The interaction distances (D_{ik}) were calculated in the hard sphere approximation by a method given elsewhere [1]. A least mean squares fit gives the set of parameters: $B_{mm} = 8 - (2K = 4.08 \pm 0.13)$; $B_{dd} = -4.3 \pm 6$; $B_{md} = 7.3 \pm 5$; $L = 6.2 \pm 1$ Å; (Here L is the distance between the TMU molecules).

From these data it follows that a remarkable number of TMU molecules take part in dimer formation. The low values of B_{dd} and B_{md} indicate that the dimer–dimer and monomer–dimer interactions are rather attractive. The relatively large value of L tempts one to interpret this value as a distance between the oxygen atoms of two TMU molecules connected by intermediate water molecules via hydrogen bonds (see Fig. 4).

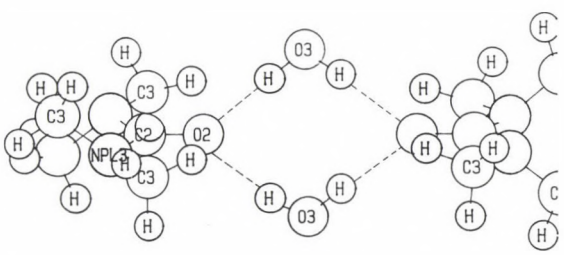

Fig. 4. A possible view of the hydrogen bonded dimer of the TMU molecules

In the frame of the second approach one takes into consideration that in the dilute solutions the interactions between the solute molecules can be approximated by pair formation of two types: solvent separated and contact ones. In this case three different types of particle are present in the solution. In consequence, many more components appear in the pairwise interaction. It is evident that one has to decide which of these interactions are negligible. The answer to this question will be dealt with elsewhere.

Despite giving relatively good approximation of the experimental data, even the first model suffers from an abundance of rough assumptions. However, the main advantage of our second approach is that its basic assumption allows us to connect all observed data over the whole range of concentration into one ensemble, for which one can use the same parameters.

References

1. V. Yu. Bezzabotnov, L. Cser, T. Grósz, G. Jancsó, Yu. M. Ostanevich, J. Phys. Chem. *96*, 976, 1992.
2. A. Guinier, G. Fournet, Small-Angle Scattering of X-Rays, J. Wiley, New York, 1955.
3. H. L. Friedman, A Course in Statistical Mechanics, Prentice-Hall, Englewood Cliffs, New Jersey, 1985.

Acta Physica Hungarica 75 (1–4), pp. 317–320 (1994)

POSTERS (NUCLEAR PHYSICS)

NEUTRONS FOR FISSION-TRACK DATING AND FISSION TRACKS FOR NEUTRON SPECTRUM MONITORING

F. BELLEMANS, F. DE CORTE and P. VAN DEN HAUTE[1]

Laboratory for Analytical Chemistry
Institute for Nuclear Sciences, Gent University
Proeftuinstraat 86, B-9000 Gent, Belgium
[1] *Laboratory for Mineralogy, Petrogr. and Micropedology*
Geological Institute, Gent University
Krijgslaan 281, B-9000 Gent, Belgium

An account is given of our experiences in the absolute calibration of Fission-Track dating, based on coirradiation with the sample either of metal monitors or of uranium-doped glass monitors. Secondly, the (Corning) CN3 and CN5 glasses, with a largely different Th/U ratio, were used to characterize the neutron spectrum in channel 4 of reactor Thetis (Gent) by means of fission-track counting. The results obtained with this technique were in good agreement with those obtained by the activation method.

The absolute calibration of the Fission-Track dating method

The Fission-Track (FT) dating method is based on the spontaneous fission of ^{238}U, which leads to linear trails of damage in the crystal lattice of natural minerals. The density of the spontaneous fission tracks, which can be counted under an optical microscope after etching, depends on the age of the sample and its U concentration. The latter can be eliminated by irradiating the sample with thermal neutrons and counting the tracks originating from the induced fission of ^{235}U. The age is thus a function of the spontaneous to induced track density ratio and the thermal neutron fluence, among other parameters.

In the absolute calibration of the FT method, the thermal neutron fluence is determined by coirradiating the sample either with metal monitors such as Au and Co or with U-doped glasses. In the latter case, the thermal neutron fluence is obtained by comparing the track density in this glass with the density in an identical glass which was pre-irradiated with a well specified neutron fluence (as determined with metal monitors). This technique makes the FT geochronologist independent of the availability of a γ-spectrometric system with a Ge-detector.

As shown by publications reporting on inter-laboratory comparisons [1,2] the SRM glasses produced by the National Institute of Standards and Technology, Gaithersburg (Washington, D.C.) and the CN glasses offered by J. Schreurs at Corning Inc., Corning (New York) are most often used for this purpose. From the SRM glasses, which exist in four different U concentrations, pre-irradiated discs

with a certified thermal neutron fluence were made available. Surprisingly, in the NIST certificates two "certified" fluence values are quoted, respectively obtained via Au and Cu, which show a difference of about 10 % [3,4]. This discredited among FT geochronologists the use of metal monitors for absolute neutron fluence determinations and stimulated the application of the ζ-calibration method [5] which is based on age standards, the age of which is determined with other isotopic methods. This procedure eliminates the need for determining the neutron fluence but also deteriorates the FT method as an independent dating technique. Van den haute et al [6], however, proved that the neutron fluence can be determined in an accurate and reproducible way by means of Au and Co, which are generally accepted as primary standard monitors in neutron metrology. Later on, De Corte et al [7] even achieved a consistency between the Au and Co monitors and Cu, which is not an internationally accepted standard, by reassuring a complete annihilation of the positron emitted by ^{64}Cu and by introducing up-to-date nuclear data for activation and decay. As concluded, this does not turn Cu into an adequate fluence monitor because one has to take into account the uncertainty of all nuclear constants involved. Recently, the ^{235}U(n,f) reaction rate was calculated using the Au and Co fluences and compared with the one determined via γ-spectrometry of the fission products after irradiation of an Al–U alloy (IRMM SP89010). The very good consistency which was observed between both results again stimulates the use of Au and Co for neutron fluence monitoring. Next, it was argued that the inconsistencies shown in the NIST certificates may have been contributed to by the use of relatively thick metal foils without correction for thermal and epithermal neutron self-shielding and by the lack of correction for the contribution of epithermal activation. Hence, doubt can be cast on both the Au and Cu fluences and this discredits the practical use of the SRM glasses as standard material for the determination of the thermal neutron fluence in the absolute approach of FT dating. In order to overcome these difficulties , we are presently performing cooperative work with the Institute of Reference Materials and Measurements (IRMM, Geel) of the European Community in order to produce, characterize and certify new and accurate sets of U-doped glass standards.

Of the CN glasses, which exist in six different types (CN1 to CN6), no pre-irradiated specimens are available.

Neutron spectrum monitoring

During irradiation in a nuclear reactor, epithermal and fast neutrons also produce fission tracks, respectively from ^{235}U and from ^{238}U and ^{232}Th. This can lead to systematic errors in the age determination of a sample when the irradiation is performed in an insufficiently thermalized neutron spectrum. Instead of using the activation method for the characterization of the neutron spectrum, this can in principle also be performed by means of FT counting after irradiation of a U-doped and a Th-doped glass, and this was investigated in the present work by making use of Corning CN glasses with largely different Th and U content.

The number of fission tracks n_f after irradiation depends on the Th and U concentration in the glass monitor and on the thermal, epithermal and fast neutron fluences:

$$n_f = N_{235}[\sigma_{f,232}\Phi_f I_{Th} + \sigma_{0,235}\Phi_{th} + I_{0,235}\Phi_e + \sigma_{f,235}\Phi_f + I_{0,238}\Phi_e I_U + \sigma_{f,238}\Phi_f I_U], \quad (1)$$

where N is the number of atoms, σ_f the cross-section for fast neutrons [8], σ_0 the cross-section at 2200 ms^{-1} neutron velocity [9], I_0 the resonance integral [8], Φ_f, Φ_{th}, Φ_e the fast, thermal and epithermal neutron fluence, respectively, I_{Th} the N_{232}/N_{235} ratio and I_U the N_{238}/N_{235} ratio. The subscripts 232, 235 and 238 refer to ^{232}Th, ^{235}U and ^{238}U, respectively.

The Th and U concentrations in the Corning glasses were determined by means of k_0-standardized neutron activation analysis [10]. In order to check the accuracy of the method the concentrations of Th and U were also determined in the NIST-SRM glasses 611, 613, 615 and 617 which have certified Th and U contents [3,4]. The nominal concentrations in these glasses range between 20 ppb and 500 ppm and a good consistency was observed for each glass type [11]. Of the CN glasses, CN3 and CN5 showed the largest difference in Th and U content, namely 39.9 ppm and < 0.020 ppm, respectively, for Th and 0.681 ppm and 12.4 ppm, respectively, for U.

In channel 4 of reactor Thetis (Gent) a CN3 and CN5 glass were irradiated under a Cd cover in order to eliminate the influence of thermal neutrons, followed by irradiation of a bare CN5 glass. Prior to irradiation a muscovite sheet with low U content was firmly attached to each glass. The muscovite then also registers the induced tracks and serves as an external detector. To reveal the tracks after irradiation, the glasses were etched in 16 % HF at 25 °C for 1 min and the muscovite detectors in 48 % HF at 25 °C for 20 min. The tracks were counted under an optical microscope with transmitted light at 1250× magnification. For the muscovite detectors an oil objective was used.

Rewriting Eq. (1) for each of the glass monitors (or for their muscovite detectors) yields a set of three equations and three unknows. For the irradiations under a Cd cover the second term of the equation can be dropped and it should be taken into account that the CN3 and CN5 glasses have a different Th and U content. From the track densities in the CN5 and CN3 glass irradiated under a Cd cover the fast to epithermal neutron fluence ratio can be determined. The track densities for both CN5 glasses then give a value for the thermal to epithermal neutron fluence ratio. For the determination of the thermal and epithermal neutron fluence by means of the activation method, an Al-0.1 % Au alloy (IRMM-530 certified reference material [12]) and a Zr foil (Goodfellow 00412) were coirradiated with the glasses. The fast neutron fluence was determined by irradiating an Al-0.819 % Th alloy (IRMM SP91091) and counting the activity of up to 15 different fission products of the ^{232}Th(n,f) reaction, all yielding consistent values. All measurements were performed on an efficiency calibrated Ge(Li) detector. The results of both techniques are shown in Table I.

It can be seen that the neutron spectrum characterization by means of FT counting and neutron activation is consistent. There is, however, a small difference between the results obtained with the glasses and those obtained with the muscovite detectors. This is probably due to a difference in track etching efficiency between the CN5 and CN3 glass, which is indicated by a difference of the etch pit diameters although both glasses were etched under the same conditions. This problem does not occur when the tracks are counted in the adjacent muscovite detectors, for which the etching efficiency is the same.

Table I
Comparison of the characterization of the neutron spectrum by means of fission track counting in glass and muscovite and by means of neutron activation. The uncertainties quoted are 1σ standard deviations

	Track counting in glass	Track counting in muscovite	Activation method
Φ_{th}/Φ_e	38.8 ± 2.2	36.5 ± 1.8	35.9 ± 0.5
Φ_f/Φ_e	2.13 ± 0.21	1.89 ± 0.22	1.90 ± 0.05
Φ_{th}/Φ_f	18.2 ± 2.1	19.3 ± 2.4	18.9 ± 0.4

Conclusions

According to our experiences in the absolute calibration of the FT method, the metal monitors Au and Co are very well suited for an absolute determination of the neutron fluence and the confusion among FT users was only due to inaccuracies in the certification of the NIST fluences. Secondly, the neutron spectrum can be accurately characterized by means of FT counting in muscovite detectors which are placed in close contact with glasses possessing largely different Th/U ratios. This could be a solution to the geochronologists who wish to determine the thermalization of their neutron spectrum without using a Ge detector. Finally, the IRMM will also produce a Th-doped glass in which the U content is negligible in order to improve the accuracy of this technique.

Acknowledgements

Thanks are due to K. Masumoto for his assistance in counting the fission tracks and to J. Schreurs for supplying the Corning glasses. The financial support of the Institute for Scientific Research in Industry and Agriculture (F.B.) and of the National Fund for Scientific Research, Belgium (F.D.C. and P.V.d.h.) is gratefully acknowledged.

References

1. D. S. Miller, N. Eby, R. McCorkell, P. E. Rosenberg and M. Suzuki, Nucl. Tracks Radiat. Meas., *16*, 237, 1990.
2. P. Van den haute, A. Chambaudet, Nucl. Tracks Radiat. Meas., *17*, 247, 1990.
3. S. B. Carpenter and G. M. Reimer, Natn. Bur. Stand. Spec. Publ. 260–49, 1974.
4. S. B. Carpenter, Natn. Bur. Stand. Spec. Publ. 260–92, 1984.
5. P. Wagner and P. Van den haute, Fission-Track Dating, Kluwer Academic Publishers, Amsterdam, 1992.
6. P. Van den haute, R. Jonckheere and F. de Corte, Chem. Geol. (Isot. Geosci. Sect.), *73*, 233, 1988.
7. F. De Corte, P. Van den haute, A. De Wispelaere and R. Jonckheere, Chem. Geol. (Isot. Geosci. Sect.), *86*, 187, 1991.
8. J. H. Baard, W. L. Zijp and H. J. Nolthenius, Nuclear Data Guide for Reactor Neutron Metrology, Kluwer Academic Publishers, Amsterdam, 1989.
9. N. E. Holden and K. A. Holden, Pure Appl. Chem., *61*, 1505, 1989.
10. F. De Corte, A. Simonits, A. de Wispelaere and J. Hoste, J. Radioanal. Nucl. Chem., *113*, 145, 1987.
11. F. Bellemans, F. De Corte and P. Van den haute, Nucl. Track Radiat. Meas., in press
12. C. Ingelbrecht, F. Peetermans, F. de Corte, A. de Wispelaere, C. Vandecasteele, E. Courtijn and P. D'hont, Nucl. Instr. Methods Phys. Res., *A303*, 119, 1991.

Acta Physica Hungarica 75 (1-4), pp. 321-324 (1994)

BIOLOGICAL EFFECT OF p(18 MeV) + Be FAST NEUTRONS

A. M. DÁM, L. G. GAZSÓ, M. RÉTLAKI, A. FENYVESI[1] and T. MOLNÁR[2]

Frédéric Joliot-Curie National Research Institute for Radiobiology and Radiohygiene
Budapest, Hungary
[1] *Institute of Nuclear Research of the Hungarian Academy of Sciences (ATOMKI)*
Debrecen, Hungary
[2] *Biochemical Cyclotron Laboratory, Medical University School*
Debrecen, Hungary

The application of fast neutrons in radiotherapy has been stimulated by the expectation that, in comparison with low LET radiations, differences in radiobiological factors might result in a larger relative biological effectiveness (RBE) and lower oxygen enhancement ratio (OER). The biological effects of a mixed neutron–gamma field, due to the nuclear physics reaction, depend on the physical parameters (energy spectra, fluxes, fluences, etc.) of the component of the radiation determined by the facility and the high LET particle used, releasing from the nuclear reaction. Accepting that the biological effects of the low and high LET radiation are different the knowledge of the most important RBE and OER values is critical in application of fast neutron irradiation facility for radiobiological research and therapeutical purpose.

Basic radiobiological study was carried out at the MGC-20E Cyclotron of ATOMKI (Debrecen). RBE and OER were determined for survival of bacterial (E.coli B/r) and mammalian cells (CHO), using ^{60}Co γ-rays as a reference radiation. RBE was found 2.46 for E.coli and 5.1 for CHO cells. The calculation of OER resulted in a lower value by about 60 %, than it was obtained with gamma radiation (gamma = 2.1 neutrons = 1.31). Reduced effectiveness was found for different chemical modifying agents such as thiol reactive, radiosensitizing, radioprotecting compounds, compared to γ-radiations, which was due to the differences in the radiochemical processes at high LET radiation.

Introduction

Most of the malignant tumours contain hypoxic but viable cells which are more radioresistant to low LET (Linear Energy Transfer) radiations. The application of high LET radiations in radiotherapy might have the advantage to overcome the problem of hypoxic resistance, having lower oxygen enhancement ratio (OER). The differences in radiobiological factors might result in a larger relative biological effectiveness (RBE) for impairment of the integrity in function of normal cell. Because of their relatively simplest production, at present fast neutrons are the most frequently used high LET particles for cancer therapy. Due to the nuclear physics reaction the neutron production is always accompanied by gamma radiation component. The biological effects of a mixed neutron-gamma field depend on the energy spectra, the fluxes and fluences (or dose rates and absorbed doses) of the component of the radiation, determined by the facility. The MGC Cyclotron has been in operation at the ATOMKI in Debrecen since 1985. Its physical parameters

are adequate for medical applications, in particular for radiotherapy. To introduce fast neutron radiotherapy a basic radiobiological study has to be carried out on different organisms endpoints.

The characteristic RBE and OER values were determined for bacterial and mammalian cell system. The effect of chemical dose modifying agents such as sensitizers and protectors were also investigated. The results obtained with fast neutrons were compared with those of gamma irradiation.

Materials and methods

Fast neutrons were generated bombarding a thick beryllium target by 18 MeV protons of the MGC-20E cyclotron of ATOMKI, Debrecen. The average neutron energy (E_n = 3.7 MeV), thick target yields ($Y_n = 1.8 \times 10^{10}$ $ns^{-1}s^{-1}\mu A^{-1}$) and the absorbed dose (D_n = 2.5 mGy $min^{-1}\mu A^{-1}$) and the gamma to neutron ratio ($D_\gamma/D_n = 0.1$) were determined at 1 m of source–sample distance at zero degree. Measurement and evaluation of the separate dose components were done on the basis of the recommendation of ECNEU of the EORTC.

Escherichia coli B/r (ATCC No.23227) were grown to early stationary phase in liquid minimal medium. Cells were filtered, washed and resuspended in TRIS-buffer. The plating medium was minimal medium supplemented with 1.5 % Oxoid agar No.1. Cell suspensions were equilibrated with pure nitrogen or air for 30 min before irradiations and then the glass containers were closed during the experiments. Misonidazole and WR1065 was dissolved in TRIS-buffer. 10 mM and 6 mM was added, respectively. The survival curves were described by the analytical formula $S/S_0 = n\exp(-kD)$. The inactivation constant (k) and the extrapolation number (n) are characteristic of the organism and the irradiation conditions. OER and RBE were calculated from the linear part of the survival curves.

CHO cells were cultivated in Eagle's Minimal Essential Medium (GIBCO) supplemented with 10 % of Foetal Calf Serum. The cells in exponential phase were trypsinized and placed into Bellco tubes. When the cells were pretreated by buthionine sulfoximine (BSO), the media were changed 20 hours in earlier time and replaced to fresh ones before irradiation. After attachment the media were changed to fresh one, containing appropriate concentrations of AK2123 or Misonidazole half an hour before irradiations. After irradiation the media were changed and the cells were incubated in CO_2 incubator for one week. The colonies were stained with methylene-blue and counted. The survival curves were fitted to the linear quadratic model in case of gamma irradiation and using log–linear fitting for neutron irradiation. The RBE values were calculated from the survival curves using the slope ratio α_n/α_γ.

Results and discussion

The summarized data for survival curves of E.coli are shown in Fig. 1. The dose-survival curves for gamma irradiation were characterized by a broad shoulder, meanwhile with fast neutrons the shoulder was considerably smaller. Similiar findings are shown in Fig. 2, obtained with mammalian cells (CHO). The evaluation of the data resulted in a relative biological effectiveness of 3.92 under anoxic condition

and 2.46 under oxic condition for E.coli and 5.17 for CHO cells in oxia. The oxygen enhancement ratio, which is a measure of the dependence of the effect on the presence of oxygen, was found to be 1.31 for mixed $n-\gamma$ field and 2.1 for reference radiation using bacterial system.

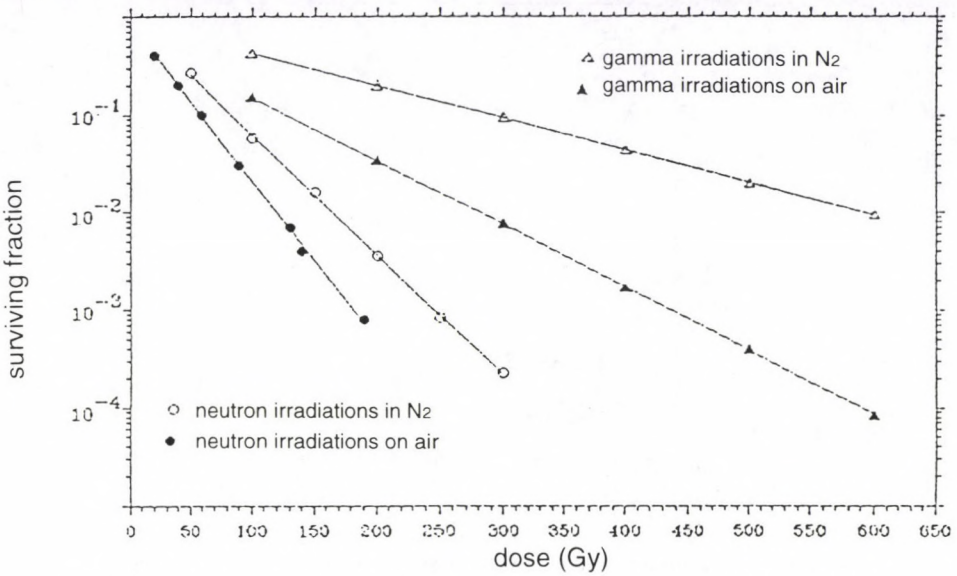

Fig. 1. Survival curves of E.coli after exposure to fast neutrons or gamma rays

Chemical modification of the radiation response has received renewed interest as a possible adjunct to radiation in the treatment of cancer. This involves selective sensitization of hypoxic tumor cells and/or protection of normal cells with minimal effect on the radiosensitivity of malignant tissues. Screening of these compounds has shown some agents to be good sensitizers and protectors at low LET radiation. Some of the electron affinic sensitizers are widely used in clinical practice, such as Misonidazole (MISO) and the newly synthetized AK2123. These hypoxic sensitizers were tested and their effect was found to be reduced in case of high LET radiation in E.coli system, under anoxic condition. The effectiveness of MISO and AK2123, expressed in SER values (Sensitizer Enhancement Ratio) were found to be MISO $SER_n = 1.07$ $SER_\gamma = 1.84$; AK2123 $SER_n = 1.15$ $SER_\gamma = 1.76$. The radioprotective agent WR1065 is able to defend the normoxic cells against the low LET radiation. The aminothiol compound exerted in E.coli system also a reduced effect of radiation protection under oxic condition. This chemical was able to prevent the radiation damage at high LET radiation by 17 % of the reference radiation.

One of the determining factors of the cellular radiosensitivity of cells is the gluthatione (GSH), which is an intracellular defensive agent. GSH is able to prevent the radiation damage at a certain level. If the GSH level is reduced, the radiosensitivity of cells increases. The inhibition of GSH synthesis by BSO or depletion of cellular GSH (by other thiol-reactive agents) could lead to the enhancement of cell

killing. The sensitizing effect of BSO pretreatment was studied on E.coli and CHO cells. The reduced gluthatione level (by about 40 %) caused only 10 % enhancement of radiation damage of both systems. The increase of radiosensitivity was found to be smaller in case of neutrons compared to data obtained with gamma rays.

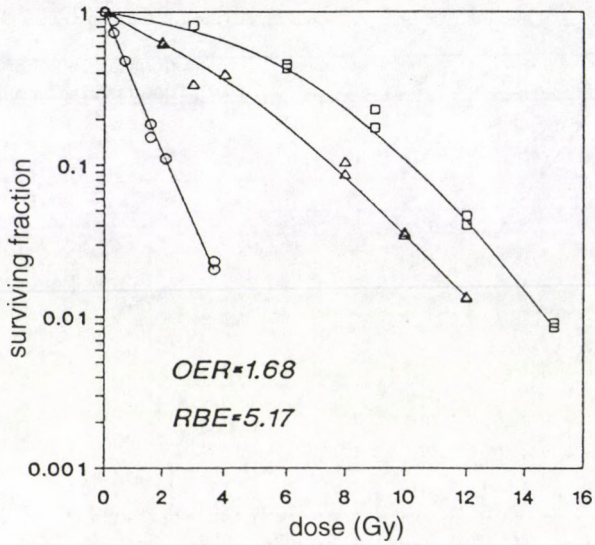

Fig. 2. Determination of the OER and RBE for survival of CHO cells

Neutrons having higher LET generate biological damage primarily by forming densely ionizing tracks which result in less indirect damaging processes that cause e.g. gamma-rays. The radiosensitization being mediated primarily through indirect effect would be anticipated to be greater for gamma rays than neutrons. Electron affinic sensitizers are true mimics of oxygen since they specifically sensitize hypoxic cells to radiation damage and this sensitization is dependent on radiation quality in the same way as the sensitization produced by oxygen. If the limited role of oxygen sensitization has been accepted we must appreciate the same for the oxygen mimetic sensitizers. The effect of radioprotective agent is somewhat different. Its effect is being mediated not exclusively by chemical modification of the radiation damage, but the enzymatic repair processes and stabilization of chromatine structure, binding of DNA, etc. are also involved.

It can be concluded that the effect of chemical modifying agents is being mediated primarily through indirect ways, and it would be anticipated to be greater for low LET radiations than neutrons, due to the different pathway of the radicals induced by the mixed neutron gamma field. Irradiations with fast neutrons result in a proportionally greater amount of nonlethal damage than lethal damage compared with radiations of low LET. This is true for irradiations under both aerobic and hypoxic conditions and indicates that the biological response to fast neutrons primarily depends on the effects of the more densely ionizing events in such a mixed field. This has potential consequences of practical importance for the use of fast neutrons in the radiotherapy of human tumours.

Acta Physica Hungarica 75 (1–4), pp. 325–327 (1994)

POSSIBILITY OF OBSERVING CONVERSION LINE SHIFTS DUE TO IONIZATION OF RECOIL NUCLEI IN (n,γ)-REACTIONS OF THERMAL NEUTRONS (PLANNED EXPERIMENT)

A. FEOKTISTOV and V. KUPRYASHKIN

Institute for Nuclear Research
Prospect Nauki 47, 252028 Kiev-28, Ukraine

It is suggested to carry out an experiment to clarify the question in which state (neutral or ionized) the recoiling atom is supposed to be after leaving the crystal cell as a result of (n,γ)-reaction of thermal neutrons. Information about it is expected to be received by measuring the energy difference of specially selected pairs of transitions in gamma and conversion spectra.

Introduction

The Bohr criterion [1] for ionization states that, when the recoil velocity is bigger than the velocity of the bonding electrons, the atom will lose some electrons. Based on this criterion, Jolie [2] suggested to consider the recoiling atom in (n,γ)-reaction to be neutral as the electron velocity in the atom for loosely bound electrons is of the order of the velocity of the electron in the hydrogen atom ($\sim 7\cdot 10^{-3}c$) and is approximately two orders of magnitude higher than the recoil velocity. That could be correct if the recoiling atom were moving in vacuum. But when such an atom is placed in crystal structure and is surrounded by other atoms and electrons and then it promptly leaves the crystal cell, electrons can lag behind from the moving atom and, besides, the shake-off effect for upper shells may occur. So, the question remains, in which state the atom will be after (n,γ)-reaction of thermal neutrons (neutral or ionized). We suggest to carry out this experiment to clarify it.

Task formulation

After the emission of primary γ-ray in the (n,γ)-thermal neutron reaction the recoiling atom starts to move and leaves the crystal cell if the target is in solid state. At that moment the atom can be in neutral state or in ionized state with a charge equal q. If the atom is ionized, the bonding energy ε of deep atom shells (further we will consider only K-shell) will increase. In our estimate it should be 5–7 eV on one charge of ionization. Ionization disappears very rapidly. In our estimate it disappears with a lifetime $\tau_a = \sim 10^{-14}$ s. The K-electron bonding energy ε_k will change nearly with the same velocity.

If we measure the energy of secondary γ-rays E_γ and the energy of their conversion electrons E_k we can determine the average shift of bonding energy $\overline{\Delta\varepsilon_k}$ from the following equation:

$$E_\gamma + O_\gamma = E_k + \varepsilon_k^0 + \overline{\Delta\varepsilon_k} + O_k.$$

Here O_γ and O_k are the nuclear recoil energy after the secondary γ-ray and the conversion electron emission, ε_k^0 is the K-electron bonding energy in the neutral atom.

The average value $\overline{\Delta\varepsilon_k}$ is determined form the equation:

$$\overline{\Delta\varepsilon_k} = \int_0^\infty \Delta\varepsilon_k(t)\frac{1}{\tau_n}e^{-\frac{t}{\tau_n}}dt,$$

where $\Delta\varepsilon_k(t)$ is the change of K-electron bounding energy in the moment of time t, τ_n is the lifetime of the investigated level. Using mean value $\overline{\Delta\varepsilon_k}$ we can draw conclusions about the value of ε_k and q.

Measurements should be made with an accuracy of several eV. It is very hard to measure conversion electrons with such an accuracy. That is why the difference method of measurements of energy should be applied. We have been successfully using this method for precise measurements in our laboratory for a long time. For that purpose we have worked out a special package of spectra processing program in which the experimental line form is used as instrumental response function [3,4].

Difference method of energy measurements

Let us find the case when there are two γ-transitions, which are close in energy. One of them is the investigated γ-transition. For the second γ-transition it is known a priori that the energy shift of K-line in conversion spectra is absent. For example, it can be the primary γ-transition or it can be the secondary γ-transition when it depopulates the level with a long lifetime $\tau > 10^{-13}$ s. If we measure the energy difference of such line doublets in γ-spectra (energy shift always absent) and in conversion spectra we can find $\overline{\Delta\varepsilon_k}$ from the equation:

$$(E_{\gamma_2} - E_{\gamma_1}) = (E_{k_2} - E_{k_1}) - \overline{\Delta\varepsilon_k}.$$

We can take in consideration also recoil energies by adding $(O_{\gamma_2} - O_{\gamma_1})$ and $(O_{k_2} - O_{k_1})$ to both parts of the above equation if it is necessary.

The β-spectrometer BILL and γ-spectrometer GAMS in Grenoble are the most suitable tools for these purposes. What should be the difference energy of line doublets to provide an accuracy of several eV? In our laboratory for β-spectrometer $\pi\sqrt{2}$ the difference energy of K-lines in conversion spectra should be $E_{k_2} - E_{k_1} \leq$ 8 keV. We suppose that it should be less than 10 keV for the BILL spectrometer. We think that there will be no problems in measuring γ-lines difference energies with high accuracy if the GAMS spectrometer will be used.

Selection of doublets

So, we should perform such main conditions:

1. We should carry out measurements of the same transitions on BILL and GAMS spectrometers.

2. Difference energy of investigated line doublets should be less than 10 keV.

3. Investigated γ-transition should be fast ($\tau_n \leq 10^{-14}$ s) and the second transition should be slow ($\tau_n \geq 10^{-13}$ s) or it can be a primary γ-transition.

To begin with, it is possible to process some measurements of conversion and γ-spectra in reaction $^{155}\mathrm{Gd}(n,\gamma)^{156}\mathrm{Gd}$ which were conducted with the help of BILL and GAMS spectrometers [5]. In the decay scheme of ^{156}Gd there are two transitions which can be analysed: the first is the fast E1-transition $\gamma 1366$, which depopulates the level 1366 keV ($\tau_n = 3.4 \cdot 10^{-14}$ s) and the second is the slow E2-transition $\gamma 1373$, which depopulates the level 1462 keV (band $K_3^\pi = O_3^+$).

After that it will be possible to plan such experiments more purposefully by selecting suitable pairs of transitions in the (n,γ)-reaction of thermal neutrons.

References

1. N. Bohr, Det. Kgl. Danske Videnskabernes Selskab Mat.-fys. Med., *13*, 8, 1948.
2. J. Jolie, Nuclear structure at high level densities: theoretical studies and a new method to measure short lifetimes, Universiteit Gent-1992-Part 1, p. 18.
3. V. V. Bulgakov, V. I. Gavriluk, V. T. Kupryashkin et al, Izv. Akad. Nauk, ser. fiz., *51*, 1874, 1987.
4. Yu. E. Koshutski, V. T. Kupryashkin, N. V. Strilchuk et al, Izv. Akad. Nauk, ser. fiz., *53*, 2125, 1989.
5. J. Klora, H. G. Borner, T. von Egidy et al, Nucl. Phys., *A561*, 1, 1993.

Acta Physica Hungarica 75 (1–4), pp. 329–333 (1994)

NUCLEAR PHYSICS AND APPLICATIONS AT BUDAPEST NEUTRON CENTRE

G. MOLNÁR, T. BELGYA, I. DIÓSZEGI, B. FAZEKAS, ZS. RÉVAY, Á. VERES and L. DABOLCZI

Institute of Isotopes, Hungarian Academy of Sciences
1525 Budapest, Hungary

After major reconstruction and upgrading the 10 MW nuclear research reactor at KFKI Budapest was opened to users on 22 November 1993. Based on the research reactor, the new Budapest Neutron Centre (BNC) is intended to become a national and international centre for neutron-based research in the fields of physics, chemistry, biology and engineering. Thermal neutron fluxes averaging over 10^{14} n cm^{-2}s^{-1} in the core and 2×10^9 n cm^{-2}s^{-1} at the exterior of radial beam ports, as well as the neutron guide system and planned cold neutron source will provide unique possibilities also for nuclear physics and applications.

The nuclear physics research program will focus on neutron capture physics, with special emphasis on measurements of nuclear level lifetimes using novel fast $\gamma_n\gamma\gamma(t)$ coincidence and Doppler-shift timing techniques. The (n,γ) station and the Compton suppression/pair spectrometer will alternatively be used for neutron-capture promt-gamma activation analysis (PGAA). Joint development of an ultra-fast rabbit tube system for activation analysis on very short-lived nuclides is also envisaged. For nuclear astrophysics, s-process capture cross-section measurements are planned using a filtered beam, to be constructed at one of the radial beam ports. A fundamental physics programme, such as tests of fundamental symmetries with polarized neutrons, as well as activities in nuclear solid state physics are also envisaged as soon as a polarized neutron guide becomes available.

1. Introduction

The WWR-SM type research reactor at KFKI Budapest is a beam reactor, equipped with all kinds of irradiation facilities to which a neutron guide system has been added during the recently accomplished reconstruction and upgrading [1]. Thermal power has been raised to 10 MW with provisions for a future 20 MW operation with more efficient fuel. A peak thermal neutron flux of 1.6×10^{14} n cm^{-2}s^{-1} in the core, an average flux of 2×10^9 n cm^{-2}s^{-1} at the exterior of the radial beam tubes and the prospect of a new liquid hydrogen cold neutron source offering a 10^9 n cm^{-2}s^{-1} cold neutron flux at the guides make it an attractive facility for research utilizing neutron beams. The beam ports will be used for research in the fields of condensed matter physics, materials science, radiography, nuclear and fundamental physics, nuclear analytical chemistry, nuclear solid state physics and health physics. The recently established Budapest Neutron Centre (BNC) [2,3] provides an ideal framework for those activities.

The present paper describes how the unique possibilities of the Budapest reactor, as an intense source of fast, thermal and – in the future — cold neutrons, are being explored for various kinds of nuclear physics related research projects. Polarized and unpolarized neutron-induced nuclear reactions, viz. radiative neutron

capture, can be utilized in the studies of problems related to nuclear and fundamental physics, as well as astrophysics. Implementation of unique nuclear analytical methods such as neutron-capture prompt-gamma activation analysis (PGAA) and other methods will also be accounted for. Finally, nuclear instrumentation development and some other future possibilities will be touched briefly.

2. Nuclear and fundamental physics

Our nuclear physics research program is focused on the radiative neutron capture process and its use as a spectroscopic tool for the characterisation of low-energy nuclear excitations. Being statistical in nature, the neutron capture process conveniently populates single-particle and collective levels of atomic nuclei, irrespective of their nature. On the other hand, observation of the capture-gamma radiation makes the wide arsenal of gamma-ray spectroscopy available for the characterisation of excited nuclear levels and their decay. One of the main objectives is the unravelling of multiphonon states in spherical and deformed nuclei. Construction of complete level schemes is also important for the test of various nuclear structure and statistical level density models.

The high neutron flux and extremely low background expected at the end position of curved neutron guide No.1 will provide unique possibilities for neutron-capture gamma-spectroscopic studies with an external target geometry. Since no bulky shielding is necessary, detectors can be moved close to the sample. This yields higher coincidence efficiency, thus making γ–γ coincidence-based methods like angular correlation, linear polarization and coincidence timing measurements more effective. Even conversion electron measurements with a thin strip target are feasible, utilizing the large rectangular beam size.

The main emphasis of the (n,γ) spectroscopy work will be put, however, on measurements of nuclear level lifetimes using novel techniques which expand greatly the time range attainable with conventional methods. This is of paramount importance, since electromagnetic transition rates derived from lifetimes, provide sensitive tests for nuclear structure models.

One of the recent successes of capture gamma-ray spectroscopy has been the development of the Gamma-Ray Induced Doppler Broadening (GRID) technique [4] for the measurement of short (<ps) lifetimes in (n,γ) reactions. While the GRID method requires extremely high luminosity and the use of a crystal spectrometer, in light and medium-heavy nuclei the Doppler shift can be measured with a Ge detector when the recoil direction is determined by the primary capture γ-ray detected in coincidence, as demonstrated recently [5] for nuclei as heavy as ^{56}Fe and for lifetimes of several fs to several hundred fs. Relying on our experience with $(n,n'\gamma)$ Doppler-shift lifetime measurements, which also involve low recoil velocities, we plan to pursue such experiments.

For longer lifetimes the delayed coincidence method has so far been used in capture γ-ray spectroscopy, Due to the poor timing properties of Ge detectors, however, the attainable time range has a lower limit of a few tenths of a nanosecond. In fission fragment beta decay spectroscopy the $\beta\gamma\gamma(t)$ fast coincidence timing

method [6] has been worked out recently to attain subnanosecond nuclear lifetime ranges, down to a few picoseconds. This method is based on a triple coincidence measurement, utilizing the excellent timing properties of BaF_2 scintillators and the high energy resolution of Ge detectors. In principle, it can be adopted to the (n, γ) reaction if both the feeding primary and the deexciting decay γ-ray are detected by separate BaF_2 scintillators and the level of interest is identified uniquely by observing a third γ-ray in the cascade using a Ge detector. Implementation and use of this method will be one of the most important goals for our nuclear spectroscopy program.

Neutron capture also has high importance for nuclear astrophysics as a mechanism of stellar nucleosynthesis. The (n, γ) spectroscopy station will also be used for the investigation of structural problems of nuclei, important for the understanding of branching points of the s-process responsible for the synthesis of most neutron-rich nuclei at the stability valley. The main emphasis will be, however, on neutron-capture cross-section measurements at several energies in the range relevant for the s-process, using the activation method. For this purpose a filtered beam facility will be constructed using the radial beam tube No. 4, looking directly at the core. Scandium, iron and silicon filters will be installed externally to provide monochromatic neutrons with energies 2, 24 and 144 keV, respectively. The filtered beam technique is well understood [7], and it has already been successfully applied for astrophysical cross-section measurements [8].

The study of fundamental problems — such as time reversal and parity violation in polarized neutron capture, or a measurement of the neutron lifetime — is another field of interest. A fundamental physics programme will be developed as soon as a polarized neutron guide becomes available.

3. Applied nuclear methods

In spite of advanced nuclear analytical methods developed in the past two decades (PIXE, XRF, etc.) classic reactor-neutron activation analysis (NAA) is still preserving its leading role, as it offfers mostly nondestructive, multi-element routine analysis needed in such areas as environmental control, geology, medicine and technological processes. Among its favourable characteristics are negligible matrix effect, excellent selectivity and high sensitivity — for about 75 elements less than 0.01 μg can be determined. In order to extend the capabilities of the rabbit tube system to subsecond half-lives, construction of an ultra-fast rabbit tube system in one of the free horizontal beam tubes is being considered. Thermal neutron flux as high as 3×10^{13} n $cm^{-2}s^{-1}$ has been measured at the inner end of the beam tubes, hence radial beam port No.1 would be ideal for this purpose.

The main emphasis is, however, on the alternative use of our capture γ-ray spectroscopy station for neutron-capture prompt-gamma activation analysis (PGAA). This novel nuclear analytical method [9] is based on the observation of prompt gamma radiation from neutron capture, and it replaces conventional activation analysis when no suitable radioactive daughter products are available. To this class belong most of the light elements (H, C, Si, P, S, etc.) as well as many

important toxic trace elements (Cu, Cd, Hg, etc.). Using clean, guided cold neutron beams the sensitivity increases tremendously due to low background and increased capture cross-sections. This method will be fully developed and exploited through implementation of the k_0 standardisation method [10]. When the cold neutron source is completed, the sensitivity of the prompt-gamma system is expected to increase by one order of magnitude. Thus the combined techniques of classical NAA and PGAA will provide highly sensitive and nondestructive determination for nearly all elements of the periodic table.

The main targets for PGAA will be the determination of light trace elements. H in metals and metal catalysts seems to be one of the most exciting fields. Determination of tracer elements such as B, Rb, Sm and Gd in geological samples is also investigated. Finally, a special programme will be developed for the measurement of all accessible toxic trace elements in environmental samples.

Apart from the nuclear analytical program there are plans to extend research activities to nuclear solid state physics using one of the future polarized guided beams. The most probable candidates are perturbed angular correlation (PAC) and beta-NMR.

4. Nuclear instrumentation

The experimental station for (n, γ) spectroscopy and PGAA is being constructed at the end of guide No.1, the last 17 m section of which will be bent to decrease direct background radiation. A twin station is envisaged, with both wide and narrow beam collimators. This arrangement accommodates for various sample requirements and also enables running activation analysis and nuclear physics experiments simultaneously. Installation of a beam chopper is also considered for activation analysis utilising ms-living isotopes. A temporary experimental station will be available for tests in June 1994 while full construction of the Ni-coated bent borosilicate glass neutron guide will be finished by September 1994.

A Compton suppression γ-ray spectrometer is being installed as the main detector. It consists of a BGO shield and a HPGe detector. As the BGO is split into eight optically isolated parts it can be operated also in pair spectrometer mode with proper coincidence gating. The BGO crystal has just arrived and missing parts of the system are being purchased. This main gamma-spectrometer should be complemented with various Ge and BaF_2 scintillator detectors for γ–γ coincidence, angular correlation and timing measurements.

For data acquisition and processing a PC-based analyser system and Unix workstations are available. It is planned to purchase a PC-based multiparameter MCA system with a magneto-optical backup device. All computers are — or will be — connected to the Ethernet-based local area network.

References

1. F. Gillemot, I. Vidovszky et al, The Budapest Research Reactor, IAEA Interregional Seminar on Research Reactor Centres — Future Prospects, Budapest, Hungary, 22–26 November, 1993. IAEA TECDOC, in press.

2. L. Rosta et al, Budapest Neutron Centre, A Research Reactor User Facility for the Central European Region, IAEA Interregional Seminar on Research Reactor Centres — Future Prospects, Budapest, Hungary, 22–26 November, 1993. IAEA TECDOC, in press.
3. Proc. Central European Initiative Workshop on the International Use of Centres of Excellence and Joint Projects on Materials Science, 26–27 April 1993, Budapest, Hungary, ELFT Budapest, 1993.
4. H. G. Börner, J. Jolie, J. Phys., *G19*, 217, 1993, and references therein.
5. V. Kupryashkin and A. Feoktistov, in: Workshop on Applications of High Resolution Gamma Spectroscopy in Studies of Atomic Collisions and Nuclear Lifetimes, eds. H. G. Börner, J. Jolie, M. Pendlebury and S. Ulbig, Report ILL 92HGB16T, ILL Grenoble, 1992.
6. H. Mach et al, Nucl. Phys., *A523*, 197, 1991, and references therein.
7. R. C. Greenwood and R. E. Chrien, Nucl. Instr. Meth., *138*, 125, 1976; R. B. Schwartz, in: Neutron Standards and Applications, NBS Special Publ. *493*, 250, 1977.
8. T. Bradley, Z. Parsa, M. L. Stelts and R. E. Chrien, in: Nuclear Cross Sections for Technology, NBS Special Publ., *594*, 344, 1980.
9. R. M. Lindstrom, R. Zeisler and M. Rossbach, Proc. of the 7th Int. Conf. Modern Trends in Act. Anal., 277, 1986.
10. F. De Corte, A. Simonits, J. Radioanal. Nucl. Chem., Articles, *133*, 43, 1989.

Acta Physica Hungarica 75 (1–4), pp. 335–340 (1994)

UPGRADING THE NEUTRON/GAMMA RATIO AT THE HORIZONTAL CHANNELS OF THE 'RA' REACTOR

M. PEŠIĆ, M. DAVIDOVIĆ, S. CUPAĆ and S. MILOVANOVIĆ

Institute of Nuclear Sciences 'VINČA'
P.O.B. 522, 11001 Belgrade, Yugoslavia

The idea of upgrading the ratio of thermal neutron flux to gamma and fast neutron flux at the horizontal channels of the 'RA' reactor is based on the advantage of the reactor fuel element composition. Reducing gamma and fast neutron flux can be achieved by splitting the reactor core in axial direction by replacement of one fuel segment into some of the fuel elements in the reactor core with the dummy one at the horizontal channel level. The calculation process and the first results of the upgrading characteristics of the 'RA' reactor horizontal channels are presented in this paper.

Introduction

The 'RA' nuclear reactor was built in 1959 at the Vinča Institute of nuclear sciences as 6.5/10 MW heavy water reactor with 2 % enriched metal uranium fuel [1]. This low-enriched metal uranium fuel was, in the late seventies, replaced by high-enriched (80 % ^{235}U) uranium dioxide fuel. During replacement of the reactor fuel, a new steady-state operation power of 4.6 MW (corresponding to thermal neutron flux of approximately $5 \cdot 10^{13}$ n/cm^2/s in the centre of the reactor core) was determined [2]. It is the consequence of the reactor primary coolant system performances and maximum allowed power density in the high-enriched UO_2 fuel.

In 1960–1984 period, the neutron research and applications at the 'RA' reactor were numerous: thermal neutron spectra determination, inelastic neutron scattering, neutron diffraction, material characteristics investigation, isotope production, NAA, etc. A few neutron spectrometers were built up around the reactor core and put into operation: single-crystal spectrometer for small angle neutron scattering (SANS), two triple-axis spectrometers, time-of-flight spectrometer and neutron diffractometer. The first experiences with cold neutron sources are acquired. Co-operation projects with researches from the former Soviet Union, Poland, Hungary, Romania, Sweden and United States were carried out and valuable results were published [3].

Research reactors in the south-east region of Europe [4], with characteristics similar to the 'RA' reactor in Vinča, were built almost in the same time when the 'RA' reactor was built. In 1959 in Budapest, Hungary, a 5 MW light water WWR-SZM type reactor was built. In 1957 in Bucharest, Romania, a 3 MW light water WWR-C type reactor and in 1961 in Sofia, Bulgaria, a 2 MW light water reactor were constructed. In the same year in Athens, Greece, a GRR-1 5 MW light water reactor was completed. Excluding the reactor in Greece which is of US origin, all these reactors are former Soviet design. Most of them were modernized (control and safety systems and use of low enriched uranium fuel) in the late eighties.

Advantages of the 'RA' reactor for upgrading the neutron characteristics of the horizontal channels

Currently, a modernization process of the control, dosimetry, safety and few auxiliaries systems of the 'RA' reactor has been in effect for the last few years. Parallel to that, an improvement of the 'RA' reactor neutron characteristics of the horizontal beam channels is considered (Fig. 1). For application of neutron beams in condensed matter physics, a high ratio of thermal neutron flux to gamma flux at the channel output, with low fast neutron flux intensity, is essential.

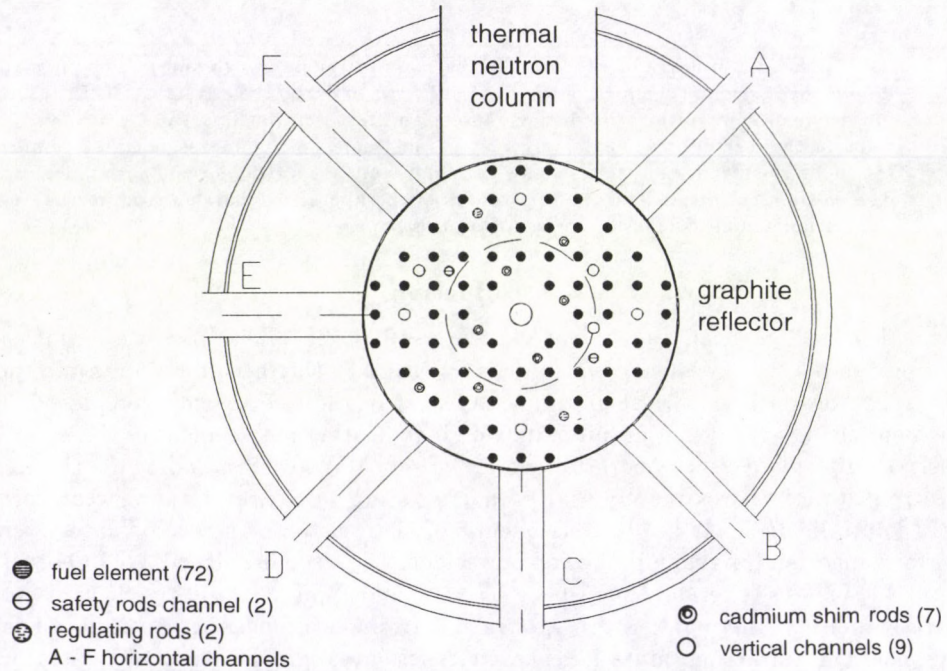

Fig. 1. Horizontal cross-section of the 'RA' research reactor in Vinča Institute

The idea of upgrading of the thermal neutron/gamma flux ratio at the channel output is based on the advantage of the 'RA' reactor fuel element composition over the research reactors in the region mentioned above. Namely, each fuel element (Fig. 2A) in the 'RA' reactor core is formed from ten independent fuel segments (Fig. 2B, each 11.25 cm long) placed one on top of the other in the fuel element tube. The last 11-th segment is a dummy one (Fig. 2C). It has the same geometry as the authentic fuel segment, but the uranium material is replaced by the aluminium. The reducing gamma and fast neutron flux can be achieved by splitting the reactor core into axial direction, at the height of the horizontal channel (1100 mm from the reactor floor level), replacing the only one fuel segment into some of fuel elements in the reactor core with the dummy one. As the result of the removing of the gamma and fast neutron source (fuel segments) from the horizontal channel input (in the reactor core), the ratio of the thermal neutron flux to the gamma flux is upgraded.

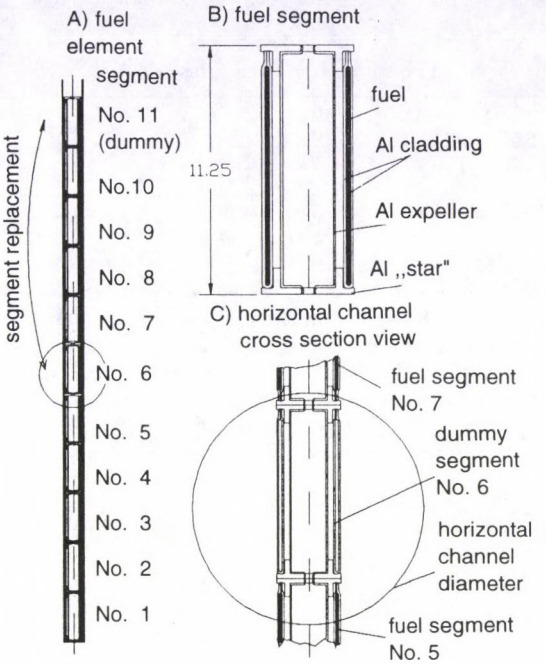

Fig. 2. Vertical cross-section of the 'RA' reactor fuel element

At the same time, it is expected that the fast neutron flux be reduced at the channel output.

Six horizontal channels with 150 mm circle diameter are designed in the graphite and light water reflector of the 'RA' reactor core. Replacing the 6-th fuel segment into each of 56 peripheral fuel elements (a total of 72) of the reactor core with the dummy one, only a small part of the 5-th (3 cm) and 7-th (1 cm) fuel segments is positioned in the optical view of the aperture of the horizontal channels. The parts of the remaining fuel material that is seen through the horizontal channels hole can be reduced, with a careful "fuel element (No. 5 and 7) packing procedure", if the ends without fuel material in the vicinity of these fuel segments are set with their faces to the dummy segment in each fuel element (Fig.2C). Other variants of the fuel replacement (exp. only in the direction of the particular horizontal channel) can be arranged also in the reactor core.

Calculation

The first calculations are carried out by 2D few group diffusion computer codes in $r - z$ geometry. The 'RA' reactor cell and supercell (automatic control rods, shim rods, vertical channels surrounded by fuel elements and moderator in the

Table I
Preliminary results of the calculation

Case	Core centre					Core edge				
	ϕ_{th}	ϕ_f	ψ_γ	$\frac{\phi_{th}}{\phi_f}$	$\frac{\phi_{th}}{\psi_\gamma}$	ϕ_{th}	ϕ_f	ψ_γ	$\frac{\phi_{th}}{\phi_f}$	$\frac{\phi_{th}}{\psi_\gamma}$
I	5.05	1.01	1.00	5.01	5.05	2.53	0.60	1.00	4.22	2.53
II	5.58	1.14	0.98	4.89	5.69	2.53	0.47	0.61	5.41	4.15
II/I	1.11	1.13	0.98	0.98	1.13	1.00	0.78	0.61	1.28	1.64

Notes: I case: 6-th segment in the fuel element is the authentic fuel segment; II case: 6-th segment in the fuel element is the dummy segment; II/I case: Calculated ratio in both cases; ϕ_{th}: Thermal neutron flux [10^{13} n/cm^2/s], for $E_n \leq 0.465$ eV; ϕ_f: Fast neutron flux [10^{13} n/cm^2/s], for $E_n > 0.465$ eV; ψ_γ: Gamma flux [relative units]; At the channels output, because of design a long pathway through the channel hole (3.30 m), only direct components of neutron and gamma flux exist, attenuated by the same factor [8]: $4.69 \cdot 10^{-4}$.

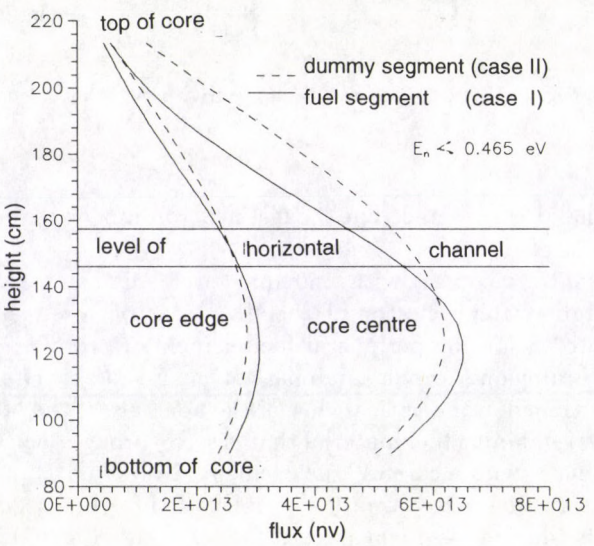

Fig. 3. Thermal neutron flux distribution at the centre and edge of the 'RA' core

reactor core) parameters are computed by VESNA, DENEB and VEGA computer codes developed in Nuclear Engineering Laboratory [5] in Vinča Institute. These calculations are done in 44 energy groups in one (VESNA, DENEB codes) and two (VEGA) dimensions. The neutron flux calculations are carried out by 4 group $r - z$ diffusion computer codes GALER [6], while gamma flux is estimated using

SABINE-3 [7] multi-group shielding computer code. All calculations are run for the 4.6 MW steady state power of the reactor and approximation of fresh fuel and average temperature distribution. In these calculations the ratio of thermal neutron flux to the fast (i.e. epithermal, $E_{edge} = 0.465$ eV) is calculated at the reactor core centre and at the reactor core edge (i.e. at the input of the horizontal channels). The ratio of gamma flux at the same core positions is determined using the results of the SABINE-3 code. The neutron and gamma transport and attenuation in the horizontal channels, in these preliminary calculations, are carried out using engineering methods [8]. The results of the calculation are presented in Table I.

The first analyses show also that the replacement of the fuel segments with the dummy ones cannot be done into all 72 elements in the core, because that replacement will put the reactor in deep subcritical condition from which it cannot be brought to the critical level by control rods. This was the reason that the replacement was done only into 56 peripheral fuel elements so that this change in the core composition has no significant influence on the reactor operation characteristics in respect to the power, temperature and coolant flow distributions. As an example the axial distribution of thermal and fast ($E_n > 0.465$ eV) neutron flux are shown in Figs 3 and 4, respectively. It can be seen that axial thermal neutron distribution in the core is not symmetrical due to insertion of the 'RA' control rods in the upper part of the core, while the fast neutron flux is reduced in the Case II at the horizontal channel input (core edge).

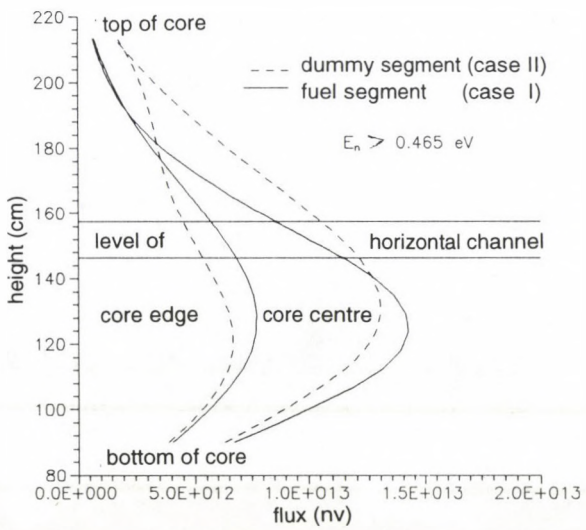

Fig. 4. **Fast neutron flux distribution at the centre and edge of the 'RA' core**

Conclusion

The computer codes and the first results of the calculation of upgrading characteristics of the 'RA' reactor horizontal channels are presented in this paper. More data for further detailed calculation are under preparation (by MCNP code [9]) to achieve more reliable results and the optimal reactor core design for increasing the thermal neutron/gamma flux ratio at the horizontal channels output. The advantages of the 'RA' reactor fuel element composition from fuel segments over usual full rods of the similar reactors, mentioned above, are confirmed.

Acknowledgements

This work is supported through the Contracts No. 0812 and 1903/93 with the MST of the RS. Authors are grateful to Mr. M. Milošević for his development of the computer codes and valuable discussions regarding objectives of the paper.

References

1. Directory of Nuclear Reactors, Vol. V, p.217, IAEA, Vienna, Austria, 1964.
2. O. Šotić et al, The 'RA' Nuclear Reactor Safety Report, (in Serbian), Vinča, 1986.
3. Conference on Utilization of Research Reactors in Yugoslavia, (in Serbian), Proceedings published by Institute of Nuclear Sciences 'Boris Kidrič', Vinča, 1978.
4. Directory of Nuclear Research Reactors, IAEA, Vienna, Austria, 1989.
5. M. Milošević, Reports Vinča-NET-26, -30, (in Serbian), Vinča, 1989–1992.
6. M. Milošević, Report IBK-NET-29, (in Serbian), Vinča, 1989.
7. C. Ponti, R. van Heusden, Report EUR 5159e Ispra, Italy, 1974.
8. V. N. Mironov, E. A. Panov, Prognozirovanie perenosa ionizuyushchego izluchevaniya metodami fotometrii (in Russian), Atomizdat, Moscow, 1979.
9. MCNP 3B, A Monte Carlo Neutron and Photon Transport Code System, ORNL-SIC Los Alamos CCC-200, 1989.

Acta Physica Hungarica 75 (1–4), pp. 341–344 (1994)

IREN – A NEW INTENSE SOURCE OF RESONANCE NEUTRONS

V. L. Aksenov, N. S. Dikansky[1], A. K. Krasnykh, V. L. Lomidze, V. A. Novokhatsky, Yu. P. Popov, V. T. Rudenko, A. N. Skrinsky and W. I. Furman

Frank Laboratory of Neutron Physics, JINR
141980 Dubna, Moscow Region, Russia
[1] *Institute of Nuclear Physics, Siberian Branch of RAS*
Novosibirsk, Russia

The IREN neutron spectrometer is currently being constructed in Dubna. It is a pulse neutron source optimized for investigations by the time-of-flight method in the resonance neutron energy range. It will provide opportunities for measurements with fast and thermal neutrons.

The parameters of the a neutron source are discussed and it is compared with the other sources of resonance neutrons. The research program for the IREN might cover a wide range of scientific interests.

Introduction

The modern neutron spectrometer of Frank Laboratory of Neutron Physics (FLNP) consists of the electron LINAC (LUE-40) and IBR-30 pulsed reactor, which is working in a subcritical mode as a multiplier of neutrons (multiplication coefficient $\sim$ 200). Such a combination of pulsed reactor and electron LINAC was born in Dubna a quarter of a century ago which gave the possibility to have a spectrometer for resonance neutrons using the time-of-flight method with high intensity neutron fluxes [1].

The same principle for a neutron spectrometer has now been applied to the IREN project. The creation of a more powerful electron LINAC with a 10 times shorter electron pulse duration allowed us to build a modern spectrometer for resonance neutrons. The parameters of this spectrometer would be comparable to LANSCE, the best analog, which is based at the Los Alamos Meson Facility and proton storage ring.

Neutron spectrometer

The present IREN [2] project as an economical, intense resonance neutron source is optimized for investigations in the resonance neutron energy range. Nevertheless, it could provide good opportunities for experiments with fast neutrons ($E_n \leq 5$ MeV). The new neutron source will form a complement to the stationary neutron sources of Grenoble, Gatchina, etc., at which experiments with thermal neutrons are carried out (as was the case with the study of parity violation effects

in neutron interactions), and to the pulsed neutron sources: GELINA FAKEL, LU-50, operating with linear electron accelerators, which provide optimum conditions for investigations of individual resonances and various averaged effects in the fast neutron range.

Realization of the IREN project will pave the way for a world-wide collaboration in neutron-aided nuclear physics to essentially supplement the spectrometer at Geel [3].

The suggestion to use the combination of an electron accelerator as an injector and a subcritical reactor as a neutron multiplication target as a neutron source is not only a tribute to tradition, but is also reflects our desire to have some advantage over the other time-of-flight, high resolution neutron spectrometers, in particular, over proton accelerator based ones. The proposed combination allows:

- a reduction of requirements for electron accelerator parameters to permit one to have a safer operating machine;
- a reduction (by an order of magnitude or even more) of construction costs;
- to have a much cheaper operating machine, both with respect to power consumption and to the necessary maintenance staff; and
- use of the whole of infrastructure of the existing spectrometers, including buildings, flight paths, experiment pavilions, some of the research instruments and the accelerator power supply system.

Modern technology permits an order of magnitude increase in the intensity of photoneutron generation in the target of an electron accelerator. Therefore, we may use a lower multiplication of neutrons (by only a factor of 30) in the target surrounded by fission material. This would make it possible to reach a pulse duration of the order of 0.5 μs.

The main parameters of the IREN spectrometer are specified in Table I.

Table I
Main parameters of IREN

Accelerated electron energy, MeV	200
Electron beam power, kW	10
Electron pulse duration, ns	250
Pulse repetition rate, Hz	150
Peak electron current, A	2
Neutron multiplication rate	28
Integral neutron yield, n/s	1×10^{15}
Fast neutron pulse duration, ns	400

The new electron accelerator will be installed vertically in place of the present LUE-40 and the building now occupied by the IBR-30 reactor will be utilized for the booster, This will save money and time and allow adaptation of a wide network to the needs of the new spectrometer: vacuum neutron guides, experimental pavilions, currently operating instruments for the polarization of neutrons and target nuclei, and for detection and spectroscopy of neutrons, together with a rich set of detectors and spectrometers for the products of interactions of resonance and slow neutrons with nuclei under investigation. In fact, one will get a multipurpose neutron factory.

We consider as the principal characteristics of resonance neutron spectrometers the integral yield per second in 10^{15} n/s, ($< I_n >$), the coefficient, C, which characterizes the neutron flux (of the energy E in eV at a distance L (in m) from a moderator) incident on a sample area of 1 cm^2 according to the formula

$$\phi(E) = C/EL^2,$$

and is given in 10^7 units, the duration of a primary neutron flux, (τ), the real neutron pulse duration, Δt, e.g., at 100 eV, which is larger due to the neutron moderation process.

Table II shows that in the resonance neutron range IREN is to become one of the world's best spectrometers as concerns the neutron flux incident on a sample at optimum energy resolution, being inferior (by a factor of 4–5) only to the LANSCE neutron spectrometer on the proton storage ring of the Meson Facility at Los Alamos.

Table II

Neutron flux data of several neutron spectrometers

Spectrometer, Laboratory	$< I_n > \times 10^{-15}$	$C \times 10^{-7}$	τ ns	Δt (100 eV) ns
FAKEL (IAE, Russia)	0.003	0.03	50	200
ORALE (ORNL, USA)	0.13	1.5	30	180
LUE-40/IBR-30 (Dubna)	0.5	6	4000	4100
LANSCE (LANL, USA)	10	40	150	300
IREN (Dubna, project)	0.9	9	400	430

The comparison of neutron yields in different energy ranges at one and the same "optimum" resolution [4], made by Steve Wender at LANL [5] showed that in the region of 10 and 100 eV, when compared to LANSCE, the IREN would have like luminosities, but which are lost at higher energies and in the thermal region (see Fig. 1). All this at a cost of construction and operation differing by a factor of one or two orders of magnitude. So, the resonance neutrons from IREN seem destined to become the cheapest in the world.

Physical research program

The research program for IREN elaborated on the basis of discussions and suggestions made at meetings will cover a wide range of scientific interests:

- properties of the neutron as a fundamental particle, including electric polarizability of the neutron and the n–e interaction;
- violation of the symmetry of fundamental properties in nuclear interactions, particularly, the effects on the enhancement of these processes in neutron resonances;
- the laws governing the change from "order" to "chaos" following the transition from near-ground-state excitations to N. Bohr compound states (neutron resonances), and further, to a new type of "order" — the collective excitations of giant resonances;

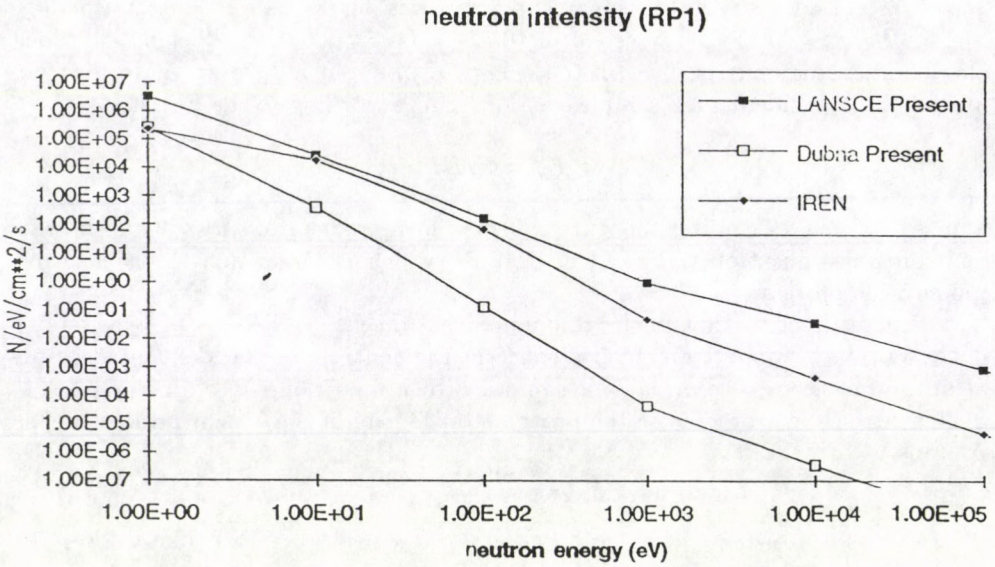

Fig. 1. Neutron intensity vs neutron energy

- cluster phenomena preserving processes at high excitations of a nucleus;
- multiparameter study of nuclear fission processes in the whole of their complexity;
- "rare" neutron reactions and the role they play in the nucleosynthesis processes, happening in space, in particular;
- interactions of resonance neutrons with isomers and radioactive nuclei, which are important to investigate for clarification of the possibility of "burn out" (transmutation) of radioactive and, especially, long-lived isotopes contained in the wastes of nuclear power energetics, which is vital for the future of this energy.

IREN will give us the possibility to investigate many other interesting problems (the optics of resonance neutrons, radiography of resonance neutrons, creation of a gamma-laser with neutron pumping, neutron induced atomic excitations and so on). But realization of these investigations is not planned now due to the lack of finances and available people.

References

1. I. M. Frank, in: Physics of Elementary Particles and Nuclei, 2, p. 807, Dubna, 1972.
2. V. L. Aksenov, N. S. Dikansky, V. L. Lomidze et al, JINR Report E3-92-100, Dubna, 1992.
3. H. Weigmann, F. Corvi, E. Sharapov, IREN and GELINA, Complementary Neutron Sources, Proc. Inter. Workshop on Time Reversal and Parity Violation in Neutron Reaction, Dubna, May 4–7, 1993 (to be published).
4. A. F. Michaudon, S. A. Wender, LANL Communication La-UR-90-4355, Los Alamos, 1990.
5. S. Wender, private communication, 1992.

Acta Physica Hungarica 75 (1–4), pp. 345–350 (1994)

PROMPT GAMMA COLD NEUTRON ACTIVATION ANALYSIS (PGCNAA) – THE USEFUL SUPPLEMENT FOR THE CHARACTERIZATION OF SPECIMEN BANK MATERIALS

M. ROSSBACH

Institute of Applied Physical Chemistry, IPC, Research Center KFA-Jülich
52425 Jülich, Germany

Basic considerations for the sensitive application of PGCNAA to biological materials in general are outlined. Some examples are given where the method has particular advantages over other analytical approaches related to the characterization of Environmental Specimen Bank (ESB) material. As a nuclear technique the method is nondestructive, rapid, and inexpensive when a beam of cold neutrons is available. The instrument is easy and fast installed and the amount of information obtained per spectrum is large. Certain elements like H, N, B, S and some rare earth elements cannot be nondestructively determined by other analytical techniques so far.

Introduction

When nuclei of some elements in a sample interact with neutrons of a guided beam scattering and absorption occur simultaneously according to their respective cross-section. In absorbing a neutron a compound nucleus is formed which can decay to the excited state of an isotope with a higher mass number by emitting prompt (within $\leq 10^{-14}$ s) gamma rays and decay with a certain half life to the ground state by a beta/gamma decay chain. Both types of gamma radiation are used for chemical analysis since decades; the delayed gammas in conventional activation analysis and the prompt gammas in PGNAA respectively using almost the same equipment. As the energy of the emitted gamma ray is characteristic for an isotope, easy identification with a calibrated detector/analyser arrangement is feasible together with quantification using the relative (standard comparison) or absolute (k_0)-techniques. As some of the isotopes with high absorption cross-section produce only stable daughters the prompt gamma approach offers the only possibility to detect these elements nondestructively. As an example, ^{1}H captures a neutron to form an excited state of ^{2}D which decays spontaneously to the ground state by the emission of a 2223.2 keV gamma ray. No radioactive product will be formed. This peak can be used for quantification of hydrogen (and hence for water in some samples) by a simple peak area comparison with a standard of known composition, or a k_0-factor.

Problems arise from scattering of neutrons in the same samples. If the exciting beam is strongly scattered by the sample properties (hydrogen being the strongest scatterer again) the illumination of the sample cannot longer be considered as homogeneous. Scattered neutrons interact with materials surrounding the sample (holder, support, shielding, etc.) and contribute to the background of these elements. The background is therefore not stable but depending on the sample itself. Such effects can be minimized by the experimental design and shielding but not totally avoided.

Experimental

Due to the scarcity of filtered neutron beams PGNAA facilities are restricted to research establishments with access to a research reactor and available neutron guides. As guiding technology and cold sources have been introduced recently at several nuclear research centers the technique is rapidly expanding. In Table I a number of facilities are listed from where reports on PGNAA instruments are published during the last two years.

Table I
Some recent applications of PGNAA using reactor based or isotopic neutron source excitation

Neutron source	Flux	Site	Notes	Reference
NIST-NBSR	$5 \cdot 10^8$	NIST Gaithersburg, USA	thermal	[1–3]
NIST-NBSR	$5 \cdot 10^8$	NIST Gaithersburg, USA	cold	[4,5]
JRR-3M	$1.2 \cdot 10^8$	JAERI, Tokai-mura, Ibaraki	thermal	[6,7]
JRR-3M	$2 \cdot 10^8$	JAERI, Tokai-mura, Japan	cold	[6,7]
BER II	$9.2 \cdot 10^8$	HMI, Berlin, Germany	cold	[8]
FRJ-2	$1.5 \cdot 10^8$	KFA-Jülich, Germany	cold	[9–11]
Triga Mark II	$3.5 \cdot 10^6$	Dalat, Vietnam	thermal	[12,13]
Triga Mark II	$\approx 10^5$	Musashi Inst. Techn. Asao-kku Kawasaki-shi, 215, Japan	thermal	[14]
THMER	10^4	Nat. Tsing-Hua Univ. Hsinchu Taiwan, R.O.C.	mobile reactor	[15]
1,5 μg ^{252}Cf		Nat. Tsing-Hua Univ. Hsinchu Taiwan, R.O.C.	In Situ Cl in lake water	[16,17]
740 GBq ^{238}Pu/Be	$4.4 \cdot 10^7$	University of Birmingham, UK	in vivo N	[18]
5 μg ^{252}Cf		ICEN-LNETI, Sacavem, Portugal	multi-ele. in coal	[19]
100–200 μg ^{252}Cf		Henan, P. R. China in Al production	process contr.	[20]
282 GBq ^{238}Pu/Be	10^7	Auckland Hospital, New Zealand	total body Cl	[21]
39 GBq ^{241}Am/Be		USDA/ARS Baylor College Med. Houston, Texas, USA	N, H, C in pigs	[22]
1 GBq ^{252}Cf	$1.1 \cdot 10^8$	Royal North Shore Hospital, Sydney, Australia	total body N	[23]
2 GBq ^{252}Cf	$2 \cdot 10^8$	USSR Acad. Sci. Vladivostok, USSR	ocean sediment mobile source	[24]
2 x 6 g ^{252}Cf	$5 \cdot 10^6$	Toronto General Hospital, Toronto, Ontario, Canada	total body N	[25]

In general, neutron fluence rates range from some 10^6 $Ncm^{-2}s^{-1}$ (for Triga reactors) to slightly above 10^9 $Ncm^{-2}s^{-1}$ at high flux research reactors. The sensitivity as a function of the exciting media hence is orders of magnitude lower for prompt than for delayed gamma ray measurements. Nevertheless, by optimizing the geometry and the counting efficiency of the device in a long measurement of 12 to 24 hours some 20 elements can be determined simultaneously at the level of ≤ 10 μg/g in biological materials [4]. Several elements like C, N, S, P or Mg have poor detection limits (between 200 and 4000 μg/g) but as they constitute the bulk of organic materials PGNAA is, however, capable of their quantification.

There are numerous applications of PGNAA in industry, process control, and in medical application [26–28] but we will restrict the discussion mainly to the case of environmental monitoring applications.

The German Environmental Specimen Bank (ESB) has been operating for 8 years collecting, processing and storing selected environmental materials from certain representative areas all over Germany. The materials are collected according to precise sampling protocols [29] and are maintained under cryogenic conditions from the sampling site until final use for analysis [30]. A great armoury of analytical techniques including AAS (various varieties), electrochemical and mass-spectrometric methods, and instrumental NAA are regularly applied for the inorganic characterization of these specimens. A number of elements like Pb, Hg, Cd, Cu and Zn are very well covered in that at least 3 different techniques are capable to determine it accurately even at low biological concentrations. Other elements like Cr, As, Sn or Tl are only covered by one method and a number of elements of similar environmental relevance are not being determined because no suitable technique exists up to now.

Therefore continuous attempts are made to extend the number of elements being characterized in ESB materials. In principle every element of the periodic table might be of interest not only from a toxicological but also from a scientific point of view. Interaction of elements (not only the so-called "essential" elements) in biological materials has been confirmed by several investigations [31,32].

Prompt Gamma Cold Neutron Activation Analysis (PGCNAA) is one of the most advanced analytical multielement techniques that enables us to extend the element spectrum for characterization of ESB materials considerably. Elements like H, B, C, N, Si, Ti, V, I and Gd are hitherto not determined by other techniques at all in the ESB materials. Elements like Al, P, Cl, Cr, Se, Cd and Hg can be determined in biological materials and PGCNAA hence can be considered as a reference method in critical cases. In principle the prompt gamma approach has a much broader applicability — every element of the periodic table emits prompt gamma rays [33] – and particularly the light elements offer new perspectives in ESB analytical work. For example, the hydrogen determination can be used to monitor the water loss in different drying procedures. As PGCNAA is a nondestructive technique samples can be analysed prior to and after freeze drying to check for element losses during the process (e.g. boron as a rather volatile element [34]).

Results and discussion

The principle of the setup of the detector, sample and electronics for PGCNAA is described in several publications [8–10] and remains for each experiment virtually the same. Installation and calibration at different irradiation positions is possible within a day or two making PGNAA a very flexible technique.

Several ESB materials have been studied using the PGCNAA technique including brown algae [*Fucus vesiculosus*], bream [*Abramis brama*], poplar leaves [*Populus nigra*], beech leaves [*Fagus sylvaticus*] and Norway spruce shoots [*Picea abies*]. The results of these investigations have been reported elsewhere [10,35]. In medical investigations the concentration of hydrogen is an indicator for water

content, carbon for fat, nitrogen for protein and sulfur for amino-acid if appropriate conversion factors are applied. Of course such relations can only be applied in special cases and control measurements have to be applied to check the results. In fact PGNAA nitrogen determination has been used to estimate the protein content in different grain species and other materials [36, 37]. Using the conversion factor of $6.25 \cdot N \cdot L_w$ (L_w = water loss factor) one arrives at protein equivalents in ESB materials as shown in Table II. It is rather difficult to compare these results with reported values except for bream: In dietary materials such information is given and values for protein in sweet water fish vary between 15 and 20 %. The values for the plant materials might, however, be more representing nucleic acids than high molecular weight proteins. Such information — although highly relevant for ecological research – hitherto is not obtained by any other technique in ESB materials so far. As the method is still under exploration similar applications of the element informations gained might well appear.

Table II

Estimated protein equivalent from total nitrogen determined by PGCNAA. Protein [in %] = $6.25 \cdot C_N$

Algae	Bream	Poplar 1	Beech 1	Spruce shoot I	Spruce shoot II
13.7	16.3	4.85	5.68	8.18	7.58

One of the major drawbacks of the technique is due to the influence of the sample itself on the element sensitivity [38,39] and the background by scattering of neutrons. Particularly in using the standard comparison approach (synthetic standards or certified reference materials) where standard and sample can have hardly the same scattering properties such influences can cause bias of the results up to 30 % or more. Up to now most applications of PGNAA were carried out in this manner, A new idea came up recently to apply the well established technique of k_0-values in delayed gamma ray spectroscopy for the prompt case as well [40,41]. The values have to be established once by measuring pure elements with a well calibrated instrument and extracting a single comparator value from the physical parameters. Future measurements of unknown samples can make use of these values to determine concentrations and detection limits using only a flux monitor as an indicator of the total neutron dose the sample was exposed to. No comparison with standards of any kind is therefore necessary.

First attempts to obtain such k_0-factors have been conducted recently at the research reactor BER II at the Hahn–Meitner Institute in Berlin by us and will be reported elsewhere [8]. Hopefully we will soon be able to demonstrate the reliability of such values and others can make use of them, too. The approach clearly enlarges the output of PGNAA spectra (by giving "smaller than" values for additional elements being not detected) and improves the speed of analysis as no standard has to be measured separately.

Conclusion

The flexibility of the technique using portable detectors and computers makes it independent of one particular reactor site. It has been demonstrated that the

equipment can be mounted and calibrated within 2 days at any available neutron beam of sufficient intensity.

The technique is purely instrumental, implying that small amounts of valuable materials as well as very large objects can be investigated without sacrificing the original sample [42]. Furthermore samples can be analysed prior to and after physical or chemical processing to detect changes in composition caused by those manipulations. Samples normally render inactive after irradiation.

The amount of information gained per spectrum lies around 15 to 20 element concentrations and additional "less than" information of as many elements as k_0-values for capture gamma reactions are available. The applications of PGCNAA to ESB materials adds at least 8 additional elements to the range already investigated and acts as a reference method for 12 others. PGNAA as a true multielement technique adds valuable information for the fingerprinting of inorganic constituents in ESB material.

Several elements determined by PGCNAA can be used to estimate components of a specimen which otherwise are difficult to obtain such as residual water, fat or protein. The determination of boron, a possible essential element [43], by methods based on a wet digestion of the samples is hampered by the high volatility of the element. PGNAA is so far the only method to overcome this problem by its purely instrumental nature.

The method has by far not reached its bottom end. As it is still a very young technique further improvements in sensitivity and accuracy can be expected by improving the efficiency of the gamma counting (including high count rate electronics and improved background reduction) or improvements in the spectra evaluation. Introduction of the k_0-concept is expected to be an important step towards such development. The combination of prompt and very short-lived (ns–ms) gamma ray emitters by the use of a neutron chopper will introduce additional information on a number of elements.

Some of the problems related to scattering are already successfully attacked by other groups working on PGNAA [2,39] and the combined effort in the field of neutron capture prompt gamma measurements certainly will help to render PGNAA soon a generally accepted and useful analytical tool for environment research.

Acknowledgements

M. R. is very grateful for financial support by the Bundesminister für Umwelt, Reaktorsicherheit und Naturschutz, Bonn and the Umweltbundesamt, Berlin.

References

1. E. A. Mackey, E. G. Gordon, R. M. Lindstrom, D. L. Anderson, Anal. Chem., *63*, 288, 1991.
2. E. A. Mackey, E. G. Gordon, R. M. Lindstrom, D. L. Anderson, Anal. Chem., *64*, 2366, 1992.
3. D. L. Anderson, W. C. Cunningham, G. H. Alvarez, J. Radioanal. Nucl. Chem., *167*(1), 139, 1993.
4. R. M. Lindstrom, J. Res. Natl. Inst. Stand. Technol., *98*, 127, 1993.
5. R. M. Lindstrom, R. Zeisler, D. H. Vincent, R. R. Greenberg, C. A. Stone, E. A. Mackey, D. L. Anderson, D. D. Clark, J. Radioanal. Nucl. Chem., *167* (1), 121, 1993.
6. C. Yonezawa, M. Hochi, Y. Ito, E. Tachikawa, in: Proc. 3rd Asian Symp. Research Reactors (JAERI-M 92-028) JAERI, Tokai, Japan, 1992, pp. 573–579.

7. C. Yonezawa, M. Hochi, Reactor Neutron-induced Prompt Gamma-ray Analysis – Review and Research Program at the Neutron Guide Beam of JRR-3 (Upgraded) JAERI-M-91-087, 1992.
8. M. Rossbach, L. N. Chau, K_0-factors for Some Prompt Gamma Reactions (in preparation).
9. M. Rossbach, Anal. Chem., *63* (19), 2156, 1991.
10. M. Rossbach, in: M. Rossbach, J. D. Schladot, P. Ostapczuk (eds), Specimen Banking: Environmental Monitoring and Modern Analytical Approaches, Springer Verlag, Heidelberg, New York, 1992.
11. M. Rossbach, N. T. Hiep, Fresenius J. Anal. Chem., *344*, 59, 1992.
12. P. D. Hien, L. N. Chau, V. H. Tan, N. T. Hiep, L. B. Phuong, in: Proc. 3rd Asian Symp. Research Reactors (JAERI-M 92-028) JAERI, Tokai, Japan, 1992, pp. 590–599.
13. L. N. Chau, N. T. Hiep, V. T. Ha, N. C. Hai, J. Radioanal. Nucl. Chem. Let., *165*(6), 351, 1992.
14. T. Matsamoto, O. Aizawa, Appl. Radiat. Isot., *41*, (9), 897, 1990.
15. Chien Chung, Chen-yi Chen, Nucl. Technol., *92*, 159, 1990.
16. Jiunn-Hsing Chao, Chien Chung, Nucl. Instr. Meth., *A299*, 651, 1990.
17. Jiunn-Hsing Chao, Chien Chung, Appl. Radiat. Isot., *42* (8), 723, 1991.
18. I. E. M. Stamatelatos, D. R. Chettle, M. C. Scott, Phys. Med. Biol., *38*, 411, 1993.
19. C. Oliveira, J. Salgado, J. Radioanal. Nucl. Chem., *167* (1), 153, 1993.
20. Liu Yuren, Lu Yanxin, Xie Yali, Wang Yonghai, Du Youling, Tan Jin, Meng Bonian, R. S. Seymour, J. Radioanal. Nucl. Chem., *151* (1), 83, 1991.
21. S. Mitra, L. D. Plank, G. S. Knight, G. L. Hill, Phys. Med. Biol., *38* (1), 161, 1993.
22. K. J. Ellis, R. J. Shypailo, H. P. Sheng, W. W. G. Pond, J. Radioanal. Nucl. Chem., *160* (1), 159, 1992.
23. L. A. Baur, B. J. Allen, A. Rose, N. Blagojevic, K. J. Gaskin, Phys. Med. Biol., *36* (10), 1363, 1991.
24. V. V. Ivanenko, V. V. Kovalenko, V. N. Krustov, A. I. Grigor'ev, A. Yu. Metelev, J. Radioanal. Nucl. Chem., *147* (2), 321, 1991.
25. S. S. Krishnan, K. G. McNeill, J. R. Mernagh, A. J. Bayley, J. E. Harrison, Phys. Med. Biol., *35* (4), 489, 1990.
26. W. Herzog, Nucl. Geophys., *3* (4), 467, 1989.
27. G. Glorieux, V. Lanz, W. Woodward, Rec. Conf. Papers, IEEE Cement Industry Tech. Conf. XXXII (Cat. No. 90CH2880-3) New York, NY, USA, 1990, pp. 187–205.
28. S. J. S. Ryde, W. D. Morgan, J. E. Compston, A. J. Williams, C. J. Evans, A. Sivyer, J. Dutton, Basic Life Sci., *55*, (In Vivo Body Compos. Stud.) 353, 1990.
29. Standard Operation Procedures, SOP's from the German ESB, in preparation.
30. J. D. Schladot, M. Stoeppler, G. Kloser, M. J. Schwuger, Analysis, *20*, M45, 1992.
31. M. Rossbach, in: M. Stoeppler, H. W. Dürbeck (eds) Beiträge zur Umweltprobenbank, 1986, JÜL-Spez-365, KFA-Jülich, Germany.
32. B. Markert, Fresenius J. Anal. Chem., *345*, 318, 1993.
33. M. A. Lone, R. A. Leavitt, D. A. Harrison, At. Data Nucl. Data Tables, *26* (6), 511, 1981.
34. T. Ishikawa, E. Nakamura, Anal. Chem., *62*, 2612, 1990.
35. M. Rossbach, M. Stoeppler, A. R. Byrne, Sci. Total. Environm., *139/140*, 411, 1993.
36. P. N. Tiwari, Radiochem. Radioanal. Letters, *6* (6), 363, 1971.
37. J. F. Sutcliffe, Phys. Med. Biol., *36* (12), 1681, 1991.
38. E. A. Mackey, Ph. D. Thesis, University of Maryland, Dept. of Chem. and Biochem., 1991.
39. D. Trubert, G. Duplatre, J.-C. Abbé, Int. Radiat. Appl. Isot., *42A*, 699, 1991.
40. R. M. Lindstrom, R. F. Fleming, R. L. Paul, E. A. Mackey, Proc. Int. k_0 Users Workshop held at Astene, Belgium, Sep. 30 to Oct. 2, 1992. Inst. Nucl. Sci., Univ. Gent, Belgium, 1992, pp. 121–124.
41. M. Rossbach, F. De Corte, Proc. Int. k_0 Users Workshop, see [40], pp. 125–129.
42. C. O. Fischer, J. Kelch, C. Laurenze, W. Leuther, K. Slusallek, Kerntechnik, *51* (1), 9, 1987.
43. F. H. Nielsen, in: R. Zeisler, V. P. Guinn (eds) Nucl. Anal. Meth. Life Sci., Humana Press, Clifton, New Yersey, 1990, pp. 599–611.

Acta Physica Hungarica 75 (1-4), pp. 351-353 (1994)

AUSTRON
A PULSED NEUTRON SPALLATION SOURCE IN CENTRAL EUROPE

M. SCHUSTER and A. COLOTTO

AUSTRON Planning Office
c/o Atominstitut der Österreichischen Universitäten
Schüttelstrasse 115, A-1020 Vienna, Austria

The Austrian Federal Government is promoting the installation of an international research centre in Austria. The AUSTRON project, supported by renowned scientists throughout Europe, is one of the candidates.

In December 1992 the Austrian Federal Government expressed its support for a proposal made by the Minister of Science and Research, E. Busek. This proposal stated that the Austrian Government would be prepared to finance the AUSTRON project by up to 1 billion Austrian Schillings (about one third of the estimated construction costs) provided that partner countries assume the remaining costs.

The facility proposed

To be attractive, the neutron spallation source must offer a performance equal to or better than the ISIS facility at the Rutherford Appleton Laboratory, which is considered the present world leader in this field. This implies a power of the proton beam at the target of at least 150 kW. Other important requirements that have been set forth are the following:

- Pulse repetition rate ≤ 25 Hz
- Proton pulse length < 1 μs
- Use of field-proven technology to allow for a short construction period.

The accelerator complex consists of a radio frequency quadrupole (RFQ), a drift tube linac (DTL) and a rapid cycling synchrotron (RCS, 1.6 GeV, cycling at 25 Hz and delivering ~ 126 μA). Thus, we are currently aiming at a beam power of 200 kW, twice as much as in our original design (Green Book of 1992).

The proposed accelerator complex allows for the acceleration of light ions at a modest additional cost. Therefore, a light-ion option (up to about 400 MeV/nucleon and some 10^9 ions/s) is included in the proposed facility. This option will include computer-controlled variation of the ion beam intensity.

This light-ion option will allow to carry out cancer therapy and research. Light-ion treatment appears to be largely superior to X-ray therapy and seems to be the most promising treatment in cancer therapy.

The proposed machine is already competitive with regard to existing pulsed neutron sources. It offers a rather slow repetition rate (high peak power) and a high potential for further development.

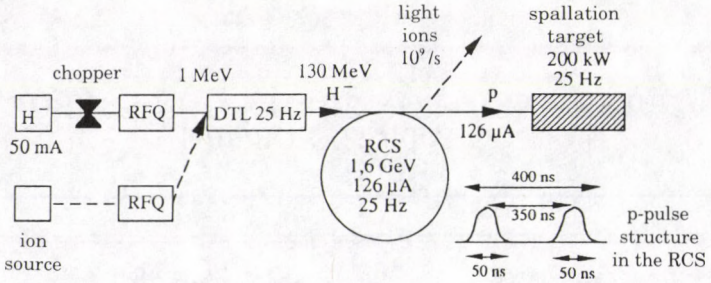

Fig. 1. AUSTRON accelerator design

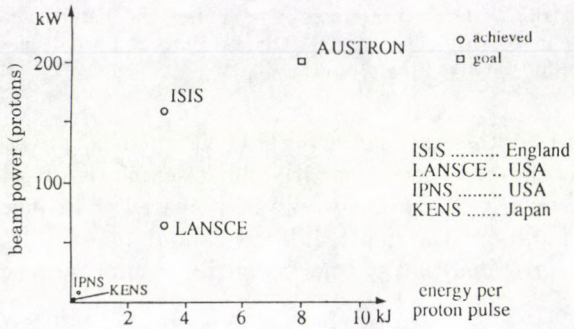

Fig. 2. Comparison of pulsed spallation sources (Proton beam power)

The present situation of the AUSTRON project

The AUSTRON Planning Office in Vienna was established in May 1993. At the same time the Accelerator Study Group at CERN took up its operation. Also in May 1993, an international *Meeting on an Advanced Neutron Spallation Source* took place. This meeting marked the start of AUSTRON as an international project.

AUSTRON is projected as an international research facility to be visited by scientists from many countries. Moreover, Austria will only be able to pay for one third of the costs while a major part of the necessary funding will have to be provided by other countries. Therefore it is particularly important to promote the idea of AUSTRON on an international scale and to inform Austria's potential partners all over the world about the possibilities offered by a new powerful spallation neutron source in Central Europe. With this in mind, the Chairman of the AUSTRON study group and Rector of Vienna's Technical University, Prof. P. Skalicky, and the AUSTRON Project Leader, Prof. M. Regler, have been visiting many European research centers. The result of these visits was the unrestricted support by many leading facilities all over Europe such as ISIS, CERN and PSI.

On the other hand, an International Scientific Council chaired by Prof. Albert Furrer (Vice Chairman is Prof. Helmut Rauch) was set up in Vienna at the end of October 1993. The members of this Council are renowned scientists form 13

European countries and the United States. All of them agreed that in Europe there is a strong demand for a facility like AUSTRON, especially in such a central location as in Austria. The Council discussed and evaluated the project's prefeasibility study, which had just been finished. The feasibility study will be finalised by the end of November 1994. A detailed technical design study will follow the feasibility study. The construction period is planned to be only 5 to 6 years after project approval and the commissioning of AUSTRON could begin in the year 2002.

The project has been presented in several European capitals (Bern, Budapest, Paris, Bonn, Bratislava, London, Rome and Brussels) where it met with great interest. A fund-raising team started discussions in Germany and Italy this winter, and further meetings are scheduled for Switzerland, France and Eastern Europe. The idea of AUSTRON is based upon a European partnership inspired by Austria's favourable geographical situation as a bridge between East and West. In other words: AUSTRON is the right project at the right time.

Acta Physica Hungarica 75 (1-4), pp. 355-359 (1994)

COMMERCIAL k_0-BASED NEUTRON ACTIVATION ANALYSIS AT DSM RESEARCH (THE NETHERLANDS)

R. VAN SLUIJS, D. A. W. BOSSUS, D. VERVECKEN and G. KLOK[1]

DSM Research B. V.
Radioisotope Applications and Support
[1] *Organic and Inorganic Analyses*
P.O.B. 18, 6160 MD Geleen, The Netherlands

Instrumental Neutron Activation Analysis (INAA) is often considered to be an old and expensive analysis technique, but its virtues still stand today: it is an effective, non-destructive, reliable, highly sensitive and multi-element technique. INAA is mainly used at universities or atomic energy research institutes which have a nuclear reactor at their diposal. Although DSM Research does not have a nuclear reactor, INAA has become one of its key analytical techniques because it was introduced via a commercial approach and because INAA is a highly suitable technique for the range of samples analysed at DSM Research.

Introduction

In this article an example is given of the use of Instrumental Activation Analysis in an industrial research environment. Although it is often considered to be an old-fashioned technique, INAA can be very effectively used for routine element analysis thanks to modern equipment, powerful software and absolute techniques.

DSM

DSM is an international chemical group. It employs around 22 000 people spread over Europe, the USA, Japan and Asia Pacific. The company's head office, its largest production site and its central research organization are located in The Netherlands. Annual sales total roughly NLG 9 billion. DSM's activities are divided over 25 business units, which operate independently. The company's main products are plastic, synthetic rubbers, fibre intermediates, fine chemicals, fertilizers, resins, plastic consumer products, packaging materials and engineering plastics. DSM is also involved in the exploration and extraction of oil and natural gas.

DSM Research

DSM Research is one of the five largest industrial research centres in the Netherlands. It works mainly for the various business units of DSM. Its main research goals are to find ways of lowering cost prices, adapt product quality to market demands, extend DSM's product range and operate production installations with the greatest possible care for safety and the environment. At DSM Research about 1100 research scientists are employed.

Element analysis at DSM Research

Inorganic elemental analysis is a key expertise at DSM Research. A group specializing in element analysis performs over ten different types of analytical techniques, from classical titrations to ICP-MS including XRF, GF-AAS, flame-AAS, ICP-AES and INAA. Being a relatively new technique at DSM Research, INAA has had to compete with all these in-house techniques.

The major drawbacks of NAA, the facts that the irradiations could not be performed in-house and the waiting time between irradiation and measurement (2–4 weeks) had to be overcome. Therefore, a commercial approach was needed from the very beginning. This implied that agreed delivery dates had to be met at all times and prices had to be competitive while still allowing the operation to at least break even. So not only the technique but also the analysts had to be reliable. Because DSM Research did not have a nuclear reactor, the analytical technique had to be independent of the nuclear reactor used; therefore the k_0-standardization technique was introduced.

Neutron Activation Analysis

Instrumental Neutron Activation Analysis was introduced at DSM Research in the mid-seventies. The technique was occasionally used for the analysis of rare earth elements in water. In 1986 the technique was revived. At that time there was a demand for an analytical technique for fluorine in all kinds of matrices and a multi-element trace element analytical technique for silica matrices. In the same year a system for fluorine analysis was built on top of the Belgium Reactor No. 1 at the Nuclear Research Centre in Mol, Belgium. Fluorine was analyzed using ^{20}F with a half-life of 11 seconds using a fast rabbit system. In 1987 it was established that NAA was the best method for multi-element trace element analysis in silica, in particular NAA using the k_0-standardization method [1]. The same year a crew of two people was trained for two weeks by Dr. F. De Corte at the University of Gent at the Institute for Nuclear Sciences. This resulted in the implementation of the k_0-standardization method at DSM Research. Some INAA highlights were:

- 1988: calibration of the first two detectors and the first version of the PC-program KAYZERO for neutron activation analysis according to the k_0-method [2].
- 1989: NAA fully operational for silica matrices.
- 1991: acceptance of NAA as a competitive analysis technique for all kinds of matrices.

Of course, some techniques are more efficient for a specified sample than others. But in 1994 NAA is fully integrated in the range of analytical techniques because it is

- directly applicable to liquids as well as solids (no destruction or sample handling);
- a multi-element technique;
- very sensitive and accurate.

NAA is performed on some 2500–3000 samples a year, representing about 30 % of the total number of samples offered for element analysis. The analytical work takes close to 1.5 person year. Technical support and development takes around 0.5 person year. Samples are irradiated in five different types of sample vials and measured in ten different standardized counting vials (see Fig. 1) on four high-purity germanium detectors.

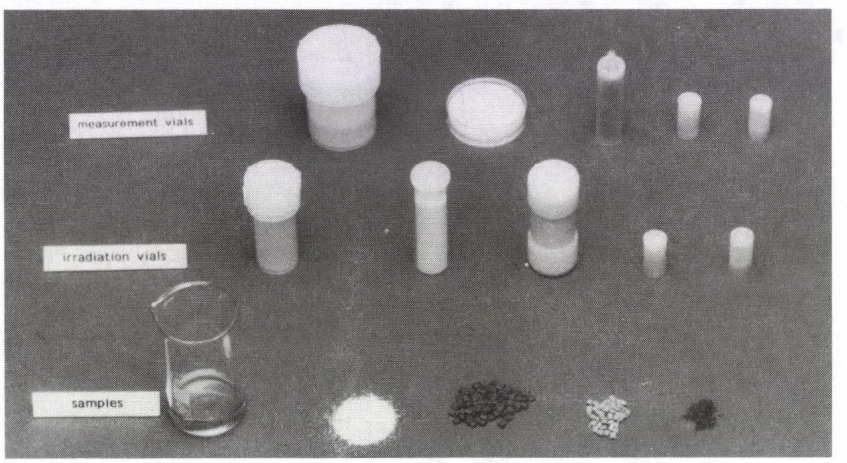

Fig. 1. Some standardized sample irradiation and measuring vials

NAA technique

NAA is performed using the k_0-standardization method developed by Dr. F. De Corte of the Institute for Nuclear Sciences at the University of Gent (Belgium) and Dr. A. Simonits of the Atomic Energy Centre in Budapest (Hungary). This method was chosen because of its reactor and matrix independency and multi-element character. The implementation was performed strictly according to the principles formulated by the INW. The technique for absolute multi-element NAA was incorporated into the DSM standard NAA software program KAYZERO. Both short-lived and long-lived radioisotopes are used. Gamma-ray spectra are evaluated using standard spectrum deconvolution software for PC (Sampo 90). For an efficient analysis sample vials have been standardized (see Fig. 1). Detection efficiencies are calculated using a matrix interpolation technique based on the calculation of effective solid angles by Moens et al [3]. This interpolation technique greatly reduces calculation time without significantly affecting accuracy [4].

Nuclear reactors for neutron activation analysis

In the vicinity of DSM Research there are several reactors that can be used for neutron activation. Within a distance of 200 km there are six reactors (see

Fig. 2). In the past six years most of the irradiations took place at the reactor BR1 at the Nuclear Research Centre in Mol (Belgium). The short distance between Geleen (NL) and Mol, approx. 90 km, the facilities available there, the good collaboration with the staff of BR1 and the very stable neutron flux with a very low gradient are some of the main reasons for this.

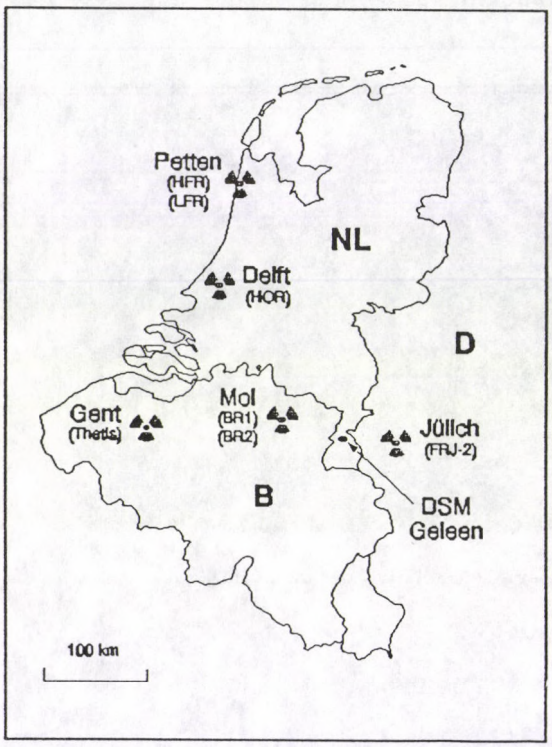

Netherlands Energy Research Foundation ECN, Petten (NL):
HFR; H_2O, 45 MW, $\sim 1 \cdot 10^{14}$ $cm^{-2}s^{-1}$
LFR; graphite, 10 kW, $\sim 3 \cdot 10^{11}$ $cm^{-2}s^{-1}$

Interfaculty Reactor Institute, Delft University of Technology, Delft (NL):
HOR; H_2O, 2 MW, $\sim 10^{13}$ $cm^{-2}s^{-1}$

Nuclear Research Centre, Mol (B):
BR1; graphite, 1 MW, $1-4 \cdot 10^{11}$ $cm^{-2}s^{-1}$
BR2; Be/H_2O, 56 MW, $1-3 \cdot 10^{14}$ $cm^{-2}s^{-1}$

Institute for Nuclear Sciences, University of Gent, Gent (B):
Thetis; H_2O, 250 kW, $1-2 \cdot 10^{12}$ $cm^{-2}s^{-1}$

Nuclear Research Establishment KFA, Jülich (D):
FRJ2; D_2O, 23 MW, $5 \cdot 10^{13}$ $cm^{-2}s^{-1}$

Fig. 2. Nuclear reactors close to DSM Research

Some other practical reasons are that liquid samples can be irradiated and that the flux is well thermalized, with only small fractions of fast and fission neutrons. Every month approx. 25–50 samples are irradiated for several hours at BR1. At the BR1 a fast rabbit system is used for short period irradiations. Once a week approximately 50–60 samples are analysed using short-lived radioisotopes. Occasionally, samples were irradiated at the Institute for Nuclear Sciences, University of Gent, Belgium, when a higher flux is necessary.

Typical NAA samples and applications

The application of NAA has changed dramatically over the past six years: from a multi-element trace element analytical technique for only one matrix it has now become a routine technique for all kinds of samples. It is currently being used for all types of analyses, ranging from all trace elements (ngrams/gram) to only one major component (%). Sample sizes range from some tens of milligrams to several

grams. Part of the success of INAA at DSM Research can be attributed to the type of samples to be analysed at DSM. Since DSM mainly produces polymers and chemical products, the samples offered for analysis are mainly polymers, slurries and catalysts.

Another reason is the fact that the technique is very flexible and can be used for:

- the analysis of samples for which no other in-house technique has been calibrated;
- the analysis of standards for comparative analytical methods;
- the development of analytical procedures for other in-house analytical techniques;
- providing a second opinion: INAA is totally different from other in-house analysis techniques and can thus be very useful.

Typical samples are water solutions containing high concentrations of (in)organic salts, hydrocarbon liquids, catalysts (slurries and solids) and all sorts of plastics, from virgin polyethylene to complex engineering plastics containing high concentrations of additives (e.g. flame retardants, stabilizers, glass fibres, pigments), chemicals, etc.

Some analysis examples are panoramic trace element analysis in polymers and hydrocarbons (feedstocks); analysis of high concentrations of inorganic additives in polymers; high concentration panoramic analysis of 'foreign' substances in unknown matrices (such as deposits or mud found in vessels, reactors or pipelines); analysis of magnesium, chlorine, aluminium and titanium in Ziegler–Natta catalysts and several other elements in newer kinds of catalysts.

Conclusion

Having been introduced on a commercial basis, in competition with other in-house analytical techniques, INAA has become a key analytical technique at DSM Research. This was possible thanks to the implementation of k_0-based NAA and time-saving software, KAYZERO, developed at DSM Research.

References

1. F. De Corte, A. Simonits, A. De Wispelaere, A. Elek, J. Radioanal. Nucl. Chem., *133*, 3, 1989.
2. D. Bossus, R. Van Sluijs, D. Vervecken, Proc. of the Int. k_0 Users Workshop-Gent, Lab. Anal. Chem., Inst. Nucl. Sci., Univ. Gent, pp. 15–18, 1992.
3. L. Moens et al, Nucl. Instr. and Meth., *187*, 451, 1981.
4. R. Van Sluijs, D. Bossus, D. Vervecken, Proc. of the Int. k_0 Users Workshop-Gent, Lab. Anal. Chem., Inst. Nucl. Sci., Univ. Gent, pp. 11–14, 1992.

Acta Physica Hungarica 75 (1–4), pp. 361–368 (1994)

THE SPECTRUM OF ONE- AND TWO-DIMENSIONAL NEUTRON SCINTILLATION DETECTORS DEVELOPED IN JÜLICH

A. SZEPESVÁRY[1,2], R. REINARTZ[1], K. D. MÜLLER[1], J. SCHELTEN[3]
E. JANSEN[2], W. SCHÄFER[2] and G. WILL[2]

[1] *Zentrallabor für Elektronik, Forschungszentrum Jülich (KFA)*
52425 Jülich, Germany
[2] *Mineralogisches Institut, Arbeitsgruppe Neutronenbeugung, Universität Bonn*
Poppelsdorfer Schloß, 53115 Bonn, Germany
[3] *Institut für Schicht- und Ionentechnik, Forschungszentrum Jülich*
52425 Jülich, Germany

Design and physical characteristics of the position-sensitive neutron scintillation detectors manufactured in Jülich are described. The detector spectrum comprises three different types each of linear and area detectors. Neutron absorption with an efficiency of 65 % for 1 Å neutrons is achieved in 1 mm ^{6}Li-scintillator glass. The linear detectors with lengths from 200 mm to 940 mm and one type of area detector of 600 x 600 mm are based on a modified Anger technology. Two other small area detectors of either 55 x 45 mm or 100 mm diameter are constructed with position-sensitive photomultipliers. The linear detectors have spatial resolutions between 1.2 and 3.0 mm, the large area detector 8.0 mm and the small area detectors 1.0 mm.

Introduction

The development of position-sensitive neutron scintillation detectors started in Jülich in 1980 with respect to applications in neutron scattering instrumentation at both steady state reactors and pulsed spallation sources. The solid state scintillation detectors are aimed at high detection efficiencies over a rather wide wavelength spectrum of epithermal, thermal and subthermal energies. Further aspects in favour of scintillation detectors are high spatial as well as time resolution, a thin detection zone for time-of-flight applications and last but not least easy maintenance and repair.

The neutron absorber, which is used so far as a standard in the Jülich scintillations detectors is Ce activated ^{6}Li-glass of 1 mm thickness; the absorption efficiency is about 65 % for 1 Å and 85 % for 2 Å neutrons. The $^6\mathrm{Li}(n,\alpha)^3\mathrm{H}$ absorption reaction results in 4.6 MeV energy of the reaction products. A small fraction of this energy is converted into light of about 400 nm wavelength. The number of photons created per capture event is about 4000; the decay time of the light spot is about 60 ns. The scintillation light is transferred to a photomultiplier (PM), where it is converted to an anode signal with a photon to electron efficiency of about 10 %.

Three different technologies using ^{6}Li scintillator glass and PMs have been applied in our Institutes to construct position-sensitive linear or area neutron detectors. The first technology used with a prototype detector was an assembly of

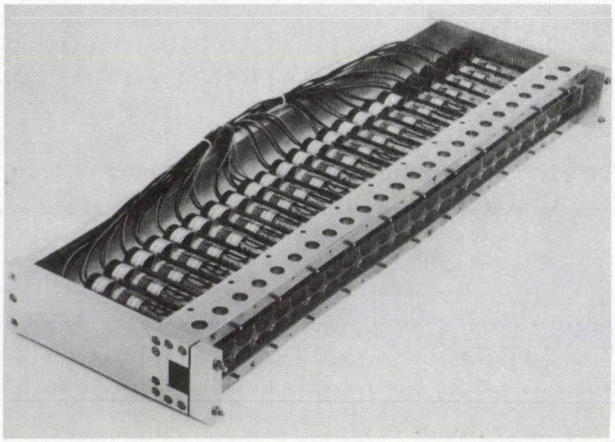

Fig. 1. Photograph of the JULIOS detector in its standard version (without light-proof box)

small scintillator elements, which were connected via a system of light guides to an assembly of PMs (Kurz et al [1]). This technology was abandoned early because of the rather small amount of light reaching the photocathodes. Much more effective with respect to the light output is the so-called Anger technology, where the detector window is formed by a plane continuous area of scintillator glass and a one- or two-dimensional arrangement of PMs behind it. The position analysis is performed by the determination of the center of the light spot on the photomultipliers; this is done by calculating the relation of the anode currents of adjacent PMs (Schelten et al [2]). This technology is used to construct three different types of linear detectors and a large area detector. Two small versions of area detectors are built from position-sensitive photomultipliers. The different detectors and their applications will be described in the following.

Linear detectors

The linear detectors are known under the designation JULIOS, which stands for '*JU*elicher *L*inear *O*rtsauflösender *S*zintillationsdetektor'. The JULIOS detector (Fig. 1) is built from a linear row of 24 PMs, whose photocathodes face the backside of a rectangular transparent light disperser with the ^{6}Li scintillator glass coupled optically on the front side. The scintillator light of an absorbed neutron is confined to a cone of about 90° by means of total reflection at an air gap between scintillator and disperser (Fig. 2). Disperser thickness and PM widths are matched to concentrate the light spot of each neutron event on the photocathodes of three adjacent PMs. The spatial resolution of the detector, which depends on the total light output of the scintillator, the quantity of light transferred to the photocathodes and the light-to-photoelectron conversion of the PMs, can be described empirically by the full width at half maximum (FWHM) of a Gaussian function according to FWHM

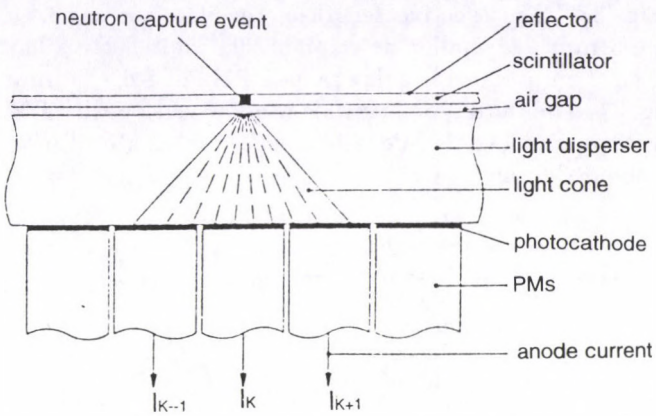

Fig. 2. Linear detector construction and scheme of the light distribution from a neutron capture event

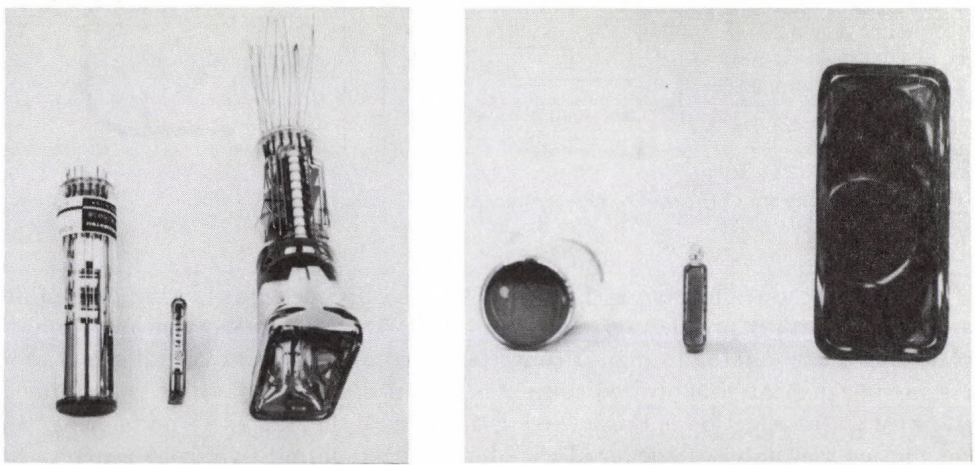

Fig. 3. Top view (left) and front view of the photocathodes (right) of the three types of photomultipliers used for different JULIOS detectors: type a (left), type b (middle), and type c (right)

$= ca/\sqrt{N}$. N is the total number of photoelectrons per capture event, a is the linear size, i.e. the separation of adjacent PMs, and c is a constant; for details see Schelten and Kurz [3] and Szepesváry et al [4].

Besides the quality of the neutron scintillator (see [5,6]) it is the type of photomultipliers to influence the physical characteristics and the effective size of the JULIOS detector. Three different PM types (Fig. 3) are used to construct different detector heads consisting of 24 PMs each. JULIOS in its standard version (Fig. 1)

is constructed with PMs of 28.5 mm diameter and circular shaped photocathodes (type a in Fig. 3). The effective length of the detector is 682 mm; the spatial resolution is 2.3 mm. A smaller detector of 200 mm effective length, but higher resolution of 1.2 mm uses rectangular shaped PMs of 8.6 × 24 mm photocathodes (type b in Fig. 3). The third type is a wide window version with PMs of 40 × 80 mm cross-section (type c in Fig. 3) and a total effective length of 940 mm; its spatial resolution is about 3.0 mm.

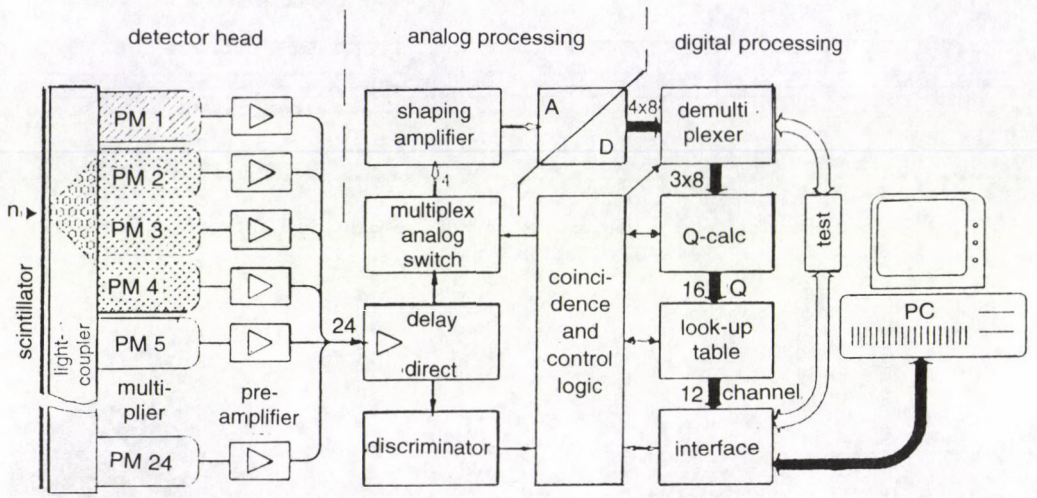

Fig. 4. Block diagram of the read out electronics and the signal processing of the JULIOS detector

The read out electronics (Fig. 4) of the JULIOS detector is composed of an analog part with a preselection of the highest PM event signals, which are multiplexed into four analog to digital converters, and a subsequent digital signal processing in a dedicated hardwired computer. The position computation is performed stepwise by (a) selection of those three PMs yielding the largest output signals, (b) calculating the center of gravity Q with the digitized output signals by using a fast look-up table procedure and (c) correcting Q according to non-linearities and inhomogeneities of the scintillator or the photocathodes by means of a special look-up table. Look-up tables are generated once by a calibration measurement. Long term stability of the detector is achieved by a completely automatic gain stabilisation of the PMs. For further details of the electronics we refer to [7,8]. There is now a ten years experience in the operation and practical application of JULIOS detectors at a powder and a texture diffractometer in Jülich, see Schäfer et al [9,10,11].

Large area detector

The same Anger-type technology of the linear JULIOS detectors is used for a large two-dimensional detector [12], which has been built for a small angle scattering

instrument at the research reactor in Jülich. 64 photomultipliers of 3 inch diameter each are arranged in a 8 × 8 square matrix (Fig. 5). The light disperser in front of the PM photocathodes is a glass plate of 70 mm thickness. The front side of the disperser is covered with the ^{6}Li glass scintillator in form of 16 plates of 150 × 150 × 1 mm. The sensitive detector area is 600 × 600 mm. The spatial resolution, resulting from the 84 mm separation of adjacent PMs, is 8 mm.

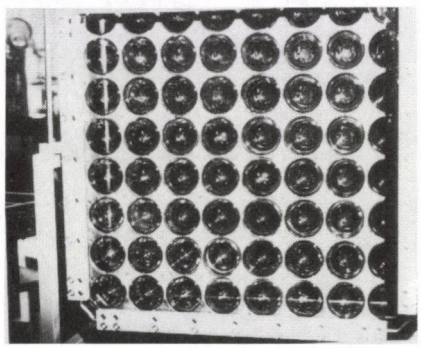

Fig. 5. Photograph of the large area detector showing the 64 PMs behind the glass disperser

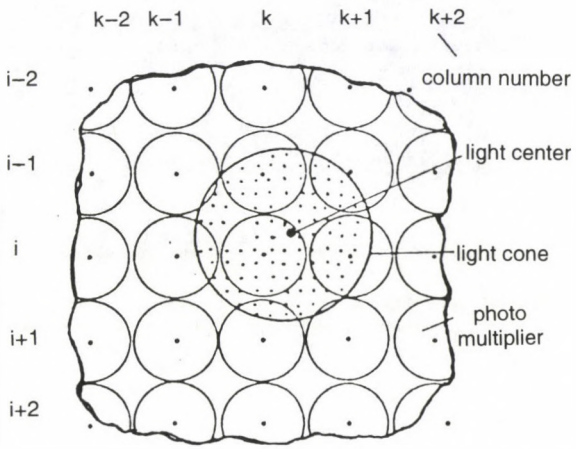

Fig. 6. Projection of the light cone of an event on the array of photocathodes of the area detector

The position coordinates of a neutron capture event are determined analogous to the procedure for the linear detector. After the determination of the coarse address of an event by preselection of the $PM_{i,k}$ (Fig. 6) with maximum anode signal, the fine addressing is obtained from the relation of the digitized output signals of the three adjacent PMs in both the x and the y direction. Again, the position computation is made by means of a fast look-up table procedure. The count rate capability of the area detector is 100 KHz. Details of detector construction, electronics, calibration, stabilization, physical properties and first experiences of application are reported by Heiderich et al [12].

Small area detectors

A new type of a two-dimensional handy neutron detector (Fig. 7) is based on a position-sensitive photomultiplier. So far, there are two types of such PMs, i.e. Hamamatsu R2487 with a rectangular shaped and R3292 with a circular photocathode. The PMs contain 12 dynode and 2 anode planes consisting of crossed wires (Fig. 8). The PM front glass housing is optically coupled to the neutron absorbing

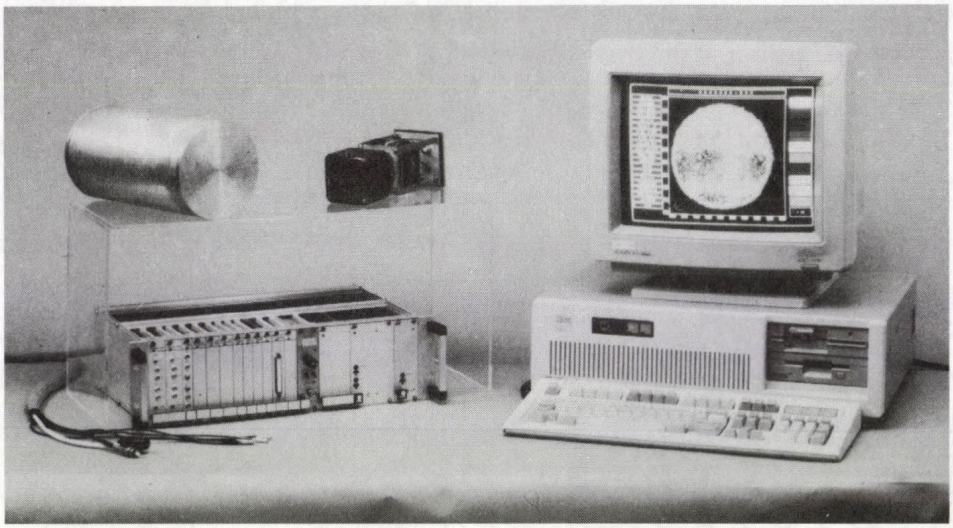

Fig. 7. Assembly of the area detector built with a position-sensitive PM. Two different detector heads (upper left) can be connected to the same electronic unit (lower left) and the PC (right) for data storage

^{6}Li-glass scintillator of 1 mm thickness. The neutron sensitive area is 55 × 45 mm for the rectangular PM and 100 mm diameter for the circular one.

Both ends of the x and y resistor chains (Fig. 8) are connected to charge sensitive preamplifiers, whose inputs are linear functions of the position coordinates of the electron beam pulse in the anode plane. The amplifier output signals are proportional to the charge in the two branches. The four amplifier signals are fed to two pulse dividing flash ADCs via main filter amplifiers (Fig. 9). The flash ADC output events are triggered by the discriminated sum signal of the four amplifier outputs in order to discriminate against gammas before the neutron event storage in a PC. The spatial resolution of the detector is measured to 1.0 mm; see Kurz et al [13].

Because of position dependence of the PM gain, which has been determined to change by about ±25 % across the position-sensitive detector area, a digital differential discrimination unit has been developed. The digital upper and lower discrimination levels are set dynamically due to the position dependent PM amplification, which is obtained from calibration measurements. Narrow discrimination windows are used to reduce simultaneously the gamma background of the neutron detector. The practical realisation of the new discrimination method and its function are described by Kanyo et al [14]. The neutron sensitivity across the detector area is measured close to unity and independent of position. The gamma background is reduced by a factor of 3 to 5 without the expense of neutron count rate.

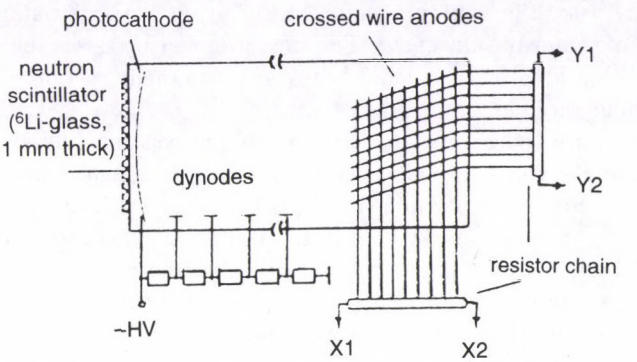

Fig. 8. Construction of the area detector using a position-sensitive photomultiplier

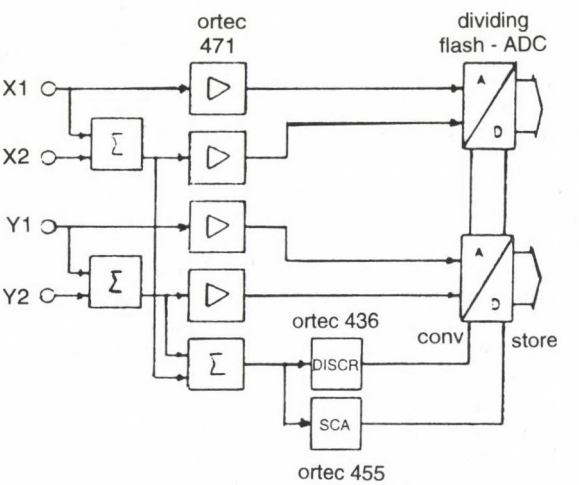

Fig. 9. Read out electronics of the position-sensitive PM with dividing flash ADCs

Discussion and prospects

Nine linear JULIOS detectors have been or are being built, so far. Six are in operation at diffractometers installed at thermal beams of the FRJ-2 and FRG-1 reactors and at the pulsed white beam of the ROTAX spectrometer at ISIS. The JULIOS electronics provides for a high resolution timing module to synchronize detector activities with the time structure of a neutron source or with time dependent sample environment conditions, e.g. outer electrical or magnetic fields. The application of the JULIOS detector in white beam time-of-flight diffractometry at ISIS

is described by Schäfer et al [15,16,17]. Actually, the JULIOS electronics is being extended to register the neutron events in 28 bit data words using 12 bit position and 16 bit time information each. The detector can be operated as a standalone system controlled by a PC with EISA-bus and the memory under the control of a 32 bit increment module.

The small area detectors are also standalone systems connected to a PC performing control of signal processing and data storage. The position-sensitive photomultipliers are handy as neutron counting tubes; they are aimed at adjustment and profile analysis purposes in neutron diffractometry, at reflectivity measurements, at focussed small angle scattering and at neutron microscopy, (see Alefeld et al [18]). Developments are in progress to improve the spatial resolution of these detectors to the μ-scale by installing a light amplifying channel plate and a lense optics between the neutron scintillator and the position-sensitive photomultiplier.

Acknowledgement

The detector project was funded by the German BMFT under contract Nos. Wl1BON, Wl2BON and Wl3BON.

References

1. R. Kurz, K. D. Müller, F. Pfeiffer, W. Schäfer and G. Will, Nucl. Instrum. Meth., *196*, 279, 1982.
2. J. Schelten, R. Kurz, I. Naday and W. Schäfer, Nucl. Instrum. Meth., *205*, 319, 1983.
3. J. Schelten and R. Kurz, in: Position-Sensitive Detection of Thermal Neutrons, eds. P. Convert and J. B. Forsyth, Academic Press, London, 1983, pp. 203–208.
4. A. Szepesváry, R. Reinartz and J. Schelten, Nucl. Instrum. Meth., 1994 (in press).
5. R. Kurz and J. Schelten, in: Position-Sensitive Detection of Thermal Neutrons, eds. P. Convert and J. B. Forsyth, Academic Press, London, 1983, pp. 192–196.
6. E. Jansen, W. Schäfer, A. Szepesváry, G. Will and R. Kurz, Physica B, *156 & 157*, 584, 1989.
7. R. Kurz, K. D. Müller, J. Schelten, A. Szepesváry, W. Schäfer and G. Will, IEEE Trans. on Nucl. Science, *35*, 78, 1988.
8. I. Naday and W. Schäfer, in: Position-Sensitive Detection of Thermal Neutrons, eds. P. Convert and J. B. Forsyth, Academic Press, London, 1983, pp. 197–202.
9. W. Schäfer, E. Jansen, F. Elf and G. Will, J. Appl. Cryst., *17*, 159, 1984.
10. W. Schäfer, E. Jansen, G. Will and R. Kurz, Physica, *136B*, 110, 1986.
11. W. Schäfer, P. Merz, E. Jansen and G. Will, Textures and Microstructures, *14–18*, 65, 1991.
12. M. Heiderich, R. Reinartz, R. Kurz and J. Schelten, Nucl. Instrum. Meth., *A305*, 423, 1991.
13. R. Kurz, R. Reinzartz, S. Widdau, J. Schelten, A. Scholz and W. Schäfer, Nucl. Instrum. Meth., *A273*, 273, 1988.
14. M. Kanyo, R. Reinartz, J. Schelten and K. D. Müller, Nucl. Instrum. Meth., *A320*, 562, 1992.
15. W. Schäfer, E. Jansen, R. Skowronek, G. Will, K. S. Knight and J. L. Finney, Nucl. Instrum. Meth., *A317*, 202, 1992.
16. W. Schäfer, E. Jansen and G. Will, J. Appl. Cryst., *26*, 660, 1993.
17. W. Schäfer, E. Jansen, A. Szepesváry, P. Skowronek, G. Will, R. Reinartz and K. D. Müller, Proc. ICANS-XII, 24–28 May 1993, RAL-Report, 1994 (in press).
18. B. Alefeld, D. Schwahn and T. Springer, Nucl. Instrum. Meth., *A274*, 210, 1989.

Acta Physica Hungarica 75 (1–4), pp. 369–372 (1994)

NEUTRON DEPTH PROFILING FACILITY AT NUCLEAR PHYSICS INSTITUTE ŘEŽ

J. VACÍK, J. ČERVENÁ, V. HNATOWICZ, V. HAVRÁNEK and D. FINK[1]

Nuclear Physics Institute
25068 Řež near Prague, Czech Republic
[1] *Hahn-Meitner Institute*
Glienickerstr. 100, Berlin 39, Germany

The neutron depth profiling technique and device installed at the Nuclear Physics Institute Řež is described. This technique provides sensitive analysis of some light elements in solids.

Principle of the technique

Neutron depth profiling is one of the nondestructive techniques for the measurement of concentrations of some light isotopes as a function of the depth in the near-surface region of solids. It exploits the existence of prompt exothermal non-resonant nuclear reactions of certain light isotopes with thermal neutrons (see Table I). The resulting reaction products (proton or alpha particle and a recoiling nucleus) are emitted with a kinetic energy determined by the nuclear disintegration energy of the reaction. The particles escaping from the sample are registered by detectors placed facing the target. From the energy loss spectra of the emitted reaction products, their depth of origin and hence the depth distribution can be reconstructed according to:

$$x = \int_{E_x}^{E_0} dE/S(E), \tag{1}$$

where E_0 is the initial energy of the particle originating from the depth x, E_x is its residual energy upon emerging from the sample surface and $S(E) = dE/dx$ is its stopping power which is a characteristic material quantity that varies strongly with the energy. Tabulations of stopping powers have been compiled by Ziegler [1] and others [2,3].

The counting rate Z in this technique is proportional to the total number N of reacting nuclides in the sample, their isotopic abundance c, their nuclear reaction cross-section σ with thermal neutrons, the thermal neutrons flux ϕ and the solid angle Ω between the sample and the detector

$$Z = N \cdot c \cdot \sigma \cdot \Phi \cdot \Omega. \tag{2}$$

The detection limit of NDP is inversely proportional to the cross-section of the reaction and the total neutron fluence. It is advantageous that the cross-sections

of some of the isotopes (He, Li, Be, B, Na) are high which makes the measuring technique quite sensitive (see Table I).

The emission of reaction products is isotropic and the detector can be placed at any angle with respect to the sample surface. The depth resolution of this technique is typically 20 nm for the vertical observation and about 10 nm for the tilted angle observation geometry.

The detection sensitivity can be increased by several orders of magnitude by the large angle coincidence spectrometry [4]. In this method both reaction products emitted from the sample in opposite direction are measured simultaneously with two detectors placed in the promixity of the target.

Table I
List of suitable isotopes exploited in NDP analysis [5]

Elem.	Reaction	% Abundance or (at./mCi)	Cross-section (barns)	Energy of react. products (keV)		Detection limit (at./cm^2)[b]
He	^{3}He$(n,p)^3$H	0.00014	5333	572	191	1.5×10^{12}
Li	^{6}Li$(n,\alpha)^3$H	7.5	940	2055	2727	9.0×10^{12}
Be[a]	^{7}Be$(n,p)^7$Li	2.5×10^{14}	48000	1438	207	1.7×10^{11}
B	^{10}B$(n,\alpha)^7$Li	19.9	3837	1472	840	2.1×10^{12}
N	^{14}N$(n,p)^{14}$C	99.6	1.83	584	42	4.5×10^{15}
O	^{17}O$(n,\alpha)^{14}$C	0.038	0.24	1413	404	3.5×10^{16}
Na[a]	^{22}Na$(n,p)^{22}$Ne	4.4×10^{15}	31000	2247	103	2.3×10^{11}
S	^{33}S$(n,\alpha)^{30}$S	0.75	0.19	3081	411	6.0×10^{16}
Cl	^{35}Cl$(n,p)^{35}$S	75.8	0.49	598	17	1.7×10^{16}
K	^{40}K$(n,p)^{40}$Ar	0.012	4.4	2231	56	1.9×10^{15}
Ni[a]	^{59}Ni$(n,\alpha)^{56}$Fe	1.3×10^{20}	12.3	4757	340	7.0×10^{14}

[a] radioactive species
[b] Detection limits in Table I are based on 0.1 counts/s, 0.1 % detector solid angle and a neutron intensity 6×10^9 s^{-1}.

NDP instrument

A basic condition for high-sensitivity NDP measurements is a low background of unwanted events resulting mainly from nuclear reactions with fast neutrons, as well as with electrons and photons. This condition is best satisfied at a neutron guide tube.

In the Nuclear Physics Institute at Řež a 5.6 m long neutron guide was installed at the LWR-15 nuclear research reactor. The guide internal cross-section is 4×150 mm^2 and its radius of curvature is 825 m. At 6 MW reactor power, the thermal neutron flux was 7×10^6 n cm^{-2}s^{-1} and the measured cadmium ratio $R = 10^5$. A schematic layout of the neutron guide and NDP arrangement is shown in Fig. 1. A well-collimated neutron beam enters a large target chamber with a diameter of 500 mm installed just behind the neutron guide end and evacuated to a pressure of 10^{-2} Torr. For routine measurements, only prevacuum is required, to prevent errors due to the particle's energy loss in the space between the sample

and the detector. Four independent spectrometric systems with the possibility of two-dimensional data handling (coincidence spectroscopy) can be used in the vessel simultaneously. Up to 14 samples can be inserted into the special holders, 12 of them into a changer for automatic measurements. The sample area can range from about 1 mm^2 to about 10 mm^2. Large area PIN photodiodes or silicon surface barrier detectors are used in a close geometry with targets. The solid angles between the samples and the detectors are usually about 1 % – 10 %. The data acquisition can be performed via PC or ND MCA. Monitor information is fed into all acquisition systems automatically.

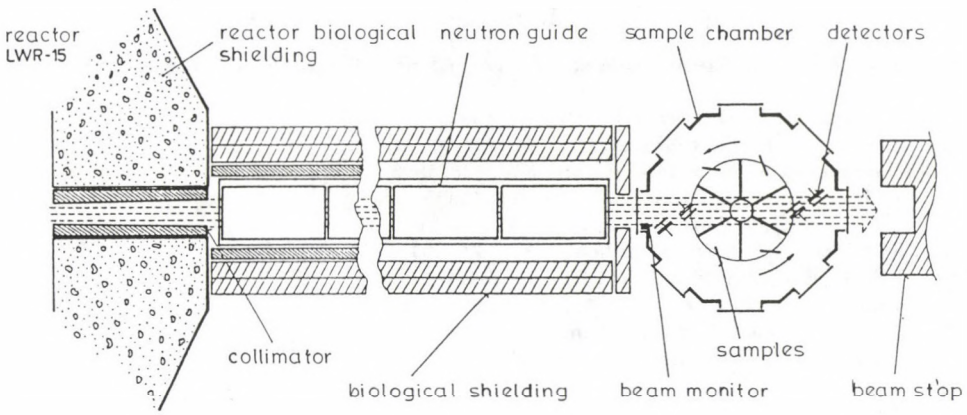

Fig. 1. A schematic sketch of the thermal NDP arrangement

At present, there exist only a few NDP devices in operation in the world: at the National Institute of Standards and Technology Gaithersburg, USA, at the National Laboratory Chalk River in Canada, at the Hahn–Meitner Institute Berlin in Germany, at the Musashi Institute of Technology Kawasaki in Japan and at the Nuclear Physics Institute Řež. In the last decade these facilities have subsequently advanced and the applications greatly expanded.

Applications

The NDP method has been used to investigate numerous questions from different areas of material science [5]. This covers the fields of the basic solid-state research (stopping powers, implantation profiles, damage distributions, sputtering, diffusion, precipitations and segregations), polymer science (conducting polymers, polymer doping, polymer destruction by ion beam irradiation), tribology and corrosion (protective surface development), microelectronics (boron in silicon, GaAs, etc), microoptics (waveguides), metallurgy (metallic glasses), ecology (determination of Li, B and N in life materials), etc. All these activities indicate that NDP

has significant potential for research where light nuclei play a role or can be applied as sensitive tracers.

In the Nuclear Physics Institute at Řež the NDP technique has been used for more than a decade. The depth profiles of boron in photoresists and SiO_2 have been measured to determine range values for implants in several types of films [6]. The diffusion across interfacial boundaries has been studied [7] for boron implanted into the Si/SiO_2 system. Similar NDP experiments [8,9] have been performed on Si/metal and SiO_2/metal systems. The NDP method has been exploited also for the biomedical study of cancer cell doping [10]. At present, the doping of latent ion tracks in polymers using the NDP technique are investigated [11].

References

1. J. F. Ziegler et al, The Stopping and Ranges of Ions in Solids, Pergamon Press, New York, 1985.
2. J. F. Janni, At. Nucl. Data Tabl., *27*, 147, 1982.
3. D. I. Thwaites, Radia. Research, *95*, 495, 1983.
4. V. Havránek et al, Nucl. Instr. Meth., *B73*, 523, 1993.
5. R. G. Downing et al, J. Res. NIST, *98*, 109, 1993.
6. J. Červena et al, Tesla Elect., *14*, 16, 1981.
7. J. Kvitek et al, Radiochem. Radioan. Lett., *24*, 205, 1976.
8. L. Pelikán et al, Phys. Stat. Sol., *72*, 369, 1982.
9. V. Rybka et al, Phys. Stat. Sol., *83*, 165, 1984.
10. V. Mareš et al, Eur. J. of Histochem., *36*, 33, 1992.
11. D. Fink et al, Rad. Eff. Def. Sol., *126*, 247, 1993.

Acta Physica Hungarica 75 (1–4), pp. 373–380 (1994)

TO THE PROBLEM OF THE COHERENCE LENGTH OF NEUTRONS

P. VARGA

KFKI Institute for Materials Science
P.O.B. 49, 1525 Budapest, Hungary

The challenge of the high accuracy of certain optical measurements, the long coherence length of light provokes one to search for possibilities to enlarge the neutron coherence length. A proposal is made to achieve this by using a five or a four plate Bonse–Hart interferometer. A further problem is, whether the neutron beam is composed of wave packets or of overlapping independent monochromatic waves; it is considered that the former is more likely.

1. Introduction

The interference of light has deliberately been studied for nearly two centuries, whereas the interference of neutrons for only two decades. The triumphal path of light interference was crowned by the new definition of the meter. This can be attributed to the excellent work of Michelson even for two reasons: The experiment named after him proved that the speed of light does not depend on the velocity of the inertial frame. Moreover, he began to compare the wavelength of spectral lines with the standard of the meter. This initiative meant that the wavelength of the atomic time standard could be compared by contemporary means with the ancient standard of the unit of length. The fact that the speed of light could be standardized to an accuracy of nine decimals is due to the large coherence length of the light emitted by atoms.

The path of neutron interferometry is nevertheless triumphal. Experiments proved the power of this method by showing the influence of the gravitational field [1], the rotation of the frame [2], and the motion of the medium [3] on he phase of neutron interference pattern; the 4π rotational invariance of the spinors was demonstrated [4]; loss of the visibility of the interference pattern was observed, when the experimentator wanted to delude the Nature by trying to hit the tail of Schrödinger's cat [5].

To stress the analogy between the interference of neutrons and light or acoustic waves we refer to [6]. The visibility of neutron interference fringes was measured, it decreased with increasing path difference and vanished after certain delay. By further increasing the delay the visibility recovered. Moreover, the phase of the interference pattern had a jump of π, when the visibility returned. Fizeau studied the yellow light of sodium in 1863 by interferometer and observed that Newton's rings disappeared at the 500th fringe, but afterwards they turned back and vanished at every 500th fringe. He could follow this up to the 5000th one. Fizeau explained that this observation was caused by a twin spectral line: it was the discovery of

the Na doublet. The disappearance and the returning of the visibility, observed in [6], was explained in the same way: the output spectrum of the monochromator was analysed, the spectrum showed deviation from Gaussian shape and it could be decomposed with reasonable good fidelity into two shifted Gaussian spectra.

The jump of the phase is the same, which happens when sound is beating: whenever the volume of sound falls to zero, the envelope of the carrier wave changes its sign, which occurs in the phase of the carrier as a jump.

These analogies provoke the idea of finding further interference effects with neutron waves, similar to those of the classical waves.

However, there is a difference between light and neutron interference: in contrast to that of the light, interference length measured with neutrons is in the order of hundred wavelengths [6,7] because no line source exists for neutrons, the coherence length is defined by the bandwidth of the device used to produce the spectrum [8].

2. Methods for enlarging coherence length

Spectrum and coherence function are bound by the Wiener–Khintchine theorem. It is obvious that any attempt to increase coherence length will will reduce the flow rate of particles because the lengthening is equivalent to cutting off a smaller part of the continuous spectrum offered by the source. Now we analyse some possibilities for increasing the coherence.

1. The simplest way is to enlarge the resolving power of the monochromator by using a better quality crystal.

2. The other way is to select neutrons by the time-of-flight method. This method enables a relative spectral width of 10^{-3}–10^{-4} to be achieved.

3. In spite of the statement in [9] the dispersion in a medium may help to make the coherence longer. In that article the coherence length of light waves was analysed to see whether it depended on the length of the dispersive medium D. Here, besides the difference between phase and group velocities, the second order dispersion $d^2k/d^2\omega^2$ was taken into account. The authors stated that " ... using a simple-minded picture of spreading wave packets, one could easily be misled into thinking that the coherence length will also spread upon propagation in a dispersive medium."

The error was caused by the voluntary change of variables. In Eq. (18) of [9] the mutual coherence function is expressed as a function of the length D of the dispersive cell, put into one arm of the interferometer, and of the path difference X due to the phase shifter introduced into the other arm of the interferometer. The change of the variables comes after Eq. (18) of [9]: new variables T and $\overline{X}$ are introduced by

$$T = (X + D)/c,$$

$$\overline{X} = D,$$

consequently the length of the dispersion cell disappears. T is called time delay. In [9] an example is given for a wave packet which has a Gaussian spectrum at the

entrance of the interferometer and all the spectral components have the same initial phase. At this stage the Fourier components of the spectrum have no additive phase, for such a wave packet interference fringes are equidistant, when measured without the dispersion cell. Using the mentioned transformations the authors obtained an expression (25) for the coherence function observable at the output of the interferometer

$$\gamma_{12}(X,T) = \frac{\exp[i\omega_0(X/u_0 - T)]}{[1 - i(\Delta\omega)^2(d^2k/d\omega^2)_{\omega_0}X]^{1/2}} \times \exp\left[-\frac{\frac{1}{2}(\Delta\omega)^2(X/v_0 - T)^2}{[1 - i(\Delta\omega)^2(d^2k/d\omega^2)_{\omega_0}X]}\right],$$

where $\Delta\omega$ stands for the initial line width, u_0 and v_0 are phase and group velocities, respectively. Here we have omitted the bar over the X to make the formula identical with the original expression. It seems, it is the path difference X (i.e. the lengthening of one of the arms of the interferometer) which has an effect on the line width. If we do not use the transformations mentioned, instead of (25) we obtain

$$\gamma_{12}(X,D) = \frac{\exp[-i\omega_0[X/c - (1/u_0 - 1/c)D]]}{[1 - i(\Delta\omega)^2(d^2k/d\omega^2)_{\omega_0}D]^{1/2}} \times \exp\left[-\frac{\frac{1}{2}(\Delta\omega)^2[X/c - (1/v_0 - 1/c)D]^2}{1 - i(\Delta\omega)^2(d^2k/d\omega^2)_{\omega_0}D}\right].$$

The shape of the coherence function remains Gaussian but the coherence length becomes longer than the initial one. Also the phase of the interference fringes is no longer constant, it shows a slight variation along the interference curve. In reality, the spectrum (a real nonnegative quantity) does not change as a consequence of the dispersion, but each Fourier component gains an additive frequency dependent phase. Nevertheless, the interference can be observed for larger arm-length differences.

4. Now we come to the interferometric method which seems to be possible to implement. The optical analogy of the proposed experiment was perfected in 1961 [10]. The authors demonstrated that a longer coherence than that offered by the light source can be obtained with the aid of an additional interferometer. They put a Fabry–Perot pair into a beam and the output was analysed by a Michelson interferometer (Fig. 1). At the input of the Fabry–Perot interferometer the coherence length of the emitted light was less than twice the spacing of the parallel plates. The interference pattern measured with nearly equal arm lengths of the Michelson interferometer vanished when one of the arms was lengthened by an amount which was measured with the same source but without the F–P interferometer. The pattern came back, when the arm-length difference approached the separation of the Fabry–Perot interferometer plates. The effect was repeated for every multiple of the separation. Interference was observed up to the eighth order. The visibility of the interference in the individual orders was reduced in accordance with the exponential law, as the amplitude of the output wave of the F–P interferometer is also reduced exponentially after each round-trip. (The same effect can be observed when measuring the longitudinal interference of a laser beam, containing several longitudinal modes.)

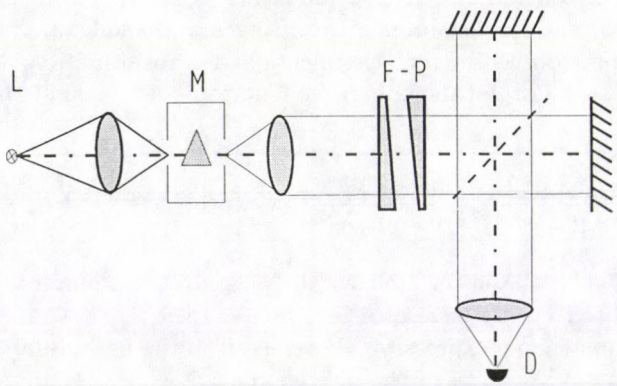

Fig. 1. Experimental set-up used in [10]. L – mercury spectral lamp, M – monochromator, F–P – Fabry–Perot interferometer, D – detector

The effect of the interferometer is principally the same as the effect of a better monochromator: the spectral transfer function of the Fabry–Perot acts like a comb-like filter on the initial spectrum, by cutting off periodic parts of the spectrum.

Though the neutron storage device [11] can in principle be regarded as a Fabry–Perot interferometer, in practice it is virtually impossible to store neutrons without spoiling the phase of the neutron wave. It seems to be realizable to enlarge the coherence length with the aid of a five or a four plate Bonse–Hart device (details of the latter were reported in [12]). Let us take a five plate interferometer (Fig. 2) and put two media into the arms of loop A between plates II and III, one with attractive, the other with repulsive pseudopotential. The first speeds up the wave packet, the other slows it down. Consequently, the wave train leaving point X on plate III will consist of two superimposed packets, shifted with respect to each other. In loop D, a third packet with no slowing down/speeding up is added to the twin train, and three superimposed packets reach point Y. If the phase plate is placed between plates IV and V, after mixing at point Y on plate V a pair of trains consisting of three superimposed wave packets interferes, this can be measured at ports 5 and 6. At points Z and Z' one train of three packets is mixed with a single packet, at ports 2, 3, 6 and 7 the interference length is shorter than in the previous case, but longer than with a three plate interferometer.

Let ψ_+, ψ_0 and ψ_- be the wave functions of the neutron with speeding up, with no speeding up/slowing down and with slowing down, respectively. The wave function of the train at port 5 is,

$$\psi = \psi_+ + \psi_0 + \psi_- + \overline{\psi}_+ + \overline{\psi}_0 + \overline{\psi}_-,$$

where the bar denotes the phase shift in loop D. Let the speeding up/slowing down introduced in loop A be longer than the coherence time, but the shift introduced in

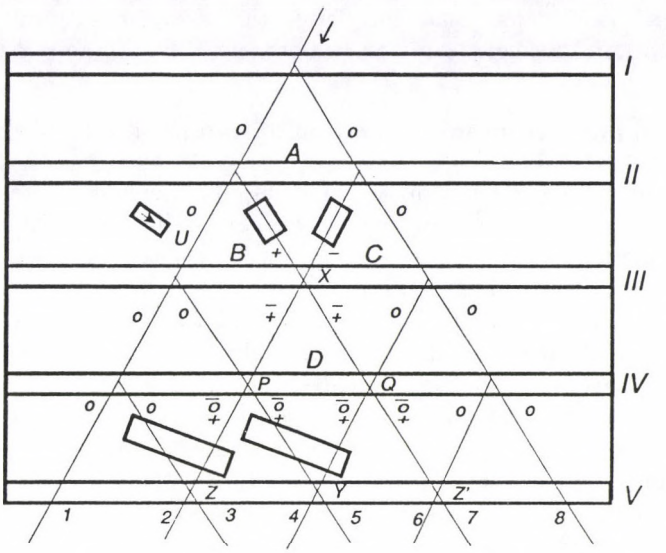

Fig. 2. The five-plate neutron interferometer

loop D is less than the coherence time (i.e. all the packets overlap). The residual density is

$$|\psi|^2 = S + 2\mathcal{R}(\psi_+\overline{\psi}^*_+ + \psi_0\overline{\psi}^*_0 + \psi_-\overline{\psi}^*_-),$$

where

$$S = |\psi^2_+| + |\psi^2_0| + |\psi^2_-| + |\overline{\psi}^2_+| + |\overline{\psi}^2_0| + |\overline{\psi}^2_-|.$$

If the shift in D is nearly equal to the speeding up/slowing down, (only two packets overlap) the density is

$$|\psi|^2 = S + 2\mathcal{R}[\psi_0\overline{\psi}^*_- + \psi_+\overline{\psi}^*_0].$$

Finally, for the shift of double speeding up/slowing down,

$$|\psi|^2 = S + 2\mathcal{R}\psi_+\overline{\psi}^*_-.$$

The contrast takes its maximum value only in the first case. In the second order it is more than 2/3 part of that of the first; in the third order not more than 1/3. Nevertheless, interference can be observed around five positions of the phase shifter.

At ports 2, 3, 4 and 7 a triple train interferes with a single one, the phase shifter has only three positions, around which interference can be observed but the

contrast does not differ in various orders, if the absorption of the media is small. If an absorber is put into loop B to cover the path with no slowing down (location U) a triple packet will be combined with a double one at Y on plate V, but the number of orders remains 5. A four plate interferometer offers similar results: interference between a twin and a single train can be observed behind points P and Q.

3. Wave packets or superposition of independent infinite waves

In the discussion [8] following the publication of the first coherence experiment [7] it was cleared that the last experiment cannot distinguish[1] between two models of neutron waves: Does the neutron beam consist of nearly identical wave packets, or is it a simple superposition of infinite sinusoidal waves, where the modulus of the amplitude of the Fourier components is the square root of the spectral density, but the initial phase of each component is independent of the other?

The first case corresponds to a model of electromagnetic wave packets emitted by atoms (the length of the packet is determined by the emission process), the second to the radiation of an incandescent lamp. There is no model for the elementary radiation process of the latter, we have a model for a black body in the equilibrium state only. In this model the spectral components are cavity modes, the energy change between modes is perfected by a small soot particle. These modes (Fourier components) can be regarded as independent. Nor can optical interferometry distinguish between the two ideas, but in optics there is a possibility to measure higher order momenta.

In both cases, however, we have a priori knowledge about the source and about the interactions undergone by the agent under observation. Neutrons, produced somewhere inside the reactor suffer collisions or, at least, they interact with the monochromator crystal that acts as a grating. Every atom of the grating scatters the neutron, the atoms are periodically arranged, the wave reaching the observation point is influenced by this periodicity.

For electromagnetic radiation no dispersion takes place in a vacuum, the periodicity at each point (far enough from the grating or in the focal plane of a lens) is conserved. The finite interference length is defined by the textbook formula for the resolution power of the grating, or in a spectacular way: the coherence length is equal to the path difference of the boundary rays (Fig. 3).

If the radiation impinging on the grating has no periodicity, it will be produced by the periodic elements of the grating itself. If there is a periodicity in the primary radiation (spectral line source) intensity is observed only in directions for which the periodicity offered by the grating equals that which was present in the incident light.

Neutrons, as produced in the fission process and scattered inelastically afterwards, can be taken into analogy with the thermal radiation. The last interaction with the monochromator defines the initial form of the wave function, which obeys on the further path the Schrödinger equation of free particles. There is no reason

[1] Nor can the experiment proposed in the previous section help.

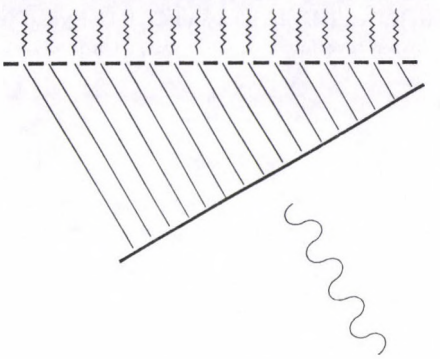

Fig. 3. The effect of a periodical structure on the field

to doubt the existence of wave packets, but a real experiment would help to clear up this problem.

Acknowledgement

Thanks are due to Dr. G. Kiss for suggesting the concrete scheme for enlarging the coherence of neutrons.

References

1. A. G. Klein and S. A. Werner, Reports on Progress in Physics, *46*, 259, 1983; J. L. Staudenmann, S. A. Werner, R. Colella and A. W. Overhauser, Phys. Rev. A, *21*, 1419, 1980.
2. S. A. Werner, J. L. Staudenmann and R. Colella, Phys. Rev. Lett., *42*, 1103, 1979; D. K. Atwood, M. A. Horne, C. G. Shull and J. Arthur, Phys. Rev. Lett., *52*, 1673, 1984.
3. M. Arif, H. Kaiser, R. Clothier, S. A. Werner, W. A. Hamilton, A. Cimmino and A. G. Klein, Phys. Rev. A, *39*, 931, 1989.
4. H. Rauch, A. Zeilinger, G. Badurck, A. Wilfing, W. Bauspiess and U. Bonse, Physics Letters, A, *54*, 425, 1975; S. A. Werner, R. Colella, A. W. Overhauser and C. F. Eagen, Phys. Rev. Lett., *35*, 1053, 1975; H. Rauch, A. Wilfing, W. Bauspiess and U. Bonse, Z. Physik B, *29*, 281, 1978.
5. J. Sumhammer, H. Rauch and D. Tuppinger, Phys. Rev. A, *36*, 4447, 1987; H. Rauch, J. Sumhammer, M. Zawisky and E. Jericha, Phys. Rev. A, *42*, 3726, 1990; H. Rauch and J. Sumhammer, submitted to Phys. Rev. Lett.
6. S. A. Werner, R. Clothier, H. Kaiser, H. Rauch, H. Wölwitsch, Phys. Rev. Lett., *67*, 683, 1991; R. Clothier, H. Kaiser, S. A. Werner, H. Rauch and H. Wölwitsch: Phys. Rev. A, *44*, 5357, 1991; H. Kaiser, R. Clothier, S. A. Werner, H. Rauch and H. Wölwitsch, Phys. Rev. A, *45*, 31, 1992.
7. H. Kaiser, S. A. Werner, E. A. George, Phys. Rev. Lett., *50*, 560, 1983.
8. A. G. Klein, G. L. Opat and W. A. Hamilton, Phys. Rev. Lett., *50*, 863, 1983; George Comsa, Phys. Rev. Lett., *51*, 1105, 1983; H. Kaiser, S. A. Werner and E. A. George, Phys. Rev. Lett., *51*, 1106, 1983.

9. W. A. Hamilton, A. G. Klein and G. I. Opat, Phys. Rev. A, *28*, 3149, 1983.
10. J. Bakos, K. Kántor and Zs. Náray, KFKI Közlemények, *9*, 307, 1961 (in Hungarian).
11. M. Schuster, H. Rauch, E. Seidl, E. Jericha and C. J. Carlyle, Physics Letters, *144*, 297, 1990.
12. Michael Heinrich, 4-Platten Interferometer, Thesis, Atominstitut der Österreichischen Universitäten, 1987.

Acta Physica Hungarica 75 (1–4), pp. 381-385 (1994)

APPLICATION OF NEUTRON ACTIVATION ANALYSIS IN STUDIES OF CHEMICAL ELEMENT DISTRIBUTION IN RĪGA (LATVIA) DRINKING WATER

M. VIRCAVS*, I. TAURE, G. EGLĪTE and Ž. BRIKE

Nuclear Research Centre, Latvian Academy of Sciences
31, Miera st., Salaspils, LV-2169, Latvia

The method of instrumental neutron activation analysis is applied in order to estimate the distribution of major, minor and trace elements in drinking water of Rīga. The chemical composition of drinking water varies considerably in different districts of Rīga. The greatest concentration differences for Zn and Al are observed. Median concentrations of determined elements are less than maximum permissible concentrations (MPC). Although in some cases the concentration of Al and Fe are more than their MPC.

Introduction

The quality of drinking water is evaluated firstly in terms of parameters which are or may be of significance to public health, and secondly in terms of parameters that affect the acceptability of water to consumers because of effects on appearance, taste, odour or other properties not directly related to health but important in relation to normal water use. Health-related parameters may be subdivided into microbiological, chemical and radioactive components (Packham [3]). Inorganic and organic compounds of different chemical elements play an important role among various chemical substances influencing the quality of drinking water. The results of many experimental studies suggest a correlation between element concentrations in drinking water and human health. For instance, small amounts of As in the environment, especially in drinking water supplies, can cause skin cancer (Pearce [4]). In order to reduce the concentration of As to below 0.01 mg/L fundamental principles and the stage development of As removal from drinking water is reported by Stöver and Roennefahrt [5]. Besides, in the 1993 guideline values of World Health Organisation (WHO) have been revised in respect to maximum permissible concentrations (MPC) of As and Pb in drinking water, i.e. the new guideline values of he mentioned elements are 0.01 mg/L (Packham [3]). Lanciotti et al [2] have discussed the problem of Ba concentrations in Italian drinking water supplies. Experimental investigations show a correlation between levels of Ba in drinking water and high blood pressure (Kopp et al [1]).

The contamination of drinking water sources both surface and ground waters is connected with the development of industry and its intensification as well as with

*Correspondence: M. Vircavs, Ministry of Environmental Protection and Regional Development of Latvia, 25 Peldu St., LV-1494, Rīga, Latvia

the growth of urban concentration. As a consequence drinking water sources are polluted with different chemical substances including various element compounds. In this connection Weideborg et al [6] have reported that acid precipitation affects surface water sources. As a result the concentrations of trace metals, especially lead, increase in drinking water sources.

In Latvia one of the areas most influenced by the industry is Rīga with the surrounding districts where different kinds of industry are concentrated. In order to estimate the influence of industrial activities on the quality of drinking water of Rīga an analysis with respect to major, minor and trace elements contents is necessary.

The state control institutions which test and determine the suitability of drinking water have information about only a few chemical elements (Fe, Pb, Cd, Zn, Hg, Mn, Al) and only at the pumping stations. In order to obtain maximum information about element concentrations in Rīga drinking water we chose instrumental neutron activation analysis (INAA) with pile neutrons using Research Nuclear Reactor (RNR) at Salaspils, Latvia; an ordinary water–water pool reactor with a nominal thermal power of 5 MW. Besides, we analyse drinking water samples collected in different dwellings of Rīga and water pumping stations as well as some water samples of wells whose water is used for drinking.

This paper presents the analysis of data obtained by INAA which characterize the concentration level of chemical elements in drinking water.

Experimental

Water samples for the present study were collected in the daytime during 1991 and 1992 from 24 dwellings of Rīga, 8 wells and 4 water pumping stations. The wells (depth 3–4 m) are located in the surroundings of Rīga. Polyethylene screw-cap bottles were used as containers for water samples. After slow evaporation 50–100 mg of the obtained remnants were irradiated with neutrons.

Short irradiations were made using the RNR horizontal experimental channel with a pneumatic transport facility (2–3 s transfer time) at the following fluxes of thermal and resonance neutrons: $F_{th} = 1.6 \times 10^{13}$ n·cm^{-2}·s^{-1}; $F_{res} = 8.5 \times 10^{11}$ n·cm^{-2}·s^{-1}. Gamma spectra of the irradiated samples and standards were recorded using a Ge(Li) detector (energy resolution 2.8 keV (FWHM) for the 1332 keV ^{60}Co gamma-ray) coupled to a 4000-channel analyser (NTA-1024, Hungary). Samples for short irradiation were packed in polyethylene containers and counted directly. The irradiation (t_i), delay (t_d) and measurement (t_m) times of samples and standards were the following: $t_i = 30$ s, $t_d = 3$ min and $t_m = 200$ s.

Long irradiations were performed in the RNR vertical experimental channels at the fluxes $F_{th} = (1.2–5.2) \times 10^{13}$ n·cm^{-2}·s^{-1}; $F_{res} = (2.1–4.2) \times 10^{11}$ n·cm^{-2}·s^{-1}. A high purity Ge detector (2.1 keV energy resolution) connected to a 4000-channel analyser (Nokia LP-4900, Finland) was used. Samples and standards were wrapped in Al foil for irradiation. Before measurements the radioactive Al foil was removed. The following analytical scheme was used: $t_i = 17$ h, $t_d = 72$ h and $t_m = 10$ min; $t_i = 17$ h, $t_d = 21$ d and $t_m = 15 - 30$ min.

Results and discussion

The drinking water of Rīga consists of surface (lake and river; 60 %) and ground water (artesian waters from 100-200 m depth in Devonian sedimentary rocks; 40 %). The dry remnant of drinking water varies from 180–530 mg/L with median concentration of 250 mg/L. Surface water does not correspond to drinking water standards. Therefore it is purified before the water supply system. In return ground water quality corresponds to the existing standards with the exception of Mn whose concentration in some sources is up to 2 times more than MPC. Considering that Rīga drinking water is a mixture of surface and ground waters in the water supply system the elemental concentrations level out, for instance, the concentration of Mn in the water supply system is less than MPC.

The chemical composition of drinking water from different surface and ground water sources varies considerably. For example, the maximum : minimum concentration ratios in surface and ground water sources are 30 for Fe and 29 for Al, the concentration of Mn only in ground waters varies by a factor 42.

26 chemical elements (Mg, Al, V, Sc, Ti, Cr, Mn, Fe, Co, Ni, Cu, Zn, As, Se, Cl, Rb, Sr, Ag, Sb, Cs, Ba, La, Ce, Hg, Th, U) were found in wide concentration ranges in drinking water samples collected in different dwellings of Rīga. Some of these elements were determined only in some samples but 11 elements were quantified in all drinking water samples (see Table I). In spite of the fact that Rīga drinking water is a mixture as it is indicated above elemental concentrations differ also in different districts of the city. The greatest concentration differences were observed for Zn and Al: the lowest concentration of Zn was 0.001 mg/L and the highest was 0.256 mg/L; the lowest concentration of Al was 0.015 mg/L and the highest was 0.89 mg/L. Besides, the latter exceeds the MPC (see Table I). The highest concentrations of Al may be connected with the use of $Al_2(SO_4)_3$ for drinking water purification as well as with the changes of surface and ground water distribution in the water supply system. The obtained data show that the highest concentrations of Zn and Al were observed in relatively new housing areas. In the case of Zn this can be explained by decreased leaching of Zn from the pipe-lines as they grow older. In connection with the obtained data it is possible to conclude that one of the main reasons of elemental concentration changes in drinking water is the quality of pipe-lines. It follows that the concentrations of elements differ even within the same street, for example, the concentration of Zn differs by a factor 5 but the concentration of Fe by a factor 2.

There are no clear differences in elemental concentrations between hot and cold pipe-line water. The data show that the shortage of coagulants used in the water treatment does not essentially influence the concentrations of chemical elements in the drinking water.

The elemental composition of wells and pipe-line water does not differ with the exception of well water which is located in some wells situated near the old dumping ground of Rīga (approx. at a distance of 2 km). There were observed high concentrations of Al (0.7 mg/L), Mn (0.7 mg/L), Fe (17 mg/L), Zn (0.66 mg/L), Cr (0.036 mg/L), Rb (0.088 mg/L) and lanthanides (e.g. La, Ce, Eu, Tb, Yb).

The water of the mentioned wells is not used for drinking but only for splashing of vegetables.

One of the criteria of the suitability of drinking water is the MPC of chemical elements which are established in standards. MPCs are not given for all elements and norms in different countries and organisations are established according to their own criteria. Four different sets of standards are given in Table: the former USSR (GOST), Sweden (SW), the European Community (EC) and the WHO. At present the standards (GOST) of the former USSR are valid in Latvia. Comparing elemental concentrations in the drinking water with the standards of the former USSR and others (see Table I) we ascertained that with few exceptions, the concentrations are lower than the MPCs in all sorts of standards. The limits of detection of the INAA method are considerably lower than the MPCs for all mentioned standards (see Table I).

Table I

Concentration ranges, median concentrations of chemical elements in Rīga drinking water, their limit of detection and maximum permissible concentrations

Elements	Concentr. ranges	M_c	LOD	GOST Ref [9]	SW Ref [10]	EC Ref [7]	WHO Ref [8]
Mg	1.1 – 27*	10*	500		30*	30*	
Cl	3.3 – 92*	11.2*	1	350*	100 – 300*	250*	250*
Al	15 – 890	65	1	500	100		200
Fe	40 – 700	190	7	300	100	200	300
Zn	1 – 256	29	0.7	5000	300		5000
Mn	9 – 102	36	0.2	100	50	50	100
Sr	4.3 – 47.3	11	0.2	7000			
Co	0.03 – 0.7	0.07	7×10^{-4}				
Sb	0.04 – 0.2	0.06	7×10^{-4}				
Sc	$(5 - 28) \times 10^{-3}$	9×10^{-3}	5×10^{-4}				
Cr	0.2 – 7.7	0.7	0.05		50	50	50

LOD – Limit of detection, calculated as $3 \cdot N_f^{1/2}$, where N_f is background level under photopeak

M_c – Median concentrations; * – Concentrations in mg/L, other concentrations in μg/L.

Using the method of INAA the composition of Rīga drinking water (in dwellings and water pumping stations) and of well water in respect to major, minor and trace elements is carried out. INAA is appropriate for drinking water monitoring in respect to content of chemical elements. Quality of Rīga drinking water with few exceptions corresponds to the indicated standards (see Table I). Besides, it is necessary to note that the control services should not monitor water quality only at the supply stations, but also in selected cases in dwellings.

Acknowledgements

This work was financially supported by a grant form the Latvian Council of Science (Scientific Project – The Application of Nuclear Analytical Methods in Solution of Ecological Problems Connected with the Environmental Pollution).

Thanks are due to Dr. T. P. Flaten (University of Trondheim) for fruitful comments of the manuscript and useful discussions concerning the problem of drinking water.

References

1. S. J. Kopp, H. M. Perry, J. M. Feliksik et al, J. Pharmacol. Exp. Ther., *177*, 433, 1985.
2. E. Lanciotti, N. Comodo, L. Gambassini et al, Bull. Environ. Contam. Toxicol., *43*, 833, 1989.
3. R. F. Packham, J. of the Instit. of Water and Environ. Management, *7*, 532, 1993.
4. F. Pearce, New Scientist, *5*, 1897, 1993.
5. T. Stöver and K. Roennefahrt, Vom Wasser, *78*, 363, 1992.
6. M. Weideborg, D. Hongve and E. Andruchow, Verh. Internat. Verein. Limnol., *24*, 2180, 1991.
7. EC Drinking Water Standards, Directive 80/778/EEC.
8. Guidelines for Drinking Water Quality, WHO, Geneva, 1984.
9. Sources of Centralized Drinking Water Supply, Hygienic, Technical Requirements and Instructions of Choice, GOST 2761–84 (in Russian).
10. Underlag for Bedömning av Dricksvatten efter Mikrobiologisk Undersökning, Norrköping, Sweden, 1985.

Acta Physica Hungarica 75 (1–4), pp. 387-396 (1994)

POLARIZED NEUTRON SET-UP

M. I. TSULAYA, M. S. GABELYA and S. I. DJAMASPISHVILI

Institute of Physics of the Academy of Sciences of Georgia
6, Tamarashvili St., 380007 Tbilisi, Georgia

A monochromatic polarized neutron set-up for study of neutron precession was constructed at the Institute of Physics of the Academy of Sciences of Georgia in Tbilisi in cooperation with the Institute of Nuclear Research (INR) in Swierek, Poland [1]. The set-up can basically be used for other experiments in nuclear and solid state physics. Description and physical parameters of the instrument including superconducting spin-flipper operation principle, its design and results of experimental check of this flipper are described.

1. Spectrometer

The general lay-out of the instrument is shown in Fig. 1. The polarized neutron beam is obtained by means of the (200) Bragg reflection from a ferromagnetic crystal of $Co_{0.92}Fe_{0.08}$ alloy. The primary neutron beam is formed by a Soller collimator, with 20′ horizontal and 3° vertical divergence. The beam size at the polarizer is 50×30 mm^2.

Two Co–Fe single crystals set in transmission for (200) reflections serve as polarizer and analyser. The crystals have been grown at INR. The original orientation of the single crystal plates was determined by means of back-reflection of X-rays with an accuracy of 30′. The plates have been finally cut along the required crystallographic directions with a precision of about 2′. The method applied was first invented by Beiel et al [2]. A plate with dimensions of $3 \times 34 \times 34$ mm^3 was selected for the monochromator-polarizer from several plates available. Two other Co–Fe plates with dimensions of $3 \times 35 \times 53$ mm^3 and $0.86 \times 32 \times 42$ mm^3 were selected for polarization analysis. Hereafter we shall refer to the first as the "thick analyser". Similarly, the second plate will be called a "thin analyser". The polarizer and analyser crystals are magnetized along the [110] direction.

A radio-frequency (R–F) spin-flipper is placed between the polarizer and analyser crystals. In the first experiments, carried out in order to determine the main parameters of the unit, a long magnetic guide field of 65 Oe covered the whole distance form the flipper to the analyser. The construction of this, as well as all the other magnetic guiding fields used in the experiment consists of two long coils made of a copper wire 0.6 mm in diameter. The core is made of soft-iron ARMCO. Each coil has 450 turns. Except for the use of the core, the overall construction is the same as described in [3]. The use of such a system makes it easy to select an optimal value of the guide field intensity.

After R–F spin-flipper Mezei's flipper is displayed (Fig. 2). The construction of the magnetic system of the flipper is designed from ARMCO alloy. Two right-angle coils, giving horizontal magnetic fields with the opposite direction, are made of a copper wire 0.63 mm in diameter.

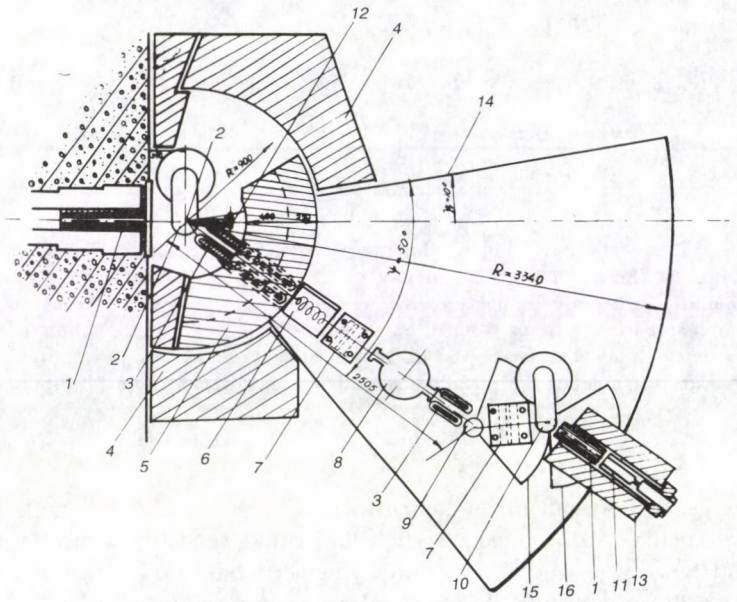

Fig. 1. General lay-out of the instrument. 1 – Soller collimator; 2 – polarizer in an electromagnet; 3 – magnet guiding field; 4 – immovable biological shield; 5 – mobile biological shield; 6 – resonance spin-flipper; 7 – Mezei spin-flipper; 8 – cryostat; 9 – goniometer; 10 – analyser with electromagnet; 11 – neutron detector; 12 – monitor; 13 – detector shield; 14 – base of set-up; 15 – base of sample; 16 – base of detector shield

In the first version whole set-up polarizer table, guiding magnetic fields, spin-flippers and analyser table are designed on the same base. The rotation axis of this base coincides with polarizer rotation axis.

The set-up was developed as follows: a superconducting neutron spin-flipper was constructed and one more axis of sample rotation was added (9, Fig. 1). An analyser, a neutron detector and an additional spin-flipper (if necessary) are placed on the basis of the added axis of sample rotation.

A ^{3}He neutron counter of CHM-18 type (made in USSR) is used to detect the diffracted neutron beam, while a fission chamber RM-70 (made in INR, Poland) is used as a monitor. The location of a preamplifier and an amplifier in single block directly at the outlets of the detectors greatly facilitates the service of this part of the electronic system.

The described polarized neutron set-up is located at the IRT-M type reactor in the Institute of Physics of the Georgian Academy of Sciences in Tbilisi.

2. Basic parameters of the diffractometer

The most important experimental parameters of the polarized neutron set-up are listed in Table I.

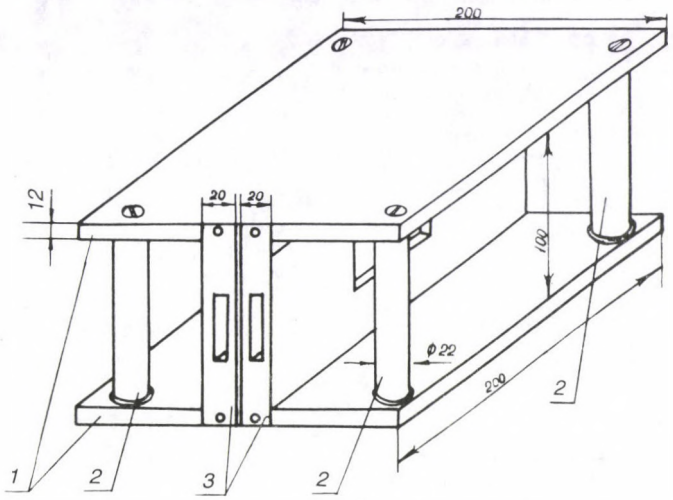

Fig. 2. Mezei spin-flipper. 1 – electromagnet poles; 2 – electromagnet coils; 3 – right-angle coils with the opposite direction of magnetic fields

Estimation of the neutron polarization and flipping efficiency has been carried out by comparing the polarization ratios $R = I_+/I_-$, i.e. the ratio of intensities obtained with the spin-flipper "off" and "on", respectively, measured separately for the two analyser crystals described in the previous Section.

The polarization ratio obtained with the "thick" analyser was $R = 67.5 \pm 1.5$. However, in order to relate this R to the polarization of the monochromatic beam one should first determine the amount ξ of the second-order neutron in the beam.

The estimated value is $\xi = 0.032 \pm 0.001$, where the error reflects the statistical errors of measurements and does not include any systematic errors inherent in the estimation method itself.

Having obtained ξ, one can calculate the amount of second-order neutrons scattered by the analyser when the spin-flipper is switched on. Since in this case the crystal reflectivity is very low, the secondary extinction can presumably be neglected. Following the above speculations, the polarization ratio for the thick analyser after correcting for the second-order scattering is $R = 80.4 \pm 1.8$.

Similar measurements have been carried out for the second, thin analyser. Correcting for the second-order scattering determined from measurements on the thick analyser one gets $R = 146.4 \pm 3.6$. For the experimental data handling one can assume that the beam polarization is $P = 0.993 \pm 0.007$ and the flipping efficiency $k = 0.996 \pm 0.004$, both values characterizing first-order neutrons, of course.

Table I
Basic parameters of the experimental set-up

Neutron wavelength λ	0.111 nm
Fraction of second-order neutrons	0.032 ± 0.001
Neutron polarization:	
1st order neutrons	0.993 ± 0.007
2nd order neutrons	0.506
Flipping efficiency:	
RF spin-flipper	0.996 ± 0.004
Mezei spin-flipper	0.992 ± 0.005
Polarizer	
Co–Fe	$3 \times 34 \times 34$ mm^3
Analysers:	
Co–Fe thick	$3 \times 35 \times 53$ mm^3
Co–Fe thin	$0.86 \times 32 \times 42$ mm^3
Magnetized field on the polarizer	0.35 T
Magnetized field on the analyser	0.195 T
Magnetic guide fields:	
Before the spin-flipper	42 Oe
After the spin-flipper	65 Oe*
Copper wire diameter	0.6 mm
Number of turns in one coil	450
RF spin-flipper:	
Permanent magnetic field	140 Oe
Length of the coil	168 mm
Coil diameter	50 mm
Copper wire diameter	1 mm
Number of turns	158
Resonance frequency	408.9 kHz

*In the experiment with the neutron nuclear precession this field is separated into two fields: before and after the sample placed in the cryostat (see Fig. 1). The intensities of the guide fields in these two sections are then 55 Oe.

3. Superconducting neutron spin-flipper

The superconducting neutron spin-flipper is of a type of spin-flippers, which operate in connection with the fast overturn of guide magnetic field method (Majorana method [4]). In this method it is necessary to create conditions of non-adiabatic neutron flying through the magnetic fields region with the opposite direction

$$K = \frac{\omega_L}{\omega_0} = \frac{\omega_L L}{\pi v} \ll 1,$$

i.e.

$$\omega \ll \omega_0. \tag{1}$$

Here $\omega_L = \gamma_n H$ is the frequency of Larmor precession of the neutron in the neutron in the magnetic field $\mathbf{H}$, $\omega_0 \frac{\pi v}{L}$ is the frequency of the turn of the field vector H in the system of coordinates connected with neutron, L is the length of the region in which the vector H turns by 180°, v is the velocity of the neutron, γ_n is the gyromagnetic ratio for the neutron.

In 1971 one of us (M. Tsulaya) suggested that a superconductor of the first kind should be used for the conservation of the condition in Eq. (1) instead of an aluminium thin foil [6] used before on thin copper wires with a strong direct electric current [7].

The idea of operation of superconducting spin-flipper [5] consists in the following. According to the Meissner effect when a superconductor is cooled in constant magnetic field up to the temperature below critical T_c, the magnetic force lines are ejected from it and the metal becomes the ideal diamagnetic. Consequently, magnetic induction inside the metal in superconducting state is always equal to zero ($B = 0$). The penetration of the external magnetic field into the superconductor is of an exponential character of dumping and is characterized by the depth of penetration, which is $5 \cdot 10^{-6}$ cm for copper at $T = 4.2$ K.

If we place the shield of first kind superconductor on the way of a polarized neutron beam perpendicular to its direction the magnetic field lines will penetrate only to the depth $5 \cdot 10^{-6}$ cm and the condition of nonadiabaticity will be fulfilled (Eq. (1)).

If the conditions of nonadiabaticity are fulfilled, the neutron, passing through the screen, keeps the direction of its spin in the presence of magnetic field of any direction behind the screen which differs from that of the spin of the neutron before the screen.

In case the magnetic field H makes a certain angle with the direction of the spin of the neutron behind the superconducting screen the spin of the neutron will begin to precess with certain frequency in this field, and depending on the value of field H and distance L, it wil turn by a certain angle.

Proceeding from the above said, a superconducting spin-flipper was created [8], the principal chart of which is presented in Fig. 3. It consists of superconduction magnetic dipole 4 and two lead glasses 2 and 3, placed inside the magnetic dipole. The bottoms of the glasses face each other on fixed distance. The field H created by the magnetic dipole, is perpendicular to the spin of the neutron.

The beam of polarized neutrons emerging from Mezei flipper 1 enters the superconducting glass 2 of the superconducting flipper and, keeping the diffraction of the spin in it, leaves it through the bottom with the spin perpendicular to the direction of the magnetic field H existing between the bottoms of superconducting glasses 2 and 3.

Further, on the distance L between bottoms of glasses 2 and 3 the spins of the neutron will precess around direction of field H of dipole with Larmor frequency ω_L and will turn by angle

$$\varphi = \omega_L t = \frac{\omega_L L}{v} = \frac{\gamma_n H L}{v},$$

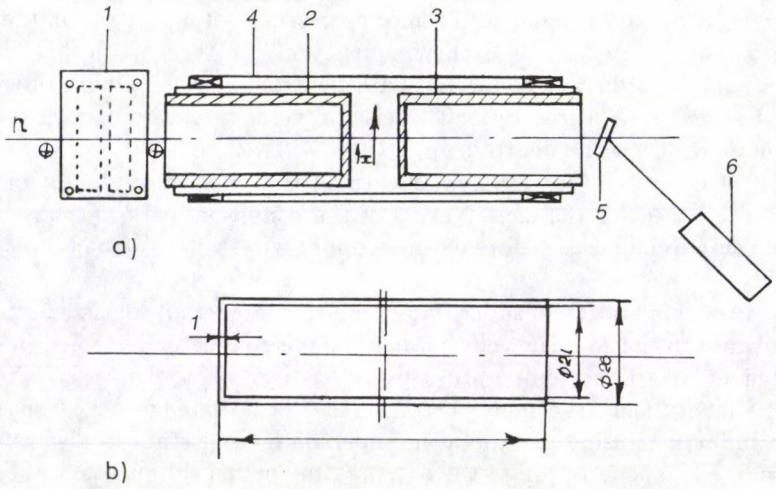

Fig. 3. Schematic diagram of superconducting neutron spin-flipper. a – general schematic diagram, 1 – Mezei flipper, 2,3 – lead glasses, 4 – superconducting magnetic dipole, 5 – neutron spin analyser, 6 – neutron detector, b – lead glass design

where v is the velocity of the neutron, and neutrons with spins turned by angle φ will reach the second glass 3.

If glass 3 is also in the superconducting state, then during the motion inside the glass, the neutron will keep the direction of the spin with which it entered glass 3, and with the same direction it will reach neutron analyser 5. Since analyser 5 lets the neutrons with spins directed along its magnetization and does not let neutrons with opposite spins, the number of neutrons will vary from maximum value to minimum on neutron detector 6 depending on the angle φ according to the law $\frac{1-\cos\varphi}{2}$. The distance between the bottoms of lead glasses 2 and 3 is fixed and the change of value of magnetic field H will cause the change of angle that, in its turn, determines the change of the number of neutrons on detector 6.

4. Experimental unit

The experimental testing and determination of parameters of superconducting spin-flipper were carried out on the unit of polarized neutrons [1] using a helium cryostat with superconducting magnetic dipole.

The helium cryostat (Fig. 4) with replaceable superconducting magnetic systems was designed for neutron investigations. The basic construction material for the cryostat was stainless steel 1X18HIOT. The upper flange 1, the carrying construction on which all units of the cryostat are suspended, nitrogen bath 5, helium bath 9 and vacuum casing 2 are made of the above material. Central steel tube 3 with dimensions 40 × 0.5 mm for pumping of He vapours is used for hanging of helium bath and superconducting magnet. Through the tube an electromagnetic

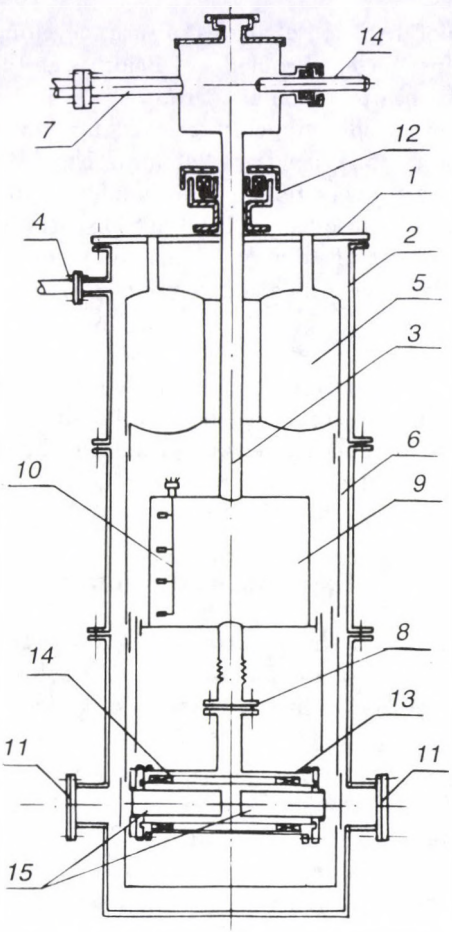

Fig. 4. Helium cryostat. 1 – upper flange, 2 – vacuum casing, 3 – central steel tube for pumping the vapours, 4 – vacuum pumping line, 5 – nitrogen vessel, 6 – thermal screen, 7 – line of pumping the vapours, 8 – indium sealed joint (like tight connection with indium seal), 9 – helium vessel, 10 – helium level gauge, 11 – aluminium flange, 12 – vacuum seal, 13 – spin-flipper casing, 14 – current leaders, 15 – lead glasses

guide system 14 is installed. Thermal shields 6 are manufactured of sheet copper, the thickness of which equals 3 mm. Various superconducting magnetic systems and experimental devices can be easily connected to helium bath 9 through a dismountable joint with indium seal. The level of helium is controlled by carbon resistors of Allen–Bradley type according to the Lavrent'ev–Churakov scheme [9].

In order to minimize the losses of neutrons on their way, the flanges of aluminium alloy AD thinned over the perimeter of the neutron beam to 0.3 mm are placed.

Vacuum Wilson seal 13 with the use of teflon allows to rotate the cryostat with liquid helium and the current leaders of the magnet around its axis within the range

0–360°, and the system of direction of angles of turn, developed by the scientists at the Research Institute for Nuclear Problems of Belorussian State University, allows to adjust the cryostat with a precision 10^{-6} rad.

The magnetic field of spin-flipper is created by superconducting magnetic dipole of a diameter 41 mm and a length of 245 mm. The dipole sections were manufactured of superconducting wire HT-50 of a diameter of 0.3 mm. The magnetic field is measured by a Hall transducer of ПХ3 S0S118A trade mark.

The spin-flipper magnetic field may be created by any magnetic systems (constant magnet, Helmholtz coil) generating a uniform magnetic field between the bottoms of the lead glasses.

Lead glasses (Fig. 3b) were cast.

The penetration of magnetic force lines inside lead glasses from the open end was checked separately. It was established that on the distance of 20 mm (an inner diameter of the glass) the magnetic intensity falls down to zero.

The whole superconducting spin-flipper is placed into the case of stainless steel and is connected to helium bath 9.

5. Experimental results

The beam of polarized thermal neutrons of wavelength $\lambda = 1.11$ Å($v = 3.56 \cdot 10^5$ cm/s) was transmitted through spuperconducting spin-flipper and for various values of the magnetic field between the bottoms of glasses the polarization ratio was determined:

$$R = \frac{N_1}{N_2},$$

where N_1 and N_2 are the numbers of neutrons (with account of the background) at switched on and switched off Mezei flipper, respectively.

The efficiency of the turn over of the spins of superconducting spin-flipper is determined from the expression:

$$K_{eff} = \frac{1 - D}{2},$$

where the value of depolarization is:

$$D = \frac{1 + eR_0}{R_0 - 1} \cdot \frac{R_i - 1}{1 + eR_i}.$$

Here R_0 is the polarization ratio at the beginning of the experiment, when the magnetic field $H = 0$; R_i is the polarization ratio corresponding to the magnetic field H_i; e is the efficiency of the turn over of Mezei flipper. Results of the experiments are presented in Fig. 5, demonstrating the dependence of the efficiency of flipper K_{eff} turn over on the value of the magnetic field between the bottoms of superconducting glasses.

At the fixed distance L between the bottoms of lead glasses and at the velocity of neutrons $v = 3.56 \cdot 10^5$ cm/s the complete turn over of the neutron spin must

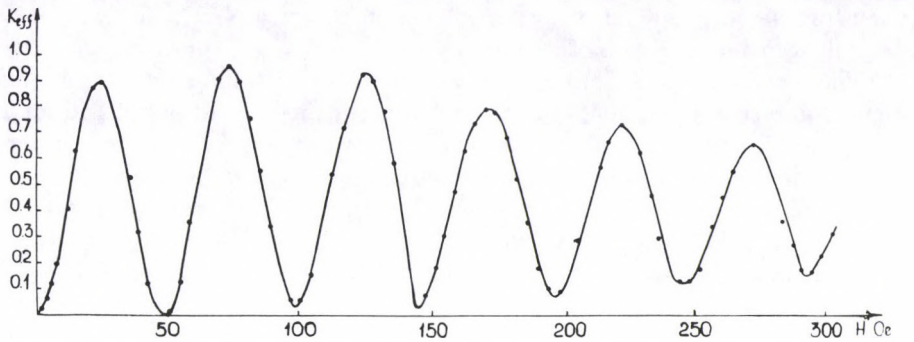

Fig. 5. Dependence of efficiency of inverted flipper K on the magnetic field flux H

occur at the magnetic field intensity $H = n \cdot 60.25$ Oe ($n = 1, 2, 3, \ldots$) As Fig. 5 shows, the periodicity is strictly observed, but the distance between maxima is not 60.25 Oe, but 50 Oe.

We suppose that the reason for that is the following:

1. The exact flux of the magnetic field H is not known. It is connected with:

a) As the Hall transducers were not adjusted strictly perpendicular to the magnetic field flux the magnetic field of superconducting magnetic dipole was not precisely calibrated. Therefore the magnetic field between the bottoms of the lead glasses is greater than the measured one.

b) The transition of lead glasses into superconducting state distorts the magnetic field between the bottoms of glasses, the magnetic force lines are concentrated in the centre, and H increases.

2. Distance L between the glasses in not exactly 20 mm and when cooling it decreases.

It is seen from Fig. 5 that K_{eff} on the first harmonic is less than on the second one. The cause of this phenomenon has not been researched yet. The decrease of the amplitude after the second harmonic can be explained by the not ideal monochromatization of the beam.

The maximum value of efficiency of spin-flipper turn over is:

$$K_{eff} = 0.9643 \pm 0.0033.$$

It is obvious that by means of resonance curve (Fig. 5) we may determine the value of the magnetic field H providing the required direction of the spin of neutrons at the exit from the bottom of glass 3 at fixed value L between the bottoms of superconducting glasses.

By means of the unit proposed the direction of the spin of neutrons at the entrance to the region with arbitrary directions of magnetic fields can be retained. For this purpose the presence of superconducting glass 2 or a plate of superconductor of first kind (Pb, Nb) in the unit described above is enough, placed on the boundary

of two magnetic fields of opposite direction, as it was done in paper [10]. In this case the neutron passing through the spuperconductor, which is in a superconducting state, will keep the direction of its spin.

The superconducting spin-flipper described above is very simple in production and even simpler in operation, especially in experiments carried out at helium temperatures and lower. To produce the superconducting flipper the superconducting material of the first kind with a high value of critical field H_c is required.

The unit proposed provides the nonadiabaticity of the vector of polarization of neutrons at their passage through the magnetic fields of arbitrary direction and also the required direction of the spin of neutrons in the given point of the space.

Acknowledgement

Authors are grateful to Prof. M. I. Podgoretsky for permanent attention to this paper and valuable comments.

References

1. M. I. Tsulaya, M. S. Gabelya, S. I. Djamaspishvili, L. Dobrzyn'ski, K. Blinovski, L. Chelmicki, Nucl. Instr. Meth., *185*, 497, 1981.
2. H. Beill, P. Carlos and R. Genin, J. Phys. Suppl., No. 3, *24*(3), 15A, 1963.
3. K. Blinovski, F. Maniavski, D. Sikorska, S. Vrotislav and L. Dobrzyn'ski, Report INR 931/II/PS, 1968.
4. E. Majorana, Nuovo Cimento, 9, 1932.
5. M. I. Tsulaya, Author's Certificate No 1358610 8.08.1987.
6. A. D. Gulko, C. C. Trostin, A. Hudoklin, Nucl. Instr. Meth., *34*, 88, 1965.
7. K. Abrahams, D. Steinsvoll, P. J. M. Bongarts et al, Rev. Sci. Instr., *33*, 524, 1962.
8. M. I. Tsulaya, M. S. Gabelya, S. I. Djamaspishvili, Author's Certificate No 1519385, 28.01.1988.
9. V. N. Lavrent'ev, V. V. Churakov, PTE, *5*, 196, 1984.
10. N. S. Sotya Murthy, L. Madhav Rao, Pramana, *22*(3,4), 313, 1984.

Acta Physica Hungarica 75 (1–4), p. 397 (1994)

BOOK REVIEW

GEORGE MARX: *The Voice of the Martians*
Roland Eötvös Physical Society, Budapest, 1994

It is a fact of history that the great figures of human culture are not distributed evenly in space and time. In the twentieth century, Hungarians played an outstanding role in physics, especially in nuclear physics. As Fritz Houtermans wrote: "The galaxy of scientific minds which worked on the liberation of nuclear power, were really visitors from Mars. They found it difficult to speak English without an alien accent, which would give them away, and therefore they chose to pretend to be Hungarians, whose inability to speak any language but Hungarian without a foreign accent is well known." This myth is proudly recalled by Edward Teller in his Epilogue written to the book.

The first part of the book outlines the history of the chain reaction from the thirties, focusing upon the contributions of the Martian Hungarians. This Hungarian version of the human quest for nuclear power is based mostly upon interviews. The author, Professor Marx of the Roland Eötvös University in Budapest, knew most of these men personally, visited, invited and interviewed them. He journeyed to Chicago and Los Alamos, to Hiroshima and Nagasaki, to Chernobyl and Paks.

Tourist brochures advertise Hungary as a country of Tokaj wine, red hot paprika, gypsy music, czardas dancing. It is less acknowledged that the coach and the match, the ball-point pen and Rubik's cube, alternating current technology and the transformer, tungsten filaments and krypton filling in light bulbs, radioactive tracing and nuclear reactor, electronically programmable computers and the BASIC language, among others, emerged from brains born and schooled in Hungary. The author discussing the myth of the Martians, gives the profiles of ten Hungarians having landed in the United States in the 20th century (George de Hevesy, Theodore von Kármán, Leo Szilard, Eugene P. Wigner, Edward Teller, John von Neumann, John G. Kemeny, Cornelius Lanczos, Zoltan Bay, Albert Szent-Gyorgyi). In the third part of the book George Marx examines the role that the Hungarian high school – the gymnasium — played in the career of world famous Hungarian scientists. The last chapter is an introduction of the Eötvös Physical Society and a short history of Hungarian physics research from the Middle Ages up to the present.

The book can be ordered at the Roland Eötvös Physical Society, telefax: 36-1-2018682.

L. Jéki

Manuscript received by Akadémiai Kiadó:
25 July 1994
Manuscript received by TYPOTEX Ltd for TEX typesetting:
22 August 1994
Date of publication: 20 February 1995
PRINTED IN HUNGARY
Akadémiai Kiadó és Nyomda Vállalat
Budapest

AN OLD NEW JOURNAL

The old Acta Physica Hungarica is transformed into a new topical journal having the name:

HEAVY ION PHYSICS

Among the main areas to be covered one may find:

Nucleus—nucleus reactions,
Ion—atom collisions,
Hadronic matter under extreme conditions,
Quark physics,
Heavy ion induced fusion, etc.

Papers—both experimental and theoretical—are invited by the Editorial Board formed by:

István Kovács
Valentin Telegdi
István Lovas
Gordon Baym
Andrzej Białas
Jakob Bondorf
Jean-Pierre Coffin
Judah Eisenberg
Mark Gorenstein
Walter Greiner
Hans Gutbrod
Miklos Gyulassy
Ole Hansen
Ulrich Heinz
Jörg Hüfner
Nicholas Kürti
Edward Teller
Nikola Cindro
Yuri Ivanov
László Jenkovszky
Keijo Kajantie
Joseph Kapusta
Joachim Maruhn
Larry McLerran
Igor Mishustin
Ulrich Mosel
Berndt Müller
Shoji Nagamiya
Judit Németh
Imre Tarján
Eugene Wigner
László Csernai
Wolfgang Nörenberg
Yuri Oganessian
János Polonyi
Jørgen Randrup
Renato Ricci
Vesa Ruuskanen
Werner Scheid
Dan Strottman
Domenico Vinciguerra
Hannspeter Winter
József Zimányi
Valeriu Zoran

The subscription price is 96 US $ per volume. (Four issues per volume.)

The address of the Editorial Office:

István Lovas (lovas@heavy-ion.atomki.hu)
Department of Theoretical Physics, Kossuth Lajos University
H–4026 Debrecen, Bem tér 18/C, Hungary

Akadémiai Kiadó, Budapest

AKADÉMIAI KIADÓ

Publishing House of the Hungarian Academy of Sciences
H–1117 Budapest, Prielle Kornélia u. 19–35, Hungary

Order form

for HEAVY ION PHYSICS
(Subscription price USD 96/vol.)

Please send this order form to your bookseller, a subscription agency or directly to AKADÉMIAI KIADÓ, P.O. Box 245, H–1519 Budapest, Hungary (Journals Export Department).

❑ Please enter my/our subscription
❑ Please enter my/our standing order
❑ Please send me/us a specimen copy of the first issue

Name: .....
.....
Address: .....
.....
(Ship to address if different from the above: .....
.....)

Method of payment:

❑ Please send pro-forma invoice
❑ Cheque enclosed USD_____ (Airmail delivery is available at an extra charge: USD 20)
❑ Charge to my ❑ VISA ❑ American Express

Please print:

Name as it appears on credit card, as applicable _____
Credit card number _____
Expiry date _____
Address _____
City/State/Country/Postal code _____

Date and Signature _____

NOTES TO CONTRIBUTORS

I. PAPERS will be considered for publication in Acta Physica Hungarica only if they have not previously been published or submitted for publication elsewhere. They may be written in English, French, German or Russian.

Papers should be submitted to

Prof. I. Lovas, Editor
KFKI Central Research Institute for Physics,
H–1525 Budapest, Konkoly Thege u. 29.
Fax: (36–1)–1–696 567
E-mail: LOVAS @ RMKI.KFKI. HU

Papers may be either articles with abstracts or short communications. Both should be as concise as possible, articles in general not exceeding 25 typed pages, short communications 8 typed pages.

II. MANUSCRIPTS

1. Papers should be submitted in three copies.
2. The text of papers must be of high stylistic standard, requiring minor corrections only.
3. Manuscripts should be typed in double spacing on good quality paper, with generous margins.
4. The name of the author(s) and of the institutes where the work was carried out should appear on the first page of the manuscript.
5. Particular care should be taken with mathematical expressions. The following should be clearly distinguished, e.g. by underlining in different colours: special founts (italics, script, bold type, Greek, Gothic, etc.); capital and small letters; subscripts and superscripts, e.g. x^2, x_3; small *l* and 1; zero and capital capital O; in expressions written by hand: *e* and *l*, *n* and *u*, ν and v, etc.

A List of Symbols on a separate sheet should be attached to each paper.

6. References should be numbered serially and listed at the end of the paper in the following form: J. Ise and W. D. Fretter, Phys. Rev., *76*, 933, 1949.

For books, please give the initials and family name of the author(s), title, name of publisher, place and year of publication, e.g.: J. C. Slater, Quantum Theory of Atomic Structures, I. McGraw-Hill Book Company, Inc., New York, 1960.

References should be given in the text in the following forms: Heisenberg [5] or [5].

7. Captions to illustrations should be listed on a separate sheet, not inserted in the text.
8. In papers submitted to Acta Physica all measures should be expressed in SI units.

III. ILLUSTRATIONS AND TABLES

1. Each paper should be accompanied by three sets of illustrations, one of which must be ready for the blockmaker. The other sets attached to the copies of the manuscript may be rough drawings in pencil or photocopies.
2. Illustrations must not be inserted in the text.
3. All illustrations should be identified in blue pencil by the author's name, abbreviated title of the paper and figure number.
4. Tables should be typed on separate pages and have captions describing their content. Clear wording of column heads is advisable. Tables should be numbered in Roman numerals (I, II, III, etc.).

IV. RETURN OF MATERIAL

Owing to high postage costs, the Editorial Office cannot undertake to return *all* material not accepted for any reason for publication. Of papers to be revised (for not being in conformity with the above Notes or other reasons) only *one* copy will be returned. Material rejected for lack of space or on account of the Referees' opinion will not be returned to authors outside Europe.